UNIVERSITY OF LIVERPOOL

SCHOOL OF ENGINEERING

Structural Behaviour of Ultra High Performance Fibre Reinforced Concrete Slabs

Thesis submitted in accordance with the requirements of the University of Liverpool for the degree of Doctor in Philosophy in Civil and Structural Engineering

Goran Hassan Mahmud

December 2015

ABSTRACT

This study presents an experimental and numerical contribution to the understanding of the structural behaviour of slabs and beams made of ultra-high performance fibre-reinforced concrete (UHPFRC).

One of the main factors affecting the use of UHPFRC in major construction projects is not having an accepted design method due to the lack of understanding of the structural behaviour of this material, especially for slabs. Therefore, a major part of this thesis focuses on the static flexural behaviour of slabs. A novel experimental technique is developed and employed within an extensive series of experiments to better understand the structural behaviour of UHPFRC. Tests are conducted on one-way and two-way slabs with both fully fixed (FF) and simply supported (SS) boundary conditions; these are of interest in structural applications such as bridge decks and the floors of buildings. Details of tests conducted on 660 mm square slabs with thicknesses of 25, 35, 45 and 60 mm are presented. The effect of geometries on steel fibre distribution in the UHPFRC specimens was investigated using physical fibre counting at the location of the cracks. It was found that the fibre distribution and orientation changes as the specimen size changes. Moreover, the number of fibres that bridged between the two cracked faces reduced as the specimen thickness increased.

A numerical model using advanced finite element modelling techniques in ABAQUS is also presented. A nonlinear concrete damage plasticity (CDP) model is used for the simulation and it was found to agree well with the experimental results in terms of load-displacement behaviour of statically indeterminate UHPFRC slabs. In addition, the model was also found to accurately capture the peak-load carrying capacity of the slab specimens. Parametric studies were carried out for slabs with thicknesses up to 120 mm. The experimental results confirmed the reliability and accuracy of the FE modelling. The numerical model was further validated by the uniaxial tensile and compressive data and it was found that the model accurately reproduced the material properties behaviour.

The thesis also includes an investigation of size effect on the structural strength of UHPFRC elements. This concerns the static flexural behaviour of similar notched

UHPFRC beams with various depths under a three-point bending test and the prediction of load-crack mouth opening displacement (CMOD) behaviour. Nonlinear finite element simulations using the CDP model were also conducted and it was found the model can predict full load-CMOD curves, peak-load and crack propagation processes with good agreement with experimental data. Furthermore, a parametric study considering larger sizes of specimens up to a depth of 300 mm was carried out and it was found that the size effect on the beam's nominal strength is negligible due to the relatively high ductility of UHPFRC compared to other types of concrete.

ACKNOWLEDGEMENTS

This PhD study was financially supported by the UK Engineering and Physical Science Research Council (EPSRC) through a DTA studentship.

I am very grateful to my supervisors; Dr Graham K Schleyer and Dr Steve W Jones at the University of Liverpool.

Dr Graham K Schleyer and Dr Steve W Jones have provided help, guidance, encouragement and supervision in delivery of this research project. Their knowledge, experience and expertise have made a significant contribution to all aspects of this research, and I am extremely grateful for that.

I am also grateful for the help and guidance of my previous supervisor Dr Zhenjun Yang now at Coventry University.

I would like to extend my thanks to all my friends and the staff of the University of Liverpool.

And last but not the least, I would like to thank my family, for their support, love and encouragement at all time and who always believed in my success.

PUBLICATIONS

- **MAHMUD, G. H., YANG, Z. & HASSAN, A. M. T.** 2013. Experimental and numerical studies of size effects of Ultra High Performance Steel Fibre Reinforced Concrete (UHPFRC) beams. *Construction and Building Materials,* 48**,** 1027-1034.

- **HASSAN, A. M. T., JONES, S. W. & MAHMUD, G. H.** 2012. Experimental test methods to determine the uniaxial tensile and compressive behaviour of ultra high performance fibre reinforced concrete (UHPFRC). *Construction and Building Materials,* 37**,** 874-882.

- **HASSAN, A. M. T., MAHMUD, G. H., JONES, S. W. & WHITFORD, C**. 2015. A new test method for investigating punching shear strength in Ultra High Performance Fibre Reinforced Concrete (UHPFRC) Slabs. *Composite Structures*, 131, 832-841.

- **MAHMUD, G. H., YANG, Z. & HASSAN, A.** Modelling UHPSFRC Beams using Concrete Damage Plasticity Model. Proceedings of the 20th UK National Conference of the Association for Computational Mechanics in Engineering, 2012. The University Of Manchester, 47-50.

The first paper discusses the investigation of size effect of UHPFRC members. This paper was based on the work presented in Chapter 3 and Section 7.1 of this thesis. The second and third papers are related to an experimental investigation of UHPFRC material properties and punching shear behaviour. The author's contribution involved the preparation of the specimens, conducting the experimental work and interpreting the results. Two more papers, one on one-way slabs and the other on two–way slabs will be submitted.

LIST OF SYMBOLS

Symbol	***Units***	***Description***
a	mm	side length of cubic load
B	mm	constant, can be found from the experiment
b	mm	span length of slab, beam width
C_{TL}	mm	total length of cracks
c	mm	distance from the support to the slab edge
d	mm	characteristic size (height or length), beam depth
d_c		compressive damage
d_f	mm	cross sectional diameter of fibre
d_n	mm	notch depth
d_0		constant, as found from the experiment
d_t		tensile damage
E	GPa	damaged elastic modulus
E_i		measured increase in number of fibres
E_0	GPa	initial elastic modulus
E_m		measured number of fibres
$E_{d,r}$	GPa	dynamic elastic modulus
$E_{d,u}$	GPa	dynamic modulus
F	kN	external load acting on slab and beam
F_b	kN	Experimental beam peak load
F_n	kN	beam numerical ultimate load
F_s	kN	slab ultimate load
F_{cr}	kN	cracking load
F_{ns}	kN	slab numerical ultimate load
f_c	MPa	compressive strength
f_f	MPa	beam nominal flexural strength
f_{st}	MPa	slab effective flexural strength
f_t	MPa	tensile strength
f_{ctf}	MPa	effective flexural strength
G	MPa	shear modulus

h	mm	height of specimen
L	mm	overall specimen length
l	mm	distance between two support
l_f	mm	length of fibre
M_{ult}	kNm/m	ultimate moment
m	kNm/m	moment
m_{cr}	kNm/m	cracking moment
N		Number of fibre
n	Hz	frequency in the longitudinal mode of vibration
S	MPa	stress in slab
S_{cr}	MPa	cracking stress
s	mm	yield line length
t	mm	slab thickness
u	mm	pull-out width
$V_{p,s}$	m/s	compression wave velocity
W_A	kg	weight of specimen in air
W_W	kg	weight of specimen in water
w	mm	slab centre deflection
w_{ns}	mm	numerical slab centre displacement at ultimate load
w_s	mm	experimental slab centre displacement at ultimate load
z	mm	compression depth after the crack
α		moment capacity function factor
ε		strain
ε_c		total compressive strain
ε_t		total tensile strain
ε^{el}		total elastic strain
$\tilde{\varepsilon_c}^{in}$		inelastic strain
$\tilde{\varepsilon_t}^{ck}$		cracking strain
$\varepsilon_{0c}{}^{el}$		compressive elastic strain
$\varepsilon_{0t}{}^{el}$		tensile elastic strain
ε^{max}		maximum cracking strain
ζ		compression zone parameter
θ		hinge rotation of the corresponding segment

v		Poisson's ratio
ξ		cracking parameter
ρ	kg/m^3	concrete density
ρ_f		volumetric reinforcement ratio
ρ^{close}		retention factor
σ	MPa	stress
σ_c	MPa	compressive stress
σ_N	MPa	nominal strength at peak load
σ_0	MPa	initial stress
σ_s	MPa	splitting tensile strength
σ_t	MPa	tensile stress
τ_b	MPa	bond shear stress

LIST OF ABBREVIATIONS

ACI	American Concrete Institute
CARDIFRC	High Performance Fibre-Reinforced Cementitious Composite
CDP	Concrete Damage Plasticity
CMOD	Crack Mouth Opening Displacement
COD	Crack Opening Displacement
CPS4R	Reduced Integrated 4-node Plane Stress Element
CSC	Concrete Smeared Cracking
C3D8R	Reduced Integration 8-noded Element
DSP	Dense Silica Particles
ECC	Engineered Cementitious Composites
FE	Finite Element
FF	Fully Fixed
SIFCON	Slurry Infiltrated Fibre Concrete
FPZ	Fracture Process Zone
FRC	Fibre Reinforced Concrete
GGBS	Ground Granulated Blast Furnace Slag
HPFRCC	High Performance Steel Fibre Reinforced Composite
HSC	High Strength Concrete
LEFM	Linear Elastic Fracture Mechanics
LVDT	Linear Variable Displacement Transducers
MDF	Macro-defect Free
NLFM	Nonlinear Fracture Mechanics
OC	Ordinary Concrete
PS	Plastic Strain
PVA	Polyvinyl Alcohol
RC	Reinforced Concrete
RPC	Reactive Powder Concrete
S4R	Reduced Integration 4-noded Stress Element
SF	Silica Fume
SFRC	Steel Fibre Reinforced Concrete

SIMCON	Slurry Infiltrated Mat Concrete
SS	Simply Supported
UHPFRC	Ultra High Performance Fibre Reinforced Concrete
YL	Yield Line
SD	Standard Deviation
SE	Standard Error

LIST OF TABLES

Tables **Page no.**

LIST OF FIGURES

Figures **Page no.**

TABLE OF CONTENTS

CHAPTER 1

INTRODUCTION

This study investigates the structural behaviour of Ultra High Performance Fibre Reinforced Concrete (UHPFRC) for application of highway bridges and buildings. To introduce a new material in construction, it is essential to understand the structural behaviour of that material. Therefore, the aim of this study is to improve the understanding of the behaviour of slab made of this concrete when subjected to static loading.

In ordinary concrete (OC), understanding slab behaviour was one of the most challenging and complicated tasks that faced design engineers. After, intensive research and development, the behaviour of concrete is now well understood. However, throughout history, structures have been built based on strength, durability, economy and aesthetics. Therefore engineers and researchers have been striving to develop new structural designs and materials that can increase the strength, ductility and durability, so that taller, stronger, safer structures can be designed and constructed.

In the field of concrete technology, from the beginning of the 19^{th} Century, engineering designs have exploited developments in material science to provide a better insight into advanced properties of materials. Many investigations and studies have been conducted to explore innovative materials for the construction industry. Thus, many materials have been discovered and studied intensively.

Gathering information from previous studies and the appearance of steel fibre in the market from the early 1960s, allowed material engineers to develop fibre reinforced concrete (FRC). However, adding discrete fibres as reinforcement has been a challenging task due to the availability of various types of fibre in the market. Moreover, selecting the right volume of fibre in the mix has required extensive experimental investigation. This has resulted in the appearance of numerous different types of FRC. Furthermore, all these fibre concretes have a similar behaviour with significant improvement in their mechanical properties compared to OC. Due to the feasibility in construction, only a few types of these fibre concretes have been considered for the replacement of OC (Donatello et al., 2009, Richard and Cheyrezy, 1995, Rao et al., 2010, Zeng et al., 2000, Lepech and Li, 2008, Karihaloo et al., 2002). This is mainly due to the high initial cost and lack of recognised design standards (Li, 2003, Spasojevic, 2008, Hassan, 2013). The high cost of the material is related to the use of high volumes of steel fibre, cement and admixtures in the mix as well as the high sensitivity of this concrete during the mixing procedure (Chanh, 2004, Spasojevic, 2008). In addition, the material is considered to be more suitable in precast applications which requires high energy consumption during the manufacturing process thus increasing the cost. However, studies on cost effectiveness conducted by (Racky, 2004, Hassan, 2013) have shown the potential advantage of using UHPFRC in construction rather than OC. Furthermore, another reason that limited the structural use of UHPFRC is due to the conservative nature of design engineers in the construction industry who are familiar with use of OC and the industry's reluctance to adopt UHPFRC when there is a lack of practical design experience of using this material (Spasojevic, 2008).

During the last two decades, a relatively new type of fibre concrete, Ultra High Performance Steel Fibre Reinforced Concrete (UHPFRC) has appeared on the market with significantly improved mechanical properties. It has number of advantages over conventional concrete such as higher strength, fracture resistance and ductility (Dugat et al., 1996, Habel et al., 2006, Karihaloo, 1999, Richard and Cheyrezy, 1994, Rossi et al., 2005). UHPFRC is characterised by much higher compressive strength compared to the other types of concrete. It exhibits strain softening in tension which distinguishes the material from other FRC materials (Spasojevic, 2008). This is due to the material's capability to sustain significant tensile force in bending, this allows it to be used without normal bar reinforcement. Eliminating the bar reinforcement reduces the use of labour

and increases production speed, and corrosion deterioration often associated with OC, is mostly avoided except for those fibres that may appear on the structure surface. The recent study has found that fibre concrete with high water-cement (w/c) ratios greater than 0.5, fibres within 1 mm cover can be affected by corrosion deterioration (Balouch et al., 2010). However, it is proposed that to prevent surface corrosion to minimum cover of as low as 0.2 mm, the w/c ratio of less 0.5 and smooth impermeable formwork or galvanised steel fibre should be used (Balouch et al., 2010). The mix design used in this study has a w/c of 0.15 which is much smaller than the 0.5 recommended. A smooth and impermeable formwork was also used to cast all the specimens. Therefore, the casting procedure and mix design used in this study will minimise surface corrosion to as low as 0.2 mm depth. This means, only fibres that are embedded in less than 0.2 mm depth are expected to be affected by surface corrosion if this UHPFRC is to be used extensively. This increases the service life of the structure and reduces maintenance costs significantly. In addition, the improvement of tensile and compressive strength allows the size of the UHPFRC members to be minimised and this reduces the overall use of material in construction.

Although many aspects of UHPFRC have been investigated previously, this new concrete has not gained that much popularity in construction. Apart from the cost of the material, this is because of a lack of design guidelines for structural components made from UHPFRC. This seriously limits its widespread acceptance in the construction industry especially in building and highway bridge applications. Lack of understanding of its structural behaviour is one the reasons why UHPFRC does not have robust design guidance and means design engineers usually prefer to focus on more familiar materials. Moreover, existing recommendations only provide modifications to the existing design standards for reinforced and prestressed concrete structures of a particular country such as France and Japan. These recommendations do not provide any specific guidelines about the design of unreinforced or prestressed UHPFRC. In terms of a standard stress-strain relationship for design at the serviceability limit state (SLS) and ultimate limit state (ULS), these recommendations suggest a conventional bilinear relationship with a horizontal yield plateau. Detailed information of the softening part, which is a crucial material property, is not given. Therefore, experimental studies to thoroughly understand its structural behaviour, especially in bending are required so that an appropriate model can be defined that can accurately capture the material's bending resistance.

In the literature, it is shown clearly that the tensile behaviour is characterised by the strain hardening phenomenon which makes UHPFRC differ from other concrete. To fully understand the material behaviour, the tensile strength must be considered in the design, thus the existing models for OC or FRC cannot be applied (Spasojevic, 2008).

Understanding the true boundary conditions of slabs in engineering structures such as bridges and buildings, is difficult and concerns design engineers. In FRC structures, where fibres are randomly mixed in the matrix, this concern is increased. The effect of boundary conditions, which are known to be significant, requires further investigation. Moreover, the response of FRC under point loads is of interest in a variety of applications in both two-way and one-way slabs, such as wheel patch loading on a bridge deck, heavy machinery in a warehouse, laboratory machines in a building, office cabinets and concrete pavements. There are few studies on these types of applications in the literature. In addition, understanding crack development and propagation within FRC is a complex phenomenon. Since fibres are randomly mixed in the matrix, the fibre orientation and distribution can change from one geometry to another (Wille and Parra-Montesinos, 2012, Spasojevic, 2008). Therefore, experimental and analytical studies of different sizes with different boundary conditions under point loading are essential to examine the effect of geometry and support conditions on the structural behaviour of UHPFRC members.

The work presented in this thesis is continuation of a research started in 2008 at the University of Liverpool. Since the material is new in the market, various mix designs of UHPFRC have been investigated and proposed. The research conducted by (Le, 2008) was proposed to design the preliminary mix proportions in term of strength and cost effectiveness. In that study a significant number of different mix designs were investigated by making changes in the mix constituent. Finally, a mix design with a compressive strength ranging 150-170 MPa and tensile strength 9 to 12 MPa was proposed. Building on the Le study, further research was undertaken by (Hassan, 2013). In Hassan's study, the primary focus was given to investigate the material properties using dog bones, 4-point beam bending and cylinder tests. Another part of Hassan's study was to investigate the punching shear resistance of UHPFRC. The current study builds further on Hassan's work and investigates the overall structural behaviour of UHPFRC beams and slabs under static loading. The current study builds on the previous work conducted by Hassan and others.

The mix design used to prepare all the specimens in this study was the same as that proposed by (Le, 2008) and material properties used in the modelling part were also obtained from the experimental work conducted by (Hassan, 2013). In this study, an experimental investigation has also been conducted to improve the mix design as well as to understand material behaviour using three-point beam testing.

1.1 Scope

The study includes two experimental phases and one numerical modelling phase using the ABAQUS finite element (FE) software. The first experimental phase is focussed on determining the size effect behaviour of UHPFRC. The investigation included the testing of 15 notched beams under 3-point bending with 5 different geometries, with the emphasis towards determining the size effect behaviour and reliability of the existing theory of OC to be used for UHPFRC. The testing procedures were conducted according to British Standards (BS). However, slight modifications were made to accurately capture the relevant behaviour of the concrete. The test results of this phase were used in the FE analysis to validate the developed numerical modelling.

In the second phase, one-way and two-way slabs with Fully Fixed (FF) and Simply Supported (SS) boundary conditions with four different geometries were tested. In total, 52 slabs were tested and analysed. The results were used to investigate the structural behaviour of UHPFRC including load-displacement relationship in all stages and failure modes. The results reported provide a detailed understanding of UHPFRC behaviour. In addition, the data was used for the validation of the FE analysis using 3D modelling.

1.2 Objectives of the Thesis

The main aim of this study is to investigate the structural behaviour of UHPFRC slabs under static bending to obtain the complete and reliable load-displacement response and failure modes. This knowledge should allow a better understanding of this material in the structural design of bridges and buildings. Furthermore, as the performance of UHPFRC is known deviate from that of conventional concrete, it is aimed to shed some light on the examination of the size effect phenomenon using three-point bending tests. This study

was built upon previous research conducted at the University of Liverpool (Le, 2008). The specific objectives of this study are as follow:

i. Measure the nominal strength of UHPFRC structural members to investigate the size effect behaviour using three-point bending test methods.
ii. To obtain a better understanding of structural behaviour of UHPFRC slabs under static bending tests accounting for the slab boundary conditions and dimensions, using experimental investigation on both one-way and two-way slabs with fully fixed (FF) and simply supported (SS) boundary conditions and
iii. Development of validated 2D and 3D numerical models for both beams and slabs using finite element (FE) analysis, to predict the static loading behaviour.

1.3 Outline of the Thesis

In order to investigate the structural behaviour of UHPFRC in bending a study of size effect was undertaken. This provided an understanding of material behaviour in bending with differing dimensions. Since, the structural behaviour of UHPFRC is still largely unknown, it would be interesting to test a real life size structure to capture the exact behaviour of this concrete. However, due to the limitations of laboratory equipment and time, only a limited range of beam sizes and slab thicknesses were examined. The sizes of the specimens were chosen based on the capacity of the test machine available in the laboratory. Moreover, the size of the specimens were chosen based the size proposed by the French recommendation (Association Francaise de Genie Civil–Service d'etudes Techniques des Routes et Autoroutes (AFGC/SETRA). 2002). The high cost of fibre and cementitious material used in the mix were another factor to limit the size of the specimens. In addition, since this research is a continuation of previous work conducted at the University of Liverpool, the same mix constituent has been used. Notwithstanding these limitations, an extensive amount of specimens with different thicknesses and boundary conditions were prepared and tested.

This first chapter gives a brief background to the development of UHPFRC. It also describes the main aim, objectives and contribution to the advancement of knowledge of this study. The remaining chapters in the thesis are structured as follows:

Chapter 2 gives details of existing fibre reinforced concretes (FRC) and reasons for choosing UHPFRC in this research study. Since UHPFRC is a relatively new construction material, a clear understanding was required to undertake this research study. Therefore, in Chapter 2, a thorough literature review on UHPFRC is given covering its first appearance, properties, application and existing design guidelines. It also details relevant experimental work, numerical modelling and theoretical works on the flexural behaviour of UHPFRC beams and slabs. Also included is an introduction on existing size effect and yield line (YL) theory for conventional concrete which are investigated in this study.

Chapter 3 investigates the size effect, which describes the phenomenon that the nominal structural strength decreases as the structural size increases. Since the strength and ductility of UHPFRC is significantly greater than ordinary concrete, the existing size effect theory (Bazant, 1984) may no longer be valid. Random fibre orientation, distribution and matrix bond might also affect the behaviour of this concrete compared with conventional concrete. Therefore, this chapter is concerned with the results from the experimental investigation of similar notched beams with different depths under three-point bending tests.

Chapter 4 details the results of the experimental studies on one-way slabs under bending. A novel experimental technique and the process used to manufacture the one-way slabs are also detailed. To demonstrate the possible failure modes, the results for both SS and FF slab boundary conditions are analysed and discussed. The effect of slab thickness and boundary condition on failure modes, crack propagation and fibre orientation and distribution are discussed. Finally, the effect of slab thickness on the effective flexural strength is discussed.

Chapter 5 details the results of the experimental tests carried out on two-way slabs for both FF and SS boundary conditions. The reason for choosing specific boundary conditions and different specimen thicknesses as well as the effect of slab thickness on fibre orientation and distribution are explained. A better understanding of structural behaviour of UHPFRC, including the complete load-displacement behaviour, crack propagation and failure modes are discussed. Also, the size effect on effective flexural strength is discussed.

The development of full 2D and 3D numerical models using ABAQUS to simulate slabs and beams subjected to the bending loads are presented in Chapter 6. The procedure to create the model including, part creation, step analysis, element types, mesh convergence studies and contact behaviour as well as the implementation of load and boundary conditions are also provided. Details of the numerical models using two different methods and input data extracted from material testing are discussed. The reliability of these numerical models are also discussed.

Chapter 7 presents the results of the FE analysis of the experimental work mentioned in Chapters 3, 4 and 5. The results of the numerical simulation to predict the complete and reliable response of load-displacement, load-crack mouth opening displacement (CMOD) and failure modes are also presented. Due to the high volume of steel fibres in UHPFRC, the cost of experimental studies is relatively high, especially for large-sized structures. Parametric studies using the FE analysis are thus carried out to model beams and slabs with greater depths that are too expensive to be tested. The potential use of numerical models as an alternative to experimentation to capture UHPFRC structural behaviour is discussed.

Chapter 8 concludes the thesis with a summary of the main conclusions from the work undertaken alongside some recommendations for future work.

CHAPTER 2

LITERATURE REVIEW ON FRCs AND UHPFRC

In this chapter the formation of UHPFRC which has been developed from high strength concrete and steel fibre is described. The mechanical properties, design guidelines and mix design as well as the effect of mix constituents of UHPFRC are described in detail. A brief history of the use of fibre in concrete which includes; the discovery, the purpose of using, the types and various shapes of fibre are also discussed in this chapter. Since UHPFRC is just one of the types of concrete that uses steel fibres, it was essential to investigate other types of FRC that are similar to UHPFRC and available in the open literature. Reasons for not choosing other types of FRC and their drawbacks are provided. The purpose of investigating a particular type, namely UHPFRC with respect to other concrete materials is also provided.

Since only limited studies have been conducted on the structural behaviour of FRC, especially UHPFRC, a particular attention is given to experimental, analytical and numerical studies that are available in the literature, especially for slabs. The accuracy, limitation and drawback of these studies are given. Furthermore, determination of the ultimate moment of resistance was considered in this study, therefore, Yield Line (YL) analysis which is one of the design methods is studied. In addition, there is very little in the literature on the effect of size on nominal strength in FRC, thus Section 2.6 discusses

the size effect phenomenon. The existing size effect theory and its limitation on FRC and UHPFRC in particular are discussed.

2.1 Background

Throughout history, concrete has been combined with fibres of other materials to increase its strength. Concrete is a mixture of crushed stone or gravel, sand and water bonded together by hydrated cement or filler that fills the voids between the coarser particles. The role of cement when hydrated is to form a paste which bonds the aggregate particles together. The hydration occurs when the cement's chemical components react with water to form products such as calcium-silicate hydrate, ettringite, iron ettriginite, calcium monosulfoaluminate, calcium hydroxide and magnesium hydroxide. However, calcium-silicate hydrate is the main hydration product for strength development. In the past many different types of fibres have been used and studied in detail. The use of fibres goes back at least 3500 years (Labib and Eden, 2006). In ancient times, straw was used to reinforce sun baked bricks and used in the 57m high hill of Aqar Quf near Baghdad (Newman and Choo, 2003). Later on, masonry mortar was reinforced with horsehair (ACI Committee 544.1R., 2002) and it is believed that the oldest house in the U.S. is a Pueblo house, which was built around 1540. Later, asbestos fibres were used in cement construction products for over a hundred years. However, in the early 1960s, asbestos was found to be a health hazard, and its use is now banned in most countries (Labib and Eden, 2006).

The enhancement of concrete properties such as high strength and ductility has been one of the greatest challenges in the field of civil engineering for many decades. Extensive experimental works have been conducted to obtain a new variety of concrete which can offer such properties. Attempts to improve strength in cement paste goes back to the 1960s and 1970s, by heat curing treatment or using low water cement ratios (Spasojevic, 2008). However, the development of improved concrete properties was restrained by a lack of understanding of the material microstructure.

Attempts to increase the strength and concrete ductility have increased significantly after the development of steel fibres in the 1960s as a replacement for traditional steel bars (Roumaldi and Batson, 1963). Material additives such as superplasticisers and fillers were also introduced to increase the strength of concrete (Mielenz, 1984, Malhotra, 1989).

These admixtures increased the material's durability and ductility as well as the strength (Bache, 1981, Dugat et al., 1996, Neville, 2011). Because these admixtures are extremely fine, their particles fill the gaps between the cement particles, voids around the steel fibres and pack against the sand surface. This minimises the voids within the matrix and enhances the bond between matrix constituents thus stresses can transfer better (Neville, 2011). The improvement in the bond between the matrix and the fibres, increases the fibre pull-out force, thus enhancing the strength (Bache, 1981).The work conducted by (Dugat et al., 1996) reported that the combination of a cementitious admixture such as silica fume (SF) and ground granulated blast furnace slag (GGBS) with superplasticisers reduce the w/c ratio to a value less than 0.15 in fibre concrete and this will reduce the total voids of the matrix hence improving the durability. In an OC paste, hydrated calcium aluminate and/or calcium hydroxide reacts with sulphates that may penetrate the concrete due to contact with ground or rain water, leading to expansion, cracking in the concrete and weakening the bond between the cement paste and the aggregate (Skalny et al., 2002). Having SF in a concrete mix such as UHPFRC reacts with the hydrated calcium aluminate and/or calcium hydroxide and it also results in a higher resistance to sulphate attack (Skalny et al., 2002). SF increases the formation of calcium silicate hydrate (CS-H) gel which is responsible for the high strength and high durability of concrete structures (Ter Maten, 2011). This development led to investigators producing matrices which have high strength with more ductile behaviour.

Since then, extensive research has been carried out to exploit and increase the use of steel fibres in concrete. This was conducted by manufacturing different types and shapes of steel fibres to improve the fibre-matrix bond characteristics. Steel fibres can be classified into five general types based upon their manufacturing process, as follows (ASTM Standard A820., 2011):

1- Cold-drawn wire
2- Cut sheet
3- Melt-extended
4- Mill cut
5- Modified cold-drawn wire

Figure 2.1, shows different types of steel fibres. Rounded fibres typically have a diameter between 0.25mm and 1.0mm. Flat, straight steel fibres have cross-sections with 0.15 to 0.64mm thickness and 0.25 to 1.14mm width. Their tensile strength, length and aspect ratios range from 345 to 1700 MPa, 19 to 60 mm and 30 to 100, respectively. Some of the fibres have been produced with both full length crimps or enlarged ends only, while others have been deformed to increase the mechanical bond (Knapton, 2003).

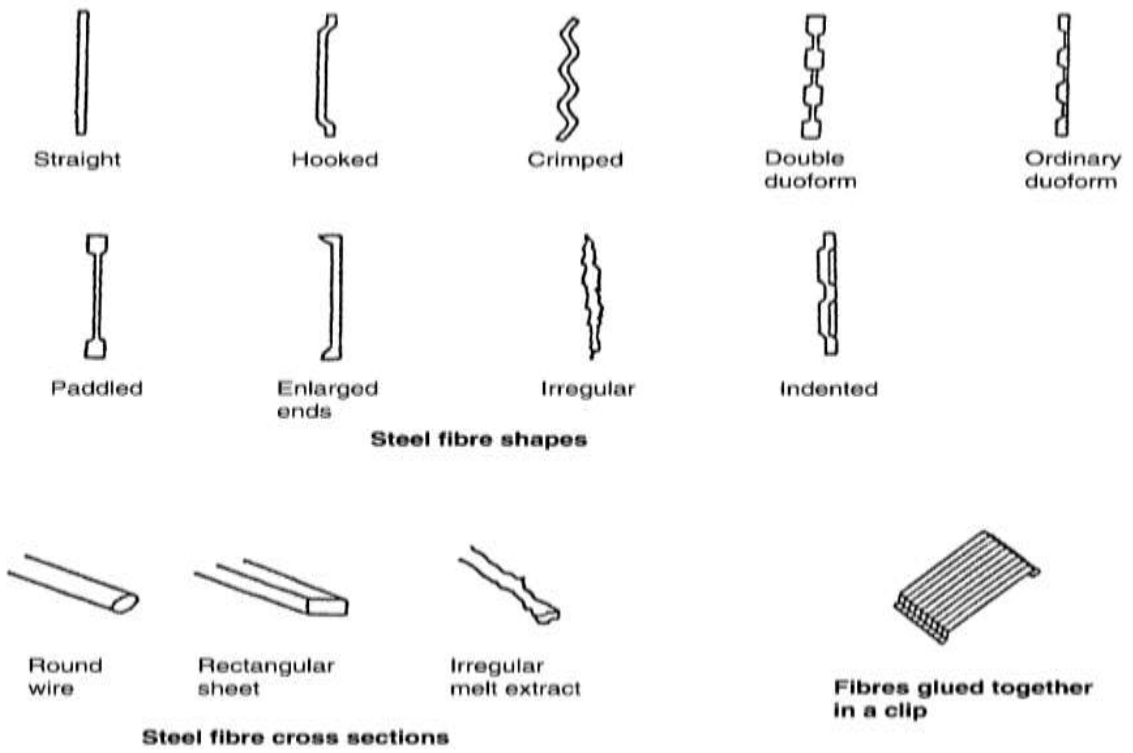

Figure 2.1: Different types of steel fibres, from (Knapton, 2003).

Gathering information from previous studies from the 1960s to 1990s and collaboration between structural engineers and material scientists have resulted in an understanding of fibre reinforced concrete (FRC). Different types of FRC have been developed with different mix designs and fibre percentages, in order to enhance mechanical and durability properties.

2.2 Types of FRCs

In the past few decades, several types of FRC have been developed and studied extensively. However, herein, concern has only been given to that fibre concrete that are acknowledged in the open literature. The reasons for choosing one type over the others in this study are presented. The advantages and drawbacks of these concretes are also presented.

2.2.1 Macro-defect Free

High-strength macro-defect free (MDF) cementitious materials were formulated by using Ordinary Portland Cement (OPC) or calcium aluminate cement and a water soluble polymer with a very low water cement ratio of (0.1-0.2) (Shah and Young, 1990). The most employed polymers are polyvinyl alcohol (polyvinyl acetate) (PVA) and hydroxypropyl methyl cellulose (Lewis, 1993, Popoola et al., 1991). This material has a high flexural strength due to the removal of large voids with a lower overall porosity, and strong chemical bonding between polymer and cement grains (Kendall et al., 1983).

MDF has a tensile strength and an elastic modulus of 150 MPa or more and 40-45 GPa, respectively. The fracture energy was also improved significantly to 300-1000 J/m^2 compared to 20 J/m^2 in normal concrete (Donatello et al., 2009). The selection of an appropriate water soluble polymer is very critical in designing MDF. It has been suggested that both the strength and the water resistance of MDF cementitious will increase with both decreasing degree of hydrolysis of the polymer and with decreasing molecular weight (Santos et al., 1999). However, in the last 30 years since its first appearance, the incorporation of MDF has been limited due to its high sensitivity to moisture or humidity (Drabik et al., 2002, Poon, 1998). In addition, it has a shrinkage problem due to dehydration of the polymer by reaction with unhydrated cement particles. Furthermore, it has been reported that the MDF materials have difficulties with being processed on a commercial scale (Donatello et al., 2009).

2.2.2 Dense Silica Particle (DSP)

Dense silica particles (DSP) are densely packed cementitious materials and this was first conceived by Bache (1981). It was developed by the Danish cement producer, Aalborg

Portland-Cement. These cementitious materials are formed by the hydration of densely packed particles of inorganic binder such as clinker, gypsum or ground granulated blast furnace slag (GGBS) with ultra-fine particles. Even with binder particle sizes ranging between 1and 100μm, voids remains in the materials and they can only be filled with materials with particles size ranging between 0.1 to 0.2 μm such as silica fume (microsilica) (SF) (Odler, 2005). The ultra-fine particles in DSP materials fill the void spaces between the cement particles, making the matrix extremely dense and thus the strength is improved significantly. Due to the very low amount of water used in a DSP mix design, superplasticiser is essential to improve the workability (Bennett, 2002).

DSP has a compressive strength of more than 150 MPa up to 280 MPa. In addition, it has a flexural strength and an elastic modulus of 30-60 MPa and 50-60 GPa, respectively. Furthermore, the mechanical behaviour of DSP is purely linear-elastic with a fracture energy of about 30 J/m^2 (Richard and Cheyrezy, 1995). It also has a high tensile strength of up to 25 MPa (Shannag and Hansen, 2000). Due to the brittleness of the material, steel fibres are required to improve the tensile properties and increase the ductility of this material. However, there have been reports that the material seems to have some drawbacks such as it may explode when it is heated or it may expand if exposed to repeated wetting and drying due to alkali-silicate reaction (Hertz, 1984, Odler, 2005).

2.2.3 Slurry Infiltrated Fibre Concrete (SIFCON)

Slurry infiltrated fibre concrete (SIFCON) is a high performance material containing a relatively high percentage of steel fibres up to 20% by volume and first discovered by Lankard Material Laboratory (Lankard, 1984, Lankard and Newell, 1984).

The matrix in SIFCON has no course aggregates, but high cement content. However, it may contain fine or coarse sand and additives such as fly ash, microsilica and latex emulsion (Dagar, 2012, Naaman, 1992). The preparation of SIFCON is relatively different from other SFRC due to the high volume of steel fibre used in this concrete. Fibre placement in the formwork moulds is the initial step in preparation of SIFCON and this can be accomplished using hand or a fibre dispensing unit. Cement based slurry is then poured onto the fibre networks with light vibration (Lankard and Newell, 1984). The material possesses high ductility and tensile strength with a high strength cementitious

matrix coupled with greater energy absorption characteristics (Farnam et al., 2010). Due to its excellent ductility, SIFCON is used where structures might be subjected to impact and dynamic loading (Rao et al., 2010). In addition, SIFCON has an ultimate flexural and compressive strength of 27 MPa to 69 MPa and 103 MPa to 207 MPa, respectively (Lankard, 1984). Furthermore, due to the high content of steel fibre, crack widths in these materials are greatly reduced and fracture failure modes are improved from a single crack to irregular multicracks in flexure (Yan et al., 2002). However, the high cost involved in the preparation of this material is due to the large volume of discrete steel fibre used in its manufacturing process. Therefore, the use of SIFCON is limited to some special applications such as military shelters, refractory concretes, loading docks, high traffic airport pavements and other specialised concrete pavements (Hackman et al., 1992). In addition, its strength reduces due to its weak resistance to freeze-thawing (Balaguru and Kendzulak, 1987).

2.2.4 Slurry Infiltrated Mat Concrete (SIMCON)

Slurry infiltrated mat concrete (SIMCON) is a high performance steel fibre cementitious material, which is very similar to SIFCON but with a relatively lower fibre volume percentage of 3% to 6% (Hackman et al., 1992). The key differences between the two cementitious materials is that in SIMCON steel fibres are placed in a mat while in SIFCON, as discrete fibres (Hackman et al., 1992).

Coarse aggregate is eliminated in the matrix of this material and cement based slurry is used to infiltrate this concrete. The fibre aspect ratio which is the ratio of fibre length to fibre diameter plays an important role in reducing crack widths. The higher the fibre aspect ratio, the finer the cracks in concrete, and this can be as high as 500 in SIMCON (Hackman et al., 1992). As little as 5.7% steel fibre volume in SIMCON can achieve the same flexural strength as SIFCON with 14%. This is due to the use of longer fibres in the mat in SIMCON compared to the short discrete fibres in SIFCON (Coskun, 2002). The tensile and compressive strength of up to 17 MPa and 81 MPa, respectively, can be achieved depending on the fibre volume percent (Krstulovic-Opara and Malak, 1997b, Krstulovic-Opara and Malak, 1997a). In addition, it has high strength, toughness and excellent crack control as well as an increase in energy absorption and durability with fracture energy of greater than 10 J/m^2 (Krstulovic-Opara et al., 1997). It has an elastic

modulus of 30 GPa (Murakami and Zeng, 1998). However, the applications of this high performance cementitious composite are limited to repair and retrofit of existing structures such as deteriorated highway bridges and pavements (Zeng et al., 2000).

2.2.5 Engineered Cementitious Composites (ECC)

Engineered cementitious composites (ECC) are high performance fibre reinforced cementitious composites with pseudo strain-hardening and significantly improved ductile behaviour due to the microstructure of its constituent composition (Li and Kanda, 1998).

The ECC matrix contains water, cement, sand, fibres and some other chemical admixtures but with no course aggregate. Various fibre types can be used in ECC and fibre type and geometry has a significant effect on its behaviour. In general it is characterised by up to 2% by volume of discrete short random fibres of polyvinyl alcohol (PVA) fibres. However, in order to achieve the optimised behaviour of ECC, consideration must be given to its composition in terms of fibre, cementitious matrix and fibre interface (Li, 1993). It exhibits an ultimate strain capacity of between 3% and 7%, which is 300-600 times greater than normal concrete (Li et al., 2006, Johari et al., 2013). In addition, it has an ultimate tensile strength greater than 5 MPa, flexural strength greater than 15 MPa, fracture toughness greater than 30 kJ/m^2, elastic modulus greater than 20 GPa and compressive strength greater than 70 MPa (Li and Kanda, 1998, Wang and Li, 2005). It also has an ability of self-healing of microcracks when exposed to natural environmental conditions (Herbert and Li, 2013). Due to its high ductility and durability, ECC materials are best suited for structural applications such as seismic-resistance, bridge decks, pavements and other infrastructure exposed to harsh environmental conditions (Lepech and Li, 2008, Li, 2003). Although, a low percentage of fibres are used in ECC, the use of this cementitious composite is limited to specific applications due to the high cost of PVA fibre, which is more expensive compared to steel fibre (Li, 2003).

2.2.6 CARDIFRC

CARDIFRC is a class of high performance short steel fibre reinforced cementitious composite (HPFRCCs) under the trade name of CARDIFRC developed at Cardiff

University. The material is characterised by the use of two different types of fibres and low water/ cement ratio (Benson and Karihaloo, 2005a). Similar to other high performance concretes, CARDIFRC's constituents are cement, microsilica, quartz sand, water, fibres and some other chemical admixtures. Large amounts (of up to 8% volume) of short steel fibre length of 6 mm and 13 mm with 0.16 mm diameter are used. A special mixing procedure that allows uniform fibre distribution is used in the preparation of CARDIFRC materials (Benson et al., 2005). This unique combination offers a compressive and tensile strength greater than 200 MPa and 12 MPa, respectively. It has a flexural tensile strength of up to 30 MPa. In addition, it has a fracture energy and an elastic modulus between 17000 to 20500 J/m^2 and 45 to 56 GPa, respectively (Benson and Karihaloo, 2005b). It is shown that the CARDIFRC material is best suited for retrofitting damaged concrete structures (Karihaloo et al., 2002). However, due to the large volume of steel fibre used in manufacturing this high performance concrete compared to the other UHPFRCs, it may give some drawbacks using CARDIFRC in major construction works.

2.3 Ultra High Performance Fibre Reinforced Concrete (UHPFRC)

Ultra High Performance Fibre Reinforced Concrete (UHPFRC) or Reactive Powder Concrete (RPC) is a high performance fibre reinforced material which exhibits a great enhancement in strength and durability properties compared to conventional reinforcement. UHPFRC is a combination of High Strength Concrete (HSC) and a relatively light amount of steel fibres. It contains most of the constituent materials of ordinary concrete along with some other admixtures such as superplasticiser and GGBS (Graybeal and Hartmann, 2003). It was invented in the early 1990 by two independent French contractors, Bouygues Construction and Eiffage Group (EGI), with the aid of construction materials companies Lafarge Corporation and Sika Corporation (Association Francaise de Genie Civil–Service d'etudes Techniques des Routes et Autoroutes (AFGC/SETRA). 2002).

UHPFRC is characterised by steel fibre content of 2% of diameter 0.15-0.20 mm, and high tensile strength in the range of 859-2000 MPa (Le, 2008). Having fibres significantly

reduces brittleness of this concrete because the fibres transmit stress across the two cracked faces and this makes UHPFRC suitable in construction (Khaloo and Afshari, 2005). It often has a cement content as high as 900-1000 kg/m^3 (Collepardi et al., 1997). Very fine sand or quartz powder size 0.1-0.6 mm (Graybeal, 2006, Richard and Cheyrezy, 1994, Wille et al., 2011b) and silica fume are also essential to achieve a high particle packing density (Wille et al., 2011a). GGBS can be added to increase the compressive strength further, and superplasticisers are also added to improve workability (Habel, 2004). Most importantly, the lack of coarse aggregate significantly improves the homogeneity of the material. This composition leads to very high compressive strength and tensile strength, typically over 150 MPa and 7 MPa, respectively (Graybeal, 2006, Bonneau et al., 1997, De Larrard and Sedran, 1994, Habel et al., 2006, Magureanu et al., 2012, Rossi et al., 2005). However it was reported by Richard and Cheyrezy (1994) that the compressive strength can be as high as 200 to 800 MPa. Recently, Wille et al. (2011) showed a direct tensile strength of up to 15 MPa could be achieved with 1% high strength steel fibres of 3500 MPa. These properties make normal steel bar reinforcements unnecessary in most UHPFRC structural members, especially shallow beams, slabs and walls (Richard and Cheyrezy, 1994, Lei et al., 2012).

UHPFRC also maintains a high resistance to acid attack, very good impact strength, it has an excellent resistance to freeze-thaw cycles and reduces creep and shrinkage when compared to conventional concrete (Toutlemonde and Resplendino, 2011, Li and Yao, 2001, Magureanu et al., 2012, Acker and Behloul, 2004). Furthermore, a recent study conducted by (Forth et al., 2014) reported that in OC, shrinkage causes the neutral axis position to move downward and this affects the prediction of shrinkage curvature using current theoretical models. In that study, a new analytical approach was proposed which takes into account the effect of shrinkage and dismisses the assumption that the neutral axis position is fixed, thus obtaining the true effects of shrinkage. This shows that using steel fibre in UHPFRC will eliminate the effect of shrinkage as steel fibres limit the concrete to shrink (reduction in specimen size) during the hardening stage and improving fatigue resistance (Meda and Plizzari, 2004). It has a high flexural strength of 20 to 40 MPa and fracture energy of around 20000-40000 J/m^2 compared to 3-5 MPa and around 100 J/m^2 for traditional concrete (Schleyer et al., 2011, Toutlemonde and Resplendino, 2011). UHPFRC is a durable material with very low permeability leading to a longer service life than the OC structure. It also requires less maintenance and thus could save

money over the life of the structure. It has been used in several projects around the world especially in the United States, Australia and Canada.

The aim of developing a high performance cementitious material and UHPFRC in particular, is to replace the traditional concrete so that it can be utilised effectively and efficiently in the construction industry and, in particular for bridge construction. However, UHPFRC is a relatively expensive material and its use is limited to parts of structures subjected to severe environmental conditions or where the use of traditional concrete is not possible (Spasojevic, 2008). Therefore, since its first appearance, various test methods and mix designs have been applied and developed to determine the key characteristics of UHPFRC, attempting to reduce its cost. The cost of the material can be between 5 to 10 times more expensive than conventional concrete on a volumetric basis. The high cost is related to the use of a high volume of steel fibre, which is relatively very expensive. The detailed study of UHPFRC cost by (Ter Maten, 2011) reported that the total costs of UHPFRC are for approximately two thirds governed by the addition of steel fibres. The study also reported that determining the cost of UHPFRC is complicated because there are several factors which influence the cost. For example, since the material is considered to be most suitable for precast applications in the current production process, this increases the initial cost of UHPFRC. Because precast applications require high energy consumption because current curing time is 48 hours at high temperatures of 90 ^{O}C during the manufacturing process and this is very expensive. Since the UHPFRC member is usually precast, it needs to be delivered to site and this increases the transport cost considerably. High sensitivity of this concrete during the mixing procedure is another factor which increases the cost of UHPFRC (Spasojevic, 2008). Having a high amount of cement in the mix design as well as additional admixtures is also another factor which makes a significant contribution to the high cost of UHPFRC. However, the overall cost reduces as the volume of UHPFRC required to meet strength criteria will be less than that of conventional concrete (Hassan, 2013, Racky, 2004). The improved material properties of UHPFRC will also ensure lower maintenance costs and a longer design life of the structure compared to conventional concrete. In addition, the current precast production contributes to its high cost significantly but recently Hassan (2013) has shown the cost can be minimised by utilising this material for cast in-situ applications.

Although this new composite concrete has outstanding qualities, researchers have also conducted extensive experimental studies to further enhance its mechanical properties. It is reported by Spasojevic (2008) that the structural behaviour of UHPFRC results from the properties of its constituents: cementitious matrix, fibre type and shape and fibre-matrix bond. In recent decades, several mix designs have been developed and studied rigorously. The primary sources for these enhancements are the volume of steel fibre percent, highly compacted cementitious matrix and mixing procedures.

Each type of FRC has its own draw-backs in terms of its use in major structural applications. In addition, research previously conducted by Le (2008) at the University of Liverpool resulted in the development of an UHPFRC mix design with tensile and compressive strength of greater than 150 MPa and 9 MPa, respectively. It has an elastic modulus of over 45 GPa. The availability of this mix design and material properties was another reason to investigate this type of UHPFRC in this current study. Therefore, this mix design was employed for all the experimental works undertaken in this present study. To show a direct comparison between the FRC types, the mechanical and physical properties are shown in Table 2.1. Alongside studies to develop of enhanced high performance cementitious materials, researchers have also made significant efforts to determine the effect of concrete constituent materials and other factors such as high curing temperature and water cement ratio on the properties of UHPFRC.

Table 2.1: Direct comparison of FRCs mechanical properties.

Properties	MDF	DSP	SIFCON	SIMCON	ECC	CARDIFRC	UHPFRC
Tensile strength	>150 MPa	25 MPa	14 MPa	17 MPa	5 MPa	>12 MPa	15 MPa
Compressive strength	300 MPa	>170 MPa	103-207 MPa	81 MPa	70 MPa	>200 MPa	150-800 MPa
Elastic modulus	40-45 GPa	50-60 GPa	27 GPa	30 GPa	20 GPa	45-56 GPa	>45 GPa
Bending/flexural strength	200 MPa	30-60 MPa	27-69 MPa	19-23 MPa	15 MPa	30 MPa	20-40 MPa
Fracture energy	300-1000 J/m^2	30 J/m^2	30-64 J/m^2	>10 J/m^2	30000 J/m^2	17000-20500 J/m^2	20000-40000 J/m^2

2.3.1 The Effect of Aggregate Size

In ordinary concrete, coarse aggregate provides volume stability to the hardened concrete and reduces shrinkage and cracking by interlocking the cement matrix. In most of the high performance cementitious materials, coarse aggregates are eliminated and fibres provide the functions similar to coarse aggregate in conventional concrete. As the size of the aggregate decreases, the specific surface area of the matrix increases. The use of fine sand creates a dense matrix and less air voids, thus the strength significantly improves as illustrated in Figure 2.2.

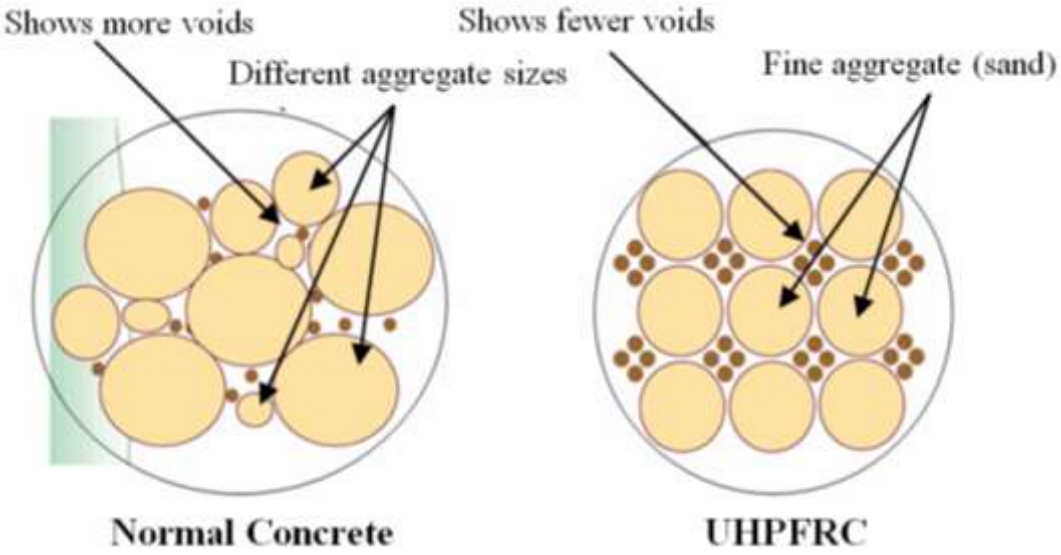

Figure 2.2: Matrix structures of conventional concrete and UHPFRC (Perry, 2003).

In UHPFRC, similar to the other cementitious composites and unlike conventional concrete, it uses only very fine aggregate like silica sand. This fine aggregate sand contains a high proportion of silica, normally more than 95% SiO_2. It is produced from both loosely consolidated sand and by crushing weak cemented sandstones (British Geological Survey, 2004). To avoid loosening cement and other admixtures, fine sand with sizes between from 0.1 to 0.5 mm, are most often encountered in UHPFRC mixes. The pozzolanic activity of UHPFRC using quartz sand was 40% higher than that of the concrete without quartz sand, after 48 hours of heat treatment at 90^{o}C (Zanni et al., 1996). This was one of the main reasons Le (2007) selected silica sand instead of ordinary sand

in his developed UHPFRC mix design, which was employed in the preparation of slab and beam specimens in this study.

2.3.2 The Effect of Cement

In concrete, it is known that the main role of cement when hydrated with water is to form a concrete paste. In UHPFRC, the selection of cement type is very important to ensure that it is compatible with the concrete admixture in the mix design. With the development of the cement industry, different types of cement are now being produced. Cements are grouped into five main types CEM 1, CEM II, CEM III, CEMIV and CEM V (British Standards Institution BS EN 1997-1, 2000). It is reported that cement types CEM I or CEM II 52.5 can be used in the manufacture of UHPFRC (Bonneau et al., 1997, Richard and Cheyrezy, 1994), as well as cement types of CEM I and CEM II 42.5 (Collepardi et al., 1997, Corinaldesi and Moriconi, 2003, Ji et al., 2004).

2.3.3 The Effect of Silica Fume

Silica fume (SF), also known as microsilica, is a by-product of the reduction of high-purity quartz with coal in electric arc furnaces in the production of silicon and ferrosilicon alloys. It consists of very fine vitreous particles approximately 100 times smaller than the average cement particle. Because of the extreme fineness of SF, their particles pack tightly against the surface of the aggregates and fit between the cement particles, thus reducing the size and volume of voids within the matrix. This improves the bond between the cement paste constituents allowing for better stress load transfer (Neville, 2011).

Silica fume is recognised as a highly reactive pozzolanic material and it is effective in enhancing the mechanical properties to a great extent (Malhotra and Carette, 1982). In an ordinary cement paste, calcium hydroxide crystallizes out as a separate and relatively weak phase, and this reacts with penetrated sulphates that may occur through ground water for example, resulting in extensive cracking, expansion, and loss of bond between the cement paste and the aggregate (Skalny et al., 2002). Adding SF in cement paste not only reacts with the surplus of calcium hydroxide and results in a higher resistance to sulphate attack (Skalny et al., 2002), it also improves the transition zone between the bulk

hydrated cement and the aggregate particles in concrete, resulting in a denser mix as shown in Figure 2.3.

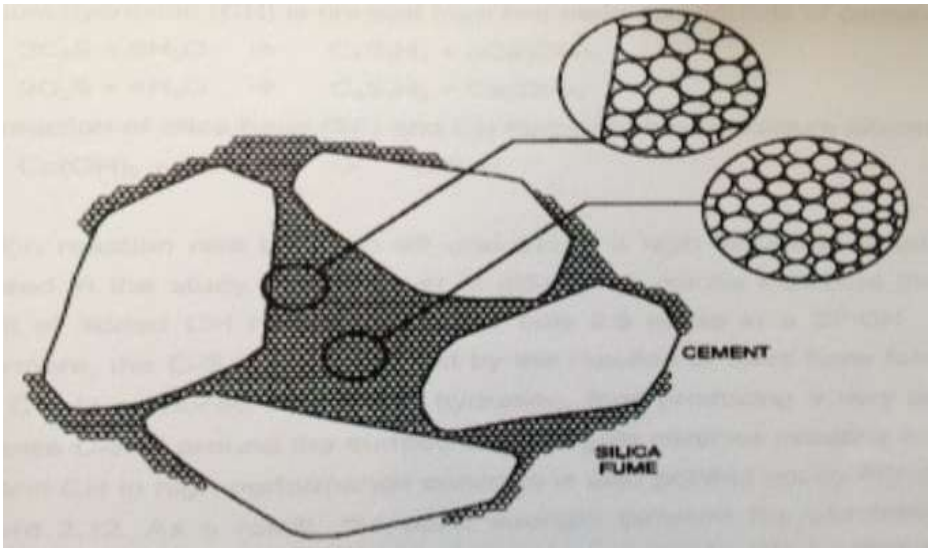

Figure 2.3: Silica fume particles filled the gap of larger cement particles (Bache, 1981).

The American Concrete Institute (ACI) defines SF as a "very fine non-crystalline silica produced in electric arc furnaces as a by-product of production of elemental silicon or alloys containing silicon" and according to (ACI Committee., 1987), the advantages of silica fume in concrete are; improved long-term strength, freeze and thaw resistance, sulphate resistance and preventing alkali-silica reactions.

The SF in combination with superplasticisers in cementitious material enhances the rheological characteristics by the lubrication effect resulting from the perfect spherical shape of the SF particles packing tightly against the surface of the sand and they fit in between the cement particles when they are well deflocculated by the right dosage of superplasticiser, resulting in an increase in the strength of the cement paste (Bache, 1981, Graybeal, 2006). The combination of the two makes the UHPFRC more cohesive and less prone to segregation than the concrete without SF and it also improves the bond between steel fibres and the matrix by increasing the contact area.

In cementitious materials, silica fume protects the randomly distributed steel fibres from chemical attack, which causes corrosion, especially in bridges, parking decks and marine

structures (Siddique and Khan, 2011). Due to the high bond strength, low permeability and improvements in durability, this all makes SF concrete an appropriate repair material, especially in severe environments (Luther, 1990). Silica fume is used in a variety of cementitious composite materials and it is recognised as one of the essential ingredients for all cementitious composite structures, especially in UHPFRC structures.

2.3.4 The Effect of Ground Granulated Blast-furnace Slag (GGBS)

Ground granulated blast furnace slag (GGBS) is manufactured from blast furnace slag, a by-product from the making of iron. This finely ground, off-white powder is insoluble in water. It is normally mixed with cement and water for construction purposes. It consists principally of non-crystalline oxides of aluminium, calcium, silicon and magnesium together with sulphur compounds and small quantities of alkalis. It was discovered in the late 19th century and it has been widely used in the cement manufacturing industry for over 100 years. In the UK, GGBS is supplied as a separate component for concrete. GGBS can be blended with cement or used as a replacement cementitious material. The use of GGBS in concrete improves long-term strength development, enhances durability and reduces the risk of cold joints which is particularly useful in warm weather concreting (Osborne, 1999).

The presence of GGBS in UHPFRC mix design delays the setting time of concrete and the concrete will remain workable longer (Le, 2008). Furthermore, the use of GGBS in the UHPFRC mix and concrete in general has the potential to reduce the environmental impact i.e. CO_2 emissions, caused by the industrial production of cement. Using only 50% GGBS as a cement replacement, the CO_2 will reduce by approximately 40% compared to CEM I as reported by the Concrete Centre, UK. For every tonne of cement, approximately 900 kg of CO_2 emissions are produced compared to GGBS where 0 kg is produced as shown in Figure 2.4. In addition, the use of GGBS also benefits in reducing the depletion of natural resources i.e. for every tonne of Portland cement produced, 1.6 tonnes of limestone/shale are removed from the landscape, while GGBS production involves no quarrying of limestone or clay (David, 2011) .

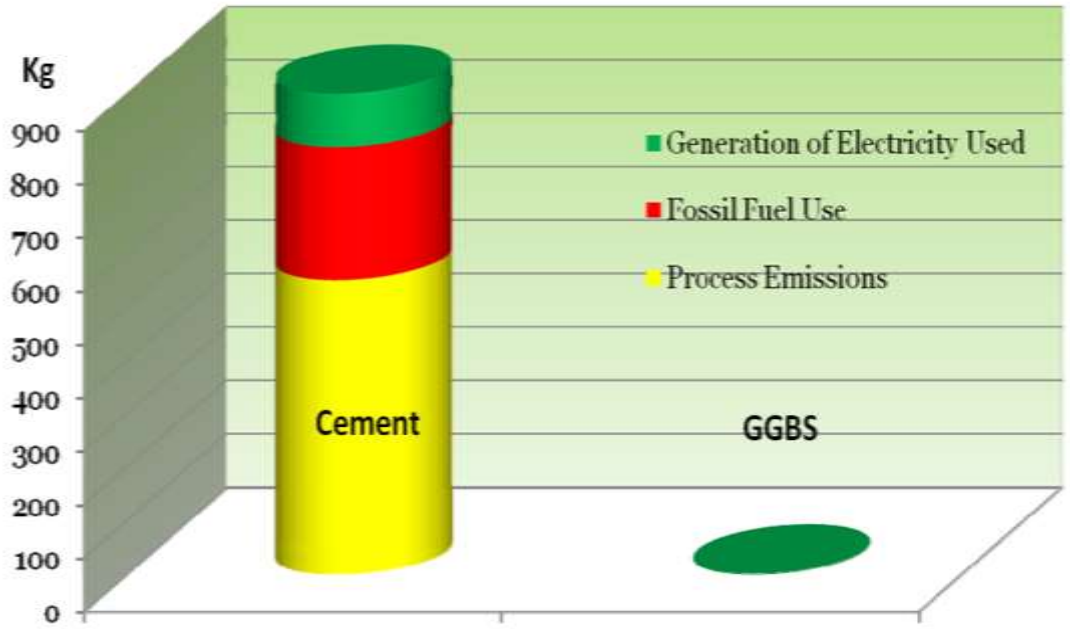

Figure 2.4: CO_2 emission for Portland cement and GGBS production (David, 2011).

GGBS reduces the possibility of thermal cracking in hardened concrete, due to the reduction in the amount of heat released and the delay in the timing of the heat release. It also enhances the resistance to internal chemical attack such as alkali silica reaction and alkali carbonate reaction (Higgins, 2005). It is reported that at standard room temperature the early age concrete containing GGBS cement has a lower strength than concrete made with Portland cement with the same binder content but as the curing period was extended, GGBS concrete strength was higher (Oner and Akyuz, 2007). This was due to the pozzolanic reaction, which is slower as the formation of calcium hydroxide requires more time to react compared to Portland cement. However, Barnett et al. (2006) reported that the early age strength development of GGBS concrete is highly dependent on the temperature and the pozzolanic reaction is more rapid as the curing temperature increases.

2.3.5 The Effect of Superplasticiser

Superplasticiser is a water reducing agent. It is used to reduce the water content of a concrete mixture while maintaining a constant workability. Superplasticiser in cement paste avoids particle aggregation, and improves the flow characteristics in concrete (Le, 2008). Superplasticisers are long and heavy molecules, which alter the attraction forces

between the cement particles by giving them highly negative electrical charges so that the cement particles repel each other, resulting in better dispersing of the cement particles as depicted in Figure 2.5, thus improved workability (Nicolaides, 2005).

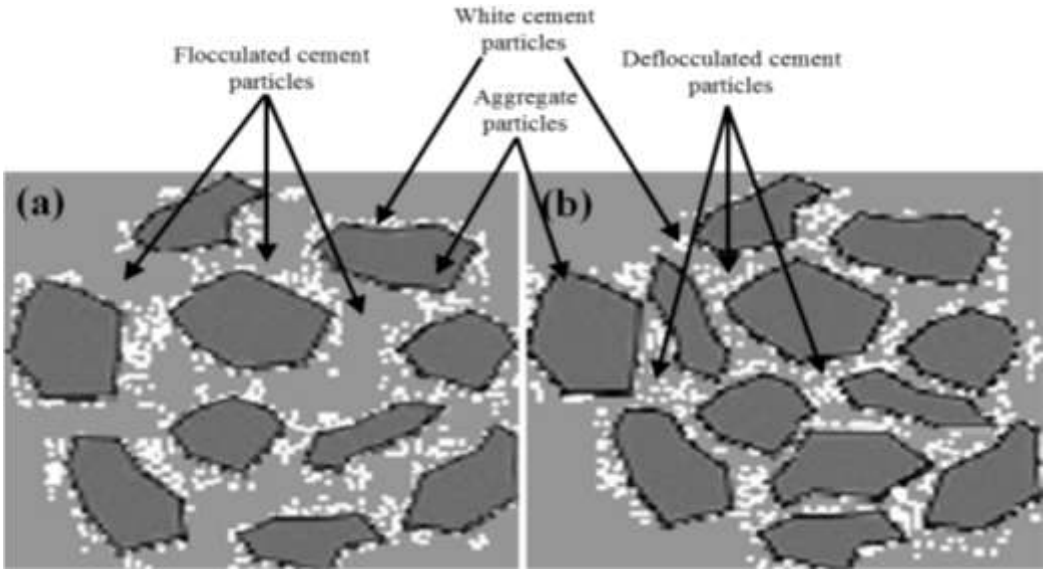

Figure 2.5: Cement paste (a) without superplasticiser (b) with superplasticiser (Nicolaides, 2005).

Since a very low w/c ratio is used in UHPFRC mix designs, workability can be an issue during casting UHPFRC members. In addition, having steel fibres in UHPFRC mix can also reduce workability (Le, 2008). To ensure that the workability of UHPFRC is sufficient, the use of superplasticiser is essential. However, the effect of superplasticiser on cement is influenced by the amount of aluminate (C_3A) content and soluble alkali in cement regardless of the type of the superplasticiser. The amount of C_3A content in cement of at least 8% is required for superplasticisers to work effectively (Sakai et al., 2008).

The combination of superplasticisers with microsilica in the UHPFRC mix results in an increase in the strength of the cement paste. It is also reported that the superplasticiser decreases void size and gives better distribution of the different components in the cement paste (Mehta and Aitcin, 1990, Puertas et al., 2005)

Superplasticisers comprise several water-soluble organic polymer groups, mainly napthanlene based and polycarboxylate superplasticiser (Spiratos et al., 2003). In UHPFRC, carboxylate-based superplasticiser are widely used due to their weaker acid and effective complexant for di and tri-valent metal ions compared to napthanlene groups (Le, 2008). An experimental study showed that the polycarboxylate polymers in both powder and liquid form are more efficient than the napthanlene polymers (Soutsos et al., 2006).

2.3.6 The Effect of Steel Fibres

Fibre has a long history going back to ancient times, when horsehair was first used to reinforce masonry mortar and plaster. The fibre volume in UHPFRC has a great effect on both the fresh and hardened state. Fibres cause a reduction in workability leading to the possible problem of balling in the concrete mix. Therefore, in UHPFRC modifications had to be made to the shape of the steel fibre by making it approximately four to eight times smaller than the fibre used in Steel Fibre Reinforced Concrete (SFRC). However, to overcome the balling problem, coarse aggregates are also eliminated in UHPFRC and only fine sand is used (Hannant, 1978, Marković, 2006).

The effect of steel fibres in cementitious composites (UHPFRC in particular) depends upon the type, shape and geometry of the structural member. Short steel fibres in UHPFRC are to prevent microcrack growth and provide high tensile strength and ductility as illustrated in Figure 2.6 (Barros and Figueiras, 1998, Perry, 2003). Whereas the presence of long fibres in concrete has greater pull-out strength and will bridge wider cracks, thus ductility is significantly improved (Lappa et al., 2006). Recently, Willie and Naaman (2012) reported that the use of hooked-end with smaller diameter and twisted fibres are a better choice for UHPFRC and it can provide higher tensile strength and ductility. A higher fibre aspect ratio (length/diameter) was found to be significant in increasing compressive strength and ductility (Gopalaratnam and Shah, 1986). The longer the fibres, the greater the tensile strength and ductility of the resulting concrete (Nicolaides, 2005). However, it is reported that the most fundamental property of a fibre reinforced concrete is the fibre bridge between the two cracked faces (Nicolaides, 2005). Therefore, fibre volume and geometry have a significant influence on the fibre-bridging action, and thus the tensile strength. As the fibre volume increases, the possibility of fibres

dispersing uniformly increases and this limits the growth of microcracks and delays the macrocrack with a consequent substantial increase in the tensile strength (Balaguru and Shah, 1992). Furthermore, the increase in fibre volume leads to higher fracture toughness in the matrix and a higher peak load (Mobasher et al., 1990). These studies have shown that the higher the number of fibres contributing in the cracked area, the higher the peak load. Moreover, in thinner structures, fibres tend to align to be parallel to the surface and perpendicular to the line of action of the force, and thus the number of fibres contributing to the cracked area is considerably higher. Therefore, the strength is improved greatly in thin elements compared to a thick element with the same fibre volume ratio.

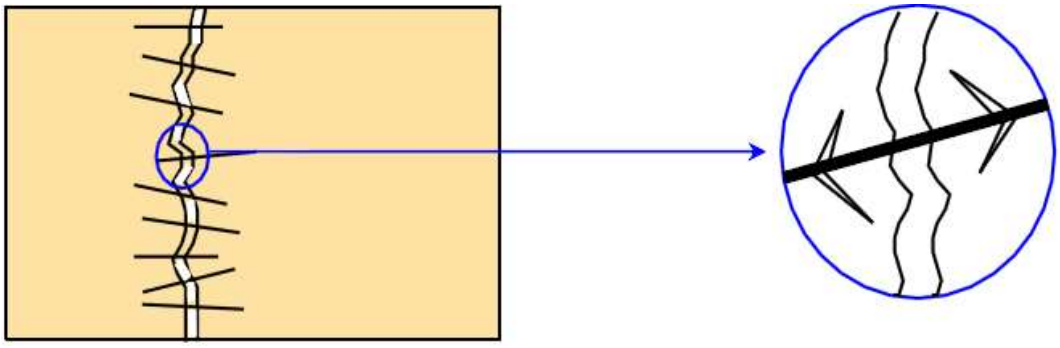

Figure 2.6: Representation of fibre bridging (Perry, 2003).

2.3.7 The Effect Water Cementitious Material Ratio

The required water content of concrete is influenced by a number of factors: aggregate size, shape and texture, slump, air content, cement material type and content, admixtures, and environmental conditions. The use of water reducing admixtures or cementitious admixtures such as GGBS or silica fume will reduce water demand. On the other hand, a decrease in the proportion of coarse aggregate to fine aggregate or increase in temperature will increase water demand (Kosmatka et al., 2002). Water in UHPFRC is one of the most crucial ingredients to form the concrete paste, as it is in conventional concrete. In general, the water content in UHPFRC concrete is much smaller compared to conventional or high strength concrete due to the admixture used in UHPFRC mix design. In addition, in UHPFRC consideration should be taken into account with regards to the quantity of water dosage in superplasticiser and water absorbed by the aggregate. The water quantity in a

UHPFRC mix design should include for both especially the former, where the dosage of the mix is too high (Le, 2008).

2.3.8 The Effect of High Temperature Curing Regime

Temperature affects the concrete strength because of its effect on the rate of hydration, the nature of the concrete structure and the rate of evaporation, resulting in drying out of the concrete. The increased rate of evaporation, associated with elevated temperatures, reduces the amount of water available and thereby retards the rate of hydration and may even cause its complete termination. Hence, in practice, the effect of temperature on strength varies and depends upon the specific conditions considered.

In cementitious materials, high curing temperature accelerates hydration reaction and material hardening at early ages (Barnett et al., 2006). An increase in the curing temperature speeds up the chemical reaction of hydration, resulting in early strength gain. In UHPFRC heat treatment achieves high strength in 7 days rather than in 28 days at room temperature. An early age compressive strength of 225 MPa can be achieved for UHPFRC specimens with a 90ºC curing temperature after 6 days, while a strength of 200 MPa is attainable for the specimens with heat treatment of 50 to 65 ºC (Schachinger et al., 2008). This is because heat treatment at 90 ºC accelerates the hydration process by activating the pozzolanic reaction of silica fume and reducing the curing time of concrete to 7 days. As the strength of concrete depends on the porosity of the cement paste, it is to be expected that the rate of strength growth and concrete early age strength will both increase with a rise of temperature (Aïtcin, 1998). However, Hassan et al. (2012) have recently shown the UHPFRC mix with heat treatment of 90ºC has almost the same strength in 5, 14 and 28 days when the specimens were cured for two days starting 24 hours after casting. This shows that two days heat treatment is enough to accelerate most of the pozzolanic reaction.

2.4 Mechanical Properties of UHPFRC

In order to use these materials in construction, the mechanical properties of the materials must be well established. Therefore, significant experimental investigations on material

mechanical properties are required. The most important mechanical properties in concrete and UHPFRC in particular are tensile strength, compressive strength, elastic modulus and flexural behaviour. In addition, it is also important to establish other mechanical properties such as freeze-thaw resistance, creep and shrinkage.

2.4.1 Tensile Strength

To determine the stress-strain or stress-crack mouth opening displacement (CMOD) relationships, extensive experimental investigations are required. Determining tensile strength is not a straightforward task. This is because it is difficult to design an appropriate test method to obtain pure material properties without the influence of the test method and specimen geometry effecting the results (Spasojevic, 2008). For instance, conducting direct tensile test is inherent to a number of difficulties such as fracture at the glued end of the tensile specimen or load eccentricities are difficult to avoid (Walraven, 2009).

Generally, tensile strength properties of concrete are determined using two methods either directly using dog bone (or splitting) tests and indirectly using flexural tests on prisms. Both methods can be performed on either notched or un-notched specimens. In UHPFRC, there have been numerous studies to determine the tensile strength using both methods, direct tensile tests using dog bone shaped specimens or indirect tests using prisms (Hassan et al., 2012). To date the AFGC French recommendation (2002) which uses dog bone shaped specimens is the most recognised test method for determining tensile strength and the stress-deflection curve is shown in Figure 2.7.

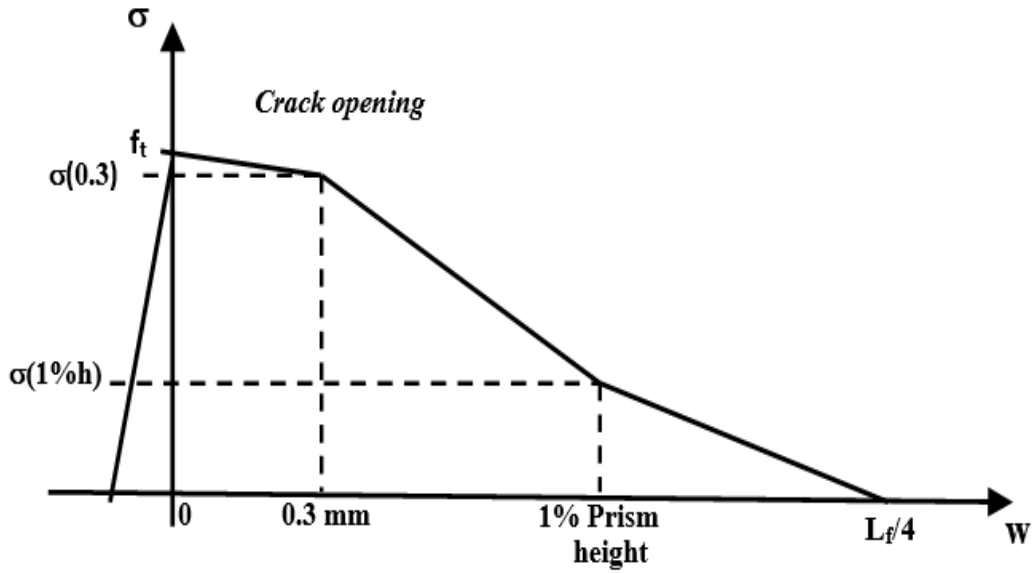

Figure 2.7: Tensile strength relationship from (AFGC/SETRA, 2002).

Figure 2.7 is based on the three-point flexural test on un-notched prisms where f_{tj} is the tensile strength and w is the CMOD. Tensile strength is the stress at the end of the initial linear behaviour of the force-displacement curve and dominates most of the flexural strength as shown in Figure 2.8 which is approximately 85% of the ultimate strength. To simplify the design method, the strain-hardening behaviour is not shown in Figure 2.7. UHPFRC compressive strain capacity is reached at a strain of approximately 0.4% while that of ordinary concrete is only 0.2% (Spasojevic, 2008, Le, 2008). Direct tensile tests for both notched and un-notched specimens are complicated to perform due to the complexity of experimental setup but it can provide more reliable results compared to the flexural test (Mallat and Alliche, 2011). Furthermore, due to the variation of tensile strength from flexural tests, the direct tensile test is the only test than can give the true tensile properties (Hillerborg et al., 1976). However, Hassan et al. (2012) recently showed the true tensile strength of UHPFRC can be obtained using dog-bone shaped specimens under the direct tensile test. Two different sizes were selected, as shown in Figure 2.9, and the result showed that both specimens give a similar result and geometry had no effect on the results. This test data was used to validate the numerical modelling presented later in Chapter 6.

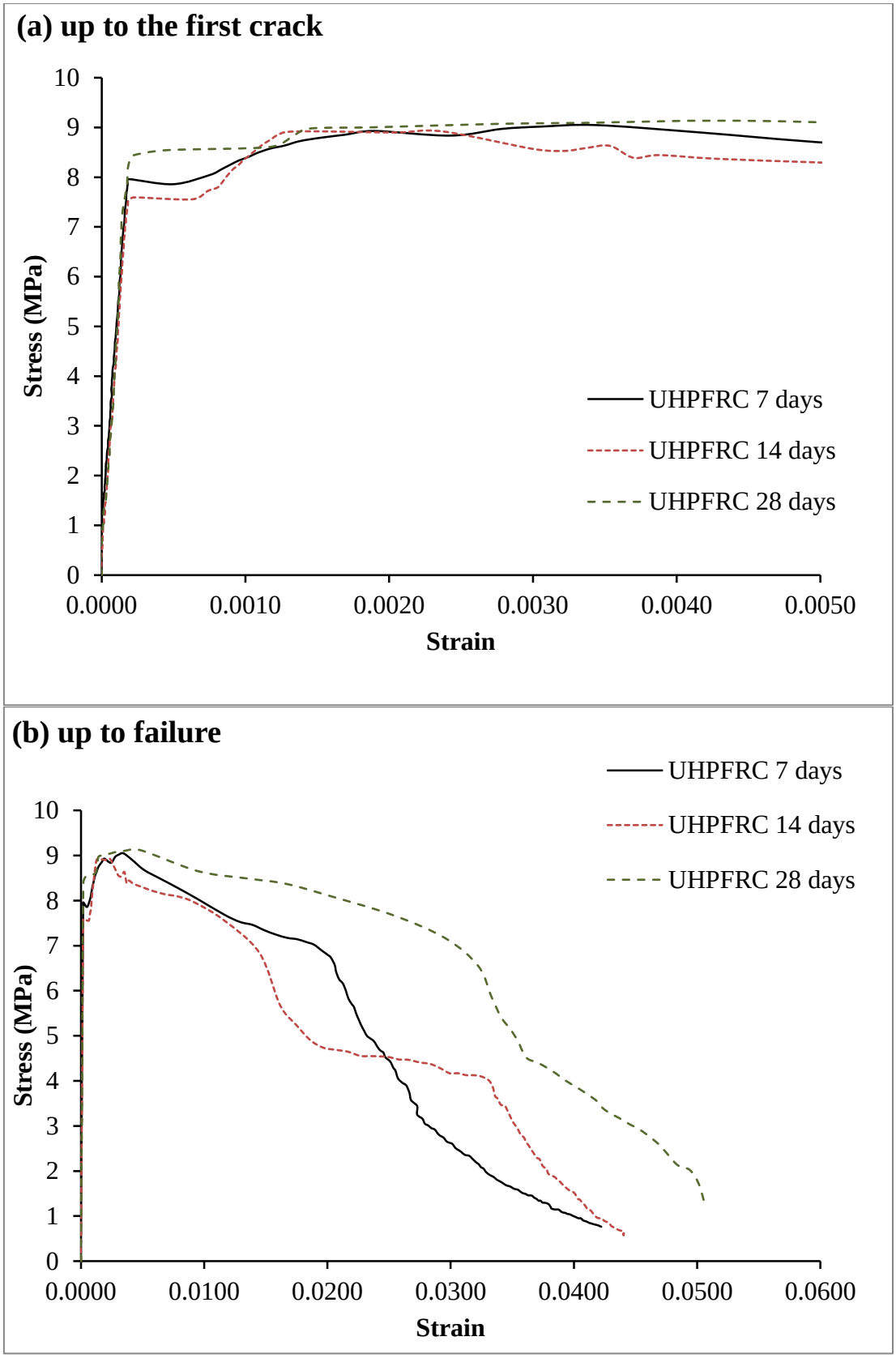

Figure 2.8: Tensile stress-strain curve (Hassan et al., 2012).

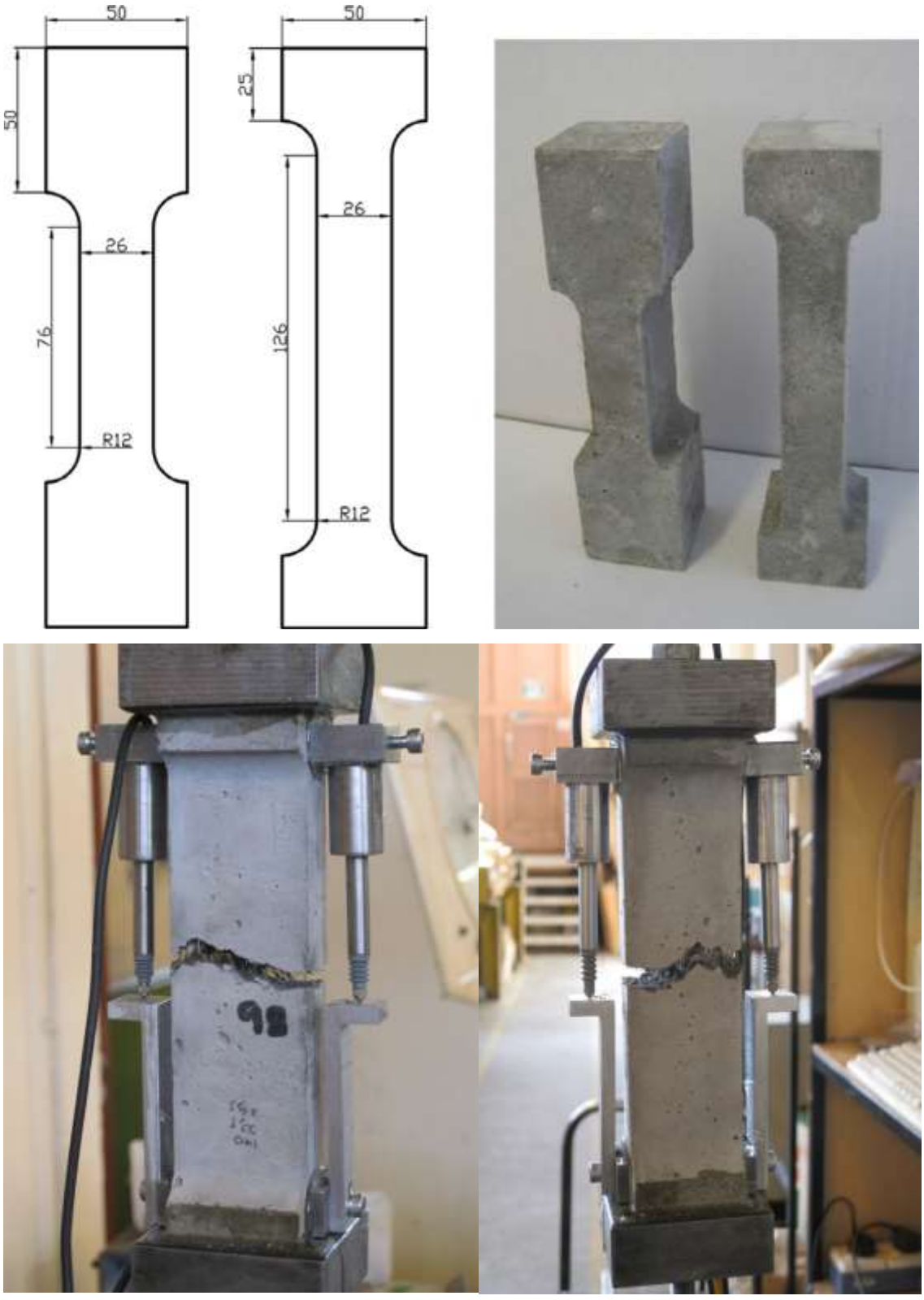

Figure 2.9: Dog-bone shaped tensile strength specimens with the failure mode, all dimensions are in mm (Hassan et al., 2012).

The results of Hassan's (2012) tensile tests showed at the beginning of the test, the specimens underwent a linear elastic phase with no permanent deformation. They showed that the major part of the tensile strength is achieved in this stage with very small deformation, see Figure 2.8a. As the load increased, the appearance of microcracks became more apparent and localised at the weakest point of the section. This took place at approximately the middle of the prismatic section of the specimen as shown in Figure 2.9. As the crack formed, fibres bridged between the two cracked surfaces to transfer stress. This was continued until the crack width became so extreme that fibres were no longer able to hold two cracked faces together and then fibre pull-out action progressed. The maximum tensile strain attained at this stage was reported in the range 1.5-2.8% with corresponding tensile strength of approximately 8.5 to 9.0 MPa. The fibre pull-out action took place mainly in a relatively small volume of the concrete matrix surrounding the steel fibre. It was also reported that as the fibre pulled-out, the stress-strain curve was affected by localised deformation and can no longer be expressed as a function of average deformation. Because point strain is not evenly distributed across the specimen, the measurement of deformation is obtained using the crack mouth opening relationship and this was important for the modelling stage of this study.

2.4.2 Compressive Strength and Elastic Modulus

For design purposes, in ordinary concrete compressive strength is the principal parameter to define a constitutive law whereas in UHPFRC, tensile behaviour is also relevant to the design of structures (Spasojevic, 2008). The compressive behaviour of UHPFRC is defined by its compressive strength of 150 to 250MPa, which is approximately 10 times greater than ordinary concrete and elastic modulus of greater than 55GPa (Association Francaise de Genie Civil–Service d'etudes Techniques des Routes et Autoroutes (AFGC/SETRA). 2002, Gowripalan and Gilbert, 2000).

In UHPFRC, steel fibres prevent the sudden explosive failure which occurs in ordinary concrete and cementitious material without fibres, thus a softening region can be obtained in the stress-strain curve. It is reported by Spasojevic (2008) that with an additional improvement in compressive strength, the fibres transfer the stress between the crack faces, and the nonlinear region is also more pronounced in comparison to high strength concretes without fibres. Moreover, the compressive failure mode in UHPFRC is

influenced by the element sizes as well as fibre volume, types and matrix bond. To determine the nonlinear and post-peak behaviour before and after failure in compression is not a straightforward task and obtaining reliable data has been challenging. However, a recent study conducted by Hassan et al. (2012) developed a simple and accurate way to determine a full stress-strain curve for UHPFRC under compression behaviour as shown in Figure 2.10. The result of the study also showed that differences in compressive strength after 7, 14 and 28 days were small if the concrete had been subjected to the hot curing process.

The elastic modulus of plain concrete is usually found using both destructive and non-destructive tests. For UHPFRC, many studies have been conducted to derive the elastic modulus from the compressive strength. The most recent study conducted has shown that non-destructive tests of plain concrete such as ultrasonic pulse velocity and resonant frequency methods can be employed to obtain the elastic modulus of UHPFRC (Hassan and Jones, 2012). In addition, the study included destructive testing, using cylinders and cubes. The results of dynamic and static tests were compared and it showed that the dynamic methods can produce an accurate result of elastic modulus *E* using the following relationship (Hassan and Jones, 2012):

$$V_{p,s} = \sqrt{\frac{E_{d,u}}{\rho}\frac{(1-\nu)}{(1+\nu)(1-2\nu)}} \qquad \textbf{(2.1)}$$

where $V_{p,s}$, v_u, ρ and $E_{d,u}$ are compression wave velocity, Poisson's ratio, concrete density and dynamic modulus of elasticity, respectively. Using the resonant frequency of vibration in the longitudinal mode, dynamic modulus of elasticity $E_{d,r}$ can be found using the following equation.

$$E_{d,r} = 4n^2L^2\rho 10^{-6} \qquad \textbf{(2.2)}$$

where n, L and $E_{d,r}$ are the fundamental frequency in the longitudinal mode of vibration, specimen length and dynamic elastic modulus, respectively.

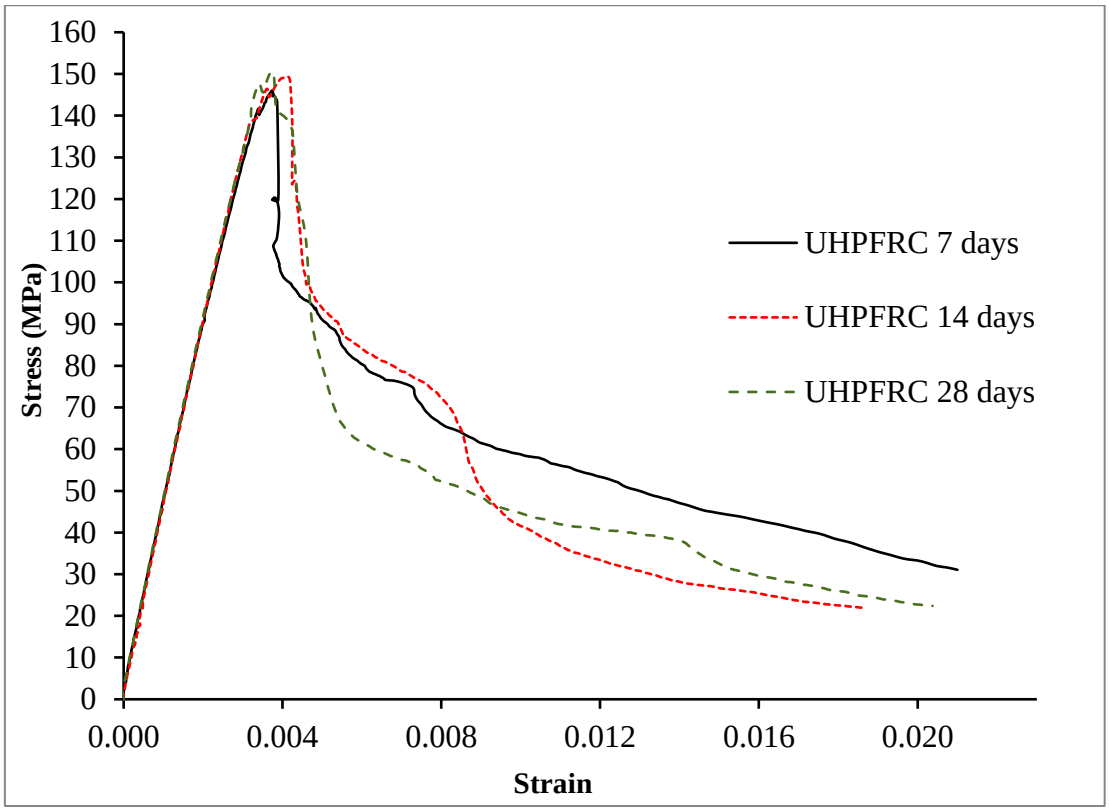

Figure 2.10: Stress-strain under compression (Hassan et al., 2012).

2.4.3 Flexural Tensile Behaviour

Since the appearance of UHPFRC, experimental studies have been conducted to investigate its mechanical behaviour. In order to describe its mechanical behaviour accurately, the material behaviour needs to be observed. The material behaviour varies depending on the fibre volume and aspect ratio with the most common fibre being the 13 mm short steel fibre. It has been reported that the flexural or direct tensile behaviour of UHPFRC can be divided into three main phases of behaviour (Association Francaise de Genie Civil–Service d'etudes Techniques des Routes et Autoroutes (AFGC/SETRA). 2002, Hassan, 2013, Spasojevic, 2008, Karihaloo and Wang, 2000). These phases are shown in Figure 2.11 and can be described as:

- Linear elastic behaviour,
- Pseudo-strain hardening behaviour, and
- Strain softening behaviour.

However, in a brittle material such as unreinforced concrete, the strain-hardening and softening cannot be obtained and the material behaves linearly until the material cracks when a sudden failure occurs, as indicated in Figure 2.11. Whereas, the stress-strain curve in ductile materials such as steel as well as alloys of other metals, shows a linear elastic behaviour until the yield point after which the material begins to deform plastically. As the material yields, the curve gradient decreases corresponding to a reduction in stiffness due to the breaking of bonds between the particles. As the deformation continues the stress increases on account of strain hardening until it reaches the ultimate strength, at which point the material ruptures. In the case of reinforced concrete, after the matrix cracks, the steel reinforcements carrying the stress between the two cracked faces increases until the steel fibre yields as shown in Figure 2.11.

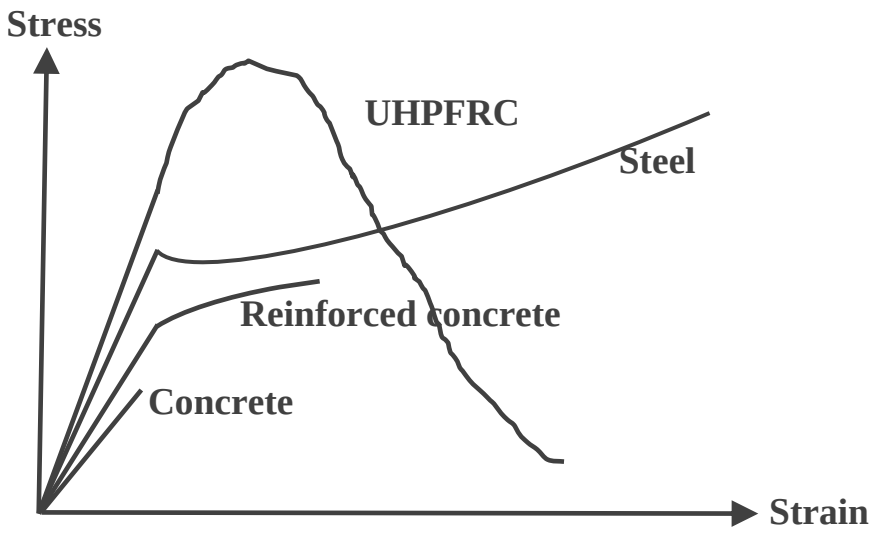

Figure 2.11: Typical stress-strain relationships for different ductile and brittle materials.

Notwithstanding extensive experimental studies on its mechanical properties and after two decades since its first appearance, only a limited number of studies have been conducted on the structural behaviour of SFRC members and UHPFRC in particular. This is mainly due to the high cost of the material. Developing a theoretical or numerical model, which can reasonably predict the behaviour of a SFRC such as UHPFRC has been challenging. Analytical work (Ghalib, 1980) determined the ultimate moment capacity and the cracking moment, assuming a certain failure mechanism. A similar method has been

recommended by the ACI committee 544 (1999) for the design of slabs with small spans (ACI Committee 544., 1999)**.** Detailed analytical work was conducted by Marti et al. (1999) which showed that the softening behaviour of SFRC can be modelled. Experimental and theoretical work by Khaloo and Afshari (2005) indicated that the energy absorption depends on fibre length and volume.

Furthermore, a study conducted on SFRC showed that the tensile cracking loads of plain and SFRC slabs were found to be similar, but there was a significant increase in the flexural strength of SFRC slabs, relative to plain concrete slabs (Roesler et al., 2004). While the study conducted on glass-fibre reinforced concrete indicated that the flexural strength was not improved by the glass-fibre compared to the normal concrete (Sravana et al., 2010). An experimental study using blast testing and numerical analysis was conducted to investigate the behaviour of UHPFRC slabs (Schleyer et al., 2011). An attempt to model the pre-peak bending response of a UHPFRC slab using the FE method is also conducted (Fairbairn et al., 2006b, Fairbairn et al., 2006a). However, the above mentioned studies only investigated a limited range of geometry experimentally and with the exception of the work by Schleyer et al. (2011), can only predict the elastic and hardening behaviour numerically. Therefore, there are too few of these studies to provide sufficient information to determine the structural behaviour of UHPFRC structures, especially for slabs.

Full experimental investigations or a numerical model that can predict full behaviour of UHPFRC two-way and one-way slabs do not exist. Moreover, a definitive technique for analysing reinforced concrete has been difficult to develop. It has been acknowledged that developing a finite element method that can predict the behaviour of UHPFRC is not a straightforward task (Biggs et al., 2000).

2.4.3.1 Linear Elastic Behaviour

Linear-elastic behaviour covers a region, where both matrix and fibres behave elastically. The maximum tensile strength attained in this stage corresponded to the matrix strength only and fibres have little or no influence on the structural behaviour as shown in Figure 2.12.

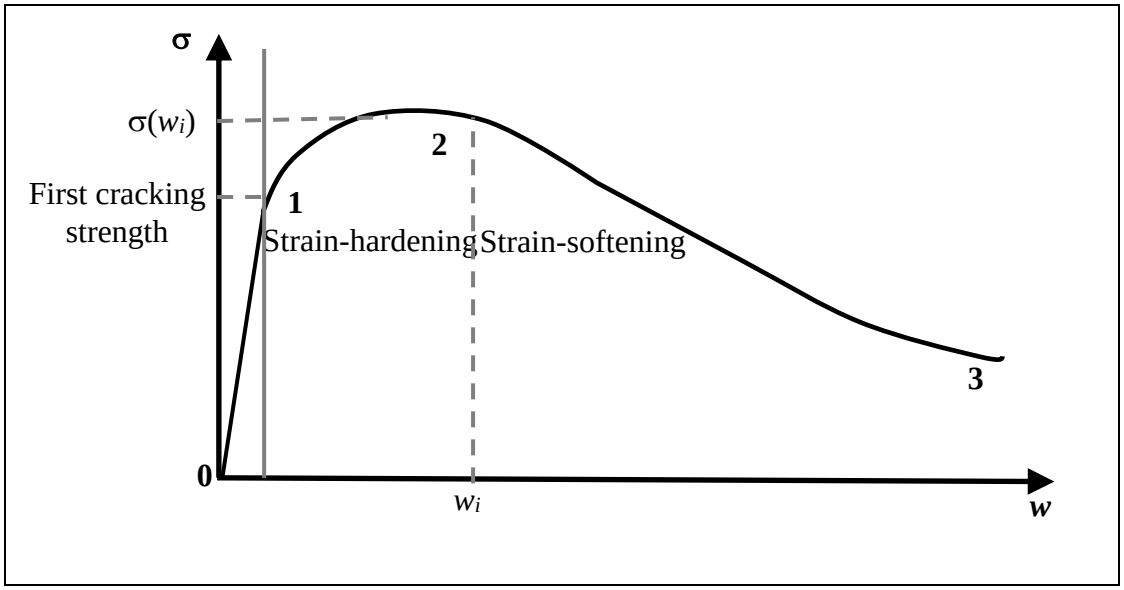

Figure 2.12: Tensile constitutive law of a UHPFRC from (AFGC/SETRA).

2.4.3.2 Pseudo-strain Hardening Behaviour

The second stage of the load or stress-displacement curve starts with the occurrence of microcracks and is located between points 1 and 2 in Figure 2.12. After the stress reaches the end of the elastic part, microcracks start to appear in the weakest section. As load increases, these microcracks widen resulting in fibre bridging action (Spasojevic et al., 2008). Furthermore, high deformation takes place during this stage due to the formation of a large number of microcracks and this phenomenon is called the pseudo-strain hardening behaviour. This strain hardening behaviour distinguishes UHPFRC from conventional types of concrete.

In this region, the tensile strength increases at a much lower rate compared to the elastic region and this small portion of tensile strength is carried mainly by the fibres. The appearance of microcracks depends on the fibre volume, geometry and matrix interface. Ultimate flexural and tensile strength and maximum deformation before strain softening are obtained at the end of the pseudo-stain hardening region, where from this point forward fibres are no longer capable of sustaining the tensile strength. The maximum deformation mainly depends on the fibre length, matrix interface and angle of pull-out. The occurrences of microcracks in this region are arbitrarily orientated, due to the random distribution and angle of rotation of the fibre within the matrix. Analytically or numerically modelling the constitutive behaviour of UHPFRC, especially in flexure is a

complicated and a challenging problem. Therefore, very few studies can be found in the literature and as such this behaviour is investigated experimentally and numerical in this study.

2.4.3.3 Softening Region

A combination of microcracks to form a macrocrack occur when the ultimate tensile stain of the material has been reached and fibres are no longer capable of holding the two cracked faces, resulting in some of the fibre debonding from the matrix. This region is called strain-softening and can be seen between points 2 and 3 in Figure 2.12. Stress from this point forward starts to decrease and is similar to the previous region where fibre geometry within the matrix bond influences the softening behaviour. The behaviour of this region is governed by the fibre pull-out action and it is also influenced by the element size (Spasojevic, 2008)

Strain softening behaviour of FRCs in both direct tension and flexure have been investigated experimentally and analytically (Naaman et al., 1974, Nammur Jr and Naaman, 1989, Ortiz, 1988, Horii et al., 1989, Li et al., 1991, Karihaloo et al., 1996, Hassan et al., 2012, Marti et al., 1999, Khaloo and Afshari, 2005, Zhang and Li, 2004). However, several assumptions are made in the developed analytical work and they all have limitations in terms of predicting the softening behaviour. Furthermore, due to the large number of steel fibres randomly distributed in the SFRC matrix such as UHPFRC and the resultant complicated fibre–matrix interaction, discrete modelling of fibres and matrix is difficult to model. Assuming fibres are uniformly distributed in the matrix, the softening behaviour of FRC can be modelled as a homogeneous material. However, this requires an accurate determination of material properties. Therefore, developing a numerical model that can reasonably predict the SFRC load-displacement curve and softening behaviour in particular is difficult. Only a few numerical studies that predict the softening behaviour of SFRC such as UHPFRC are available in literature (Al-Azzawi et al., 2006, Swaddiwudhipong and Seow, 2006, Yang et al., 2011a, Hong et al., 2010, Kang et al., 2010) and these studies can only be applied for a single geometry. In addition, several unrealistic assumptions are made in the above numerical models and they can only be used for simple geometries such as beams. Al-Azzawi et al (2006) used simulations for two beams; one with fibre reinforcement and the other unreinforced. In

the former, the FE results only agreed with the experiment in the elastic region while there were considerable differences in the strain-hardening region. In the latter, significant differences can be seen in both the elastic and stain-hardening regions. Swaddiwudhipong and Seow (2006) proposed an analytical approach which predicts the stress and strain failure of steel fibre reinforced beams and slabs with different fibre volume ratios and the results were incorporated into the FE analysis using ABAQUS. The results show that the analytical method can only predict some of the slabs accurately while considerable differences were observed in the beam models in both the elastic and strain-hardening regions. Yang et al (2011a), Hong et al (2010) and Kang et al (2010) used inverse FE analysis using a poly-linear approximation method. This is a method for estimating the tension softening diagram using data from experimental load-displacement curves. The method is only suitable for softening regions as it uses an assumed stress at which the crack propagation occurs. It also assumes the softening curve is appropriate as input data of the FE analysis. This means that all UHPFRC structures exhibit similar fibre-bridging action regardless of geometry. However, researches have shown that the fibre bridging action changes as the geometry of the structure changes and this makes this method inappropriate to model UHPFRC structures. Therefore, for the advancement of knowledge of UHPFRC behaviour, extensive numerical and experimental investigations are conducted in this study.

2.5 Yield Line (YL) Analysis

The vast majority of slab structures around the world, especially those which were constructed before the Second World War were designed based on elastic theory (Megson, 2005). However the elastic method has its limitations as it gives no indication of the ultimate load carrying capacity of a slab. It cannot give an accurate result because the material may show plastic behaviour.

An alternative technique, the YL analysis is an analysis approach for determining the ultimate load capacity of reinforced concrete slabs of any shape. The main advantage of YL is that it can predict a realistic value of collapse load of the slab irrespective of the slab shape or loading configuration. The method predicts several failure patterns, which

have been substantiated experimentally and the design is based on the most critical failure pattern. These failures depend upon the slab restraint and loading position.

YL was first introduced in 1921 by Ingerslev in Danish (Ingerslev, 1921) and then in 1923 in English (Ingerslev, 1923). They were described as a line of rupture that occurs in the slab along which the bending moment is constant. This approach simply assumes only bending moment acts along the yield-line and hence can be applied only if yield patterns are a straight line. It also assumes that once the most critical failure has been found for a given YL pattern, individual rigid regions between the yield-patterns are in equilibrium solely due to the moment along the yield-line, as illustrated in Figure 2.13.

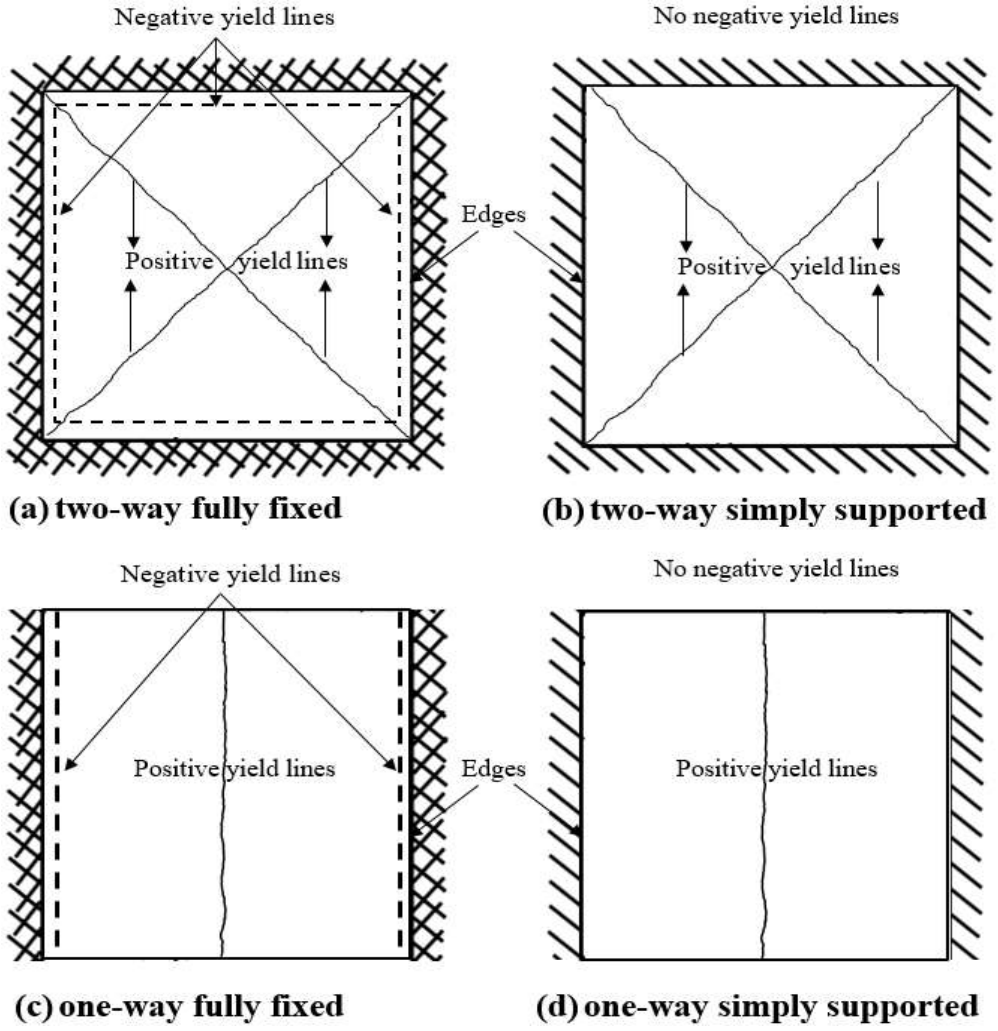

Figure 2.13: Regions in equilibrium due to the moment action along yield line in slab.

In 1932, Professor Johansen developed the YL method (Johansen, 1932) and published an introductory theory in 1943 (Johansen, 1943). Therefore, Johansen must be acknowledged as the pioneer of YL analysis. This theory was then adopted by the Danish concrete code. There is anecdotal evidence that YL analysis allowed the Danish engineers to produce an efficient design of reinforced concrete slabs of any shape while engineers around the world were struggling with tables of elastic moments and influence surfaces (Braestrup, 2010). Until about 1950, there still remained a certain disconcerting feature about the use of yield line (Sandhu, 1970). This was a belief that even if the YL method found the most critical layout of a particular pattern, it always seemed possible to discover another pattern, which could give an even lower collapse load. Fortunately, this argument was answered when in 1951 Prager and Hodge published a book, which stated the rules for limit analysis. These rules indicated that the lowest failure load had been reached if one could find coincidental upper or lower bound solutions (Prager and Hodge, 1951).

Furthermore, Johansen's paper (Johansen, 1932) was published in Germany in 1932, the thesis (Johansen, 1943) was also translated to Portuguese for the first time. In the 1960's YL theory had attracted engineers around the world especially in the United Kingdom (UK) and became a significant subject for design engineers. As a result, in 1962, Johansen's thesis was translated to English (Johansen, 1962) by the Cement and Concrete Association (C & C A) under the name of *Yield-Line Theory*. A decade later, the C&CA also published a catalogue of solutions under the name of YIELD-LINE FORMULAE FOR SLABS (Johansen, 1972). To evidence that the method was quickly spread in the UK, in 1964 Nielson's thesis was published in English (Nielsen, 1964), in 1965 the Magazine of Concrete Research issued a special publication on this method (Cement & Concrete Association C&CA., 1965), and in 1967 Jones and Wood published a book by the name of *Yield Line Analysis of Slabs* (Jones and Wood, 1967).

YL analysis assumes that slabs fail at their ultimate load in a near straight line (Megson, 2005). It allows the design engineer to estimate the ultimate flexural strength of reinforced concrete slabs and it makes it possible to analyse a large variety of slabs with a minimum of mathematical effort (Hognestad, 1953). The main reason that made the YL a successful design method was that it allowed designers to produce efficient designs of reinforced concrete slabs of any shape and loading (Sandhu, 1970). Whereas other methods such as elastic plate and standard tables of bending moment distribution, gave no indication of

the ultimate load carrying capacity of a slab and was only applicable to rectangular slabs, respectively. However, there is a lack of information in concrete construction in regards to using UHPFRC in slab design with the use of YL analysis. The YL method can be considered applicable for use in slab systems that are reinforced uniformly. Assuming that UHPFRC satisfies this requirement due to the randomly distributed fibre in the matrix, this method can be applicable for designing UHPFRC slabs (Harris, 2004).

Using the YL principle, external work done by the applied force on the slab to cause deflection must be equal to the internal work done by the plastic hinges which are created by the moment of resistance along the YL pattern with the angle of rotation. The moment of resistance is calculated at a load where the material reaches its ultimate strength. In UHPFRC, this is the peak load calculated when fibres begin to pull-out. To simplify the calculation the failure pattern is usually assumed to be a straight line. In OC, the relationship between moment and applied force can be obtained for the two-way and one-way slabs with both simply supported and fully fixed edges using the above principle (Park and Gamble, 2000). However, in UHPFRC, the above method is only applied for the simply supported case (Marti et al., 1999, Khaloo and Afshari, 2005). The effects of boundary conditions are significant in a YL analysis and the angle of rotation at the centre must be equal to the angle of rotation at the supports as the YL analysis principle normally assumes constant yielding moment values along each yield pattern. Due to the occurrence of crack patterns on the compression face, internal work done by the plastic hinges which are created along the yield pattern in FF boundary conditions are greater than for the SS boundary condition, Figure 2.13a. In conventional concrete and after the steel bar yields, the moment at any deformation point is constant as there is no softening behaviour. Therefore, the FF boundary condition in conventional concrete satisfies the YL requirement and yielding moment values along the support is equal to those at the centre. However, due to the random mix of high yield strength steel fibres, this concrete has a stain softening region, which allows the strength of the section to reduce steadily despite having cracks in the structure. Therefore, it would be unrealistic to apply YL method to determine the ultimate moment of resistance of UHPFRC.

2.6 Size-effect Law of UHPFRC

Enhancement of the mechanical properties of concrete for higher strength and ductility has received a great deal of attention in recent years in the context of building a sustainable society. A variety of new types of concrete, such as high performance/strength concrete and steel/polymer FRC, have been developed for such purposes. However, some other concrete phenomenon behaviour such as size effect has been ignored, with the assumption that the existing concrete size effect law can be used for SFRC.

Although many aspects of FRC and UHPFRC in particular have been investigated, understanding the size effect of structures made up of UHPFRC is largely lacking. The size effect describes the phenomenon that nominal structural strength decreases as the structural size increases. The first theory of size effect for a broad class of brittle structures was developed by Weibull (1939, 1951) where the strength of the structure depends upon the volume of the test specimens (Weibull, 1951, Weibull, 1939). In a quasi-brittle material such as concrete, the size effect was first introduced by Hillerborg, et al (1976) where the size effect in normal concrete was based on the properties of the material as well as geometry (Hillerborg et al., 1976). In the early 1980s, it became clear that the classical Weibull analysis of the size effect on nominal strength in brittle failure is invalid for quasi-brittle materials such as concrete, rock masses or ice sheet (Bazant and Xi, 1991, Bazant et al., 1991). This was because the Weibull approach ignored the stress distribution and energy released after a large stable crack growth prior to failure, as these were the main causes of size effect in concrete. Theories and equations for size effects in normal concrete and reinforced concrete beams are further studied and established, mainly by Bažant and his co-workers (Bazant, 1984, Bažant and Kim, 1984, Bažant and Sun, 1987). The size effect theory proposed (Bazant, 1984) is based on the energy released during crack propagation:

$$\sigma_N = Bf_t(1+\frac{d}{d_0})^{-\frac{1}{2}} \qquad \textbf{(2.3)}$$

where σ_N is the nominal strength at peak load, f_t the tensile strength of the material, d the characteristic size of the structure, and B and d_0 are constants that can be determined from

experiments or numerical analyses. The theory is based upon three distinct types of fracture regimes, which are linear elastic fracture mechanics (LEFM), nonlinear fracture mechanics (NLFM) and strength theory, as illustrated in Figure 2.14. This shows the change in σ_N from the smallest structure where the size effect is governed by the strength criterion to large structure where the size effect is governed by the LEFM theories.

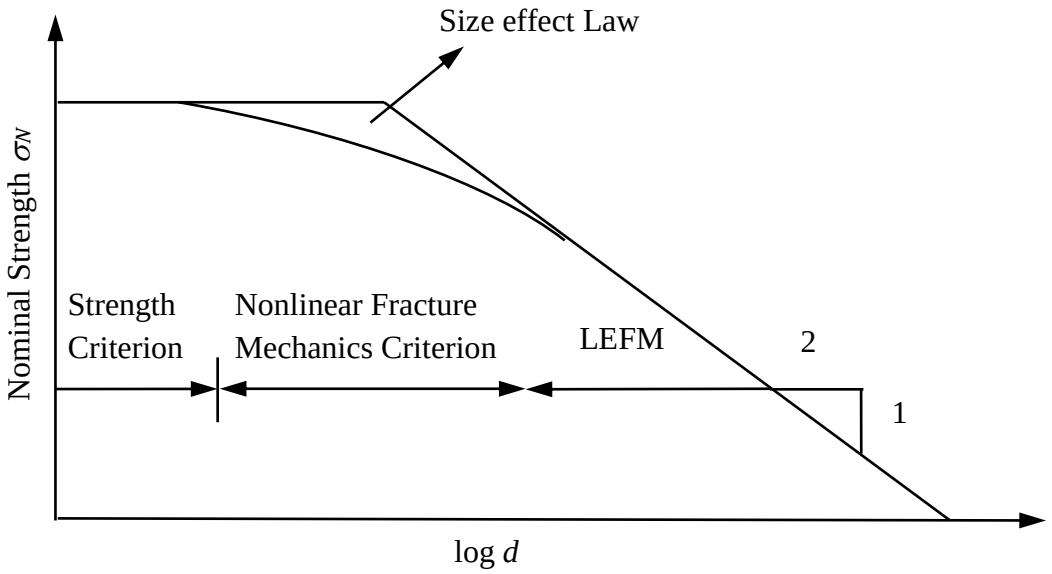

Figure 2.14: The current generalised size effect law (Bazant, 1984).

Furthermore, researchers came to the conclusion that the failure of normal concrete in tension is caused by the macrocrack in the fracture process zone (FPZ) (Kim and Yi, 2002). Ever since, size effect has received a great deal of attention for concrete in both tension and compression and many studies have been conducted experimentally and analytically (Barr and Tokatly, 1991, Bazant, 1991, Bažant, 1989, Bazant and Cao, 1987, Bazant and Chen, 1997, Bazant and Kazemi, 1991, Bazant and Sener, 1988, Kim and Yi, 2002, Van Mier, 1992, Vonk, 1992, Yu, 2007). The size effect exists in the nominal strength of concrete structures (Ooi and Yang, 2010).

To date, a limited number of analytical and experimental studied have been undertaken on the size effect for FRC and UHPFRC. Analytical work has shown that the size effect of the FRC is dominated by the fibre bridging and fibre-matrix interface parameters (Li et al., 1998). Experiments have shown that the size effect appeared to be less significant for FRC than for reinforced concrete (Lepech and Li, 2003). Furthermore, experimental

studies have also shown that the size effect on the bending strength of UHPFRC members was characterised by a pseudo-plastic behaviour in tension and dependent on the ratio of total crack-surface area to the cross-section area of beam (Spasojevic et al., 2008) and (Le, 2008). However, the importance of size effect on the structural implication for UHPFRC members has not been studied sufficiently and more research is needed to gain a better understanding. Therefore, another part of this study investigates the size effect phenomenon for UHPFRC members.

2.7 Design Guidelines of UHPFRC

The mechanical properties of cementitious materials in terms of ductility, durability and strength differ from those of ordinary concrete and this makes the existing concrete design guidelines invalid to be applied to UHPFRC. Since the development of this cementitious material, only limited research has attempted to develop design guidelines to be used in designing UHPFRC structures. This is a significant reason why this new concrete has not gained popularity in construction and this seriously limits its widespread acceptance in the construction industry, especially in building and highway bridge applications.

In the last decade, several design guidelines have been developed, but they have not yet been used widely in construction. This is because these guidelines are only related to a limited range of UHPFRC engineering structures. The first recommendations were developed by the French (Association Francaise de Genie Civil–Service d'etudes Techniques des Routes et Autoroutes (AFGC/SETRA). 2002). This can be divided into three sections; material characterisation, design and analysis of structures and durability. These recommendations only provided modifications to the existing French design standards for reinforced and prestressed concrete structures and these were not developed specifically for highway bridges and building structures. Reinforcing steel bars are not required, due to the superior mechanical properties of UHPFRC. However, the recommendations do not provide any specific guidelines about the design of non-reinforced or prestressed UHPFRC. In additions, the revised version by Toulemonde and Resplendino (2011) shows that considerable modifications were made in the recommendations. This indicates that the recommendations are not ready to be employed in designing major structures. A second guideline for the design and construction of UHPFRC structures was developed and published in Japan (Japan Society of Civil

Engineers(JSCE). 2008). This guideline gives design and construction recommendations to meet the requirements of safety, serviceability, durability and the resistance to fatigue of structures made of UHPFRC. Material manufacturing, behaviour and mechanical properties were included. These recommendations were not developed according to the European design standards and do not provide detailed information for unreinforced UHPFRC. The document states that the recommendation only provides basic provisions for designing UHPFRC structures, especially footbridges in accordance with the Japanese test methods which are different from the European test methods. In addition, in terms of the stress-strain relationship for design at SLS and ULS, both the French and Japanese recommendations suggest conventional bilinear relationships with a horizontal yield plateau. Detailed information of the softening part, which is an important material property, is not given. A set of design recommendations based on a particular application for UHPFRC structures were also released in Australia (Gowripalan and Gilbert, 2000), in Germany (Deutscher Ausschuss Fur Stahlbeton/ German Association for reinforced Concrete (DAfStb). 2003), and in the United States (U.S Deparment Transportation/The Federal Highway Administration (FHWA). 2006). However, none of these recommendations and guidelines are specific for the use of UHPFRC design especially in highway bridges. Moreover, some of these documents identify the issue but do not give a specific recommendation on how to deal with it. Therefore, further research is required to find a more suitable and safe design guideline for UHPFRC, so that UHPFRC can be used in the construction industry more often.

2.8 Applications of UHPFRC

The first ever UHPFRC structure designed was the Sherbrooke footbridge in Sherbrooke, Canada, which was built in 1997 (Resplendino and Petitjean, 2003). This precast pre-stressed bridge had spans of 60 m and had a cross section width of 3.3 m with the main span of 10 m. The bridge was designed using web truss shape and a ribbed slab cross section of 30 mm thickness, as illustrated in Figure 2.15. The structure became an inspiration to designers and engineers leading to several other footbridges, highway bridges and architectural applications being built with UHPFRC around the world. Some of the projects are shown in Figure 2.15 to 2.18 (Toutlemonde and Resplendino, 2011).

(a) Sherbrooke footbridge in Canada

(b) Glenmore footbridge in Canada

(c) Gartnerplatz footbridge in Germany

(d) Niestetal footbridge in Germany

(e) Sakata Mirai footbridge in Japan

(f) Papatoe footbridge in New-Zealand

(g) Kampung Linsum bridge in Malaysia

(h) Peace footbridge in South Korea

(i) Buchanan County bridge in USA

(j) Wapello County bridge in USA

Figure 2.15: Bridge applications (Toutlemonde and Resplendino, 2011).

Figure 2.16: Jean Bouin stadium in France (Toutlemonde and Resplendino, 2011).

(a) INELFE tunnel between Spain and France

(b) Spiral stairs in Denmark

(c) Shawnessy LRT Station in Canada

(d) Thiais building facade in France

Figure 2.17: Architectural applications (Toutlemonde and Resplendino, 2011).

(a) UHPFRC portal frame in Malaysia

(b) Martel tree in France

(c) Millau viaduct toll gate in France

(d) Sunshades in France

(e) Haneda airport in Japan

(f) The Folly in Netherland

Figure 2.18: Other applications (Lei et al., 2012, Toutlemonde and Resplendino, 2011).

There are a few more UHPFRC projects that have not been mentioned in the above list such as Cattenom Power Station beams, France 1997-1998, Monaco station panels, France, 1999, La Reunion soil anchorage plates, France, 1999 Rhodia panels, France, 2000, Seonyu footbridge, Korea, 2001-2002, Shower cabins, France, 2002-2003, Sofia Queen Museum, Madrid, Spain, 2003, Eraring Power Station, Australia, 2004, Papatoe Railways Station, New Zealand, 2005 and many more. Moreover, these applications are mainly footbridges and single span highway bridges or architectural structures. UHPFRC is partially used to build the above structures, mainly in the form of prestressed or post-tensioned girders or UHPFRC is used mostly in cases where OC barely meets the design requirements, due to UHPFRC's lightness or resistance to aggressive environments.

However, this new concrete has yet to gain broader recognition in the construction industry and design methods for structural components and systems made from UHPFRC remain largely unknown, the leading obstacles being the high cost, energy consumption during the manufacturing process and lack of structural exploitation. However, an increase in the service life of the structure, reduction in maintenance and reduction in material used as the volume of UHPFRC required to meet the strength criteria will be less than that of OC, can overcome the cost obstacles. Since the current precast production contributes to its high cost significantly but recently it has been shown that the cost can be minimised by utilising this material for cast in-situ applications (Hassan, 2013). Therefore, studies to exploit its structural behaviour, especially for slabs in bending are required. An appropriate model that can accurately capture the material resistance can be defined so that design engineers can consider the use of UHPFRC in practice.

2.9 Existing Studies on Flexural Behaviour of UHPFRC Slabs

A slab system, unlike beams and columns is different due its geometry. Slab failure mechanisms occur either due to flexure or punching shear. In reinforced concrete slabs, flexural failure occurs due to the cracking in the concrete and yield in the reinforcement, in the most highly stressed zone (Mosley et al., 2012). This will then act as a plastic hinge as the loads are distributed to other regions of the slab, resulting in crack formation. If the loaded area is small compared to the concentrated load such as column under/on slabs, punching shear failure could occur.

Conventional reinforced slab structures can be divided into two types of internal load distribution, a one-way and a two-way type slabs. A one-way slab is usually supported on two opposite sides and has a much larger dimension in one direction than in the other and can be assumed to be supported only along its long sides. The main steel bars are placed in the long direction and are assumed to carry load in one direction. They may be designed as a unit width beam spanning in the short direction for uniformly distributed loads. A slab supported on four sides is called a two-way slab, which generally is designed by empirical methods. In this type of slab, steel bars are designed and placed in both direction and can carry load in both directions. In UHPFRC structures, the amount of reinforcement cannot be controlled. Therefore, the assumption can be made that the

reinforcement in the UHPFRC slab is uniformly distributed due to the randomly distributed fibres in the matrix (Harris, 2004).

Previously, researchers have attempted to develop design methods for the use of FRC in the construction industry. However, these studies are limited and only a few experimental and theoretical works have been conducted to determine the flexural behaviours of UHPFRC slabs. Therefore, this study attempts to investigate slab flexural behaviour under a central point load and different boundary conditions.

2.9.1 Spasojevic Study

The Spasojevic study investigated the bending behaviour on several slabs with various thicknesses between 40 to 60 mm and a square shape with 900 mm sides. The boundary conditions of the specimens consisted of 8 radial point supports, which were placed symmetrically around the perimeter of 450 mm radius. A point load with a contact surface of 30 mm by 30 mm was applied in the centre, as shown in Figure 2.19.

Figure 2.19: UHPFRC slab under central point load in bending (Spasojevic, 2008).

In order to apply and extend the theory of plasticity to UHPFRC, both compression and tension must be considered. In this study, compressive behaviour is assumed to be similar

to that of OC, with consideration given to the effect of fibre as fibres enhance compressive strength. Tensile behaviour was found to be capable of large deformation after the occurrence of microcracks similar to steel bar reinforcement in OC. Furthermore, a simplified moment- curvature relationship of UHPFRC was also found to be similar to that of conventional RC. In addition, it was noted that the failure patterns for UHPFRC were similar to the ordinary concrete slabs. These observations allowed the authors to consider and apply the existing plasticity equations for reinforced concrete to be extended to UHPFRC with a slab thickness of less than 100 mm. To design thin UHPFRC slabs, the study applied the yield line pattern failure mechanism as shown in the following relationship.

$$\iint_A F.w(x,y)dxdy = \sum (m.s).\theta \qquad \textbf{(2.4)}$$

where F and w are the external load and slab displacement, respectively, m is the moment along yield line length s and θ is the hinge rotation of the slab segment. The results from the experiment showed that all the UHPFRC slabs failed in the same manner as OC with the development of four yield lines, which divided the slab into four smaller panels with almost the same sizes, as shown in Figure 2.20.

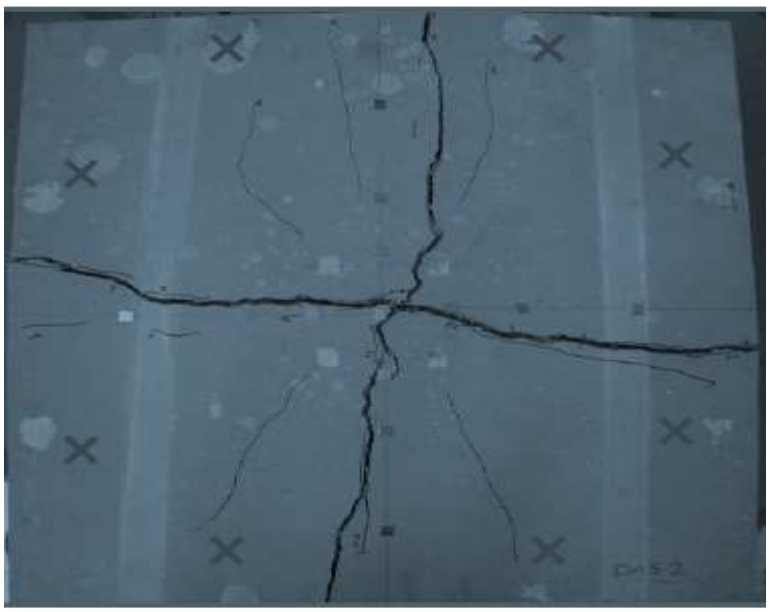

Figure 2.20: UHPFRC slab failure under central point load (Spasojevic, 2008).

The analytical equations assumed that the slabs develop perfect plastic hinges. However in reality, the hinges in the UHPFRC element were different and hence the applicability of the theory of plasticity must be limited. In addition, the study can only be used to design thin UHPFRC in nonlinear elastic region with limited crack width. The effect of boundary conditions is significant on the accuracy of the model as it can only be used when the failure is in bending. This seriously limits the use of the model in the structural design of slabs and in bridges in particular as the bridge boundary condition differ from those used in this study.

2.9.2 Harris Study

In this study the YL method was performed based on moment-curvature relationship for slabs with various thicknesses approximately of 51, 63.5, and 76 mm. The YL analysis was applied based upon the assumption that steel fibres are uniformly distributed in the matrix. The load was applied over a small area to simulate the effect of standard tyre patch loading with several different restraint conditions.

Based on the experimental results, the author came to the conclusion that slabs with a fixed edge would require a higher load to result in flexural failure. It was also observed that the predicted failure loads for all the specimens were much higher than the actual loads as illustrated in Table 2.2. A significant variation can be seen especially in series two and three. According to the study, this variation in the results could be attributed to the use of ACI (2011) YL method equations of conventional concrete and this could be inadequate to analyse UHPFRC slabs. Furthermore, YL analysis based on moment – curvature relationship was not ideal for designing UHPFRC slabs. The use of assumptions made by the study to analyse the failure mode or the lack of knowledge during the time of the study could also be a reason for the variation between the experimental and predicted results. In addition, the uses of YL methods in OC design is to reduce the amount of steel bar reinforcement but the amount of fibres in UHPFRC matrix cannot be controlled. Hence, the YL method is not an ideal approach to be employed in UHPFRC slab designs. Therefore, in this study UHPFRC slabs with different boundary conditions and specific loading arrangement under static loading will be investigated experimentally and numerically.

Table 2.2: Comparison between predicted and actual loads (Harris, 2004).

Test series one							
Test	Slab thickness **(mm)**	Punch plate size **(mm)**	Predicted Failure Load **(kN)**			Actual Failure Load **(kN)**	
			Punching failure	Flexural failure	Failure mode	Failure mode	Failure Load
1	**55.1**	**38.1**	**155.7**	**169.9**	Punching	Punching	**103.6**
2	**58.9**	**50.8**	**196.2**	**197.1**	Flexure	Flexure	**120.9**
3	**53.8**	**27.9**	**129.4**	**160.6**	Punching	Punching	**100.5**
Test series two							
Test	Slab thickness **(mm)**	Punch plate size **(mm)**	Predicted Failure Load **(kN)**			Actual Failure Load **(kN)**	
			Punching failure	Flexural failure	Failure mode	Failure mode	Failure Load
1	**66.3**	**50.8**	**236.0**	**248.0**	Punching	Punching	**146.8**
2	**65.5**	**76.2**	**281.1**	**248.6**	Flexure	Flexure	**159.7**
3	**64.5**	**38.1**	**201.1**	**231.0**	Punching	Punching	**135.7**
4	**70.1**	**63.5**	**284.7**	**280.7**	Flexure	Flexure	**152.1**
Test series three							
Test	Slab thickness **(mm)**	Punch plate size **(mm)**	Predicted Failure Load **(kN)**			Actual Failure Load **(kN)**	
			Punching failure	Flexural failure	Failure mode	Failure mode	Failure Load
1	**78.7**	**63.5**	**340.3**	**350.5**	Punching	Flexure	**173.5**
2	**71.9**	**38.1**	**240.2**	**285.6**	Punching	Punching	**156.6**
3	**76.9**	**25.4**	**239.7**	**321.6**	Punching	Punching	**178.4**
4	**72.4**	**50.8**	**270.9**	**293.6**	Punching	Flexure	**170.8**
5	**83.1**	**44.4**	**321.6**	**379.9**	Punching	Flexure	**175.3**

2.9.3 Marti Study

An experimental investigation was conducted on circular (C) and square (S) slabs as well as four-point (R) beams under flexural tensile testing to determine the behaviour of SFRC. Test configurations and specimen sizes are shown in Figure 2.21 and Table 2.3. A general theoretical approach using flexural analysis, which can predict the softening behaviour, was also proposed with careful consideration for random fibre-distribution and pull-out action. In the past, to determine the mechanical properties of both OC and SFRC, three or four-point flexure and square slab tests are used. In this study, Marti et al. (1999) attempted to determine the strength and ductility properties of SFRC using circular test

slabs and the relationship between four-point loaded beam, square slabs and circular slabs was also investigated using the proposed theoretical approach.

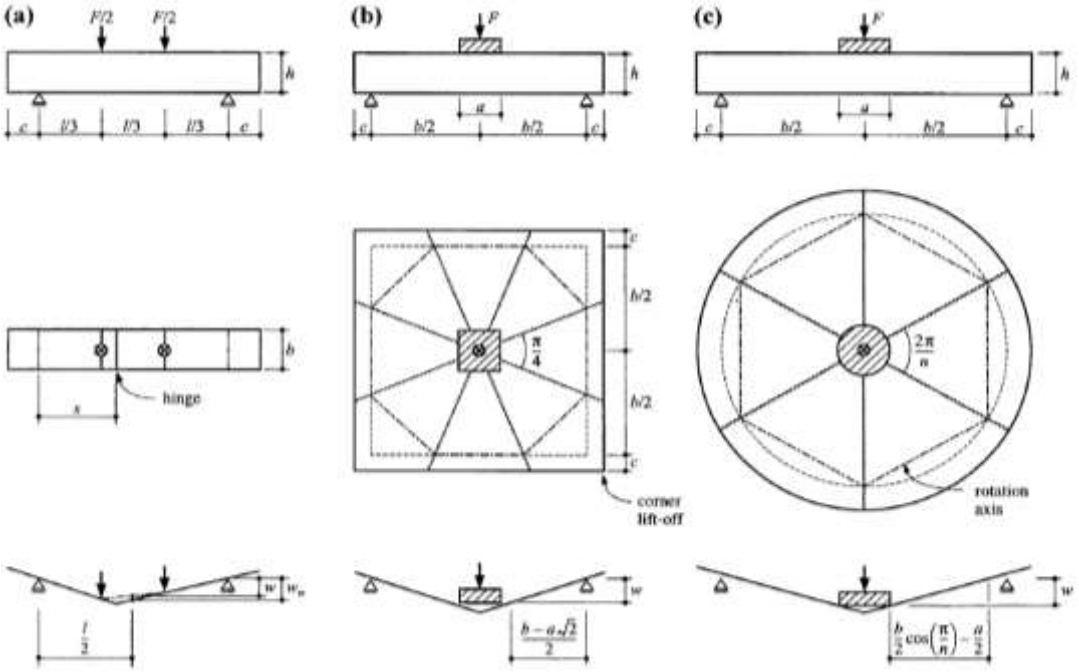

(a) modulus of rupture test (b) square slab test and (c) circular slab test

Figure 2.21: Test set-up and failure modes (Marti et al., 1999).

Table 2.3: Specimens sizes used in Marti study.

Test	A (mm)	B (mm)	c (mm)	h (mm)	L (mm)
Four-point beam	-	100	75	100	450
Square slab	100	520	40	100	-
Circular slab	120	680	60	100	-

In this study, fibre geometry and the bond properties were considered and it was assumed that the fibre pull-out occurs on the side of the shorter embedment length, this resulted in the following relationship for initial stress

$$\sigma_0 = \frac{\rho_f l_f \tau_b}{2d_f} \quad \textbf{(2.5)}$$

where the bond shear stress is:

$$\tau_b = 2 f_t = 0.6(f_c)^{2/3} \quad \textbf{(2.6)}$$

where l_f and d_f are the length and circular cross sectional diameter of the steel fibre and ρ_f is volumetric reinforcement ratio in the matrix. f_t and f_c are the tensile and compressive strength, respectively. As the loading is increased, cracks became bigger and fibres start to pull-out until the stress became zero and the pull-out width $u = l_f/2$ as shown in Figure 2.22a. Due to the reduction in fibre-matrix bond linearly, a parabolic relationship between stress σ and pull-out width can be obtained $0 \leq u \leq l_f/2$ as illustrated in Figure 2.22b.

$$\sigma = \sigma_0 (1 - \frac{2u}{l_f})^2 \quad \textbf{(2.7)}$$

If d is the overall depth of the specimen and z is the compression depth after crack occur, over 80% of the compression depth is assumed to be the compressive stress of $0.85f_c$ as shown in Figure 2.22d. Thus the cracking parameter ξ was introduced based upon the angle of rotation θ and compression depth, see Figure 2.22, as shown in the following relationship.

$$\theta(h - z) = \frac{\xi l_f}{2} \quad \textbf{(2.8)}$$

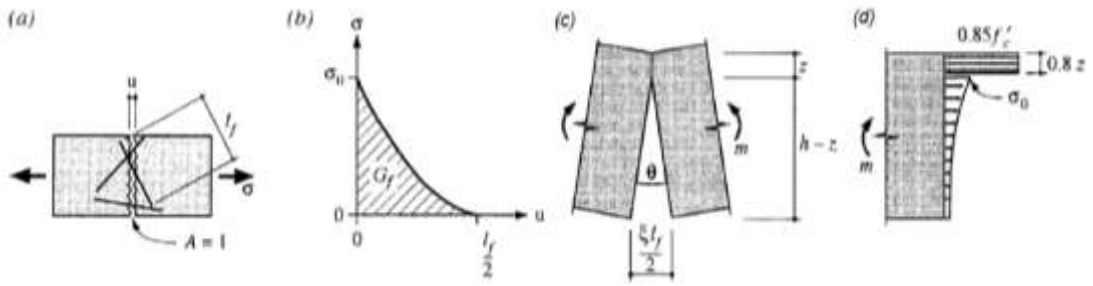

Figure 2.22: (a) fibre pull-out in uniaxial tension (b) stress against crack opening (c) flexural hinge (d) stress distribution (Marti et al., 1999).

Using the tensile stress distribution in Figure 2.22b, a cracking parameter can be assumed for $0 \leq \xi \leq 1$ before and $\xi \geq 1$ after fibre pull-out. Based on the assumption the compression zone depth and moment *m* are obtained using following relationships.

$$z = \frac{h}{1 + \dfrac{2.04\, f_c}{\sigma_0 (3 - 3\xi + \xi^2)}} \tag{2.9}$$

$$m = 0.85\, f_c \times 0.8z \left[0.6z + (h - z) \frac{6 - 8\xi + 3\xi^2}{12 - 12\xi + 4\xi^2} \right] \tag{2.10}$$

$$z = \frac{h}{1 + \dfrac{2.04\, f_c \xi}{\sigma_0}} \tag{2.11}$$

$$m = 0.85\, f_c \times 0.8z \left[0.6z + \frac{(h - z)}{4\xi} \right] \tag{2.12}$$

The nominal stress distribution in Figure 2.22d, is assumed to be uniform as shown in Figure 2.23, hence the effective flexural strength f_{ctf} is obtained using the following relationship:

$$f_{ctf} = f_c \frac{0.68\zeta}{1-\zeta} \quad \textbf{(2.13)}$$

where the compression zone parameter is

$$\zeta = \sqrt{0.25 + \frac{m}{0.68h^2 f_c}} - 2.5 \quad \textbf{(2.14)}$$

The general f_{ctf} can be determined using the following equations:-

$$f_{ctf} = \frac{F(b-a)}{(b+2c)4h^2} \quad \textbf{(2.15)}$$

where F and h are slab applied force and thickness, respectively. The parameters of a, b and c are the slab geometries as shown in Figure 2.21.

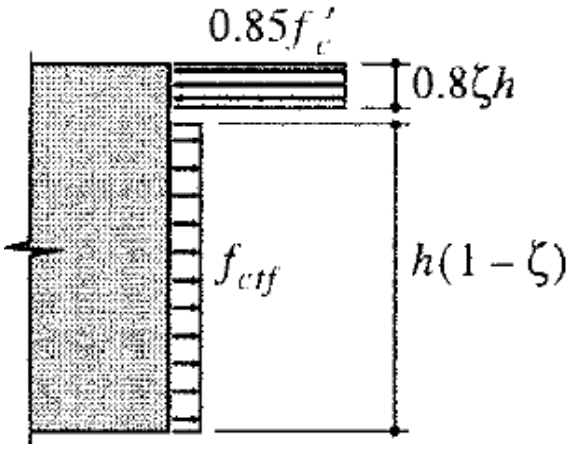

Figure 2.23: Nominal stress distribution (Marti et al., 1999).

The relationships between nominal flexural strength and the angle of rotation using a theoretical approximation are plotted against the experimental data. The results show that

some of the calculated values are conservative and they did not predict some of the test results as shown in Figure 2.24. Furthermore, the proposed method uses the effective flexural tensile strength at a deformation for a certain crack opening and this may only be true for the specific boundary conditions and fibre type, used in the study. A suggestion for the calculation of both the SLS and ULS resistance is included, stating that cross-sectional force and moment may be determined from elastic analysis or other solutions satisfying equilibrium but no detailed information is given. It also states that the method is rather onerous for the material tested and it may be revised based on future findings.

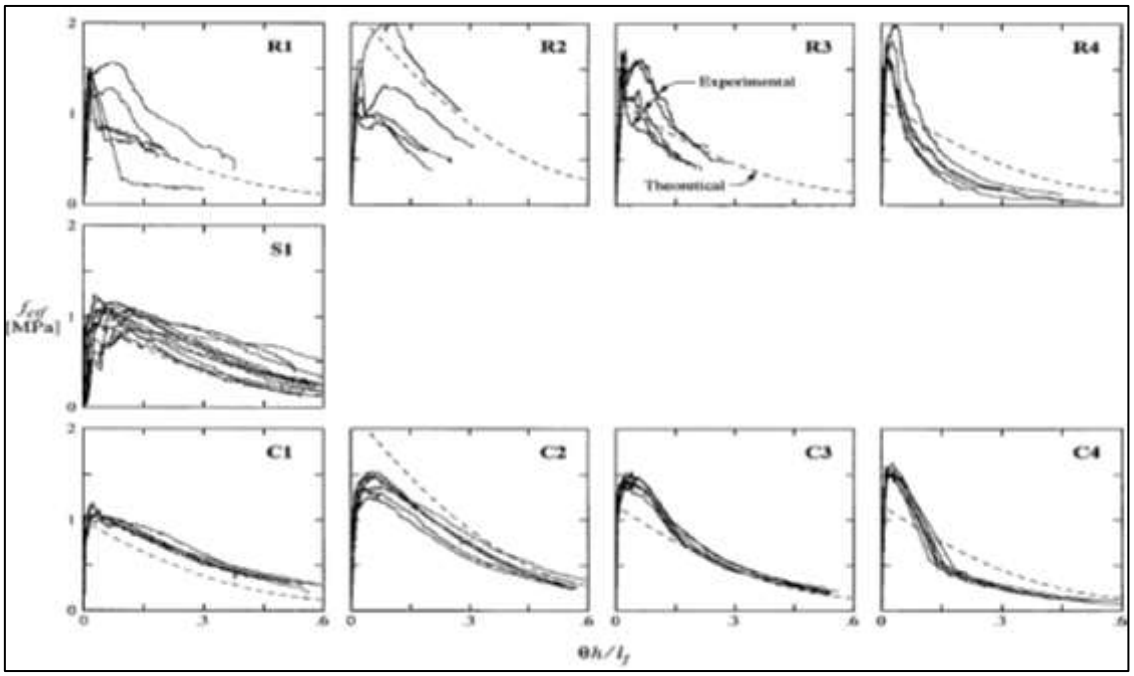

Figure 2.24: Experimental and theoretical effective flexural tensile strength versus hinge rotation (Marti et al., 1999).

Further investigation of Marti study was later carried out by Khaloo and Afshari (2005) using the principle of virtual work. Slabs tested in this study had a thickness (t) of 80 mm with corners supported as shown in Figure 2.25a. Slab dimensions for a, b and c were 80, 680 and 70 mm respectively. A design method based on allowable deflection was proposed for SFRC slabs.

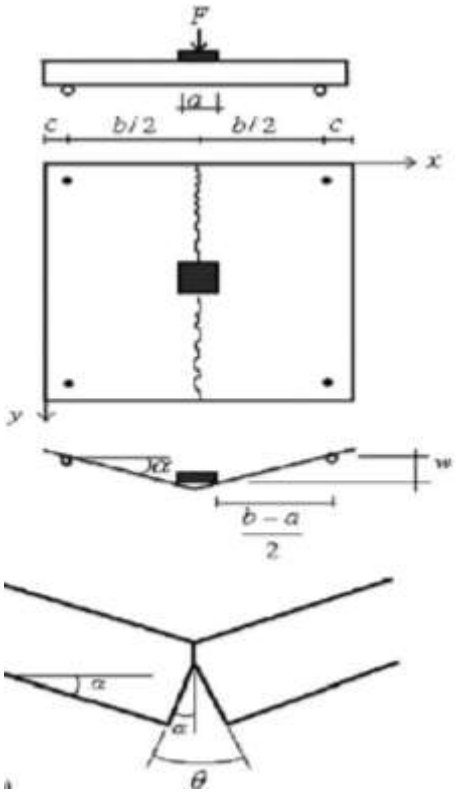

Figure 2.25: Slab analysis using yield line analysis (Khaloo and Afshari, 2005).

By inspection of Figure 2.25 and using YL analysis, where the sum of external work is equal to the internal work, the following relationship was obtained:

$$\theta = \frac{4w}{b-a} \qquad \textbf{(2.16)}$$

Using yield line analysis, external work done by the applied force is equal to the internal work done by plastic hinges as follows:

$$\sum F\delta = \sum m\theta s \qquad \textbf{(2.17)}$$

By combing and re-arranging the above equations:

$$F = 5.467\,m \qquad \textbf{(2.18)}$$

Finally using equations 2.5 to 2.8 and 2.16 to 2.18, the following relationships between load-deflection were obtained. For $0 \leq \xi \leq 1$:

$$F = 3.718\, f_c z \left[0.6z + (h-z)\frac{6 - 8\xi + 3\xi^2}{12 - 12\xi + 4\xi^2} \right] \quad \textbf{(2.19)}$$

$$w = \frac{\zeta l_f (b-a)}{8(h-z)} \quad \textbf{(2.20)}$$

and $\xi \geq 1$

$$F = 3.718\, f_c z \left[0.6z \frac{(h-z)}{4\xi} \right] \quad \textbf{(2.21)}$$

$$w = \frac{\zeta l_f (b-a)}{8(h-z)} \quad \textbf{(2.22)}$$

The theoretical results based on equations 2.19 to 2.22 showed that some of the predicted values were both over and under estimated in the test data as shown in Figure 2.26. Only the simply supported boundary condition is included in this study and detailed information for other boundary conditions are not given. The modified method covers only the fibre volume within the range 0.5-1.75% which is smaller than the fibre volume used in this research study. In addition, the main objective of this study was to investigate experimentally the flexural strength, load deflection curves and energy absorption of small slabs with different fibre volumes rather than presenting design methods. Generally, the theoretical methods proposed by Marti el at. (1999) and developed by Khaloo and Afshari (2005) were not capable of determining the flexural behaviour of SFRC and slabs in particular. Therefore, thorough experimental investigations on flexural behaviour of UHPFRC slabs are undertaken in this study.

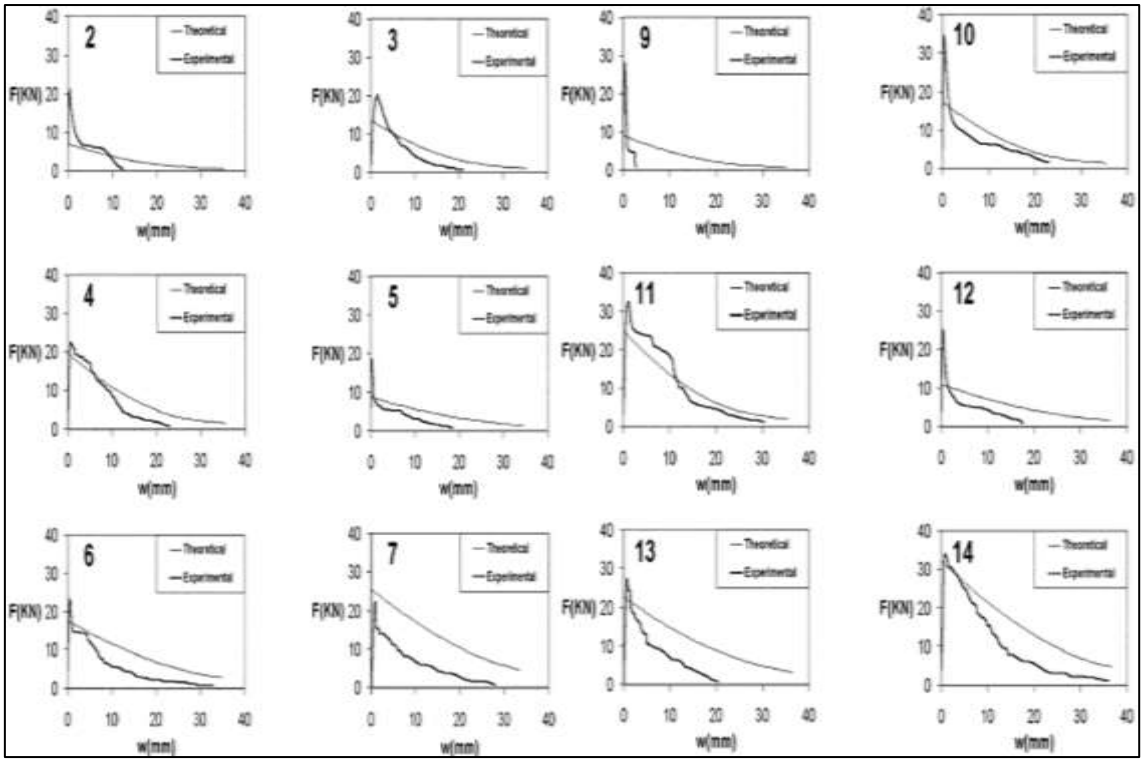

Figure 2.26: Comparison between theoretical and experimental load-displacement curves (Khaloo and Afshari, 2005).

2.9.4 Ghalib Study

An analytical approach based on experimental data was proposed by Ghalib (1980) to determine the ultimate and cracking moment capacity of FRC slabs. One-way slabs under two line loads and two-way slabs under concentrated loads were tested. One-way slabs were 20 mm thick, 150 mm wide and 500 mm in length. The loads were applied 200 mm apart symmetrically placed with respect to the centre of the slab and the slab had simply supported boundary conditions. Two-way slabs were 33 mm thick and 960 mm square with corner support boundary conditions. In addition, cylinders and long prisms were tested under direct and indirect compression and tension to determine material properties.

An assumption of failure mechanism was essential to develop the analytical approach and fibre geometry and fibre volume ratio were also given significant consideration in prediction equations. The analysis in this study was divided into two sections. In the first section, analytical calculation of cracking moment, which occurs at the end of elastic

stage, was obtained. In the second section, detailed procedures of prediction equations of both one-way and two-way slabs were shown.

For a homogenous material and using classic beam flexural theory under a four-point bending test, the elastic and resisting bending moment acting on the slab can be expressed as follows (Ghalib, 1980):

$$m = \frac{Fx}{2b} \quad \textbf{(2.23)}$$

and

$$m = \frac{St^2}{6} \quad \textbf{(2.24)}$$

where F is the external load, x is distance between the load and the nearest support, b is the width of the slab, t is the slab thickness and S is the stress in the slab. The above equation can only be used if the material is purely elastic and the neutral axis must lie in the middle of the cross section. Since determining the cracking moment was the aim of this study, Ghalib substituted cracking load F_{cr} for F in equation 2.23 and equated equation 2.23 and 2.24, thus the following relationship was expressed to obtain cracking stress and moment:

$$S_{cr} = 0.90\sigma_s \quad \textbf{(2.25)}$$

$$m_{cr} = 0.15\sigma_s t^2 \quad \textbf{(2.26)}$$

where σ_s is the splitting tensile strength. Taking into account the fibre geometry, adhesive bond and volume ratio, ultimate resisting moment per unit width was expressed

$$M_{ult} = \alpha E_0 \sigma_t \quad \textbf{(2.27)}$$

where E_0 is the initial elastic modulus, σ_t tensile stress and α is the moment capacity function factor, which is explained in detail in Ghalib's work. Using YL theory, ultimate resisting moment for two-way slabs is also proposed using the following relationship:

$$m = \frac{7}{24}\sigma_s t^2 \quad \textbf{(2.28)}$$

The above analytical approach was proposed based on experimental work on SFRC, which behaves differently from UHPFRC materials. In addition, the finding of this study is only limited to particular geometries as stated in Ghalib's study. Furthermore, an assumption of failure mechanism is required in order to use this approach. The lengths of the fibres used in this study were between 40 to 60 mm and the results, especially in two-way slabs, showed no softening behaviour but with a strain hardening behaviour over a long range of deformation as shown in Figure 2.27 and Figure 2.28. Because most of the results showed no softening behaviour, Ghalib has assumed that the material behaves linearly until cracks occur followed by a yield plateau. This allowed the author to use a conventional linear constitutive law and adopt the YL theory to determine the relationship between applied force and ultimate moment. The UHPFRC material tested in this study behaves differently from that tested by Ghalib and it would be inaccurate to apply the method to capture the UHPFRC behaviour. Therefore, experimental studies on both one-way and two-way slabs are conducted to investigate the structural behaviour for the design purposes of UHPFRC slabs.

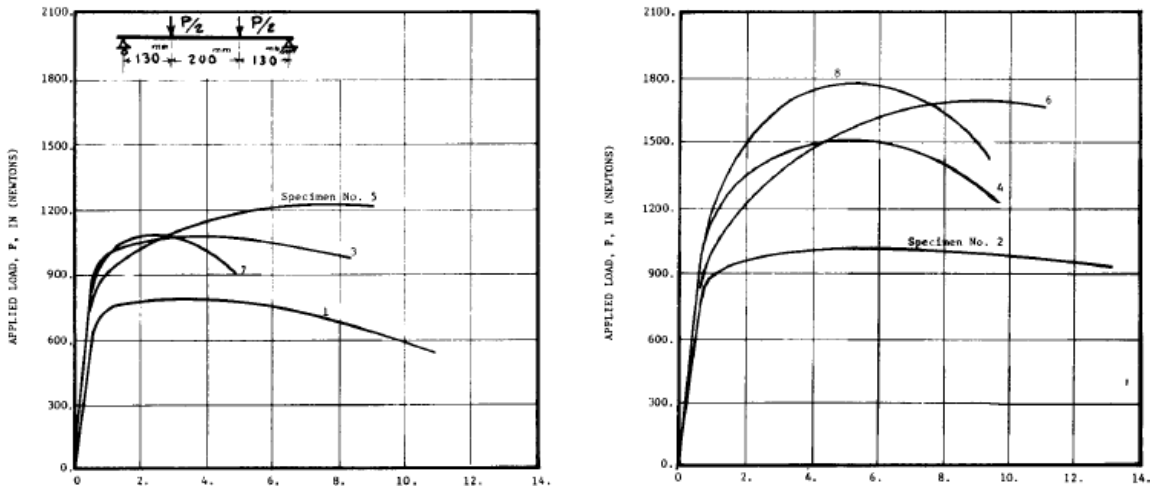

Figure 2.27: Experimental results of one-way slabs (Ghalib, 1980).

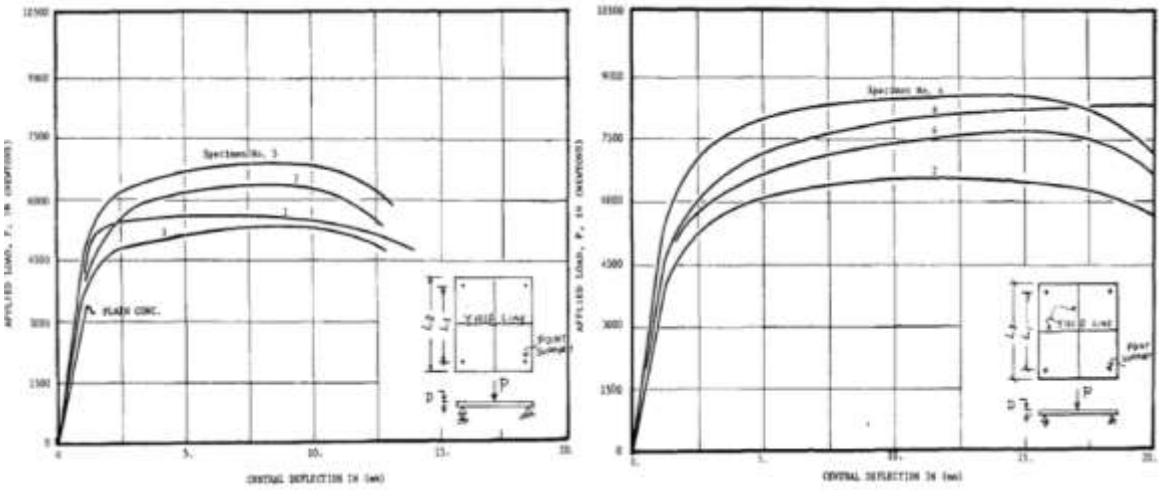

Figure 2.28: Experimental results of two-way slabs (Ghalib, 1980).

2.10 Concluding Remarks

This chapter discussed the appearance of different types of fibre throughout history as well as the available types of fibres on the market. Attention was given to selected literature on the current state of knowledge on the use of UHPFRC and its limitation in structural design. The focus was to firstly gain a full understanding of steel fibre's first appearance in the market and the development of different types of SFRC. The advantages and drawbacks of these concretes are presented. The reasons for choosing UHPFRC over other types of FRC are presented. For example, this research continues

the work of previous studies conducted at the University of Liverpool. The effect of concrete constituent materials and other factors such as high curing temperature and w/c ratio on the properties of UHPFRC are also presented in this chapter.

It became clear that SFRC and UHPFRC in particular have many advantages over conventional concrete such as higher strength, fracture resistance and ductility. UHPFRC has high flexural strength and fracture energy compared to traditional concrete. It is a durable material with very low permeability leading to a longer service life than an OC structure. It is a very promising material with its suitability in a wide variety of applications, especially for those structures where ordinary concrete is impossible.

Following this, an introduction to YL analysis is included and the potential for this design method to be extended and adapted to UHPFRC is discussed. Reasons for the incompatibly of the YL method for designing UHPFRC slabs, with FF boundary conditions in particular are also discussed. Due to the random mix of high yield strength steel fibres, even after cracks develop, this concrete produces a strain softening region. This behaviour means that the YL theory is considered to be unsuitable for UHPFRC. In terms of design, it is important to have a clear understanding on nominal flexural strength when the structural geometry changes. The question to be answered is whether or not the size effect phenomenon, which is proven to be a fact in conventional concrete, exists in UHPFRC members. Therefore, experimental and numerical investigations on size effect of UHPFRC were conducted and are presented in Chapters 3 and 7 of this thesis, respectively.

The role of the existing design guidelines to design UHPFRC structure was also investigated. The limitation and capability of these design guidelines were presented. It was found that an enormous amount of research has been undertaken to explore mechanical properties of the material. However, a concise understanding of the structural behaviour of UHPFRC is still largely lacking and this has limited the application of UHPFRC in engineering structures especially in building and bridge applications. Finally, a review of previous experimental and analytical studies on UHPFRC materials was conducted. Drawbacks of these studies were presented. Particular attention was given to the behaviour of UHPFRC slabs under flexural loading.

CHAPTER 3

THREE-POINT BENDING TEST

This chapter presents the experimental work carried out on rectangular beams. This was conducted on 15 UHPFRC notched beams under three-point bending. The specimens were notched to ensure that the local stress concentration occurred at the centre of the beam so that the CMOD could be obtained. In order to compare the results of different geometries, it was essential that all the specimens failed in a similar manner. The notch will also improve the accuracy of the flexural tensile strength (U.S Deparment Transportation/The Federal Highway Administration (FHWA). 2006). In addition, the notched prism is a standard method to measure the flexural strength of fibre concrete with fibres no longer than 60 mm. The materials, experimental set-up, applied fibre types, mixing procedures and test methods are also presented in this chapter.

Although many aspects of UHPFRC have been investigated extensively, the size effects on the structural strength of UHPFRC members remain largely unknown. This is mainly due to the lack of sufficient and reliable experimental data. This chapter aims at better understanding the size effect on flexural tensile behaviour of thin UHPFRC beams. In addition, the flexural behaviour of UHPFRC members is different from ordinary RC due to the influence of steel fibres. Therefore, the detailed investigations of bending behaviour of thin UHPFRC beams, failure mode and crack propagation are also presented in this chapter.

In the last few years some of the mix design constituents such as superplasticiser has been replaced by a new dispersing agent. Therefore, this chapter presents an investigation of this new superplasticiser. The curing treatment applied to concrete is always important, especially in the case of UHPFRC. Therefore, all the UHPFRC specimens studied in this research programme were heat treated after they reached sufficient strength to undergo the process. Finally, in order to verify that the mixing and casting procedure used to prepare the specimens resulted in the steel fibres being uniformly distributed throughout the matrix and to investigate the effect of specimen geometry on fibre distribution, an extensive examination of fibre distribution where cracks occurred during the testing was carried out.

3.1 Beams Failure Modes

As a concrete beam subject to flexure loading, two types of stresses develop in the beam, flexural and shear stresses. These stresses are influenced by many factors such as the compressive and tensile strength of concrete, the dimensions of the beam, and the amount of steel reinforcement and tensile strength of the steel rebar (Roberts and Ho, 1982). This argument may not be fully applicable to FRCs as there is no reinforcing steel rebar and steel fibres are randomly mixed in the concrete matrix. However, regardless of the types of the concrete, there are two main failure types in concrete beams and these are flexural and shear failures.

3.1.1 Flexural Failure

Flexure failure can be defined as a failure when the beam reaches its ultimate moment capacity. Because concrete is strong in compression but relatively weak in tension, concrete beams are reinforced with steel rebar placed in the tension zone to prevent explosive failure of the concrete in compression. Steel is strong in both tension and compression and this ensures that the beam failure mechanism is gradual and controlled. As the load acting on the beam increases, vertical cracks propagate to form under the applied load as shown in Figure 3.1. As the loading further increases, the concrete crack width increases and the reinforcing steel bars bridge between the two cracked faces to transfer the stress. Similarly, steel fibre concrete fails in flexure and the possibility of this

failure mode increases in UHPFRC beams (Bastien-Masse and Brühwiler, 2014). Adding steel fibre into the concrete will help to transform the shear failure to flexural failure (Li et al., 1992, Cucchiara et al., 2004).

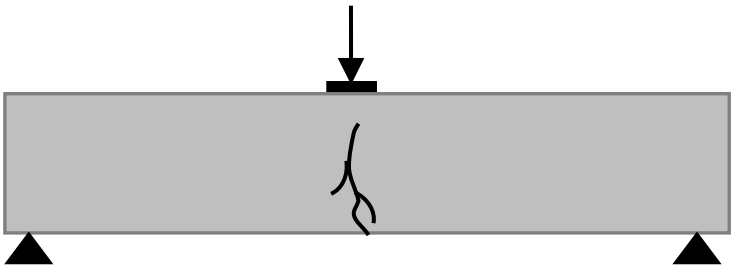

Figure 3.1: Flexural failure mode of concrete beam.

3.1.2 Shear Failure

Shear failure occurs when concrete exceeds its biaxial tension-compression stress capacity in shear dominated areas due to the shear force pushing one part of the section in one direction and another in an opposite direction (Assakkaf, 2002, Assakkaf, 2004). It is likely associated with stress conditions in the particular region of the beam section where compressive force is transmitted to the supports (Kotsovos, 1986). This creates cracks which usually appear close to the support initiating diagonally upward toward the centre of the beam. In simply supported beams, due to the load acting on the beam, the reaction force at beam supports generate vertical shear in the section as shown in Figure 3.2. There are several shear failure modes in rectangular concrete beams and these are as follows:

- If the shear strength became greater than the flexural strength, failure occurs at a point where the flexure stress is the highest usually at the centre of the beam where compression strain exceeds its capacity. This type of shear failure called flexure-compression is shown in Figure 3.2a.
- This type of failure occurs with the start of flexural cracking but as the shear increases, the crack begins to turn over and become inclined towards where the loading is acting and this is called flexure-shear failure (Sas et al., 2011, Li et al., 1992) as shown in Figure 3.2b. This failure type usually occurs in beams which do not have transverse or web reinforcement.

- Another type of shear failure called shear-compression failure which often occurs in beams with inadequate transverse or web reinforcement. In this failure mode, cracks initiate diagonally between the load and support positions penetrating the compression zones as shown in Figure 3.2c. This failure type is common in deep beams where the crack causes the compression force to redistribute onto a smaller area resulting in the compressive strength being exceeded, thus failure occurs (Zarais, 2003). The crack initially propagates at the tensile zone but due to the compression strut caused by the arch which connects the point of loading and supports as shown in Figure 3.2c, which prevents the tension crack propagating onto the compression zone (Islam et al., 2014).

Adding steel fibres leads to substantially higher ductility during failure in concrete beams and will transform the shear failure to flexural failure (Li et al., 1992, Cucchiara et al., 2004). Furthermore, it has recently been reported that the use of steel fibre can enhance the flexural behaviour in concrete beams (Islam et al., 2014, Jang et al., 2015). Having a notch in the three-point bending test will ensure that the beam splits at the point directly where the load is placed (Alani et al., 2013). Since the main purpose of this study was to investigate size effect behaviour, the failure mode was required to be similar for all the beam specimens, therefore, all the beams were notched.

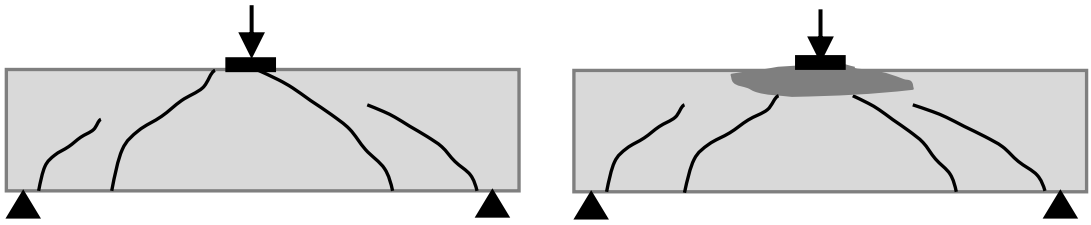

(a) flexure-compression (b) flexure-shear

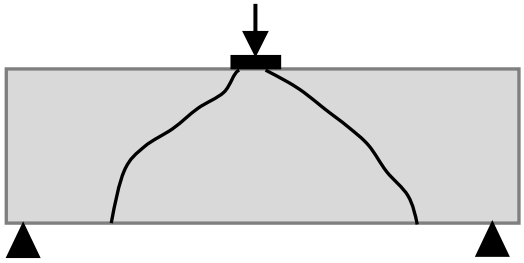

(c) shear-compression

Figure 3.2: Shear failure of concrete beams.

3.2 Review of Three-point Bending Test Method

To investigate the size effect behaviour of concrete and determine a test method to understand its effect, size effect behaviour was a subject of debate among researchers. It was concluded that in order to investigate size effect behaviour, various specimens with similar geometry but different spans or depths are required to be tested. Beams are usually used to investigate size effect phenomenon and it has now been demonstrated that size effect exists in the nominal strength of concrete structures (Lepech and Li, 2003, Ooi and Yang, 2010). In OC, Bazant and his co-workers who are pioneers in this field, have used a notched three-point bending testing method to determine the size effect phenomenon (Bažant, 1989, Bazant and Xu, 1991).

For FRCs with fine size aggregate and randomly distributed fibres, the three-point bending testing method has been used to determine the size effect behaviour (Lepech and Li, 2003, Lepech and Li, 2004). In addition, a BS standard has also recommended notched three-point bending testing method for FRC (British Standards Institution BS EN14651:2005+A1, 2007). Furthermore, despite intensive experimental investigation on material properties of UHPFRC, size effect of this concrete has been neglected and there is a lack of understanding of this behaviour. Therefore, this study aims to investigate this behaviour experimentally using a three-point bending test method.

In order to decide what parameters to choose to investigate the size effect, the following aspects were considered:

- The purpose of the experimental work
- The accuracy of the testing method
- Requirements related to undertake the experimental works
- Ease of undertaking the experimental work

With relation to the first and second aspects, it was important to consider the main aim of the investigation and in this study this was size effect. According to the previous studies mentioned and BS standard for FRC, three-point bending will give a reliable outcome to investigate the size effect behaviour. In terms of the requirement related to undertake the experimental works, softening behaviour was required to be considered in this study. To obtain the softening stage, all the tests were carried out under displacement control. According to the BS standard for the three-point bending test, displacement control is

required (British Standards Institution BS EN14651:2005+A1, 2007). The machine with displacement control is only adequate for specimens of a certain length as shown in Figure 3.3. In addition, in order to be able to do a direct comparison between the different sizes, it was important to obtain the same failure modes. Therefore, all the specimens were notched at the centre. The notching of specimens was done by wet sawing as this is a requirement in the BS standard.

In terms of the final aspect, it was important that the experimental works are executed easily so that accurate data can be obtained. Since the specimens needed to be notched using wet sawing, it would not be attainable if beams with longer spans such as 3 m or 4 m were prepared because the displacement control testing machine was not capable of testing such beams. Furthermore, the materials used in UHPFRC mixes and fibre in particular are expensive and this added another reason for testing smaller specimens. It is also desirable that the dimension of the tested specimens correspond to the commonly used sizes in previous studies and standards. However, the reliability of the results is the most important consideration. It should be expected that the testing method used in the present study gives repeatable results and have a low scatter.

3.3 Experimental Programme

All the UHPFRC beam specimens were tested under three-point bending, using a 300 kN Zwick hydraulic loading frame machine, which has a pre-load of approximately 2 kN. This pre-load is a machine default value, which is needed to open a servo valve before loading of the beam can start. The general machine set-up can be seen in Figure 3.3.

Figure 3.3: General set-up of Zwick test machine.

3.3.1 Materials and Mould Preparation

The mix design constituents used were silica sand with an average grain size of 270 μm supplied by WBB Minerals UK, Portland cement (type CEM I 52.5 N) and GGBS supplied by Hanson Heidelberg Cement Group, silica fume supplied by Elkem Materials, superplasticiser (type Eurocast200) supplied by FOSROC Ltd UK, tap water and steel fibre type OL13 with a tensile strength of 2000 MPa, 13 mm long and 0.2 mm diameter supplied by Bekaert Ltd. The mould dimensions of 150 × 150 × 500 mm were selected to be used to investigate three-point bending (British Standards Institution BS EN14651:2005+A1, 2007). The mould used to prepare the beam specimens was designed by previous researchers at the University of Liverpool, and was again used in this research study is shown in Figure 3.4.

Figure 3.4: Steel mould for preparation of prismatic elements.

The UHPFRC mix design used was determined by a previous researcher (Le, 2008) at the University of Liverpool. The type of superplasticiser used to develop the UHPFRC mix design was Structuro11180 due to the availability of this type at the time of the study. However, during the experimental work, Structuro11180 was updated for a better and more effective water reducer called Eurocast200. Therefore, an investigation to find the appropriate superplasticiser dosage was required to ensure the reliability of the UHPFRC mix design.

3.3.2 The Effect of New Superplasticiser on Mix Design

To investigate the effect of superplasticiser on the mix design, workability tests using a flow table test (British Standards Institution BS 4551-1, 1998) were conducted. The flow table test is one of the most reliable test methods to measure normal and SFRC concrete and it has been used for many decades. A total of 14 mix designs with different superplasticiser dosages and the same concrete composition were prepared and investigated. In addition, density and compressive strength tests were also conducted as mentioned in Table 3.1. The results are compared with those found using the old superplasticiser by the previous researcher (Le, 2008).

Table 3.1: Eurocast200 superplasticiser investigation.

Mix content			**Mix -1**	**Mix -2**	**Mix -3**	**Mix -4**	**Mix -5**	**Mix -6**	**Mix -7**	**Mix -8**	**Mix -9**	**Mix -10**	**Mix -11**	**Mix -12**	**Mix -13**	**Mix -14**
Cement, (kg/m^3)			657	657	657	657	657	657	657	657	657	657	657	657	657	657
Microsilica, (kg/m^3)			119	119	119	119	119	119	119	119	119	119	119	119	119	119
Ground Granulated Blast Furnace Slag, (kg/m^3)			418	418	418	418	418	418	418	418	418	418	418	418	418	418
Total Binders, (kg/m^3)			**1194**	**1194**	**1194**	**1194**	**1194**	**1194**	**1194**	**1194**	**1194**	**1194**	**1194**	**1194**	**1194**	**1194**
Silica Sand, (kg/m^3)			1051	1051	1051	1051	1051	1051	1051	1051	1051	1051	1051	1051	1051	1051
Steel Fibre 2%, (kg/m^3)			157	157	157	157	157	157	157	157	157	157	157	157	157	157
Superplasticisers, (kg/m^3)			25	25	27.5	30	30	30	32.5	35	35	37.5	37.5	37.5	40	40
Free Water, (kg/m^3)			202	197	195	208	191	193	191	188	189	185	187	187	185	185
Flow measurement (mm)			210	195	215	205	215	220	220	227	230	230	228	230	235	245
Density in 7 days (kg/m^3)	*(100x100) mm*	1- Sample one	2342	2332	2372	2407	2394	2347	2373	2390	2397	2400	2402	2395	2455	2424
		2-Sample two	2355	2335	2378	2424	2387	2351	2378	2384	2401	2409	2410	2400	2419	2411
		3-Sample three	2360	2329	2362	2429	2417	2359	2378	2386	2398	2412	2402	2403	2453	2405
	(50x50) mm	1- Sample one	2390	2347	2377	2408	2415	2346	2376	2416	2376	2393	2387	2396	2438	2428
		2-Sample two	2366	2333	2389	2431	2408	2370	2388	2385	2373	2392	2405	2376	2439	2396
		3-Sample three	2360	2342	2392	2421	2422	2372	2366	2393	2381	2395	2387	2399	2442	2422
Strength in 7 days (MPa)	*(100x100) mm*	1- Sample one	133	128	144	154	149	147	146	145	149	147	151	149	153	149
		2-Sample two	138	128	143	140	146	139	148	148	148	158	152	151	149	148
		3-Sample three	135	135	142	141	149	145	148	141	150	157	149	146	152	148
	(50x50) mm	1- Sample one	140	137	130	140	144	143	146	144	138	150	145	151	149	151
		2-Sample two	134	138	147	143	146	147	146	150	144	150	159	158	155	155
		3-Sample three	109	139	131	143	147	144	150	154	144	159	156	144	149	151

3.3.2.1 Flow Test Measurement and Cubes Preparation

All the mixes in Table 3.1 were prepared according to the mixing procedure explained by Le et al., (2007). After the flow table was cleaned and dried, the truncated conical metal mould which was 50 mm in height, 70 mm in top diameter and 102 mm in bottom diameter was placed at the centre of the table. The mould was filled with fresh concrete and it was then lifted away vertically and the table immediately jolted for twenty-five times in 15 s. Finally, four perpendicular diameters of the freshly spread concrete were measured immediately to determine the average diameter as shown in Figure 3.5a.

Alongside the flow table test, three 100 mm cubes and three 50mm cubes were cast (see Figure 3.5b) to measure the compressive strength of each mix proportion. After all the moulds were filled, they were shaken using a vibration table for less than 30 seconds. After the cubes were cast, they were covered with damp hessian sheets and kept at ambient temperature (~20^{o}C) for 24 hours before they were placed in the curing tank at 90^{o}C for 48 hours. All the specimens were tested after 7 days prior to casting.

(a) flow test (b) cube preparation

Figure 3.5: Superplasticiser investigation.

3.3.2.2 Density Measurement

Density is the physical property of material that measures the solidity of the concrete. After demoulding the cubes, the specimens were measured by recording their mass by weighing them in air (W_A) and then in water (W_W) using a steel stirrup as shown Figure

3.6. This was done by immersing the cube fully in water in the tank, ensuring that the stirrup did not touch the bottom of the tank. After the specimen was weighted in both air and water, the density was measured (British Standards Institution BS 1881-127, 1990) and is given by:

$$\rho = \frac{W_A}{W_W - W_A} \times 1000 \tag{3.1}$$

Test results may be affected by reinforcing steel fibre, by the chemical composition of concrete constituents, and by sample heterogeneity. Therefore for each mix, three samples were cast and tested. The density value was the average of the group of three specimens. The results are recorded in Table 3.1.

Figure 3.6: Density measurement.

3.3.2.3 Compressive Measurement

The compressive strength of UHPFRC mixes were measured using both 100 mm and 50 mm cube specimens. The purpose of making two different cube dimensions was to ensure that the mix had been done properly. To determine the compressive strength, the cubes

were tested according to (British Standards Institution BS 1881-116, 1983) with a 3000 kN TONIPACK compression test machine, as illustrated in Figure 3.7.

Figure 3.7: Cube positioned in the 3000 kN TONIPACK compression test machine.

After the specimens were prepared, the bearing surfaces of the testing machine were wiped clean to remove any loose grit or other extraneous material from the surface which may affect the results. The specimen was carefully centred on the lower platen of the 3000 kN compression test machine to ensure that the load would be applied to the two opposite cast faces of the cube as shown in Figure 3.7. After the specimen was positioned, the load was applied and increased continuously at a nominal rate of 0.3 kN/s until failure occurred and the results were recorded as shown in Table 3.1.

3.3.2.4 Results

The workability of those mixes with low dosage of superplasticiser Eurocast200 (25, 27.5 and 30 kg/m^3) was found to be slightly lower compared to those high dosage (32.5 to 40 kg/m^3). The lower dosages of between 20 to 35 kg/m^3 of superplasticiser also showed lower compressive strengths of 130 to 143 MPa, while the higher dosage of 37.5 and 40 kg/m^3 showed a strength around 150 MPa. Le (2008) suggested a superplasticiser dosage of 40 kg/m^3 to be used in order to obtain a compressive strength of more than 150 MPa

and density between 2400 to 2500 kg/m^3. In addition, the density results showed that the 37.5 kg/m^3 dosage of Eurocast200 was very similar to the density of the old superplasticiser reported with the density between 2400 to 2500 kg/m^3 (Le, 2008). The investigation showed that the lower dosage of new superplasticiser can be used. However, the concrete mix batches for preparing the slabs were much greater than the trial-error batches. Therefore, to avoid any workability issues, the dosage of 40 kg/m^3, which is similar to the old superplasticiser, was also selected for the new type superplasticiser in this study. As the effect of material constituents on compressive and tensile strength was explained in detail in Sections 2.3.1 to 2.3.8, the purpose of superplasticiser in UHPFRC is to improve workability due to the very low water/cement ratio used in UHPFRC mix design. Without the use of this water reducing agent, a workable UHPFRC paste cannot be obtained. As mentioned in Section 2.3.5, the combination of superplasticiser with other cementitious materials such as microsilica results in an increase in the strength of the cement paste. Superplasticiser can also decrease void size and gives better distribution of the different components in the cement paste (Mehta and Aitcin, 1990, Puertas et al., 2005). However it was shown by Le (2008), the use of superplasticiser improves the cement paste if the right volume is added in the mix. Over-dosing with this water reducing agent will have no affect on cement paste strength but will affect its workability.

3.3.3 Mix Design and Specimen Fabrication

UHPFRC beams with 2% by volume steel fibres ratio to mortar matrix were prepared. The mix design of UHPFRC investigated in this study was developed at the University of Liverpool (Le, 2008) as detailed in Table 3.2. As this study is a continuation of a wider investigation of this particular UPHRFC, it was important to use the Le (2008) mix design to further explore the structural behaviour of this UHPFRC mix design. A study by Hassan (2013), which also started before this current study was primarily focused on determining the experimental test method to obtain material properties of this UHPFRC. Therefore, it was important to use the same mix design to better understand this concrete and its applicability for future use. In addition, as explained in Chapter 2, other types of FRCs were also studied and they were found to have a number of drawbacks.

Table 3.2: UHPFRC mix design.

Mix Content	kg/m^3
Cement (CEM I 52.5)	657
Ground Granulated Blast Furnace Slag (GGBS)	418
Microsilica (Silica Fume)	119
Silica Sand	1051
Superplasticisers (Eurocast200)	40
Water	185
Steel Fibre 2% (OL13)	157
Total	2627

For the mixing process, a three-speed Hobart mixer (see Figure 3.8a) with the capacity of 90 litres was used to prepare all the specimens. Silica sand, SF, GGBS and cement were weighed and added slowly to the mixer and dry mixed for nearly 2 minutes (Figure 3.8b). Then water and superplasticiser were mixed together and slowly added to the mixture and mixing continued for another 5 to 7 minutes. After the cement paste mix became uniform, as shown in Figure 3.8c, the straight carbon steel fibres were slowly added by hand to the mixer and mixing continued for another 2 minutes to ensure the uniform distributions of the fibres, as shown in Figure 3.8c. The total mixing time was between 9 to 12 minutes depending upon the batch size. After the mixture was fully mixed, specimens were cast in moulds under a frequency vibrator for less than 30 seconds to ensure no air voids remained within the matrix. The filling of moulds was completed for all the specimens using scoops to move the UHPFRC from the mixing pan into the mould. The concrete was always placed in one end of the mould and allowed to flow to the other end in order to complete the filling and obtain uniform fibre distribution. The specimens were then covered with a damp hessian and a polyethylene sheet and allowed to harden at laboratory temperature (20^{o}C) for one day and undisturbed until final set had occurred.

After 24 hours the specimens were checked that they had adequate hardness. All the specimens were then taken out of the moulds and were placed in a special curing tank at 90˚C for two days. This high curing temperature accelerates the hydration reaction and

material hardening and results in increased strength at early ages (Schleyer et al., 2011, Barnett et al., 2006, Kamen et al., 2007). However, Hassan et al. (2012) has recently shown that the UHPFRC mix used in this study reaches its maximum strength within 7 days when heat treatment of 90ºC is applied. All the specimens prepared were tested after 28 days. Furthermore, care had to be taken during the demoulding procedure for specimens especially for thin beams to avoid cracks as their strength was not sufficient at this stage. A total of fifteen beams, with five depths d= 30, 60, 90, 120 and 150 mm, and the same width b= 150 mm and span l=500 mm were prepared, as illustrated in Figure 3.9. Three beams were prepared for each depth. Wet sawing was used to notch the test specimens. All the beams have a notch of depth $d_n = d/6$. A beam is named by its depth, for example, the beam D30 has d=30 mm.

(a) the mixer is empty (b) the mix constitutes

(c) the concrete paste (d) steel fibre added to the concrete paste.

Figure 3.8: Mixing procedure of UHPFRC

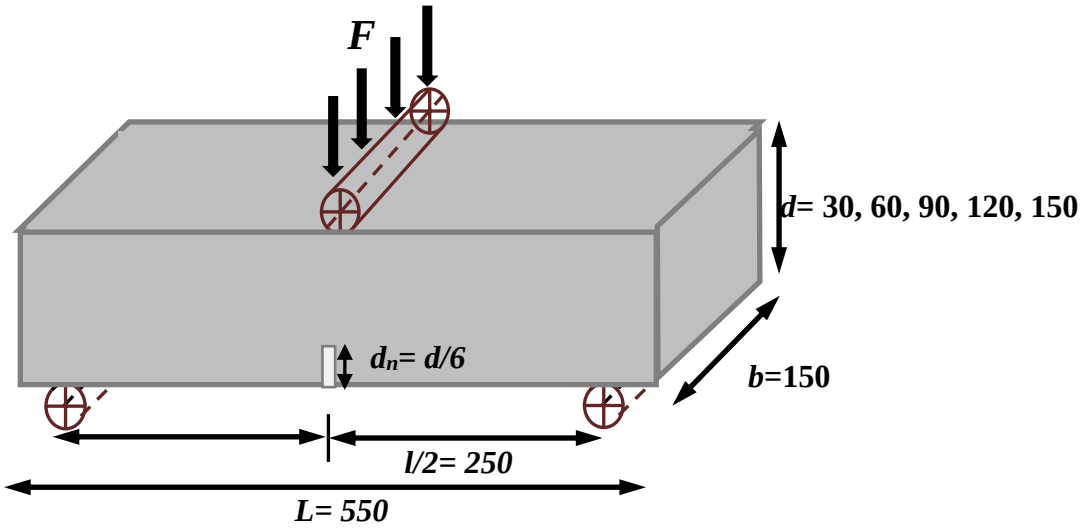

Figure 3.9: Specimen geometry (all the dimensions are in mm).

3.3.4 Testing Procedure

The testing machine shown in Figure 3.3 was adjusted to undertake the three-point bending test. The distance between the two semi-circular supports was set at 500 mm. To place LVDTs under the beam, a rectangular and an L-shaped steel member were glued to each side of the notch, as shown in Figure 3.10. The beam was loaded in a 300 kN hydraulic loading frame machine, and the load was applied through a semi-circular steel roller on the top surface of the specimen, 250 mm away from each support. Figure 3.11 shows the test set-up for the beam with d=120 mm as an example. CMOD was measured at mid-span by the two (LVDTs) with 9 mm range, which were fixed to a rectangular and an L-shaped steel support. Both LVDTs were connected to a computer, which calculated the CMOD data by averaging both LVDT values as shown in Equation 3.2. All the specimens were tested with a constant displacement rate of 0.2 mm/min.

$$CMOD = \frac{LVDT_1 - LVDT_2}{2} \qquad \textbf{(3.2)}$$

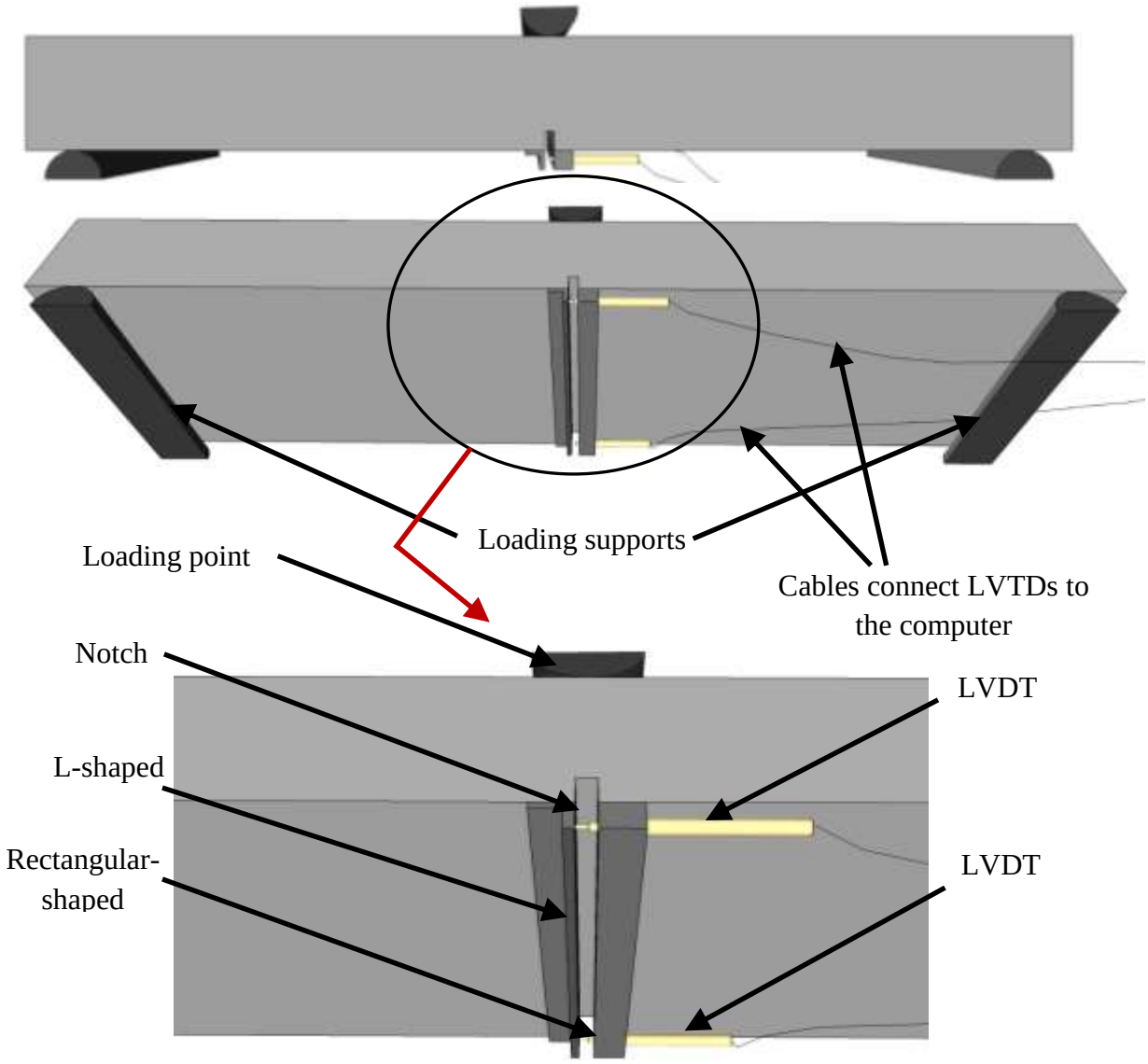

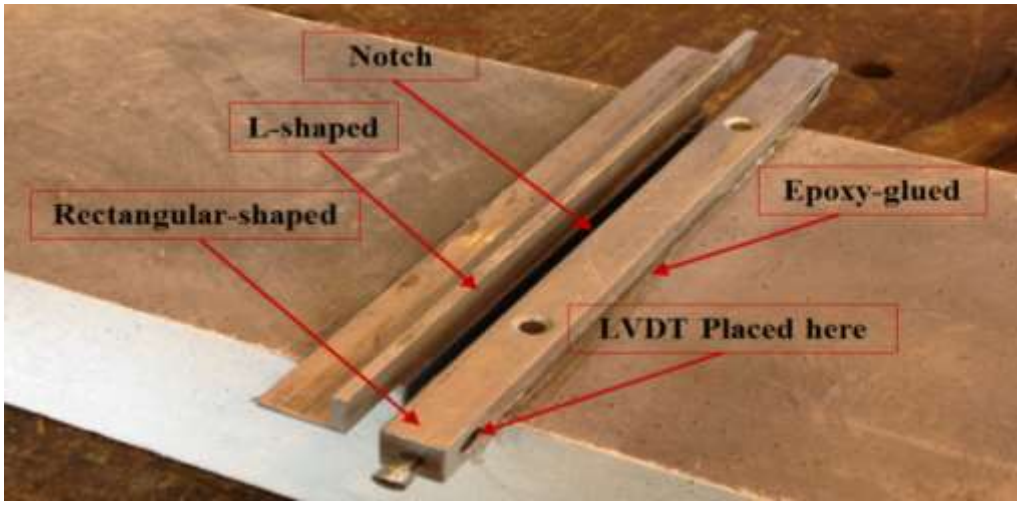

Figure 3.10: Beam specimen set-up showing the LVDT positions.

Figure 3.11: Test setup of notched 3-point flexure test of UHPFRC beams.

3.4 Results and Discussion

This section details the experimental results for beams specimens subjected to the three-point bending test. The results are for the investigation of structural behaviour of UHPFRC beam including the failure modes and load-CMOD relationship and crack propagation. The results also present an assessment of the relationship between the specimen size and nominal strength, and the relationship between this study to other related works in the literature on size effect.

3.4.1 Effect of Fibre Distribution and Orientation

It is reported that fibre distribution and orientation have a significant effect on failure modes in UHPFRC members. These effects depend on the member size, mix design, type of fibre used in the mix and pouring effect during preparation of the specimens. In order to understand this better, the results of this study and other studies reported in the literature are discussed.

A considerable number of studies have been conducted on fibre distribution in UHPFRC concrete and these studies have concluded that 100% fibre uniform distribution cannot be obtained due to the random distribution fibre in the matrix. However, there are techniques

which can be used during mixing and casting to enhance the uniformity of fibre distributions and to maximise fibre distribution. These techniques are adopted in this study as explained in Section 3.3.3.

When specimens tested with one dimension considerably smaller compared to the other two, fibres tend to align to the surface in thin specimens, thus more fibres contribute to the bridging action (Association Francaise de Genie Civil–Service d'etudes Techniques des Routes et Autoroutes (AFGC/SETRA), 2002, Dupont, 2003, Marković, 2006, Wille and Parra-Montesinos, 2012, Nezhentseva et al., 2013). The study conducted by Abdalla and Karihaloo (2003) and Ferrara and Meda (2006) reported that the geometry has an effect on fibre distribution (Abdalla and Karihaloo, 2003, Ferrara and Meda, 2006). The study conducted on fibre distribution and orientation by Pansuk et al (2008) and Kim et al (2008) also showed specimen geometry has a considerable effect on fibre distribution (Pansuk et al., 2008, Kim et al., 2008).

The most recent study of visual observations using X-ray Computed Tomography (CT) scanning by Nezhentseva et al (2013) showed that fibres in thinner sections tend to be parallel to the surface whereas in thicker sections the direction tends to be more randomly orientated. The higher the number of fibres parallel to the specimen's wall surface, the higher the number of fibres contributing to the bridging action. In addition, it has been shown that the fibre distribution orientation significantly affects fibre-bridging action and this depends on the shape of the specimen (Kang and Kim, 2011, Kang et al., 2011). It was also reported that the vertical wall effect has a significant influence on fibre distribution and the fibres tend to be parallel to the wall surface (Døssland, 2008, Wille et al., 2014, Sebaibi et al., 2014). This means in thinner specimens more fibres were aligned to the wall surface. A similar result was seen by Le (2008).

In UHPFRC, fibres are randomly mixed during preparing of the specimens and this randomness cannot be avoided due the size and amount of the steel fibres. In this study like other FRC or UHPFRC studies, fibres are randomly mixed as explained in Section 3.3. Since the first development of UHPFRC, numerous studies have been undertaken to understand how to control the fibre orientation in the UHPFRC matrix. Despite significant efforts, very little understanding has been obtained in terms of fibre orientation. The findings of some of these studies in the literature contradict each other but they all agree on two common points. First, fibre orientation is influenced by the

casting techniques and second that specimen geometry has a significant effect on fibre orientation and this is unavoidable.

The study conducted by (Petersson, 1998) on fibre orientation using X-ray photographs taken from the specimen's cross section showed that fibres were oriented into the flow direction and this was more pronounced for longer fibres. In UHPFRC, fibre pull-out behaviour depends on the orientation of fibres in the matrix. This orientation directly influences the number of fibres that contribute to the fibre-bridging action. Therefore, fibre pull-out behaviour has a direct effect on the mechanical behaviour and failure modes of UHPFRC (Grünewald, 2004, Stähli et al., 2008). Several researchers have studied the pull-out behaviour effect of different types of fibre such as hooked-end and straight. For the straight steel fibre used in this study, studies conducted by Naaman (1999) and Grunewald (2004) reported the embedded fibre length improves the pull-out strength and dissipation of energy during pull-out stage (Naaman, 1999, Grünewald, 2004). Grunewald (2004) also reported that the embedded fibre length depends on the fibre orientation and this increases with the increase in angle between the axial load and the fibres. This means that as the fibres align with the specimen's wall, the angle between the axial force and the fibre gets closer to 90º and the length of embedded fibre is the maximum. This demonstrates that the fibre orientation has a direct effect on the strength and failure modes of the specimens. Grunewald (2004) further investigated the effect of specimen geometry and fibre orientation and concluded that specimen wall effect has a considerable effect on the fibre orientation and the wall effect restricts the fibre to orientate freely in the matrix. This indicates that the thinner the specimen, the greater the wall effect on the overall fibre volume in the specimen. On the other hand, the effect of wall on the fibre volume/depth ratio in thin beams and slabs are greater compared to thick slabs. Furthermore, specimen size affects the fibre orientation as fibres are forced to align along the moulded surface (Lataste et al., 2009, Barnett et al., 2010).

Since slabs and beams with different geometries are tested in this study, it will not be surprising that fibre orientation influences the specimen ultimate strength and failure modes. In addition many studies have investigated the wall depth effect (i.e., the distance from the specimen wall to the point where fibre orientation is affected). Some studies have taken the wall affected depth as half the fibre length used in the mix (Soroushian and Lee, 1990, Association Francaise de Genie Civil–Service d'etudes Techniques des

Routes et Autoroutes (AFGC/SETRA), 2002, Dupont, 2003, Marković, 2006), while others have taken the full fibre length (Kooiman, 2000, Grünewald, 2004). For specimen thicknesses tested in this study, wall depth has a considerable effect on the ultimate strength, on thin specimen in particular. In addition, flow direction and casting technique have an influence on fibre orientation in UHPFRC specimens (Habel, 2004, Spasojevic, 2008, Yang et al., 2011b, Nezhentseva et al., 2013, Kang et al., 2011, Wille et al., 2014). Therefore, in this study careful consideration was given to casting technique during the preparation of the specimens.

In order to verify that the mixing procedure used to prepare the specimens resulted in the steel fibres being uniformly distributed throughout the matrix, an examination was carried out to investigate the fibre distribution where cracks occurred during the testing. Furthermore, to investigate the effect of specimen geometry, the physical fibres were counted at each cracked faces for each specimen thickness. To do this, specimens for each depth are opened out into two pieces where the macrocrack occurred as shown in Figure 3.12. A flow chart is used to illustrate the fibre distribution for each specimen thickness, where letter L is chosen for the left side of the beam and R for the right side. Beams are named by their depth, for example, left side of 30 mm deep beam named BL30. Fibres for each faces were counted as show in Figure 3.13.

Figure 3.12: Crack location of beam specimen with different thicknesses.

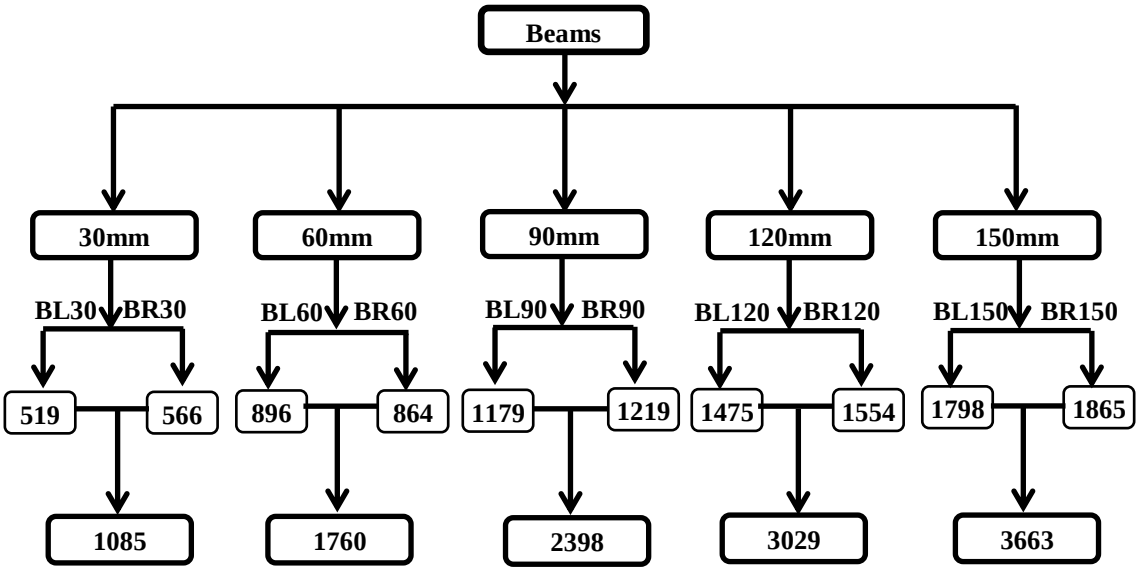

Figure 3.13: Fibre distribution of beams with different depth.

In order to compare the fibre distribution of beams with different depths (h), cross sections were analysed for the number of fibres (N) that bridge between the two cracked faces which were counted, as shown in Figure 3.12 and Figure 3.13. The more fibres that can be counted in the cracked faces the more fibres are aligned. If the fibres are perpendicular to the cross-section and uniformly distributed, this means more fibres bridged between the two cracked faces. Fibres that are parallel to the cross-section, and uniformly distributed, do not contribute greatly to the fibre bridging action.

The above figures show how the fibres are aligned in the specimen and confirmed the thinner the specimen the more fibres are uniformly distributed. The result clearly indicates uniform fibre distribution reduces as the beam depth increases. Looking at the beam with 30 mm depth, L30 has 519 fibres contributing to the fibre bridging action, while L60 for beam with 60 mm depth has only 896 fibres. A similar result was found when R30 was compared to R60. However, the comparison between the beams using one side of the crack may not give an accurate result. Depending on the fibre embedded length, one of the cracked face may have pulled-out more fibres than the other side during the fibre pull-out behaviour. Therefore, fibres on both faces were added for each beam as shown in the flow chart in Figure 3.13. The result of beams with smaller depths were compared to the larger ones. The N/h ratio of smaller beams was found to be greater than the larger beams and the amount of fibre bridging between the two cracked faces reduced in larger

specimens. The ratio for beams with 30 mm depth was found to be 36.13, while beams with 60 mm depth the ratio reduced to 29.33. Moreover, when L60 is compared to L90, L120 and L150, little difference was seen and fibre distribution was only changed by less than 3% as shown in Table 3.3. This finding can be very important in term of designing real life size UHPFRC structures. The result shows that, except for fibres close to the surface, fibre distribution at the centre of the beam with *h* greater than 5 times the fibre length (i.e., beams with 90 mm, 120 mm and 150 mm height), do not change significantly. This also demonstrates that the mixing procedure used in this study is an effective way to cast the UHPFRC specimens. However, physical examination showed that the fibre orientation at the centre for beams greater than 60 mm depth, changes from one specimen to another and fibres are not aligned over the whole area at the centre of the beam. This was not a surprise as fibre can freely rotate within the matrix in larger specimens.

Moreover Figure 3.12 shows that for beams with large depths the fibre orientation at the centre of the beam is less when compared to the areas near the wall for the same beam size. This figure clearly shows that fibres close to the wall are restricted and have to align with the beam wall. The differences in fibre orientation can also be due to the flow of the fresh concrete during the casting stage as it can be faster at the centre than near the wall (Stähli et al., 2008). In general, it was clear both fibre orientation and distribution changes as the size of the specimens changed but the rate of these changes was very minimal for beams with thicknesses greater than 60 mm. Therefore, it can be concluded that the fibre distribution of real life size beams may be similar to those tested in this study. However, this conclusion may need to be validated experimentally before it can be used extensively.

Table 3.3: Fibre distribution of different beam sizes.

Beams	Number of fibre (*N*) for both cracked faces	Increase in fibres with respect to thickness	*N/h*	Reduction in *N/h*
D30	1085	1085	36.17	-
D60	1760	675	29.33	6.83
D90	2398	638	26.64	2.69
D120	3029	631	25.24	1.40
D150	3663	634	24.42	0.82

3.4.2 Failure Modes

Since all the beams were notched in the centre, they all failed in flexure with a major crack through the beam depth. Figure 3.14a-e show the typical failure modes of the five beams. It can be seen that, although the beam geometry, boundary and loading conditions are all symmetric, the cracks in some of the beams are slightly tortuous and deviate away from the beam mid-span. This should be attributed to the random distribution and orientation of steel fibres (Wille and Parra-Montesinos, 2012, Spasojevic, 2008), which make the crack-tip stress fields complicated and the local tensile strength and fracture toughness highly heterogeneous, as in conventional concrete where the aggregates function similarly to the steel fibres (Lepech and Li, 2004). This cannot be accurately simulated by the homogenous models adopted in this study, and can only be simulated by those models considering the random heterogeneity directly (Su et al., 2011) or indirectly (Wille and Naaman, 2012). In addition, beam failure modes show that the crack deviation increased with an increase in the beam depth. This implied that most of the fibres tended to be in alignment with the direction perpendicular to the crack plane in thinner specimens, thus reducing the fibre randomness in the matrix, resulting in less deviation in crack patterns.

Referring to the photographs of crack propagation, the flexural behaviour of the UHPFRC beams was determined in the three different stages. The first was the linear-elastic stage, where both matrix and fibres behaved elastically. The maximum flexural strength attained in this stage corresponded to the matrix strength while the fibre contributed little to the overall structural behaviour (Spasojevic, 2008). The matrix at this stage has not cracked due to the axial force except for existing microcracks that may have occurred in the concrete due to the shrinkage in the hardening stage. At this stage, no permanent deformation takes place and the moduli of elasticity of UHPFRC and UHPC (without fibre) were found to be identical in an experimental investigation conducted by (Hassan, 2013). The deformation at the elastic stage is also very little in UHPFRC, therefore, it is unlikely that fibres greatly contributed to the flexural strength. Although, it must be acknowledged that this is not a proven hypotheses and it has not been shown experimentally that fibres have no contribution at this stage. Beams at this stage showed no sign of cracks in both tensile and compressive faces.

The next stage followed with the appearance of microcracks near the notch where the matrix cracking strain was exceeded. As the load increased, the microcracks merged into a single macrocrack above the notch. The crack surfaces were bridged by closely spaced steel fibres. Due to the high strength of the steel fibres and the strong bond between the fibres and the matrix, the macrocrack widens slowly in this stage, leading to a certain level of strain hardening. This strain hardening behaviour distinguishes UHPFRC from conventional types of concrete. This stage is called the pseudo-strain hardening stage.

After a considerable deflection, where the fibres were no longer capable of sustaining maximum tensile stress, due to the increase in crack width, the final stage of the beam specimen occurred as a single macrocrack localised in the section. This stage is called the descending region (softening region). Similar to the previous stage, this region is very pronounced for UHPFRC and is controlled by fibre pull-out across the concrete crack and fibre pull-out depends on the type and length of the fibre. The deformation behaviour in this stage is related to half the length of the fibre, 6.5 mm in this study. It is important to mention that, although the beam had failed at this stage, the beam segments were held by fibre-bridging at the top of the section, where the crack width is smaller than half the length of the fibre for beams with small depth and intact zone in compression zone for beams with large depth. This fibre-bridging behaviour acts in a similar manner to the top reinforced bars in OC.

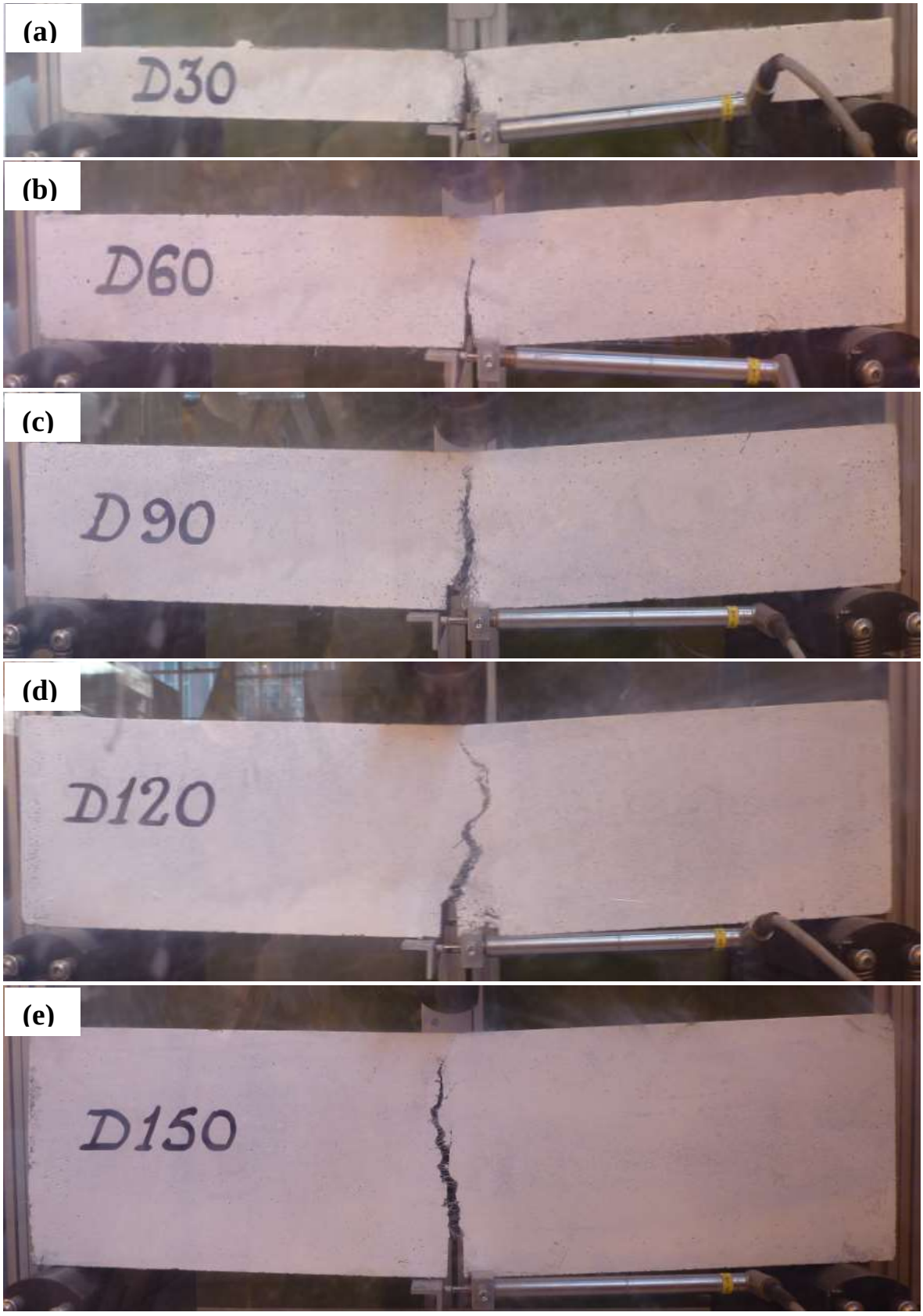

Figure 3.14: Cracks at failure of 5 beams (a) D30 (b) D60 (c) D90 (d) D120 (e) D150.

Furthermore, it was also observed that the load increased at a very small rate in the pseudo-strain hardening phase compared with the elastic phase and high deformation took place with a reduced modulus of elasticity. It is important to mention that the CMOD in the softening stage had increased significantly when compared with the strain hardening stage. This behaviour can be due to weakening of the bond between the matrix and the steel fibres during the pseudo-strain hardening phase. UHPFRC contains short, straight, high tensile steel fibres with a yield strength of greater than 2,000 MPa, in addition, the bond between the matrix (with compressive and tensile strengths of up to 240 MPa and 20 MPa, respectively) and steel fibres in UHPFRC, is approximately around 10 MPa (Wille and Naaman, 2012). Therefore, it was unlikely that fibre yielding had occurred. Closer examinations of the fracture surfaces as shown in Figure 3.15 also confirmed that all the beams failed with fibre matrix interface debonding, not fibre pull-out.

Figure 3.15: Fracture surface with pulled-out steel fibres.

Moreover, tensile testing figure obtained from the manufacturing supplier (Bekaert) shows that the fibre stress-strain curve goes under two stages as shown in Figure 3.16. The first stage is a linear elastic where stress linearly proportional to strain and it ends at

a stress of 2000 MPa which has a corresponding strain of 0.009. As the stress exceeds a value corresponding to the yield strength, the fibre undergoes plastic deformation. The stress to produce plastic deformation increases with increasing plastic strain, resulting in a nonlinear stress-strain relationship. This part of the curve ends at around 3000 MPa where the fibre reaches its peak yield stress and ruptures. Comparing the tensile strength of a single fibre used in this study to the tensile strength of UHPFRC, it would be impossible for the fibre to have yielded during the specimen testing.

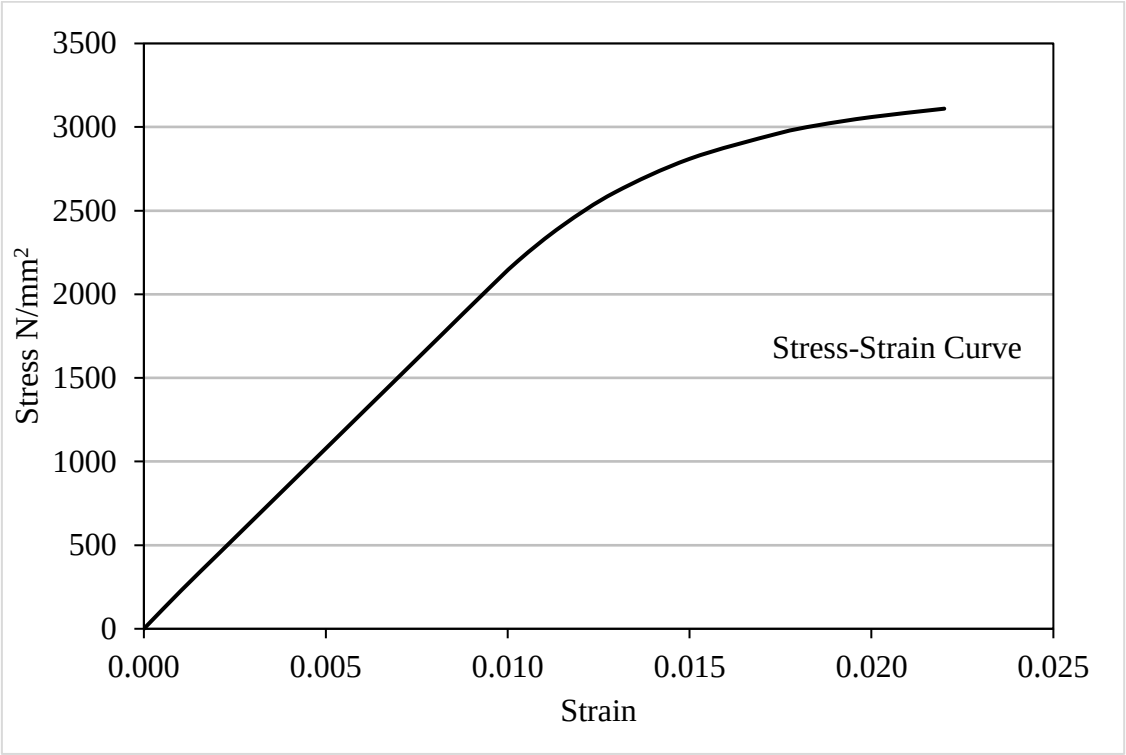

Figure 3.16: Stress-strain curve for a single steel fibre.

The failure mode in these beams was imposed by the notch at the centre of beams as shown in Figure 3.17. The notch encourages the beam to fail at a point where the loading is acting. It developed a concentrated stress at the centre point and this caused the beam to reach its flexural strength before other regions of the beam develop shear forces. On the other hand, having the notch has made a weak point at the beam centre and prevented the beam from exhibiting a longitudinal movement to develop shear stresses on longitudinal planes.

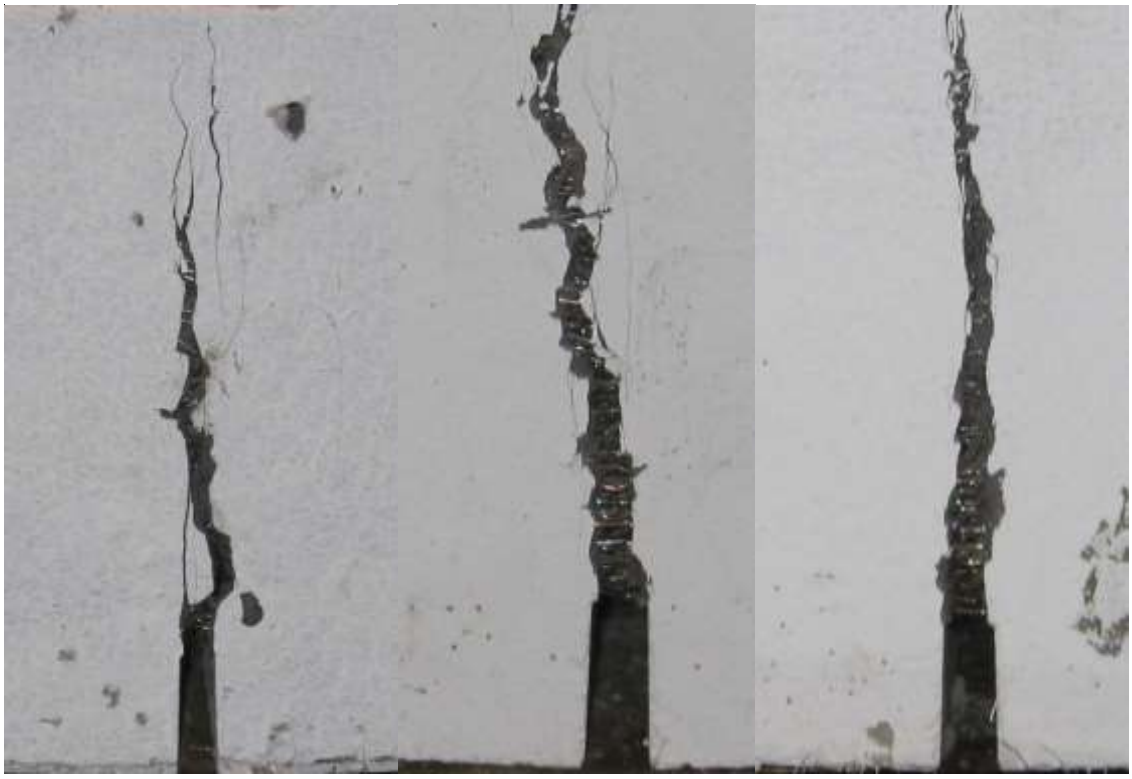

Figure 3.17: Shows fibre bridging action.

If the beams were not notched, the crack propagation would have been different. In the literature, it has been reported in many studies that OC beams with the short spans and large depths fail in shear. These shear failure modes would depend on beam geometry, concrete properties and the number of steel reinforcement bars as explained in Section 3.1.2. However, the four-point and three-point bending tests conducted by (Le, 2008) on beams without notches with depths 100mm and 150mm, respectively. The results showed all the beams failed in flexure with a single macrocrack initiating from the centre of the beam towards the compression zone. Further tests on four-point bending by (Hassan, 2013) confirmed that beams with 100mm depth failed in flexure with a single macrocrack in the tensile zone where the load was applied. This demonstrated that fibres have a transformed failure mode from shear to flexure. Furthermore, several unnotched UHPFRC beams with depths of 40mm and 100mm were tested by (Magureanu et al., 2010) using the three-point bending test and the results showed that all fail in flexure with a single macrocrack

In regards to beams with larger spans, Furlan Jr (1997) tested several fibre concrete beams with a 1000mm span and 100mm depth and the results showed all the beam failed in shear with several microcracks and macrocracks along the span of the beam (Furlan and de Hanai, 1997). However, a study conducted by Yang et al (2011) on UHPFRC beams with a span of 2900mm and 270mm depth showed a single macrocrack flexural failure with multiple microcracks initiated linearly on both side of the macrocracks (Yang et al., 2011b). Furthermore, the recent study conducted by Fujikake (2014) has shown UHPFRC beams with a 1700mm span with 200mm depth failed in flexure with a single macrocrack at a point where the load was acting (Fujikake, 2014). At each side of the macrocrack, there were also numerous microcracks covering 1100mm of the span. This clearly indicates that the failure modes of UHPFRC beams with larger spans cannot simply be predicted and there is a possibility of both flexure and shear failure modes, thus further experimental investigations are required.

3.4.3 Load-CMOD Curves

The three load-CMOD curves and the average curve from the bending tests are shown in Figure 3.18 to 3.22, for each beam depth. Due to random distributions of discontinuous short steel fibres, scatter in the experimental results of three tests for one beam design especially in the softening region were within 10% of the mean response. Therefore, the three beam specimens for investigation of bending behaviour were found to be adequate as this was a case reported in (Wille and Parra-Montesinos, 2012). Table 3.4, summarises the experimental peak loads F_b and the nominal flexural strength f_f of all the beams which were found using equation 3.3 from (British Standards Institution BS EN14651:2005+A1, 2007).

$$f_f = \frac{3F_b l}{2b(d-d_n)^2} \qquad \textbf{(3.3)}$$

where l is the span length between the two roller supports, b is the beam width, d is the beam depth and d_n is the notch depth.

Figure 3.18 to 3.22 show that all the beams exhibit linear elastic behaviour up to the appearance of microcracks around the beam notch and ends before the CMOD reaches 1 mm. In this region, the load was carried by the matrix strength alone but as the load increased, the microcracks started to form. A slow reduction of elastic modulus occurred as the curve changed from linear to nonlinear behaviour and the material entered the pseudo-strain hardening region. This continued as the number of microcracks increased with the increased applied load, and resulted in the material reaching its ultimate load carrying capacity. The increase of CMOD is very slow in this region and except for D30, which failed at a CMOD of approximately 0.4 mm, all the beams failed at CMODs between 1 to 1.5 mm. The figures show that the load-CMOD in this region reached about 80 to 90% of its ultimate load carrying capacity. The shape of the load-CMOD curves are strongly dependent on the number of fibres that were bridging between the two cracked faces. This indicates that the material properties can be improved by enhancing the bending behaviour.

After the beam failed, the strain softening region began with a considerable reduction in the applied load. In addition, as the load increased, more slipping between fibres and the matrix occurred and the increase in CMOD was significantly faster in this region compared to the two previous regions. Furthermore, as expected, the load-CMOD showed that the beams with greater depths could withstand a greater load than the shallow beams. However, a gradual change to brittle behaviour in the strain hardening then the softening region was observed in thicker beams.

Table 3.4 shows that the F_b for beams with a depth of 30 mm ranged from 2.5 to 3.5 kN, with an average of 3.17 kN. As the depth doubled, the average F_b increased significantly and a value of 10.13 kN was recorded. After the beams with 90 mm depth had been tested, the increase in average F_b was only doubled and a value of 22.03 kN was recorded. The increase of average F_b kept reducing with an increase of the beam depth, where the larger beam (d=150 mm) only increased by 48% compared to the beam with a depth of 120 mm. In other words, the effect of beam depth on average F_b reduced with the increase of specimen depth. This is due to the effect of fibre-bridging action on the pseudo-strain hardening behaviour, whereas in shallow beams more fibres contribute to the fibre-bridging action than for the beams with greater depths.

As explained, the load carrying capacity of UHPFRC members is dependent on the fibre-bridging in the pseudo-strain hardening region. In shallow beams fibres tend to align parallel to the longer side of the beam, meaning more fibres and the full fibre length contribute to the fibre-bridging action, thus an increase in the ultimate load carrying capacity of the beam. But as the beam depth increased, the fibres were positioned at larger spaces in the matrix and no longer tended to align perpendicular to the direction of the force, resulting in a smaller number of fibres available to bridge between the two cracked faces. Therefore, the fibre inclination angle increased resulting in fibre pull-out in a width smaller than the length of half a fibre. However, it is important to mention that a considerable scatter, especially in the softening region, can be observed in three beams of similar depth. Since in UHPFRC the fibres are randomly mixed during the casting procedure, apart from certain casting and mixing techniques explained in Section 3.3.3, uniform fibre distribution is highly unlikely. It is clear that 100% random fibre distribution cannot be achieved in any fibre concrete, so a considerable variation between specimens with the same geometry and fibre volume ratio is not surprising. Therefore, the possibility of scatter in the results for UHPFRC beams must be taken into account if the softening region is considered. Table 3.4 shows, except for smaller beams, the standard deviation (SD) of the flexural strength is less than 2 MPa and this gives a standard error (SE) of less than 1.5 MPa. This shows the variation between the experimental values is small and confirms the accuracy of the experiments.

As explained, fibre bridging action involves the bond between steel fibres and the matrix and this bond can be represented in segments or layers. After the concrete cracks, the first layer of fibres, which are the closest to the tip of the crack, bridge between the two cracked faces. As the crack became wider, the first layer of fibre pulls-out and the next layer bridges between the two cracked face and this process continues until the element completely fails. Figure 3.21 and 3.22 show sudden drops at the beginning of the softening stage, as can be seen for beams with depths of 120 mm and 150 mm. The reduction in load in the softening stage depends on the distribution and angle of fibres that contribute to the bridging action. As mentioned previously, fibres can orientate more freely in beams with larger depths and so are less influenced by the wall effect. Therefore, the length of embedded fibres in some parts of the cracked area can become shorter due to the angle of fibres contributing to the bridging action. This results in sudden drops of load at some parts of the softening stage for some of the beams with a larger depth.

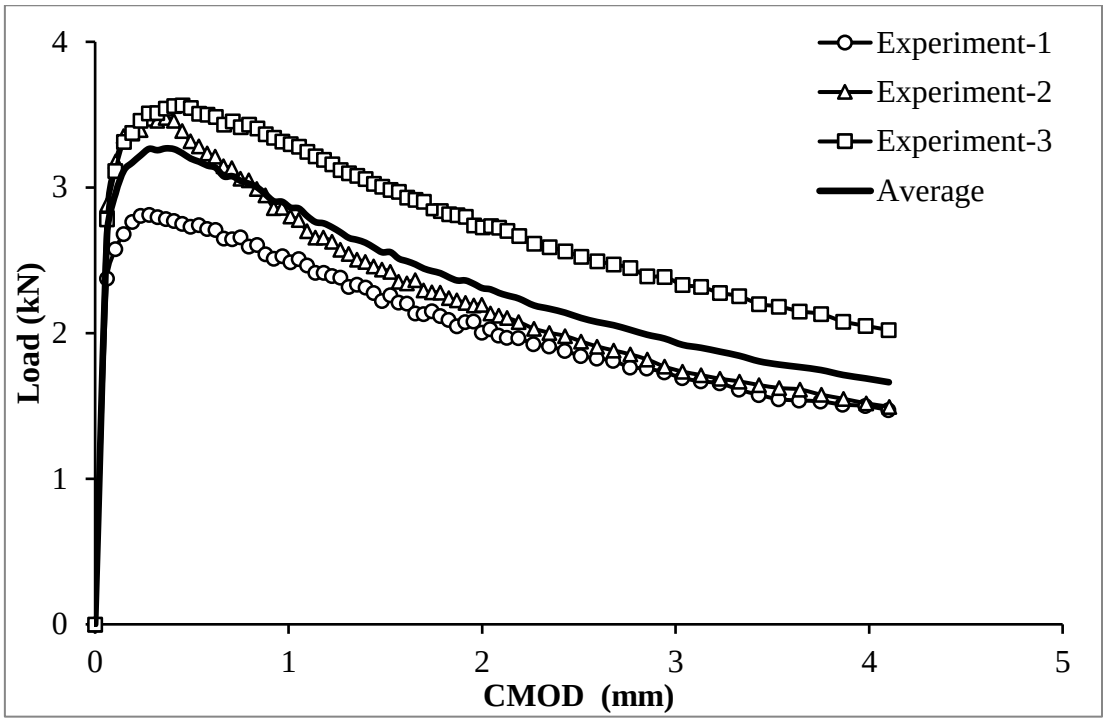

Figure 3.18: Load-CMOD curves for beams with 30 mm depth.

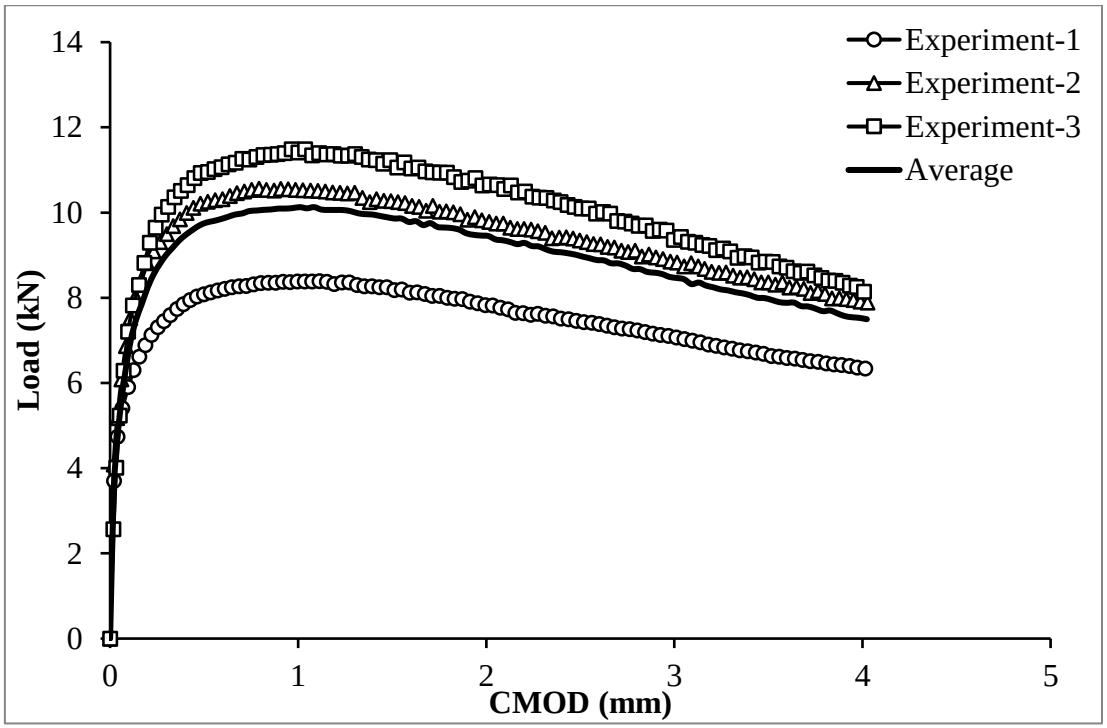

Figure 3.19: Load-CMOD curves for beams with 60 mm depth.

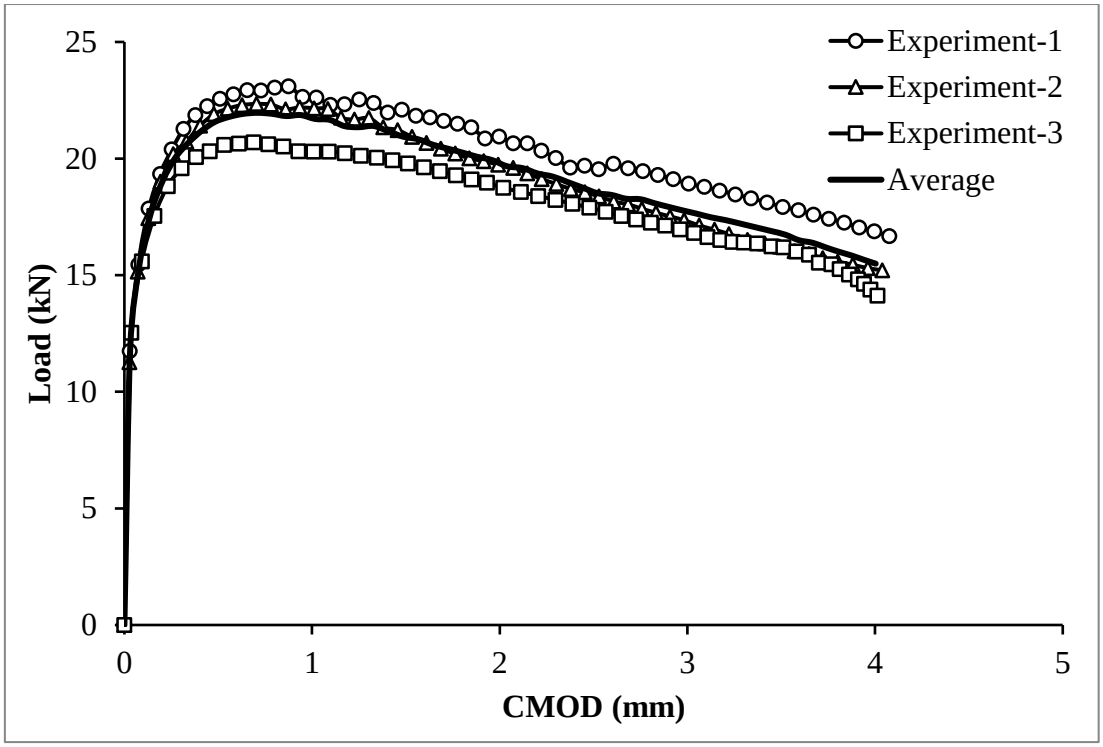

Figure 3.20: Load-CMOD curves for beams with 90 mm depth.

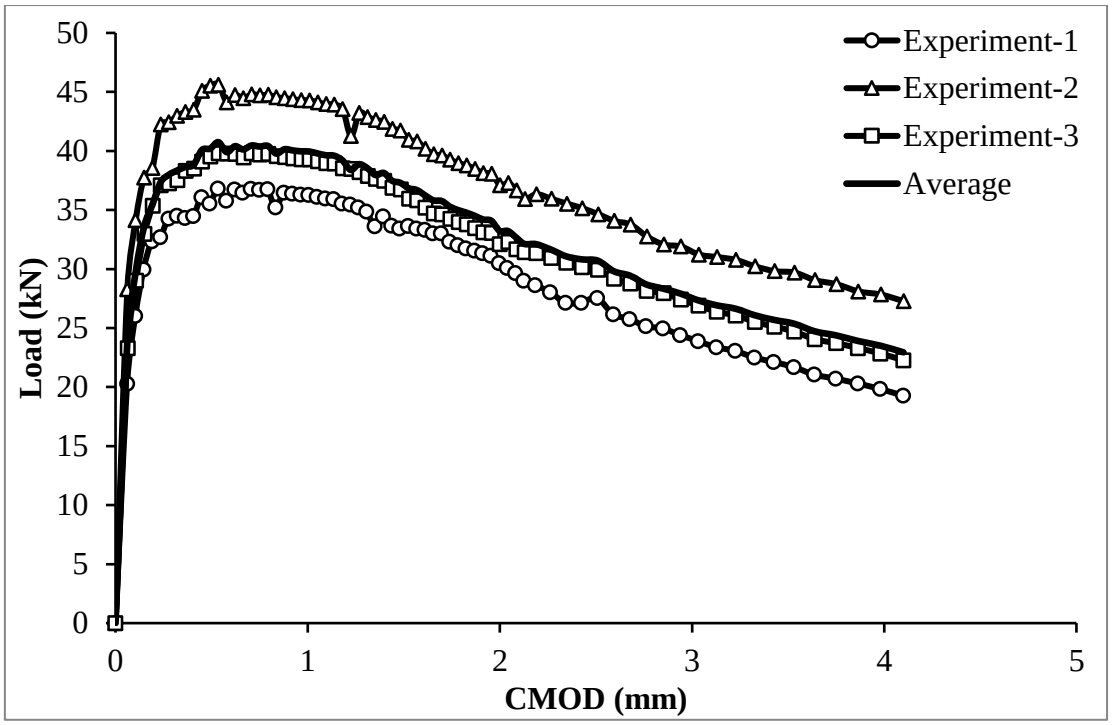

Figure 3.21: Load-CMOD curves for beams with 120 mm depth.

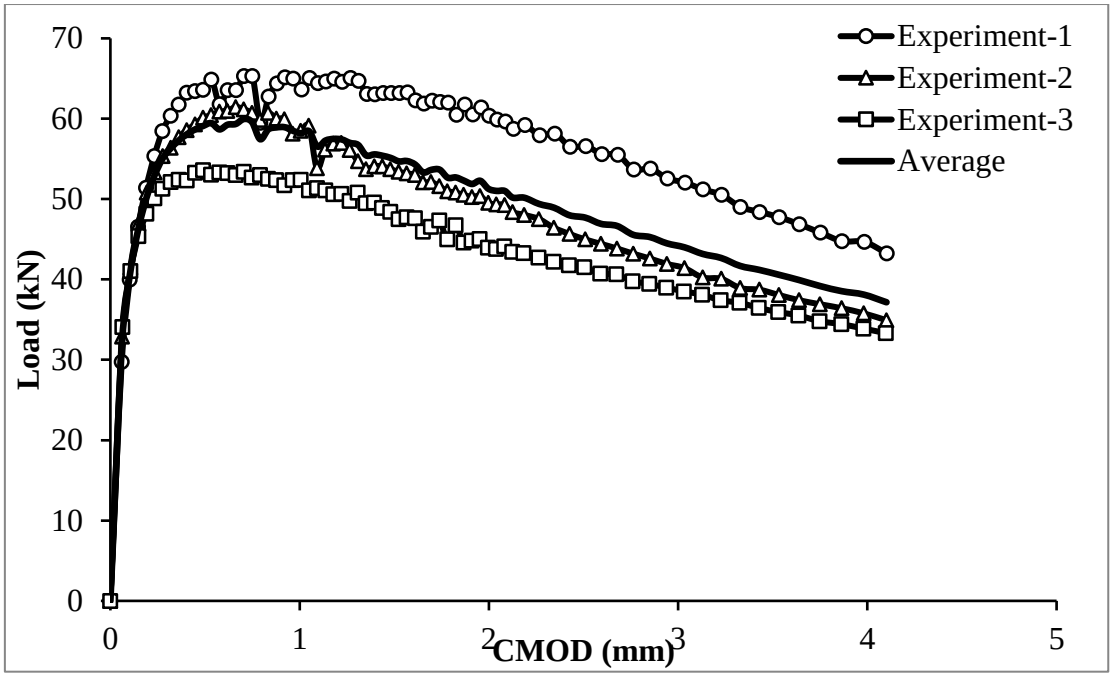

Figure 3.22: Load-CMOD curves for beams with 150 mm depth.

Table 3.4: Experimental results for three-point bending tests.

	No.	Experimental peak load F_b (kN)	Average F_b (kN)	Nominal flexural strength f_f (MPa)	Average f_f (MPa)	Standard Deviation SD/ Error SE (MPa)
D30	1	2.5	3.2	20.0	25.3	3.7/2.1
	2	3.5		28.0		
	3	3.5		28.0		
D60	1	8.4	10.1	16.8	20.3	2.5/1.5
	2	10.5		21.0		
	3	11.5		23.0		
D90	1	23.1	22.0	20.5	19.6	0.8/0.5
	2	22.3		19.8		
	3	20.7		18.4		
D120	1	36.8	40.7	18.4	20.3	1.8/1.1
	2	45.6		22.8		
	3	39.8		19.9		
D150	1	65.3	60.1	20.9	19.2	1.5/0.9
	2	61.5		19.7		
	3	53.6		17.2		

3.4.4 Size Effect

The nominal flexural strength f_f versus log d from all the experimental results is plotted in Figure 3.23. It can be seen that, except for the smallest d=30 mm, the nominal flexural strength for all the other beams is around 20 MPa and the strength does not depend on the size of the element. This is due to the scatter of results which is greater than the size effect. This clearly indicates that the size effect in concrete can be eliminated through the use of material with a high ductility such as UHPFRC. This result opposes the concrete fracture mechanics hypothesis that the ratio of the total crack surface area to the cross-section area of smaller specimens is believed to be higher than that of larger specimens. As mentioned in Section 2.6 and Figure 2.14, the generalised size effect law is divided into three different regions.

According to the theory, classical LEFM predicts the size effect for those structures, where member sizes are the largest and nominal strength is proportional to the square root of nominal member size (Lepech and Li, 2004). This represents those materials that are ideally brittle and the FPZ is very small compared to overall structure member size. In these structures, all fracture energy is consumed at the crack tips. The second part of the curve represents structures with smaller size or material which is less brittle such as concrete and rock. The theory, which was developed by Bažant through the application of NLFM showed, due to the heterogeneity of the material, the FPZ surrounding the crack tips is relatively large with respect to the overall member dimensions, while LEFM requires FPZ to be small. This result is not only contradictory with the LEFM assumption, but it is also proven that the nominal strength in normal reinforced concrete decreases with an increase in structure size. It also showed that in concrete, FPZ of the nonlinear zone is very large compared to the cross section of the structure. The final part of the curve represents the strength theory, where the specimen size becomes much smaller or the material shifts from brittle to ductile, the effect of fracture size will diminish due to the enlargement in the FPZ surrounding crack tips. Based on the results, this study places the UHPFRC material in the strength zone on the generalised size effect law curve in Section 2.6, Figure 2.14, where the material is much less brittle compared to OC. This confirms that the size effect in structures made of cementitious materials can be eliminated by adding a high volume of ductile fibres (Lepech and Li, 2003, Lepech and Li, 2004). Most recently, it has been showed that changes in beam specimen sizes had little influence on the peak flexural strength (Wille and Parra-Montesinos, 2012).

Moreover, the result is in contradiction with Bažant's hypothesis that concrete obeys NLFM. Therefore, it would appear that UHPFRC does not follow the existing size effect law of conventional concrete.

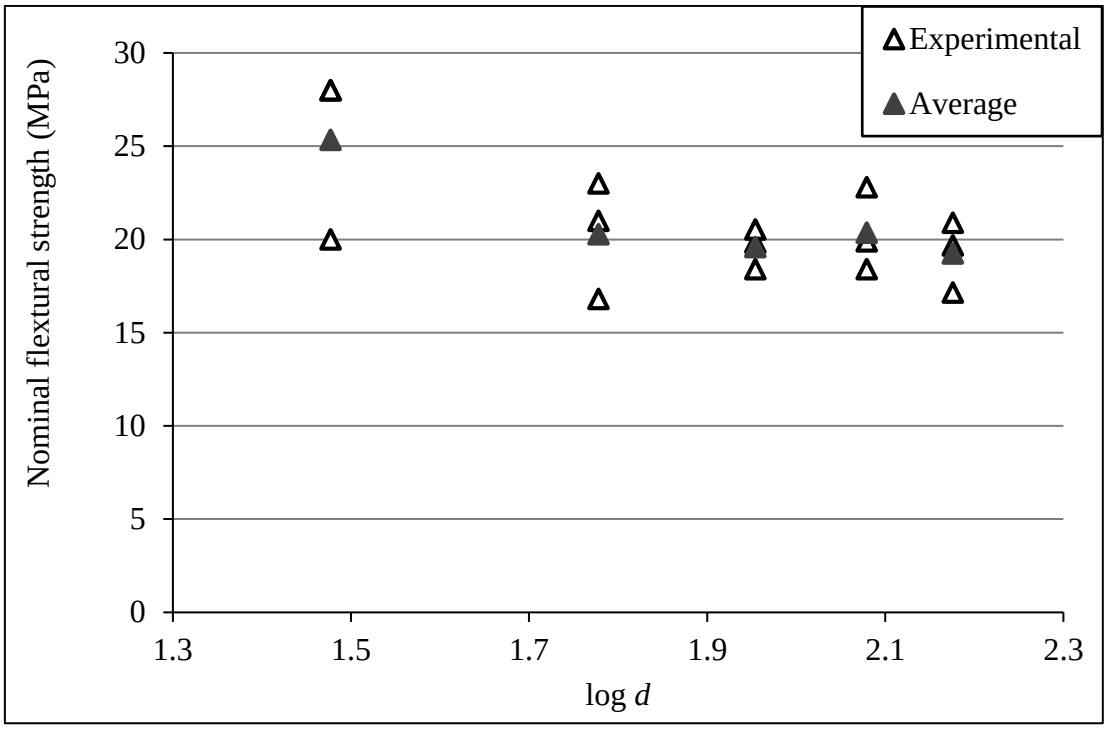

Figure 3.23: Size effect on the nominal flexural strength of UHPFRC beams.

3.5 Concluding Remarks

The effect of the new superplasticiser type Eurocast200 on the UHPFRC constituent has been studied using flow tables, density and cube compressive tests. The new superplasticiser was found to be more effective than the old one in terms of workability. The new type of superplasticiser with 40 kg/m^3 gives a compressive strength and density of greater than 150 MPa and 2400 kg/m^3 respectively, which is similar to the result of the previous type of superplasticiser used by Le (2008).

The results showed that all the beam specimens failed in flexure with a single macrocrack, propagating from the tip of the notch upward due to the loading condition imposed by the notches in the testing configuration. The load-CMOD relationship showed the beam specimens underwent three different stages and these were pure elastic, pseudo-strain

hardening and strain softening and all the failures occurred due to fibre pull-out not fibre yielding. The increase of CMOD was found to be slower in the strain-hardening region and all the beams reached their ultimate strength at a CMOD between 1 to 1.5 mm. However, the effect of beam depth on ultimate strength diminished with the increase of specimen depth due to the effect of fibre-bridging action. The length of embedded fibres during fibre bridging action when concrete cracks relies on the fibre orientation within the matrix. Therefore, the material ultimate strength and crack patterns depend on fibre orientation. The fibre orientation in thin specimens is controlled due to the effect of the specimen wall surface while in thick specimens fibre orientation is more random. Moreover, the fibre distribution investigation showed that the numbers of fibres contributing to the fibre bridging action in the cracked area changed as the specimen size changed. The examination showed fibre orientation reduces as the thickness increased. This change is only significant when the specimen thickness is less than three times the fibre length. The examination also showed the number of fibres contributing to the fibre bridging action in the cracked area were not proportional to an increase in the specimen depth.

Since the first appearance of UHPFRC, extensive experimental investigations have been conducted but the size effect behaviour which can be challenging for the design engineer, has been neglected. This study is one which thoroughly investigates the size effect behaviour using extensive experimental and numerical modelling. It advances knowledge of this particular type of UHPFFC in terms of its size effect behaviour. The finding of this study shows that the flexural strength for all sizes was found to be around 20 MPa. The results of this study also showed that the existing size effect of conventional concrete cannot be employed for UHPFRC members as concrete shifts from brittle to ductile behaviour. Therefore, the existing size effect law of conventional concrete needs to be modified or a new theory of size effect for UHPFRC members needs to be developed.

CHAPTER 4

ONE-WAY SLAB INVESTIGATION

Details of an experimental investigation of the bending behaviour of one-way spanning slabs including mould fabrication, designed experimental setup and testing procedure are described in this chapter.

The majority of engineering structures such as bridges and buildings involves designing one-way spanning slabs. To understand the response of such structures requires a comprehensive and detailed examination. Due to the uncertainty of true boundary conditions of slabs in engineering structures, especially in bridges, the experimental study was conducted with two different boundary conditions; fully fixed (FF) and simply supported (SS).

A total of twenty-six (660 × 660) mm slabs containing 2% by volume of short steel fibres were tested under bending test with four different thicknesses. The experimental work was divided into two test series of UHPFRC slabs. The first test series was conducted on 13 No. UHPFRC slabs with FF supports on two opposite edges while, the second test series was conducted on 13 No. specimens with SS supports on two opposite edges. In both series the adjacent edges were free unsupported edges. The effect of boundary conditions and geometries using an experimental approach to determine the load-displacement relationship, failure modes and crack propagation under bending test are also discussed in this chapter.

In order to verify that the mixing and casting procedures used to make UHPFRC slabs result in the steel fibres being uniformly distributed, and to determine the effect that the specimen geometries have on fibre distribution, an experimental investigation was carried out in this chapter. The investigation is based on counting the number of fibres that bridge between the two cracked faces, and to determine the relationship between the fibre distribution and slab thicknesses. The relationship between the thickest slab (60 mm) and life-sized structures in terms of fibre distribution and orientation is also discussed.

4.1 Experimental Programme

The experimental work for one-way spanning slabs was divided into two test series with 2% by volume steel fibres ratio to mortar matrix. The first test series was conducted on 13 No. UHPFRC slabs with FF supports on two opposite edges while, the second test series was conducted on 13 No. specimens with SS supports on two opposite edges, as shown in Figure 4.1. A total of twenty-six (660 × 660) mm slabs were tested with four different thicknesses (t), of 25, 35, 45, and 60 mm. However, after the specimens were measured, the planned 25 mm slabs in SS boundary condition were found to be 2 mm thicker. Although, these slabs were slightly thicker than the slab geometry planned in this study, they were kept to be tested due to the high cost of steel fibres.

Three slabs were tested for each of 35, 45 and 60 mm and four slabs with 27 mm thickness. A slab is named by its depth and boundary condition, for example, the slab ONE-WAY-SS27 has t of 27 mm and simply supported boundary conditions on two opposite edges and free edges on the other two edges. To cast the specimens, eight batches were prepared using the same mix design, four for each FF and SS boundary conditions. An additional small batch was prepared to cast the extra slab with 27 mm thickness. From each UHPFRC mix, 12 cubes, six (50 × 50 ×50) mm and six (100 × 100 ×100) mm were tested under uniaxial compression to assess the compressive strength of UHPFRC slab specimens at an age of 7 and 28 days.

All the slabs were tested using a centre point load, which is of interest in a variety of applications such as tyre patch loading on bridge decks, heavy machinery in warehouses, concrete pavements and many more.

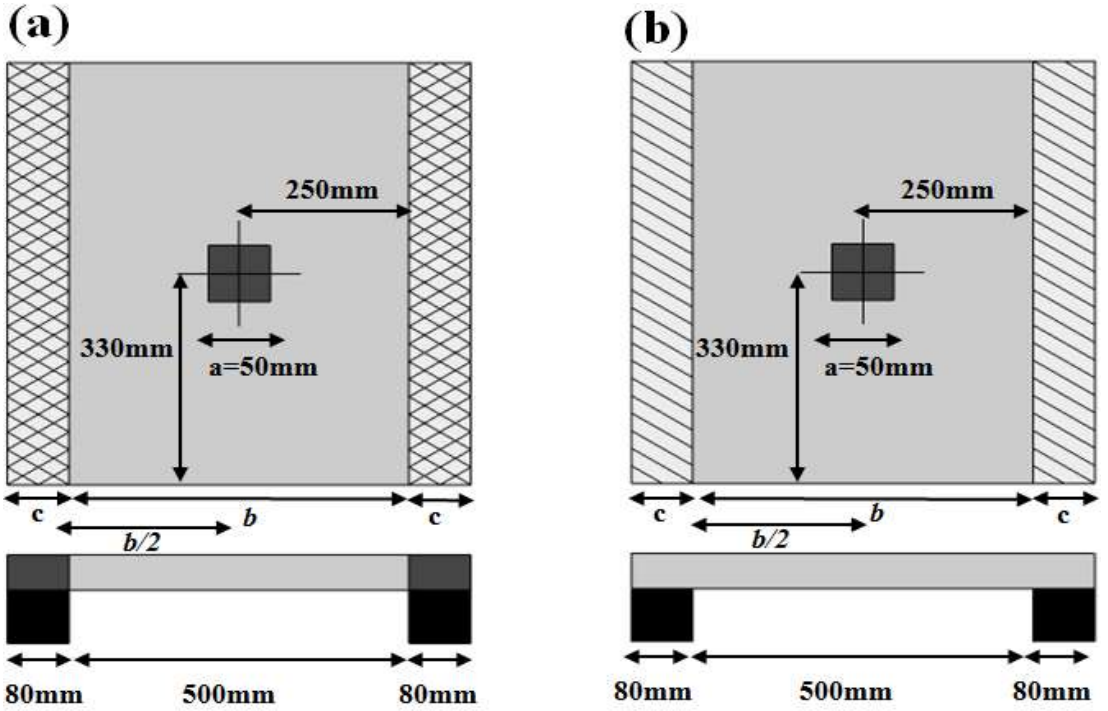

Figure 4.1: Boundary condition (a) full fixed edges (b) simply supported edges.

4.1.1 Materials and Mould Preparation

The materials used in the mix design to prepare the one-way slab specimens were described in Section 3.3.3.

To fabricate the slab specimens, a special wooden mould built by previous researchers at the University of Liverpool, was modified in this research study as shown in Figure 4.2. Because various boundary conditions were considered, steel studs with diameter of 18 mm were placed along the mould edges to allow holes to be made along the edges of the slab. The purpose of these holes was to allow the slabs to be supported, when fixed boundary conditions were required. However, these studs were reduced and removed depending on the desired boundary conditions. The moulds were steel lined with a thickness of 6 mm to ensure the smoothness in the slab specimens and to avoid difficulty that may arise during the demoulding procedure. The steel base plate was screwed to the base of the wooden mould to ensure no movement occurred during casting, especially during the vibration procedure. After the studs were lubricated and inserted into a plastic pipe with the diameter of 22 mm, they were placed along the edges of the steel plate at

the base of the mould. To ensure that the plastic pipe did not come off, a steel washer was placed on the top of the pipe and screwed to the steel stud. The wooden sides were connected using screws and they were easily removed to take the specimens out during demoulding. The dimensions of the mould, including the distance between the studs, are shown in Figure 4.3. Stud number and spacing along each side were the same and six studs were placed in each side. The height 80mm was chosen for these studs, which was greater than the largest specimen thickness tested in this study. Due to the weight of the slab specimens, two steel bars were placed above the studs in the two opposite sides for each mould. These steel bars allowed the slab to be moved easily from the mixing to the demoulding area, especially for slabs with 60 mm thickness which required a crane to move them. Along each side of the mould, six screws were used to secure the wooden edges to the base as shown in Figure 4.2. Since only three slab specimens were chosen for each parameter in this study, only three moulds were prepared. Since the two-way slabs were first investigated in this study, the moulds were designed based upon two-way slabs. However, in one-way slabs, only two opposite edges were required to be fixed for FF boundary conditions. Therefore, modification was made to the designed mould. Studs were only placed along the two opposite edges of the mould.

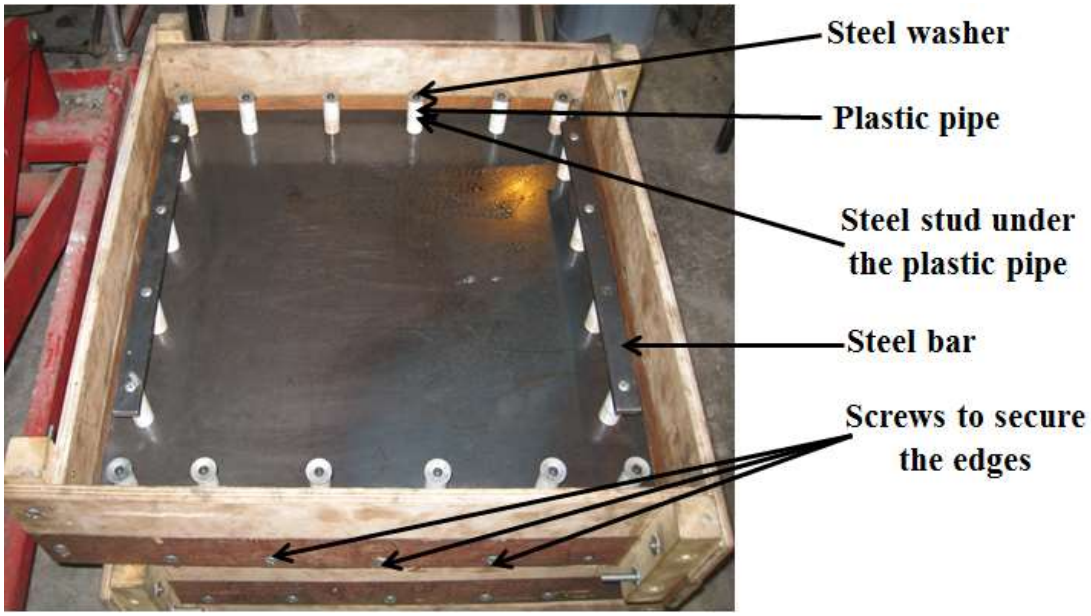

Figure 4.2: Two-way and one-way slab mould.

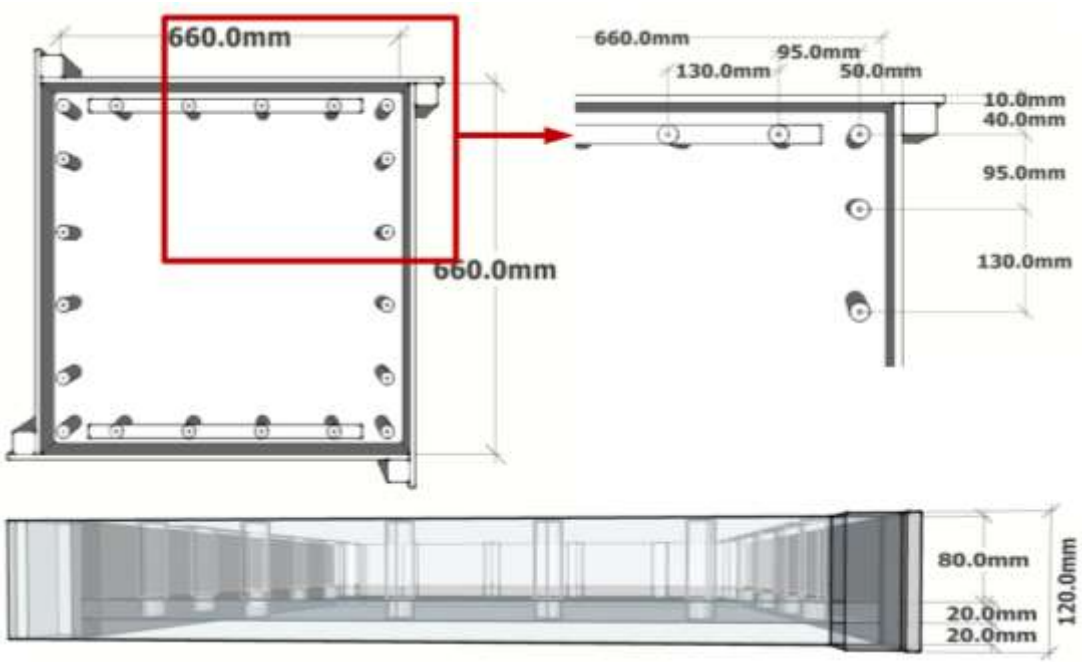

Figure 4.3: Two-way and one-way mould dimension.

4.1.2 Mix Design and Specimen Fabrication

The mix design detailed in Table 3.2 of Section 3.3.3 was used to produce the one-way slabs. The mixing procedure described in Section 3.3.3 was used to fabricate the slab specimens. However, since the size of the slabs is greater than the beams, slightly different techniques were used during the filling process. The UHPFRC was added to the centre of the mould where it flowed to the sides of the mould. This allowed the random distribution of fibres within the matrix. Demoulding the thick slab specimens needed varying amounts of time and sufficient strength to support their greater self-weight. Therefore extra time was required during demoulding.

To demould the specimens, all four sides of the mould were detached. The steel washers which were placed on the top of the plastic pipe were unscrewed so that the steel studs could be removed easily. To avoid any damage around the holes, the plastic pipes were not removed from the slab. The slabs were placed inside a steel cage and carefully placed in the curing tank for 48 hours. After two days, the slabs were taken out from the hot curing tank and left for a few hours to cool down. Finally, all the plastic pipes were removed and the specimens were ready for testing.

4.1.3 Equipment Setup Testing Procedure

A 300 kN Zwick hydraulic loading machine was employed to test the one-way slabs. To test the slab, a novel experimental setup, which was designed for two-way slabs was modified and used. The equipment for the tests consisted of two identical steel I-sections, two square steel frames with 50 mm and 40 mm thicknesses, respectively, and six pieces of steel strips, as shown in Figure 4.4. Four of the steel strips had a thickness of 25 mm and the other two were 20 mm and all had a length of 660 mm. M20 steel studs were used to fix the slab to the steel support and frame in the FF series. The steel frames had outer dimensions of (800 × 800) mm and (660 × 660) mm with inner dimensions of (500 × 500) mm, respectively. Details of the experimental setup are shown in Figure 4.4. Further details of the experimental procedure are shown in Figure 4.5.

At the start of the experimental setup, the two I-section steel beams were placed and fixed to the base of the testing machine using M20 steel studs, as shown in Figure 4.5a. The large steel frames with 50 mm thickness were placed on the top of the I-sections which were fixed to the bottom of the loading machine, as illustrated in Figure 4.5b. The small frame with 40 mm thickness was then fixed to the large frame, as shown in Figure 4.5c. Steel strips with the thickness of 25 mm were fixed to each side of the steel frame giving a clearance of 50 mm for the specimens to deflect, as illustrated in Figure 4.5d. The slab specimen was placed on the two supports and a LVDT with a range of 18 mm was placed under the slab where the load was applied. The LVDT was connected to the Zwick hydraulic loading machine and the tests were carried out as depicted in Figure 4.5e. In the FF series steel strips with 20 mm thickness were placed on the top of the slab and M20 studs were used to fix the specimen edges, as shown in Figure 4.5f. The studs were fixed to the top steel strip, slab, support steel strips and the small steel frames. Each side of the slab was fixed with 6 studs as shown in Figure 4.6a. The load was applied through a 50 mm cubic steel block at the centre of the specimen. The tests were performed under displacement control with a rate of 0.4mm/min.

The data was collected using the ‘testXpert’ software. The load-displacement curve was also obtained for each slab and the curve was monitored during the experiment to ensure that the test was conducted accurately. Once again to ensure enough data was obtained in the linear elastic range, for every second, one data point was requested. Therefore, over

2000 data points were collected for each slab and then the MATLAB software was used to analyse the data.

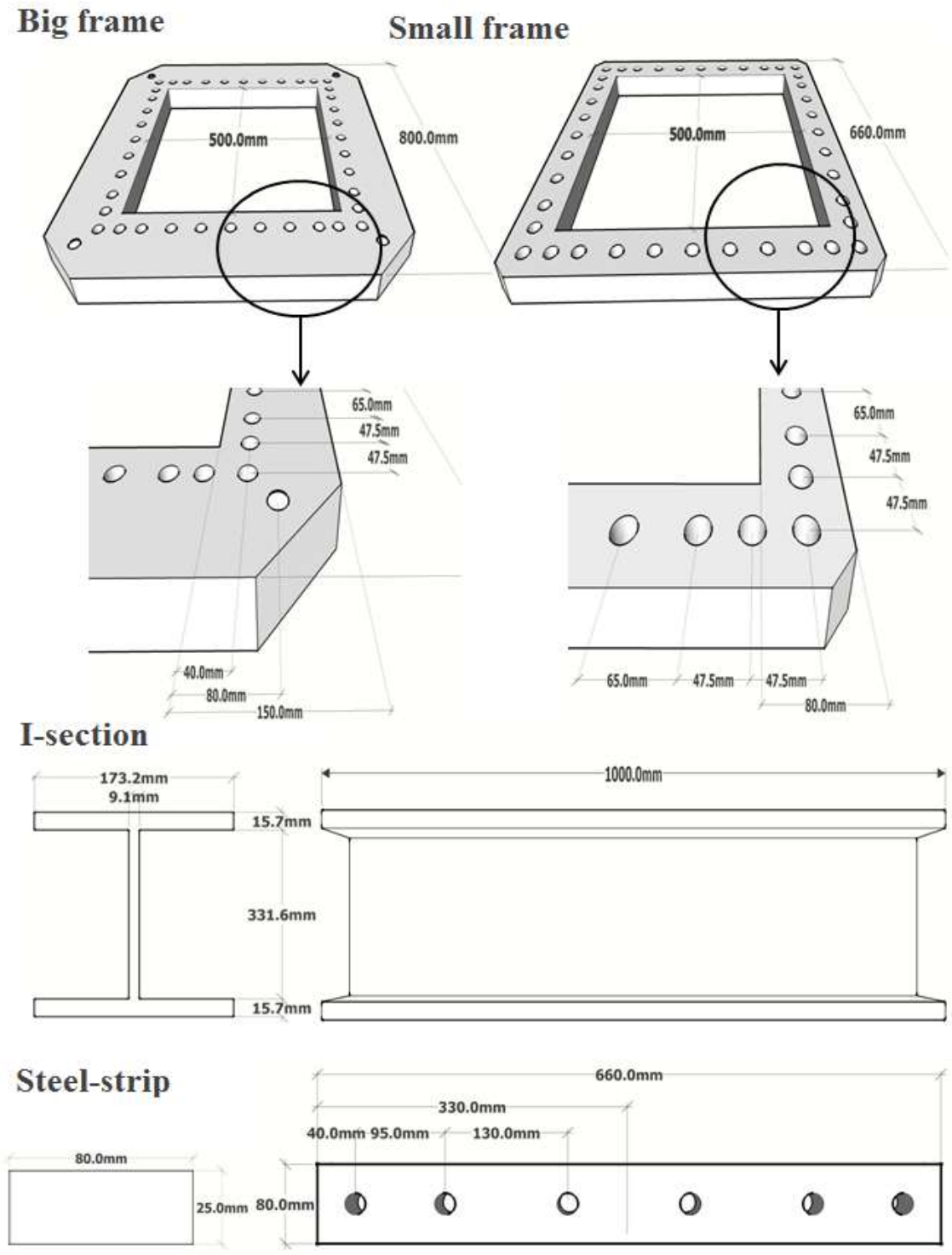

Figure 4.4: Steel I-section, frames and strip detail.

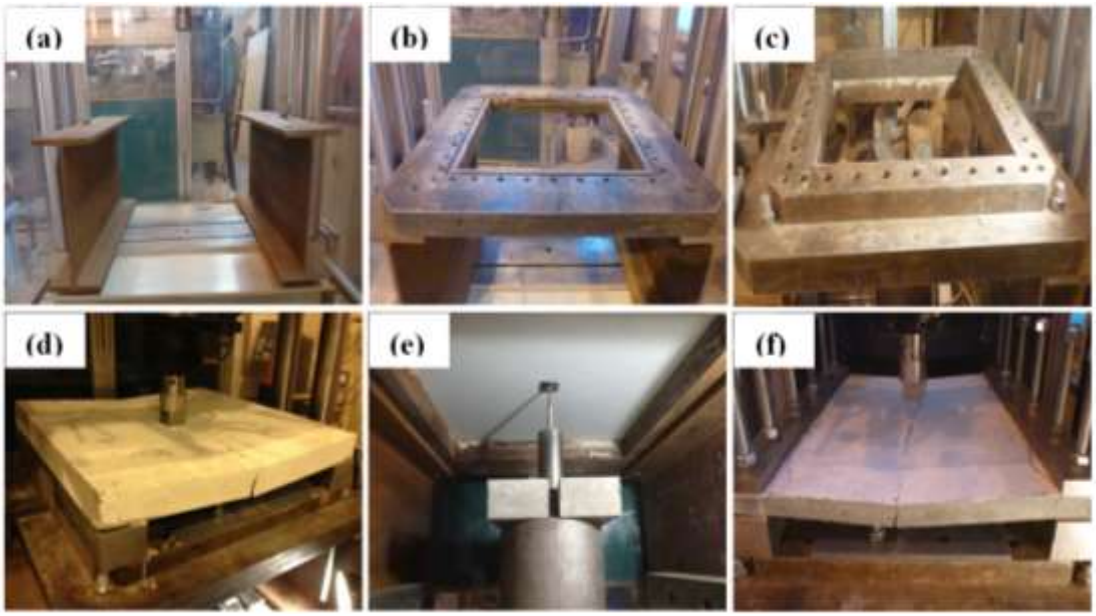

Figure 4.5: Details of experimental setup (a) I-sections placed at the machine base (b) big frame placed on the two I-section (c) small frame placed on the big frame (d) slab placed on the small frame (e) the LVDT placed at the bottom face of the slab (f) the edge restraint in FF series.

(a) fully fixed boundary condition (b) simply supported boundary condition

Figure 4.6: One-way slab boundary conditions during the test.

4.2 Results and Discussion

This section presents the experimental results of one-way slabs obtained using the novel experimental setup described above. The structural behaviour of one-way slabs with FF and SS boundary conditions under central loading in bending was investigated. The effect of boundary conditions and slabs thicknesses on the failure mode and load displacement relationship is discussed. Finally, an assessment of thickness on failure modes and effective flexural strength as well as on fibre distribution and orientation is also discussed.

4.2.1 One-way Slab Fibre Distribution and Orientation

In order to determine the effect of fibre distribution on the failure mode of the slabs, and to verify that the mixing and compaction procedures used to make UHPFRC slabs result in the steel fibres being uniformly distributed, a physical inspection of the fibres at the crack location was carried out. To do this, a specimen from each slab thickness was chosen. The slab specimens were cut open into two segments at the point where the cracks occurred and the number of fibres was then counted to determine the effect of the specimen thickness and the mixing procedures on the fibre distribution, as shown in Figure 4.7. In order to obtain better accuracy in counting the individual fibres, the crack surfaces were divided into smaller cross-sectional areas (5 mm thickness by 25 mm crack length) during the counting process, and each segment was counted three times. Each area was numbered and examined thoroughly. If there was a discrepancy between the counted values, further counts were undertaken to ensure that the correct number of fibres was counted. Similar to the beams, the slabs were referred to by their depth, for example, the left side (L) of a 25 mm deep slab (S) was named SL25. Fibres on each side of the crack were counted separately for all slab thicknesses and the results are summarised in Figure 4.8. In most of the slabs, it was observed that the number of fibres counted from one cracked face was considerably different from the other face of the same specimen. This was expected due to the pull-out behaviour influenced by the length of the embedded fibre within the matrix. Depending on the bond between the fibre and matrix at the exact location of the crack, fibre pull-out occurs from the side where the embedded length is smallest. It would not be accurate to compare one cracked face to another since more fibres may be pulled out towards one face than the other. In order to have a direct

comparison, therefore, fibres from both cracked faces were added together for each slab thickness, as shown in Figure 4.8.

25 mm 35mm

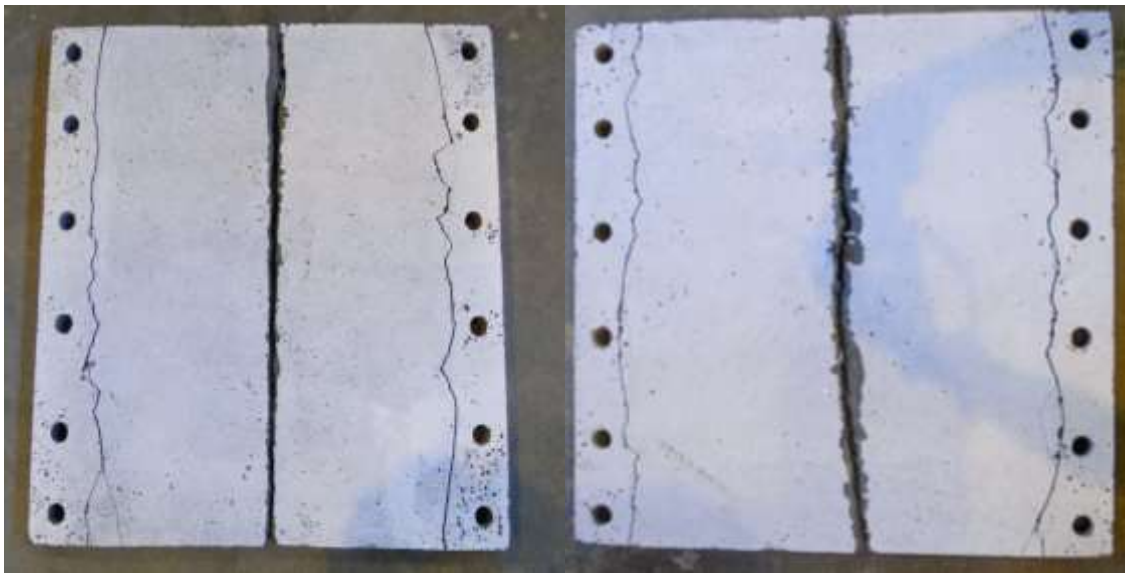

45mm 60mm

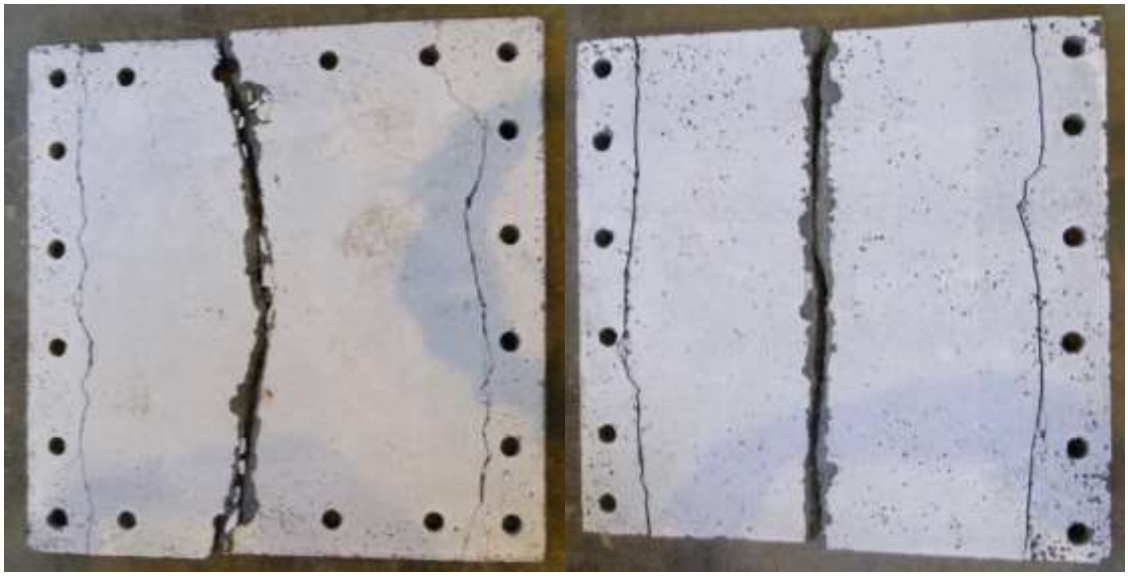

Figure 4.7: Slabs were cut into two segments at the failure crack location.

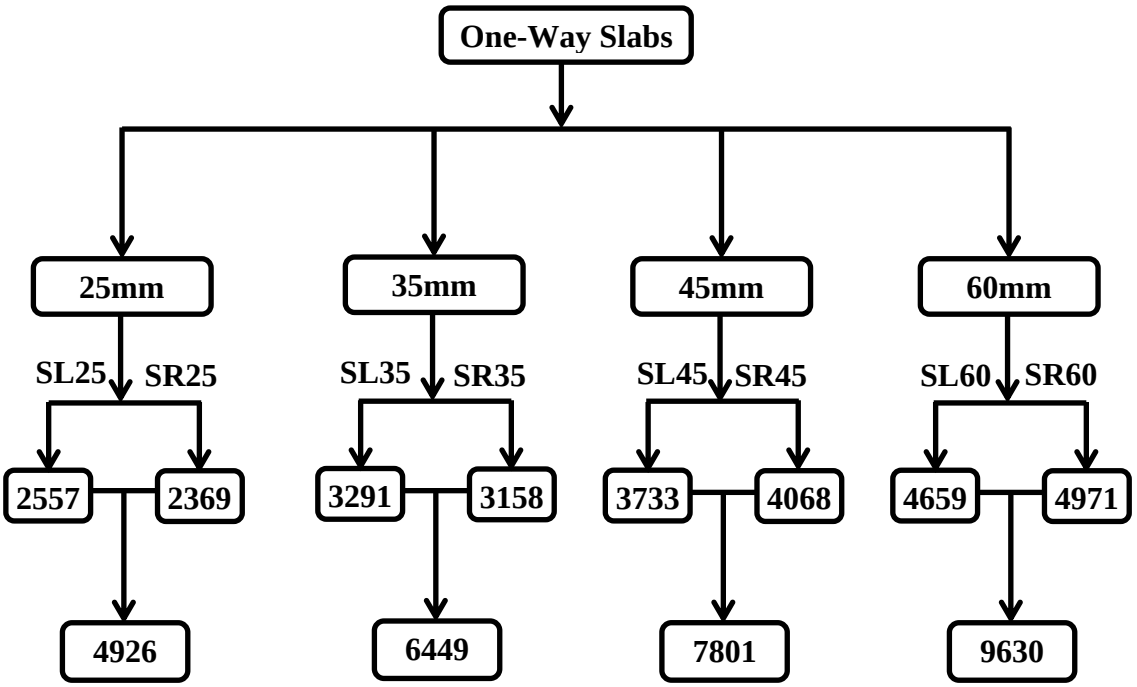

Figure 4.8: Fibre distribution for different slab thicknesses.

As explained in Section 3.4.1, many studies agree that the specimen geometry has a significant effect on fibre distribution and orientation. In this study, when the crack surface was examined, it was observed that the thinner slabs showed greater consistency of fibre distribution throughout the cracked faces than the thicker slabs. There were a few spots of poor fibre distribution in thick slabs as shown Figure 4.9. However, the spots were not predominant and cannot characterise the general picture of the fibre distribution within the crack location of the examined slabs.

From a visual inspection of the sections after cutting, it appeared that there were lower numbers of fibres at the edges in thicker slabs than in thinner slabs. This feature was more predominant at the edge close to the side wall of the mould, but this difference was not very significant and a lower number of fibres could be due to the specimen wall effect or specimen geometry, as explained in Section 3.4.1. It is also important to mention that no fibre balling was observed for any slab specimens where cracks had occurred. A careful visual inspection also confirmed only a very few visible voids on the cracked faces for all the slab specimens and this confirmed the accuracy of the mix design used in this current study.

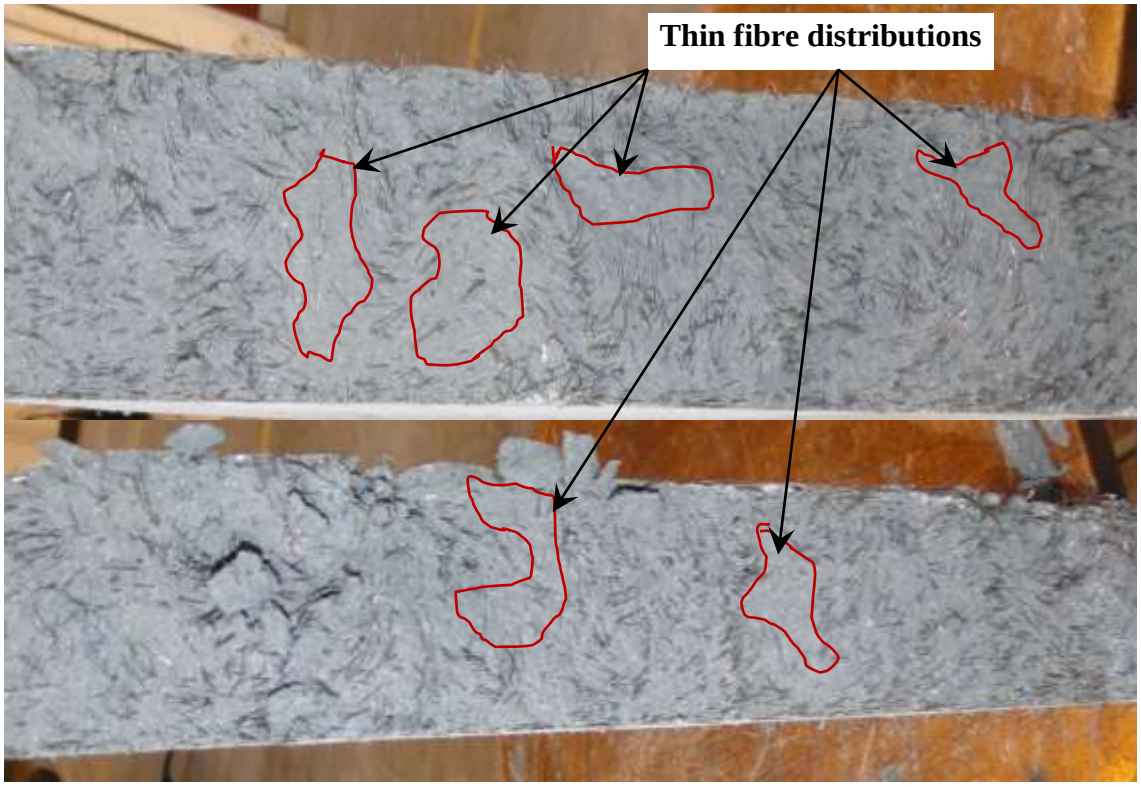

Figure 4.9: Inconsistency in fibre distribution in slabs with 45 and 60 mm thickness.

To determine whether experimental measurement of fibres are proportional to the specimen thickness, the result of the slabs were compared. This comparison provided evidence if the result of 25 mm slab can be used to accurately estimate the number of fibres that are expected to be counted for the 35, 45 and 60 mm slab. It is important to mention, however, that this comparison was based purely on the one particular area of the slab: the middle section where the crack had occurred.

Looking at Figure 4.8, the number of fibres at the crack location that had bridged between the two cracked faces, given a slab with a 25 mm thickness, was 4926. Looking at the result of the 25 mm thick slab, it was anticipated that the number of fibres should have increased by approximately 985 for every 5 mm increase in thickness. Since the slab with a 35 mm thickness had increased by 10 mm, it was expected that the total increase in the number of fibres would be 1970, as shown in Table 4.1. However, when fibres at the crack surface for a 35 mm thickness slab were counted, they were found to total 6449, which is less than the anticipated value. This means that the number of fibres in the 35 mm slab increased by 1523 when the thickness increased by 10 mm. This is less than the

expected number of fibres based on 25 mm slab by 447 as given in Table 4.1. The difference between the experimentally counted fibres and the expected value indicates that fibres in the 35 mm slabs are not orientated and distributed in the same way as the 25 mm specimens. This change in fibre orientation has a direct impact on the fibre bridging action, resulting in fewer fibres being counted in slabs with a 35 mm thickness. This clearly shows that the rate of increase in the number of fibres that bridge between the two cracked faces reduced as the thickness increased. This finding agrees well with the studies reported in the literature (Association Francaise de Genie Civil–Service d'etudes Techniques des Routes et Autoroutes (AFGC/SETRA), 2002, Dupont, 2003, Marković, 2006, Wille and Parra-Montesinos, 2012, Nezhentseva et al., 2013). Furthermore, the relationship between the specimen thickness and the experimental measurements of fibre counting continued to reduce as the slab thickness increased further. For slabs with a 45 mm thickness, the number of fibres was counted to be 7801, this gives an increase of 1352 fibres only which is less by 618 fibres if compared to the 25 mm slab. The relationship was further reduced when the 60 mm slab was investigated, counting 751 less fibres when compared to the 25 mm slabs as shown in Table 4.1. As mentioned in Chapter 3 and stated in the literature, fibres in specimens with small thickness are restricted from positioning freely within the matrix due to the wall effect, resulting in an unrealistic representation of the fibre distribution and orientation in respect to other thicknesses, especially life-sized structures. These results indicate clearly that the fibre distribution changes as geometry changes and specimen surface has a considerable effect on fibre distribution and orientation (Abdalla and Karihaloo, 2003, Ferrara and Meda, 2006, Pansuk et al., 2008, kim er al., 2008).

Comparing the results between the two thicker slabs (45 mm and 60 mm) as shown in the third column from the left, it can be seen that the increase in number of fibres in the 45 mm slab is 1352, whereas 1219 fibres were counted for the 60 mm slab. This shows the difference between the two larger slab specimens is only 133 fibres, which is considerably smaller if compared to the thin slabs (447 fibres only). This small difference in thick slabs illustrates that the change in the fibre distribution is more apparent with thin slabs than with the thick ones (Nezhentseva et al., 2013). Moreover, the result of thick slabs can provide an important finding as the difference in number of fibres between the two larger slabs is less than 10%. The number of fibres that contribute to the fibre bridging action for larger size specimens could now be estimated using the experimental measurement of

the largest slab of this study with a known level of uncertainty. This is especially useful since the fibre orientation and distribution in life-sized structures is unlikely to differ much from the largest slab tested here (by less than 10%), although these conclusions will have to be verified experimentally with life-sized structures if they are to be used extensively.

Table 4.1: Fibre distribution results in one-way slabs.

Slab	Experimental measurement (E_m)	Increase in number of fibres per 10 mm increase in thickness (E_i)	Differences $\|Ei_{25} - Ei_t\|^*$
25	4926	**1970**	0
35	6449	**1523**	447
45	7801	**1352**	618
60	9630	**1219**	751

*t =35, 45 or 60 mm

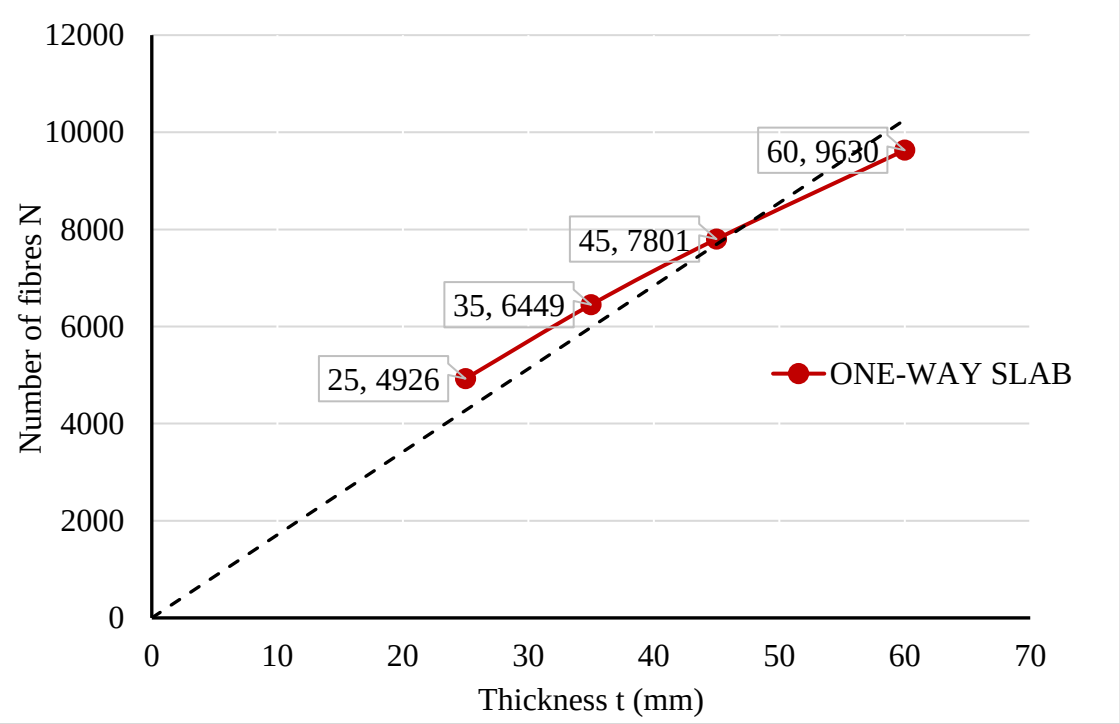

Figure 4.10: Relationship between slab thickness and fibre distribution.

4.2.2 Failure Modes

The failure modes of the one-way specimens with FF boundary conditions were found to be similar to the traditional concrete slab, as illustrated in Figure 4.11. The crack at the tensile face of the specimens failed with a single crack initiated at the location of the applied load, extending outwards to the centre of the slab's free edges. This failure normally occurs in OC (Ellobody and Bailey, 2008, Jones and Wood, 1967). During the experiment, it was observed after a deflection of approximately 0.30 to 0.40 mm, at the tensile face, several microcracks appeared around the centre of the slab specimens where the load was acting. The microcracks in the most stressed zone tended to form where the bond between the fibre-matrix became weak due to the external force, resulting in a stress concentration. As the loading was increased only a few of the microcracks formed a single crack and the others remained almost unchanged in the later stages of loading. The failure modes of thinner and thicker slabs in one-way slabs were found to be similar unlike two-way slabs where more cracks were observed in thicker specimens. In one-way slabs with FF boundary conditions, the development of microcracks to a macrocrack was found to be influenced by specimen edge restraint.

Although the slab geometry, loading and boundary conditions were similar, the cracks in some of the slabs are tortuous and deviate away from the straight line. This again could be attributed to the random distribution and orientation of the steel fibres (Wille and Parra-Montesinos, 2012, Spasojevic, 2008), which make the crack-tip stress fields complicated and the local tensile strength and fracture toughness highly heterogeneous, as in conventional concrete where the aggregates function similarly to the steel fibres (Lepech and Li, 2004). It should be mentioned that all the slabs in the FF series had a similar crack failure in the compressive face where cracks form along the two fixed edges, as illustrated in Figure 4.12a. However, in some of the specimens especially in the thicker slabs, cracks deviated from a straight line due to the fibre orientation, distribution and the fibre-matrix bond. In the SS series a single crack formed from where the load was acting and extended towards the centre of two free edges as shown in Figure 4.12b.

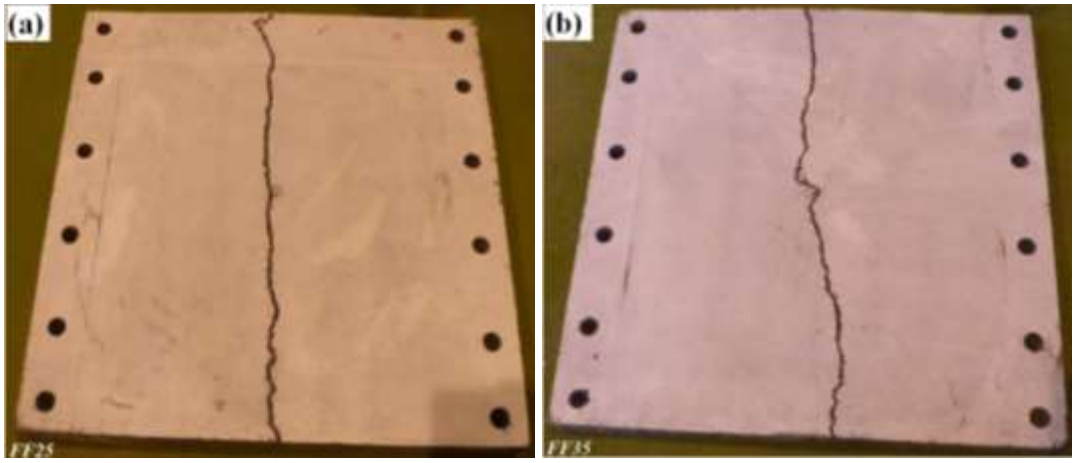

(a) tensile face crack pattern for FF25 (b) tensile face crack pattern for FF35

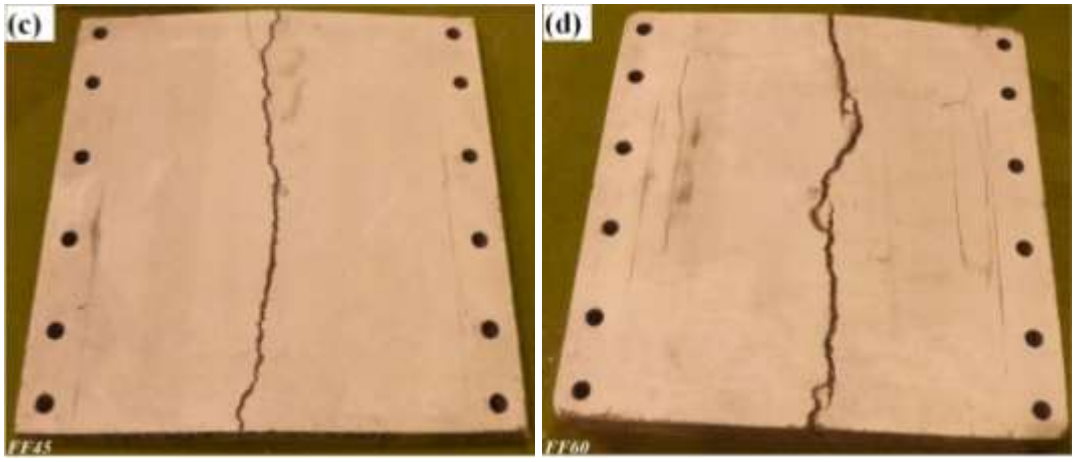

(c) tensile face crack pattern for FF45 (d) tensile face crack pattern for FF60

Figure 4.11: Cracks for one-way slabs with fully fixed boundary conditions.

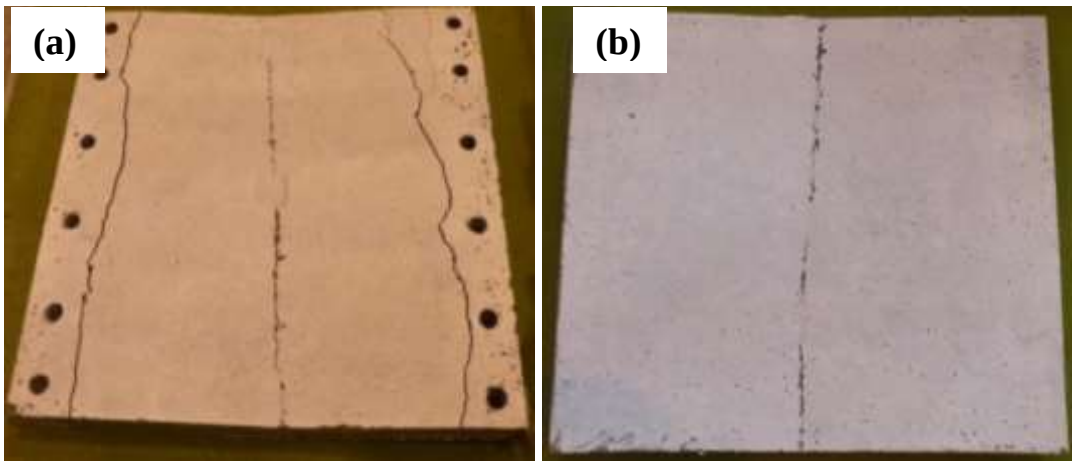

(a) compressive face crack for FF45 (b) compressive face crack for SS45

Figure 4.12: One-way slab compressive face crack pattern.

Similar to the first series, the results of the second series specimens with SS boundary conditions showed a similar failure pattern for all the thicknesses, forming a single macrocrack initiated at the location of applied force and extending towards the centre of the free edges, as depicted in Figure 4.13. A clean smooth crack through the slab is obtained with the specimen held together by the short steel fibres, which remained intact. The transformation of the microcracks to the macrocrack was observed when the specimen deflection reached 0.30 to 0.40 mm. In this series, the process from the appearance of microcracks to fibre pull-out (fibre-bridging) was slightly quicker, in thicker specimens in particular. Crack widths were more pronounced compared to those with FF boundary conditions. This can be attributed to the effect of boundary conditions, which influence the fibre pull-out behaviour. Failure took place when fibre pull-out reached its final stages, the cracks extending into the compressive zone so that no further load could be carried and the load started to decrease. As expected the load is sufficiently high in slabs with FF boundary conditions to force the slabs to fail in flexure compared to the ultimate failure load experienced by the slabs with SS boundary conditions. However the ultimate load carrying capacity was observed at around 5 mm displacement in both the FF and SS series for slabs with thicknesses of 25, 27 and 35 mm. Whereas, fibre pull-out behaviour occurred at a displacement of around 3 to 4.5 mm in slabs with thicknesses of 45 and 60 mm.

Geometry influences the fibre orientation and position within the matrix, and thus fibre bridging action at the crack locations as shown in Figure 4.14 and Figure 4.15. These figures show as the slab thickness increases the position of the fibre within the matrix changes considerably. Figure 4.14 shows slabs with 25 and 35 mm thickness tend to have more uniform fibre dispersion throughout the slab geometry. However, slabs above 35 mm thick allow fibres to be positioned more randomly within the matrix, resulting in non-uniform fibre distribution especially for 60 mm thick slabs as shown in Figure 4.15b. Furthermore, in thinner slabs due to the geometry effect, most of the fibres are parallel to the specimen surfaces and this means more fibres contribute to the bridging action at the crack location. This parallel positioning of fibres also influences the fibre effectiveness in terms of fibre bridging between the two crack faces. It allows the crack to widen to its widest before fibre pull-out occurs. Whereas, in thicker slabs such as 45 and 60 mm, fibres have little effect on load action as the slab thickness is much greater than the length of the fibre. Therefore, more randomly orientated fibres can be observed at the location

of the crack patterns. This results in fewer fibres contributing to the bridging action. Moreover, Figure 4.15 shows that many of the fibres contributing to the bridging action are not perpendicular to the crack pattern, thus they had pulled out at a smaller crack width. This observation clearly confirms that geometry influences both fibre distribution and orientation in the matrix.

Similar to the beam specimens, closer examination confirmed that all the one-way slab specimens also failed by fibre pull-out. As mentioned in Chapter 3, it is shown that the bond strength between fibres and the matrix is approximately 10 MPa and steel fibre yields at 2000 MPa. Therefore, it was unlikely that fibre yielding had occurred.

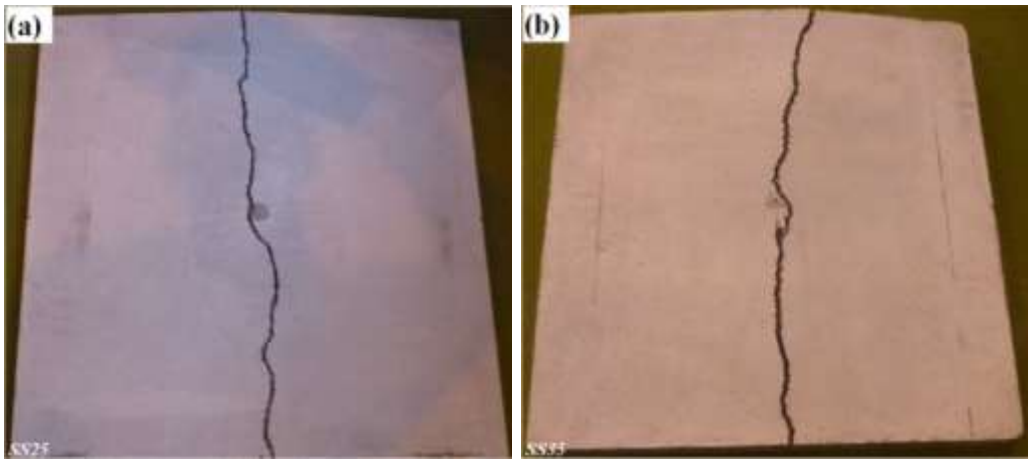

(a) tensile face crack pattern SS25 (b) tensile face crack pattern SS35

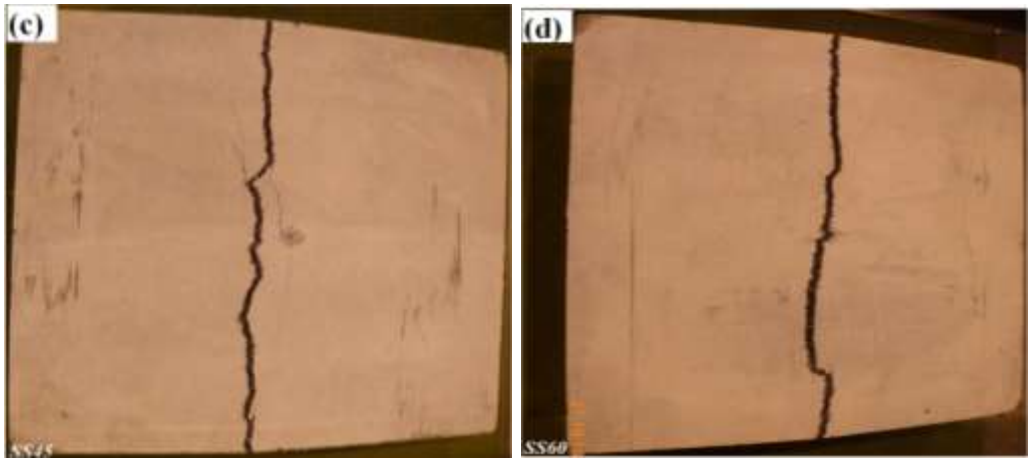

(c) tensile face crack pattern SS45 (d) tensile face crack pattern SS60

Figure 4.13: Cracks for one-way slabs with simply supported boundary conditions.

(a) Slab with 25 mm thickness

(b) Slab with 35 mm thickness

Figure 4.14: Shows a uniform fibre distribution.

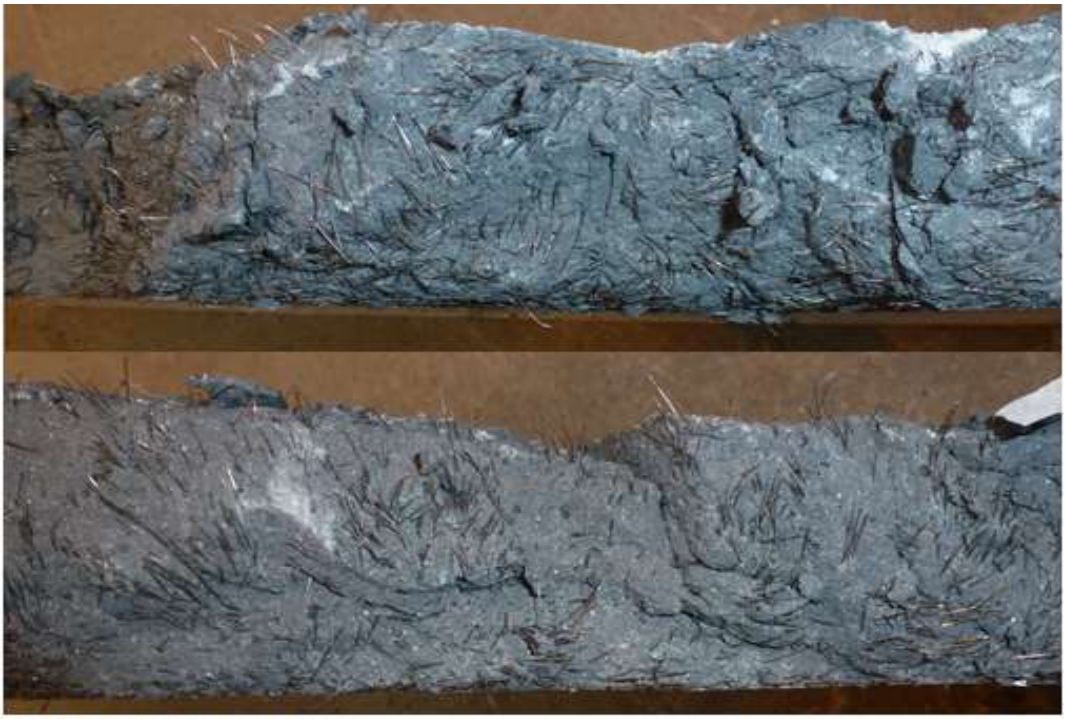

(a) Slab with 45 mm thickness

(b) Slab with 60 mm thickness

Figure 4.15: Shows non-uniform fibre distribution.

4.2.3 Load-displacement Curves

The experimental load–displacement curves for the one-way slab specimens from the bending tests and the average curve are shown in Figure 4.16 to 4.19 for FF boundary conditions and Figure 4.20 to 4.23 for the SS boundary conditions, respectively. The load-displacement curves show that the UHPFRC slabs similar to the beams underwent three main regions as previously described by Hassan et al. (2012)

4.2.3.1 Linear Elastic

In the first region, the linear response of the slabs covers the start of loading to maximum loading just before microcracks start to appear in the material. In this region, both the fibres and matrix behave elastically and the curve has a steep ascending slope. The maximum load attained in this region corresponded to the matrix strength while the fibres contributed little to the overall structural behaviour. Although the slab had symmetric boundary conditions along all the edges, the appearance of microcracks in this region was random due to the effect of the short discontinuous steel fibres.

The behaviour of UHPFRC specimens was significantly different compared to the OC: the material with a FF boundary condition showed very stiff behaviour at this stage with very little displacement. The load-displacement graph shows very little variation in displacement where this stage ends, covering a range of 0 to 0.35 mm. Due to the effect of fibre bridging in UHPFRC, a smooth transformation occurred from elastic to strain hardening regions. During the experiment it was observed that as the microcracks were propagating, the load-displacement curve began to change from linear to nonlinear behaviour, with the load at the end of this stage being approximately 11, 27, 60 and 105 kN, respectively. It is important to mention that with thin slabs (25 and 35 mm), the load carrying capacity at this stage was considerably less than the ultimate strength of the slabs, whereas with thick slabs 60 to 65% of the slab's load was achieved. This variation in loads in the linear elastic stage shows an important behaviour of UHFRC, namely; that the matrix strength does not increase linearly as the specimen thickness increases.

Similar to the FF boundary conditions, loads at the end of the linear elastic stage in the SS boundary condition were 8, 14, 20 and 59 kN. The slabs in this series, however, tend to be less stiff compared to the FF slab boundary conditions, with a greater range of

displacement of up to 0.55 mm. It is therefore important that the effect of the boundary condition be considered in the investigation of UHPFRC. In designing OC, for SLS it must remain in the elastic region and the structure must remain functional for its intended use when it is subjected to everyday loading. In designing UHPFRC, for SLS it must also be located in the purely elastic zone but, according to both French and Japanese recommendations, this must also satisfy two conditions (i) plane sections remain plane and (ii) stress is proportional to strains in the uncracked region (Japan Society of Civil Engineers (JSCE), 2008). Therefore, understanding the structural behaviour of UHPFRC in the elastic region is essential as it satisfies the SLS.

4.2.3.2 Pseudo-strain Hardening

As the load increased, the second region started where the transformation of microcracks to macrocracks began. At the end of this region, microcracks become more pronounced and the cracking strain of the structure exceeded the matrix's cracking strain. This resulted in a concentration of closely spaced microcracks that merge and form a single macrocrack and this is called the pseudo-strain hardening region. At the end of this region, a single macrocrack formed due to the combination of microcracks. In this region, stress was transferred by the fibres bridging across the faces of each crack and this depended on half the length of the fibre, 6.5 mm for the fibres used in this study. Sufficient bond between the matrix and the fibres is essential as well as an even distribution of fibres. Type and shape of steel fibre influences fibre-matrix bond, and thus the strain hardening behaviour (Yang et al., 2011c, Wille and Naaman, 2012). The resisting force due to the fibre bridging in this stage not only restrains crack opening but also leads to better interlocking between the two cracked faces. Due to the effectiveness of fibre bridging, the concrete carries more load after the matrix cracks and it covers a wider range of displacement. As mentioned in Section 3.4.1, this strain hardening phenomenon distinguishes UHPFRC from all other types of concrete and, therefore, it is important that this region is included in the design when the ultimate limit strength (ULS) is considered. Due to the brittle behaviour of OC, the ULS is usually considered to lie at the upper part of the elastic region where stress is proportional to strain. Adapting the design standard of OC directly to UHPFRC will not be practical if the true stress-strain curve of UHPFRC is considered, since a significant part of the displacement falls within this region. Figure

4.16 to 4.23 show that the displacement at the beginning of this region is very small and indeed much smaller than the allowable widths of the cracks. Although microcracks have occurred in the structure, the structural integrity of the section is not affected since the crack width is significantly small. This is only true for that small portion of the curves that start from the end of elastic region; however, for both the SLS and ULS design, the portion of the curve in this region can be considered as long as the crack width is below the allowable crack width. Looking at the material properties testing as set out in Figure 2.8 in Chapter 2, microcracking in this region accounts for 40 to 90% of the nonlinear response of the matrix, but the propagation of microcracking becomes predominant at a stress level of 70 to 90% of the tensile strength. It is important that this region is considered carefully during the design of UHPFRC. Indeed, as recommended in both the French (AFGC/SETRA, 2002) and Japanese design guidance (Japan Society of Civil Engineers (JSCE), 2008), when SLS and ULS are calculated, the stress and strain of the section must be calculated under the assumption that the material is purely elastic under compression and perfectly elastoplastic under tension. This means a linear relationship between stress-strain at the beginning of the strain hardening region may be assumed, depending on the width of microcracks. Boundary conditions also play an important role in this region. Looking at slabs with FF boundary conditions, the displacement at this region starts from the end of the elastic region to up to 3.3 mm in thin slabs (25 and 35 mm) and 4.6 mm in thick slabs (45 and 60 mm). Slabs with a SS boundary condition were found to be constant throughout the specimens with different thicknesses and displacements starting from the end of the elastic region to up to 5 mm.

4.2.3.3 Strain Softening

The third and final region started with the occurrence of a number of macrocracks, where the fibre-matrix interface was no longer capable of sustaining the maximum peak load, due to the increase in the crack width. Slippage between the fibre and the matrix occurred, resulting in fibre pull-out behaviour. Therefore, the fibres were no longer capable of transferring load between the two cracked faces and this resulted in a decrease in the load. As the load increased, more slipping between fibres and the matrix occurred and macrocracks became more pronounced, as illustrated in Figure 4.11 and Figure 4.13. The progression of fibre pull-out behaviour is dependent on the length of the fibres, the

strength of the matrix and the fibre-matrix bond. This progression of fibre pull-out behaviour allowed a smooth transition from the ultimate peak load to the strain softening region. It was also influenced by the macrocrack which occurred at the centre of the slab becoming more apparent as the loading continued. As mentioned before, fibre distribution plays an important role in this region. The length of the embedded fibre in the cracked area was dominated by the behaviour of the load-displacement curve. The decrease in the load was influenced directly by the amount of fibres that pulls out at that particular time. Looking at the curves, it can be observed that some of the slabs show a very sharp decrease in the softening region whereas less steep behaviour can be seen in the others, as shown in Figure 4.16 to 4.23. The load-displacement curves showed that the fibre pull-out behaviour also influenced the softening regions, since a little scatter can be observed for slabs with similar thicknesses and boundary conditions. It is important to mention, however, that the variation in this region is greater if compared to the pseudo-hardening region. Furthermore, the smooth transformation from elastic to strain-hardening, and then to strain softening, was also observed in all the slab specimens in both series.

These outcomes of the experiment with different specimen thicknesses provide valuable insights to assist in the understanding of the overall structural behaviour of full scale structures. The analysis of the experimental results showed the identification of failure modes of UHPFRC one-way slabs. The results prove that, despite changes in the slab thickness, the failure modes were similar in slabs with four different geometries, with a single macrocrack initiating at the middle of the slab, followed by observable fibre pull-out behaviour. It can therefore be concluded that the full scale slab would fail in a similar way to those tested in this study. Also, the experimental load-displacement response showed that all the slabs with both boundary conditions underwent three main stages: linear elastic, pseudo-strain hardening and strain softening. The curves prove that increasing slab thickness results in an increase in the ultimate flexural load carrying capacities and the first crack load, and that the slab thickness has no influence on the failure stages. Furthermore, the beam specimen results in Chapter 3 of this study have also showed that the beam underwent three stages similar to the slab failure stages. Moreover, as discussed above, the failure stages of this study were found to be similar to the failure stages of other studies which have used UHPFRC specimens with different sizes and shapes. It is suggested, therefore, that the full scale slabs would undergo similar

stages as those slabs tested in this study. These conclusions may need to be verified experimentally, however, if they are to be used extensively.

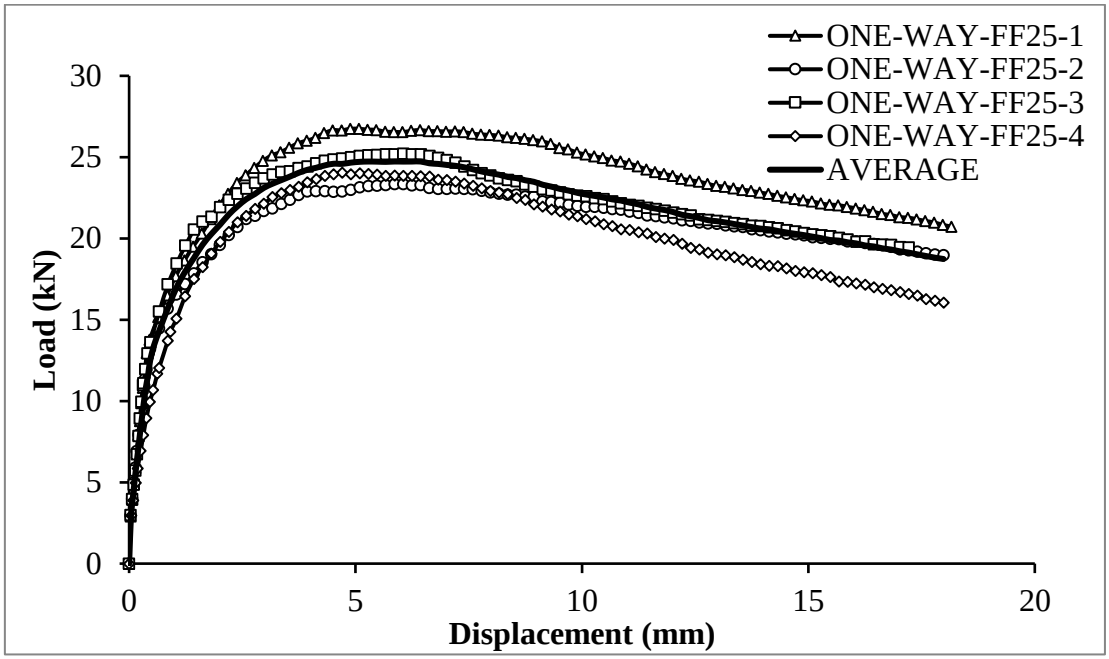

Figure 4.16: Load-displacement curves for FF25.

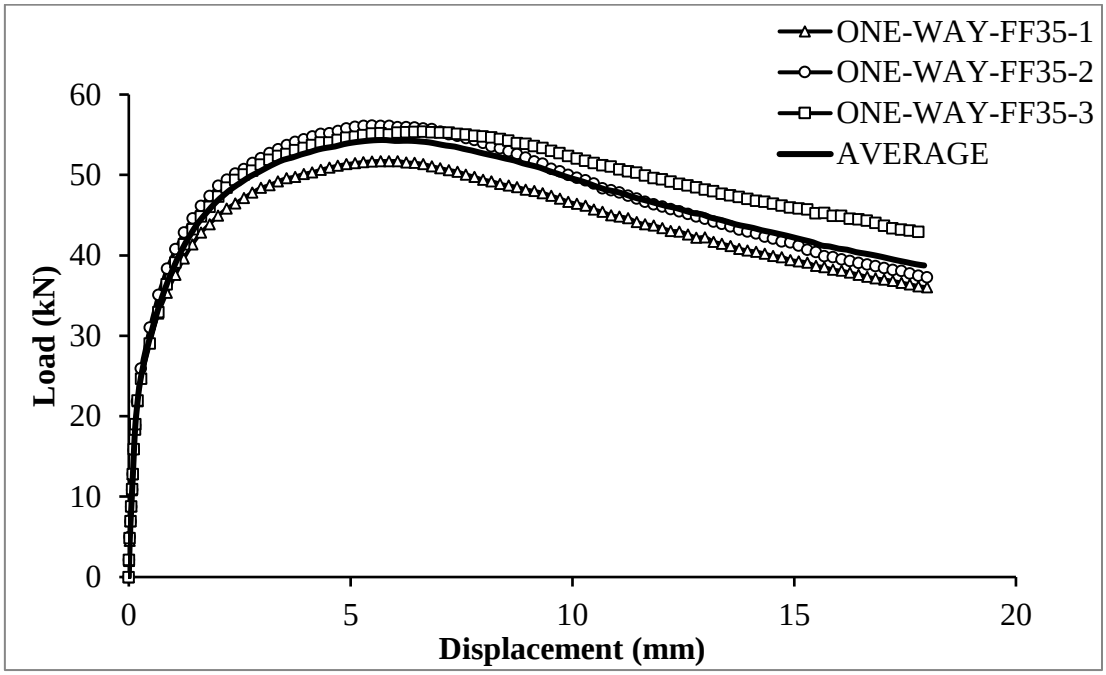

Figure 4.17: Load-displacement curves for FF35.

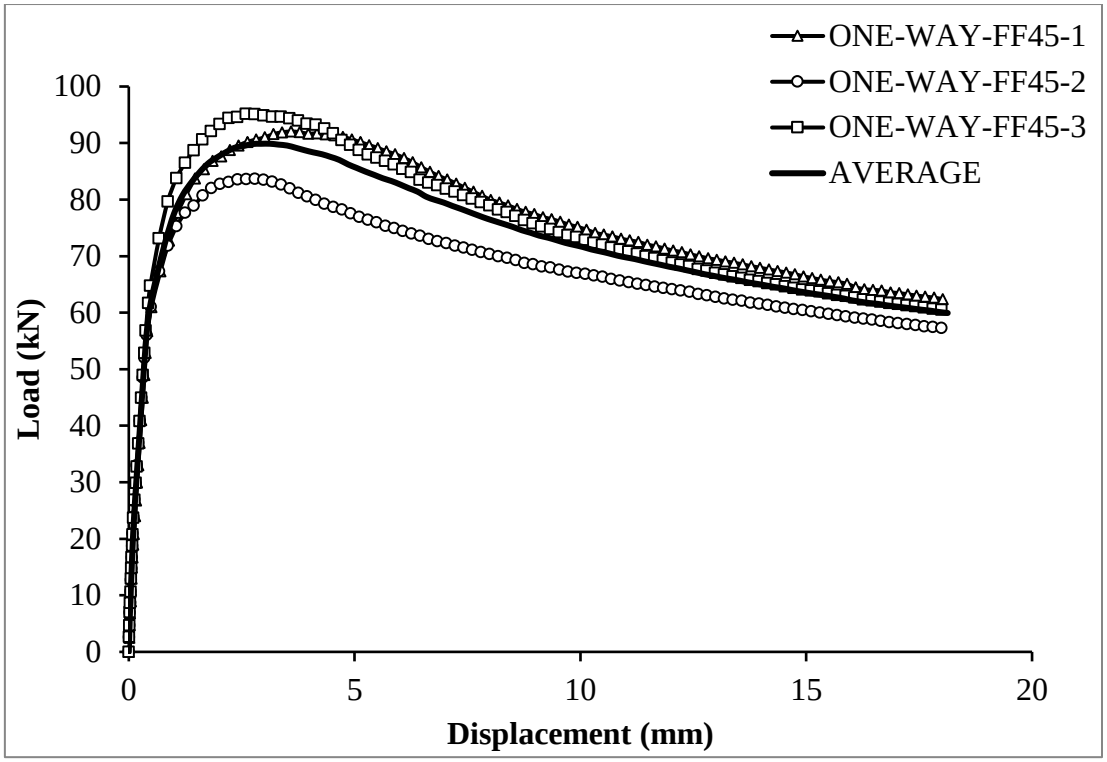

Figure 4.18: Load-displacement curves for FF45.

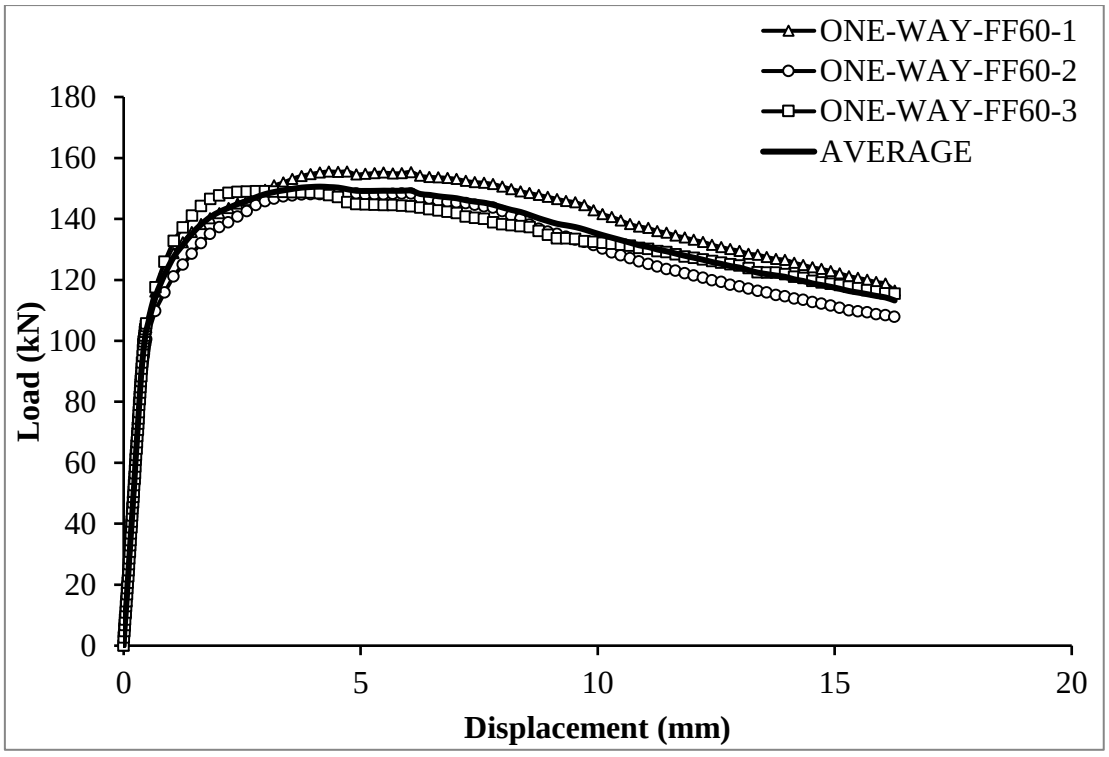

Figure 4.19: Load-displacement curves for FF60.

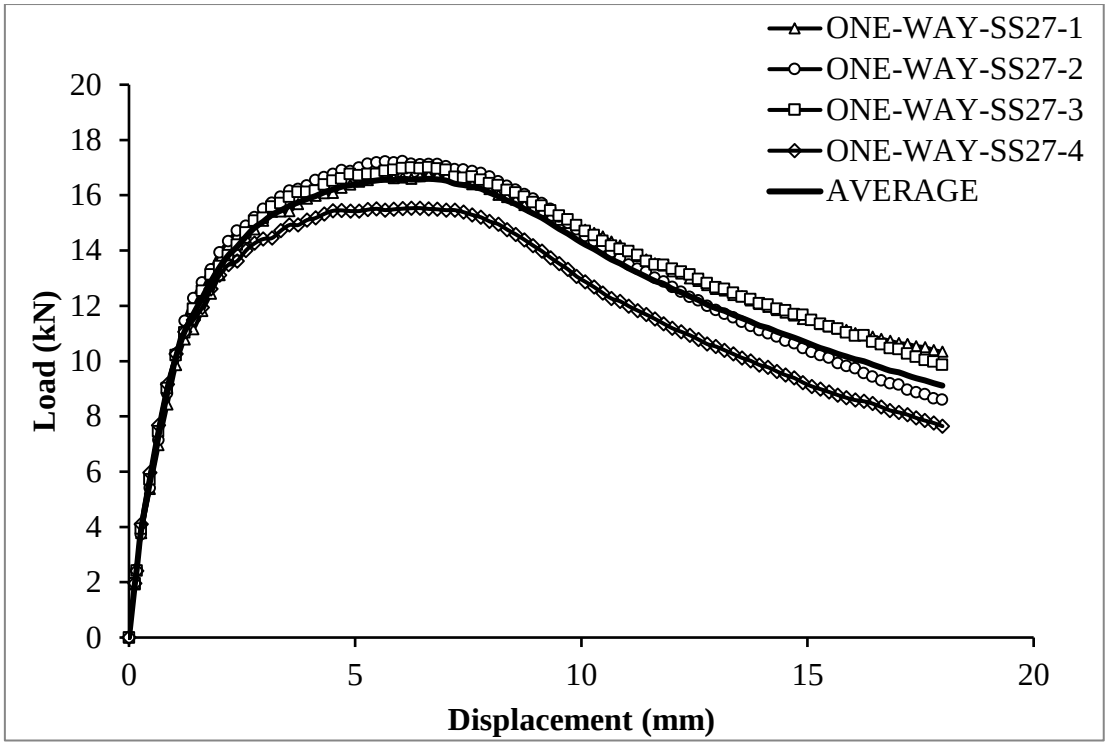

Figure 4.20: Load-displacement curves for SS25.

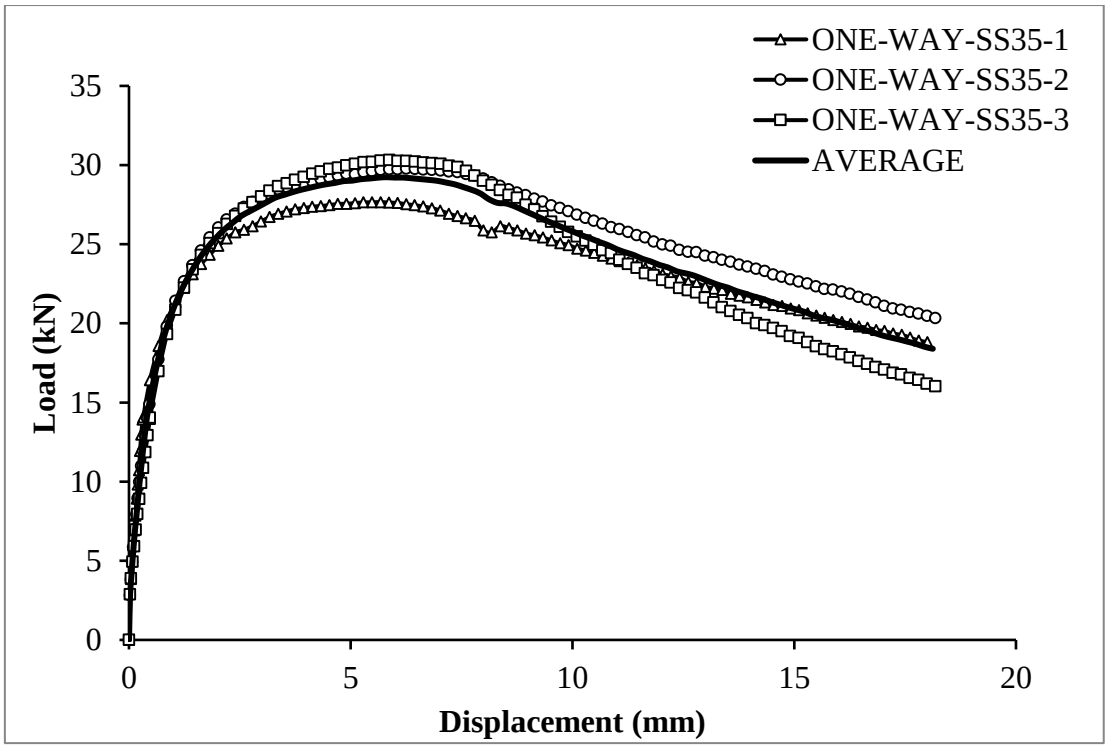

Figure 4.21: Load-displacement curves for SS35.

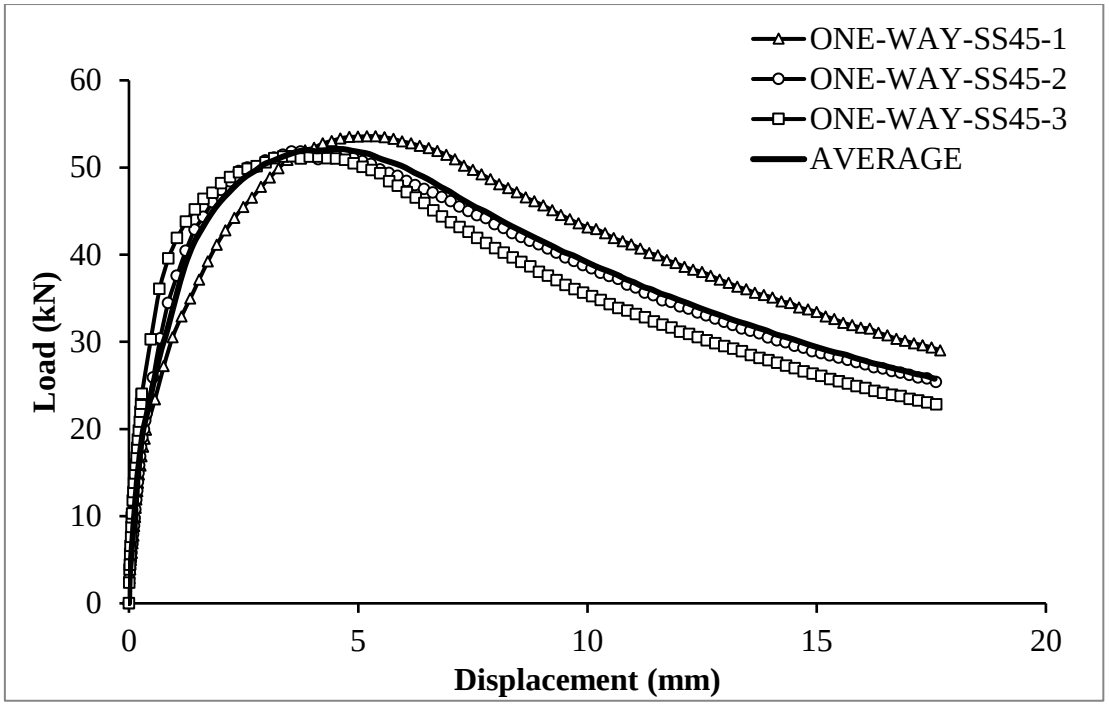

Figure 4.22: Load-displacement curves for SS45.

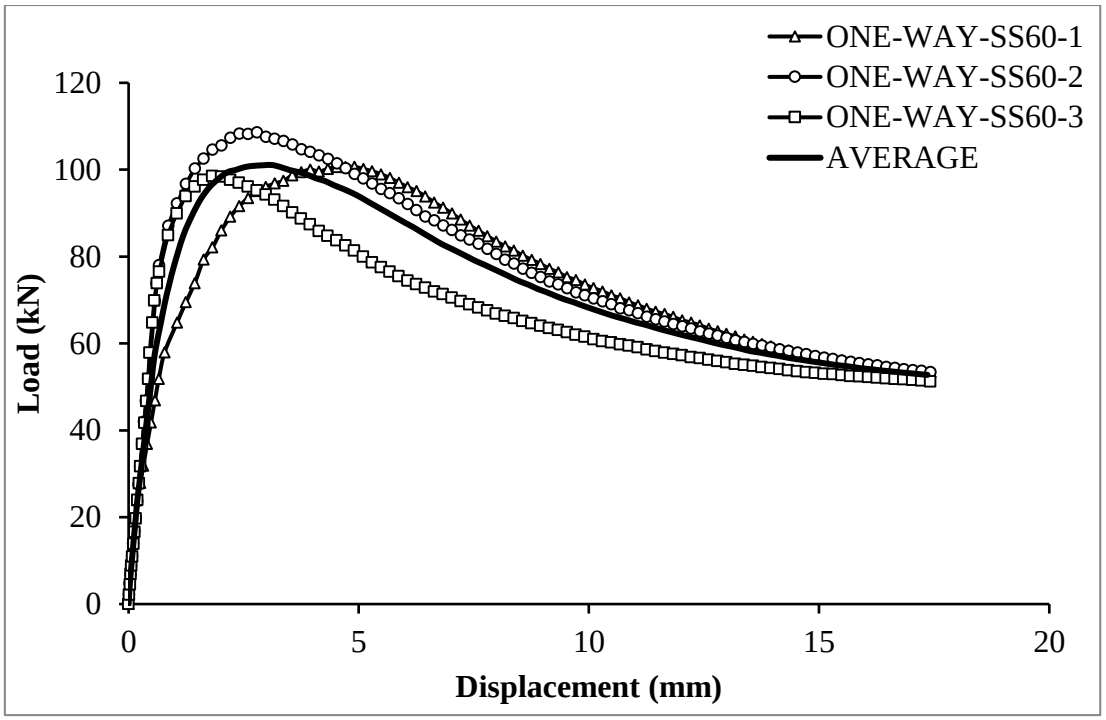

Figure 4.23: Load-displacement curves for SS60.

4.2.4 Thickness Assessment of One-way Slabs

The experimental ultimate load (F_s) for each slab specimen with an experimental average for both the FF and SS boundary conditions are recorded in Table 4.2 and Table 4.3, respectively. Displacement (w_s) at F_s for each slab and average w_s are also shown. The effect of slab thickness on the slab's ultimate load and displacement at ultimate load is discussed here. Table 4.2 illustrates the response of the four different slab thicknesses. It is clear that as the thickness increased the value of F_s required to produce a certain displacement increased. In the FF series, an average F_s required for the slab with 25 mm thickness was 24.7 kN whereas it increased by 123% when the 35 mm slab thickness was tested. For a slab thickness of 45 mm, the increase in F_s was only 64% and an average of 90.30 kN was recorded. Finally, when the 60 mm thick slab was tested, the F_s increased by 67%. These results indicate that the percentage increase in F_s reduced as the slab thickness increased.

In SS series, Table 4.3 shows that the average F_s of 16.5 kN was recorded for 27 mm thick slabs. The average F_s increased to approximately 29.1 kN for 35 mm thick slabs and this showed that the load was increased by 77% compared to the thin slabs. An average F_s of 52.1 kN was recorded for 45 mm thick slabs and the load carrying capacity in these slabs increased by 79% compared to slabs with 35 mm thickness. Finally, when 60 mm thick slabs were tested an average F_s of 102 kN was recorded, and the F_s increased by 96%. These results also showed that the percentage increase in F_s reduced with increase in the slab thickness but at a slower rate compared to FF slabs. In addition, these results showed that the F_s values are not influenced by the thickness directly, however, change in thicknesses influenced the fibre contribution, resulting in an increase or decrease in fibre-bridging behaviour. Fibre-bridging behaviour is significantly influenced by the amount of fibres in the location of the crack. Furthermore, F_s varied for slabs with similar thicknesses and boundary conditions due to the random distributions of fibre in the matrix, resulting in a variation in fibre pull-out behaviour for each specimen.

Referring to Figure 4.16 to 4.23 for slabs with FF boundary condition, it is clear that the appearance of microcracks was around an average load of 14, 28, 60 and 118 kN for slab thicknesses of 25, 35, 45 and 60 mm, respectively. The average loads were doubled as the thickness increased by 10 mm. For the slabs with SS boundary conditions, similar assessments can be conducted. Slabs with SS boundary conditions cracked at average

loads of 11, 21, 38 and 78 kN for slab thicknesses of 25, 35, 45 and 60 mm, respectively. Comparing these load values showed an approximate relationship of slab thickness to first crack load is apparent and the load almost increased by double as thickness changed. Each thickness produced an approximately linear relationship with the first microcrack load. These results are significant in terms of serviceability in designing UHPFRC as it allows designers to predict the cracking load. Consideration must be taken into account that small changes in thickness can significantly influence the serviceability load. It was also noted that the w_s at F_s in both series was approximately 5 mm for slabs with 27 mm and 35 mm thickness and 3 to 4.5 mm for slabs with 45 mm and 60 mm thickness, respectively. The difference in w between thin and thick slabs is perhaps due to the changes in stiffness, which increases in proportion to the slab thickness.

The transformation from elastic to strain-hardening for slabs with 25 and 35 mm in both series were similar and it covered a wide range of displacement approximately 0.5 to 5 mm, whereas this transformation zone was approximately 0.5 to 4.5 mm for slabs with 45 and 60 mm thickness in SS boundary conditions. In addition, the transformation from first to second region was found to be slower for slabs with 25 and 35 mm compared to slabs with 45 mm thicknesses. However, the transformations were found to be very similar for slabs with 45 mm compared to 60 mm thickness. This means fibre direction and orientation were changed within the matrix as the slab thickness increased, which resulted from the alignment of the fibres perpendicular to the direction of the force in thinner slabs. The effect of fibre orientation on the transformation of the material from one region to another appeared to reduce significantly when the slab thickness was large enough for fibres to orientate randomly, see Figure 4.14 and Figure 4.15. It seems, therefore, that having sufficient experimental data with respect to their thickness, the bending behaviour of UHPFRC slabs can be predicted.

Table 4.2: Slabs experimental results with fully-fixed boundary condition.

Specimens		Ultimate load F_s (kN)	Average F_s (kN)	Displacement (w_s) at F_s (mm)	Average w_s (mm)
Name	No				
ONE-WAY-FF25	1	26.7	24.7	5.1	5.1
	2	23.1		5.1	
	3	25.0		4.9	
	4	24.0		5.1	
ONE-WAY-FF35	1	56.1	55.0	5.3	5.2
	2	54.7		5.1	
	3	54.1		6.2	
ONE-WAY-FF45	1	92.0	90.3	3.3	3.3
	2	83.7		3.3	
	3	95.2		3.1	
ONE-WAY-FF60	1	155.6	150.8	4.9	4.6
	2	148.2		4.9	
	3	148.4		4.1	

Table 4.3: Slabs experimental results with simply-supported boundary condition.

Specimens		Ultimate load F_s (kN)	Average F_s (kN)	Displacement (w_s) at F_s (mm)	Average w_s (mm)
Name	No				
ONE-WAY-SS27	1	16.6	16.5	5.3	5.3
	2	17.2		5.3	
	3	16.8		5.3	
	4	15.5		5.3	
ONE-WAY-SS35	1	27.6	29.1	5.1	5.2
	2	29.6		5.2	
	3	30.1		5.2	
ONE-WAY-SS45	1	53.4	52.1	5.0	4.5
	2	51.5		4.5	
	3	51.3		4.1	
ONE-WAY-SS60	1	100.6	102.0	3.9	3.1
	2	107.5		3.0	
	3	97.9		2.4	

4.2.5 Size Effect and Effective Flexural Strength

In order to investigate the size effect, the effective flexural strength (f_{st}) of the slabs was calculated for slabs with both FF and SS boundary conditions using Equation 2.15 from Section 2.9.3. These equations can determine the general flexural strength only if the material behaves linearly. However, the validity of these equations diminishes as the material shifts from linear to nonlinear behaviour. Although these equations may not be valid once f_{st} is exceeded, they were used here for comparison purposes. The three and four f_{st} from the bending tests and the average f_{st} were recorded Table 4.4 for both FF and SS boundary conditions, for each slab thickness. The results were plotted against the slab thicknesses as illustrated in Figure 4.24 and Figure 4.25. Comparing UHPFRC to OC in terms of concrete fracture hypothesis, the results indicate that changes in thickness had no influence on f_{st} of the slabs. The results show that the average f_{st} for slabs with FF and SS boundary condition were 4.0 to 4.8 MPa and 6.7 to 7.1 MPa, respectively. Whereas, in OC, the ratio of the total crack surface area to the cross-section area of smaller specimens is believed to be higher than that of larger specimens. The results support the size effect finding reported in Chapter 3 in Section 3.4.4 and confirmed that the size effect behaviour which sometimes becomes a barrier in designing OC is less significant in designing UHPFRC structures in one-way slabs.

Furthermore, it was reported by Keenan (Keenan, 1969) that in reinforced concrete one-way slabs, deflection induces force on sections along hinge lines if the ends of the slab are restrained against longitudinal movement. This increases the moment resistance of sections along the hinge lines, thus significantly increasing the ultimate flexural resistance of the slab. However, it seems this behaviour was less in UHPFRC slabs as the flexural strength of SS slabs was found to be close to that of the slabs with FF boundary conditions. This was perhaps due to the effect of random steel fibre in the matrix, which reduced the effect of compressive membrane forces at the support whereas in ordinary reinforced concrete, flexural strength is enhanced by the compressive membrane forces (Tong and Batchelor, 1971)

Table 4.4: Effective flexural strength of one-way slabs.

h (mm)	Fully Fixed Slabs		Simply Supported Slabs	
	Effective Flexural Strength f_{st} (MPa)	Average f_{st} (MPa)	Effective Flexural Strength f_{st} (MPa)	Average f_{st} (MPa)
25	7.2	6.7	4.5	4.5
	6.4		4.6	
	6.8		4.5	
	6.5		4.2	
35	7.1	7.5	3.9	4.1
	7.8		4.1	
	7.7		4.2	
45	7.7	7.6	4.4	4.3
	7.1		4.3	
	8.0		4.3	
60	7.3	7.1	4.7	4.8
	7.0		5.0	
	7.0		4.6	

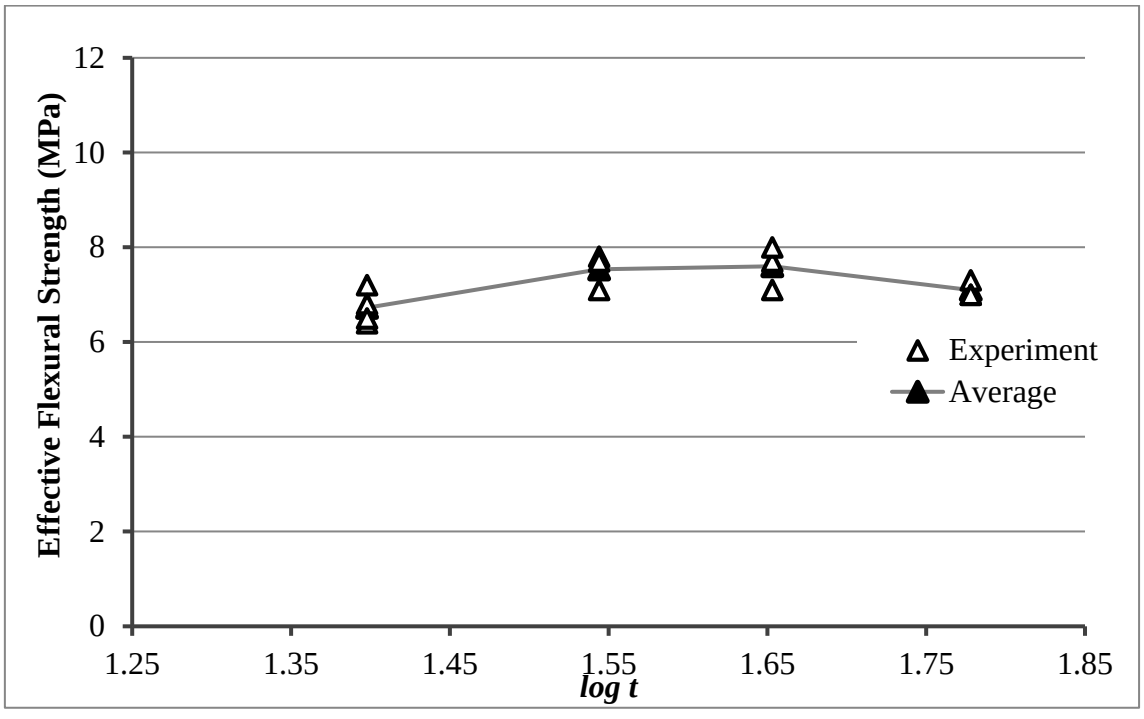

Figure 4.24: Ultimate flexural strength versus thickness for FF one-way slabs.

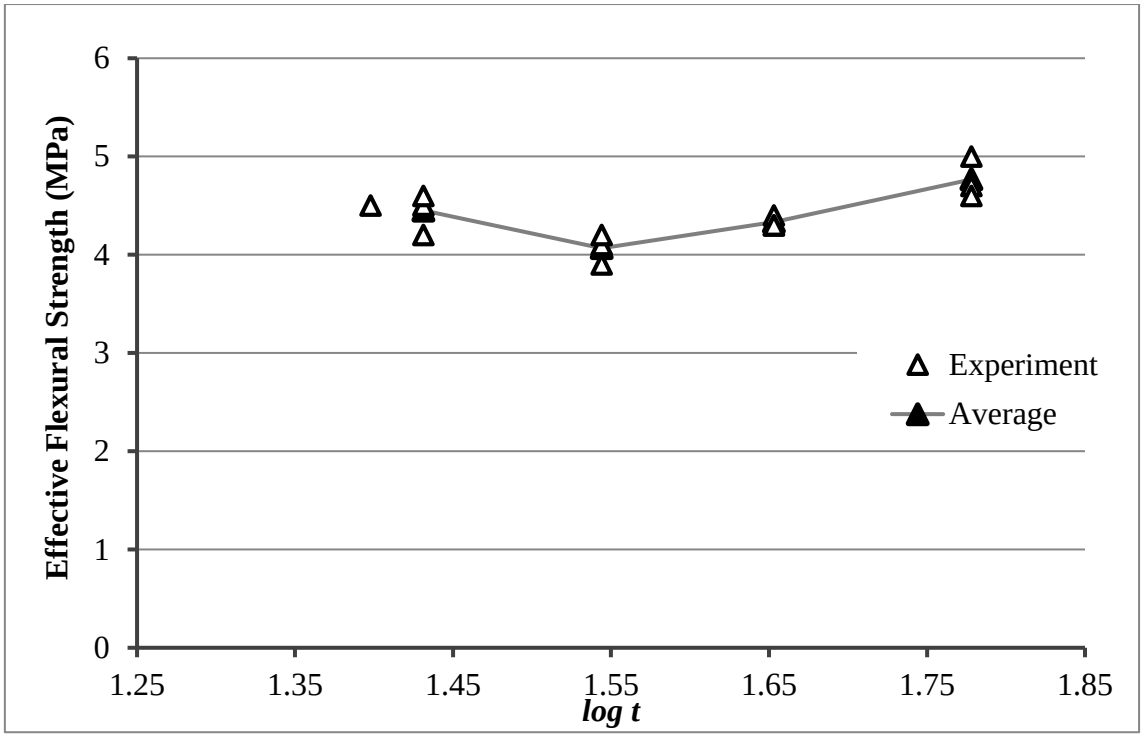

Figure 4.25: Ultimate flexural strength versus thickness for SS one-way slabs.

4.3 Concluding Remarks

The simple yet effective experiment setup showed that it is capable of determining the load-displacement curve and failure mode. Analysis of the test results has shown that changing boundary conditions from FF to SS setup are achievable.

The results from the experimental study for one-way slabs showed that boundary conditions have less effect on the pseudo-strain hardening behaviour in one-way slabs. It also showed that the failure mode in one-way slabs is not influenced by the boundary conditions and all the slabs failed with a single macrocrack on the tensile face. The results showed that all the UHPFRC one-way slabs fail in flexural behaviour. Similar to the beams, the failure mode of slabs also confirmed that the mechanical behaviour of UHPFRC goes through three main regions: (1) linear elastic (2) strain hardening, and (3) strain softening. Microcracks in both the FF and SS slab series initiated at a displacement of around 0.30 to 0.40 mm. It was found that the w at F_s in both series was approximately 5 mm for slabs with 25, 27 and 35 mm thickness and 3 to 4.5 mm for slabs with 45 mm and 60 mm thickness, respectively.

Examination of the physical distribution of fibres at the crack locations showed that fibres tended to be perpendicular to the cross-section in thin members due to the specimen wall effect, causing more fibres to bridge between the two cracked faces. In thick members, however, fibres were less affected by the specimen wall and more randomly orientated in the matrix, resulting in less fibre bridging between the two cracked faces. The physical examination also showed that few spots of poor fibre distribution can be observed in thicker slabs, especially 45 and 60 mm thick slabs, and this related to the actual fibre concentration. In addition, the examination showed that the mixing and casting procedures used in this study led to a satisfactorily uniform fibre distribution in UHPFRC.

These results also showed the percentage increase in F_s reduced with increase in the slab thickness in both series. However, these increases were slower in the slabs with SS boundary conditions compared to FF slabs. The results also showed that changes in thickness had no influence on f_{st} of the slabs in both the SS and FF series. It showed that the average f_{st} for slabs with FF and SS boundary condition were 4.0 to 4.8 MPa and 6.7 to 7.1 MPa, respectively. The results confirmed that the size effect behaviour which sometimes becomes a barrier in designing OC can be neglected when designing UHPFRC elements as one-way slabs.

CHAPTER 5

TWO-WAY SLAB INVESTIGATION

This chapter details the experimental investigation of bending behaviour of two-way UHPFRC slabs without conventional reinforcement. The slab chosen for the investigation in this study is 660 × 660 mm containing 2% by volume of short steel fibres with various thicknesses. The experimental work consists of two series. The first series was carried out on 13 slab specimens with fully fixed (FF) boundary conditions while the second series was conducted on 13 slabs with simply supported (SS) boundary conditions. To prepare the specimens, special moulds were built and details of the fabrication of these moulds are described in this chapter. The experimental programme, which includes mixing procedures, specimen fabrication, a developed experimental setup and loading procedure, is also described.

In order to understand the structural behaviour of two-way spanning UHPFRC slabs, a comprehensive and detailed examination was required, that included two different boundary conditions being considered. The aim of investigating two different boundary conditions was to demonstrate the effect of edge restraint on failure modes and crack propagation when subjected to direct transverse loading. The load-displacement relationship for both series and the effect of the specimen thickness on the load-displacement curves are also presented in this chapter.

The experimental measurement conducted in Chapter 4, were applied here to further investigate the effect of slab thickness on fibre distribution and orientation. Finally, the

influence of specimen thickness on the size effect behaviour and effective flexural strength are also discussed.

5.1 Experimental Programme

Two different test series of UHPFRC slabs were conducted under bending behaviour to identify different failure modes. A total of twenty six 660 by 660 mm slabs were tested with four different thicknesses (t): 25 mm, 35 mm, 45 mm, and 60 mm.

The first test series was conducted on 13 No. UHPFRC slabs with FF boundary conditions, while the second test series was conducted on 13 No. specimens with SS boundary conditions, as shown in Figure 5.1. Three slabs were tested with thicknesses of 35, 45 and 60 mm and four slabs with a thickness of 25 mm. As the 25 mm thick slabs were smaller than the length of two fibres, an extra specimen was tested to ensure that fibre balling did not occur and bending behaviour was obtained.

For clarity, slabs were named by their depth and boundary condition, for example, the slab TWO-WAY-FF25 is 25 mm thick and has fully fixed boundary conditions. In total, eight batches of specimens were prepared using the same mix design, four FF and four SS. An additional small batch was prepared to cast the extra 25 mm thick slabs. For each UHPFRC mix, 12 cubes, six (50 × 50 × 50) mm and six (100 × 100 × 100) mm were tested under uniaxial compression to assess the compressive strength of UHPFRC slab specimens at an age of 7 and 28 days.

All the slabs were tested using a centre point load, which is of interest in a variety of applications such as heavy machinery in warehouses, laboratory machines in buildings, office cabinets and many more.

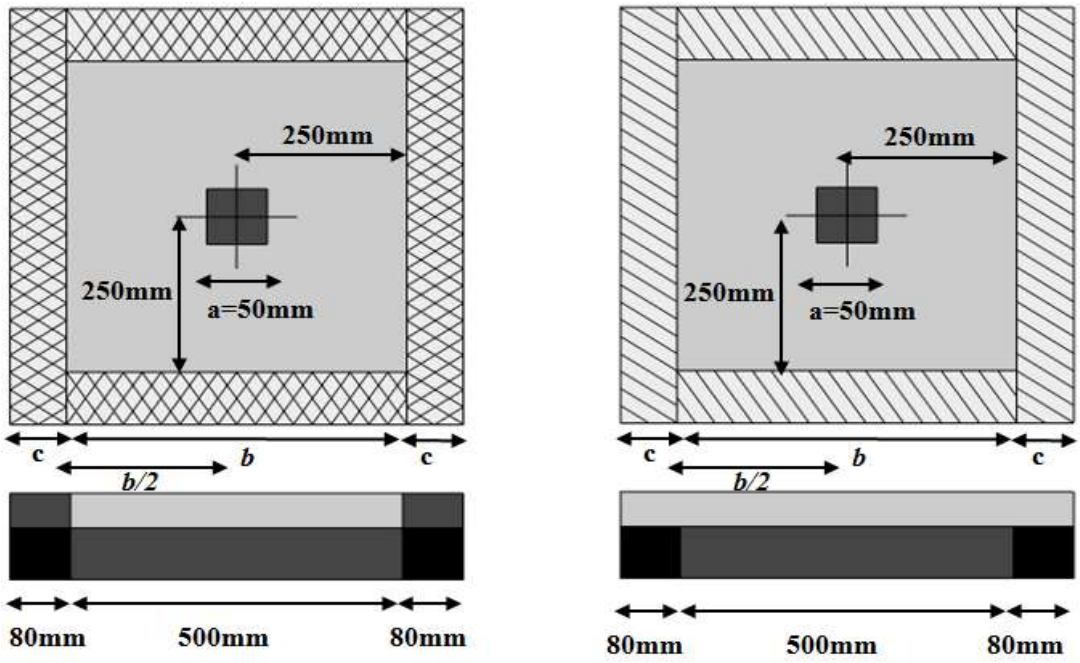

(a) fully fixed (b) simply supported.

Figure 5.1: Slab boundary conditions.

5.1.1 Materials and Mould Preparation

The materials used in the mix design to prepare the two-way slab specimens are explained in Section 3.3.3. The design of the mould used for the two-way slabs is given in Section 4.1.1.

5.1.2 Mix Design and Specimen Fabrication

The one-way slab mixing procedure described in Section 4.1.2 was employed in preparation of two-way slab specimens. The two-way slabs are also prepared using the similar procedure used for one-way slabs.

5.1.3 Equipment Setup Testing Procedure

The slab specimens were tested using the Zwick hydraulic loading machine. To test the specimens, a novel experimental setup had to be designed to apply the boundary conditions described previously. The equipment for the slab tests consisted of two

identical steel I-sections, large and small square steel frames with 50mm and 40mm thickness, respectively. In addition, for slabs with FF boundary condition, M20 steel studs to fix the slab to the steel frames were used. Details of the I-sections and steel frames are shown in Figure 5.2.

At the start of the experimental setup, the two I-section steel beam were placed and fixed to the base of the testing machine using M20 steel studs, as shown in Figure 5.3a. The large steel frame was then placed on the two I-sections and secured at the four corners using M20 studs, as illustrated in Figure 5.3b. Once the supports were fixed, the slabs were placed on the large frame, as shown in Figure 5.3c. After the setup was completed, a linear variable displacement transducer (LVDT) was placed under the centre of the slab (see Figure 5.3d). This setup was used when the slabs were tested with the SS boundary conditions. For slab specimens in the FF series, the small steel frame was placed on the slab and fixed to the setup configuration using M20 steel studs as shown in Figure 5.3e and Figure 5.3f.

The load was applied through a 50 mm cubic steel block at the centre of the specimen, as illustrated in Figure 5.4. Since the softening part of the post-peak behaviour was required in this study, the tests were performed under displacement control with the rate of 0.4 mm/min. The LVDT connected to the loading machine was placed under the slab to record the displacement during the test. The LVDT had a total movement range of 18mm and was connected to a computer to collect the load and displacement data. The data was collected using specialised software called ‘testXpert’. This software allows the user to request any desirable output curves during the testing procedure. In this study, the load-displacement curve was requested for each slab and the curve was monitored during the experiment to ensure that the test had been conducted accurately. Due to the short range of the linear elastic region and to ensure enough data was obtained in this region, for every second, one data point was recorded. Therefore, in total, over 2000 data points were collected for each slab. However, after the test was completed, the MATLAB software was used to process and analyse the data.

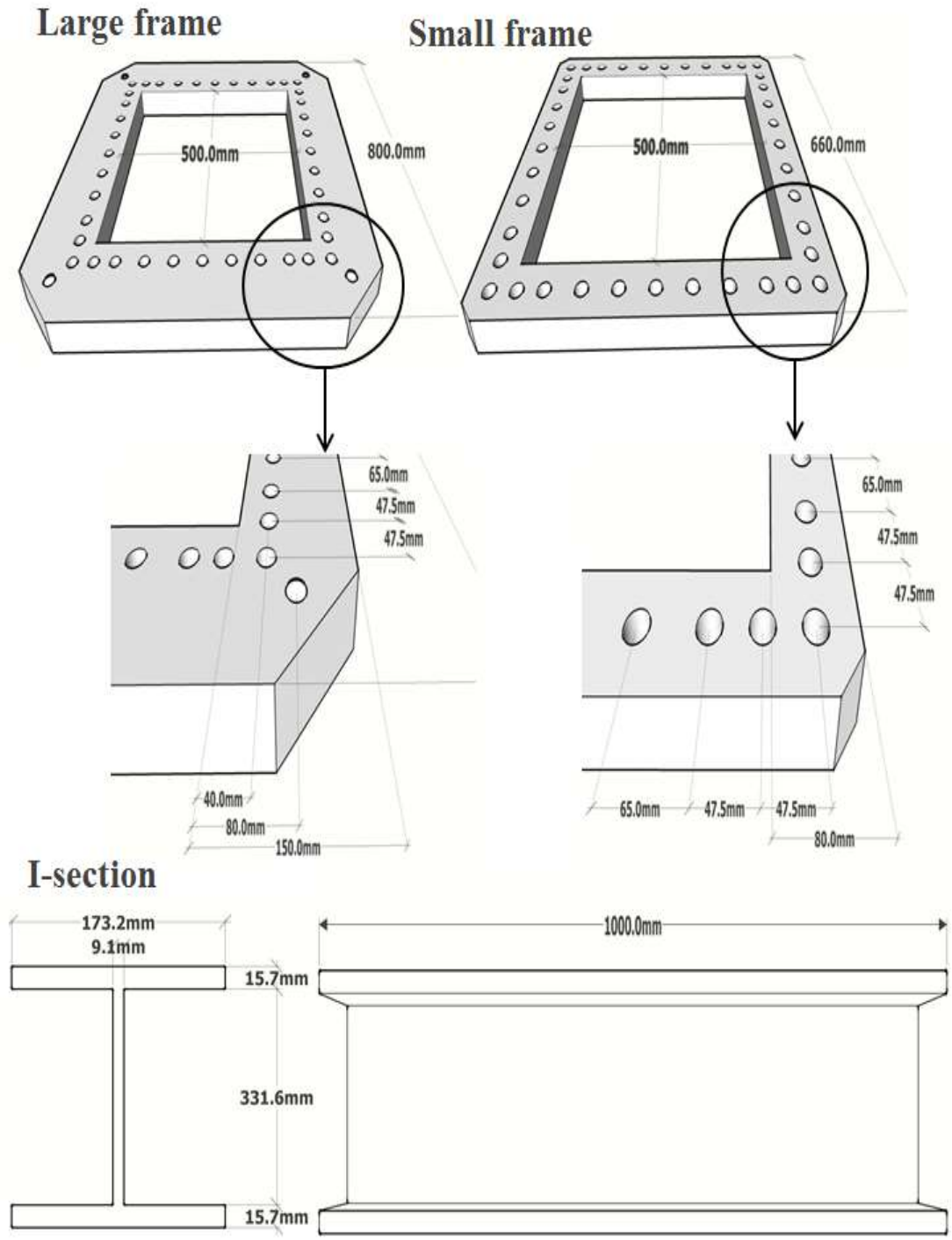

Figure 5.2: Steel frames and I-section details.

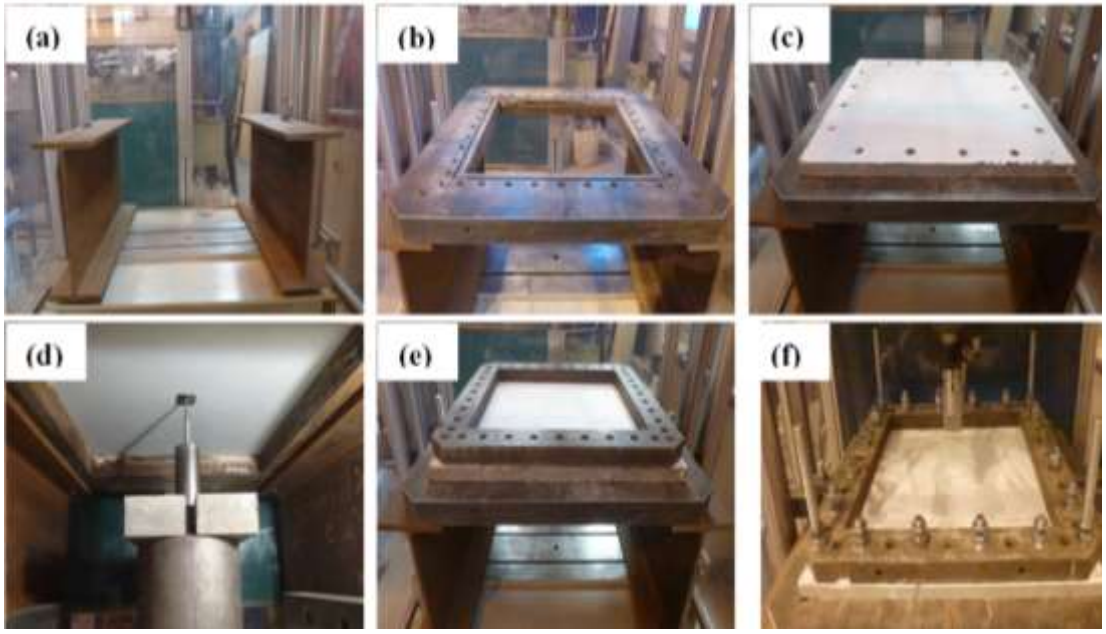

Figure 5.3: Details of experimental setup (a) I-sections placed at the machine base (b) big frame placed on the I-sections (c) slab placed on the big frame (d) the LVDT placed at the bottom face of the slab (e) small frame placed on the specimen in FF series (f) the edge restraint in FF series.

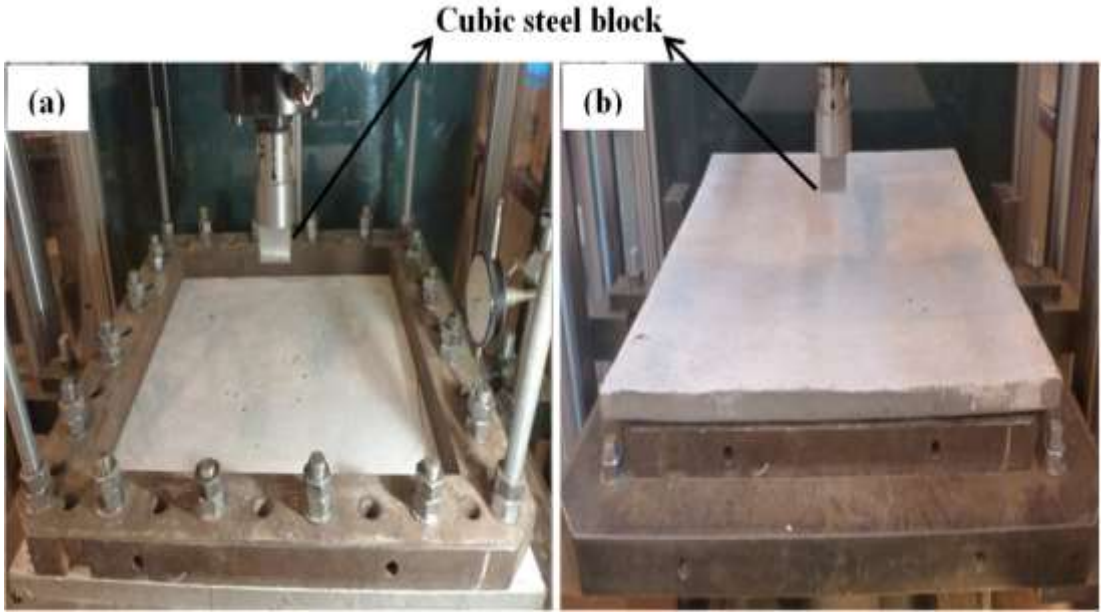

(a) fully fixed boundary condition (b) simply supported boundary condition

Figure 5.4: Two-way slab boundary conditions during the test.

5.2 Results and Discussions

This section presents the experimental results of two-way slabs subjected to bending using the designed testing setup described above. The slabs were tested under a central load with FF and SS boundary conditions that are of interest in design. The structural behaviour of UHPFRC slabs including failure modes and the load-displacement relationship is discussed. The effect of slab thickness on effective failure modes, crack formation, fibre distribution and orientation and flexural strength in the matrix is also discussed.

5.2.1 Two-way Slab Fibre Distribution and Orientation

To further determine how fibres are distributed within the slab specimens and how the slab thickness affects the fibre distribution, a specimen from each thickness was visually inspected. The results of this investigation can also be used to further clarify the findings presented in Chapter 4 regarding the effect of fibre distribution on slab failure modes. This can also further verify the mixing and casting procedure used to prepare the UHPFRC specimens in this study. In a similar process to that used to investigate the one-way slabs, one specimen of each thickness was cut into segments at the locations where cracking occurred during the experimental testing, as shown in Figure 5.5. The number of fibres present at each crack surface for each thickness were counted and recorded as shown in Figure 5.6 – 5.9. The approach used to count the fibres of the one-way slab was also adopted for the two-way slabs and the crack surface was initially divided into small sections of 5 x 25 mm. This approach allowed the fibres to be counted more easily, as well as providing more accurate results as it minimised the possibility of double counting or miscounting fibres. Since the majority of the slabs failed with four major cracks, the slab segments were labelled using geographical notation, e.g. the top segment was labelled as north as shown in Figure 5.5. Each side of the segment was labelled according to its position in the figures, e.g. the cracks labelled as NW and NE were located in the North West and North East segments, respectively.

Looking at the flow charts, it is evident that the two faces of each crack do not have the same number of fibres. As explained previously, the number of fibres on each crack face depends on the length of the embedded fibres. Fibres tend to pull out from the face where

the embedded length is the shortest, resulting in a considerable difference between the two faces of the same crack. In addition, since the crack lengths varied between cracks, as shown in the flow charts, it was important to measure the length of each crack in order to accurately evaluate the fibre distribution of different slab thicknesses.

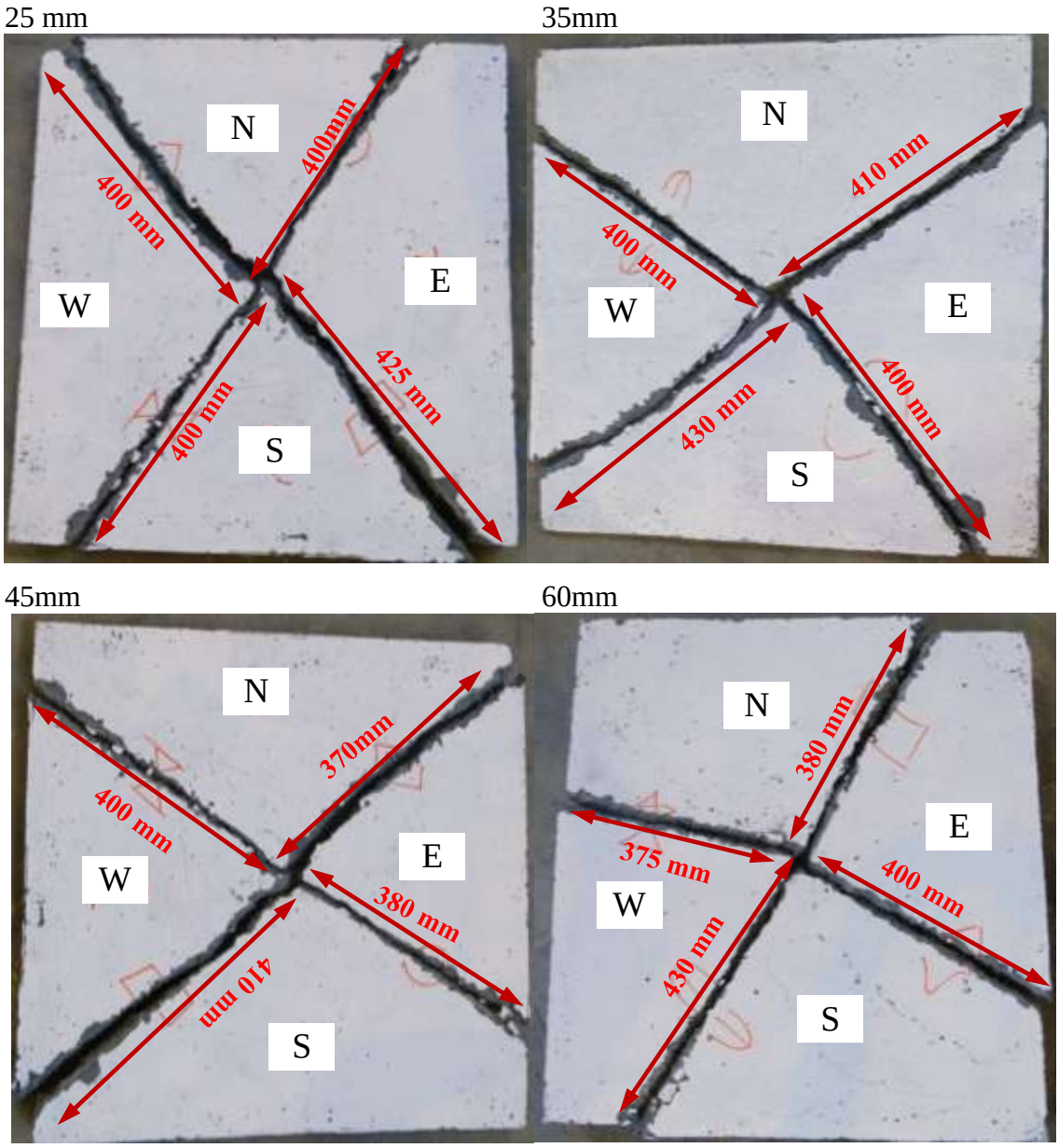

Figure 5.5: Slabs were cut into four segments at the crack locations.

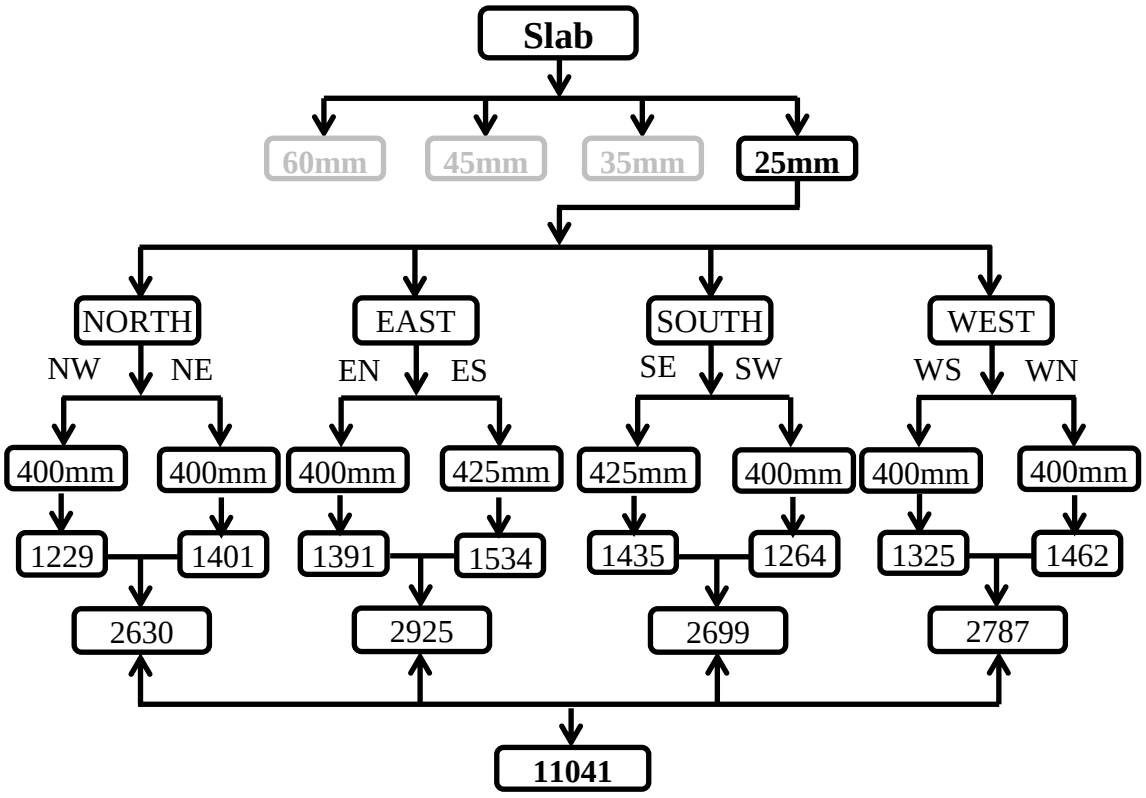

Figure 5.6: Flow chart for slab with 25 mm thickness.

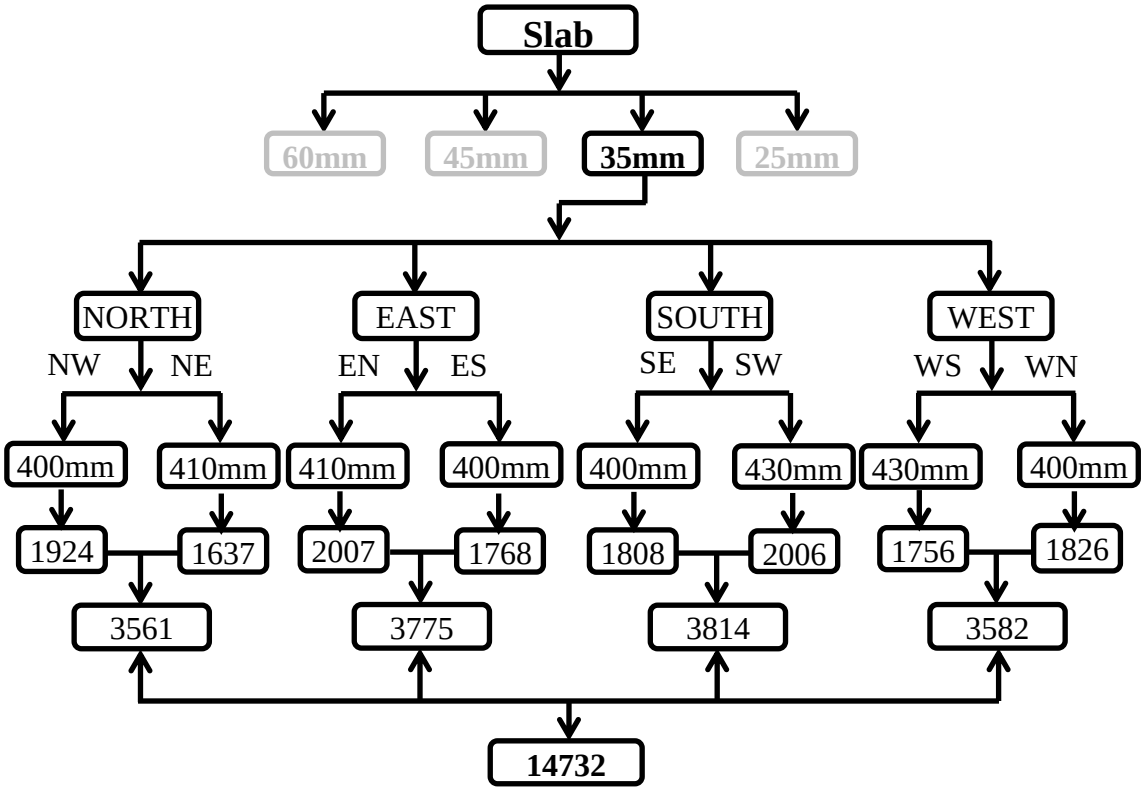

Figure 5.7: Flow chart for slab with 35 mm thickness.

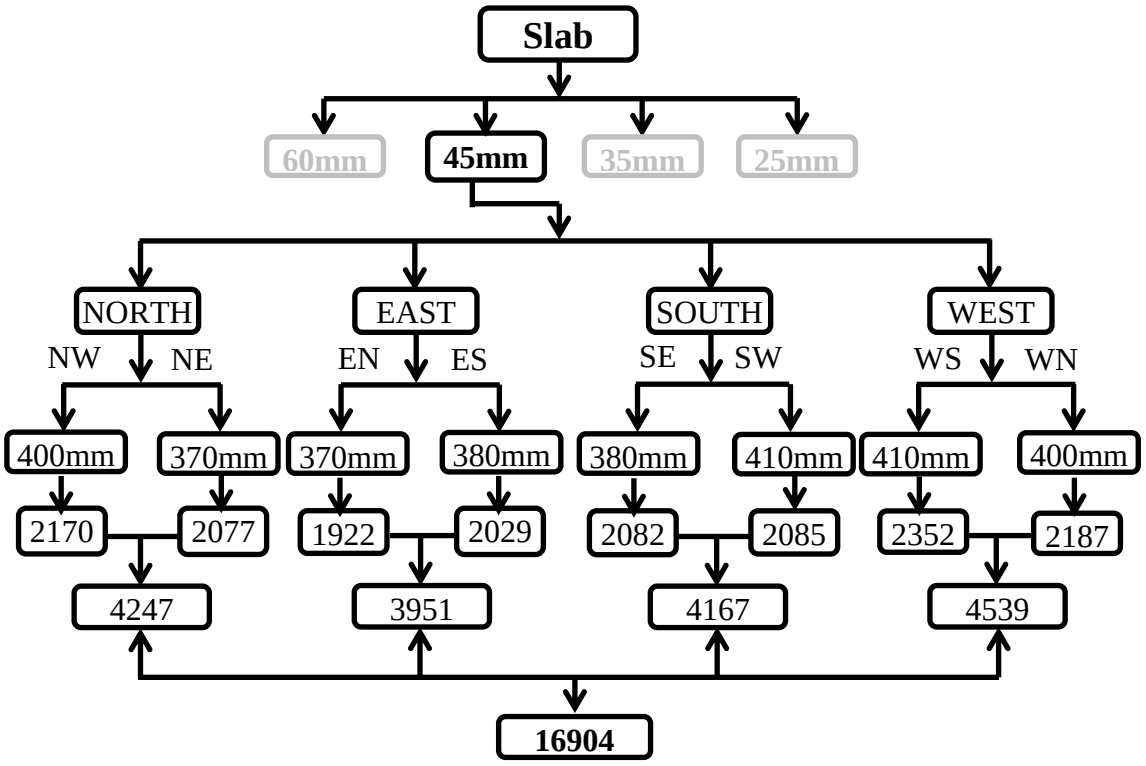

Figure 5.8: Flow chart for slab with 45 mm thickness.

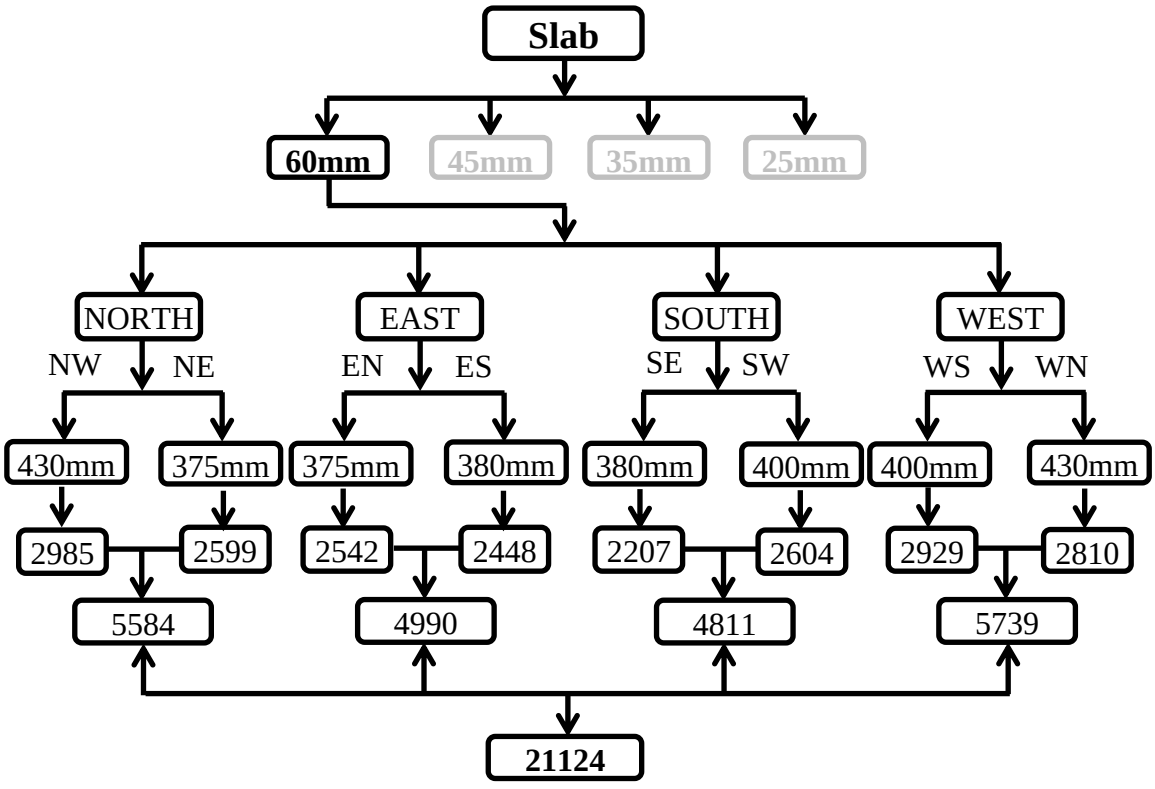

Figure 5.9: Flow chart for slab with 60 mm thickness.

Examination of the 25 mm slab specimen showed that there were 1229 fibres on the NW face of the crack, whereas there were 1401 on the NE face. Similarly, there were 1462 fibres on the WN face of the west segment which was considerably greater than the 1325 fibres on the WS face. This behaviour was observed for all the specimen thicknesses and depends on the fibre embedded length at that particular location where cracking occurred. Moreover, using visual inspection, it was confirmed that similar to the one-way slabs, there was no fibre balling in any of the slab specimens where cracking had occurred. These results further confirm the validity of the mixing process used in the current study. As mentioned above, in order to compare the results between different slab thicknesses, it was also important to consider the crack length. Because the longer the crack, the greater the number of fibres to be counted. Therefore, two cracks from specimens of different thickness (e.g. the crack in location N of the 25 mm slab and the crack in location N of the 35 mm slab) are no longer directly comparable. As a result, the lengths of the cracks were taken into account in the comparison procedure. However, to simplify the comparison between the different thicknesses and to be able to compare the two-way slab results to the one way slab data, the number of fibres were calculated for a 660 mm crack length, which is equal to the crack length of one-way slabs. This was done by adding the number of fibres at all four locations (E_m) and dividing by the total crack lengths (C_{TL}), and multiplying by 660 mm crack length as shown in Equation 5.1 and Table 5.1.

$$N_{660} = \frac{E_m}{C_{TL}} \times 660 \qquad \textbf{(5.1)}$$

For example, N_{660} for 25 mm slab was calculated as follow:

$$N_{660} = \frac{11041}{400 + 425 + 400 + 400} \times 660 = 4484 \text{ fibres}$$

Similar to the 25 mm slab, the other slab thicknesses 35, 45 and 60 mm were also calculated and recorded in Table 5.1.

Table 5.1, column two from the right also shows, the number of fibres per 10 mm thickness were counted to be 1794 for the 25 mm slab. Whereas, the number of fibres per 10 mm thickness reduces to 1444 fibres as the slab thickness increased to 35 mm. The results also show for the other thicknesses investigated, the number of fibres per 10 mm thickness further reduces to 1223 and 1096 for 45 mm and 60 mm slabs, respectively. This indicates that the fibre distribution has reduced as the slab thickness increased. This can only be explained due to the specimen wall effect in 25 mm slab restricting fibres to orientate freely within the matrix. Whereas, fibres in the thick slab matrix were allowed to orientate more freely, resulting in less fibres contributing to the bridging action between the two cracked faces. To better illustrate the relationship between the slab thickness and fibre distribution, the results of both two-way are plotted in Figure 5.10. The results are found to be similar to the one-way slabs and confirm that fibre distribution reduces as slab thickness increases.

Another important observation was that, similar to the one-way slabs, the changes in the experimental measurement was also found to be smaller (127 fibres only) when the slab thickness increased from 45 to 60 mm. In addition, to further investigate this, the results of the beam specimens in Chapter 3 were used. Using Equation 5.1, the number of fibres for a 660 mm crack length (N_{660}) were calculated for all the beam thicknesses. The (N_{660}/t) ratio for both beam and slab specimens were plotted as shown in Figure 5.11. It was found that the ratio became similar for specimen thicknesses greater than 60 mm. This clearly shows that the specimen geometry has very little effect on fibre distribution as the thickness became greater than 60 mm. This is especially useful since the fibre orientation and distribution in life-sized structures is unlikely to differ much from the largest slab and beam tested here. However, as mentioned in Chapters 3 and 4, these conclusions may need to be validated experimentally with real life sized structures before they can be used extensively. The findings of the two-way slab investigation also agree with other studies reported in the literature that geometry has a significant effect on fibre distribution and orientation (Døssland, 2008, Wille et al., 2014, Sebaibi et al., 2014).

Table 5.1: Experimental measurement of two-way slab.

t (mm)	Experimental measurement (E_m)	Total crack length (C_{TL}) (mm)	Fibre per 660 crack length (660 x E_m / C_{TL})	Increase in number of fibres per 10 mm increase in thickness (E_i)	Differences $\lvert Ei_{25} - Ei_t \rvert^*$
25	11041	1625	4484	1794	0
35	14732	1640	5929	1444	349
45	16904	1560	7152	1223	571
60	21124	1585	8796	1096	697

*t =35, 45 or 60 mm

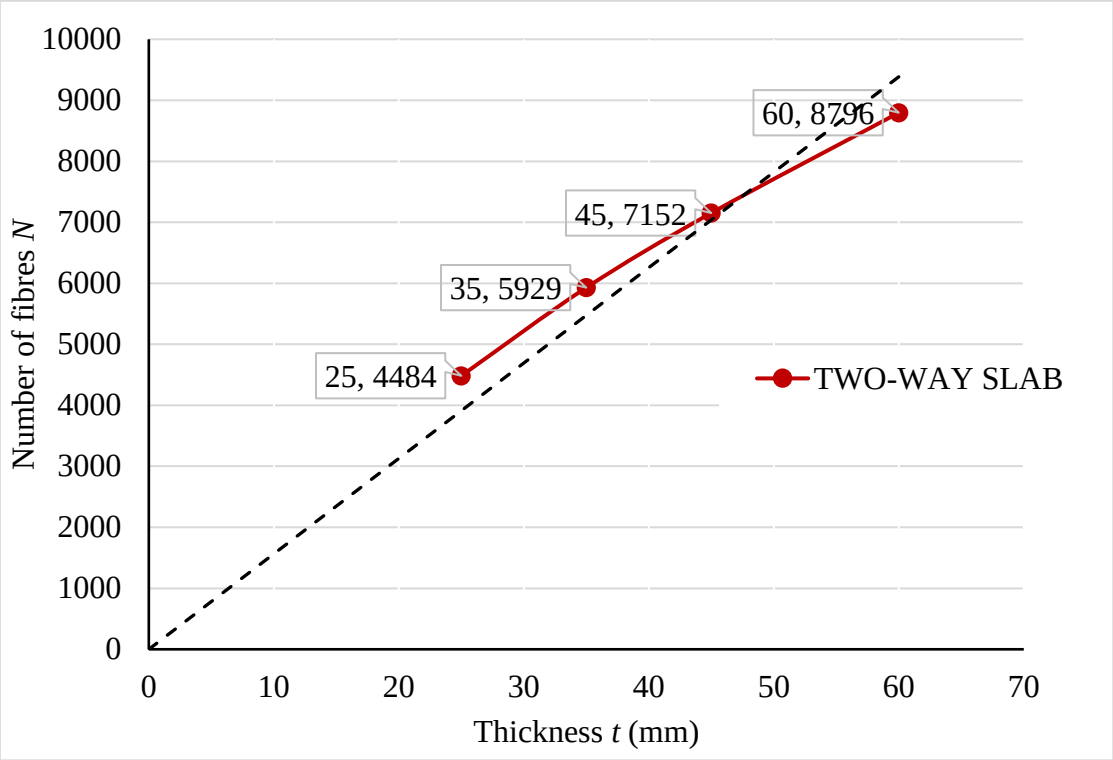

Figure 5.10: Relationship between fibre distribution and specimen thickness.

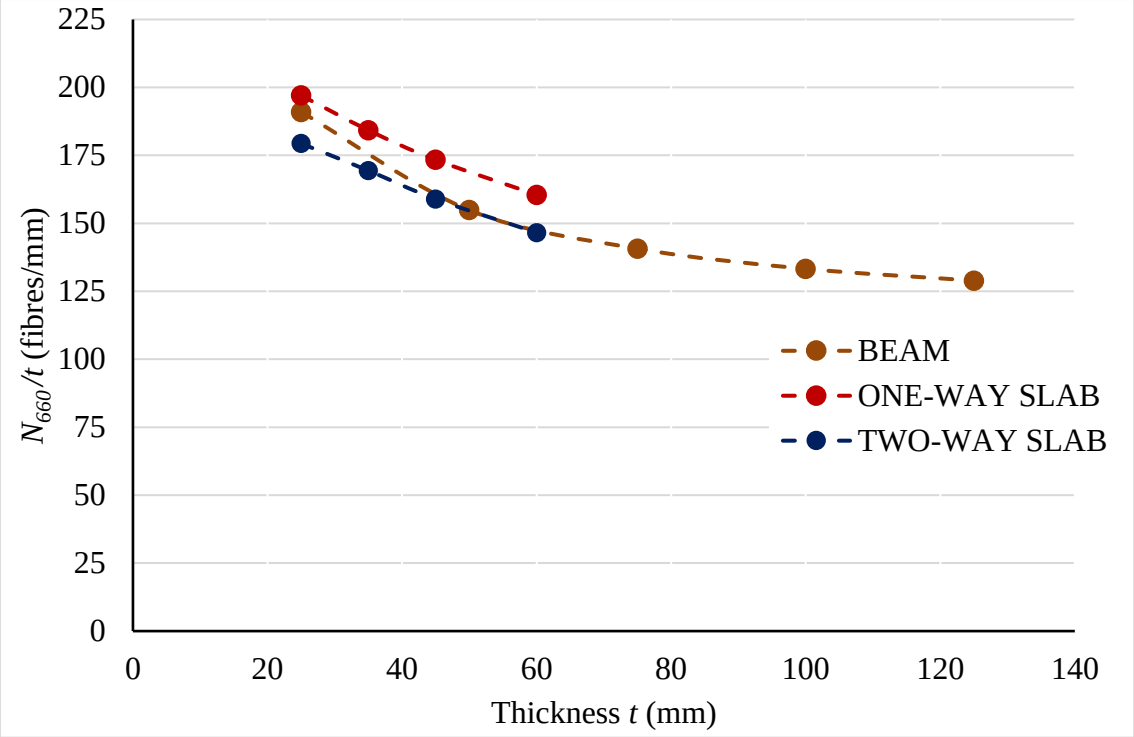

Figure 5.11: Relationship between fibre distribution and slab thickness for beams and slabs.

5.2.2 Failure Modes

During the experiments, it was observed after a deflection of approximately 0.25 to 0.30 for thin slabs (25 and 35 mm) and 0.30 to 0.40 mm for thick slabs (45 and 60 mm), on the tensile face, several microcracks appeared around the centre of the slab specimens. However, as the loading was increased, these microcracks formed several macrocracks and extended towards the slab edges. The formation of macrocracks was random and it was different from one thickness to another and even from one slab to another. As explained above, the formation of these major cracks was dependant on the fibre orientation and distribution in the crack area because cracks tend to form where the material is at its weakest. In addition, after the slab failed, it was observed that the fibres had begun to pull-out from the cracked faces by around 5 mm for all the slabs for both FF and SS boundary conditions.

Irrespective of the differences in the slab geometry, all the specimens with FF boundary conditions failed in flexure with similar failure crack patterns. On the tensile face, cracks

initiated from the centre towards the corners and edges of the slab. It was noted that four macrocracks were formed for the thinner UHPFRC slabs (25 mm, 35 mm), while six macrocracks occurred in few of the thicker specimens (45 mm, 60 mm) as depicted in Figure 5.12. This can be explained by the fibre orientation (angle of pull-out) and density within the matrix. As explained in Section 4.2.1, in thinner slabs, fibres tend to be parallel to the surface and perpendicular to the line of action of the force and this can have a considerable effect in preventing a small crack becoming a large one, resulting in fewer cracks (Rossi et al., 1987). In thicker slabs, fibre orientation can be much more random and this means less fibre contribution in fibre-matrix bond, resulting in more cracks occurring. The higher number of cracks in UHPFRC is due to the crack-bridging effect of the fibre, which results in softening behaviour where cracks localise in pronounced deformation and this was shown by Marti et al. (1999). Furthermore, although the slab geometry, loading and boundary conditions were the same, the cracks in some of the slabs are tortuous and deviate away from a straight line. In addition, the appearance of microcracks in the slab was random. This should be attributed to the random distribution and orientation of steel fibres in the concrete as was reported by Wille and Parra-Montesinos (2012) and Spasojevic (2008). This behaviour makes the crack-tip stress fields complicated and the local tensile strength and fracture toughness are highly heterogeneous, as in conventional concrete where the aggregates function in a similar way as the steel fibres (Lepech and Li, 2004). All the slabs in the FF series ended up with similar crack patterns in the compressive face where cracks formed in a circular shape along the inner part of the top steel frame. These cracks deviated from a straight line due to the effect of random steel fibre distribution within the matrix as explained above, and also as illustrated in Figure 5.13a. Whereas in the SS slab series, cracks on the compressive face were not observed as the slabs had no restriction to rotation in the opposite direction to the load as shown in Figure 5.13b. Cracks in slabs with the FF boundary condition were more pronounced compared to those with the SS boundary condition.

The importance and effect of boundary conditions need to be considered in the analysis of any structure, particularly a concrete slab. However, with regard to real life structures, determining their true boundary condition has always been challenging. Most of the slab structures, particularly in buildings and bridges, are neither simply supported nor fully fixed. Therefore, both FF and SS boundary conditions were considered in this study,

aiming to understand the behaviour of the UHPFRC slab in both cases. During the experimental work dial gauges were used on several trial slabs with a 25 mm thickness to ensure that there was no rotational behaviour at the supported areas during the testing for slabs with FF boundary conditions. The results of this trial testing showed no indication of support rotational behaviours at all four edges. Dial gauges were also used during the actual experiment and the results indicated zero rotational behaviour at the support.

Despite taking all these measures for ensuring the fixity of the support edges in the FF boundary condition, the results of some of the thick slabs (45 and 60 mm) indicate that the stiffness of the support edges may have varied. While, looking at the result of the slabs with FF boundary condition, cracks propagate from the centre of the slab toward few centimetres away from the corners. This behaviour is more pronounced in thick slabs, where more than four macrocracks occurred in some of the specimens as shown in Figure 5.12. This may be due to the fact that two edges of the slabs were supported by the two I-section beams as well as the steel frames and these provided a stiffer support than the other two edges which were supported by the steel frames only, as shown in Figure 5.3e. This variation in support stiffness was not detected in the experimental work as the smallest reading of the dial gauge is 1 mm. In order for the support rotation to be detected by the dial gauge, the reading had to be greater than 1 mm. As mentioned previously, the load-displacement curves showed that the slabs linear elastic stage ended at a displacement of less than 0.40 mm and microcracks had started when the displacement was much smaller than 1 mm. Therefore, the small rotation of the two supports which were resting on the steel frames only may have rotated less than 1 mm. Moreover, because the linear elastic behaviour of UHPFRC structures is significantly small and covers a very small range of displacement, this shows that the material is more sensitive to the support stiffness when compared to OC. Therefore, boundary conditions cannot be taken lightly during the design of UHPFRC members and must be considered carefully.

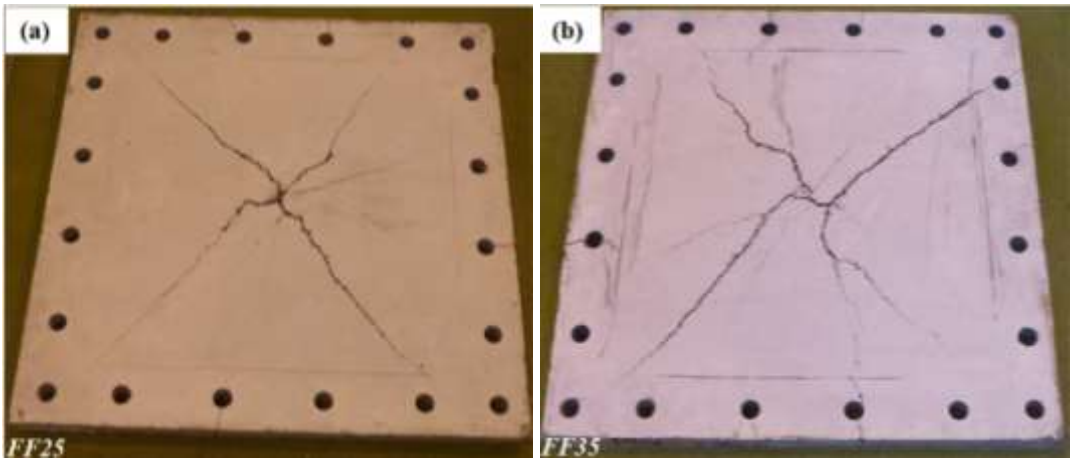

(a) tensile crack pattern of the FF25 slab (b) tensile crack pattern of the FF35 slab

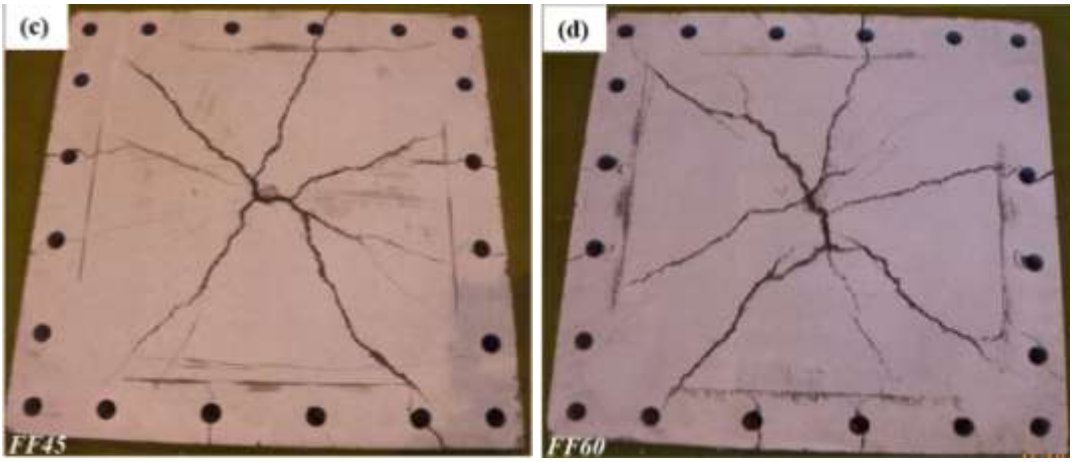

(c) tensile crack pattern of the FF45 slab (d) tensile crack pattern of the FF25 slab

Figure 5.12: Cracks on tensile face for two-way slabs with FF boundary condition.

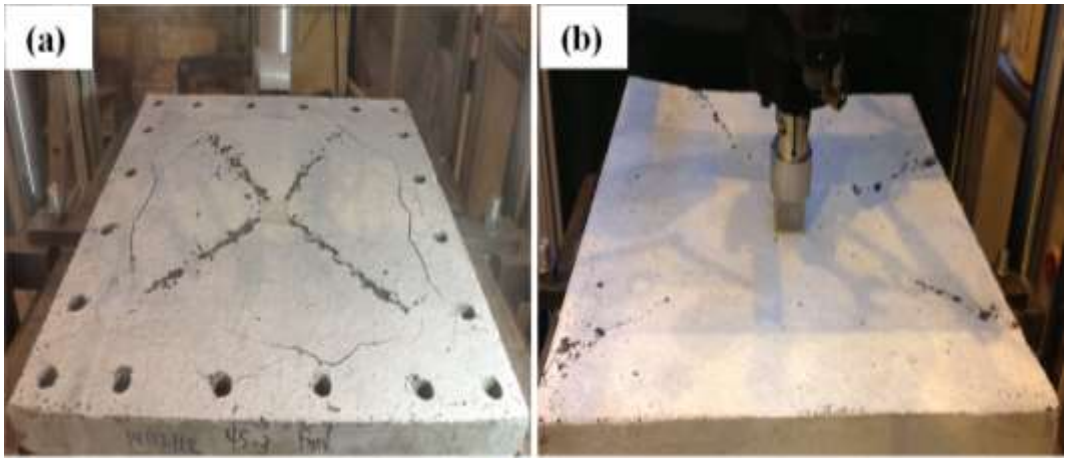

(a) compressive face crack for FF45 (b) compressive face crack for SS45

Figure 5.13: Two-way slab compressive face crack pattern.

The result of the second series of specimens with the SS boundary condition clearly shows that the diagonal cracks form from the position where the load acts towards the corner of the specimens. However the number of cracks in this test series seems to be more consistent throughout the range of varying slab thickness and all the specimens failed with four diagonal macrocracks, as depicted in Figure 5.14. This smaller number of cracks can be explained by the effect of the SS boundary condition compared to the slab specimens with FF boundary condition. This indicates that the edge restraint influences the failure mode, thus consideration must be given to the boundary condition during the design of UHPFRC slabs. In addition, a significant effect due to the boundary conditions was observed during the transformation of microcracks to a macrocrack in this series.

As the load was increased, the transformation took longer and slabs underwent a smooth transformation from the elastic region to strain-hardening where a sudden change could be observed in the slab specimens with FF boundary conditions. In general both series showed similar failure modes where cracks radiated from the centre of the slab specimens towards the edges. It is difficult to know the true boundary condition of a slab in an engineering structure, such as bridges and buildings in particular. Therefore, in slab design it is important to consider both FF and SS boundary conditions, especially in designing UHPFRC slabs.

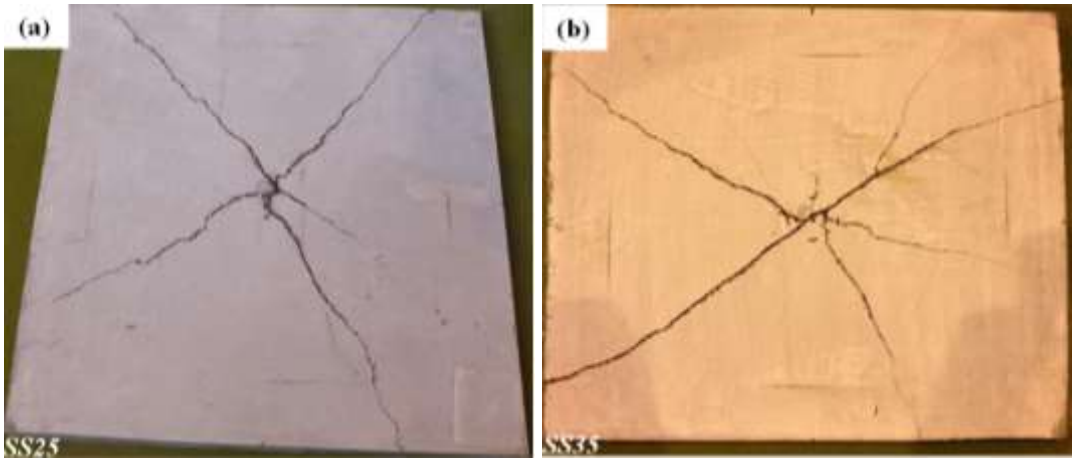

(a) tensile crack pattern of the SS25 slab (b) tensile crack pattern of the SS35 slab

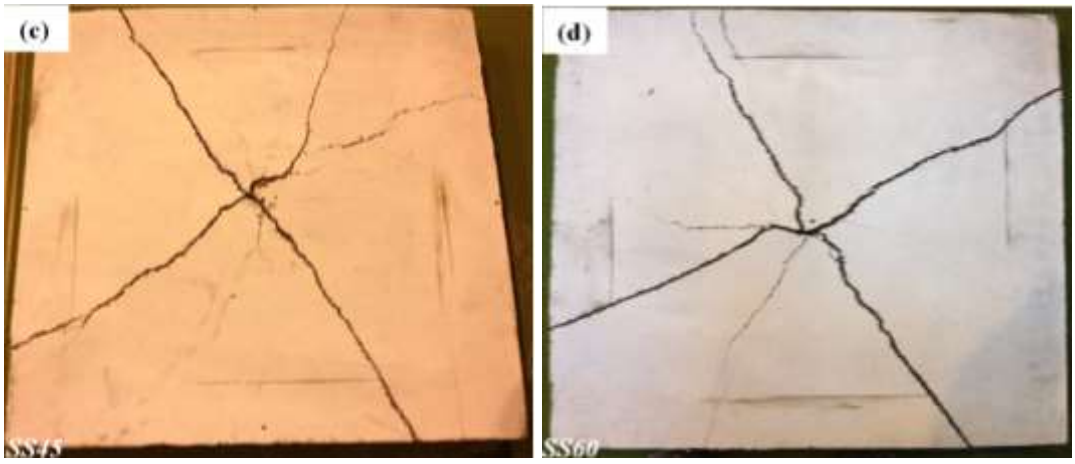

(c) tensile crack pattern of the SS25 slab (d) tensile crack pattern of the SS25 slab

Figure 5.14: Cracks on tensile face for two-way slabs with SS boundary condition.

5.2.3 Load-displacement Curves

The three and four load–displacement curves for all the specimens from the bending tests and the average curve are shown in Figure 5.15 to 5.18 for the FF boundary conditions and Figure 5.19 to 5.22 for the SS boundary conditions, respectively, for each slab thickness. A little scatter can be seen in the experimental results of the three and four tests for any one slab design and this is due to the random distributions of discontinuous short steel fibres. As expected, thicker specimens led to a significantly higher bending strength compared to that of thinner slabs. In addition, slabs with a similar geometry could withstand a greater load with the FF boundary condition compared to the SS boundary

condition, due to the development of significant tensile membrane resistance along the supporting edges.

As reported in Chapter 4, three main regions were also identified in the slab specimens. The first region covers the beginning of the load to the appearance of microcracks where the material is purely elastic. The second region follows, as the load was increased after the slab deflection reached approximately 0.30 to 0.40 mm. In this region, tensile stress was resisted completely by the fibre-matrix bond. In this region, several macrocracks developed from the centre to the slab edges and a sudden decrease in the slab stiffness was also noticed. These crack surfaces were bridged by closely spaced steel fibres. Due to the high strength of the steel fibres and strong bond between the fibres and the matrix, the macrocracks widen slowly during this stage, leading to a certain level of strain hardening as shown in Figure 5.15 to 5.22. Since slabs with the SS boundary condition were allowed to rotate freely, the transformation of microcracks to macrocracks was considerably slower compared to the FF boundary condition. The deformation is also significantly greater for the SS series compared to the FF series, and this clearly shows that the boundary condition considerably influences the strain-hardening region. The final region started when the ultimate load carrying capacity of UHPFRC is reached at the end of the strain hardening region. In this region, slabs with FF boundary conditions underwent a considerably large deflection when compared with the strain-hardening region as was reported by Hassan et al. (2012). This behaviour could be due to weakening of the bond between the matrix and the steel fibres during the pseudo-strain hardening region. However, a decrease in softening region of the curves for specimens within the FF series was considerably slower compared to specimens in the SS series for the same slab design and in thick slabs in particular. This is because the edges of the slabs in the SS series were allowed to rotate, resulting in a faster decrease in the load. There was a considerable scatter in the experimental results of the three and four tests for any one slab design in the softening region. A more detailed discussion of these regions can be found in Section 4.2.2. Similar to the beam and one-way slab specimens, closer examination confirmed that all the two-way slab specimens also failed by fibre pull-out.

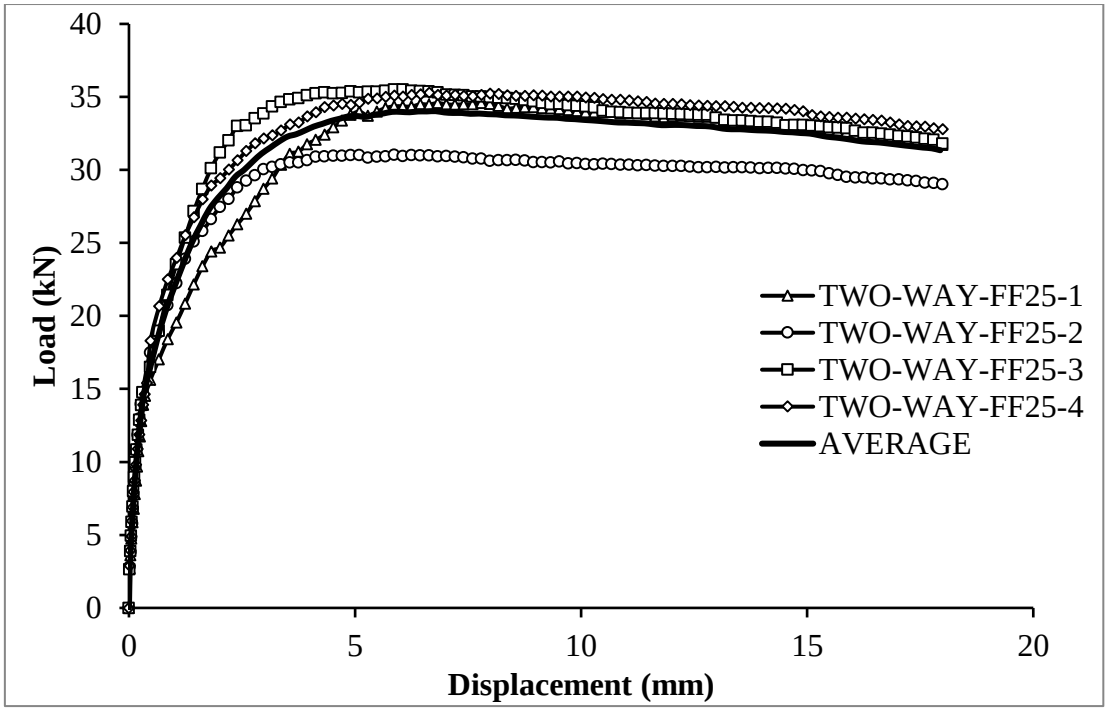

Figure 5.15: Load-displacement relationship for FF25.

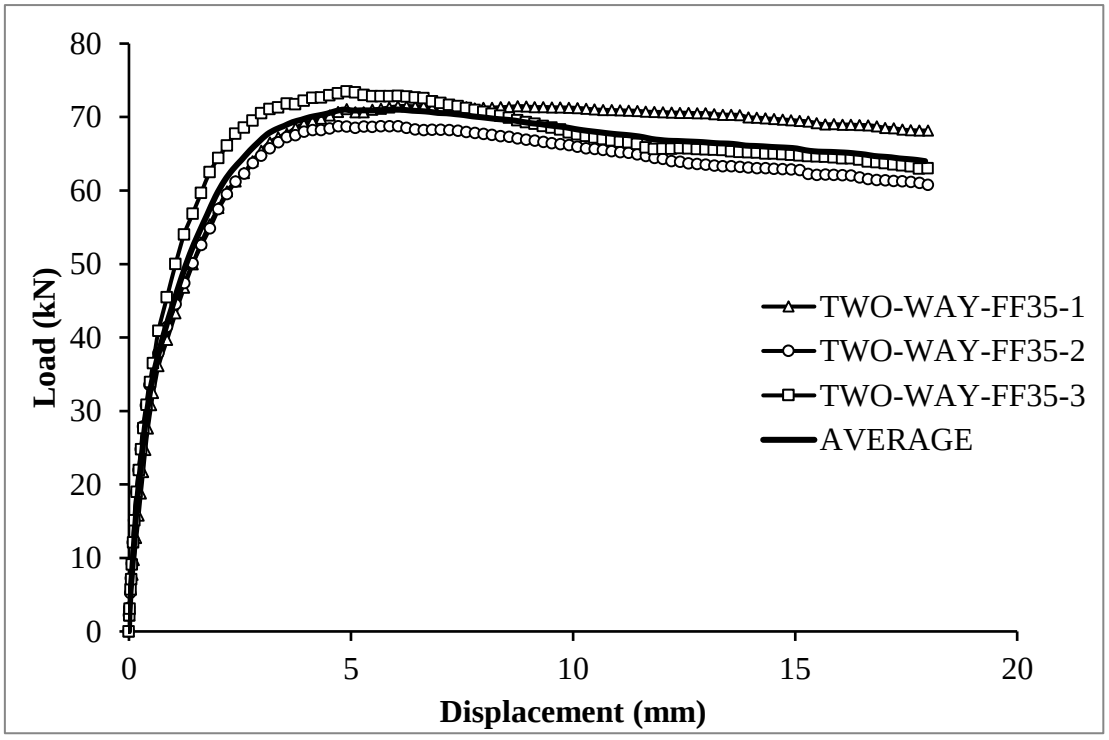

Figure 5.16: Load-displacement relationship for FF35.

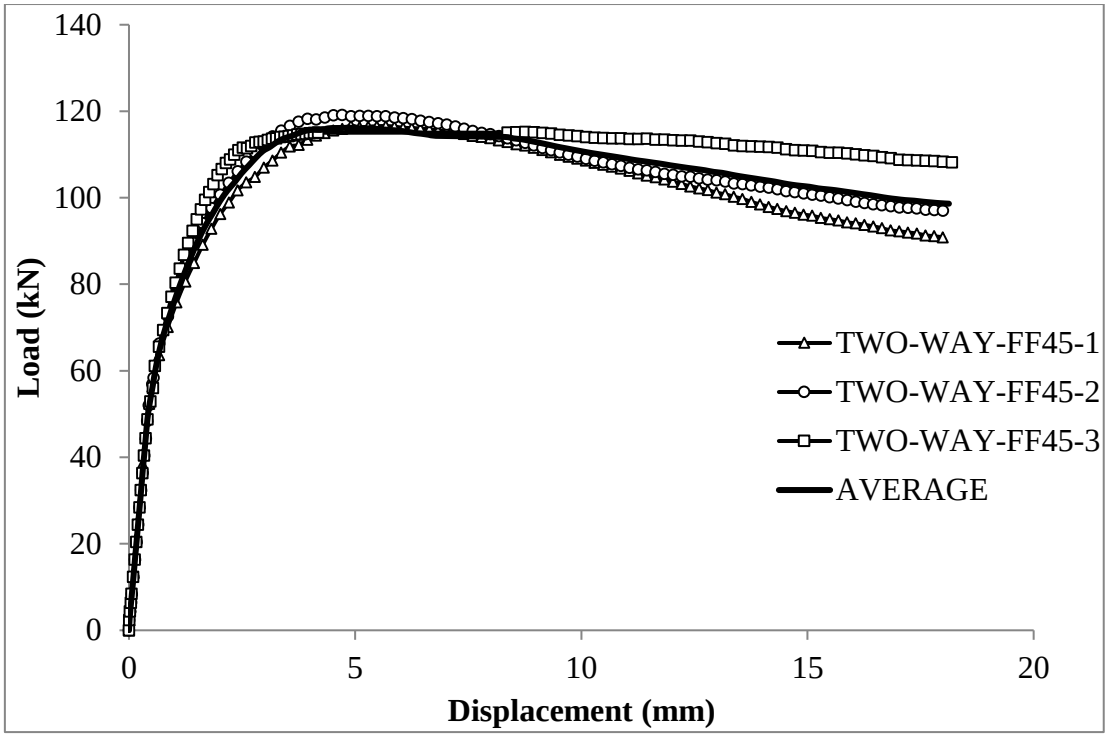

Figure 5.17: Load-displacement relationship for FF45.

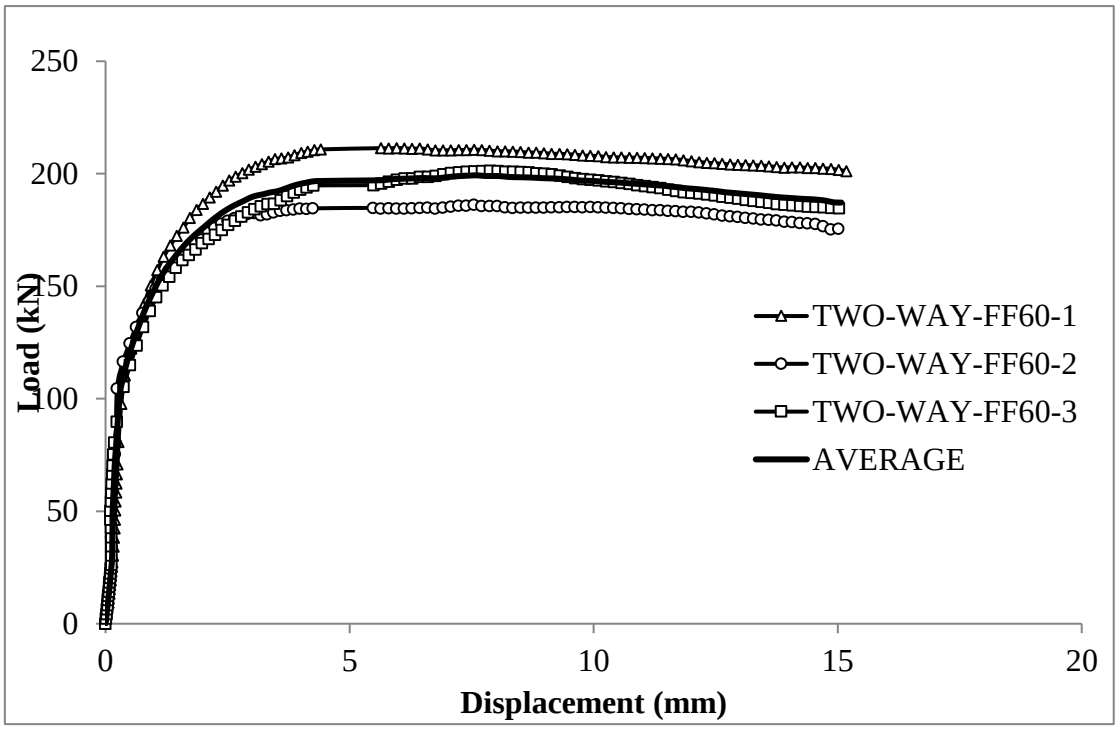

Figure 5.18: Load-displacement relationship for FF60.

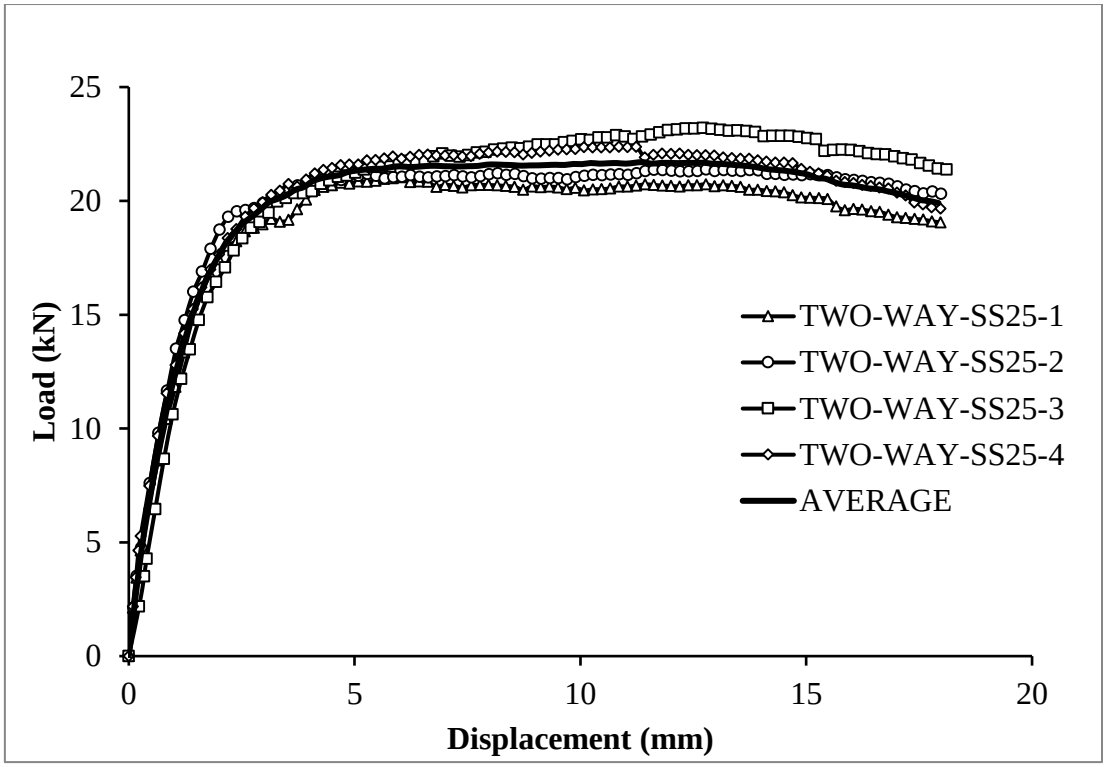

Figure 5.19: Load-displacement relationship for SS25.

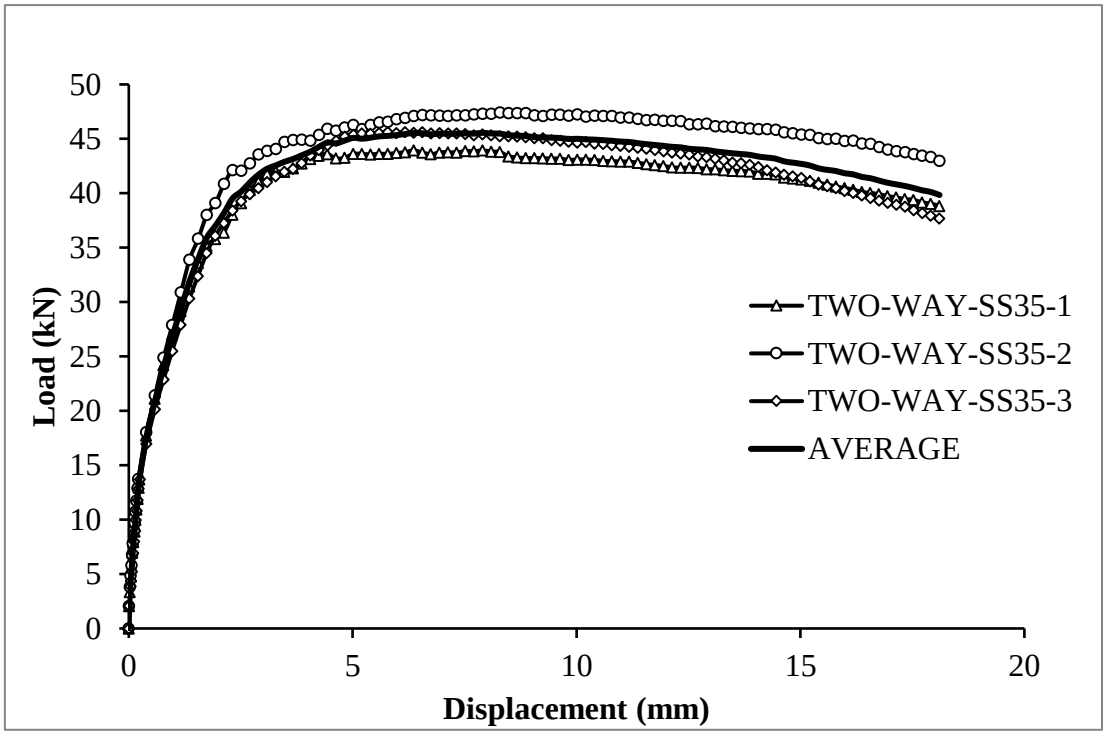

Figure 5.20: Load-displacement relationship for SS35.

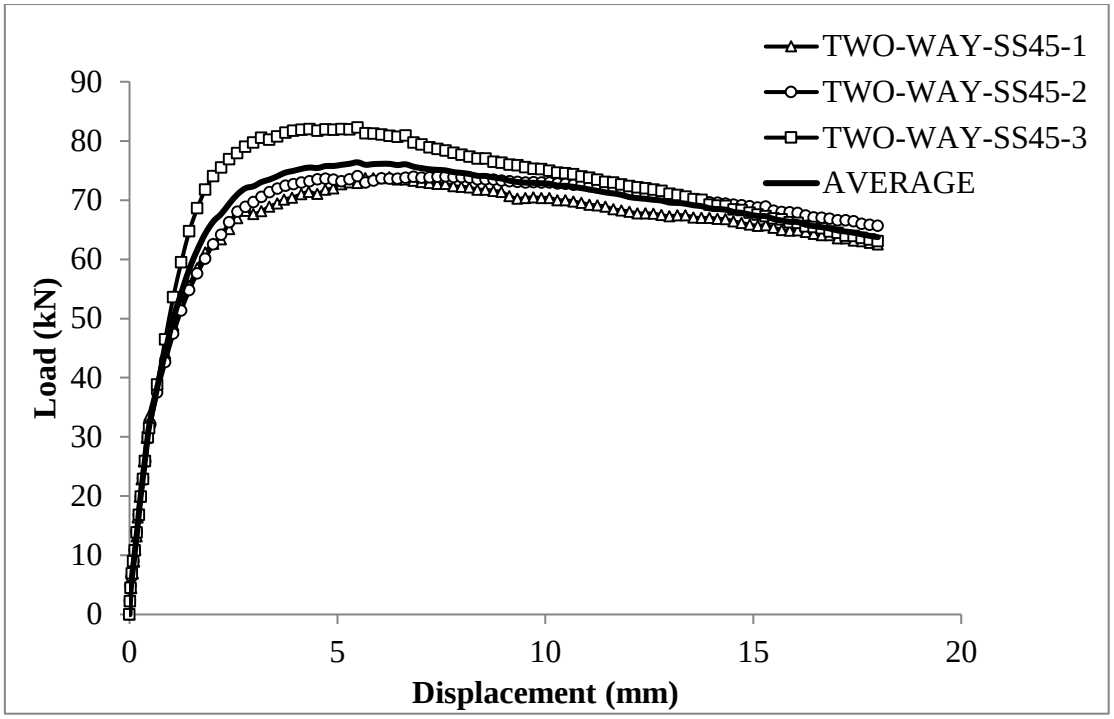

Figure 5.21: Load-displacement relationship for SS45.

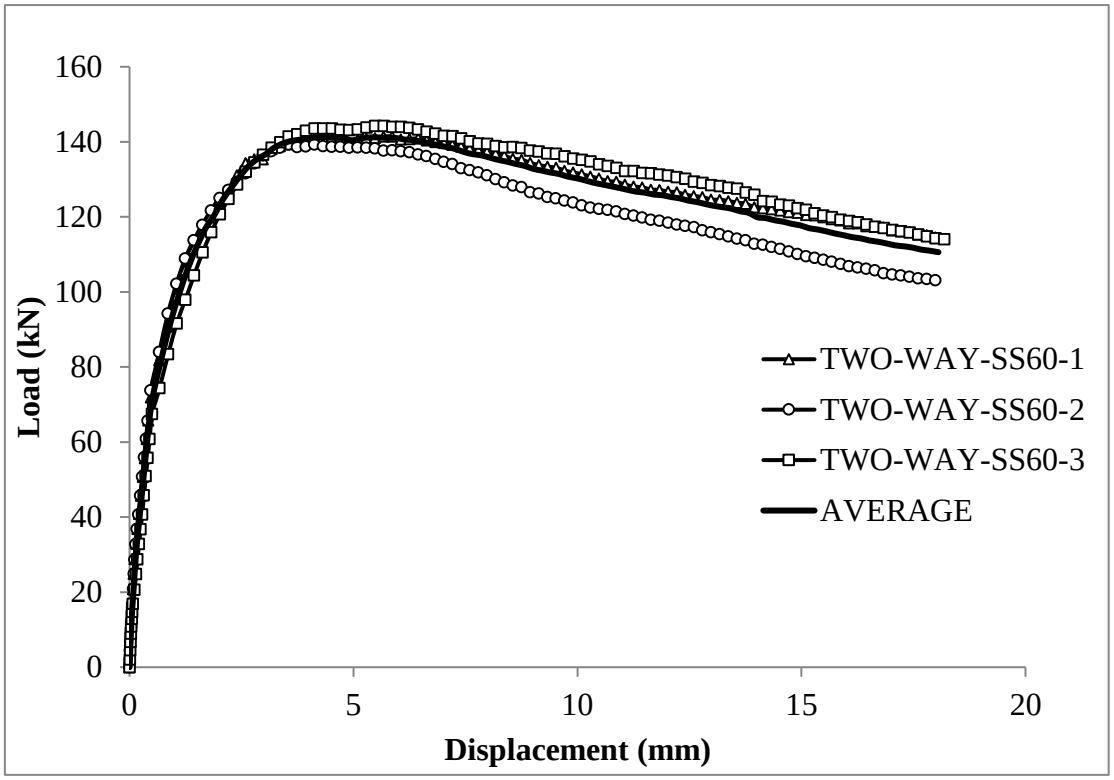

Figure 5.22: Load-displacement relationship for SS60.

5.2.4 Thickness Assessment of Two-way Slabs

The experimental ultimate loads (F_s) for each slab specimen with experimental averages for both FF and SS boundary conditions are given in Table 5.2 and Table 5.3, respectively. F_s is the load which the slab can carry before the fibre pull-out behaviour occurs where the bond between the fibre and the matrix is not sufficient to hold the two cracked faces together. Displacement (w_s) at F_s for each slab and the average are also shown. To understand the effect of thickness on bending behaviour, F_s and w_s are investigated here.

Table 5.2 shows the response for four different slab thicknesses with FF boundary conditions. As expected the thicker slabs carried higher load than the thinner slabs. The F_s for specimens with 25 mm thickness ranged between 31 to 35 kN, which gives an average of 33.7 kN. Whereas F_s increased by 112% when specimens with 35mm thickness were tested. An average F_s of 117 kN for slabs with 45 mm thickness was obtained, where an increase in F_s was only 65%. After slabs with larger thicknesses were tested, F_s only increased by 68%, although the thickness was 15 mm greater compared to slabs with 45 mm. In addition, in this series the w_s at F_s was varied from one thickness to the other. Despite the difference in the value of F_s for each slab thickness, the occurrence of w_s seemed consistence and was around 5 mm.

The results for slabs with SS boundary conditions are shown in Table 5.3. The average F_s for a slab thickness with 25 mm was 21.2 kN, whereas an average F_s of 45.0 kN was recorded when slab with 35 mm thickness was tested and this showed that the F_s increased by 114%. Slab results for 45 mm thickness indicted that the F_s increased by 69%. As the slabs with 60 mm thickness were tested, an average F_s of 141 kN was recorded and the increase in F_s was 85%. This result from both series shows that fibre-bridging behaviour plays a significant role in F_s values and an increase in the slab F_s was not necessarily influenced by the thickness alone. As the thicknesses increased, fibres were less likely to be perpendicular to the direction of the force. So fibres were distributed in the matrix more freely, thus the fibre-bridging action reduced in thicker slabs. Both series showed an increase in percentage in F_s with increasing thickness similar for all the slabs except for the thickest slabs. The F_s in slabs with 60 mm thickness with FF boundary conditions only increased by 68% whereas a higher percentage of 85% was recorded for slabs of the same geometry with SS boundary conditions. This could be due to the effect of the number of macrocracks which were less for thick slabs with SS boundary condition

compared to those with FF boundary conditions with similar thickness. The smaller the number of macrocracks, the less the fibre-bridging, resulting in less fibre pull-out behaviour, thus the member has a greater strength.

Table 5.2: Slabs experimental results with fully-fixed boundary condition.

Specimens		Ultimate load F_s (kN)	Average F_s (kN)	Displacement (w_s) at F_s (mm)	Average w_s (mm)
Name	No				
TWO-WAY-FF25	1	34.0	33.7	5.1	5.0
	2	31.0		5.1	
	3	35.3		5.0	
	4	34.5		4.9	
TWO-WAY-FF35	1	71.0	70.8	4.9	4.9
	2	68.7		4.9	
	3	72.9		4.9	
TWO-WAY-FF45	1	116.6	117.0	4.9	4.9
	2	119.1		4.7	
	3	115.2		4.9	
TWO-WAY-FF60	1	210.5	197.2	5.6	5.5
	2	184.1		5.4	
	3	193.6		5.4	

Table 5.3: Slabs experimental results with simply-supported boundary condition.

Specimens		Ultimate Load F_s (kN)	Average F_s (kN)	Displacement (w_s) at F_s (mm)	Average w_s (mm)
Name	No				
TWO-WAY-SS25	1	20.8	21.2	5.1	5.1
	2	21.1		5.1	
	3	21.2		5.2	
	4	21.6		4.9	
TWO-WAY-SS35	1	43.6	45.0	5.1	5.1
	2	46.2		5.1	
	3	45.3		5.0	
TWO-WAY-SS45	1	73.0	76.1	5.3	5.2
	2	73.3		5.1	
	3	82.0		5.1	
TWO-WAY-SS60	1	141.2	141.0	4.7	4.8
	2	138.7		4.7	
	3	143.2		4.9	

5.2.5 Size Effect and Effective Flexural Strength of Two-way Slab

Similar to one-way slabs, to investigate size effect of two-way slabs, the effective flexural strength (f_{st}) was calculated for both FF and SS boundary conditions. In both series, during the experiment, it was evident that specimens with lower span/thickness ratios exhibited significant shear failure local to the loading point when compared to thick slabs. Furthermore, shear failure in specimens with lower span/thickness ratios occurs in the strain hardening region and for higher span/thickness ratios occurred in the strain softening region. To further investigate the thickness effect on slab strength, size effect investigations were carried out.

As described in Chapter 3, in OC as the structural member size increases, the nominal strength of the member reduces, requiring the use of larger member sizes to overcome lower strength while further exacerbating the problem. For the interest of the structural application of UHPFRC, size effect behaviour is described here for two-way slabs under the bending test. The three and four values of f_{st} obtained from the bending tests and the average f_{st} were recorded in Table 5.4. The results were plotted against the slab thicknesses as illustrated in Figure 5.23 and Figure 5.24. The fact that most of the bending strength occurred during the development of pseudo-plastic phase in concrete (Spasojevic

et al., 2008) and UHPFRC is distinguished by its pseudo-strain hardening behaviour, the f_{st} of UHPFRC is not influenced when compared to OC. The figures show that changes of thickness have very little influence on the f_{st} and the size effect was very limited for two-way spanning slabs. Both FF and SS slabs showed that the f_{st} is around 8.9 to 9.8 MPa and 6.0 to 6.6 MPa, respectively. The results also show the appearance of microcracks and the occurrence of the fibre-bridging at different displacement values for each slab thickness was not significant in terms of size effect. The result for two-way slabs confirmed that the use of UHPFRC materials as a replacement of OC in structural application has an advantage to element size effect issues. However, it is important to mention that the above equations employed here to calculate the f_{st} were only for comparison purposes to investigate the size effect phenomenon.

Table 5.4: Effective flexural strength of two-way slabs.

h (mm)	Fully Fixed Slabs		Simply Supported Slabs	
	Effective Flexural Strength f_{st} (MPa)	Average f_{st} (MPa)	Effective Flexural Strength f_{st} (MPa)	Average f_{st} (MPa)
25	9.3	9.2	5.6	6.0
	8.4		5.8	
	9.6		6.3	
	9.6		6.1	
35	9.9	9.8	6.1	6.4
	9.5		6.6	
	10.0		6.4	
45	9.8	9.7	6.1	6.4
	10.0		6.2	
	9.4		6.9	
60	9.4	8.9	6.6	6.6
	8.2		6.5	
	9.2		6.7	

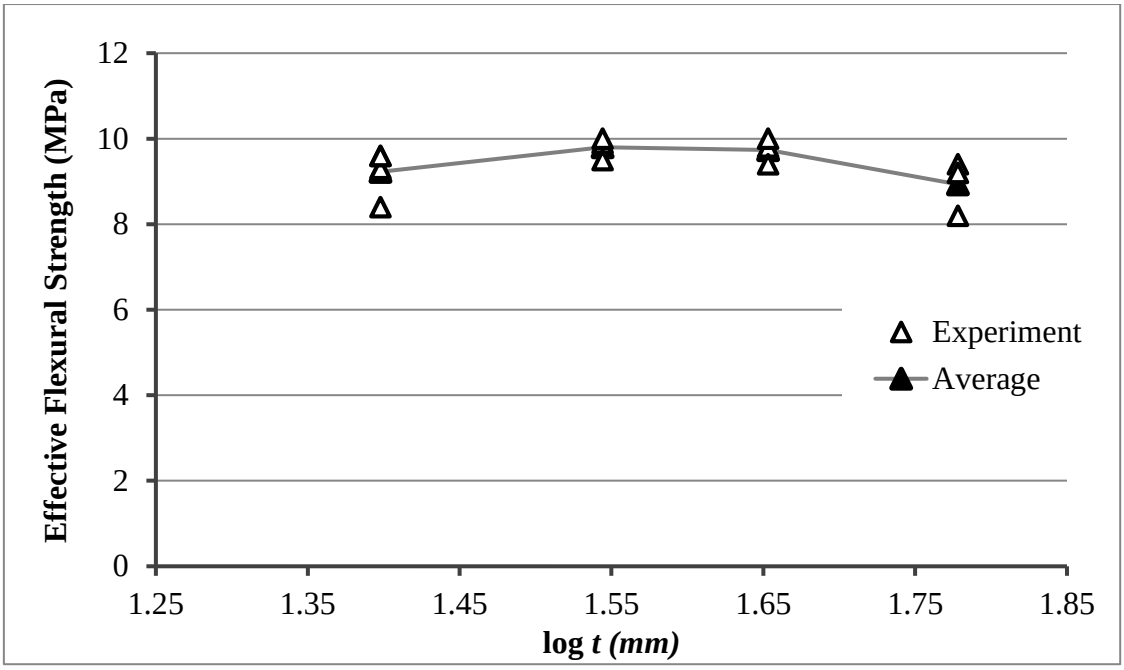

Figure 5.23: Flexural strength versus log of thickness for FF series in two-way slabs.

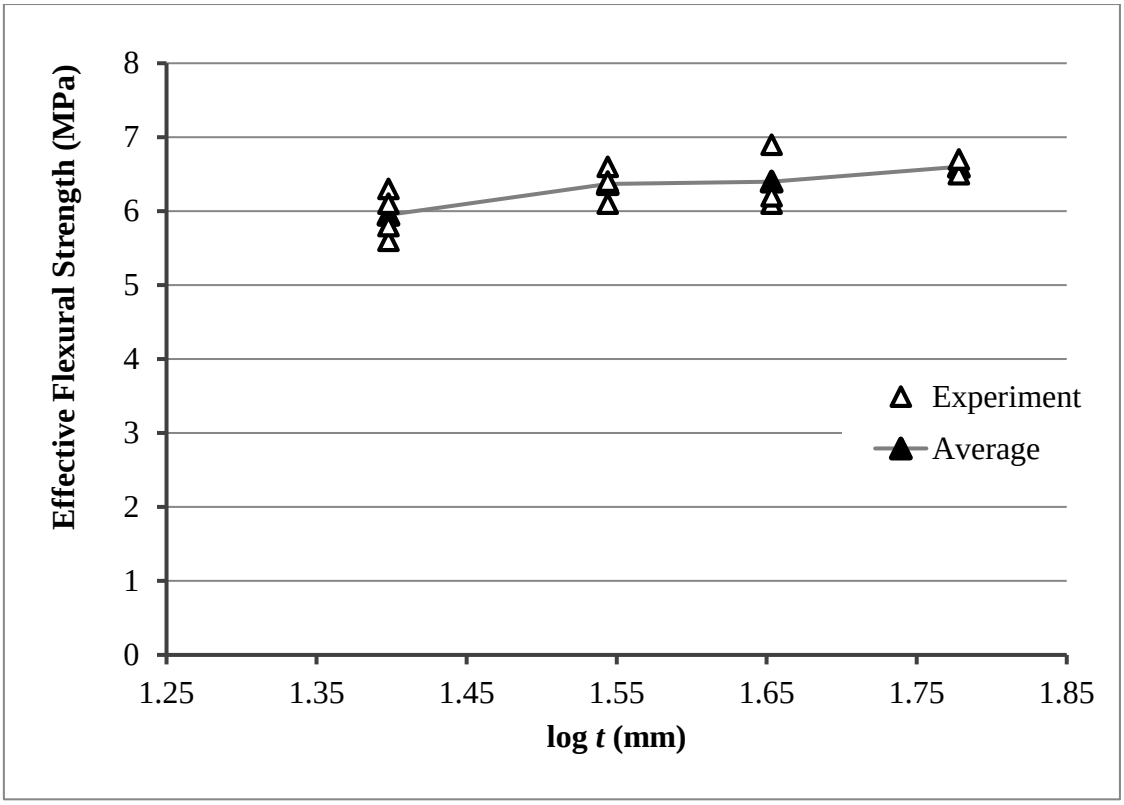

Figure 5.24: Flexural strength versus log of thickness for SS series in two-way slabs.

5.3 Concluding Remarks

The designed experimental setup showed the structural behaviour of two-way slabs with both FF and SS boundary conditions can be determined efficiently and accurately.

The results of the study presented in this chapter show that the UHPFRC slab geometry can influence the fibre distribution and orientation within the matrix as this is reported by other studies in the literature. The slab boundary conditions can have a considerable effect on the load-displacement behaviour. The results also show that the boundary conditions have a significant effect on the failure modes. The end of the linear elastic region and the appearance of microcracks in both FF and SS slab boundary conditions were observed at a displacement of around 0.25 to 0.40 mm. Moreover, the fibre pull-out behaviour had begun at a displacement of approximately 5 mm for all the slabs in both FF and SS boundary conditions. Furthermore, crack development in the FF boundary conditions seems to be influenced by the slab edge restraint stiffness. This higher number of cracks were believed to be due to the effect of boundary conditions where the support stiffness in one of the two adjacent edges are greater compared to the other two edges. Changes in thickness for the specimens tested had no influence on the f_{st} of the slabs in both FF and SS boundary conditions.

With regards to the fibre distribution, similar to the one-way slabs, the experimental measurement showed that fibres tend to be more uniform in thin slabs compared to the thick slabs. The result showed that the number of fibres that contribute to the bridging action between the two cracked faces are greater in the thin slabs due to the effect of slab geometry. However, the effect of geometry diminishes as the thickness becomes greater than 60 mm. Overall, the experimental investigation for two-way slabs provided a similar result to the beam specimens and one-way slabs. This confirms that the fibre distribution changes from one thickness to another and these changes are more predominant in slabs with thicknesses smaller than 60 mm.

CHAPTER 6

FINITE ELEMENT ANALYSIS

Previous studies conducted on the modelling of UHPFRC materials can be found in Chapter 2. It was highlighted that there are a number of analytical models available that are based on reasonable simplifications and assumptions. Generally, these are limited to a range of geometries or can only predict a part of the load-displacement curve. Such models are useful for approximation purposes but are often incapable of describing localised damaged and nonlinear behaviour. In addition, an analytical approach is only applicable for a simple structural shape, with ideal support and loading conditions unlike a FE analysis which can be applied to analyse structures of any shape, support and loading conditions. Therefore, numerical models that can predict the full structural behaviour (before and after ultimate load) of UHPFRC are required. The need of such models becomes more compelling in the light of high volumes of steel fibres required in UHPFRC, thus the cost of experimental studies is relatively high, especially for large-sized structures. However, developing a FE model that can predict UHPFRC structural behaviour is not a straightforward task due to the difficulty in modelling discrete cracking. This is due to the randomly distributed fibres in the matrix. Furthermore, modelling fibres within the matrix is a time consuming process. In addition, to accurately capturing the material behaviour of fibres, very fine meshes are required and this can lead to high computational cost. This explains why there are very few studies in the literature regarding analytical work on UHPFRC. Due to the ongoing development of FE analysis,

it is now possible to analyse the structural behaviour of UHPFRC when the true material properties are used.

This chapter presents the procedure for using a finite element (FE) analysis to simulate the structural behaviour of UHPFRC materials. The geometric and material nonlinearity as well as the material damage and failure models are included in the analysis. The description of mesh convergence studies, element and analysis type as well as applied load and boundary conditions are also included. The experimental studies presented in Chapters 3, 4 and 5 were used to validate the FE analysis using the Concrete Damage Plasticity (CDP) model in ABAQUS/Standard. The reasons for choosing the CDP model and accuracy of the model based on the previous studies are discussed. The reliability and importance of material properties extracted from uniaxial tensile and compressive laboratory tests for input into the CDP model are also discussed. The model applies to both the beams and the slabs. Boundary and loading conditions are described in the respective sections for each set of experiments.

UHPFRC beams are modelled using 2D solid elements. The FE simulations for entire load-Crack Mouth Opening Displacement (CMOD) curves are described. Slabs are modelled to simulate the structural behaviour of one-way and two-way slabs. To do this, a 3D model was developed based on the CDP material model in ABAQUS. To capture the material behaviour beyond the ultimate load, additional parameters were introduced. Formation of the equations used to calculate these parameters are presented along with the relevant experimental data.

6.1 Finite Element (FE) Analysis

Finite element (FE) analysis was first developed in 1943 by A. Hrennikoff and R. Courant, who utilised the Ritz and Rayleigh method of numerical analysis and variational methods (Papadopoulos, 2005). After the development of the digital computer, a paper published by Turner et al., (1956), which reinvented the FE method as a natural extension of matrix structural analysis. The authors of this paper (Turner et al., 1956) were pioneers and this was recognized as the start of the current FE analysis techniques. The term ‘finite element’ was first introduced by Clough, who was one of Turner’s associates at that time (Papadopoulos, 2005). In 1963, finite elements were first used in the solution of a field

problem and steady state problems were solved in the context of heat transfer, electrical fields and seepage. A few years later, the FE method attracted the attention of applied mathematicians especially those interested in numerical solution. Therefore, in 1973 the first treatise on the mathematical aspects of the FE method provided with a rigorous mathematical foundation was published (Strang and Fix, 1973).

Over the past few decades, with the rapid development of computer technology, the FE method has been subjected to intense research reported in many scientific articles and books. By the beginning of the 1990s, a great number of FE method commercial packages were developed and widely applied in many problems in the field of structural analysis, structural mechanics and solid mechanics (Papadopoulos, 2005).

The FE analysis has been used to solve linear and nonlinear engineering problems. Throughout the history of FE analysis, a variety of software tools based on FE analysis such as ABAQUS, ADINA, ATENA, DIANA, OpenSeeS, VECTOR2, ZEUS-NL and many more have been developed. These simulation tools can be used for a variety of applications ranging from the modelling of civil engineering structures to acoustics and areas of heat transfer and fluid mechanics. The FE analysis is straightforward and easy to understand, even for problems with complex geometry or complex material properties. Furthermore, it is a cheaper method to investigate structural behaviour than to do experiments. However, the use of these simulation tools depends on the nature of the problems and input values, especially the material properties used. Furthermore, the accuracy of these simulation tools to analyse a material's behaviour changes from one to another. To validate an experimental result using FE analysis, it is essential to investigate if the solution being produced is capable of describing and accurately predicting the problem being considered. The accuracy of the results in a FE analysis, especially for fibre concrete, is highly dependent on the material properties introduced into the analysis. Due to the randomly distributed fibres in UHPFRC, reliable material properties were needed to capture its structural behaviour. In the past, to analyse plain and reinforced concrete, ABAQUS has been the most frequently used and reliable software. Therefore, ABAQUS was employed to analyse UHPFRC in this study.

6.2 ABAQUS

ABAQUS is a powerful commercial package developed by David Hibbitt, Bengt Karlsson and Paul Sorensen in 1978 in Rhode Island, USA and now marketed under the SIMULIA brand of Dassault Systems. It provides a large element library and a large number of material models and is capable of analysing a wide range of engineering problems including linear, nonlinear, static, dynamic, structural and thermal. It consists of three core products, ABAQUS/Standard, ABAQUS/Explicit and ABAQUS/CAE.

In the ABAQUS program, there are two main analyses available for nonlinear quasi-static and dynamic problems: Explicit and Standard. ABAQUS/CAE only provides the analysis modules as a complete modelling, managing and visualisation environment for ABAQUS analysis products. ABAQUS/Explicit uses an explicit dynamic finite element formulation and was originally developed to solve dynamic events such as impact and blast. ABAQUS/Standard uses an implicit solution approach by solving a system of equations at each increment and is suitable for a large range of linear and nonlinear situations involving static and dynamic problems (ABAQUS, 2013). Since the problems are nonlinear quasi-static, ABAQUS/Standard analysis was employed in this study.

6.2.1 ABAQUS Standard

In ABAQUS/Standard two main behaviours are considered in modelling most of the material and these are elastic and plastic behaviour. In defining the FE analysis, a linear elastic model is only valid for small elastic strain normally less than 5% and the model can be isotropic, orthotropic or fully anisotropic (ABAQUS, 2013). Elastic models can also have material properties that depend on temperature and other field variables depending on the materials.

Stress is calculated based on the total elastic strain and elastic modulus using the following equation.

$$\sigma = E * \varepsilon^{el} \qquad \textbf{(6. 1)}$$

where σ=total stress,

E^{el} =the initial modulus of elasticity, and

ε^{el}=total elastic strain.

The linear elastic behaviour of UHPFRC was modelled as an isotropic material that is temperature independent as recommended by ABAQUS. For the isotropic case, the software calculates the stress-strain relationship based on the input values such as elastic modulus (E) and Poisson's ratio (v) using the following Equations 6.2 and 6.3.

$$\begin{Bmatrix} \varepsilon_{11} \\ \varepsilon_{22} \\ \varepsilon_{33} \\ \varepsilon_{12} \\ \varepsilon_{13} \\ \varepsilon_{23} \end{Bmatrix} = \begin{bmatrix} 1/E & -v/E & -v/E & 0 & 0 & 0 \\ -v/E & 1/E & -v/E & 0 & 0 & 0 \\ -v/E & -v/E & 1/E & 0 & 0 & 0 \\ 0 & 0 & 0 & 1/G & 0 & 0 \\ 0 & 0 & 0 & 0 & 1/G & 0 \\ 0 & 0 & 0 & 0 & 0 & 1/G \end{bmatrix} \begin{Bmatrix} \sigma_{11} \\ \sigma_{22} \\ \sigma_{33} \\ \sigma_{12} \\ \sigma_{13} \\ \sigma_{23} \end{Bmatrix} \quad \textbf{(6. 2)}$$

The shear modulus (G) is also expressed in terms of E and v as

$$G = E \big/ 2(1+v) \quad \textbf{(6. 3)}$$

However plastic behaviour is more complex as the material undergoes deformation due to the applied force when the material loses its original geometric shape. In FE analysis, ABAQUS has been used widely to capture and describe the behaviour of both brittle (i.e. concrete) and ductile (i.e. steel) materials. Since UHPFRC is a type of concrete and has a ductile behaviour, ABAQUS is a suitable tool to predict its structural behaviour.

In ABAQUS/Standard, two common approaches are available: the Concrete Smeared Cracking (CSC) and the Concrete Damaged Plasticity (CDP) models. Both models are discussed in the following sections. However, since, the study investigates the structural behaviour of UHPFRC and the main interest in this study is to gain a better understanding of the material behaviour at a structural level, a homogenous model was adopted in both approaches. Furthermore, the parameters of interest in this study are load, displacement and failure patterns, and both models using a homogenous approach, can provide these outcomes accurately, as has been reported in the literature. A more complicated model

such as a heterogeneous model would be desirable if the material was to be investigated at an element level. However, such a model requires an extensive amount of experimental testing in order to obtain the required parameters to define the model. Due to the fact that the material is new and there is a lack of experimental test data, adopting a heterogeneous model would not be achievable. However, the required input parameters for homogenous modelling can be obtained from the properties testing conducted by Le, 2007 and Hassan, 2013. Overall, it is also important to acknowledge that the developed model in this study is simplified if compared to the heterogeneous model but it can accurately predict the behaviour of UHPFRC at the structural level and contribute on the advancement of knowledge.

6.2.1.1 Concrete Smeared Cracking (CSC)

This method provides a tool to model concrete in all types of structures, including beams, trusses, shells, and solids. It can also be used to model plain concrete but it is intended primarily for analysing reinforced concrete as it allows the rebar to be used in the model. It is often used for concrete when subjected to monotonic loading but it needs to be combined with the linear elastic model properties. Cracking and post-cracking are the most important aspects of the behaviour of this model (ABAQUS, 2013). The model predicts the nonlinear behaviour based on the crack occurrence and crack detection during the analysis. The detection of cracks is assumed when the stress reaches the failure surface and this is called the crack detection surface, which has a linear relationship between the von Mises equivalent deviatoric stress (q) and the equivalent pressure stress (p) as shown in Figure 6.1.

After cracks have occurred, they remain in the calculation and the model does not consider each macrocrack and the calculations are performed independently at each integration point. The presence of cracks during the calculation affects the failure stress and the material stiffness associated with the particular integration point. This involves the modification of the material stiffness properties after the occurrence of cracking, leading to severe convergence difficulties. Therefore, various concerns have been raised which has brought the reliability of CSC into question (ABAQUS, 2013).

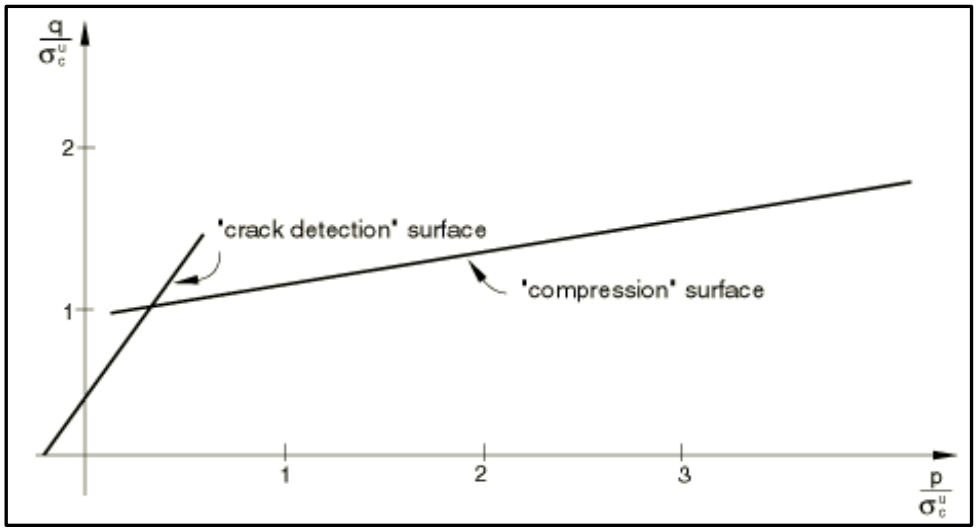

Figure 6.1: Yield and failure surfaces in the (*p*–*q*) plane (ABAQUS, 2013).

In order to capture the behaviour of the material in the nonlinear stage, compression hardening and tension softening are required. When the stress components are dominantly compressive, the concrete is modelled using elastic-plastic theory. The compression hardening behaviour is introduced in a simple form of yield stress and elastic strain behaviour in a uniaxial response and incorporated in the model to define material behaviour outside the elastic range as shown in Figure 6.2. During the loading, concrete in compression initially exhibits elastic behaviour but as the stress increases, inelastic straining occurs and the response of the material loses its stiffness and softens as the material reaches its ultimate stress. If the load is removed at some point after this inelastic strain occurs, the unloading response will be smaller than the initial elastic response. Since cracks develop so quickly in plain concrete and it is difficult to observe the actual behaviour, the model assumes the material loses strength through a softening mechanism. Therefore, open cracks can be represented by the loss of elastic stuffiness and this is input into the model as compressive hardening behaviour.

Furthermore, in multiaxial stress states that this model can provide, a failure surface which governs the plastic response of the concrete as illustrated in Figure 6.3. The failure surface determines the stress and material stiffness behaviour of every integration point in the model and these calculations are carried out independently at each integration point. For any integration point with stress values lying inside the surface perimeter, the material behaviour of the point is calculated. However, when the value lies on or outside the

perimeter, failure of the material has occurred and the ultimate strength of the material is reached.

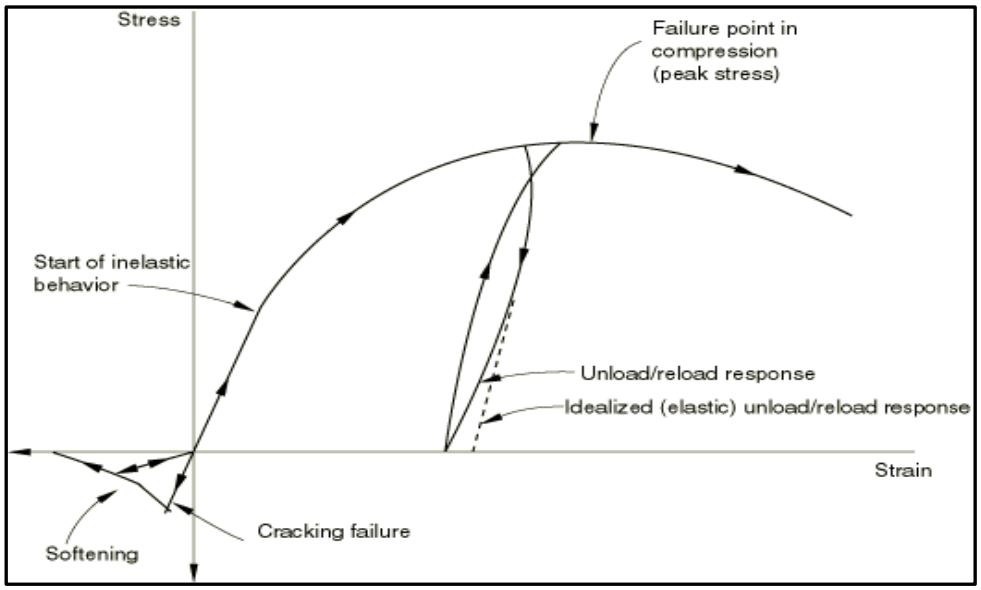

Figure 6.2: Uniaxial behaviour of concrete (ABAQUS, 2013).

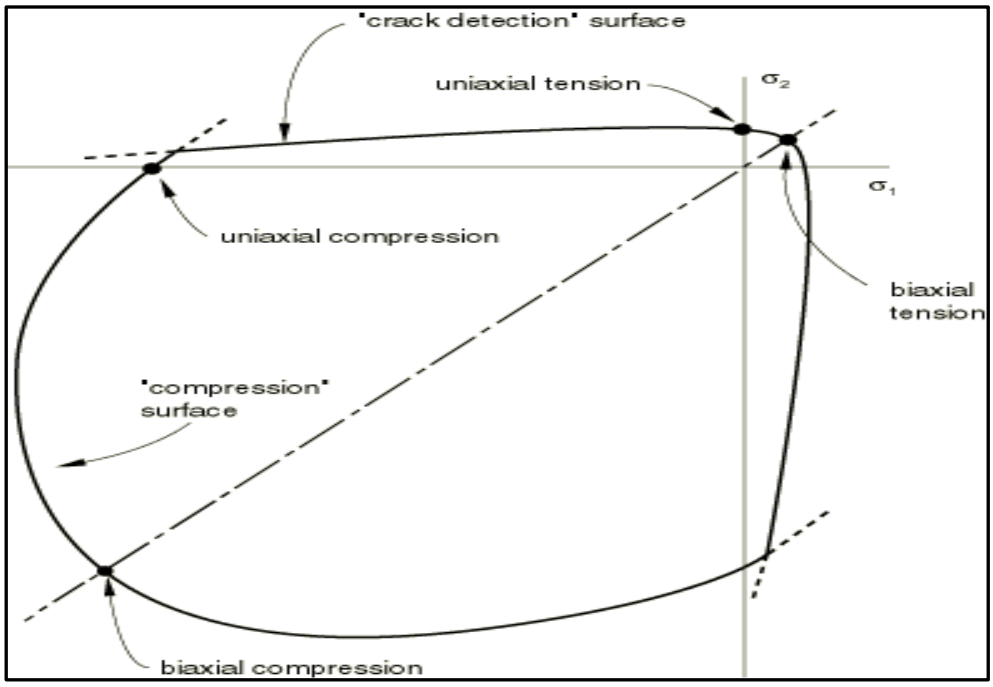

Figure 6.3: Concrete failure surfaces in plane stress (ABAQUS, 2013).

Apart from compression hardening, tension stiffening is another important parameter that needs to be included in the CSC model. This parameter captures the direct strain behaviour across cracks in the model and this allows the softening behaviour to be defined. Tensioning stiffening can be introduced by means of a post failure stress-strain relation or fracture energy cracking. In the former approach, the model assumes the stress-strain behaviour to be linear until the tensile strength (failure point) is reached. The softening behaviour will be captured by the tension stiffening as shown in Figure 6.4. This often occurs in cases with very little or no reinforcement such as in this study where a few discrete cracks initiate in the structure (ABAQUS, 2013).

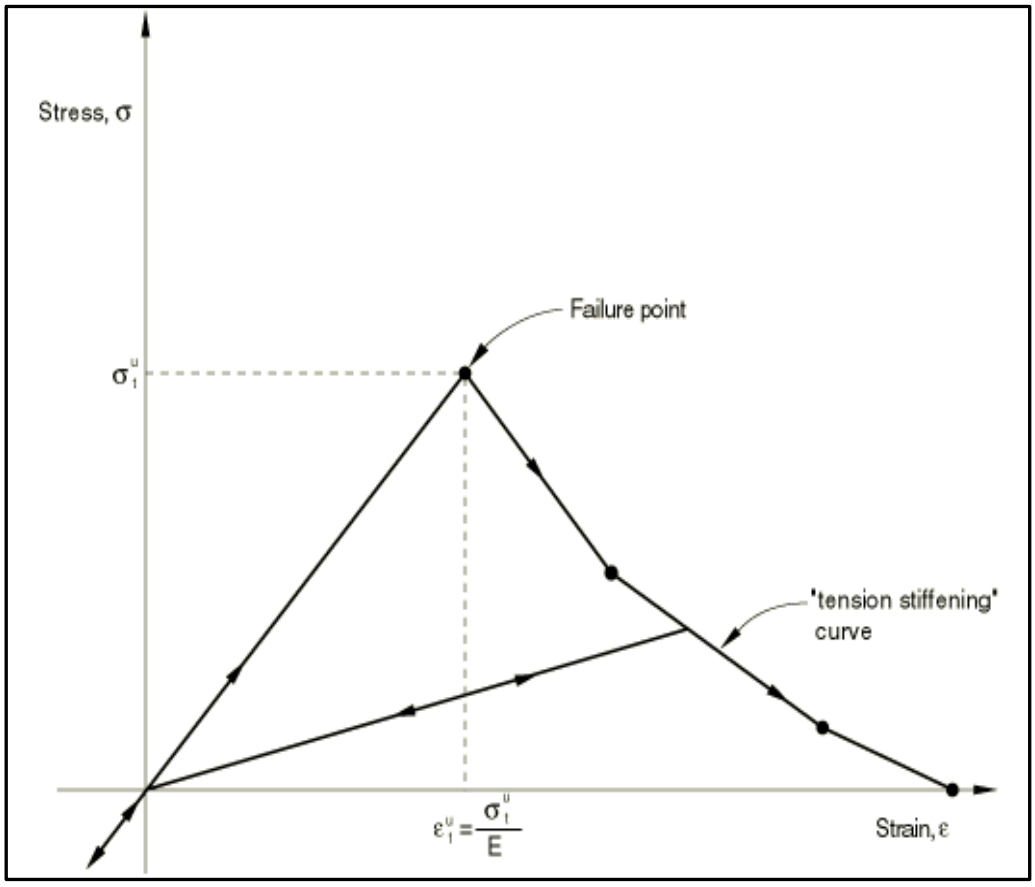

Figure 6.4: Tension stiffening model using stress-strain relation (ABAQUS, 2013).

To reduce mesh sensitivity issues, a mesh refinement is required; however, the mesh refinement leads to narrower crack bands. To overcome mesh sensitivity, the crack band proposal by Hillerborg (1976) has been accepted as an adequate approach and can provide

a reasonable solution. In the theory it is assumed that the crack propagates when stress at the tip of crack reaches the tensile strength. However, it is not assumed that stresses fall to zero after the occurrence of cracks but to decrease with the increasing crack width as shown in Figure 6.5. It is an energy balance approach where a certain amount of energy is observed at the crack surface. After the load is applied, the energy will be released and when the released energy is equal or greater than the observed energy, the crack will propagate. This means this approach relies on the crack opening displacement (COD) which is linear with the failure stress and stresses are present in the crack zone as long as the COD is small. Therefore, implementing stress-COD concept directly associated with the crack length and element geometry. However, since the direction of crack is unknown, having defined element with a large aspect ratio can lead to some mesh sensitivity. Therefore, it is recommended for elements that are as close to a square as possible (aspect ratio close to one) to be used (ABAQUS, 2013). This was adopted in this study and it will be discussed in the flowing sections.

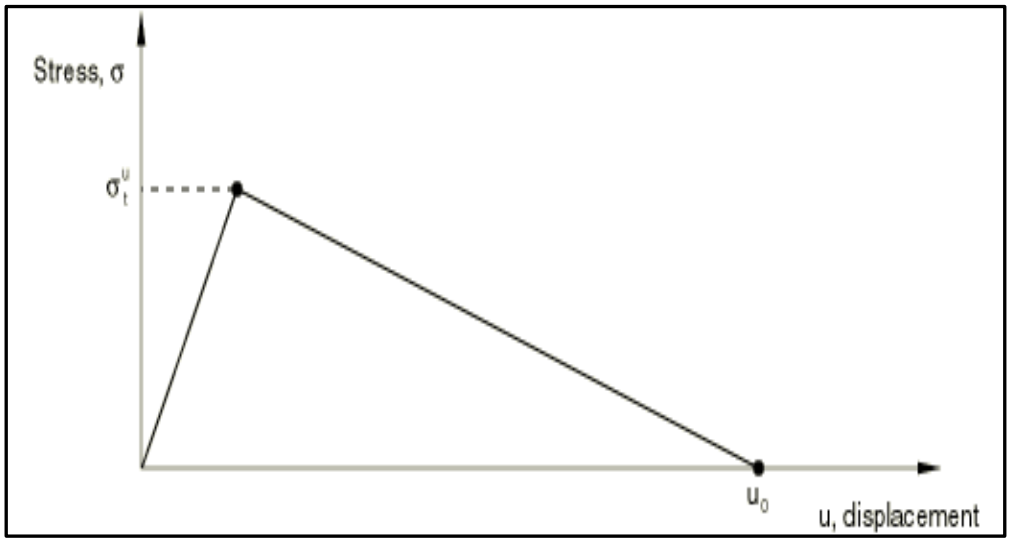

Figure 6.5: Fracture energy cracking model (ABAQUS, 2013).

In addition, there are several other parameters such as failure ratio and shear retention values can be included as input into the CSC model. As specified in (ABAQUS, 2013) four failure ratios can be defined as follows:

- *The ratio of the ultimate biaxial compressive stress to the ultimate uniaxial compressive stress and the default value is set as 1.16.*
- *The absolute value of the ratio of the uniaxial tensile stress at failure to the ultimate uniaxial compressive stress and the default value is set as 0.09.*
- *The ratio of the magnitude of a principal component of plastic strain at ultimate stress in biaxial compression to the plastic strain at ultimate stress in uniaxial compression and the default value is set as 1.28, and*
- *The ratio of the tensile principal stress at cracking, in plane stress, when the other principal stress is at the ultimate compressive value, to the tensile cracking stress under uniaxial tension and the default value is set as 0.33.*

Although these parameters are not the main parameters in CSC, it is recommended that they be included in the analysis and in concrete modelling, the default values are usually used if experimental data is not available (ABAQUS, 2013). Based on the property tested by (Le, 2007, and Hassan, 2013), the ratio of the uniaxial tensile stress to the ultimate uniaxial compressive stress can be determined and it was found to be 0.06.

Shear retention can also be defined in conjunction with the failure ratio and is generally included in the analysis to enhance the damage behaviour to reduce computing effort. It is done by specifying the shear modulus reduction as a function of the crack opening strain as cracks propagate in the structure. It is assumed that the elastic shear modulus normally reduces linearly with the increasing strain until it reaches zero. The two values are used for this parameter are the shear retention factor ρ^{close} and maximum crack opening strain ε^{max}. The default value for shear modulus is 1 and the strain is greater than zero. If this parameter is not included in the analysis, ABAQUS will automatically choose the default values and this assumption often works in many cases (ABAQUS, 2013). The relationship between ρ^{close} and ε^{max} for open cracks can be defined in the following Equations 6.3 and 6.4.

$$\rho = (1 - \varepsilon / \varepsilon^{\max}) \qquad \text{when } \varepsilon < \varepsilon^{\max} \qquad \textbf{(6. 4)}$$

$$\rho = 0 \qquad \text{when } \varepsilon > \varepsilon^{\max} \qquad \textbf{(6. 5)}$$

For cracks that subsequently close, the model assumes a reduced shear modulus and user can specify the value of both ρ^{close} and ε^{max} using the following Equation 6.6.

$$\rho = \rho^{close} \quad \text{when } \varepsilon < 0 \qquad \textbf{(6. 6)}$$

The values of ρ^{close} and ε^{max} can be included in the model with an optional dependency on temperature and other predefined field variables (ABAQUS, 2013).

6.2.1.2 Concrete Damaged Plasticity (CDP)

Concrete damaged plasticity is another model in ABAQUS/Standard which has been used widely for analysing plain and reinforced concrete and other quasi-brittle materials in all types of structures (solids, beam, truss and shells). It is primarily designed to be used to model rebar for reinforced concrete structures under monotonic cyclic and/or dynamic loading with a low confining pressure but it can also analyse plain concrete using the concept of isotropic elasticity. It was presented originally by Lubliner et al. (1989) and it is a continuum based on an internal variable formulation of plasticity theory for the nonlinear analysis model for concrete.

The CDP model assumes that the failure in both tensile cracking and compressive crushing of the concrete is characterised by damage plasticity. It uses the concept of isotropic damage evolution in combination with isotropic tensile and compressive plasticity to represent the inelastic and fracture behaviour of concrete. It allows the definition of strain hardening in compression, strain softening (or stiffening) in tension, and uncoupled damage initiation and accumulation in tension and compression, as illustrated in Figure 6.6.

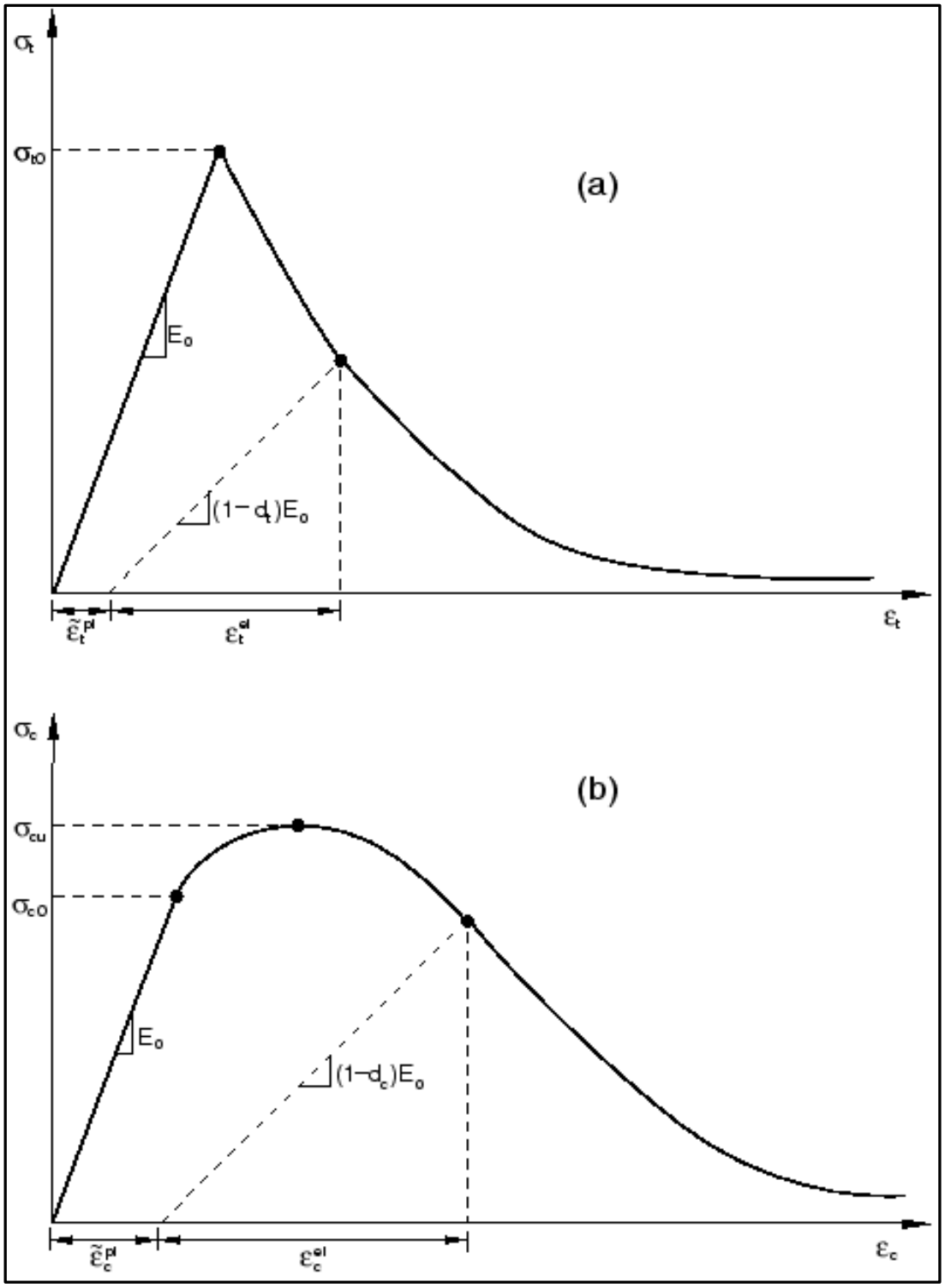

Figure 6.6: Damage curves in (a) tension (b) compression (Lubliner et al., 1989).

The accuracy of the stress-strain curves in tension and compression is crucial for realistic simulations of concrete structures. The data obtained from dog-bone specimens (for tension) and cylinders (for compression) were used (Hassan et al., 2012). However, to

model tension stiffening, the use of tensile stress-strain curves leads to mesh-dependent results as the crack tends to localise in one element width (Chen and Tao, 2011). To avoid this problem, the equivalent stress-COD curve is recommended in ABAQUS as shown in Figure 6.7. The experimental data for tensioning stiffening and compression hardening obtained from the material properties tests are shown in Figure 6.8. However, in 3D modelling for slabs, the curve was smoothed to avoid a convergence issue, as shown in Figure 6.9. This was implemented in ABAQUS by using the keyword *CONCRETE TENSION STIFFENING, TYPE=DISPLACEMENT. The concrete in compression is modelled by Figure 6.6b using the keyword *CONCRETE COMPRESSION HARDENING, TYPE=STRAIN. To include these parameters in the analysis, data were simply extracted using Equations 6.7 to 6.10 from (ABAQUS, 2013).

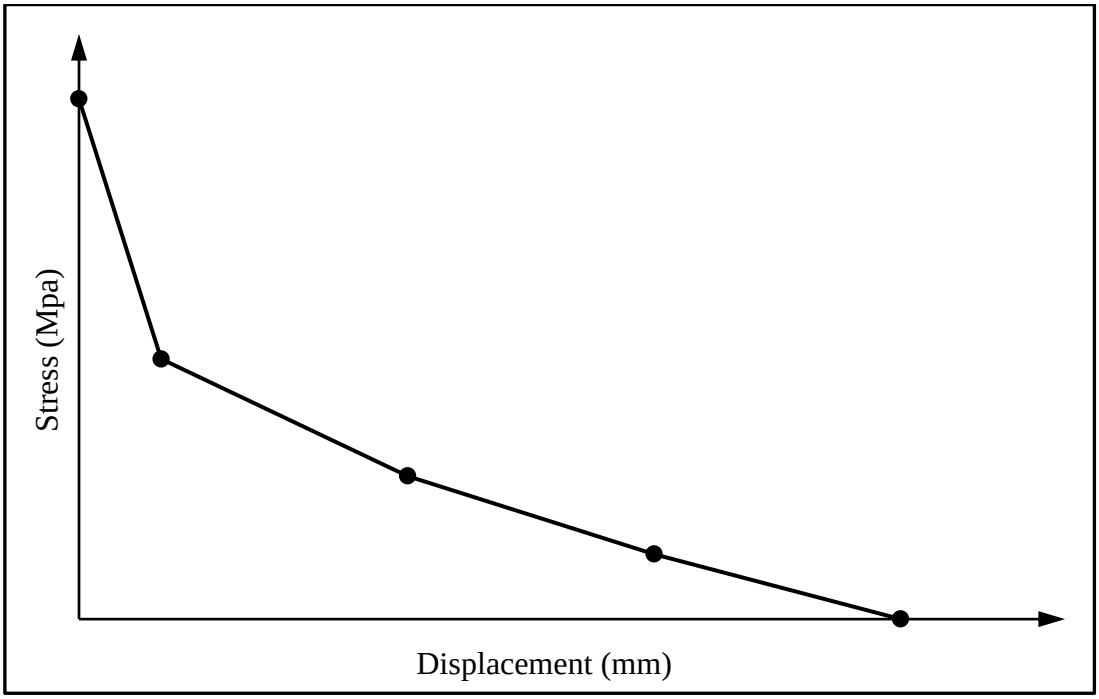

Figure 6.7: Tension stiffening model, stress-displacement approach (ABAQUS, 2013).

$$\varepsilon_t^{\approx ck} = \varepsilon_t + \varepsilon_{0t}^{el} \quad \textbf{(6. 7)}$$

$$\varepsilon_{0t}^{el} = \frac{\sigma_t}{E_0} \quad \textbf{(6. 8)}$$

$$\varepsilon_c^{\approx in} = \varepsilon_c + \varepsilon_{0c}^{el} \quad \textbf{(6. 9)}$$

$$\varepsilon_{0c}^{el} = \frac{\sigma_c}{E_0} \quad \textbf{(6. 10)}$$

where in tension $\varepsilon_t^{\sim ck}$ is a cracking strain, ε_t is a total tensile strain, ε_{0t}^{el} is the tension elastic strain, σ_t is a tensile stress and E_0 is the undamaged elastic modulus. In compression ε_c^{in} is inelastic strain, ε_c total compressive strain and ε_{0c}^{el} compressive elastic strain. The compression hardening parameter captures the pseudo strain hardening phase as the cracks start to initiate within the matrix after the material goes beyond the elastic phase. Whereas the tension stiffening parameter captures the nonlinear inelastic phase of the structure after the macrocrack propagates and fibres start to pull-out and are no longer capable of transferring the stress between the two faces.

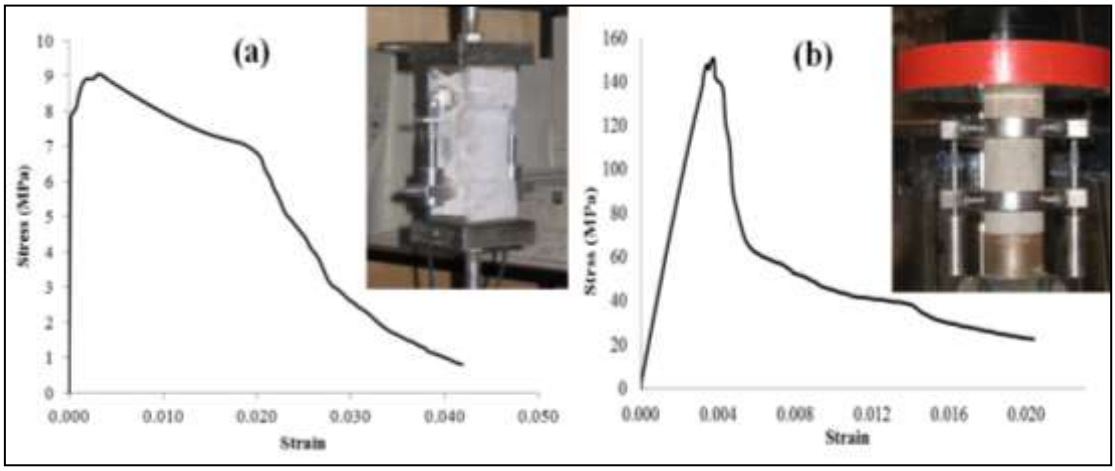

Figure 6.8: Experimental stress-strain curves relationship (a) tensile (b) compression (Hassan et al., 2012).

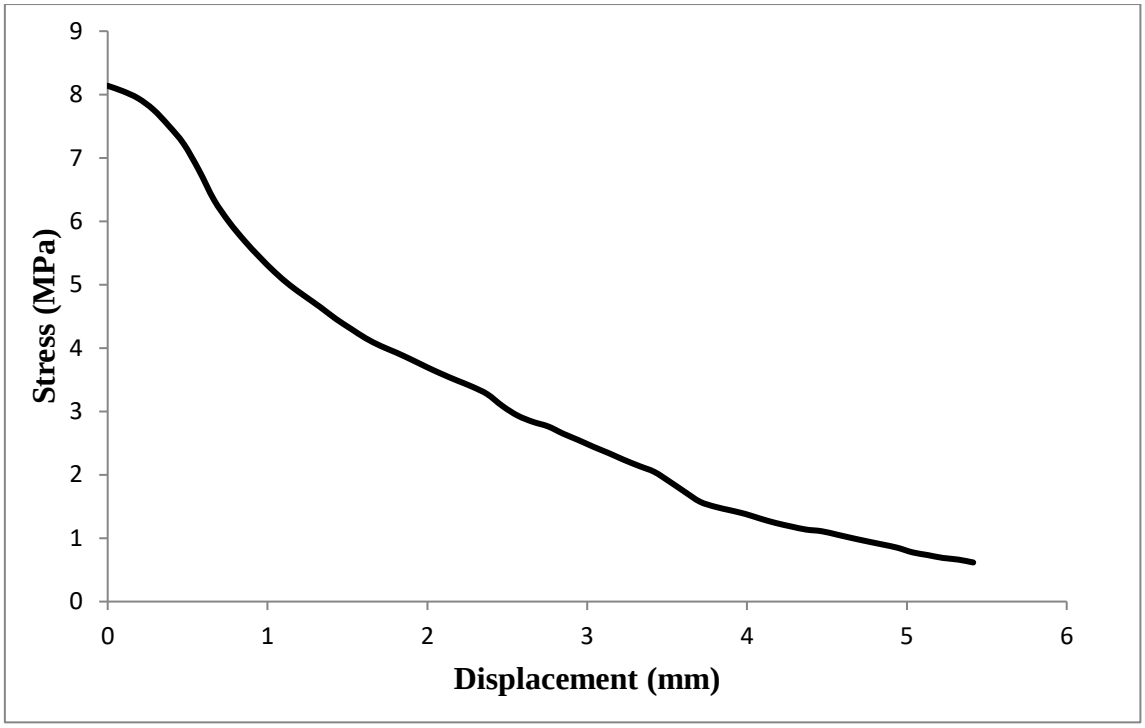

Figure 6.9: Tensile traction-displacement curve.

It should be noted that the strain and COD obtained from experiments include elastic parts but inelastic quantities are used on the data line in ABAQUS so transformation is needed. The tensile fracture and compressive plastic behaviour are completed by specifying the evolution laws of damage which represents the stiffness degradation. This degradation mechanism is obtained under uniaxial cyclic loading conditions which are quite complex. This involves the opening and closing of previous microcracks. Under uniaxial cyclic tests some recovery of the elastic stiffness can be obtained when the material is unloaded. The stiffness recovery is an important behaviour in concrete. The CDP model assumes that the damage index or the material stiffness degradation index varies from zero representing no damage to 1 representing complete failure. In this study, the tensile damage d_t is calculated by Equation 6.11 and 6.12.

$$d_t = 1 - \frac{\sigma}{f_t} \qquad \textbf{(6. 11)}$$

$$E = (1 - d_t)E_0 \qquad \textbf{(6. 12)}$$

where σ and f_t are the traction related to COD in the softening range and flexural strength, respectively. E and E_0 are the elastic modulus and degraded elastic modulus, respectively. Tensile damage is implemented in ABAQUS by using the keyword *CONCRETE TENSION DAMAGE, TYPE=DISPLACEMENT. As the compressive stress modelled in this study in both the three-point bending beams and slabs, is always smaller than the compressive strength, no definition of compressive damage index d_c is needed.

Furthermore, five other parameters are required to be defined in the CSC model. These are: the dilation angle in degrees, the flow potential eccentricity, the ratio of initial equibiaxial compressive yield stress to initial uniaxial compressive yield stress, the viscosity parameter and the ratio of the second stress invariant on the tensile meridian to that on the compressive meridian. The dilation angle of the concrete can vary from one concrete mix design to another, even among different specimens from the same batch. In previous studies, different dilation angles from 12° to 45° have been used but usually values from 30° to 40° have been used with OC. Moreover, in OC, the dilation angle values have been used mostly based on the trial/run error analysis. The effects of these additional parameters are discussed in detail in the following section.

6.2.2 Material Properties and Preliminary Analyses

To determine the ability of CSC to capture the structural behaviour of UHPFRC, preliminary analyses were undertaken using data from material properties testing conducted by Le (2007) and Hassan (2013). The input data used in the CSC model, compression hardening, tension stiffening and other parameters such as failure ratios, and shear retention are shown in Table 6.1. The CSC model predicts the post failure behaviour based on the crack occurrence and crack detection during the analyses. The model assumes, as the stress reaches the tensile strength, cracking has occurred and stress has a linear relationship with CMO. Therefore, the most important parameter in the model is the displacement at failure which was 6 mm in this study. However, looking at the material properties data Figure 6.8 and Figure 6.9, it is apparent the relationship between stress-CMO is not linear. In addition, due to the fibre pull-out behaviour the reduction in stress changes from one displacement point to another. Therefore, it was expected that the CSC may not capture the behaviour of this material satisfactorily, in particular in the

softening region. However, to ensure the credibility of the model, preliminary analyses were conducted.

Table 6.1: Material properties and parameters used in CSC model.

Tension stiffening and other parameters			**Compression hardening**	
Density (kg/m^3)		2500	119.82	0
Elastic modulus (GPa)		45.0	122.23	0.00005
Poisson's ratio		0.22	124.63	0.00011
Displacement at failure (mm)		6.00	127.03	0.00017
Failure ratio 1		1.16	129.37	0.00022
Failure ratio 2		0.06	131.67	0.00028
Failure ratio 3		1.28	133.94	0.00033
Failure ratio 4		0.33	136.16	0.00039
Shear retention	ρ^{close}	1.0	138.31	0.00044
	ε^{max}	0.1	140.39	0.00050
			142.23	0.00055
			143.85	0.00061
			145.58	0.00066
			147.35	0.00072
			148.94	0.00077

6.2.2.1 Preliminary Investigation of CSC Elements

Models with different element types as shown in Table 6.2, were investigated. In total nine different types of elements were investigated; five solid element and four shell elements. The results of all the simulation investigations are presented in Figure 6.10 and Figure 6.11 for one-way and two-way slabs, respectively.

From the preliminary results for both one-way and two-way slabs, the reliability of the CSC model appears to be limited in capturing UHPFRC behaviour. Despite attempts using different element types of both 3D solids and shells, the model experienced convergence problems, in particular with 3D solid elements. Looking at the one-way slabs in Figure 6.10, it can be seen, except for the C3D8 and C3D8I models, which only captured the linear elastic stage, none of the 3D solid models converged. During the analyses, the results of 3D solid models indicted when the displacement reached 0.25 mm,

the models appeared to have difficulty to converge. Furthermore, looking at the two-way slabs figure, none of the 3D element models converged and all the models terminated at very small displacements. Therefore, the load-displacement curves for 3D elements are not included here.

Figure 6.10 and Figure 6.11 show the load-displacement curves obtained from the CSC analyses using shell elements in the elastic region and up until the peak load are in good agreement with the experimental data, while the FE curve showed a stiffer behaviour after the displacement reached the maximum failure point. However, as the load reached its maximum, the analysis appeared to diverge and stop. This was observed for all the shell elements as shown in the figures. In general, the reduced integration elements provided a better convergence compared to the none-reduced integration elements and this was observed in both one-way and two-way slabs. These results were not surprising as the CSC model in the softening region assumes a linear relationship between damaged stiffness and crack opening width and it only takes the final failure displacement into account where the stress is zero. In UHPFRC, the assumption of linear relationship in the softening region will not be realistic as the damaged stiffness is dependent on the fibre pull-out behaviour and it changes from one displacement point to another. Furthermore, since the softening stage was of interest in this study, and is an important behaviour of UHPFRC, the CSC model was not validated by the experimental data.

Table 6.2: Element details for CSC and CDP models.

Element types	Details
C3D8	Eight-node linear brick 3D-element
C3D8I	Eight-node linear brick incompatible 3D-element
C3D8R	Eight-node linear brick reduced integration 3D-element
C3D20	Twenty-node quadratic 3D-element
C3D20R	Twenty-node quadratic reduced integration 3D-element
S4	Four-node linear shell element
S4R	Four-node linear reduced integration shell-element
S8R	Eight-node quadratic reduced integration shell-element with six degrees of freedom per node
S8R5	Eight-node quadratic reduced integration shell-element with five degrees of freedom per node

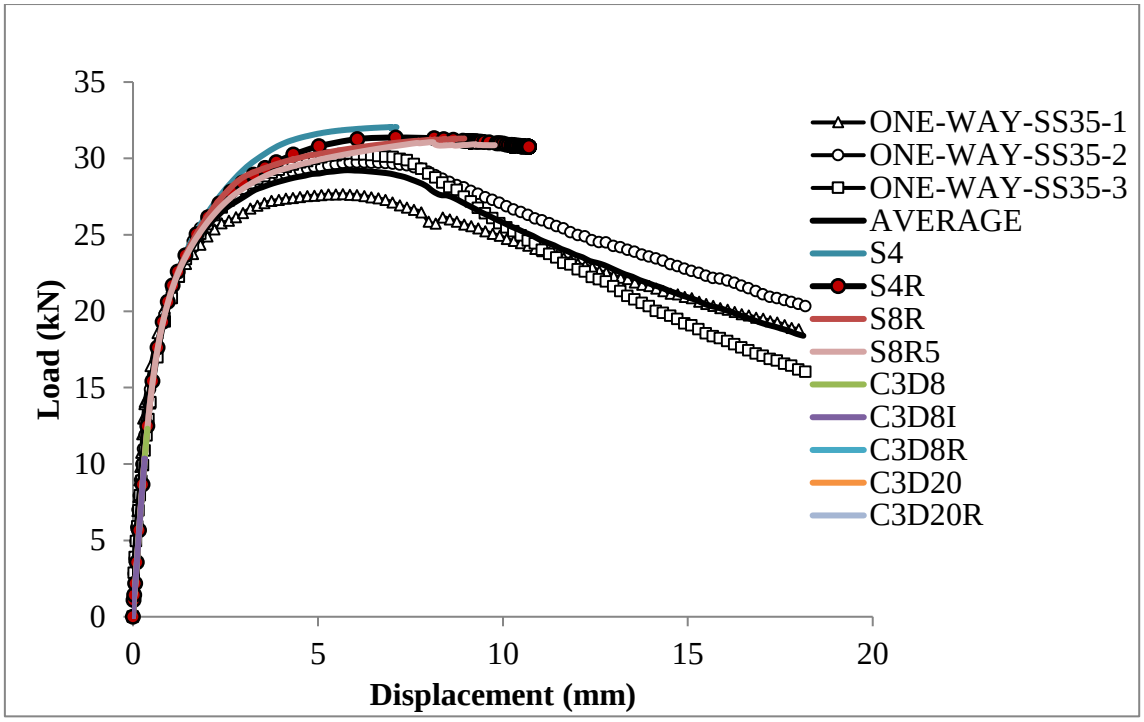

Figure 6.10: Preliminary analyses for one-way slab using CSC model.

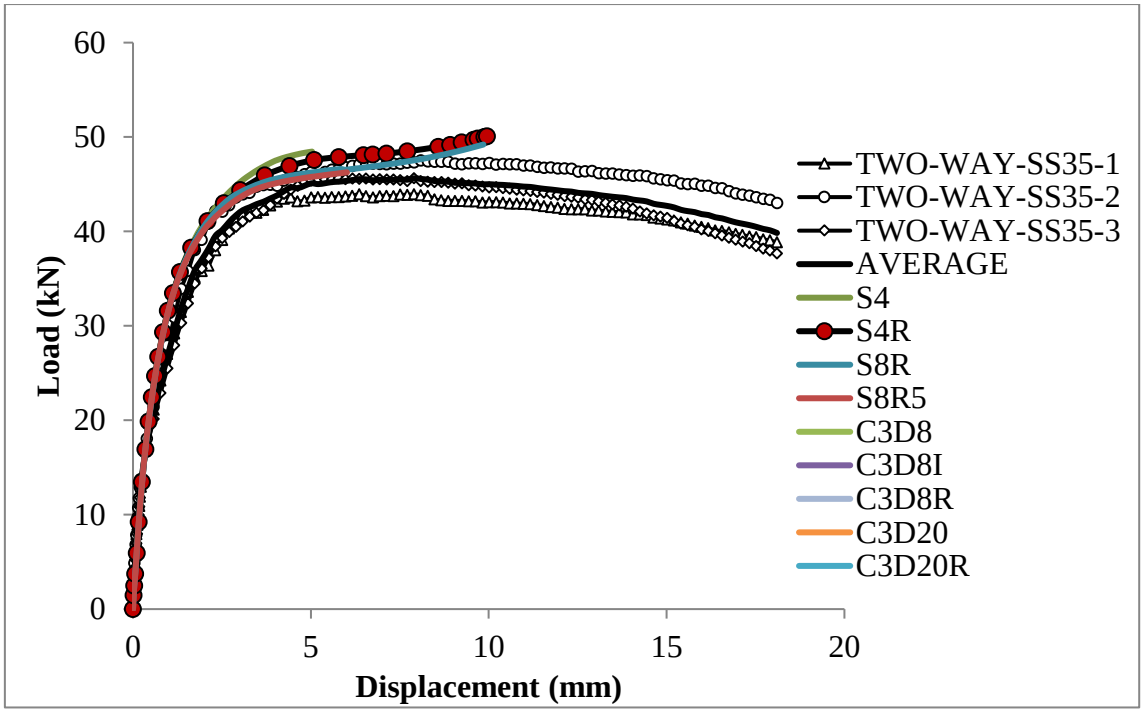

Figure 6.11: Preliminary analyses of two-way slabs using CSC model.

6.2.2.2 Preliminary Investigation of CDP Elements

Similar to the CSC, preliminary analyses were conducted on the CDP model and the input data used to capture the behaviour were obtained from material properties testing (Hassan, 2013) and are shown in Table 6.3 and Table 6.4. Concrete density was chosen based on the study conducted previously on this material (Le, 2007 and Hassan, 2013). The *E* and *v* values were also chosen based on material properties tests conducted by Hassan, (2013). The CDP preliminary results were found to have a good agreement with the experimental data. However, to determine the effect of the additional parameters shown in Table 6.3 on the accuracy of the model, a preliminary analysis was also carried out on these parameters and discussed in the following sections.

Table 6.3: Other CDP model parameters.

Other CDP model parameters	
Density (kg/m^3)	2500
Elastic modulus (GPa)	45.0
Poisson's ratio	0.22
Dilation angle (degrees)	33^o
Eccentricity	0.10
Ratio of compressive yield	1.16
Ratio of stress meridian	0.66
Viscosity	0.00

Table 6.4: Material properties used in the CDP model.

Slab				**Beam**				**Compression hardening**	
Tension stiffening		**Tension Damage**		**Tension stiffening**		**Tension Damage**			
Stress (MPa)	δ (mm)	Damage Variable	δ (mm)	Stress (MPa)	δ (mm)	Damage Variable	δ (mm)	Stress (MPa)	Strain
8.138	0.000	0.0000	0.000	8.430	0.000	0.000	0.000	119.82	0
8.053	0.095	0.0104	0.095	8.251	0.205	0.022	0.205	122.23	0.00005
7.941	0.190	0.0242	0.190	7.941	0.555	0.059	0.555	124.63	0.00011
7.764	0.285	0.0460	0.285	7.764	0.840	0.080	0.840	127.03	0.00017
7.513	0.380	0.0768	0.380	7.513	1.133	0.110	1.133	129.37	0.00022
7.223	0.475	0.1124	0.475	7.223	1.414	0.144	1.414	131.67	0.00028
6.810	0.570	0.1631	0.570	6.810	1.645	0.193	1.645	133.94	0.00033
6.338	0.665	0.2212	0.665	6.338	1.747	0.249	1.747	136.16	0.00039

5.987	0.760	0.2643	0.760	5.987	1.796	0.291	1.796	138.31	0.00044
5.695	0.855	0.3002	0.855	5.695	1.874	0.325	1.874	140.39	0.00050
5.436	0.950	0.3320	0.950	5.436	1.957	0.356	1.957	142.23	0.00055
5.198	1.045	0.3613	1.045	5.198	2.056	0.384	2.056	143.85	0.00061
4.991	1.140	0.3867	1.140	4.991	2.177	0.408	2.177	145.58	0.00066
4.816	1.235	0.4083	1.235	4.816	2.271	0.429	2.271	147.35	0.00072
4.646	1.330	0.4292	1.330	4.646	2.316	0.449	2.316		
4.465	1.425	0.4513	1.425	4.465	2.391	0.471	2.391		
4.307	1.520	0.4707	1.520	4.307	2.453	0.490	2.453		
4.154	1.615	0.4896	1.615	4.154	2.491	0.508	2.491		
4.031	1.710	0.5047	1.710	4.031	2.512	0.522	2.512		
3.929	1.805	0.5172	1.805	3.929	2.549	0.534	2.549		
3.818	1.900	0.5308	1.900	3.818	2.623	0.548	2.623		
3.701	1.995	0.5452	1.995	3.701	2.684	0.561	2.684		
3.591	2.090	0.5588	2.090	3.591	2.770	0.574	2.77		
3.489	2.185	0.5713	2.185	3.489	2.861	0.587	2.861		
3.391	2.280	0.5833	2.280	3.391	2.990	0.598	2.99		
3.272	2.375	0.5979	2.375	3.272	3.104	0.612	3.104		
3.085	2.470	0.6209	2.470	3.085	3.190	0.634	3.19		
2.934	2.565	0.6394	2.565	2.934	3.257	0.652	3.257		
2.836	2.660	0.6515	2.660	2.836	3.300	0.664	3.300		
2.764	2.755	0.6603	2.755	2.764	3.403	0.672	3.403		
2.649	2.850	0.6745	2.850	2.649	3.519	0.686	3.519		
2.548	2.945	0.6869	2.945	2.548	3.614	0.698	3.614		
2.441	3.040	0.7001	3.040	2.441	3.695	0.711	3.695		
2.342	3.135	0.7122	3.135	2.342	3.812	0.722	3.812		
2.236	3.230	0.7253	3.230	2.236	3.968	0.735	3.968		
2.139	3.325	0.7371	3.325	2.139	4.115	0.746	4.115		
2.046	3.420	0.7486	3.420	2.046	4.237	0.758	4.237		
1.894	3.515	0.7673	3.515	1.894	4.308	0.776	4.308		
1.732	3.610	0.7872	3.610	1.732	4.331	0.795	4.331		
1.576	3.705	0.8063	3.705	1.576	4.336	0.813	4.336		
1.496	3.800	0.8162	3.800	1.496	4.372	0.823	4.372		
1.440	3.895	0.8231	3.895	1.440	4.460	0.829	4.460		
1.382	3.990	0.8302	3.990	1.382	4.540	0.836	4.540		
1.307	4.085	0.8394	4.085	1.307	4.610	0.845	4.610		
1.240	4.180	0.8477	4.180	1.240	4.669	0.853	4.669		
1.185	4.275	0.8544	4.275	1.185	4.737	0.860	4.737		
1.136	4.370	0.8605	4.370	1.136	4.805	0.865	4.805		
1.111	4.465	0.8635	4.465	1.111	4.880	0.868	4.880		
1.058	4.560	0.8700	4.560	1.058	4.948	0.875	4.948		
1.003	4.655	0.8767	4.655	1.003	5.016	0.881	5.016		
0.951	4.750	0.8832	4.750	0.951	5.078	0.887	5.078		
0.902	4.845	0.8892	4.845	0.902	5.140	0.893	5.140		
0.850	4.940	0.8956	4.940	0.850	5.227	0.899	5.227		
0.777	5.035	0.9045	5.035	0.777	5.308	0.908	5.308		
0.734	5.130	0.9099	5.130	0.734	5.389	0.913	5.389		
0.689	5.225	0.9153	5.225	0.689	5.479	0.918	5.479		
0.663	5.320	0.9185	5.320	0.663	5.554	0.921	5.554		
0.617	5.415	0.9242	5.415	0.617	5.635	0.927	5.635		

ABAQUS offers a variety of elements for use with the concrete damage plasticity model such as shell, solid, plane stress, plane strain, generalised plane strain and axisymmetric elements. Therefore, assigning an appropriate element type and shape is essential in mesh modules, prior to mesh convergence studies. A thorough preliminary numerical investigation was also conducted in CDP on both 3D and shell elements and details of these element types are shown in Table 6.2. Since four different thicknesses and various different boundary conditions were tested, it would not be realistic to investigate all the tested specimens. Therefore, slabs with 35 mm thickness for both one-way and two-way slabs were chosen to investigate the effect of element size. To compare the results, it was important to use similar element sizes in all the analyses.

Except for the C3D8 element, the results showed that all the 3D elements underestimate the experimental data as they go beyond the elastic region as shown in Figure 6.12. Furthermore, the analysis for element type C3D81 terminated after approximately 70% of its total time due to convergence difficulties. Figure 6.13 shows that the C3D8 element type, which gives a reasonable result for one-way slabs with 35 mm thickness, overestimated the two-way slabs with similar thicknesses. Surprisingly, the element type C3D8I which stopped in the one-way slab analysis gave a reasonable result for two-way slabs. Therefore, the reliability of the 3D element diminished as the parameters were changed. In terms of shell elements and except for the S4R element, the accuracy of these elements changes as the parameters change. For instance element type S4 gives similar results to S4R as shown in Figure 6.13**Error! Reference source not found.**. The accuracy of this element changes considerably as the parameter changes, as shown in Figure 6.12. Furthermore, using shell elements significantly reduced computational time and memory usage compared to the 3D elements. Computational time for 3D element analyses was approximately 50 times greater than with shell elements. The results show the S4R element gives an accurate result for both one-way and two-way slabs as shown in Figure 6.12 and Figure 6.13, respectively. Therefore, it was decided to use S4R elements to model all the slabs. Each element must be labelled numerically and this was automatically assigned when the element is defined. Labelling allows the user to analyse any element on the geometry during the analysis or in the visualisation modules, especially in the models with large numbers of elements such as in this study.

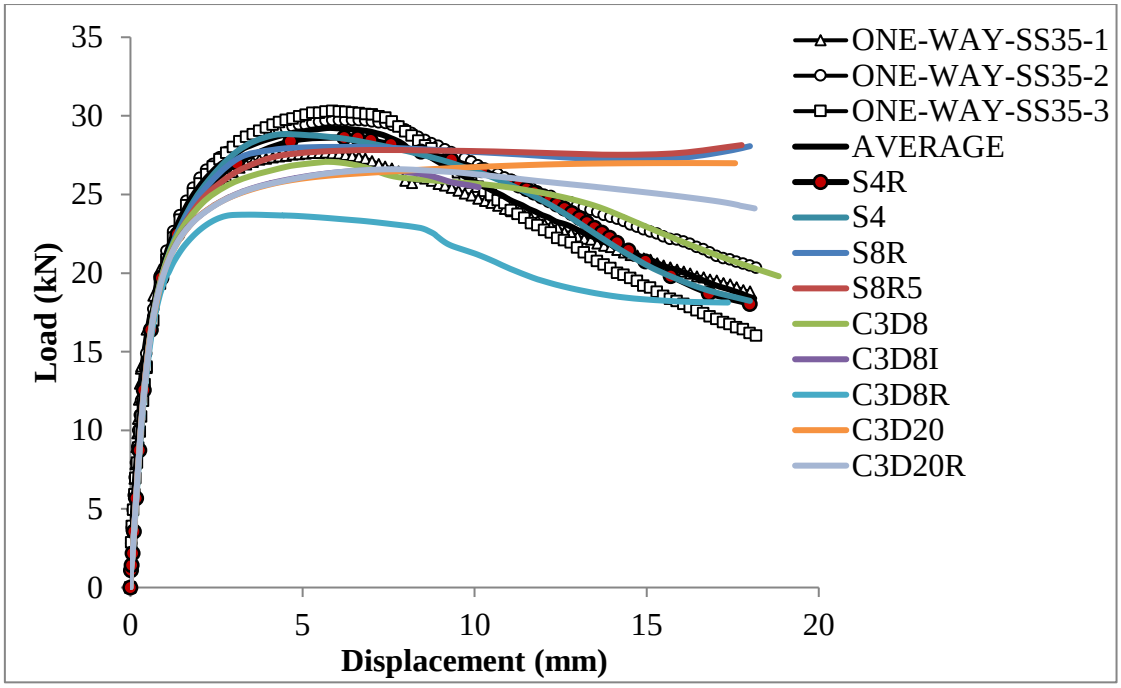

Figure 6.12: Preliminary analysis for different element types for on-way slabs.

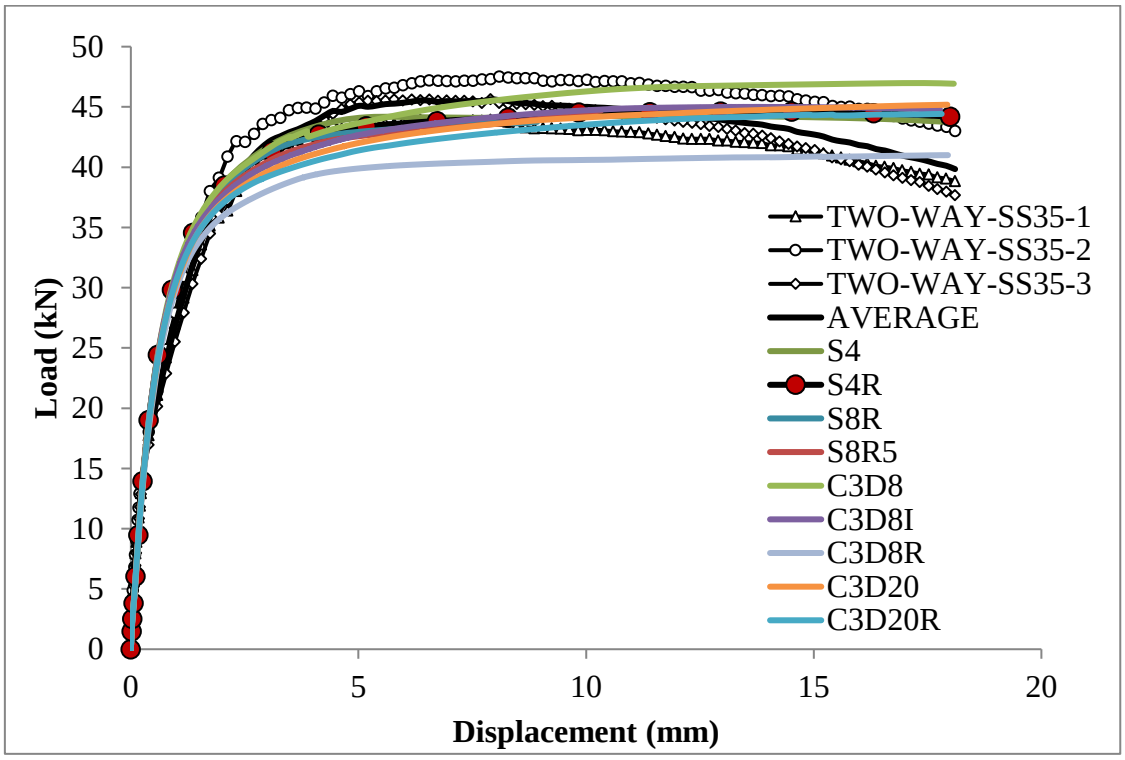

Figure 6.13: Preliminary analysis for different element types for two-way slabs.

6.2.2.3 Preliminary Investigation of Elastic Modulus and Poisson Ratio

To determine material properties of any types of concrete, a small variation in the result is expected. Material testing for UHPFRC also showed a small variation in the result. Therefore, a range of values based on material testing were chosen and used in the model. Since, E and υ can have an effect on the FE result, especially in the elastic range and the material testing by Hassan (2013) showed that the elastic modulus and Poisson's ratio results could vary between the range of 44 to 48 GPa and 0.21 to 0.24, respectively. Therefore, preliminary analyses between these ranges were carried out for both one-way and two-way slabs. The results showed these small changes in elastic modulus and Poisson's ratio, were insignificant as shown in Figure 6.14 and Figure 6.15. However, it is important to mention that changes in these parameters may have an effect if the material is to be investigated at an element level which is beyond the scope of this study. For example, considering the bond between the fibres and the matrix using a heterogeneous model.

In addition, choosing any values E and υ within the range showed in the material testing would be accepted to be used in the FE model. Hassan (2013) concluded that the average value of 45 GPa and 0.22 for both elastic modulus and Poisson's ratio, respectively could be used. Therefore, 45 GPa for E and 0.22 for υ, were used in all FE models.

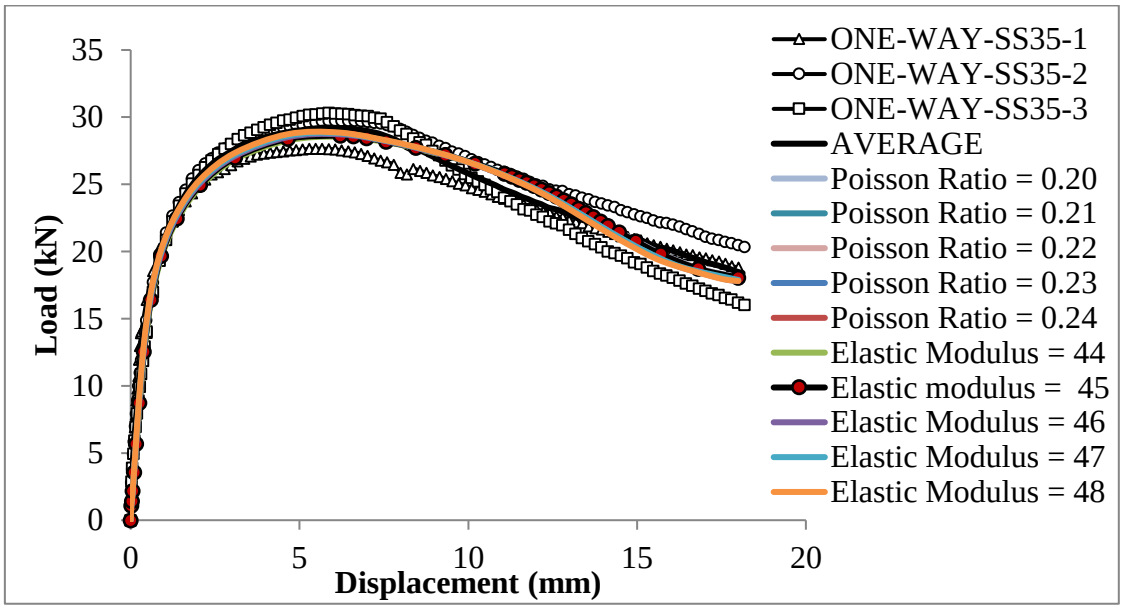

Figure 6.14: FE investigation for elastic modulus and Poisson's ratio for one-way slabs.

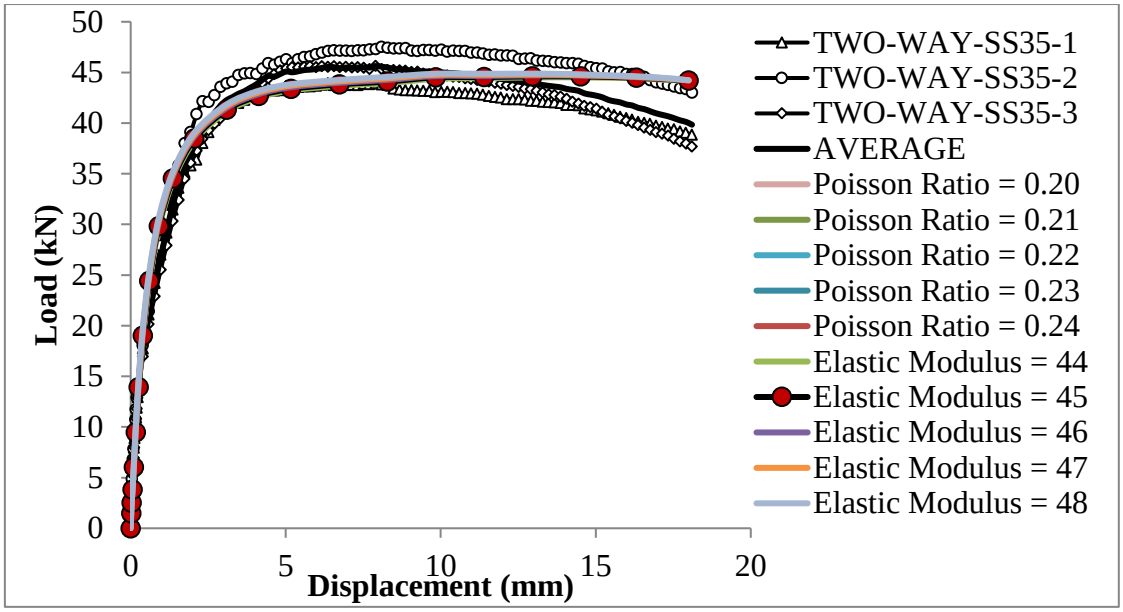

Figure 6.15: FE investigation for elastic modulus and Poisson's ratio for two-way slabs.

The other five parameters such as the dilation angle, eccentricity, f_{b0}/f_{c0}, K and viscosity that are required to be defined in the CDP model are also investigated. As mentioned, the dilation angle of the concrete can vary from one concrete mix design to another, even among different specimens from the same batch. In previous studies, different dilation angles from 12° to 45° have been used but usually values from 30° to 40° have been used with OC. Moreover, in OC, dilation angle values have been used mostly based on the trial/run error analysis. However, in this study various values of 30°, 33°, 35°, 37° and 39° were used to determine the effect of dilation angle. Slabs with 35 mm thickness in both one-way and two-way arrangements were analysed. The result of these models showed that the changes in dilation angle were insignificant and the results for both one-way and two-way setups are shown in Figure 6.16 and Figure 6.17, respectively. Viscosity is another uncertain parameter in concrete modelling. It occurs due to the collision between the material particles as they move at different velocities. It measures the material's resistance to gradual deformation by either shear stress or tensile stress. In concrete it is related to the rheological properties of the fresh concrete which can be described by its yield point and plastic viscosity. Yield point describes the force that is required to start the fresh concrete moving, whereas plastic viscosity describes the resistance of a concrete to flow under external stress when the stress is higher than the yield stress. In order to obtain an appropriate concrete rheology, it is essential to maintain the balance between

the yield point and plastic viscosity. Since concrete has to fulfil several requirements in both the fresh and hardened state, it is important to understand the properties of fresh concrete as it has a direct effect on the quality of the hardened concrete. It has always been desirable to increase the mechanical properties of hardened concrete by reducing the w/c ratio. However, reducing the w/c ratio decreases workability, therefore a modifying admixture such as a superplasticiser has been added to decrease and maintain the yield stress and plastic viscosity of the fresh concrete. In terms of the viscosity of hardened concrete, this has been the subject of debate between two groups of researchers in the literature. One group of researchers contended that amorphous solids, such as glass and many polymers, are liquid and may be considered to have viscosity. This has led some to the view that solids are liquids with a very high viscosity and flow like a liquid but very slowly. This idea is usually supported by glass flow and this can be observed in old buildings. However, other researchers dispute this hypothesis and argue that solids are elastic for small stresses while fluids are not and that glass flow in window panels of old buildings are due to the lack of manufacturing process at that time rather than to the viscosity of glass (Plumb, 1989). In order to determine the viscosity of hardened concrete, appropriate testing would be required, which is beyond the scope of this research. Therefore, using any values rather than the recommended value in ABAQUS will not be justifiable. In the literature, the viscosity parameter is defined through a numerical investigation by changing this parameter until the numerical result becomes close to the experimental data and in the most cases the value 0.0 is used. In OC modelling, a value from 0.0 to 0.1 was found to be sufficient, depending on the numerical problems. Since, in this study, the default value was found to provide satisfactory results between the numerical and experiment, the value of 0.0 was chosen.

The ABAQUS manual recommends a default value of 0.0 for concrete static modelling and uses the default value in all the solved examples in the manual. If the user excludes the parameter in the analysis, ABAQUS uses the default value of 0.0 automatically. Therefore, including or excluding this parameter has no effect on the concrete modelling. Furthermore, viscosity values greater than 0.0 can be used in ABAQUS/Standard only if the extended FE analysis using modified virtual crack closure techniques is used. However, this was not the case in this study, thus values of 0.0 for viscosity were used in all the preliminary analyses. The other three remaining parameters were also investigated and the results showed these parameters have no effect on the analyses as shown in Table

6.5. Therefore, the default values from the ABAQUS documentation 33°, 0.1, 1.16, 0.66 and 0.0 were used for each of the five parameters, respectively.

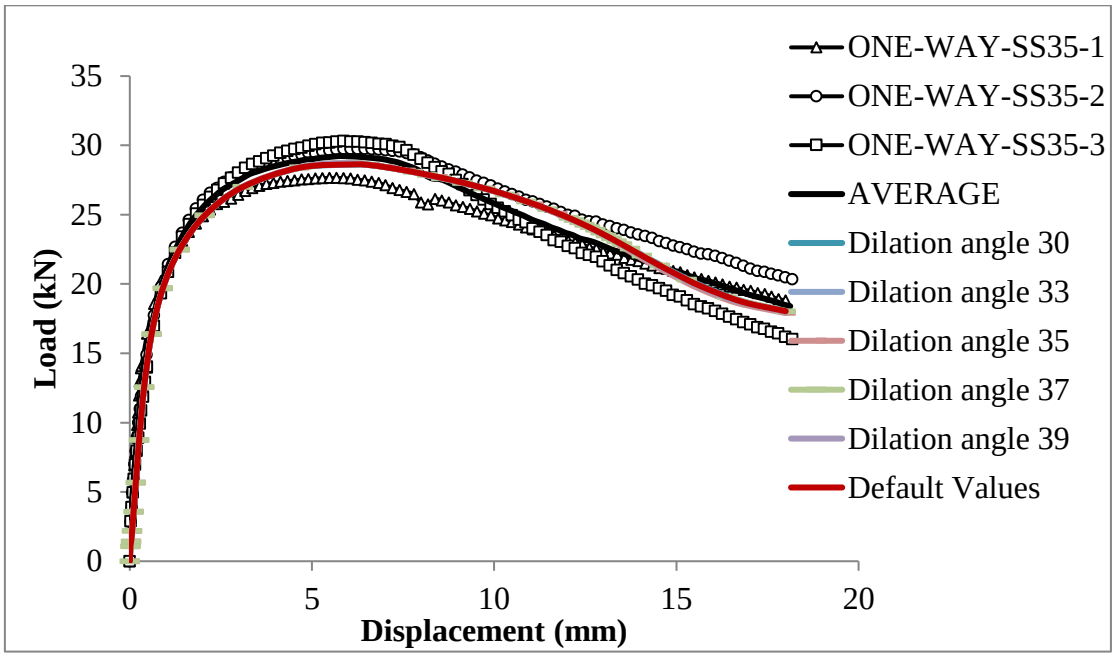

Figure 6.16: Preliminary analyses for dilation angle for one-way slabs.

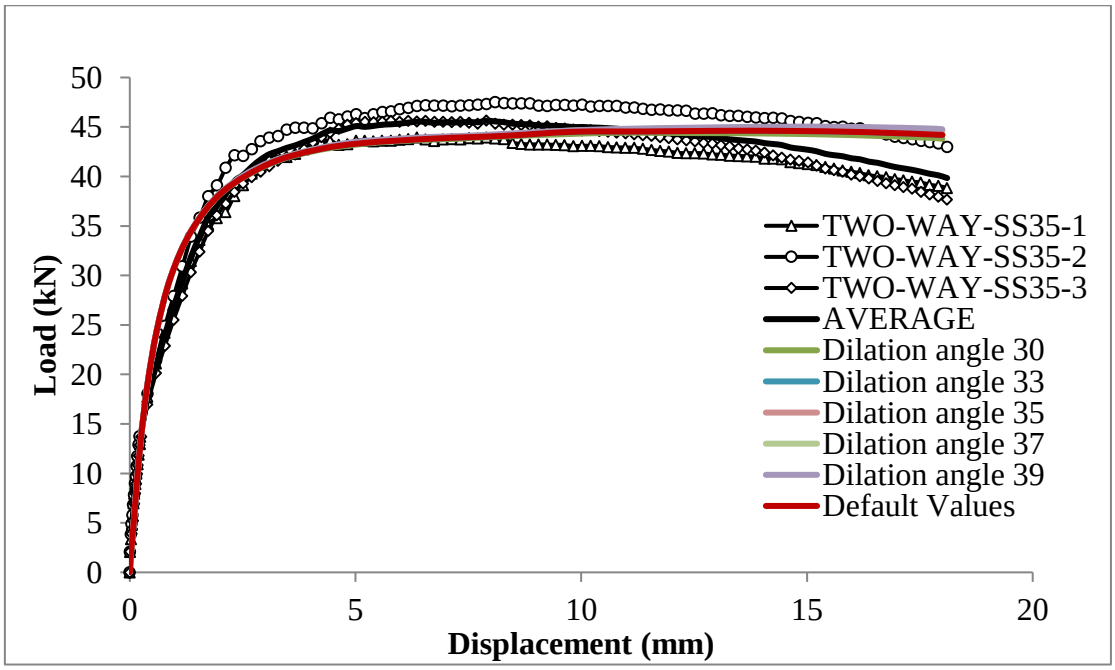

Figure 6.17: Preliminary analyses for dilation angle for two-way slabs.

Table 6.5: Values of key parameters used in the preliminary analysis.

Models	(Dilation angle, Eccentricity, Ratio of compressive yield, Ratio of stress meridian and Viscosity) parameters
Default Values	33, 0.1, 1.16, 0.66, 0.0
Dilation angle 30	30,0.0,0.0,0.0,0.0
Dilation angle 33	33,0.0,0.0,0.0,0.0
Dilation angle 35	35, 0.1, 1.16, 0.66, 0.0
Dilation angle 37	37,0.0,0.0,0.0,0.0
Dilation angle 39	39, 0.1, 1.16, 0.66, 0.0

The result of preliminary analyses showed that the CDP model provides better results compared to a CSC model to capture the structural behaviour of both one-way and two-way UHPFRC slabs. The CDP model has a better convergence solution and is capable of determining the behaviour of the material in all three stages: linear elastic, strain hardening and strain softening. The model has been used in previous studies and showed a better convergence solution as crack propagation is modelled using a continuum damage approach (Dawood, 2010). In addition, the CDP model can accurately capture the concrete failure modes in reinforced concrete structures (Liu et al., 2008). Therefore, CDP was selected in this study to simulate the behaviour of the UHPFRC beams and slabs. However, in order to further validate the reliability of the FE analysis, the tension and compression tests conducted by (Hassan, 2013) were modelled. The outcome of the CDP model are compared to the experimental data and detailed in Section 7.1 in Chapter 7.

6.3 Finite Element Procedure

This section provides a detailed overview of the modules concerned with modelling the beams and slabs. The description includes model geometry, properties, elements, mesh, surface and region interactions, support boundary conditions and loads.

6.3.1 Notched Beams Modelling

The experimental work described in Chapter 3 for all the beams with depths varying from 30 mm to 150 mm, were modelled in the ABAQUS software. Due to the high volume of steel fibres in UHPFRC, the cost of experimental studies is still relatively high, especially for large-sized structures. To establish a full size effect law, more beams with depth of 180, 210, 240 and 300 mm, in addition to the five beams tested, were also modelled using a similar procedure.

Furthermore, due to the sheer number of fibres randomly distributed in the matrix and the resultant complicated fibre-matrix interaction, discrete modelling of fibres and matrix requires substantial re-meshing (Yang et al., 2005). This re-meshing is needed to accommodate the arbitrary geometries and boundaries along newly created cracks created by the external forces, thus extensive computation is needed which is time-consuming even with the available modern computer power (Hents, et al., 2005, Su et al., 2011). Moreover, in the literature many studies attempted to model the interface between the physical aggregate and the matrix, of ordinary concrete. To do this, the interface between the aggregate and matrix was modelled using zero length elements which had a normal softening and shear component along the aggregate surface. However, the main drawback of this discrete modelling is that, these models are not suitable to determine the softening behaviour, since softening is already pre-defined in the model at the meso-level (Lilliu and Van Mier, 2003). An alternative approach based on linear-elastic fracture mechanics, proposed by Wang (1994) is to model the physical cracking between the interface and matrix. This model requires the user to describe the crack propagation in the model. This means the formation of the cracks must be known experimentally prior to running the model. Therefore, this approach may be useful for describing crack propagation of OC, where extensive research has been conducted and the behaviour of OC in terms of crack propagations is well understood. In UHPFRC, where there is a lack of understanding the structural behaviour of the material in terms of failure modes and cracks propagations, the use of such a model would not be appropriate. In addition, due to the large number of fibres within the matrix of UHPFRC, the number of cracks and crack locations changes as the geometry changes, hence the credibility of the Wang model would be limited to those sizes only where they have been validated experimentally.

Moreover, the CDP model is proven to be reliable at defining the structural behaviour of OC. It is an accurate, simple and straightforward tool for understanding the structural behaviour of concrete. In addition, in the preliminary investigation, it accurately predicted the behaviour of UHPFRC for all cases, especially in the elastic and strain hardening stages. Therefore, it is considered to be appropriate to be used in this study.

Assuming that fibres are uniformly distributed in the matrix, the UHPFRC is modelled as a homogeneous material in this study. To simulate crack propagation in the notched beams, the CDP, which has proved very powerful for modelling normal concrete structures (Chen et al., 2009, Li et al., 2012, Chen et al., 2012), is used to model UHPFRC beams.

6.3.1.1 Part Module

The part module was used to define the geometry and the beams were created by choosing a 2D deformable solid part. Due to the simplicity of the geometry, the mesh of the 2D model was generated by defining the nodal coordinates in the input file. Because the beams were symmetric, only half of the specimens were considered, as shown in Figure 6.18. Due to the simplicity of the beam geometry, an input file was created to define the part. The input file was imported directly to the processors to analyse. The properties explained above such as elasticity, density, Poisson's ratio, compression hardening, tension stiffening, and tension damage were defined. In the part module, several toolsets such as Set, Partition, and the Datum are provided. These toolsets operate on the part and allow users to create sets, partitions, and datum geometry, respectively. Partition and the Datum toolset were used to create three partitions along the x-direction and one along the y-direction for all the beams. Material properties which were the most important part of the model were also input including: elastic modulus, Poisson's ratio, compression hardening, tension stiffening and tension damage.

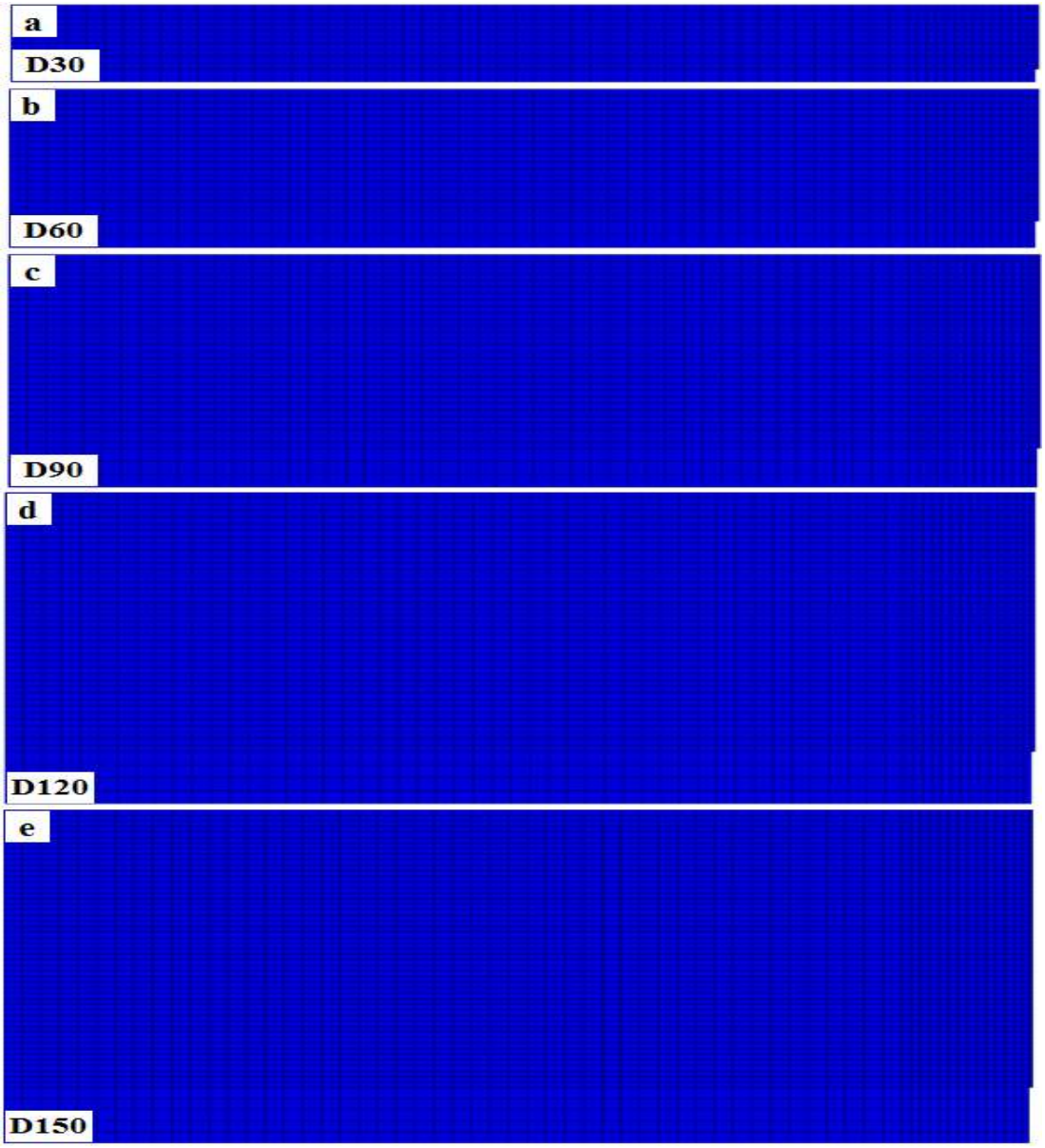

Figure 6.18: Part geometry of 5 beams (a) D30 (b) D60 (c) D90 (d) D120 (e) D150.

6.3.1.2 Assembly

In the assembly module, using the "SET" option, three sets of nodes were defined in the input files. The first set was defined for the support at a distance of 25 mm from the end of the beam and it was constrained in the vertical direction. While the top node at the centre of the beam was defined for the applied load and it was constrained in the horizontal direction. Because only half of the beam was considered due to the beam symmetry, the third set was used to define the nodes on the mid-span and these nodes

were constrained in the horizontal direction. Finally the thickness of the beam was taken into account under the "section" option and it was set to be 150 mm.

6.3.1.3 Beam Elements

Several CDP models with different analyses such as 2D and 3D in ABAQUS/Standard were built for each beam thickness and analysed. In order to be able to compare the results between the 2D and 3D models, the same mesh size was used in all analyses. Apart from an increase in the computation time, the 3D models have also shown a convergence difficultly. Therefore, the results of 3D models are not shown here. In the 2D analysis, several different elements are available in both linear and quadratic shapes. The eight node plane stress quadratic and reduced-integration elements (CPS8, CPS8R) as well as the four node linear plane stress, reduced-integration and incompatible elements (CPS4, CPS4R and CPS4I), respectively, are investigated. Taking the softening region into account, the results of the models were compared to the experimental results and the four node elements showed a better accuracy compared to the eight nodes elements. The results of the 2D models with different elements for D90 were analysed. Except for CPS4, all the other elements underestimated the softening behaviour. In addition, the CPS4I stopped due to the convergence difficulties before the analysis reached the ultimate load as shown in Figure 6.19. However, the accuracy of CPS8, CPS4I and CPS4 elements was also reduced when beams with different depth were analysed. For instance, after the D150 beams were analysed, the results showed that, except for the CPS4R elements, all the models were terminated due to the excessive distortion of the elements. In addition, reduced-integration elements significantly reduce the computation time. Therefore, all the beams were modelled using CPS4R elements. Every element node has two degrees of freedom and they can be used to model the widest variety of components as illustrated in Figure 6.20.

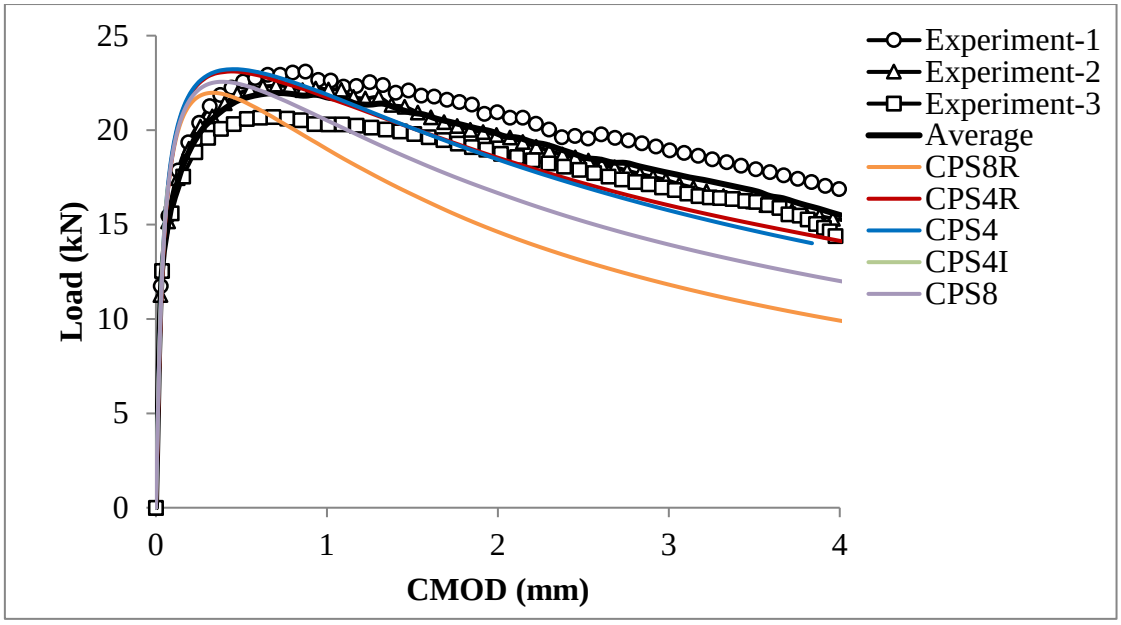

Figure 6.19: Results of the 2D models for D30 beams using different element types.

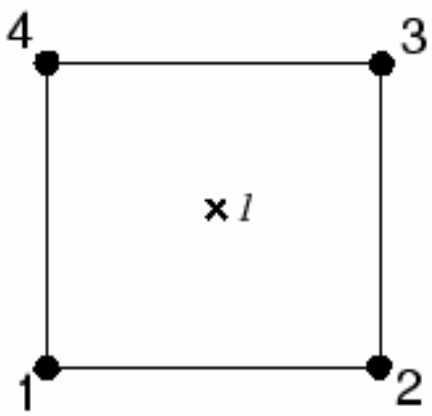

Figure 6.20: 2D elements with reduced integration element (ABAQUS, 2013).

In order to define the elements, nodes had to be defined in the input files. Since four partitions were used in the beam model, eleven node sets were defined using the "NSET" parameter for each beam. According to the beam geometry, the gaps between these node sets were filled using the "NGEN" parameter. After all the nodes were defined and based on the node sets, seven element sets were also defined using the "ELSET" option. Finally the elements were generated using the "ELGEN" parameter and it was required that each data line was given the first and last element as well as the increment in element numbers between these elements.

6.3.1.4 Beam Mesh Convergence Study

The mesh definition is a critical process in modelling, and the accuracy of the results rely on it. It is concerned with breaking down all individual parts into smaller elements. The beam was partitioned prior to the meshing stage so as to avoid unsymmetrical mesh generation. An element mesh was generated from the model geometry using the meshing tools within the ABAQUS software during the job analysis.

In FE modelling, a finer mesh typically results in a more accurate solution. However, as a mesh is made finer, the computation time increases. A mesh convergence study was carried out to obtain a mesh that satisfactorily balances accuracy and computing resources. The mesh convergence study provided an accurate solution with a mesh that was sufficiently dense and not overly demanding of computing resources. Since the beam specimens failed with the single macrocrack at the beam centre and all the beams were notched, it was apparent that the stress concentration is highest at the centre. Therefore, for each specimen, the mesh near the notch region was set to be finer than the side of the beam to reduce the computation time. Prior to the three meshes shown here, initially an element size greater than 5 mm was used to investigate the mesh sensitivity and to ensure the model ran without an error. As expected, the results of the FE analysis were found to be significantly different from the experiment in terms of the peak load and softening behaviour. Therefore, the element size was reduced by half and this process was repeated until the decrease in element size had very little effect on the result. The final three mesh sizes near the beam centre, 5 (Coarse), 2.5 (Medium) and 1.25 (Fine) mm, for the beam with d= 60 mm are shown in Figure 6.21. The result of the mesh sensitivity showed that the change in the element size in the latter two led to virtually identical results, while the finer mesh increased the computation time. Therefore, the medium mesh was adopted to model other beams in this study. Since the problem is a 2D model, only the x- and y-directions needed to be considered. In the x-direction, elements were defined to be 5 mm up to the length of 240 mm, 2.5 mm up to the length of 270 mm, 2 mm up to the length of 274 mm and 1.0 mm up to 275 mm. In the y-direction, the elements were defined in two different sizes, 5 mm up to the tip of the notch and 2.5 mm thereafter, as illustrated Figure 6.22.

In ABAQUS, by default, an aspect ratio of up to 10 is allowed. The element aspect ratio is defined as the element width divided by the element height in this study. To model the beam accurately, it was important to avoid excessive aspect ratios. To obtain a better

accuracy, it is recommended in ABAQUS to use an aspect ratio of close to 1, especially where the stress concentration is a maximum in the middle of the beam in this study. In the beam FE model, except for 5 mm close to the notch which has an aspect ratio of 0.8, the aspect ratio of 1 was used up to 30 mm from the centre of the beam. An aspect ratio of 2 was used for the rest of the beam where stresses are smaller. All the aspect ratios used to model the beams are within the allowable limit.

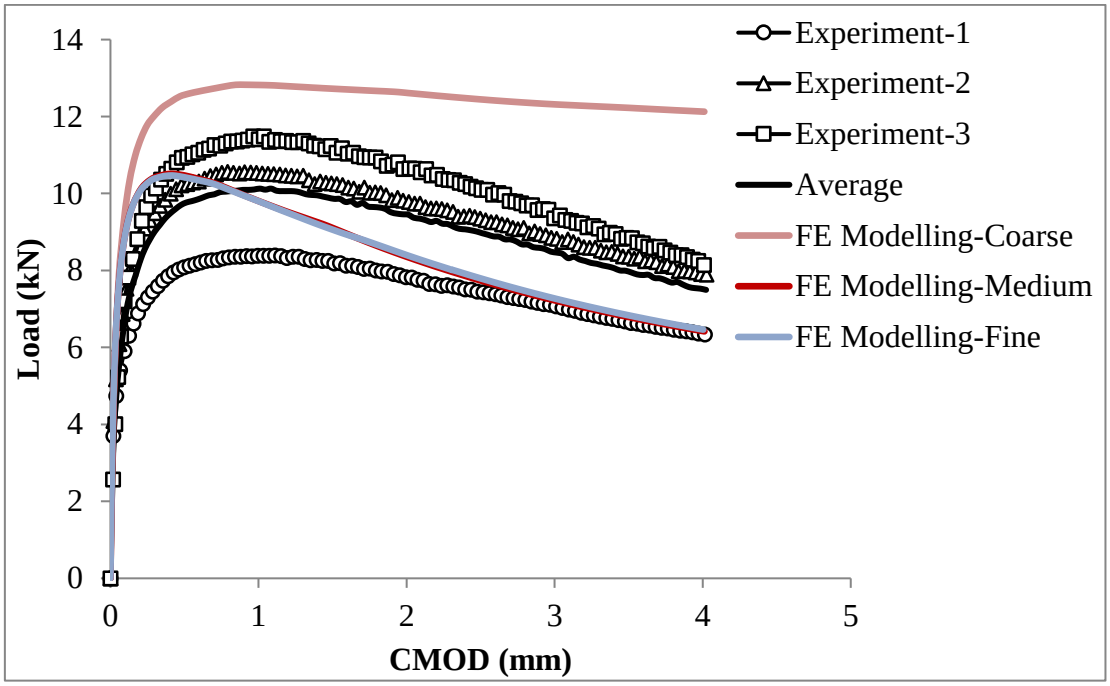

Figure 6.21: Mesh convergence study for D60 beam specimens.

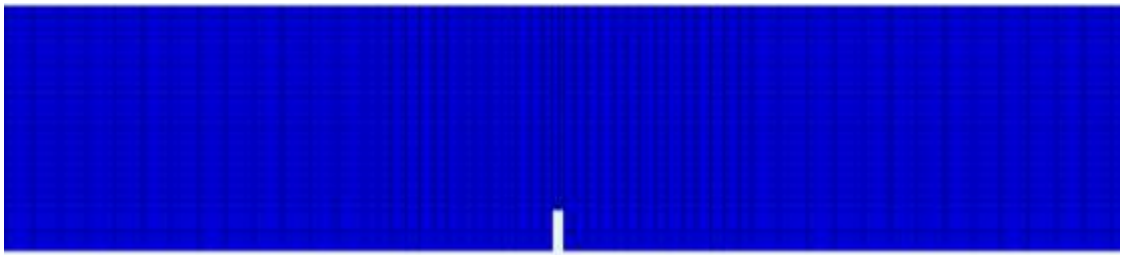

Figure 6.22: Mesh element size for D60 beam specimens.

6.3.1.5 Steps

The post-peak behaviour was considered in this study and to obtain the post-peak part of load-CMOD curves, the STATIC-RIKS method was used in all the analyses. In this step method, a parameter called NLGEOM is provided, which takes material nonlinearity into account. Therefore, in the input file the parameter NLGEOM was switched on to indicate that geometric nonlinearity was accounted for during the step. Increment parameters were specified with 0.001 as an initial value and 0.01 as a maximum. Since the problem included a nonlinear material, iterations were required to ensure convergence of the magnitude of the vector of residual force, thus the minimum length increment was set to 0.000001.

6.3.1.6 Load and Boundary Condition

In the FE analysis, only half of the length of the specimen was considered and symmetrical conditions were imposed by constraining nodes at the mid-span in the horizontal direction as shown in Figure 6.23. In the experiment, load was controlled in displacement over the semi-circular roller; so a load-displacement control method was employed in the analysis. The displacement in the FE analysis was set to be 10 mm on the centre node, which was higher than the maximum mid-span displacement recorded in the experiment. The boundary conditions were based on the support conditions used in the experiments, thus the sixth node from the end of the beam was restrained in the vertical direction as shown in Figure 6.23. To obtain the load, the reaction force at the support was measured.

To ensure that the boundary condition in the models were representative of the experimental tests. The boundary conditions for the beam specimens were fixed at one support in both x-direction in translational (U1) and y-direction in translational (U2), while the other support was restricted only in the y-direction in translational (U2). Since only half of the beam was modelled, symmetrical boundary conditions were applied to the nodes. The boundary condition for x-direction in translational (U1) was used on the nodes along the x-plane at the mid-span which restricted displacement in the x-direction. The support node is also restrained in the y-direction in translational (U2) which restricted displacement in y-direction as shown in Figure 6.23.

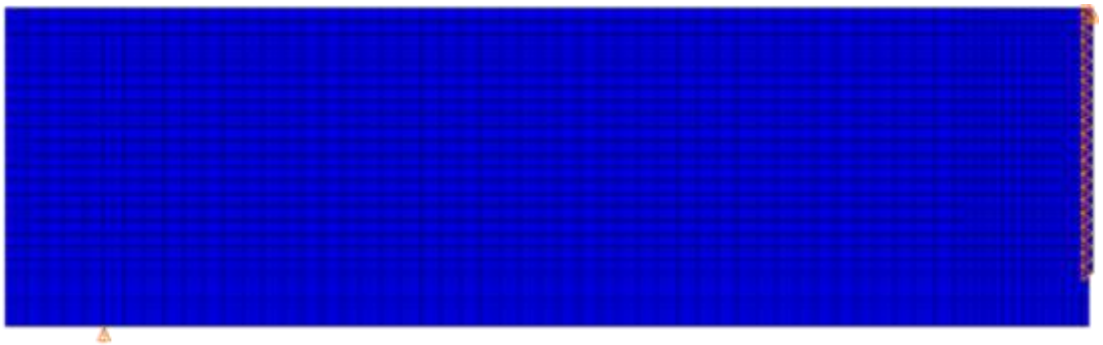

Figure 6.23: Boundary condition for D60 beam specimens.

6.3.1.7 Analysis and Visualisation

After all the tasks involving defining the model (such as defining the geometry of the model, assigning section properties, mesh and choosing appropriate steps) were finished, the "Job module" was used to analyse the model. Due to the capacity of job modules, during the analyses several jobs with different beam geometries were run simultaneously to obtain the results quicker. Using the "monitor" option, these jobs were monitored during the analyses.

Once the model was fully analysed, the visualisation module was used to interpret the results. To view the results, outputs were requested. In ABAQUS, two types of output requests are available: field output and history output and both can be specified by creating output requests. However, because the analyses can create very large amounts of output and in ABAQUS output can be controlled and managed, only data required to interpret the results of the simulation were produced. In this study, the displacement, stress, strain and reaction forces data over the whole slab model were requested. The results such as reaction forces and displacements were viewed in the visualisation module and recorded. The deformed shape with maximum displacement, damage counter and plastic strain (PE) for the beam with a depth of 60 mm are shown in Figure 6.24. These are discussed in detail in Chapter 7, Section 7.1.1.

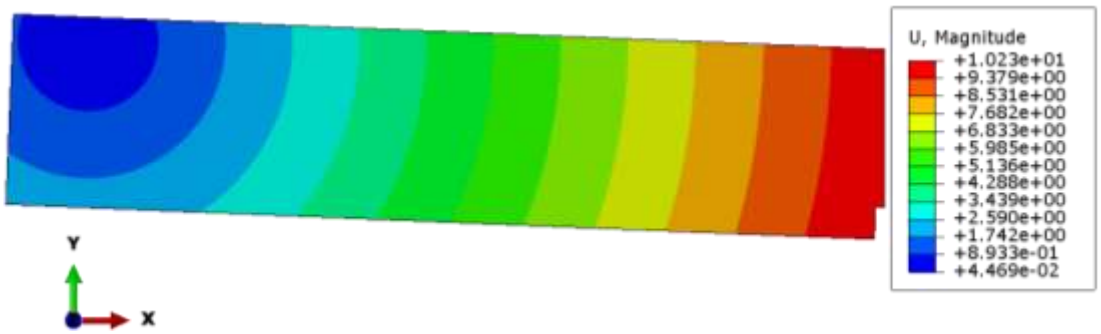

a) deformed shape

b) plastic strain (PE)

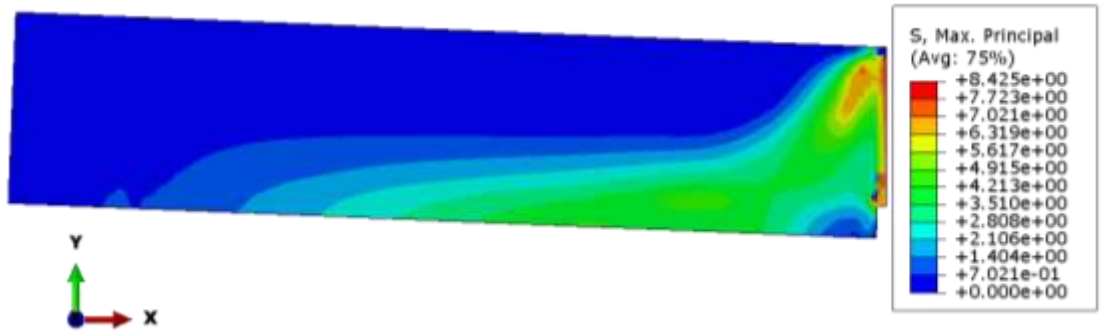

c) stress contour

Figure 6.24: The FE results for D60 beam.

6.3.2 Slab Modelling

Experimental investigations of different size specimens are expensive as a wide range of dimensions of similar structures are required to be tested to understand the true behaviour of the material. For such purposes, versatile, cost-effective numerical simulations are often used (Ooi and Yang, 2010). In addition, many physical phenomena in engineering are described in terms of an analytical approach and using analytical methods for capturing complicated material behaviour such as UHPFRC is challenging. The FE method is a numerical approach by which these behaviours can be predicted

approximately. Therefore, in this study, a nonlinear FE analysis using CDP in ABAQUS (ABAQUS, 2013) was developed and carried out to capture the bending behaviour of the one-way and two-way slabs as described in Chapters 4 and 5, respectively. The CDP model uses material properties obtained from uniaxial compression and tension tests (Hassan et al., 2012). Due to the large number of fibres randomly distributed in the matrix, discrete modelling of fibres would be too time-consuming. Similar to the notched beams, fibres are assumed to be uniformly distributed in the matrix and slabs were modelled as a homogeneous material. The model is described in the following sections.

6.3.2.1 Part Modules

The slab was first created using 3D deformable shells using the part modules box in ABAQUS/CAE. The slab was sketched using dimensions taken from the experimental data. To obtain the true structural behaviour of the slabs, it was essential to model the steel support and loading block of the test setup. Therefore, the steel support and load block were also created using 3D deformable solid elements and sketched in ABAQUS/CAE. For slabs with FF boundary conditions, the top steel frame was also created. Due to the symmetry of the slab in the x- and y-planes, only one quarter of the specimen was considered, as shown in Figure 6.25. The material properties under the "properties" parameter were defined for the slab. These properties such as elasticity, density, Poisson's ratio, compression hardening, tension stiffening, and tension damage were defined. The experimental setups such as support, loading block and top frame materials were chosen as elastic isotropic and only 2 independent variables were defined. The two variables were the elastic modulus and the Poisson's ratio. After defining materials for all parts, sections were created for each individual part. Homogenous shell sections were assigned to the slab and homogenous solid were assigned to the steel support, frame, and loading block. In the section module, the user can define which surface of the slab is to be defined using the shell offset option and "middle surface" was chosen for all the slab specimens.

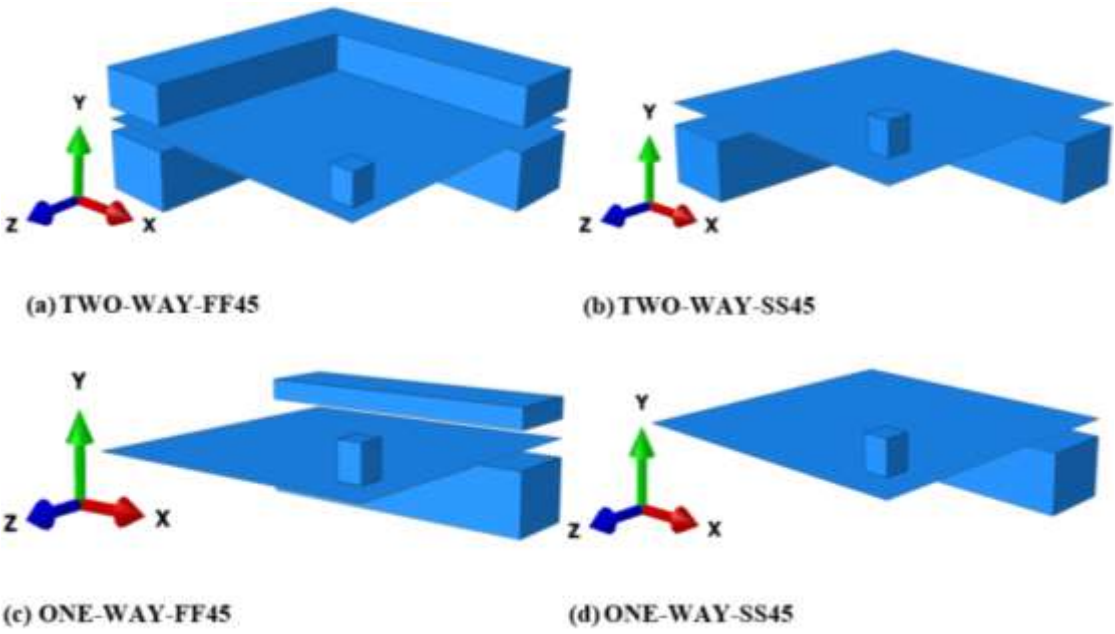

Figure 6.25: Details of symmetric loading and boundary conditions.

6.3.2.2 Assembly

In assembly, all the parts were created as instances into a global coordinate system and one instance was made for each part, using the 'instance part' function. In this module all the parts were translated and rotated to their desired positions, using the 'translate instance' and 'rotate instance', respectively, as shown in Figure 6.26. It was important that the slab was placed in its right position. For instance, Figure 6.26a shows the two-way slab with 45 mm thickness, where spaces of 22.5 mm below and above the slab were required. This is because the thickness of 45 mm was assigned to the slab in the section modules.

In order to assign regions, nodes and elements with correct load and boundary conditions and to request an output, it was important for sets to be used in the model. Set is a named region on which the user can perform various operations. It can be used to name a geometry such as cells, faces, edges and vertices or it can be used to name nodes or elements that have been selected. In ABAQUS/CAE, two different types of sets can be defined, Part and Assembly sets. Part sets are sets that the user created in the part or property module and can be accessed in "set manager" in the ABAQUS model tree. In the part module, sections cannot be assigned to regions using parts sets, however, they can be assigned in the property module. If a part contains sets, instanced in the assembly

module, its sets can only be used as a read-only access. Assembly sets are sets that the user created in the assembly, step, interaction or load module. These sets appear under assembly "set manger" in the assembly and can be used to indicate regions where the user wants to apply a load, or boundary conditions or to obtain output. Since the model involved several load and boundary conditions, different output requests and several contact interaction assembly sets were used in the slab modelling.

In all the models, sets were defined using the "set" tool box on the slab, support, loading block and top frame and these sets made it easy to apply the desirable loading position and boundary conditions in the model. They also made it easy to record the output after the analysis to obtain the data such as load, stress and displacement. Furthermore, in the assembly module, several surfaces were defined using the "surface" tool box and these were later used in the interaction section for the contact relationship between the slab and steel support and loading block, respectively, as shown in Figure 6.26. In the "surface" tool sets, two different types of surfaces can be created, geometry and mesh. However, since there are no differences between the surface types, geometry surfaces were used for all the surfaces.

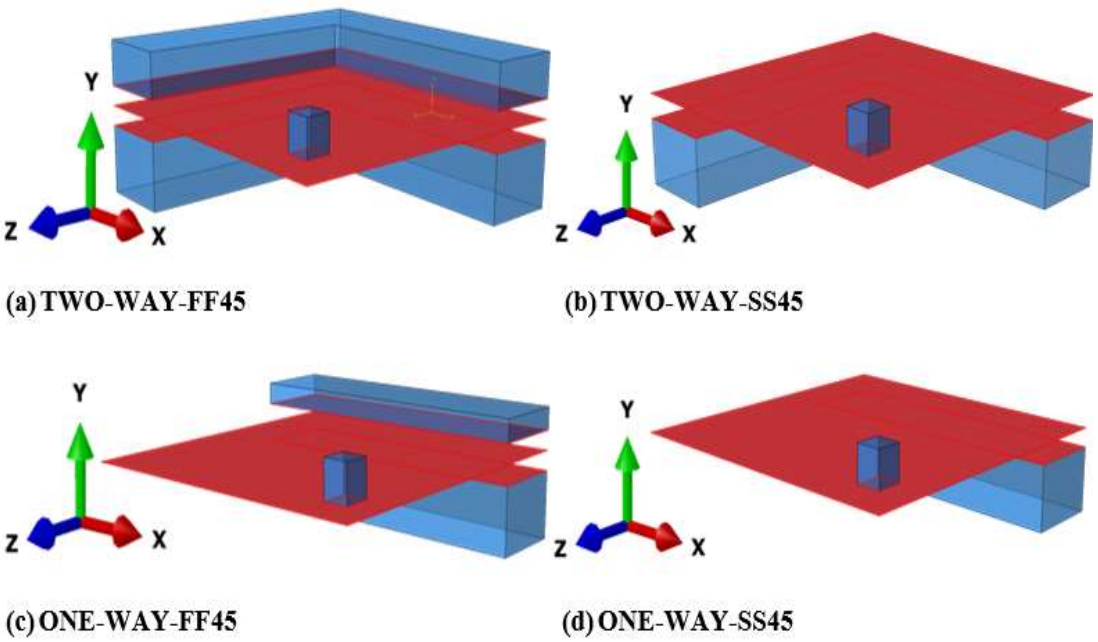

Figure 6.26: Surface contact are shown.

6.3.2.3 Step

In the FE analysis in ABAQUS a sequence of one or more analysis steps should be defined. The step sequence provides a convenient way to capture changes in the loading and boundary conditions of the model. It also provides changes in the way parts of the model interact with each other and any other changes that may occur in the model during the course of the analysis. The analysis procedure in the model of this study consists of one main step. However, ABAQUS/CAE automatically creates a special initial step, which cannot be edited, renamed, replaced, copied or deleted. This is performed at the very beginning of the model and this allows users to define boundary conditions, predefined fields and interactions that are necessary at the beginning of the analysis. Therefore, all the boundary conditions and interactions were defined in the initial step, while load boundary conditions were defined in the actual step.

Several different types of step are available in ABAQUS/Standard but the general-static method recommended by ABAQUS was used in all the analyses. Automatic stabilisation with the default parameters was employed with dissipated energy fraction set to 0.0002 and adaptive stabilising set to 0.05. It was noted that the automatic stabilisation makes the analyses become more stable after the peak load was reached as was the case in other studies (Chen and Graybeal, 2011a, Chen and Graybeal, 2011b). In the general-static analysis, the "incrimination" parameter is provided, which allows the user to modify the size and number of increment in the step analysis. In this parameter, several tabs are included and one of which is the maximum number of increments. Based on the trial run before the actual model runs, it was found that the maximum number of increments of 3000 were sufficient for the model to complete successfully. To ensure that the model was provided with the sufficient increment sizes, automatic time incrimination was adapted. In the incrimination parameter, three other tabs are provided for increment size and these are initial, minimum and maximum values. The minimum increment size of 1E-10 was chosen to ensure the model reached a convergent solution if ABAQUS needed a smaller time increment than the initial value. In order to obtain smooth curves, a sufficient amount of data was required to be produced, therefore, the maximum increment size was limited and set to 0.1, thus the model did not complete with a small number of increments.

6.3.2.4 Slab Element

The preliminary analyses showed that the shell elements, S4R in particular, provided better accuracy compared to the solid elements. Therefore, both one-way and two-way slabs are modelled using S4R elements. In shell elements, parts are discretised by a reference surface using element planer dimensions. The thickness of shell element is defined through section properties to describe the shell cross-section which allows users to calculate cross-section stiffness during or at the beginning of the analysis. To calculate stresses and strains independently at each section (integration points), ABAQUS uses numerical integration through the thickness of the shell as shown in Figure 6.27 for single integration points in the S4R (4-node, reduced integration) element which has been used in this study.

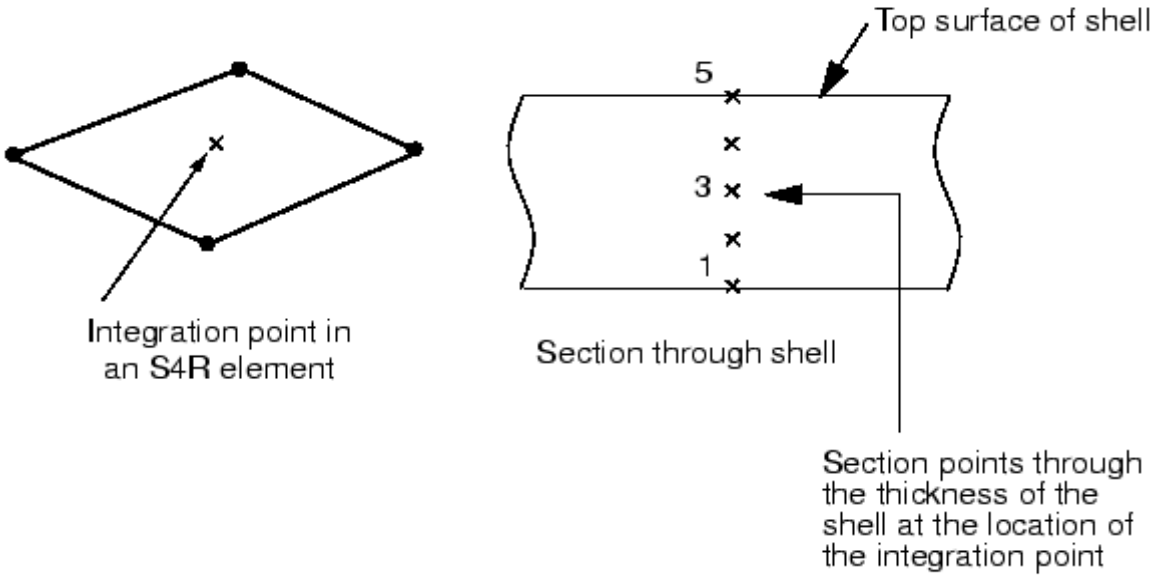

Figure 6.27: Configuration of section points in a numerically integrated shell element (ABAQUS, 2013).

The S4R shell element can be used for linear analysis and for nonlinear analyses involving contact, plasticity, and large deformations. There are two different rules available for section integration in shell elements; Simpson's and Gauss rules. The default number of five for Simpson's rule and three for the Gauss quadratic are given in ABAQUS but in general for nonlinear problems, the number of integration points of more than the default

number are recommended (ABAQUS, 2013). Nine thickness integration points are commonly used to model progressive failure of the concrete through the thickness with acceptable accuracy. The number of integration points must be an odd number for Simpson's rule and the maximum allowable number of points is 99. Whereas, the number of integration points must be less than or equal to 15 for the Gauss quadratic. However, the three integration points Simpson's rule and the two integration points Gauss quadrature are sufficient for linear problems. In all the analyses, it was found that nine Simpson's rule integration points gives an accurate result to capture the failure progress in both one-way and two-way UHPFRC slabs.

Moreover, compared to the other shell elements, reduced integration elements reduced the computing time and memory space significantly as it uses lower order integration to calculate the element matrix. For example the S4R element only uses 1 integration point compared to S4 which uses 4 integration points therefore its computation is 4 times less costly. The integration point is located at the element's centroid as shown in Figure 6.27. The element with a single reduced integration point uses the more accurate uniform strain formulation, where the value of strain components are averaged and computed over the element volume. This is not only important when the model is nonlinear, it is also significantly important with respect to the output values, thus the strains are a better representation of actual strain. In bending analyses, the reduced integration decreases the number of constraints introduced by an element to avoid element locking to stabilise the model.

To model the experimental setup such as the steel support, top frame and loading block, 3D brick elements, using reduced-integration 8-noded elements (C3D8R) were used. These solid elements have eight nodes with three degrees of freedom and one integration point as shown in Figure 6.28. These reduced integration elements are also known as centroid strain or uniform strain with hourglass and use a lower order integration to form the element stiffness.

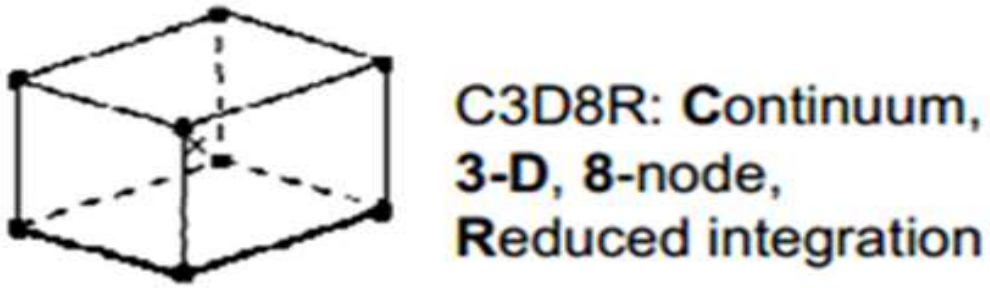

Figure 6.28: Element type for steel supports and loading plate.

6.3.2.5 Slab Mesh Convergence Study

The meshing process is considered to be critical in FE modelling. The accuracy of the numerical analysis depends strongly on the mesh size. In order to mesh the part, seeding was required, using the "Seed" tool box in the mesh modules and the slabs were seeded to a desirable element size using part seeds. To determine appropriate mesh sizes, mesh convergence studies were carried out. Both the accuracy of the prediction and the computer time were considered when choosing an appropriate element size for the model. The mesh convergence studies show that the stiffness of the structure is dependent on both the material properties and the element size. Therefore, it was essential that the same size of element's aspect ratio and material properties were used for both one-way and two-way slabs, so that the effect of element size was consistent throughout the study. In addition, it is recommended in ABAQUS that the accuracy of numerical analysis improves if square elements are used, thus all the elements were kept square.

As 16 different parameters were considered in this study, it was important that the chosen element would converge and provide an accurate result for all 16 cases, hence an extensive preliminary mesh convergence study had to be carried out. The preliminary analysis based on the experimental peak load for both one-way and two-way slabs was carried out. At the beginning of the preliminary analysis, the element size was kept to as high as 115 mm as shown in Figure 6.29 for slabs with 35 mm thickness. Although this element size was unrealistic as it is much greater than the slab thickness, this was important to ensure that the job can complete without an error message and the model built accurately in terms of the point load, supports, geometry and other parameters. After ensuring the job can run without an error message, the element size was reduced by half

and this procedure was repeated until the decrease in element size had little or no influence on the result as shown in Figure 6.29. The mesh convergence study for the slabs was much more complicated and time consuming compared to that for the beam specimens. This is because as the element size being reduced to 14 mm, it was important to check other slab thicknesses in both the one-way and two-way slabs to ensure that the model converges in all cases. This process of checking was also repeated when the element size reduced to 7 and 5 mm. It was found that an element size of slab thickness (t) /5 which is equal to 7 mm, gives an accurate result for both the one-way and two-way slabs and element sizes below this ratio had very little effect on the result as shown in Figure 6.29. However, to ensure the improvement of accuracy of the FE analysis, a ratio of t/7 which gives an element size of 5 mm was also used and investigated. It was found that the differences in terms of accuracy were very small compared to the 7 mm element size.

In addition, for element sizes with the ratio of t/5, the computation time increased and at some point convergence problems for some slab thicknesses occurred. Looking at the mesh convergence results, it can also be noted that the element size of 14 mm gives a result close to the element size of 7 mm and correlates very closely with the experimental results. However, the accuracy of the element size of 14 mm is considerably reduced when other slab parameters changed. It is recommended in ABAQUS that an element aspect ratio of close to 1.0 gives an accurate result. Therefore, all the FE analysis results presented in this study for two-way and one-way slabs with both SS and FF boundary conditions are based on an element size of t/5 which gives an aspect ratio of 1.0. Mesh convergence studies enabled the user to obtain an accurate solution with a mesh that is sufficiently fine and not overly demanding of computing resources. Figure 6.30 shows the element size for slabs with 35 mm thicknesses for both one-way and two-way slabs with FF and SS boundary conditions.

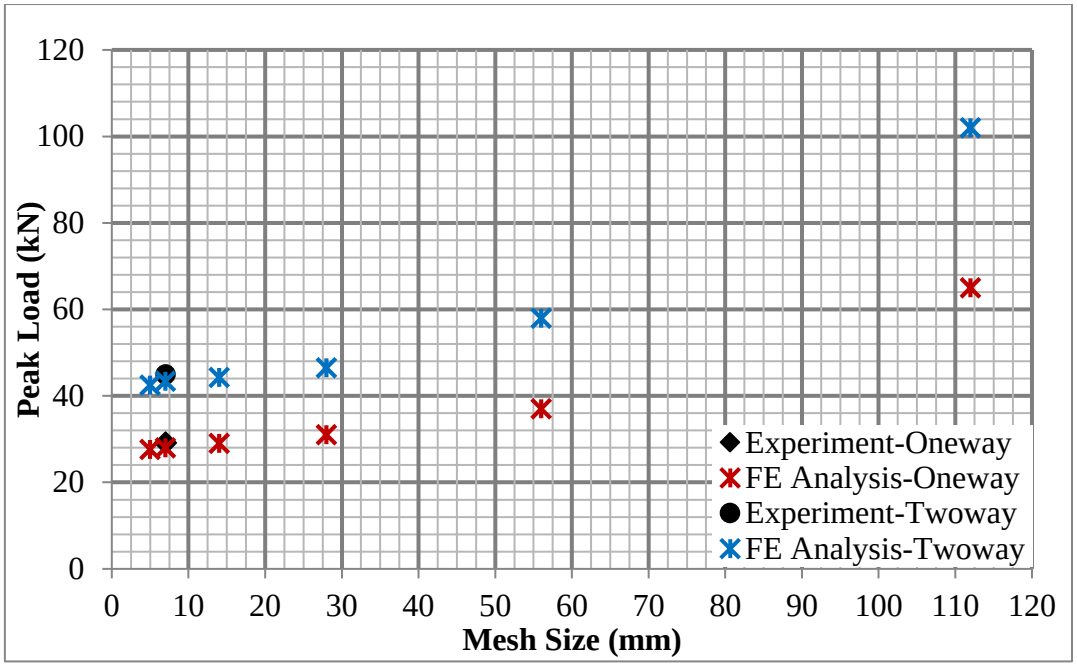

Figure 6.29: Mesh convergence analysis for both one-way and two-way slabs for 35 mm thickness.

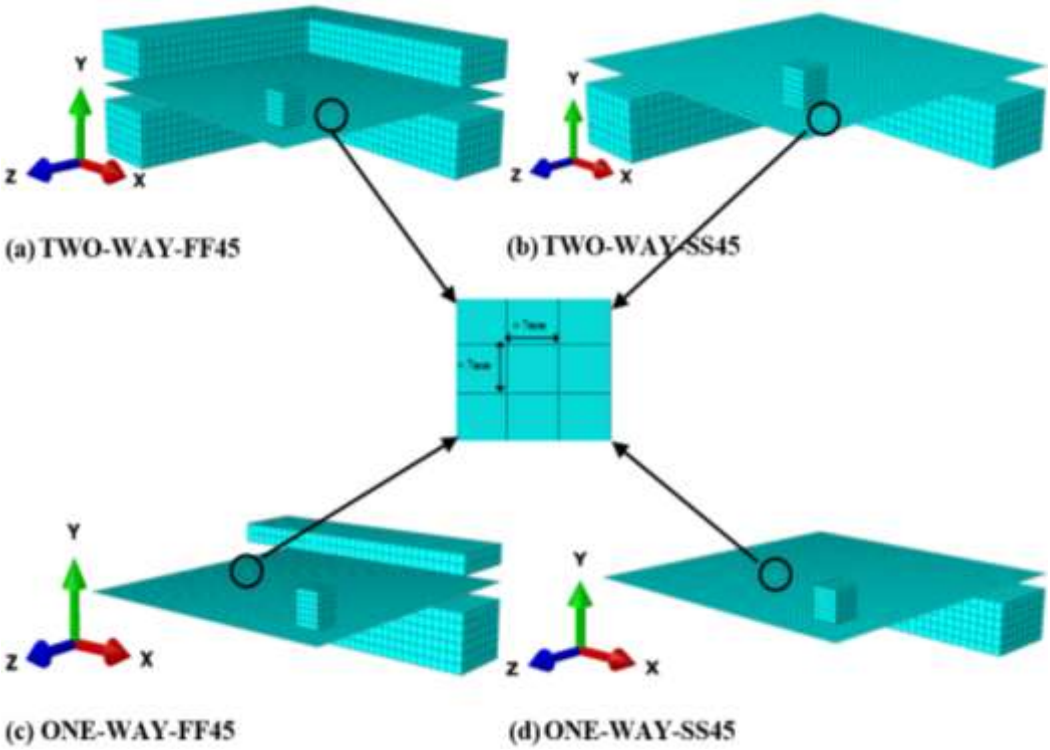

Figure 6.30: Element size used in the analysis.

6.3.2.6 Contact Interaction Modules

Contact is an interaction between two bodies or surfaces, or it can be an interaction of a single surface that may interact with itself under a set of rules to adjust the surface position at the beginning of the analysis. Contacts are usually defined in an initial step analysis. ABAQUS/Standard provides two algorithms for modelling contact and interaction problems and these are the general contact algorithm and the contact pair algorithm. General contact is very simple and it has very few restrictions on the types of surface involved. It uses tracking algorithms to ensure that proper contact conditions between the surfaces are enforced efficiently. It can also be used with contact pair algorithms as well as 2D or 3D dimensional surfaces. Whereas, the contact pair algorithm requires the user to explicitly pair surfaces that may potentially come into contact. It can consider either small or finite sliding effects while general contact only considers finite sliding effects. Since several parts were modelled, it was essential to introduce contact behaviour in the simulation. It was found that a contact pair algorithm can provide an accurate result and was used for modelling contact in the FE models. Figure 6.31 shows the contact simulation procedure in ABAQUS/Standard.

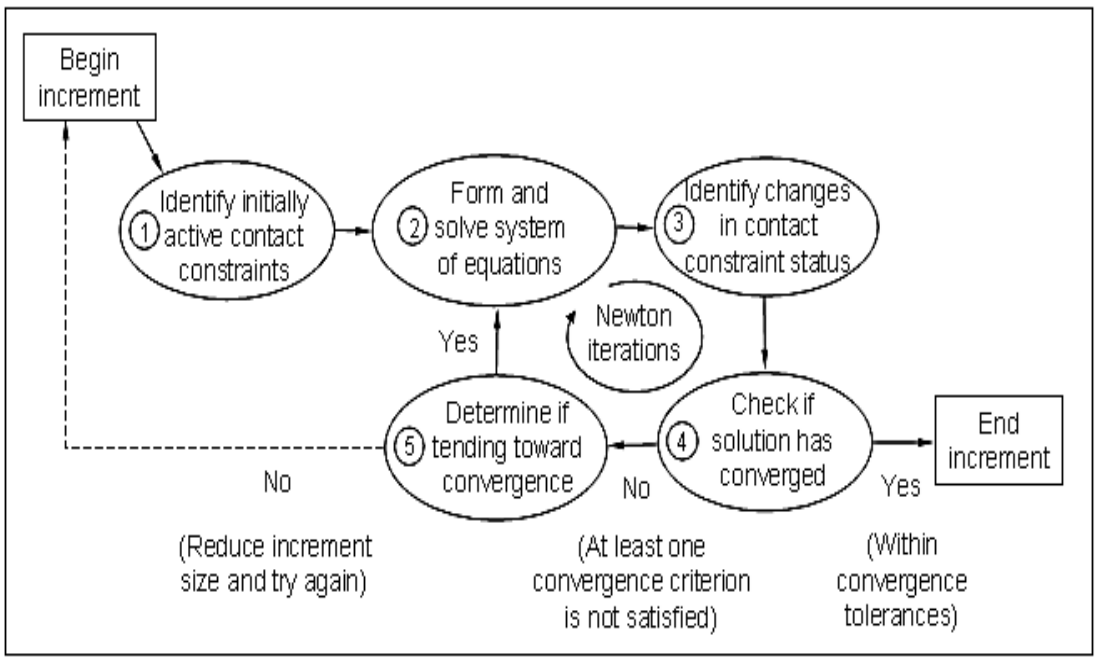

Figure 6.31: Understanding contact algorithm in ABAQUS/ Standard (ABAQUS, 2013).

In the interaction module, standard surface-to-surface contact relationships between the experimental setup and the slab were defined. In all the interactions, finite sliding formulations with contact tracking of two configurations and no adjustment in slave surfaces were used. Interaction properties were defined in order to model these contacts. Two interactions were created between the bottom-face of the slab and the steel support and top-face of the slab and the steel loading block as shown in Figure 6.32a and Figure 6.32b. An additional interaction between top-face of the slab and the top frame was created for slabs with FF boundary conditions in both one-way and two-way slabs as shown in Figure 6.32c and Figure 6.32d.

The contact pair interaction can refer to a contact interaction property. Therefore, an interaction property was defined between the steel support, the loading block and the slab in the FF series, while two interaction properties were used in the SS series. For all contacts, tangential and mechanical behaviour were employed in defining the contact properties. In the simulations, a "frictionless" formulation is used for tangential behaviour and a "hard" contact for normal behaviour for all contact surfaces for slabs with FF boundary conditions. In addition, in normal behaviour, separation after contact between the steel support and the slabs was not allowed in the FF series, while separation between support and the slab was allowed in the SS series. In slabs with SS boundary conditions, the contact between slab and steel support was not fixed. Instead, it was reasonable to model the interaction as surface-to-surface contact with allowable separation and a coefficient of friction equal to 0.25. As recommended in ABAQUS, a coefficient of friction above 0.20 can improve the convergence of the model. Furthermore, the coefficient of friction of 0.25 is sufficient to model contact between steel and concrete (Ellobody et al., 2006).

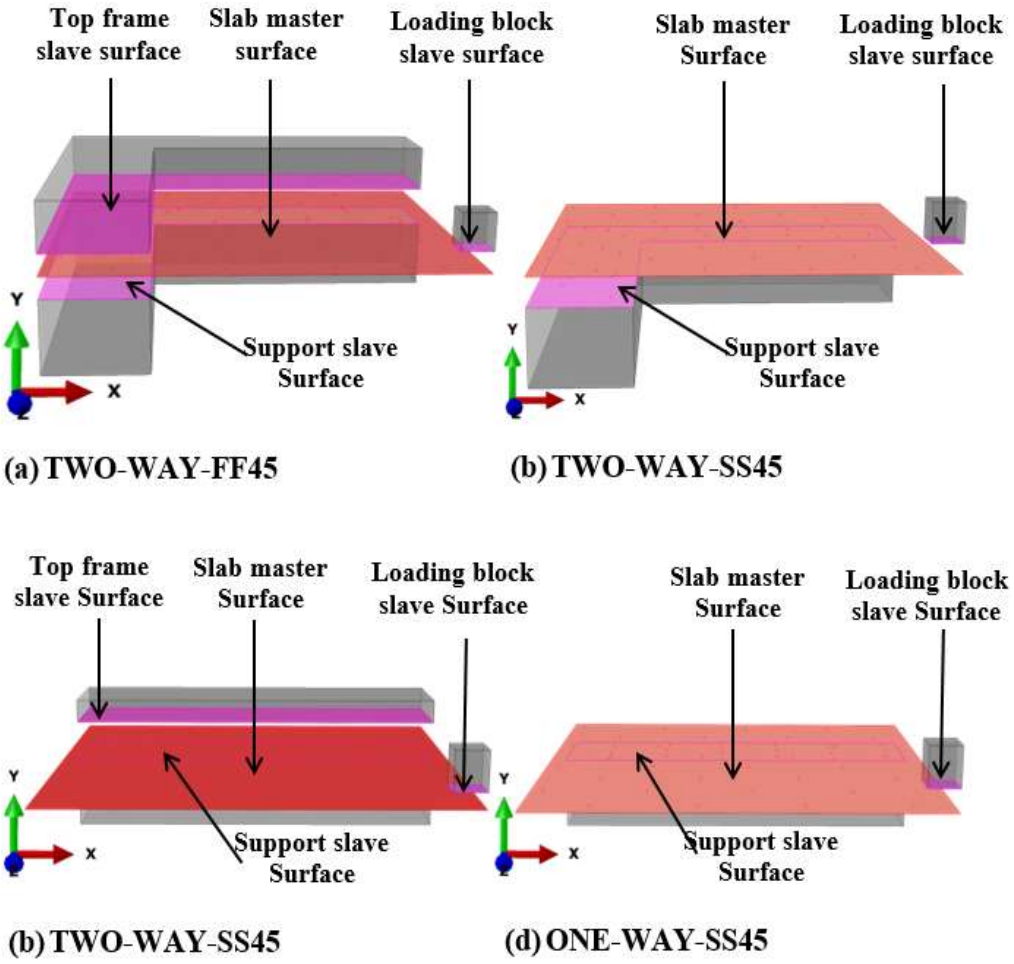

Figure 6.32: Contact interaction between the slab and steel supports.

6.3.2.7 Load and Boundary Conditions

Due to the symmetry of the experimental setup, only a quarter of the loading block was modelled. Symmetrical conditions were applied to surfaces in the x- and z-directions (Figure 6.33). The translational displacements U1 and rotational R2 and R3 in x-direction and the translation displacement of U3 and rotational R1 and R2 in z-direction for all nodes on the surfaces were restrained. In this analysis, displacement control was applied as shown in Figure 6.33. The displacement was applied at a constant rate and the slip was taken from the slab centre node as measured during the experiment. The load was measured from the reaction forces at the supports.

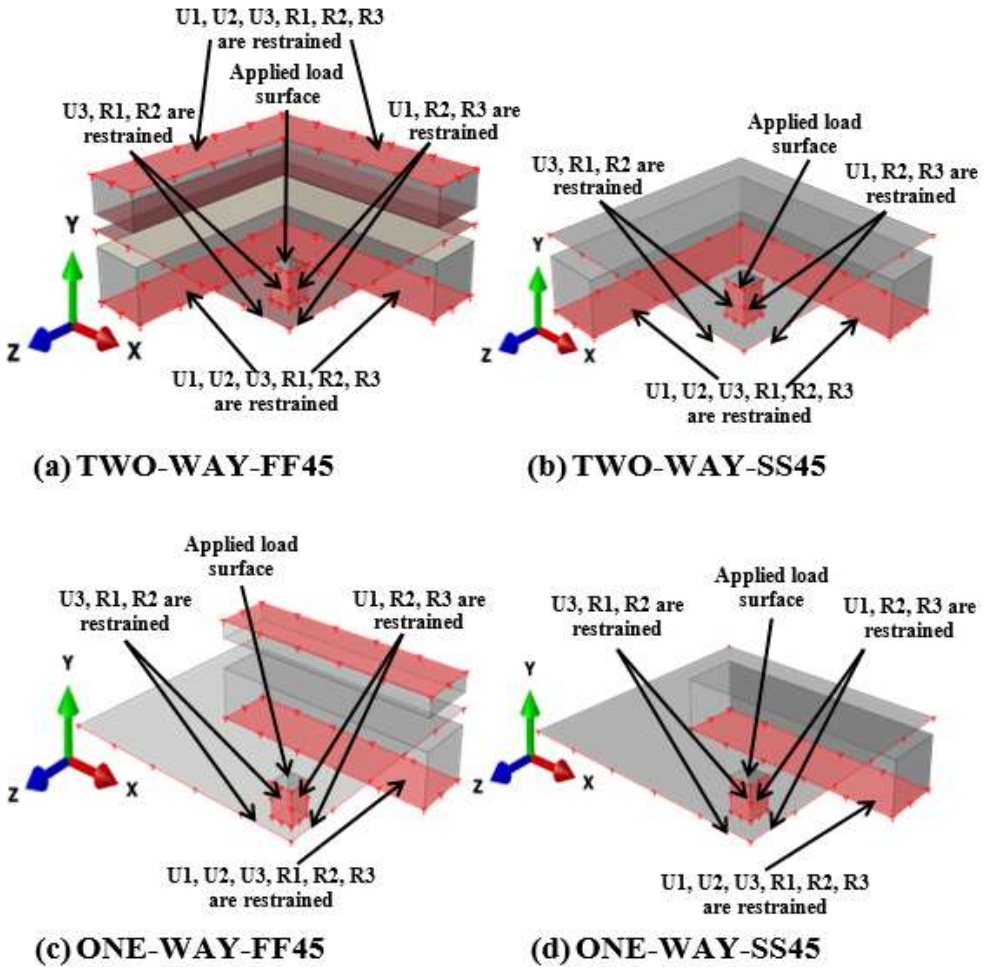

Figure 6.33: Loading and boundary conditions.

The boundary conditions were applied based on the support conditions used in the experiments. Symmetrical conditions were also imposed of the experimental setup such as support and top frame as shown in Figure 6.33. The figure also shows that the steel support was fully restrained for all the slab analyses. For slabs with FF boundary conditions, the top frame was also fully restrained as shown in Figure 6.33a and Figure 6.33c. For slabs with SS boundary conditions, the slab edges were free to rotate as shown in Figure 6.33b and Figure 6.33d. Since only a quarter of the slab was modelled, the slab was restrained in the x-direction in translational (U1) and rotational (R2 and R3) displacement. It was also restrained in the z-direction in translational (U3) and rotational (R1 and R2) displacement. The symmetric plan of steel support and top frame were not required to be restrained as they were fully fixed.

6.3.2.8 Analysis and Visualisation

After the model had been created in the pre-processing stage using the above steps, the job was defined and named for the full analysis in the "Job Manager" tool box. Using the job module, the finite element model was converted into finite element code and submitted to the solver. At the beginning of the analysis, ABAQUS/CAE first generated an input file representing the defined model and then the solver performed the analysis. Because the general-static method as described in Section 6.3.2.3 was used, the duration of the analysis was dependent on the mesh size and material properties. During the analysis, the job was monitored using the "monitor" function for any errors or warning messages. Once the analysis was run without error messages, the visualisation module was used to interpret the results. To view the results, outputs were requested. In ABAQUS, two types of output requests are available: field output and history output and both types of output can be specified by creating output requests. However, because the analyses can create very large amounts of output and in ABAQUS output can be controlled and managed, only required data to interpret the results of the simulation were produced. In this study, the displacement, stress and strain data over the whole slab model and the reaction forces for a relevant direction at the support were requested in the field output. Figure 6.34 to 6.37, shows the analysed models for a 45 mm thick slabs.

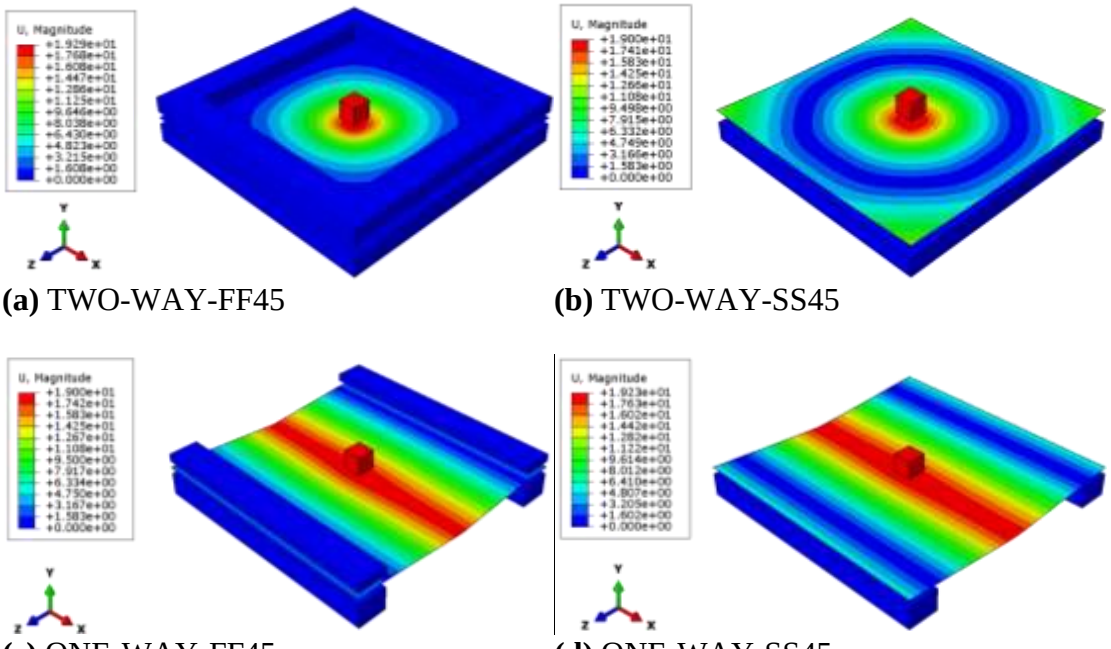

(a) TWO-WAY-FF45 **(b)** TWO-WAY-SS45

(c) ONE-WAY-FF45 **(d)** ONE-WAY-SS45

Figure 6.34: Deformed shape for 45 mm slabs.

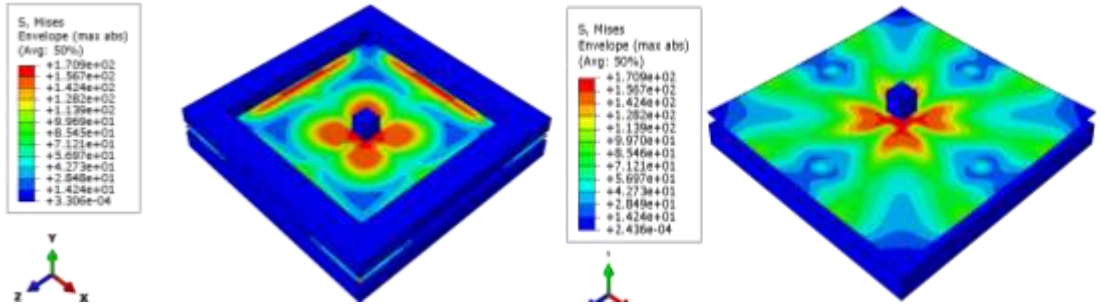

(a) TWO-WAY-FF45 **(b)** TWO-WAY-SS45

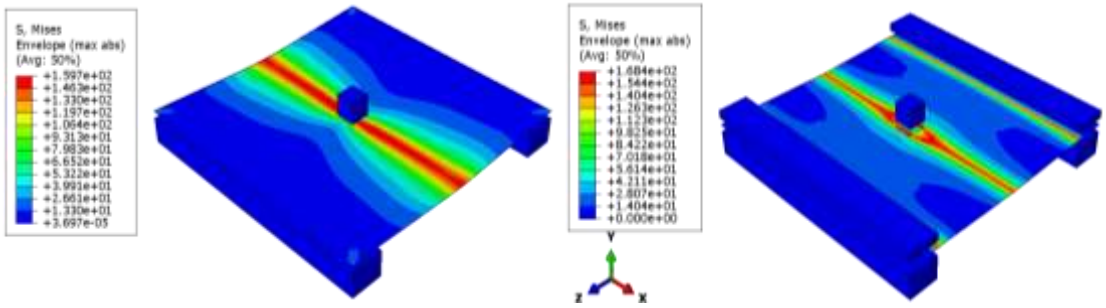

(c) ONE-WAY-FF45 **(d)** ONE-WAY-SS45

Figure 6.35: Stress contours for 45 mm slabs.

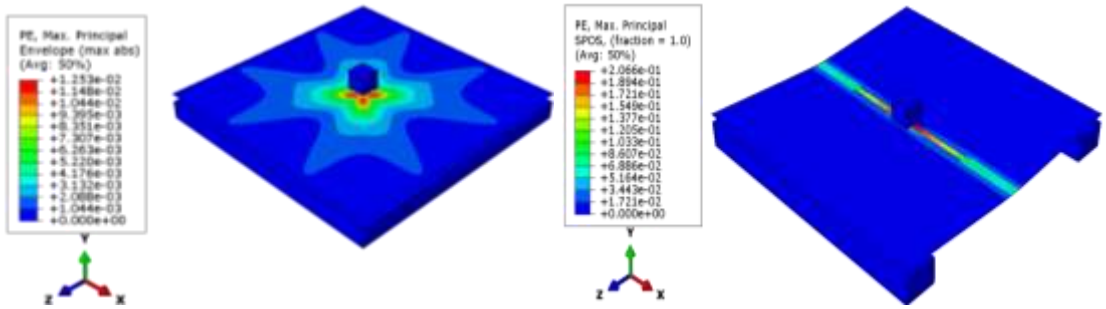

(a) TWO-WAY-SS45 **(b)** ONE-WAY-SS45

Figure 6.36: Plastic strain (PE) contours showing crack locations for 45 mm slabs.

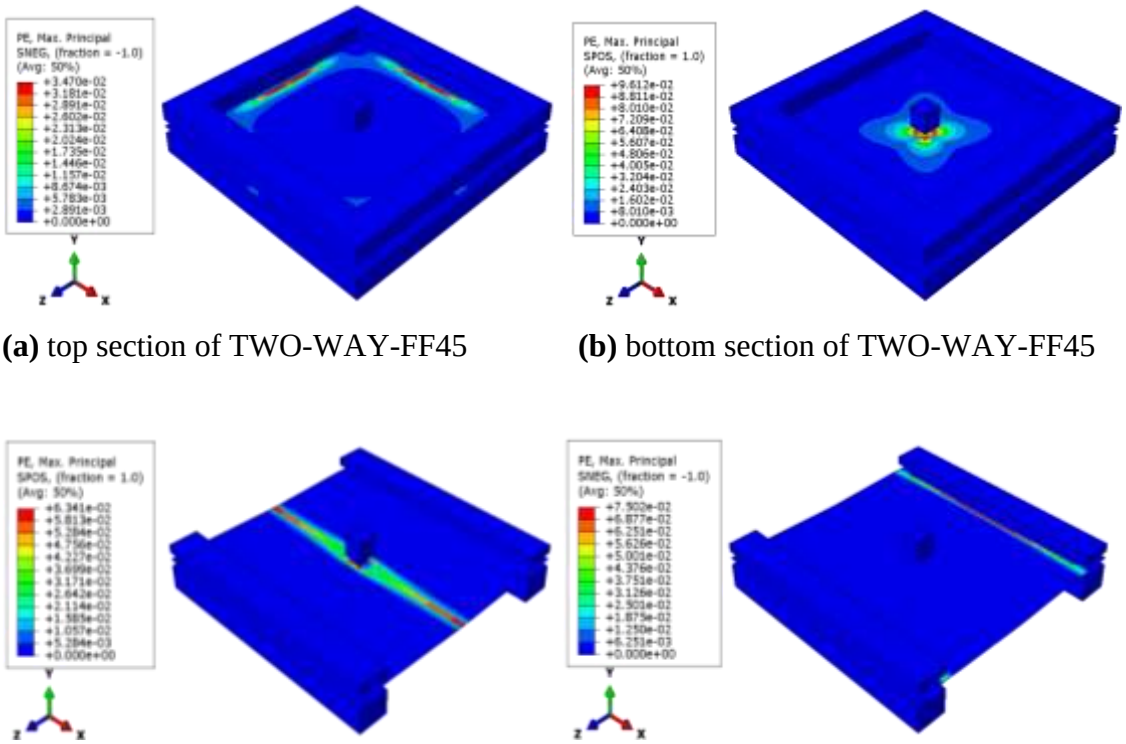

(a) top section of TWO-WAY-FF45 **(b)** bottom section of TWO-WAY-FF45

(c) top section of ONE-WAY-FF45 **(d)** bottom section of ONE-WAY-FF45

Figure 6.37: Plastic Strain (PE) contours showing the location of cracks.

6.4 Concluding Remarks

The FE analysis was carried out to examine the reliability and efficiency of ABAQUS software using both concrete smeared cracking (CSC) and concrete damage plasticity (CDP) in capturing the structural behaviour of UHPFRC. The examination showed that the CSC model is limited in capturing the behaviour UHPFRC material and its stability and efficiency reduces as the parameters of the model changed. The model experienced convergence difficultly as the load reached its ultimate peak load. Whereas the CDP model showed to be very efficient and capable of capturing the structural behaviour of UHPFRC at all stages, especially linear elastic and strain-hardening stage. Therefore, a reliable nonlinear FE analyses for notched three-point bending tests, using a CDP model in ABAQUS are developed in this chapter. Nonlinear FE analyses using CDP model for one-way and two-way UHPFRC slabs were also developed.

The procedure to create the model including: part creation, step, element types, mesh convergence studies and contact behaviour are provided. The implementations of load and boundary conditions are also provided. Preliminary analyses with elastic moduli

ranging from 44 to 48 GPa and Poisson's ratios from 0.20 to 0.24, have shown that changes in these parameters had no effect on the results. Preliminary analyses have also shown that changes in dilation angle, viscosity or other parameters had no effect on the results. Investigation of various elements in the beam model showed that the CPS4R solid element gave the most accurate results. Mesh sensitivity studies showed that an element size 2.5 mm near the centre was sufficiently accurate to model all the beam sizes.

Preliminary analysis for various element types such as 3D and shell elements were also investigated for slabs and the results showed that the S4R shell element was the most accurate element type to capture the behaviour of both one-way and two-way slabs in both FF and SS boundary conditions. Mesh convergence studies were carried out and the results showed that an element size of slab thickness t/5 gave accurate results for both one-way and two-way slabs.

In design, the required parameters are often the load-displacement relation of a structural member, especially the ultimate load carrying capacity and corresponding deflection. The CDP model using the input data such as tension stiffening, compression hardening and tension damage obtained from material testing, were able to capture the structural behaviour of beams and slabs in terms of load-displacement relationship and crack propagation. The results of this developed model agreed well with the available experimental test data and a discussion of the results is presented in Chapter 7. However, it is important to mention that these conclusions need be validated using further experimental testing, before it can be used exclusively.

CHAPTER 7

DISCUSSION OF FINITE ELEMENT RESULTS

Due to the lack of knowledge in the available literature regarding the structural behaviour of UHPFRC slabs, the main concern in this study was to investigate the structural behaviour of slabs under static loading both experimentally with custom set-up procedures and numerically using ABAQUS. In this chapter, the FE analysis results using the Concrete Damage Plasticity (CDP) model in ABAQUS/Standard are presented. The model behaviour is validated by the experimental uniaxial tensile and compressive tests and discussed in this chapter. The behaviour of the model at an element level was also investigated using single element modelling for both solid and shell elements.

The results of numerical analyses were compared to the corresponding experimental work on both one-way and two-way slabs described in Chapters 4 and 5, respectively. This was used to capture the experimental data in terms of load-displacement relationships, failure modes, cracking load and ultimate load carrying capacity. The results of the experimental data for both one-way and two-way slabs at the serviceability limit state (SLS) are compared to the no cracking SLS criterion proposed by the AFGC, which does not allow cracking to occur in the elastic stage. The practicality of the AFGC proposed recommendation in design is discussed.

As detailed in Chapter 2, this study was also concerned with an investigation of the size effect phenomenon on nominal strength of notched beams under three-point bending by a process of experimentation and FE analysis. Since only a few studies are available in the literature regarding size effect behaviour of UHPFRC, a detailed experimental

investigation described in Chapter 3 was compared to the nonlinear FE simulations described in Chapter 6.

The FE analysis was also used to predict the structural behaviour when the depth of the UHPFRC beams and slabs vary, especially for those that are too expensive to be tested. Finally, discussions and conclusions are drawn for the all the models employed to simulate the structural behaviour of UHPFRC beams and slabs. The effectiveness and limitation of the numerical model in capturing the bending behaviour of UHPFRC beams and slabs during all stages of loading as well as failure modes are also provided.

7.1 CDP Model Validation Using Material Testing

In order to further validate the CDP model, the tension and compression tests conducted by Hassan (2013) were modelled. To do this, the reliability of the model was validated using two different approaches. Firstly, to investigate the model at a structural level, the complete dog-bone shaped and cylinder specimens were modelled and compared to the experimental data. Secondly, a single element was modelled to investigate the CDP model at element level.

7.1.1 Complete Material Test Modelling

The preliminary investigation showed that the model is capable in capturing the structural behaviour of beams and slabs but to further ensure that the CDP model behaves as expected, the developed CDP model is used to model the material testing. The complete dog bone shaped specimen for tension and cylinder shaped specimen for compression conducted by Hassan (2013) were modelled. The results of the numerical model compared to the experimental tests data presented in Hassan (2013) are shown in Figure 7.1. It is important to mention that the (C3D8R) eight-node linear brick reduced integration 3D-element was used in this investigating as the four-node linear reduced integration shell-element (S4R) cannot be used to model the cylindrical shaped specimen due to its geometrical restrictions. However, the S4R element has been used in the following section to investigate the model behaviour at element level.

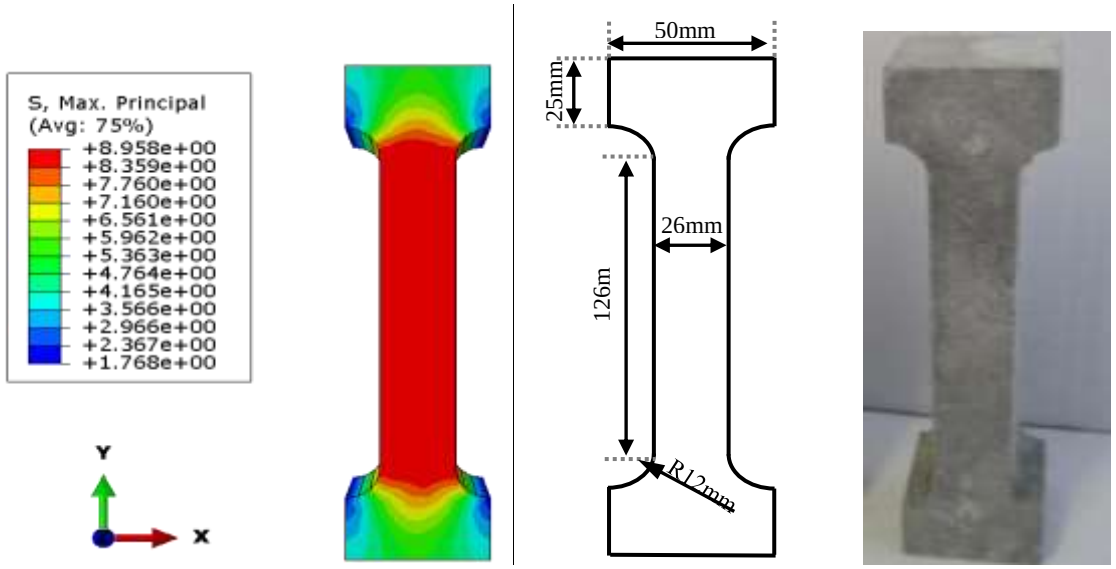

(a) Tension

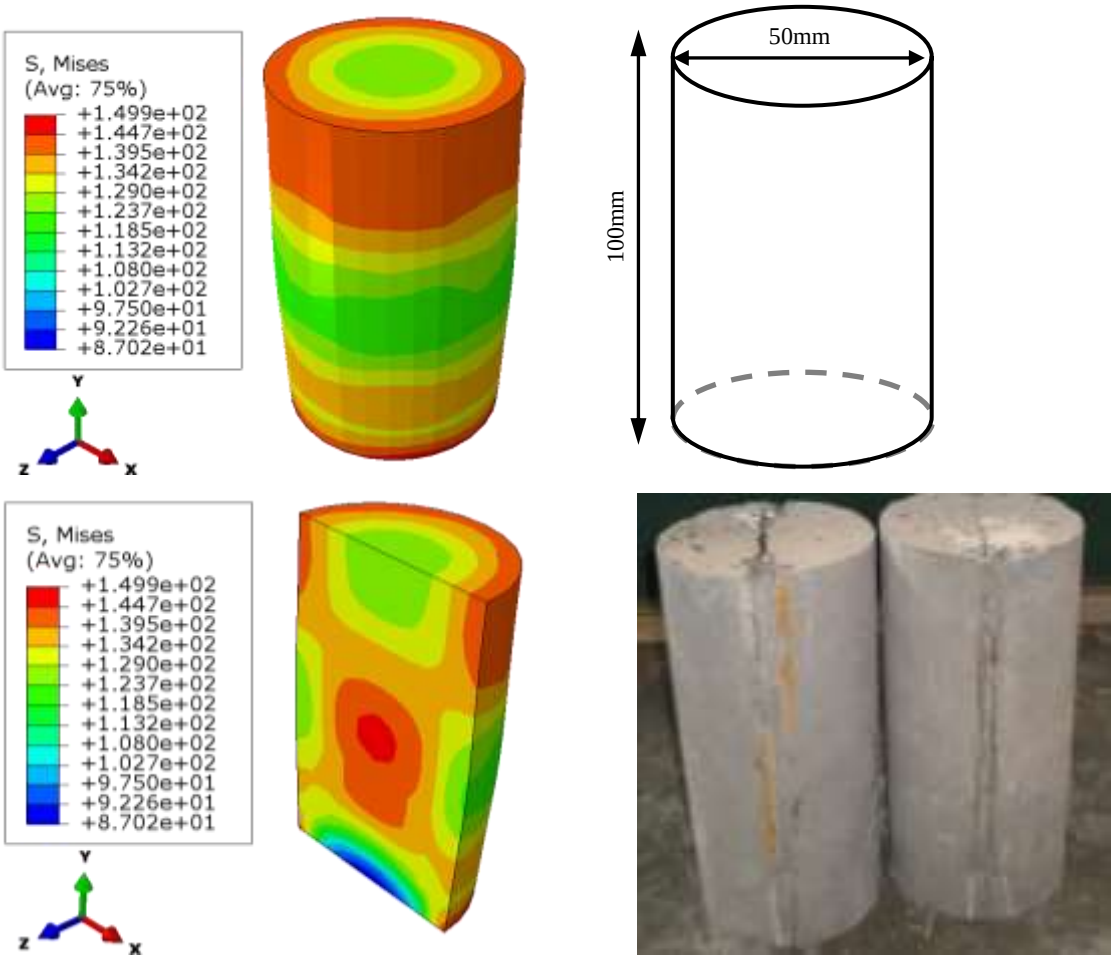

(b) Compression

Figure 7.1: Experimental and numerical outcome.

The experiment work conducted by Hassan (2013) showed all the specimens in tensile testing failed with major cracks at the neck of the specimens. However, the location of the cracks varied within the weaker section of the specimens as detailed in Hassan's thesis. Looking at the numerical outcome, it can be seen that the stress is the greatest at the neck of the dog bone specimen and the possibility of failure crack is likely to occur at the specimen neck as it happened during the experiment. Similarly the compression result showed the specimen failure occurred due to the Poisson's ratio effect. During the compression test, concrete specimens usually undergo lateral expansion whereas the steel platens do not undergo lateral expansion to the same extent as the concrete specimens. The difference in the lateral expansion between the concrete and adjacent steel platens of the testing apparatus creates a tangential force. Therefore, as a result, in addition to the compressive stress, the lateral shearing stress affects the concrete specimen's failure. Therefore, the failure modes in the experiments occurred due to several major cracks leading to disintegration of part of the concrete as well as a few wing cracks across the specimen geometry.

The main aim of these material properties investigations was to determine the capability of the CDP model in capturing the material property behaviour. The result of the numerical model in terms of stress-CMOD relationship for uniaxial tensile and stress-strain relationship for uniaxial compression test were plotted against the experimental data reported by Hassan (2013) as shown in Figure 7.2 and Figure 7.3, respectively.

The uniaxial tensile test was examined using three different meshes with an element size of 8, 6 and 4 mm with an aspect ratio close to 1, as shown in Figure 7.2. It can be observed that the prediction obtained from the developed FE model agrees well with the experimental data at all loading stages. Looking at Figure 7.2a, the model simulated the elastic and strain hardening region successfully. It can be seen that the effect of the mesh dependency on the result is also very minimal at the elastic and strain hardening stage, whereas a small discrepancy can be seen in the softening region. The discrepancy in the softening region between the two smaller meshes is less than 5%. In addition, further reduction in the element size only increased the computational time and led the model into convergence difficulties. Therefore, an element size of 4 mm is recommended to be used to model the uniaxial tensile test of UHPFRC using the developed CDP model. As explained previously and reported in the literature, due to the randomness of fibres within

the matrix, considerable scatter can be seen in the experimental data especially in the softening region. However, the results of the model in the softening region are also within the scatter region of the experimental data as shown in Figure 7.2b. Therefore, it can be concluded that the model is capable in capturing the UHPFRC material behaviour under uniaxial tension.

The model's ability to reproduce the concrete behaviour under monotonic uniaxial compression is also verified and compared to the experimental results of Hasson (2013). It is important to mention that the softening stage of compression hardening shown in Figure 6.8b were included in the model to investigate the uniaxial compression test. Similar to the tensile test, three different meshes were adopted to investigate the mesh convergence study and element sizes were 8, 6 and 4 mm with an aspect ratio of 1.05, 1.1 and 1.01, respectively as shown in Figure 7.3. The meshing techniques based on global seeding control were used to obtain results with high accuracy, in particular for the peak response.

Comparing the results, the nonlinear numerical performance predicted by the CDP model obtained stress-strain behaviour very close to the experimental results in all loading stages. However, looking at the figure, very small variations can be seen between the mesh with an element size 8 mm and meshes with 6 and 4 mm in terms of the peak load but the difference between the two finer meshes were found to be less than 1%. Using element size smaller than 4 mm only increased the computational time with no changes in the accuracy of the result. Therefore, no results for element size smaller than 4 mm are not shown here. Furthermore, the variation between the three meshes in the strain softening was found to be minimal and they all lie within the scatter of the experimental data. This again shows the capability of the model in capturing the material properties under the uniaxial compression test. It is suggested that an element size of 4 mm is sufficient to reproduce the uniaxial compression test of UHPFRC tested by Hassan (2013).

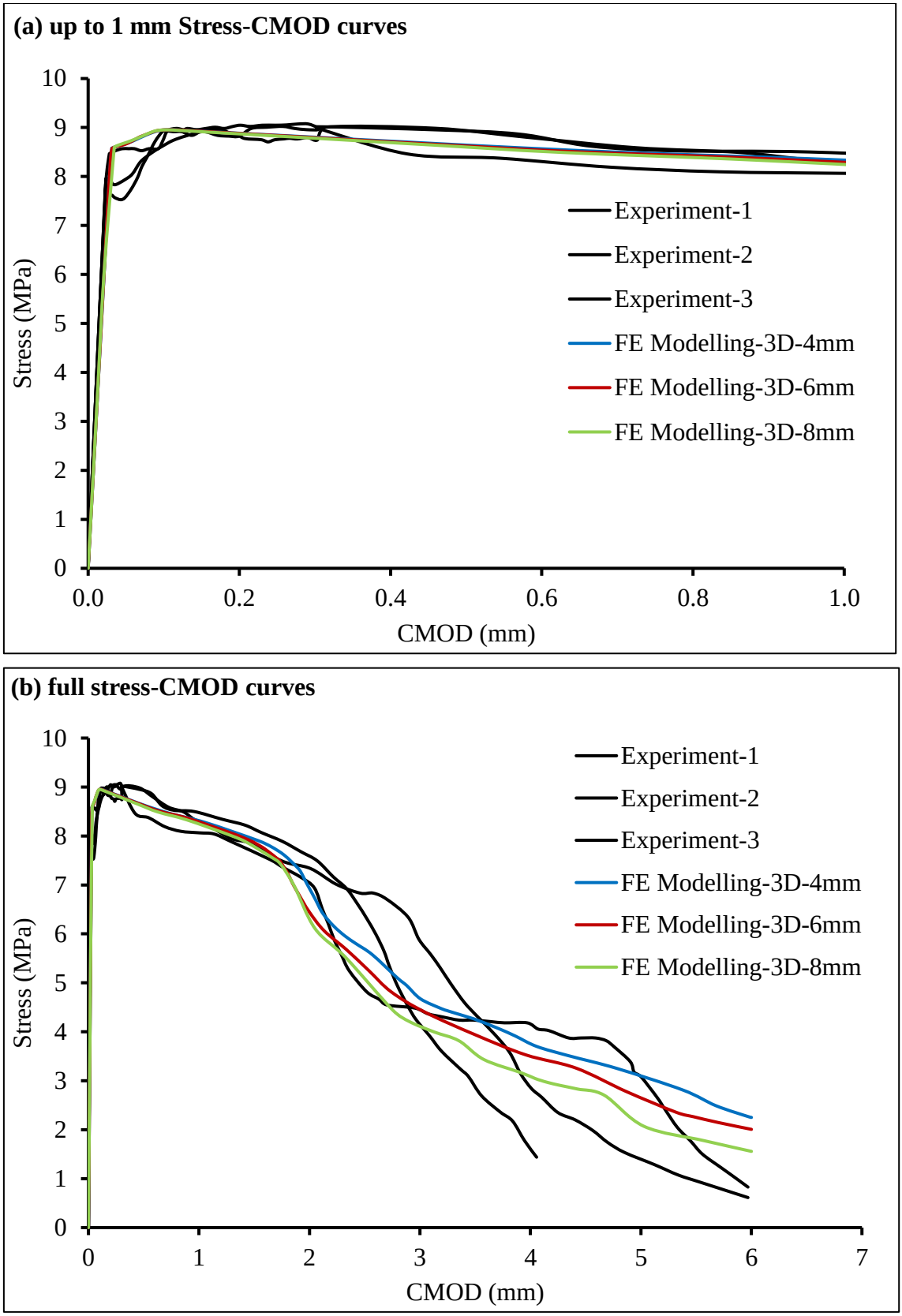

Figure 7.2: Comparison between CDP model and experimental test result under uniaxial tension test.

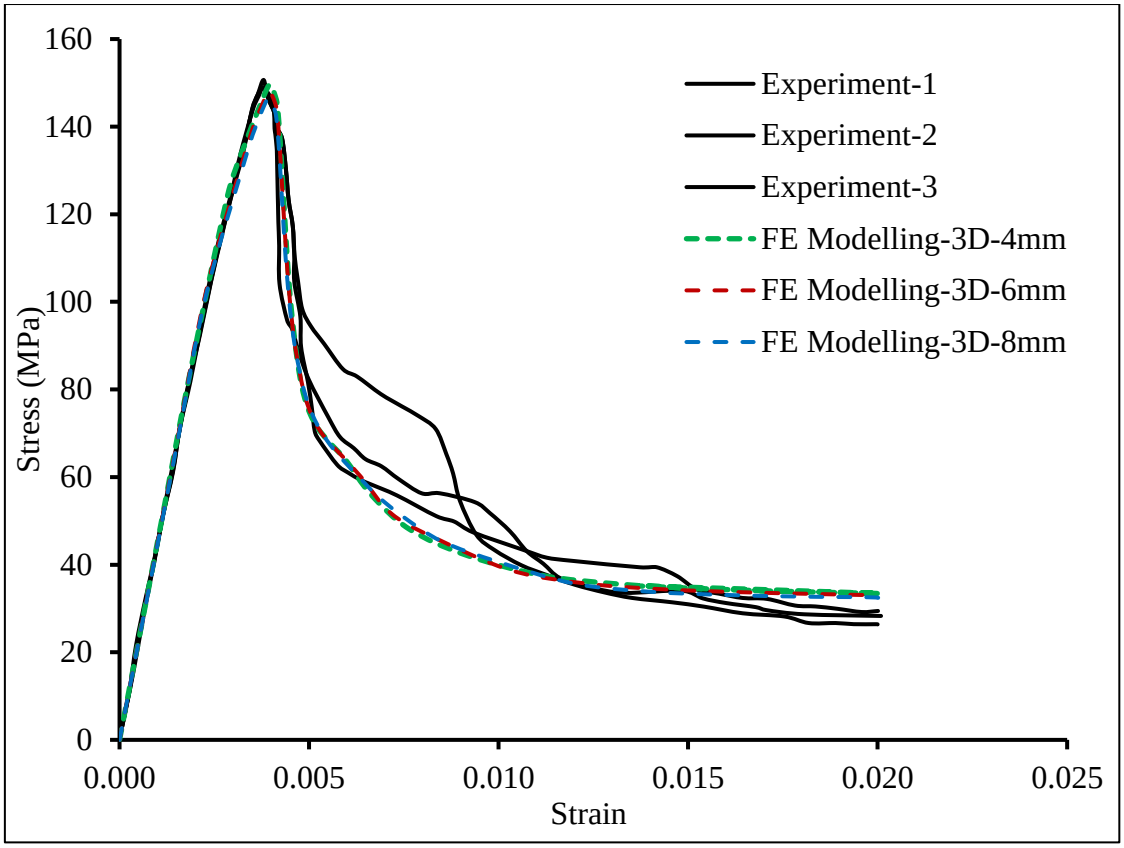

Figure 7.3: Comparison between numerical model and experimental test results under uniaxial compression.

7.1.1 Single Element Modelling

Although the main aim in this study, both experimentally and numerically, is to better understand the UHPFRC material at a structural level, it is thought that consideration should be given to the capability of the model at element level. To determine if the model behaves at element level as expected, a single element using both S4R and C3D8R elements was investigated under both uniaxial tension and compression as shown Figure 7.4 and Figure 7.5, respectively. For uniaxial tension, a single solid and shell element was fixed at the bottom and pulled from the top for up to 6 mm as shown Figure 7.4. Whereas, for uniaxial compression, the element were compressed from the top to obtain the stress-strain relationship as shown in Figure 7.5.

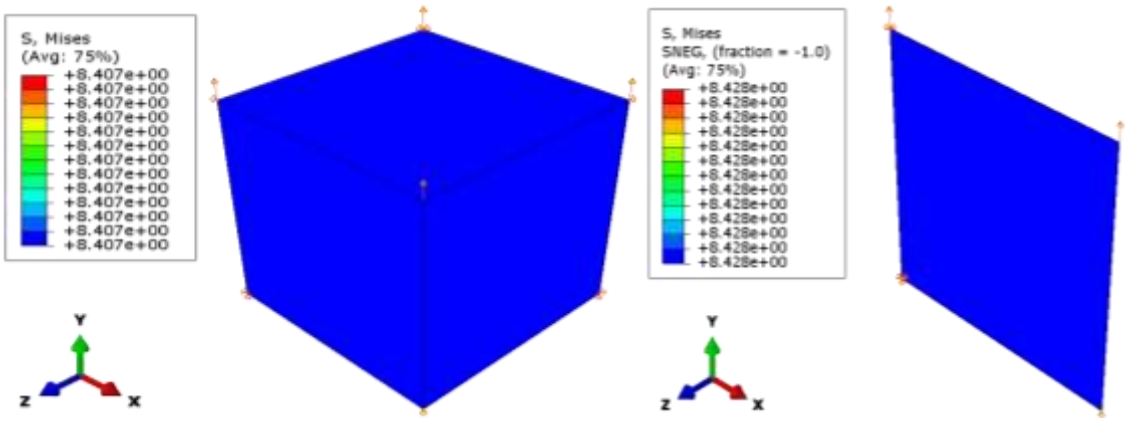

(a) C3D8R solid element (b) S4R shell element

Figure 7.4: Single element model under uniaxial tension.

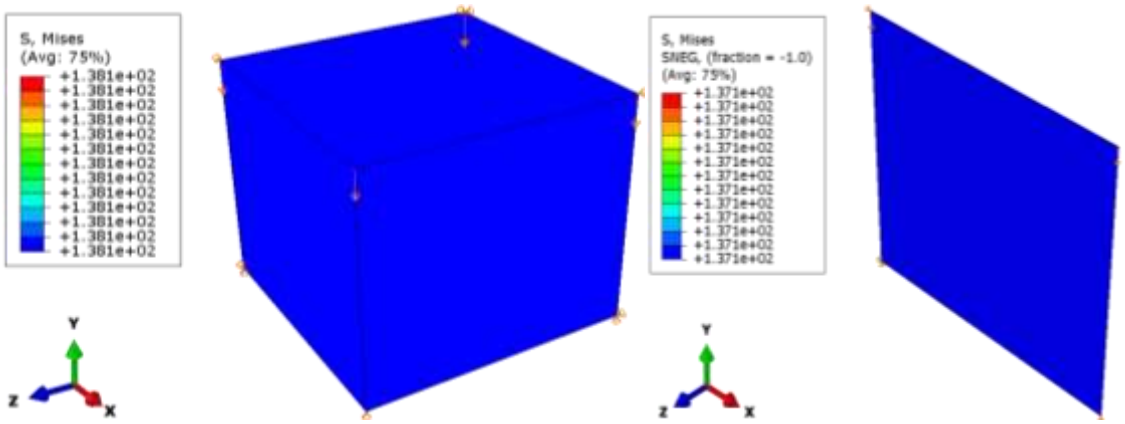

(a) C3D8R solid element (b) S4R shell element.

Figure 7.5: Single element model under uniaxial compression.

The stress-CMOD and stress-strain curves obtained from the numerical model using C3D8R solid and S4R elements for uniaxial tension are plotted against experimental data obtained from Hassan (2013) are shown in Figure 7.6 and Figure 7.7, respectively. Similarly, the results of the model for uniaxial compression are also plotted against the experimental data as shown in Figure 7.8 for the C3D8R solid element and Figure 7.9 for the S4R shell element.

Figure 7.6 and Figure 7.7 show good correlation between the model and the experimentally observed response for UHPFRC material subjected to uniaxial tension in

elastic and strain hardening stages. In general, the model shows similar behaviour for both solid and shell elements and represents the fundamental characteristics of UHPFRC material response well up to the peak load. Whereas, in the softening stage, the model underestimates the accumulation of plastic strains when compared to the experimental data and does not predict the observed reduction of elastic material modulus. Given the considerable variation in experimental data obtained by Hassan (2013) in the softening stage, in particular, prediction of the CDP model to represent the results of a single experimental test is inappropriate. Instead, the model needs to be compared to the typical response of concrete. Therefore, the result of the model is not far from the lowest experimental response. However, the lower behaviour of the model using a single element model can be classified into the following aspects. Firstly, the response of UHPFRC is determined by the formation of a continuous single crack and global mechanism such as microcracking, hence the material damage (reduced material strength and stiffness) associated with cracks which distributed over the entire volume of the dog-bone shaped specimen rather than a single element. Therefore, the fracture strain and damage evolution value which is used in the simulation was obtained by the global mechanism behaviour of the concrete, so it is very difficult to obtain the numerical results which match the experimental curve using single element modelling. Secondly, similar to the experimental procedure, in the simulation process, the stress which concentrated along the machine direction are obtained and averaged from the applied force rather than a specific area of the specimen. Finally, the single element model implies that the whole of the concrete model geometry is activated and the element is not restrained laterally, whereas in full modelling, similar to the laboratory testing, elements are partially restricted by the neighbouring elements to move laterally. This results in a higher stress requirement to converge the analysis. The aforementioned points may be the reason that the model becomes sensitive at element level, after the elastic stage.

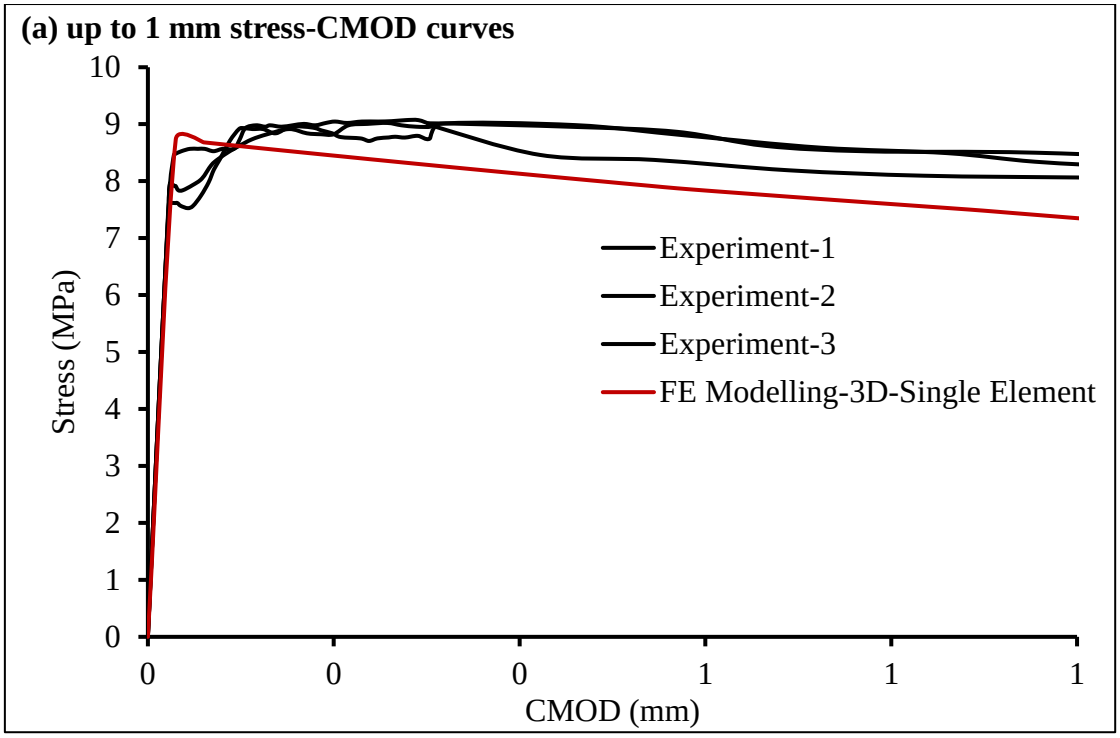

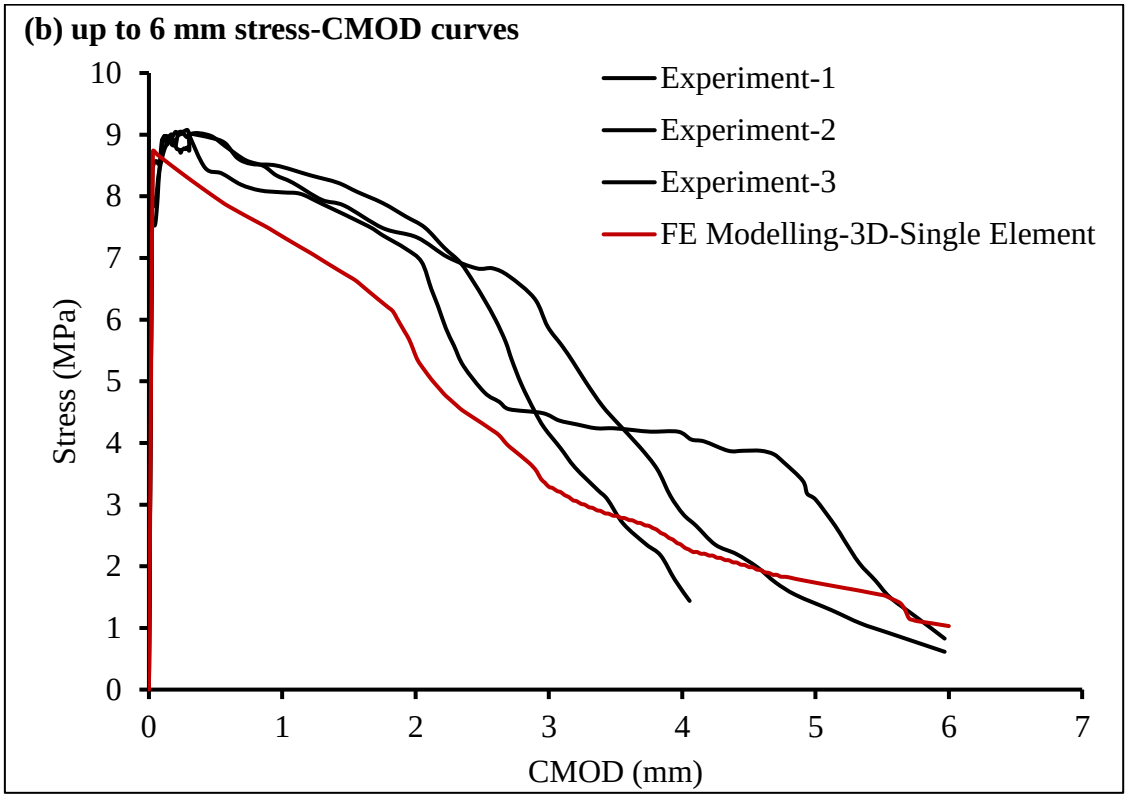

Figure 7.6: Comparison between uniaxial tension test and numerical model using single solid elements.

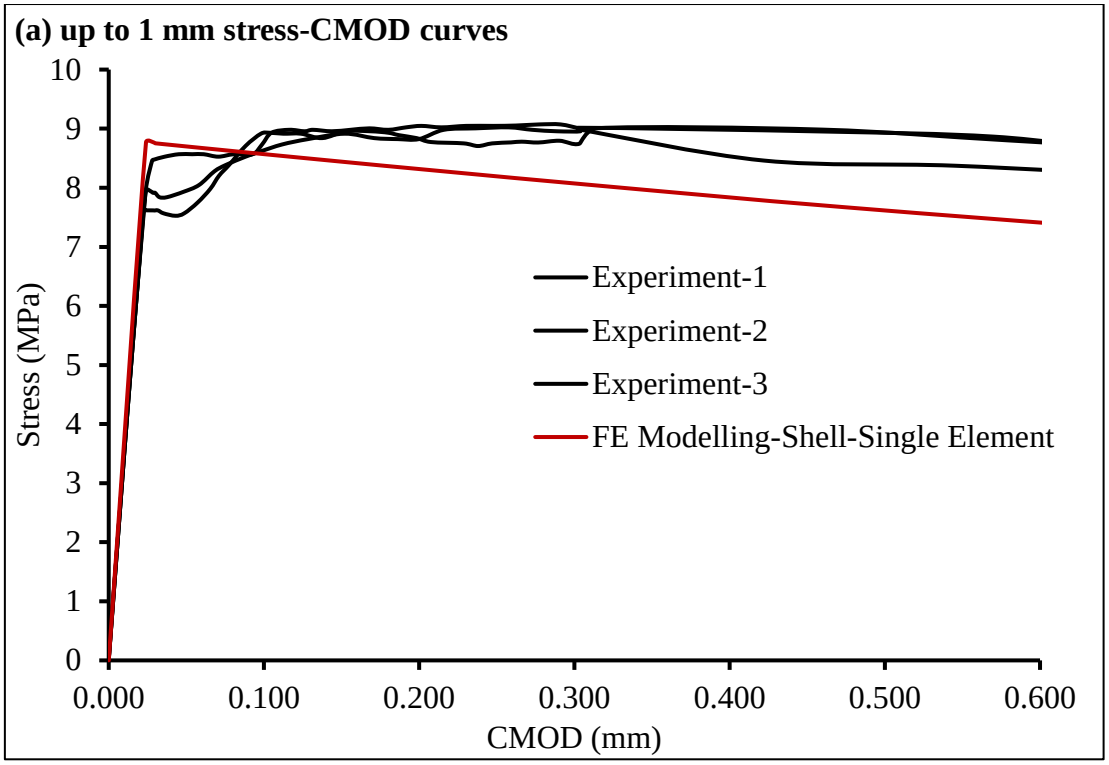

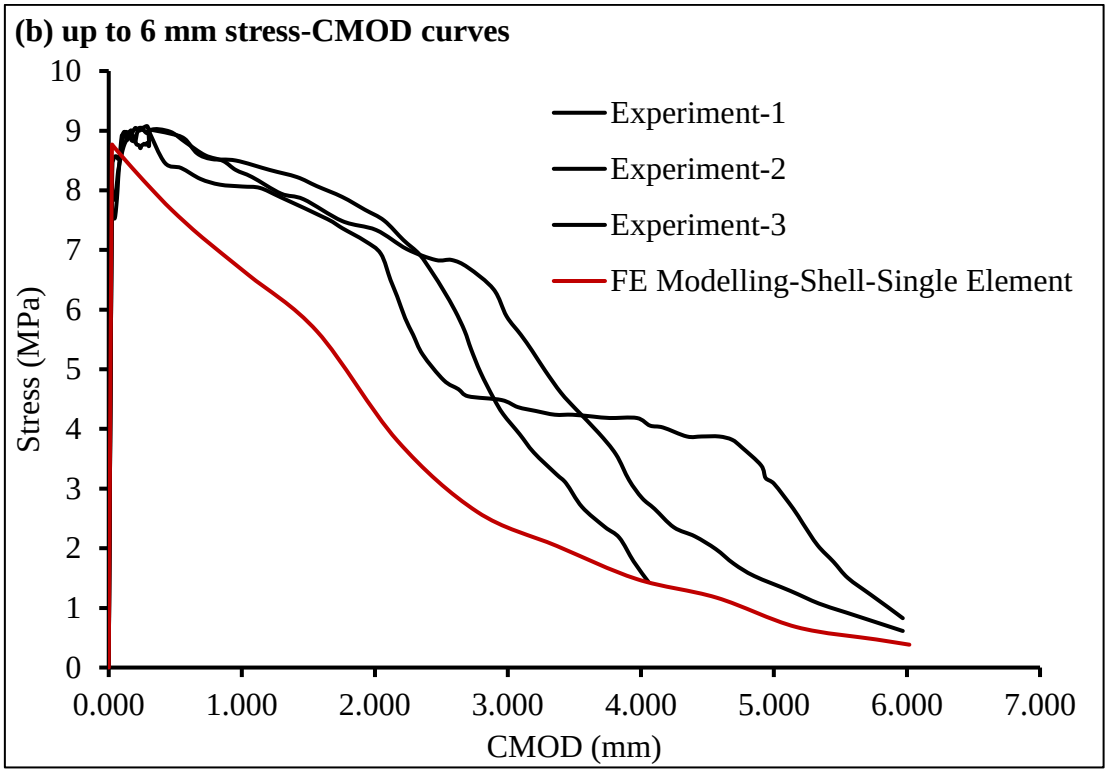

Figure 7.7: Comparison between uniaxial tension test and numerical model using single shell elements.

Figure 7.8 and Figure 7.9 show the observed and predicted stress-strain responses for UHPFRC material subjected to uniaxial compressive loading for both solid and shell elements, respectively. Similar to the uniaxial tension, the result of both solid and shell elements under uniaxial compression were found to be almost identical. Data presented in both figures show that the models represent the typical response of concrete subjected to uniaxial compression except for the peak load. The CDP model predicts a greater reduction in elastic modulus at the peak load than is observed in experiments. However, the model does predict the response of concrete in softening with good accuracy. Moreover, the difference between the model and the experimental response in tension and compression is approximately 0.5 MPa and 10 MPa, which gives 5% and 6% difference, respectively. Lower estimations of the model are preferred than overestimation for design purposes. In general the model predicts the overall structural behaviour of the UHPFRC but it shows some sensitively when the material is investigated at an element level. Therefore, it would be recommended to undertake further experimental testing such as single fibre pull-out testing to include in the model so that the model can be calibrated to investigate the UHPFRC material at element level.

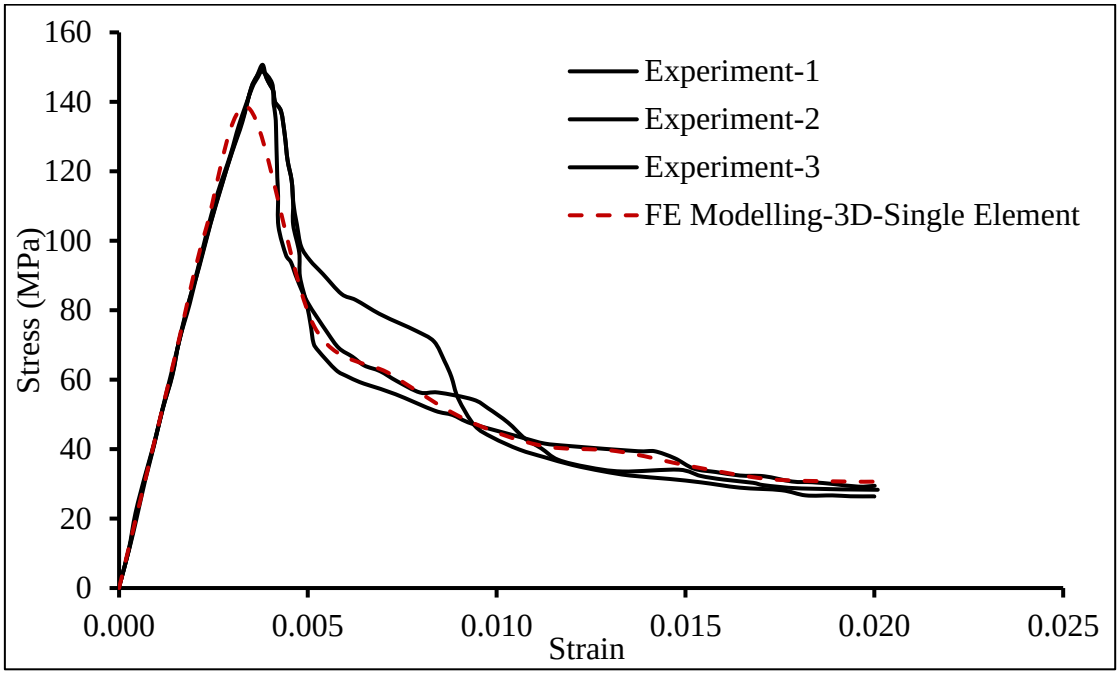

Figure 7.8: Comparison between uniaxial compression test and numerical model using single solid elements.

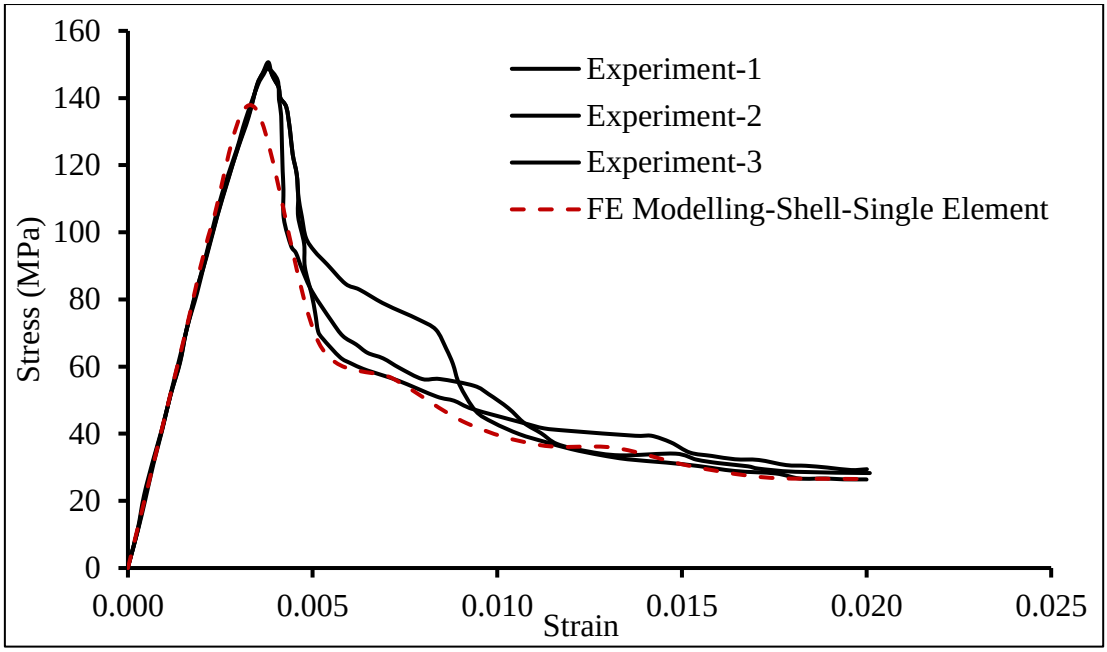

Figure 7.9: Comparison between uniaxial compression test and numerical model using single shell elements.

7.2 Comparison of Results of Notched Beams

This section discusses the FE analysis results for notched beams subjected to three-point bending. The results are compared to the experimental data. The accuracy of the model in terms of load-displacement, failure mode and size effect are discussed.

7.2.1 Failure Modes

Since all the beams were notched at the centre, microcracks occurred early at mid span around the notch. When the applied load increased, these microcracks formed into a single macrocrack that spreads vertically from the top of the notch toward the top surface of the beam. The FE analysis was able to capture this behaviour (see Figure 7.10) and showed that the crack patterns for all the beams started from the top of the notch and extended towards the top surface. As the beam reached the ultimate load, the beam failed in flexure with a single major crack. The two cracked faces of the beam were held by the intact area in the compression zone. However, the depth of the intact zone varied from one beam to another, depending on the beam depth. The CDP model effectively captured this

behaviour and the crack patterns can be seen in the visualisation module using plastic strain components (PE). Beams with 60 mm depth are shown in Figure 7.10 as an example. Furthermore, during the experimental investigation, the load-CMOD was monitored and it was observed that the microcracks began to appear at a CMOD of approximately 0.05 mm. Plotting PE in the visualisation, the FE analysis results showed that the appearance of the crack pattern compared well to that seen in the experiments.

As explained in Section 3.4.2, although the beam geometry, boundary and loading conditions are all symmetric, there is a considerable scatter in the experimental results of three tests for one beam design due to random distributions of discontinuous short steel fibres. In addition, the cracks in some of the beams are slightly tortuous and deviate away from the beam central lines, thus unsymmetrical crack paths cannot be accurately simulated by the homogenous FE models developed in this study, and can only be simulated by those models considering the random heterogeneity directly (Su et al., 2011) or indirectly (Wille and Naaman, 2012). Since it was assumed in the FE analysis that fibres are uniformly distributed in the matrix and the beam is modelled as a homogeneous material, the developed model can only predict symmetrical crack paths. Therefore, it was unlikely that the model would predict the exact crack path as it occurred during the experiment. However, the FE model appears to capture the material performance effectively and predicted the crack direction accurately as seen in the experiment. The simulated crack path for the 90 mm beam with displayed stress and tensile damage contours are shown in Figure 7.11.

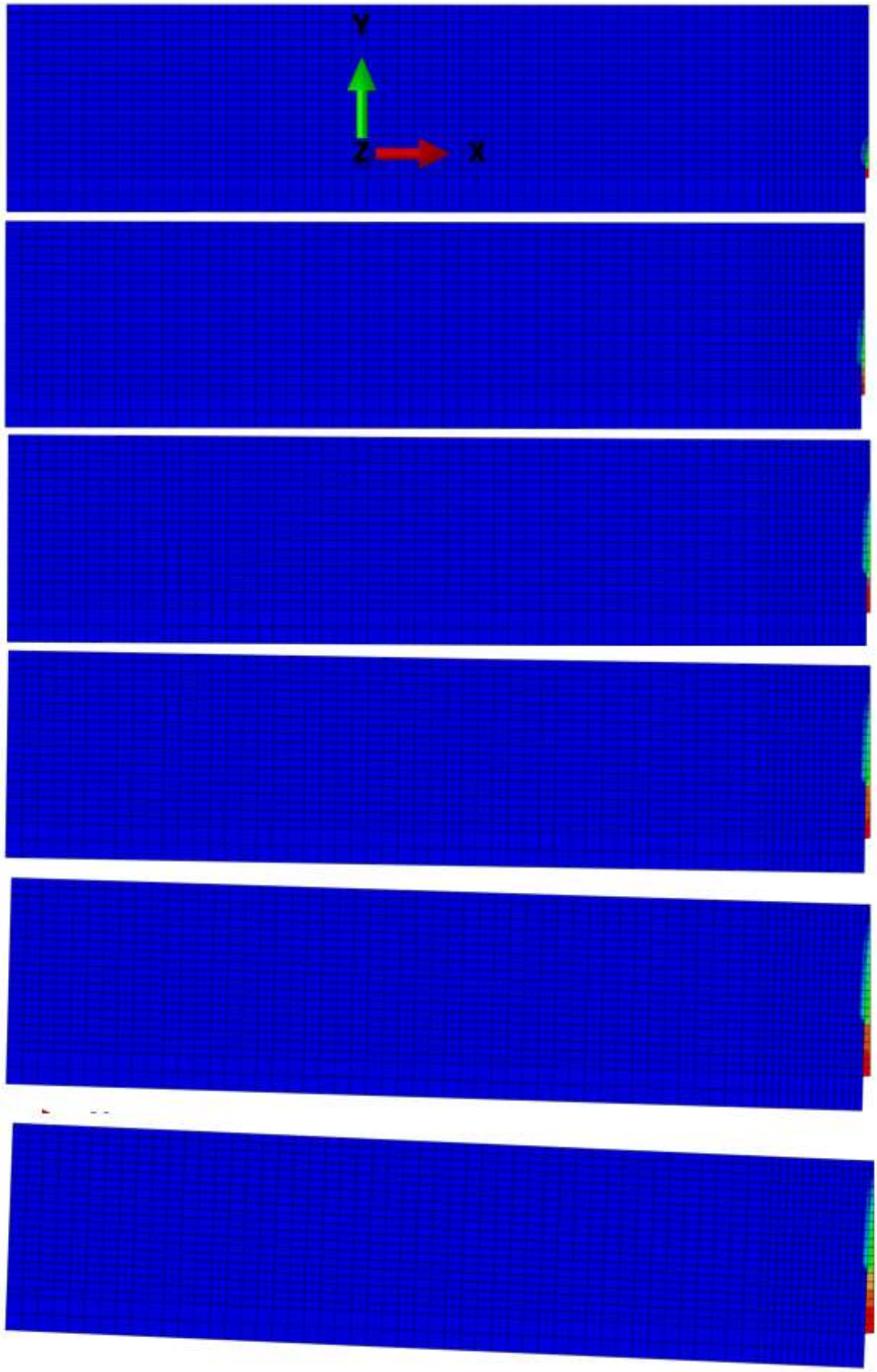

Figure 7.10: Crack pattern in process of analysis.

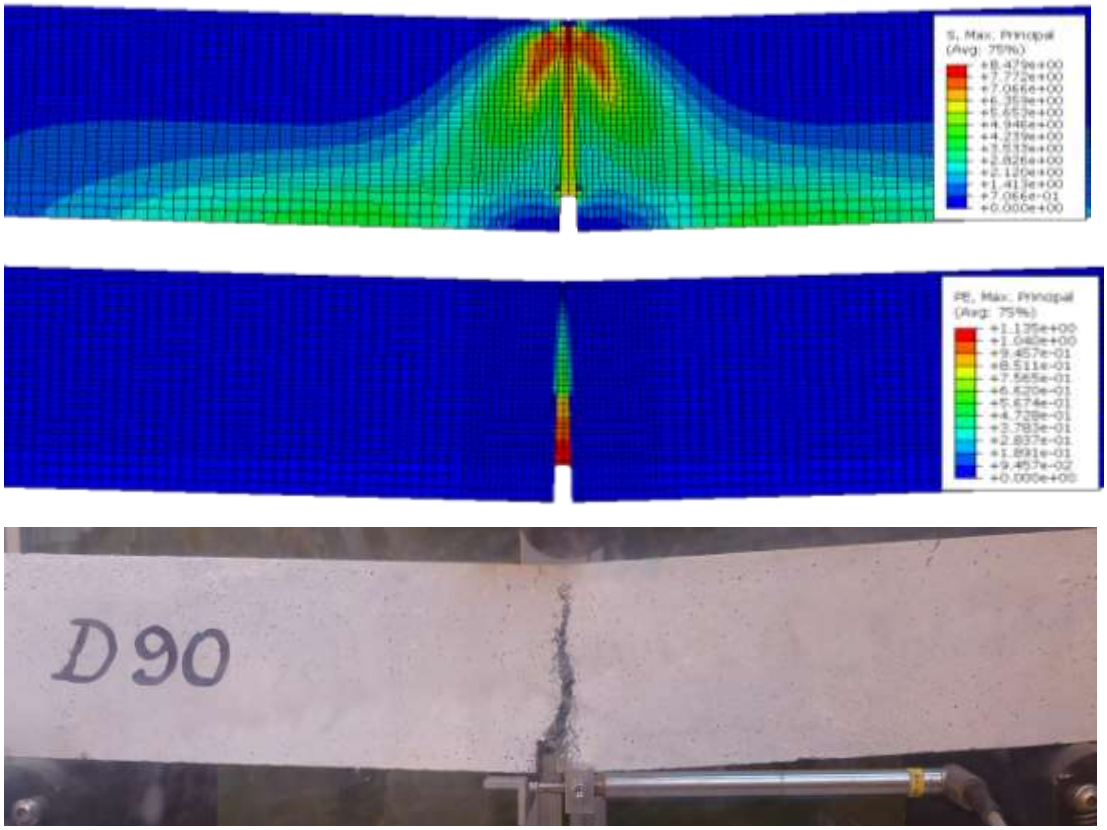

Figure 7.11: The model damaged contours compared to the experimental test results.

7.2.2 Load-CMOD Curves

The three load-CMOD curves from the bending tests and the average curve are compared with the CDP-based numerical results in Figure 7.12 to 7.16, for each beam depth. In the case of the very small displacements, all the curves follow the linear relationship between the load and the CMOD obtained from the experiment. This behaviour was observed clearly in the FE analysis for all the beam specimens shown in Figure 7.12 to 7.16. During the analysis, as the load was increased, it was noticed that the curve changes from its linear slope to a nonlinear ductility (hardening behaviour) as occurred in the experiment. During the experiment at this point, it was observed that certain areas of the concrete suffered tensile stresses larger than the matrix tensile resistance; cracks at the tension face resulted in changes in elastic modulus of the beam. This causes the curve to change from linear to nonlinear behaviour. It appeared that the material properties introduced in the model such as tension stiffening and compression hardening captured this transformation as the model follows the experimental curves in the strain-hardening region. However, for the shallowest beam with a depth of 30 mm, the model underestimated this behaviour

when compared to the experimental curves. The discrepancy may be due to the test procedure, in which the pre-load of 2 kN was too close to this beam's peak load of about of 2.5-3.5 kN, as shown in Figure 7.12. This can also be due to the effect of fibres tending to align themselves parallel to the surface and perpendicular to the line of action of the force as explained in previous chapters. Furthermore, the load-CMOD curves from the model are similar to the experiment showing a similar transformation between linear to nonlinear occurring at a crack opening of 0.05 mm. Therefore, damage contours were obtained for all the beams at a CMOD of 0.05 mm. The results show that beams with 30 mm depth are similar to the other beams and very small damage of approximately PE = 0.005 can be seen at the centre as shown in Figure 7.17.

The second stage of load-CMOD was predicted by the model and the result showed that a very small area covered in this region ended at a CMOD of approximately 0.40-0.50 mm. During the experiment, similar behaviour was seen (see Figure 7.12 to 7.16), indicating that the material properties included in the FE models were accurate. In the descending (softening) region, the FE analysis showed the curve has a steeper slope with increasing values of CMOD if compared to the experimental results. The axial load started to decrease after the beam reached its peak load and in this region, the iteration time converged faster compared to the strain-hardening region. As the analysis progressed beyond the elastic region, the elements started to change from their original shape especially those at the centre of the beam where the stress is at its greatest. According to the ABAQUS manual, these elements require a new elastic modulus and this is a complex procedure. The CDP model assumes that the reduction of the elastic modulus can be given in terms of a scalar degradation variable as shown in Equation (7.1):

$$E = (1 - d_t)\, E_0 \qquad \textbf{(7.1)}$$

where E and E_0 are the damaged and initial elastic moduli, respectively. From the above equation, E can be obtained as the beam analysis progresses as shown in Figure 7.18. This figure shows that the elastic modulus of the beam reduces significantly as the crack widens due to the slippage of fibres during the experiment. Based on the equation built into the ABAQUS software (Equation 7.1), new elastic moduli were calculated and used at each increment to capture the nonlinear region of the curve. These calculations were

based on the material properties included in the model. The results showed that the model accurately captured the ascending and descending regions with the reduced elastic modulus for all the beam specimens. Looking at Figure 7.12 to 7.16 shows that the CMOD of the peak load is under-predicted by the FE model for the beam below a depth of 120 mm but the FE results lie within the spread of the data. As reported in the literature, a considerable variation can be seen in the concrete data results for the same geometry and mix design especially in the nonlinear regions. This variation increases when short fibres are included in the concrete. Therefore, the scatter in the data in the ascending regions indicates that the variation needs to be considered in the design of UHPFRC members.

Due to the random distribution of steel fibres, a considerable scatter can also be seen in the softening region and this changes from one beam depth to another. However, except for the beams with 60 and 90 mm depth, the FE model results lie in the experimental range. The differences between the FE analysis and experimental data for specimens below 120 mm in the softening region could be due to two reasons. Firstly, softening behaviour in UHPFRC is highly dependent on the fibre-bridging action and this depends on the fibre orientation in the matrix. Since the thickness of these specimens is large enough for the fibres to orientate randomly, the orientation of fibres can change from one specimen to another, resulting in changes in the fibre-bridging action. Because there are no reinforcing steel bars in the UHPFRC and only fibres control the two cracked faces, more fibre contribution to the fibre-bridging action makes the strength reduction slower in the softening behaviour over a wide range of deflections. This results in a stiffer softening behaviour. Secondly, as shown in Equation 7.1, the prediction of the softening behaviour by the model is based on the calculation of a new effective elastic modulus. This new elastic modulus is calculated using the input data introduced to the model. Since the material input data was obtained using material testing data and does not consider the randomness in the fibre-bridging action, it may lead to an underestimation in the softening behaviour. In some of the specimens with a similar geometry a difference of up to 25% can be seen as well as a difference of up to 35% between the model and the experimental results. Therefore, a variation of at least 25% is essential to be considered in designing UHPFRC if softening behaviour is considered.

Experimental and numerical peak loads F and F_n for all the beams are shown in Table 7.1. Except for the beams with a depth of 30 mm, the simulation accurately predicted the experimental peak load. This can be due to the effect of fibre alignment or testing setup. Fibre bridging can have a considerable effect in preventing a small crack growing into a large crack, resulting in an increase in the peak load during the experiment. Whereas, in the simulation this is not the case and the load determined is based on the material parameters used. The above analyses demonstrate that the CDP-based FE models are capable of predicting the elastic range, strain hardening and ultimate load-carrying capacities of the UHPFRC beams with good accuracy. Since the aim was to investigate the size effect behaviour and size effect is determined from the ultimate load, parametric studies can then be carried out for beams with greater depths.

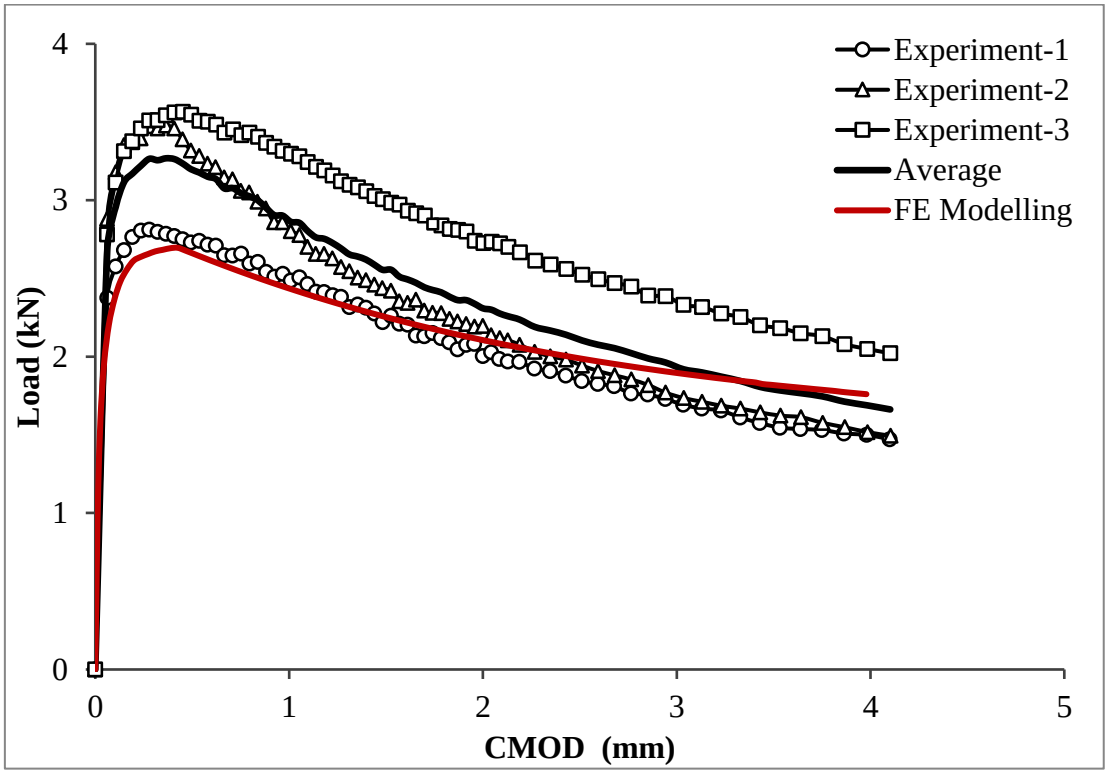

Figure 7.12: Load-CMOD curves for D30 beams.

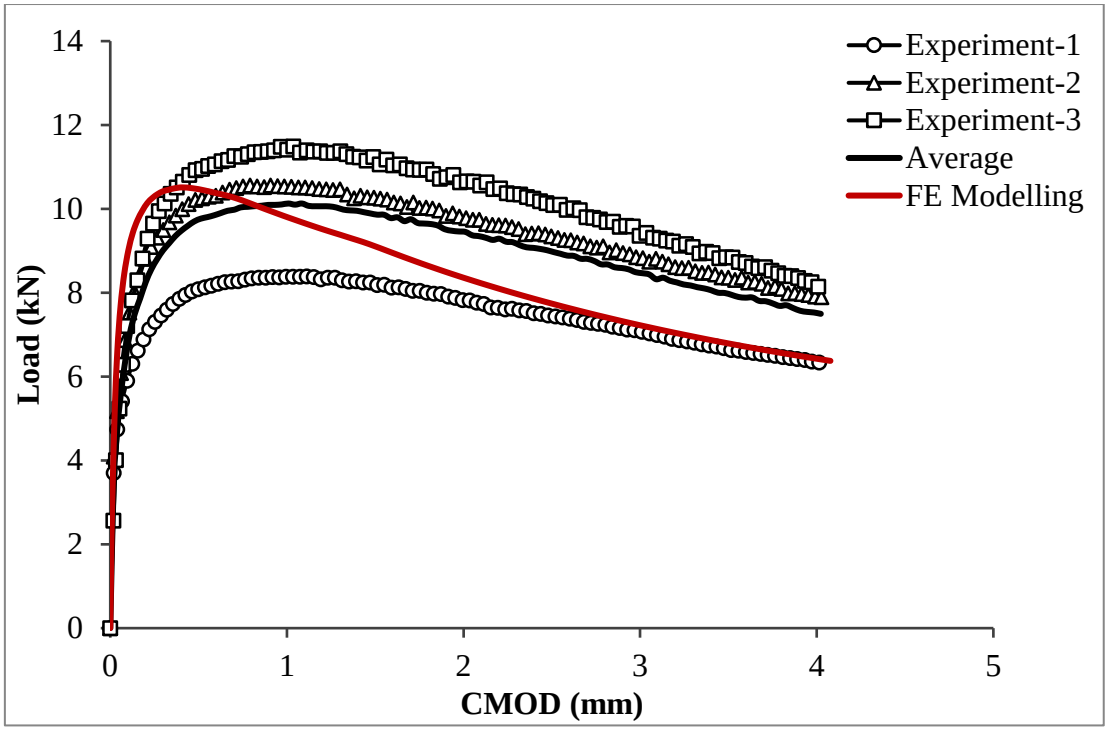

Figure 7.13: Load-CMOD curves for D60 beams.

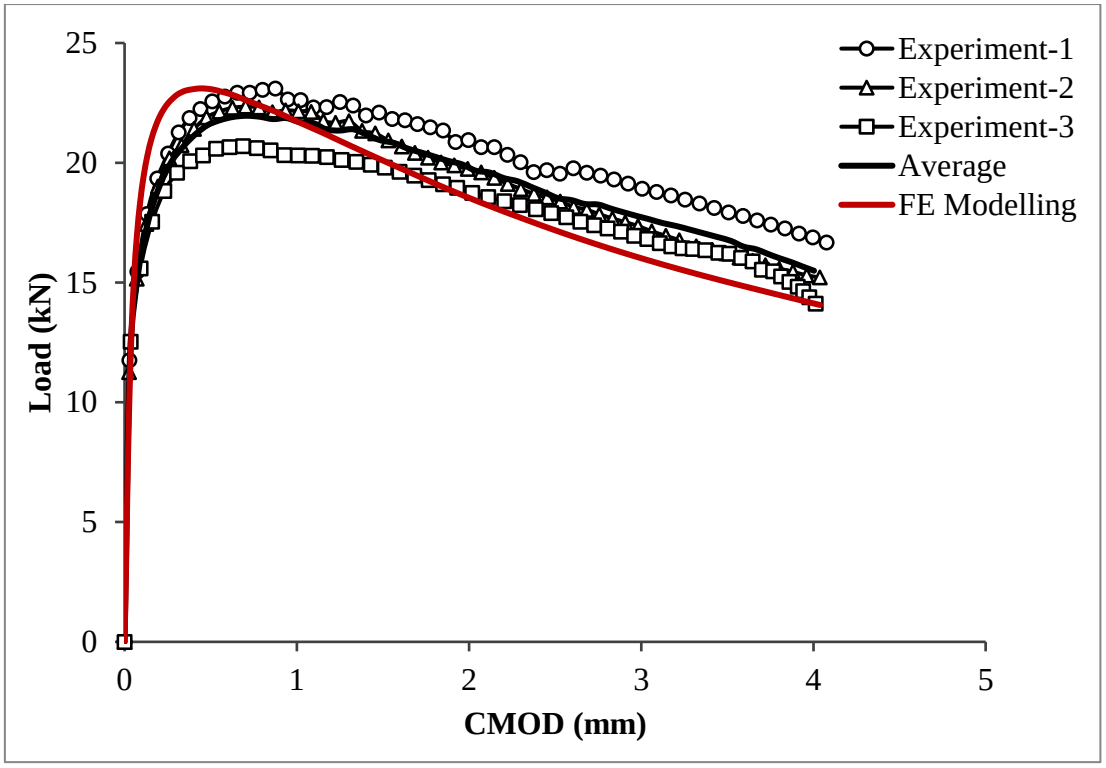

Figure 7.14: Load-CMOD curves for D90 beams.

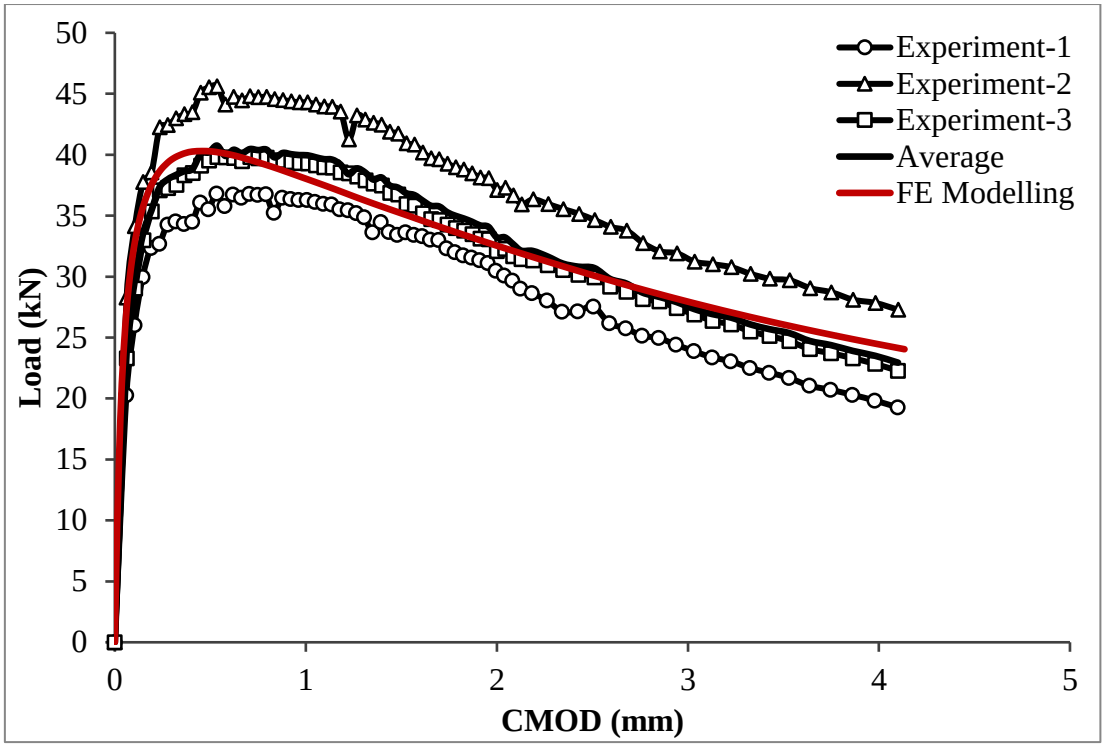

Figure 7.15: Load-CMOD curves for D120 beams.

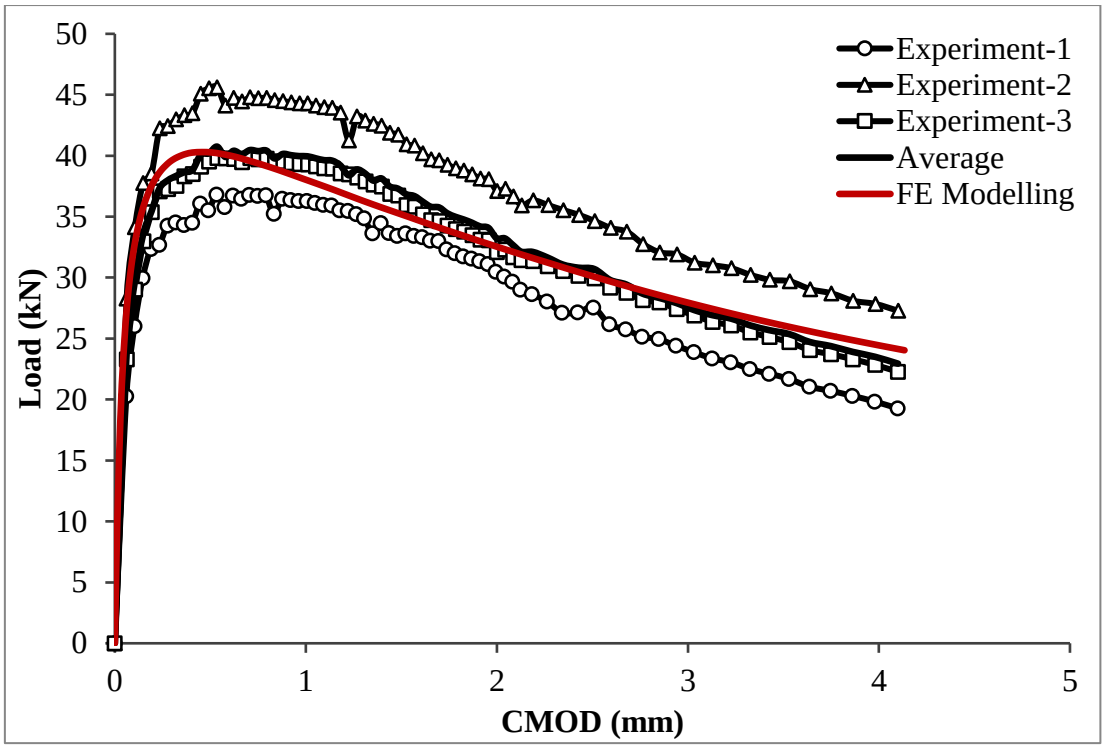

Figure 7.16: Load-CMOD curves for D150 beams.

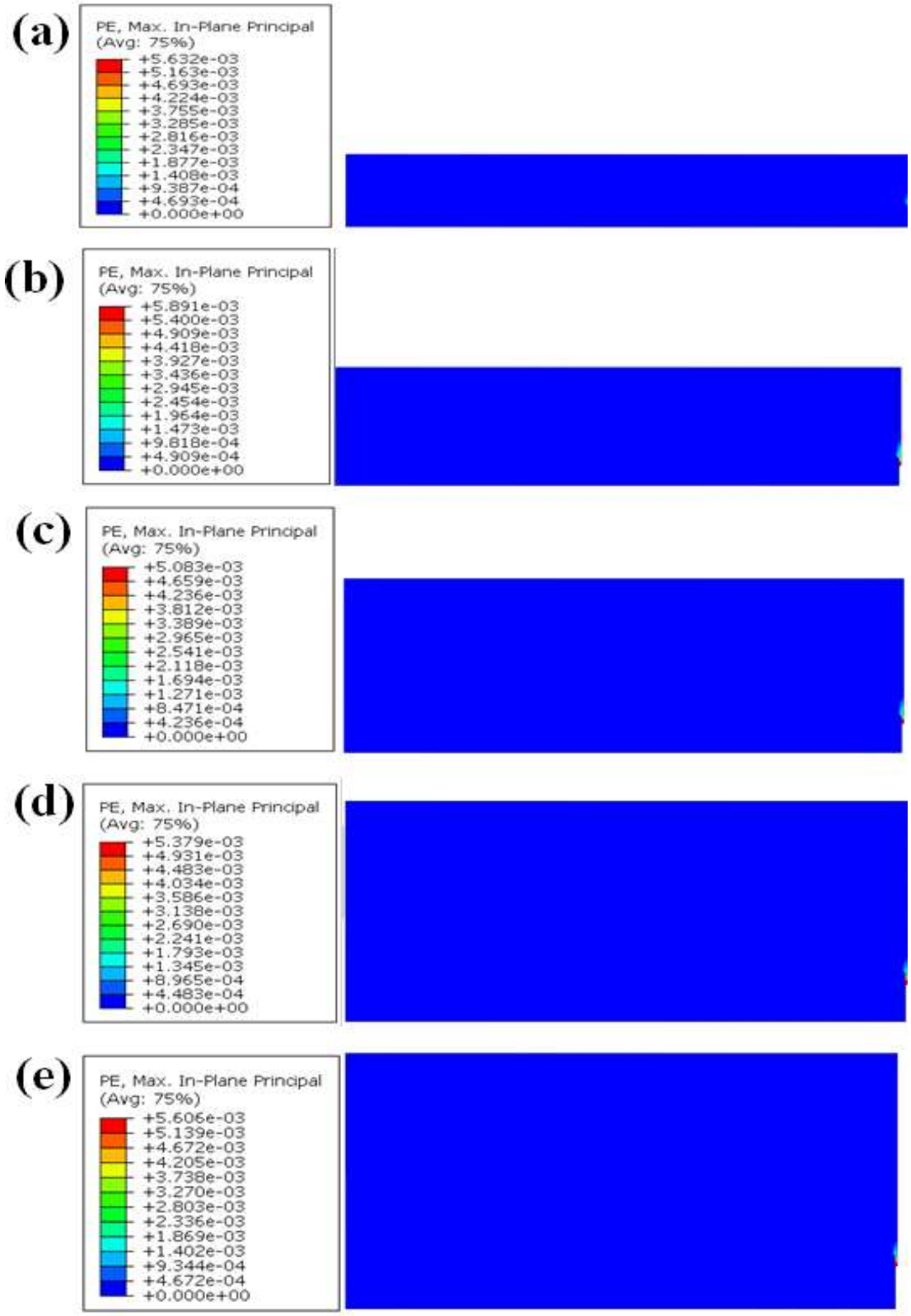

Figure 7.17: Damage at the end of linear stage (a) D30 (b) D60 (c) D90 (d) D120 (e) D150.

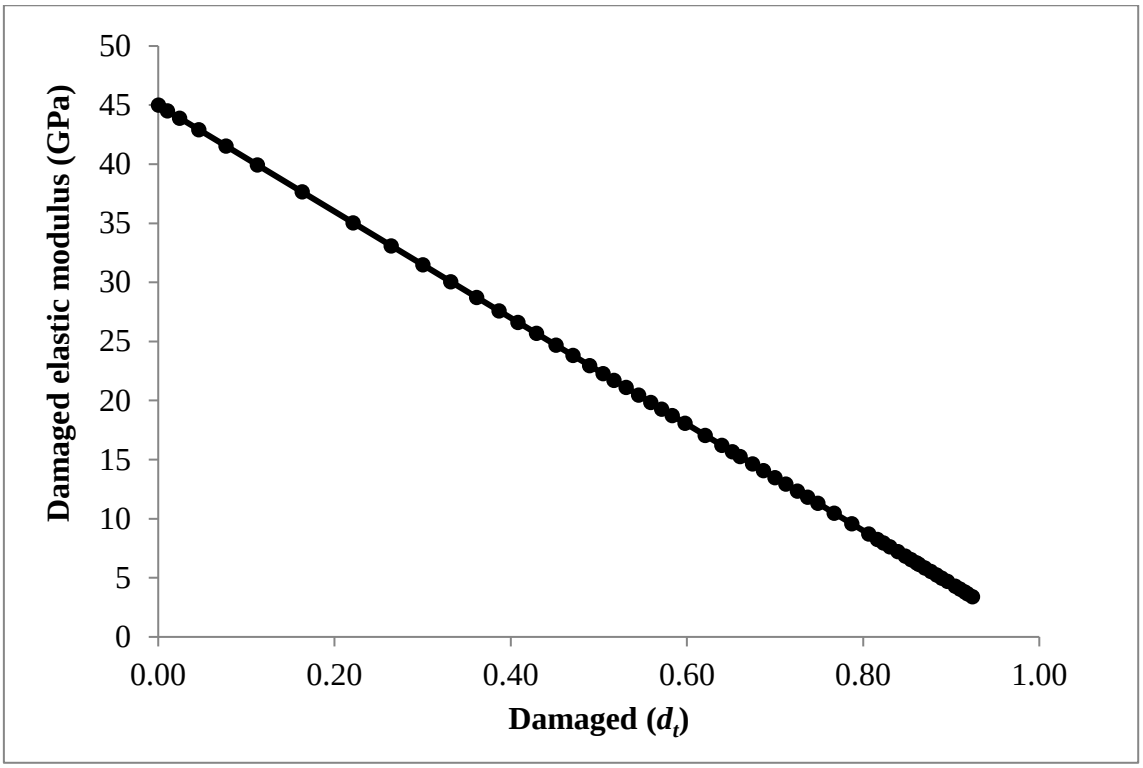

Figure 7.18: Shows reduction in the elastic modulus.

Table 7.1: Experimental and numerical results for beam specimens.

	No.	Experimental peak load F (kN)	Average F (kN)	Numerical peak load F_n (kN)	Nominal flexural strength f_f (MPa)	Average f_f (MPa)	Numerical flexural strength f_{fn} (MPa)	Log d	Error $\lvert f_f - f_{fn} \rvert / f_f$
D30	1	2.50	3.17	2.81	20.00	25.33	22.32	1.48	11.8%
	2	3.50			28.00				
	3	3.50			28.00				
D60	1	8.40	10.13	10.52	16.80	20.27	21.00	1.78	3.6%
	2	10.50			21.00				
	3	11.50			23.00				
D90	1	23.10	22.03	23.07	20.53	19.59	20.48	1.95	4.7%
	2	22.30			19.82				
	3	20.70			18.40				
D120	1	36.80	40.73	40.23	18.40	20.37	20.11	2.08	1.2%
	2	45.60			22.80				
	3	39.80			19.90				
D150	1	65.30	60.13	61.75	20.90	19.24	19.76	2.18	2.7%
	2	61.50			19.68				
	3	53.60			17.15				

7.2.3 Size Effect

As the main purpose of the beam tests was to investigate size effect behaviour, Table 7.1 summarises the experimental and numerical nominal flexural strength, f_f and f_{fn} respectively for all the beams. The f_{fn} for all the numerical models were calculated using the following equation from (British Standards Institution BS EN14651:2005+A1, 2007):

$$f_f = \frac{3F_n * l}{2b(d - d_n)^2} \qquad \textbf{(7. 2)}$$

where l is the span length between the two roller supports, b is the beam width, d is the beam depth and d_n is the notch depth. The numerical result showed that all beams failed at an f_{fn} of around 20 MPa (see Table 7.1) and proved that the strength does not depend on the size of the element. It can be seen that the numerical result agreed with the average experimental data except for d=30 mm, the differences between the two results are less than 5%. These slight differences may be caused by the assumption of material homogeneity, and the different properties used in the modelling. For example, an elastic modulus (E) of 45.0 GPa was used in numerical modelling, but the values from the experiments varied between 44.0 GPa to 47.0 GPa.

Since experimental work can be very expensive to conduct for the full-size structures and knowing that the modified CDP model can predict the behaviour of UHPFRC beams under static load, a parametric study has been performed. The change in the specimen depth is the main parameter for this study. Extra CDP-based FE simulations for beams with d =180, 210, 240 and 300 mm were then carried out for an analysis of size effect. The nominal flexural strength f_f versus log d results from all the experimental and numerical results were plotted in Figure 7.19. It can be seen that the f_{fn} from the numerical simulations for all these large sizes are also around 20 MPa. It is therefore, a finding of this study, placing the UHPFRC material on the horizontal part on the general size effect curve, namely, it follows the strength criterion which specifies that the structural failure is characterised by ductile yielding. This FE analysis confirms that the size effect in structures made of cementitious materials could be eliminated by adding a high volume of ductile fibres, as reported by Lepech and Li (2003 and 2004) in the similar material ECC. More recently, Wille and Parra-Montesinos, (2012) showed that changes in beam

specimen size had little influence on the peak flexural strength. Therefore, it can be concluded that size effect phenomenon can be ignored in UHPFRC beams up to size of 300 mm in depth or the current size effect law cannot be applied.

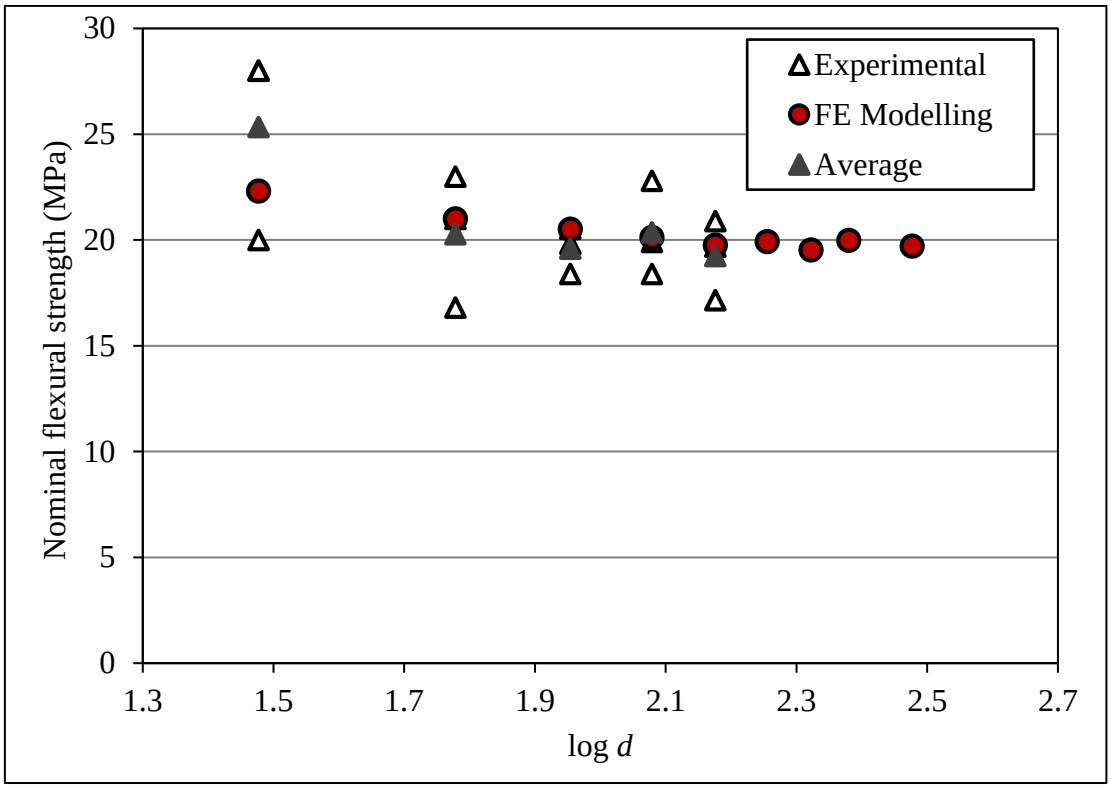

Figure 7.19: Size effect on the nominal flexural strength of UHPFRC beams.

7.3 Comparison of Results for One-way Slabs

This section discusses the FE analysis results for one-way slabs and compares them with the experimental data provided in Chapter 4. The validity of the model is examined along with its capacity to determine the structural behaviour of one-way UHPFRC slabs with different geometry and boundary conditions. To do this, nonlinear FE simulations developed for one-way slabs were employed. The FE model was then used to conduct parametric studies for slabs with greater thicknesses that were too expensive or impractical to be tested.

7.3.1 Failure Modes

On inspection of the experimental results, stress induced at the centre of the slabs resulted in a single tensile crack forming on the bottom surface of the slab for both FF and SS boundary conditions. The model predicted results in good agreement with the corresponding experimental data as illustrated in Figure 7.20 and Figure 7.21. In the case of SS boundary conditions, the slabs edges were free to rotate, resulting in lower contact with the support than the slab with FF boundary conditions. The rotational restraint and higher contact surface with the support from FF boundary conditions resulted in higher stresses (Figure 7.20) than for the SS boundary conditions (Figure 7.21) at the same displacement. For slabs with SS boundary conditions, as the initial stage of the loading subjects the slabs to pure bending, axial loads cause the slab centre to become more stressed while the edges become more relaxed but still experience small tensile stresses. As the loading continues, concrete experiences cracking in the tensile zone and does not receive any further stress in this area, while in the FF slabs in the compression surface, compressive stresses, which first occur near both supported edges, propagated along the support. It can be observed that at displacements of 0.30 to 0.40 mm, microcracks appear in all the slabs with FF boundary conditions and they all change from linear behaviour to the strain-hardening region, while the slabs with SS boundary conditions are still partly in the linear elastic region. This observation agrees well with the specimens tested in this study.

It is known that the FE analysis using CDP is not capable of capturing the failure mode of OC. In order for the model to capture the failure modes, the extended finite element method (XFEM) must be incorporated in the analysis and this is not a straightforward task. Moreover, this task gets further complicated as the fibres are randomly distributed and orientated in the matrix. To capture the failure mode of a UHPFRC structure, the CDP model needs to be incorporated with a specially designed and efficient algorithm using a computer programme such as MATLAB as well as XFEM parameters and this is beyond the scope of this study. Due to this reason, very few studies have attempted to model the fibres individually and these studies have only considered a simple and single geometry. Developing a model to capture the failure modes when boundary conditions and geometry changes is complex and challenging. Furthermore, it requires a high computational cost associated with the large number of fibre and difficulties of obtaining a fibre-matrix bond. Therefore, the FE model developed in this study is not capable of

showing the physical cracks. However, it is capable of showing the stress distributions of tensile face and compressive face as shown in Figure 7.20 and Figure 7.21. Both figures highlight the regions where the stress is the highest within the slab. The stresses increase as the load on the slab structure concentrated above, where the point load and the slab surface meet. The stress at the centre in the FF slabs is found to be greater than the stress at the slab supports.

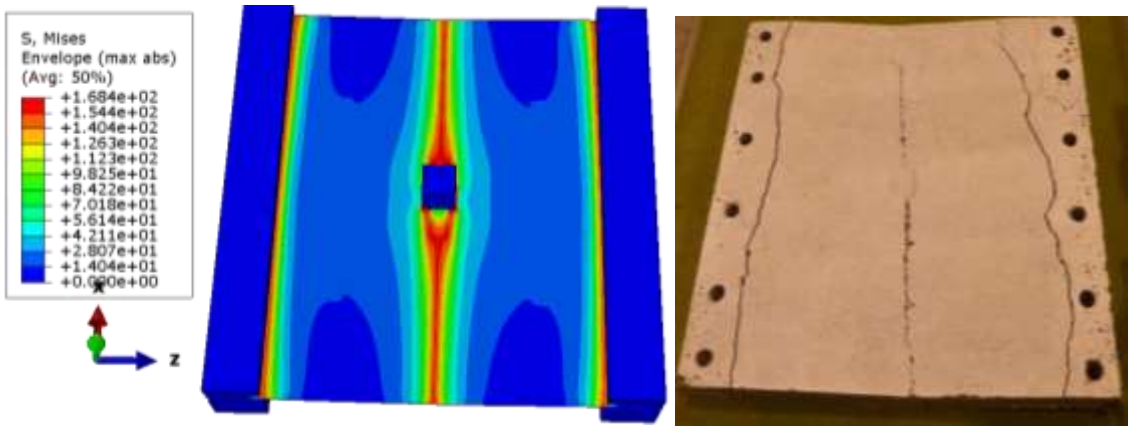

Figure 7.20: Stress distribution against test failure mode for the 45 mm one-way slab with FF boundary condition.

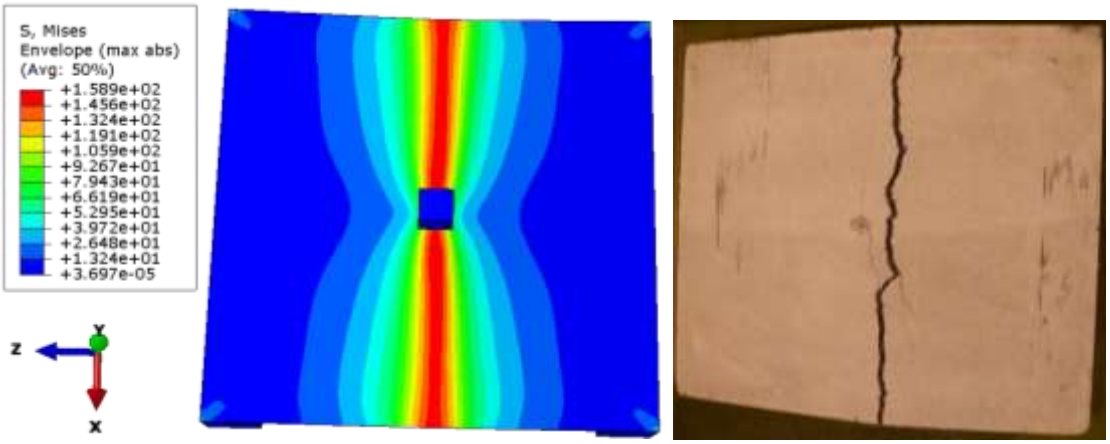

Figure 7.21: Stress distribution against test failure mode for the 45 mm one-way slab with SS boundary condition.

In addition, due to the random distribution and orientation of steel fibres in the matrix, the formation of macrocracks on the tensile face cannot be simulated by models that consider the random heterogeneity (Su et al., 2011) or those where the crack position is known in advance (Meda and Plizzari, 2004). In addition, modelling the adhesive bond stress mechanism between fibres and matrix is complicated and cannot be obtained directly from ABAQUS (Nwankwo et al., 2013). Therefore, no attempt was made to simulate discrete crack propagation in this study. When taking into consideration the difficulties, necessary time and cost to conduct an experimental test, parameterised nonlinear finite element analysis is very reliable and preferable technique to investigate nonlinear behaviour of UHPFRC.

Unlike the concrete models based on discrete crack modelling, the CDP model does not have the ability to show the physical cracks developing at the material integration points (ABAQUS, 2013). However, it is possible to obtain the concept of an effective crack direction with the purpose of obtaining a graphical visualisation of the cracking patterns in the slab structure using PE output. In order to show the damage occurrence or crack locations of the slab specimens at the ultimate level, PE were extracted from the model for both FF and SS boundary conditions. To illustrate this, the 45 mm slab is shown for both FF and SS boundary conditions as shown in Figure 7.22 and Figure 7.23, respectively. During the experimental testing, the slab with FF boundary condition experienced compressive cracking on the top face of the slab which first occurred near both supported edges, propagated along the support. It can be observed that the model reproduced the compressive crack path, as it occurred during the experiment. For slabs with SS boundary conditions, cracks only occurred at the centre of the specimens and propagated toward the specimen edges. It can be seen that the CDP model seems quite realistic compared to the experimental result and the crack growth is captured in both boundary conditions. However, it also important to mention that the determination of crack location in CDP in ABAQUS is limited and purely based on the assumption proposed by Lubliner et. al. (1989), that cracking initiates at points where the tensile plastic strain is greater than zero and the maximum principal plastic strain is positive. Therefore, further experiments with the larger sizes need to be carried out in order to use the model exclusively.

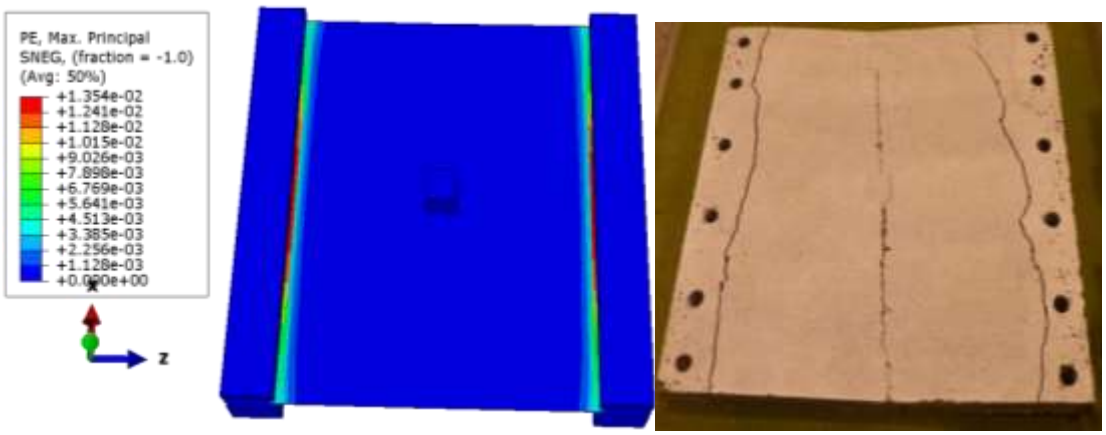

(a) FE and experimental top face

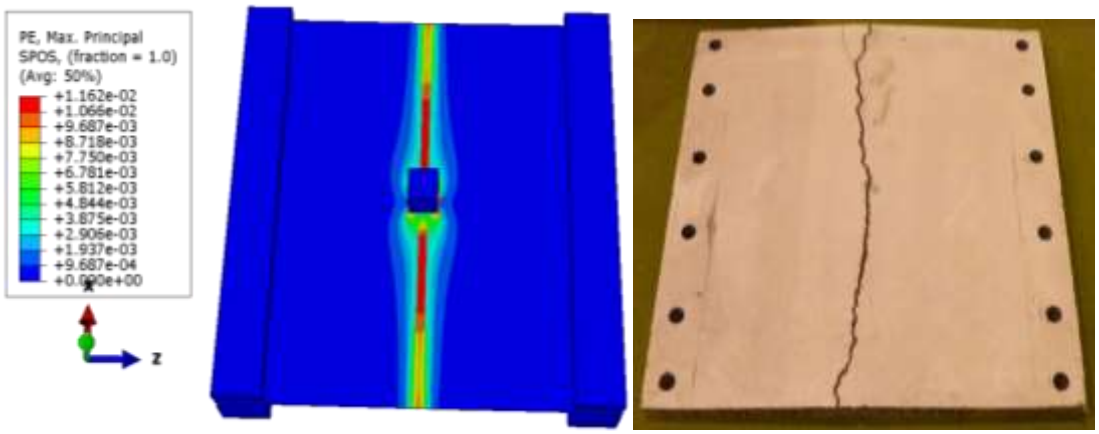

(b) FE and experimental bottom face.

Figure 7.22: Damage result for 45 mm one-way slab with FF boundary condition.

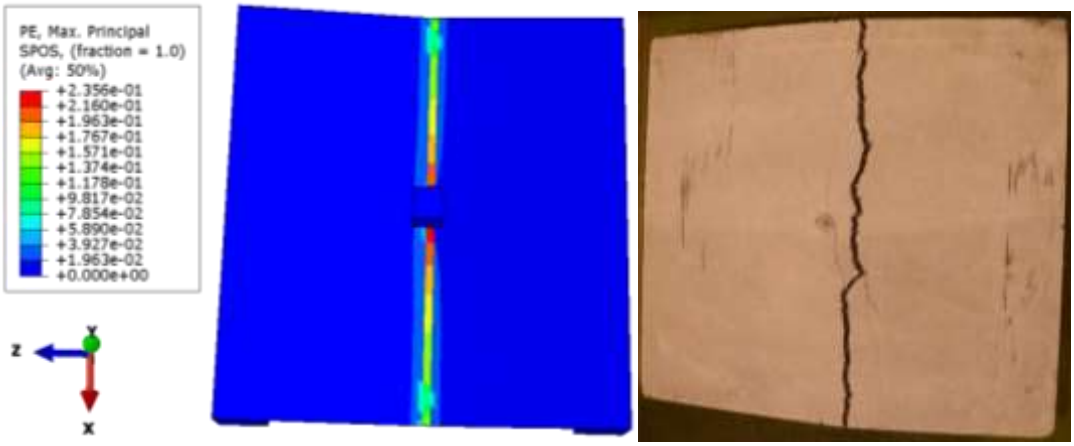

Figure 7.23: Damage result for 45 mm one-way slab with SS boundary condition.

As explained in Chapter 2, due to the random fibre distribution in the matrix, UHPFRC has high ductility compared to OC. This high ductility results in large deformations before failure. The rotation of the two edges which were resting on the support was significant compared to the slab's overall central deformation in the SS boundary condition. However, no rotation of the two fixed edges was recorded for slabs with FF boundary conditions. The FE analysis using the CDP model confirmed this behaviour and the full models for both FF and SS boundary conditions are shown in Figure 7.24. In general, when taking into consideration the difficulties, necessary time and cost to conduct an experimental test, parameterised nonlinear finite element analysis is a preferable technique Therefore, this model can make a considerable contribution in future studies to better understanding the nonlinear structural behaviour of UHPFRC.

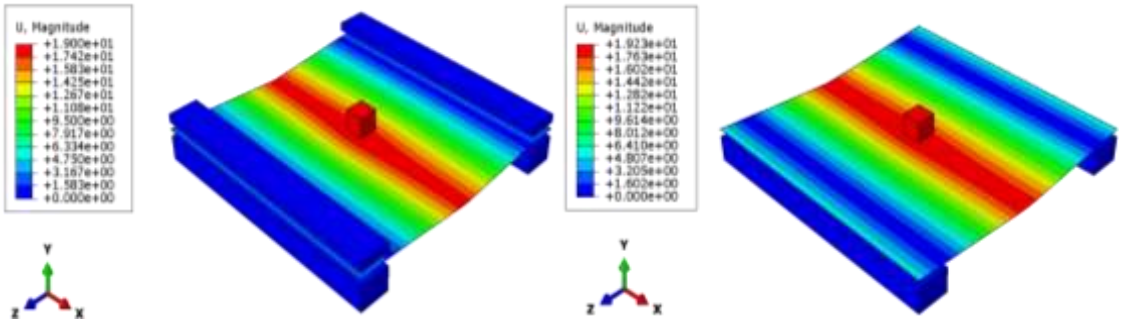

(a) FF boundary condition (b) SS boundary condition

Figure 7.24: Deformation shape for 45 mm one-way slabs.

7.3.2 Load-displacement Curves

The experimental load–displacement curves for the one-way slab specimens for each slab thickness and the average curve are compared with the CDP-based numerical results in Figure 7.25 to 7.28 for FF boundary conditions and Figure 7.29 to 7.32 for the SS boundary conditions, respectively. The experimental (F_s) and numerical (F_{ns}) ultimate load for each slab specimen with an experimental average for both the FF and SS boundary conditions are also presented in Table 7.2 and Table 7.3, respectively.

The predicted load-displacement curves in the linear elastic region are similar to the experimental load-displacement curves, where there is a steep rise in the load followed

by the strain-hardening region. It is clear that the initial elastic modulus introduced in the model very accurately captured the behaviour of the slabs in both the FF and SS boundary conditions. Both the FE simulations and experimental results show the end of the elastic region is at approximately 0.30 to 0.40 mm for both FF and SS boundary conditions. As the material extends beyond its linear behaviour, cracks begin to appear, resulting in the strain-hardening stage. It seems that the numerical simulation has accurately captured the strain-hardening behaviour of all the slabs in both the FF and SS series. It is recommended that a displacement of up to 0.40 mm can be allowed in designing UHPFRC one-way slabs in serviceability limit state (SLS) regardless of boundary conditions. It is important to mention that the UHPFRC material shows a stiffer behaviour in the elastic region with a small displacement.

As previously mentioned, the results of the optimised section proposed by the French design guidelines (Association Francaise de Genie Civil–Service d'etudes Techniques des Routes et Autoroutes (AFGC/SETRA), 2002) suggested that the slab thicknesses are categorised for two types: thin and thick slabs. This assumption is based on no cracking at SLS. Looking at the slab test results conducted here, this criterion may not be realistic. This is because the material only covers a very small portion of displacement before the occurrence of microcracks. The load at the end of elastic stage is significantly lower than the ultimate load for all the slab thicknesses with both FF and SS boundary conditions.

For slabs with FF boundary conditions, the load to cause microcracking for the 25 mm slabs, ranged from 6 to 8 kN which is significantly lower than the ultimate loads that ranged from 22 to 26 kN as shown in Table 7.2. Similarly for 35 mm slabs, microcracks appeared when the load reaches approximately 20 to 22 kN, which is considerably smaller when compared to the ultimate load that ranged from 54 to 56 kN as shown in Table 7.2. A similar behaviour was also observed for both 45 and 60 mm slabs where microcracks occurred at a load range from 56 to 58 kN and 85 to 90 kN while the ultimate loads were 92 to 95 kN and 148 to 155 kN, respectively.

This considerable difference between the first cracking load and ultimate load is also observed for slabs with SS boundary conditions. The load to cause the appearance of microcracks for 25 and 35 mm slabs ranged approximately from 4 to 5 kN and 10 to 12 kN, respectively. Whereas the ultimate load was 15 to 17 kN for 25 mm slabs and 27 to 30 kN for 35 mm slabs as shown in Table 7.2. For thick slabs (45 and 60 mm), the

cracking load was found to be 19 to 22 kN and 55 to 60 kN, respectively. Similarly, the ultimate load was significant when compared to the cracking load and ranged from 51 to 53 kN for 45 mm slabs and 98 to 107 kN for 60 mm slabs. This demonstrates that the SLS criterion proposed by AFGC may be conservative for UHPFRC slab systems. Since, the difference between first cracking load and ultimate load was at least 42% for one-way slab thicknesses, further testing such as fatigue investigations are needed to better understand the crack behaviour of UHPFRC as the no cracking criterion proposed by AFGC is highly conservative. A similar finding is also reported in the literature (Harris, 2005).

Although, in the elastic or strain-hardening region, the numerical performance predicted by the CDP model and the experimentally obtained load-displacement curves are rather close. A scatter in the pseudo-strain-hardening regions can be seen in the experimental testing. Therefore, a variation of 10% must be considered in this region in designing at the ultimate limit state, especially for slabs with the thicknesses of larger than 45 mm. This percentage allows for variations that may occur in the stain-hardening stage due to the fibre-bridging behaviour as fibres have a significant influence on the direction of microcracks. Moreover, in some of the slabs with a similar thickness, a difference of up to 25% can be seen in the softening region in the experimental results. Therefore, a variation of at least 25% should be considered in designing UHPFRC if softening behaviour is considered. Nevertheless, further experimental testing is needed in order for this recommendation to be used in design.

The differences between the experimental average ultimate load F_s and numerical ultimate load F_n are less than 5%, except for the ONE-WAY-SS27 slabs as shown in Table 7.2 and Table 7.3. As reported in the literature and investigated in Chapters 4 and 5, in thin slabs, fibres tend to be aligned more perpendicular to the direction of the load, due to the restriction in fibre orientation and distribution imposed by the thickness. Furthermore, the model agrees well with the experimental results and shows that the displacement at F_s is approximately 5 mm for slabs with 25, 27 and 35mm thickness and 3.2-4.5 mm for slabs with 45 and 60 mm in both FF and SS boundary conditions.

In general, the softening behaviour of the experimental test results for both the FF and the SS series was also reasonably predicted by the numerical simulation. However, the FE models tend to show a relatively stiffer behaviour with increasing load compared to the

experiments, especially for the ONE-WAY-SS27 slabs. This could be attributed due to the sensitivity of CDP model to one-way thin slabs with SS boundary conditions which have a thickness of only twice the fibre length. In addition, the consideration of fibre distribution in Chapter 4 showed that the fibres in thinner slabs tend to be parallel to the slab surface resulting in more fibres bridging between the two cracked faces. Whereas in the model, this behaviour could not be simulated as the concrete was assumed to be a homogenous material. Moreover, it is well-known that a variation of up to 10% can be seen in the experimental investigation of traditional reinforced concrete specimens at the nonlinear stage, where cracking has occurred. This variation may be further increased in UHPFRC specimens as the crack opening is dependent on the number of fibres that contribute to the bridging action. Therefore, a considerable difference between the numerical model and the experimental data is not surprising in the tension stiffening stage. However, this region of the material for thin members still requires further experimental testing in order for the model to adequately describe the behaviour and to better understand the softening region.

Furthermore, the SD of the F_s is less than 5 kN and this gives a SE of less than 2.8 kN. The coefficient of variation (CV) indicates that there is little fluctuation only ranging from 1.5% to 8.2% in the ratio of the experimental values to the average value and confirms the accuracy of the experiments. However, it suggests that the variation of 10% in the F_s is required to be considered in designing of both thin UHPFRC slabs ($t < 3l_f$) such as 25 and 35 mm and thick UHPFRC slabs ($t > 3l_f$) such as 45 and 60 mm when ultimate load is considered.

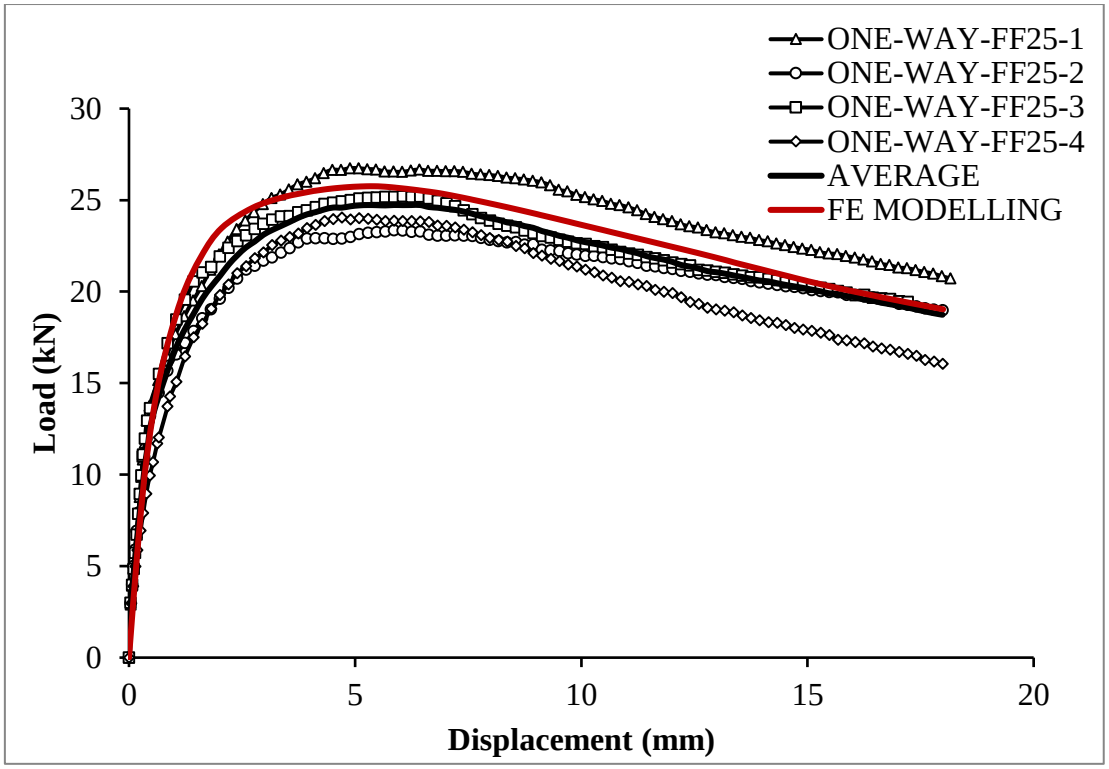

Figure 7.25: Load-displacement curves for FF25 slabs.

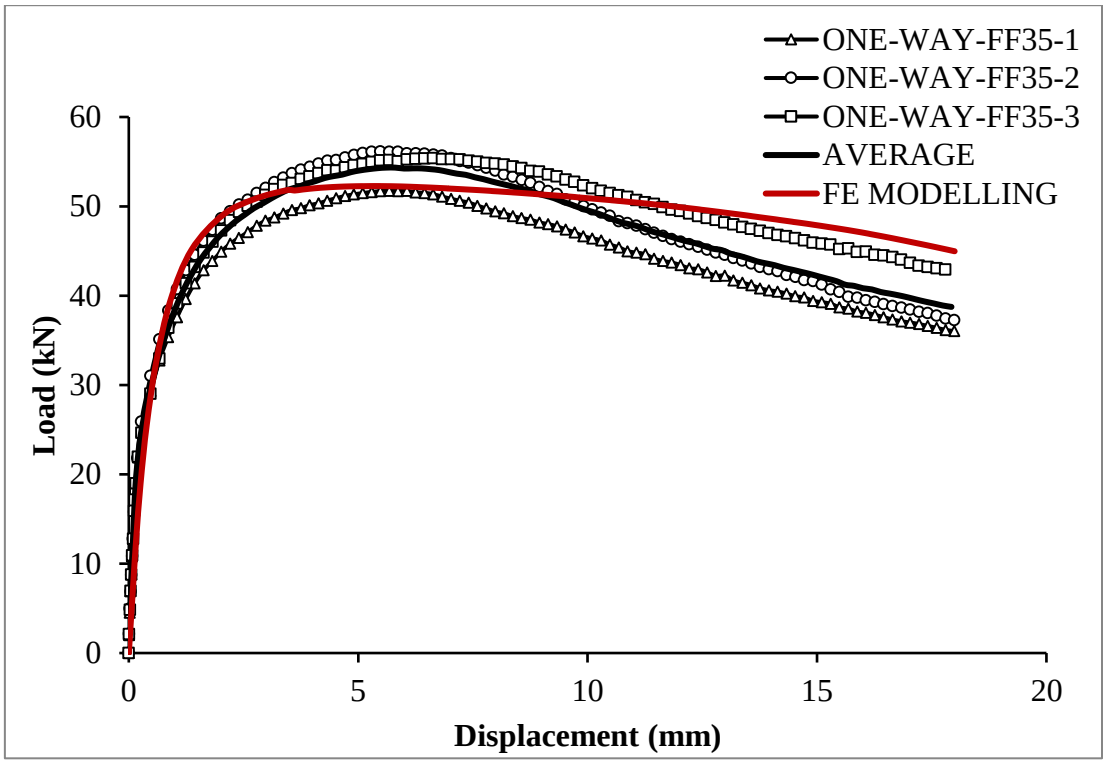

Figure 7.26: Load-displacement curves for FF35 slabs.

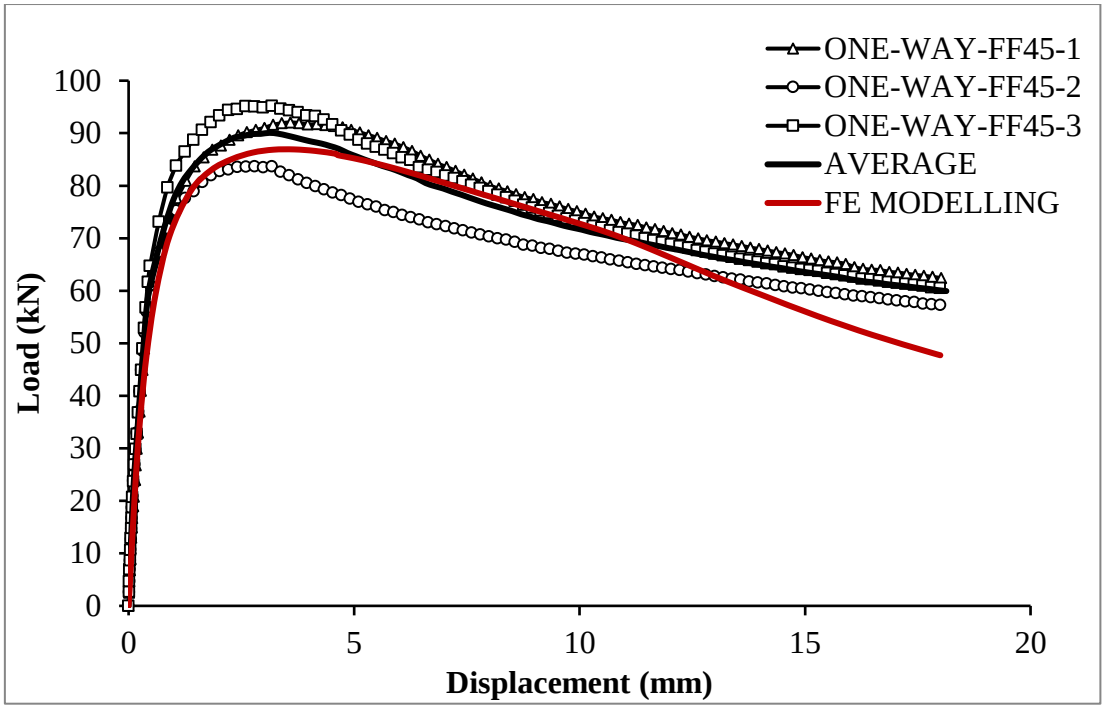

Figure 7.27: Load-displacement curves for FF45 slabs.

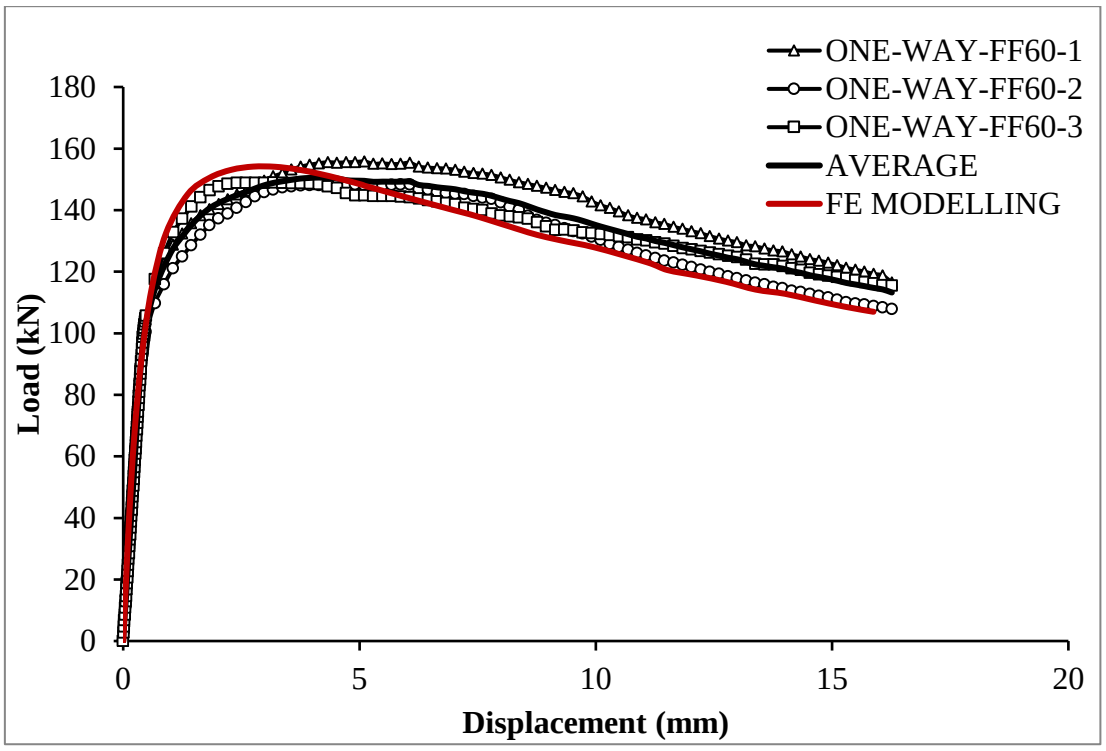

Figure 7.28: Load-displacement curves for FF60 slabs.

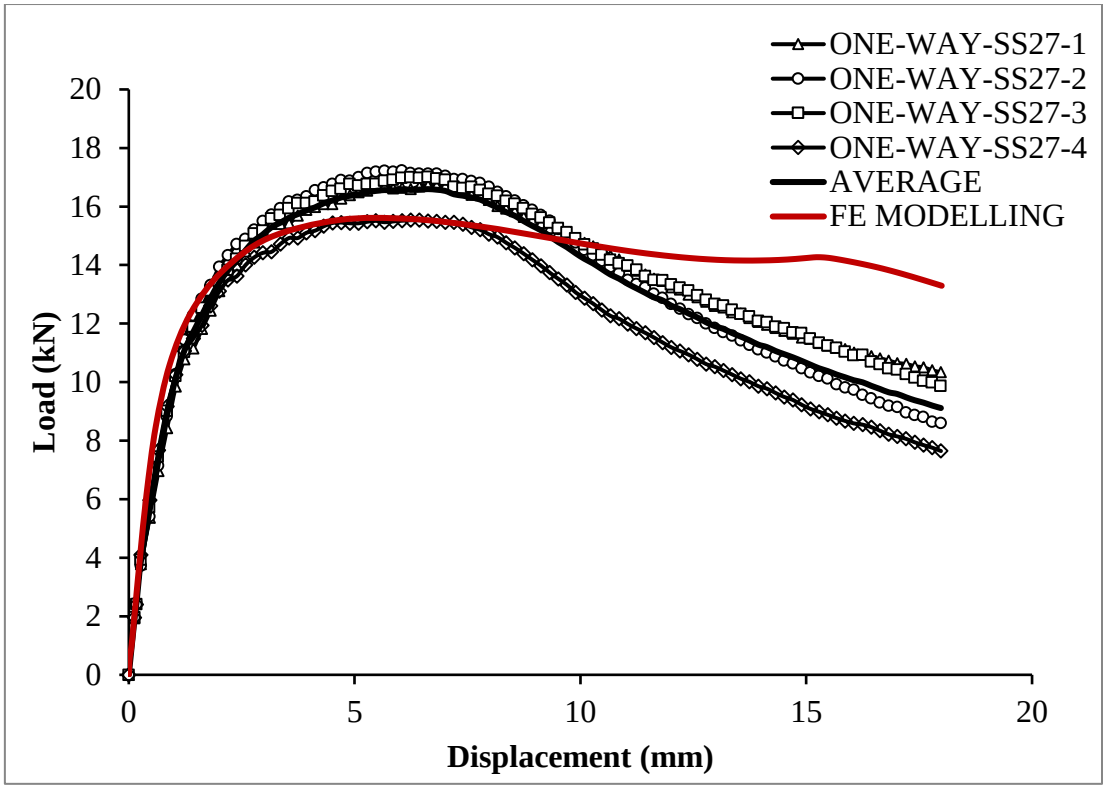

Figure 7.29: Load-displacement curves for SS27 slabs.

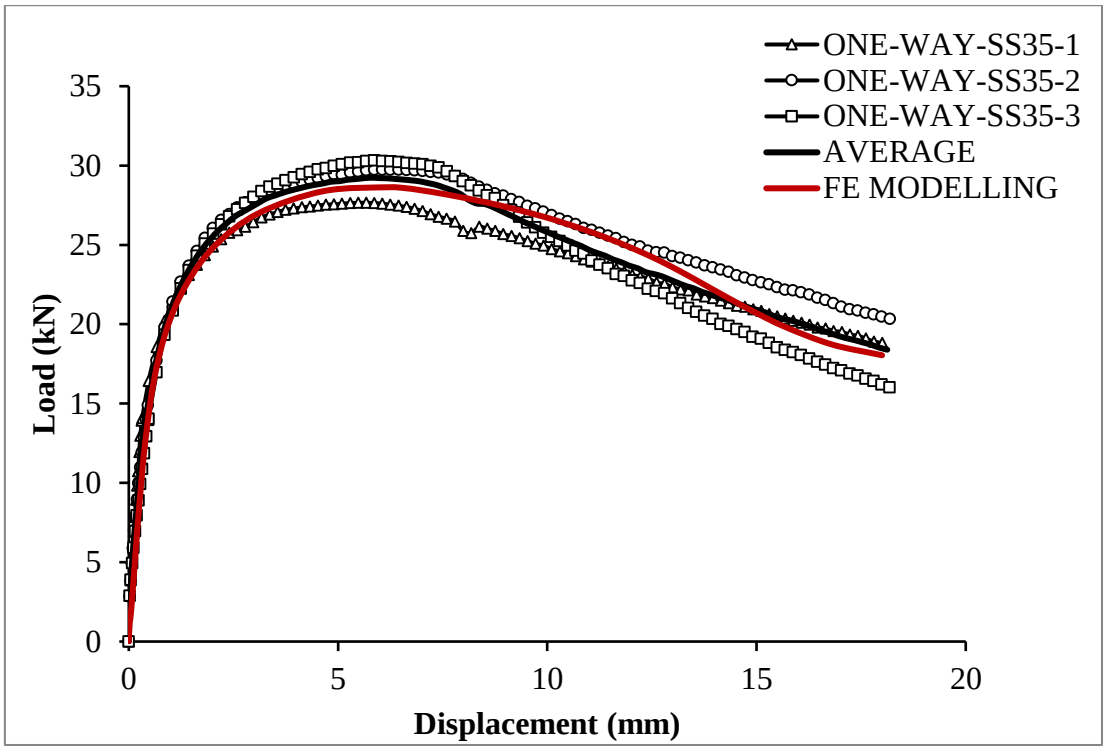

Figure 7.30: Load-displacement curves for SS35 slabs.

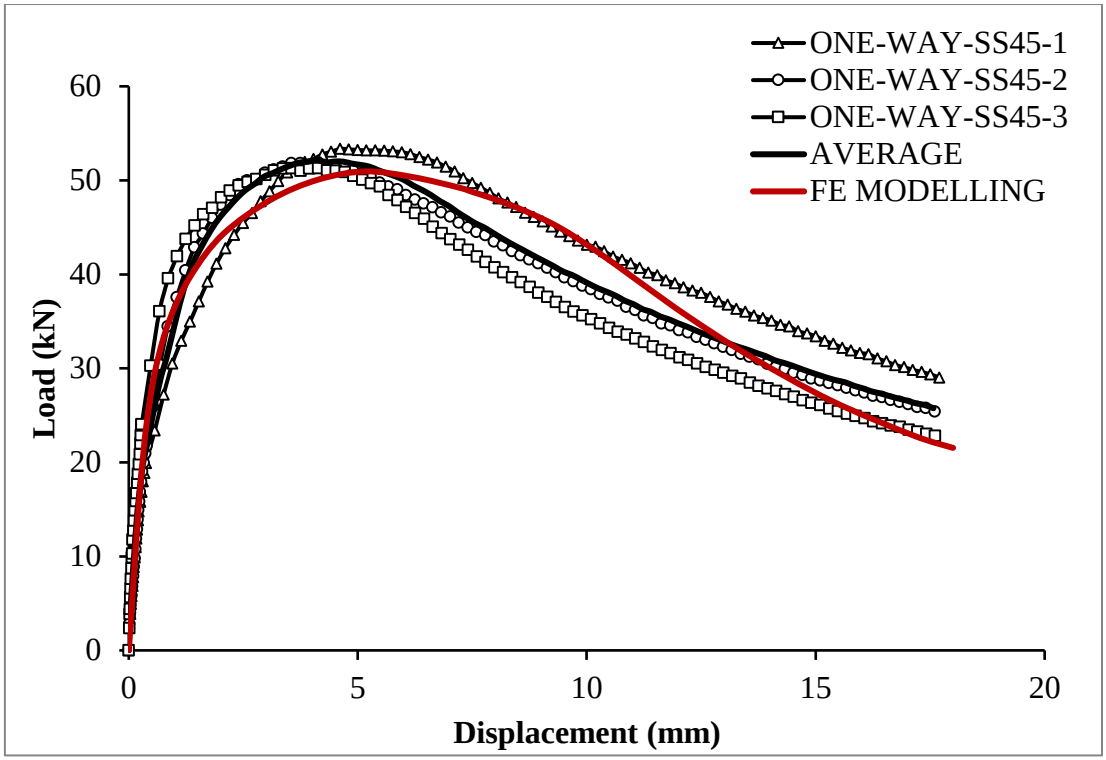

Figure 7.31: Load-displacement curves for SS45 slabs.

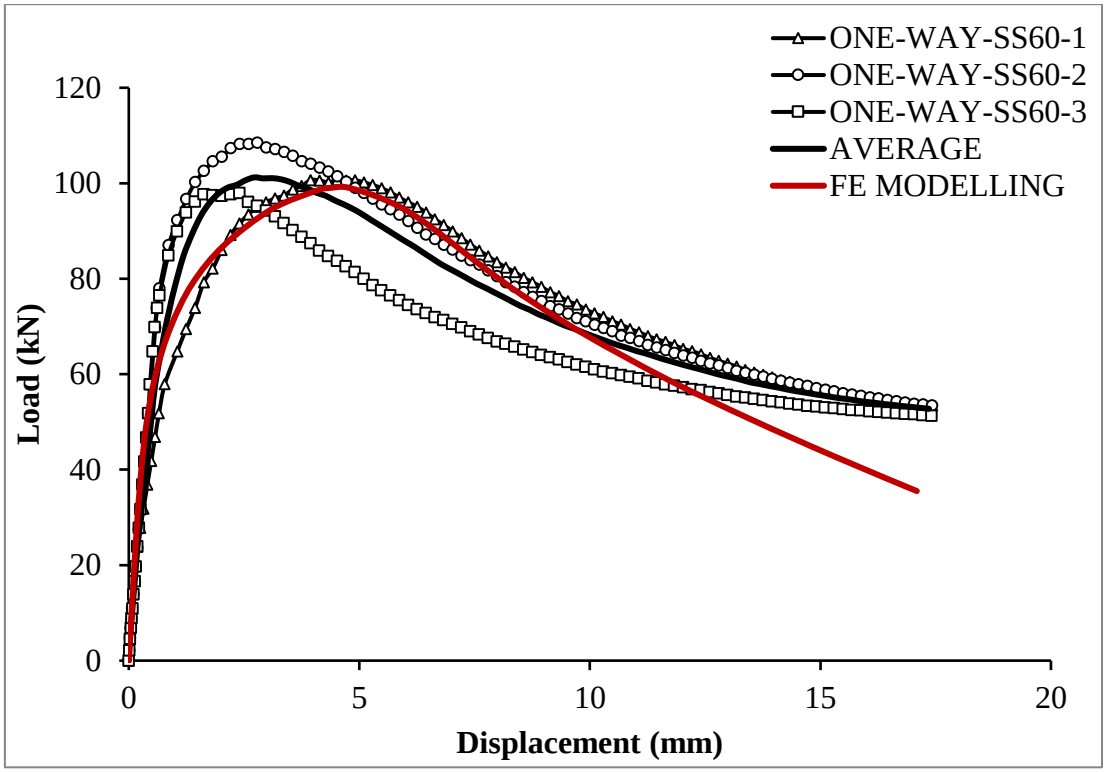

Figure 7.32: Load-displacement curves for SS60 slab

Table 7.2: Slabs experimental results with FF boundary conditions.

Specimens		Experiment				Numerical ultimate load F_{ns} (kN)	Error $(F_s - F_{ns}) / F_s$	Standard Deviation SD/ Error SE (kN)	Coefficient of Variation (CV)
Name	No	Cracking load F_c (kN)	average F_c (kN)	Ultimate load F_s (kN)	average F_s (kN)				
ONE-WAY-FF25	1	6.3	7.4	26.7	24.8	25.7	3.7%	2.0/ 1.0	8.2
	2	7.1		23.1					
	3	8.0		25.0					
	4	8.2		24.0					
ONE-WAY-FF35	1	20.2	21.3	56.1	54.4	52.3	3.9%	0.8/ 0.5	1.5
	2	21.7		54.7					
	3	21.9		54.1					
ONE-WAY-FF45	1	56.1	57.3	92.0	90.3	86.9	3.7%	4.8/ 2.8	5.4
	2	57.8		83.7					
	3	57.9		95.2					
ONE-WAY-FF60	1	85.2	87.4	155.6	150.8	153.2	1.6%	3.4/ 1.9	2.3
	2	87.3		148.3					
	3	89.8		148.4					

Table 7.3: Slabs experimental results with SS boundary conditions.

Specimens		Experiment				Numerical ultimate load F_s (kN)	Error $(F_s - F_{ns})/ F_s$	Standard Deviation SD/ Error SE (kN)	Coefficient of Variation (CV)
Name	No	Cracking load F_c (kN)	average F_c (kN)	Ultimate load F_s (kN)	average F_s (kN)				
ONE-WAY-SS27	1	4.1	4.5	16.6	16.5	15.58	6.2%	1.2/ 0.6	7.6
	2	4.2		17.2					
	3	4.8		16.8					
	4	4.9		15.5					
ONE-WAY-SS35	1	10.1	10.9	27.6	29.1	28.39	2.8%	1.0/ 0.6	3.7
	2	11.0		29.6					
	3	11.8		30.1					
ONE-WAY-SS45	1	19.0	20.0	53.4	52.1	50.95	2.3%	0.9/ 0.5	1.8
	2	19.3		51.5					
	3	21.9		51.3					
ONE-WAY-SS60	1	55.1	57.5	100.6	102.0	99.24	2.7%	4.0/ 2.3	4.0
	2	57.4		107.5					
	3	60.1		97.9					

In terms of design, it is only the linear and strain-hardening behaviour that are of interest and it appears that the discrepancy between the experimental and the numerical results is less than 5% in these regions. This discrepancy increases if the softening behaviour is considered. There is no doubt that the slab thickness has an effect on both the failure modes and load-displacement relationship. This may partly explain the slight discrepancy between the experimental and numerical results in the softening region. Overall, the good agreement between the FE simulations and experimental results presented in this study demonstrates the potential use of the CDP model to give accurate predictions of the behaviour of UHPFRC slabs.

In reality, it would be impossible to capture the exact softening behaviour using a FE simulation for FRC. This is because, as the geometry changes, the position and orientation of fibres change. Furthermore, fibre orientation and distribution may change from one specimen to another. However, having a FE model that can predict reasonable results such as the model in this study, can contribute to the advancement of knowledge in terms of designing UHPFRC, since the material is still very expensive to test.

7.3.3 One-way Slabs Parametric Study

The FE model successfully predicted the structural behaviour in terms of cracking load, ultimate load as well as the failure mode. Therefore, parametric studies were conducted to understand the structural behaviour of the slab as the thickness further increases. Parametric studies were focusing exclusively on linear elastic and nonlinear region up to the ultimate load carrying capacity. The model was used to investigate the influence of the thickness on the cracking and ultimate load. To do this, slabs with both FF and SS boundary conditions with four thicknesses (75, 90, 105, and 120 mm) but with similar geometries were considered. The material properties used for the slab investigation were taken for the parametric studies. The results of these parametric studies are shown in Figure 7.33 and Figure 7.34 for both FF and SS slabs, respectively.

Generally, there was not a significant change in the load-displacement behaviour of the slabs as the thickness increased if compared to the 25 to 60 mm slabs. As expected, when the slab thickness increased, the ultimate load of the member increased. Looking at the analysis results, it can be seen that the elastic regions began to transform to the strain-hardening region as the central displacement reaches around 0.20 mm. However, the

major transformation takes place at a displacement of approximately 0.30 to 0.40 mm for all thicknesses with both FF and SS boundary conditions, as shown in Figure 7.33b-e and Figure 7.34b-e. These results are similar to the results for these thicknesses that are investigated experimentally in this study. Once again the FE analyses confirm the linear elastic behaviour of one-way slabs and it showed that the end of the linear elastic region can be captured accurately. The loads at the end of this region were approximately 132.4, 197.9, 276.8 and 366.2 kN for slabs with FF boundary conditions and 74.2, 114.8, 164.2 and 223.6 kN for slabs with SS boundary conditions, as shown in Table 7.4.

In the experimental study, the FF slab with 60 mm thickness exhibited a 67% increase in the ultimate load compared to the 45 mm thick slab as discussed in Chapter 4, Section 4.2.4. After the parametric studies were carried out, slabs with 75 mm thickness showed that the ultimate load increased to 252.1 kN which gives a 67% increase as illustrated in Table 7.4. Whereas, the ultimate load in slabs with 90 mm thickness was only increased by 32%. Finally, when the slab with thickness of 120 mm was analysed, the ultimate load of 650.4 kN was recorded with an increase of 33% when compared to the 90 mm thick slabs. These results indicated that the percentage increase in the ultimate load reduced significantly as the thickness increased. This trend was also found in the experimental study between thicknesses of 25 and 60 mm.

As discussed in Chapter 4, Section 4.2.4, the ultimate load in slabs with the SS boundary conditions increased by 96% when the slab thickness increased from 45 mm to 60 mm. The parametric study results shown in Table 7.4, illustrate that the ultimate load of the 75 mm thick slab was 171.1 kN and increased by 68% compared to the 60 mm thick slabs. When the 90 mm thick slab was studied, the result showed an increase in the ultimate load was 57%, whereas, the increase was only 30% for the 105 mm thick slab. After the final thickness was analysed, the ultimate load of 482.5 kN was achieved. This gives an increase of 38% when compared to the 105 mm thick slabs. Similar to the FF slabs, a significant reduction in the percentage increase of the ultimate load could be seen in the SS slabs. However, it is important to mention that the values illustrated in Table 7.4, were chosen based on the transformation from the strain hardening region to the strain softening region rather than the highest point along the curves.

As expected, the results showed that the fibre pull-out load increased with the increase in the thickness but the percentage increases in the SS slabs was not as significant as for the

FF slabs. Furthermore, as explained in Section 4.2.3, experimental work showed that the fibre pull-out behaviour in thick slabs (45 and 60 mm) occurred at smaller displacements of 3 to 4.5 mm compared to thin slabs (25 and 35 mm) of approximately 5 mm. This was due to the large space in the matrix allowing fibre to position more randomly, thus the possibility of less fibre bridging was seen in slabs in both FF and SS boundary conditions.

Although, the model does not consider fibre randomness, it includes parameters such as tension stiffening, tension damage and compression hardening in order to capture the true trend of the load-displacement curve based on the damaged elastic modulus calculated by the model. The behaviour of the load-displacement curve captured in the model was based on the geometry and changes as the thickness changes. Changes in the structure geometry result in different stress distributions in the localised area (crack area) and changes in the element original shape. As the element changes its original shape, the model produces a new elastic modulus based on the parameter d_t as shown in Equation 7.1. As detailed in Chapter 6, the degradation damage is calculated according to the stress value within the damaged elements, thus a new elastic modulus is calculated. Moreover, the tension stiffening and compression hardening purpose were to capture the fibre pull-out action as the structure goes beyond the elastic region. Therefore, the behaviour of thick slabs can be captured by the FE model accurately. This confirmed and agreed with the experimental data that thick slabs reached the ultimate load at smaller displacements compared to thin slabs. The results of parametric studies for the larger thicknesses are shown in Table 7.4. The FE results also showed that the displacement for the ultimate load was reduced to as low as 2.2 mm when the 120 mm slab was studied. Therefore, in one-way UHPFRC slab designs, especially in bridge decks, it is essential to consider the influence of geometry on ultimate load behaviour. The parametric study showed that the FE model can be used to capture the structural behaviour of one-way slabs with different geometries and it can be used for evaluating the design standard of UHPFRC members. However, experiments with sizes similar to the parametric study need to be carried out in order to affirm the conclusions regarding the effect of slab thickness on the cracking and ultimate load carrying capacity.

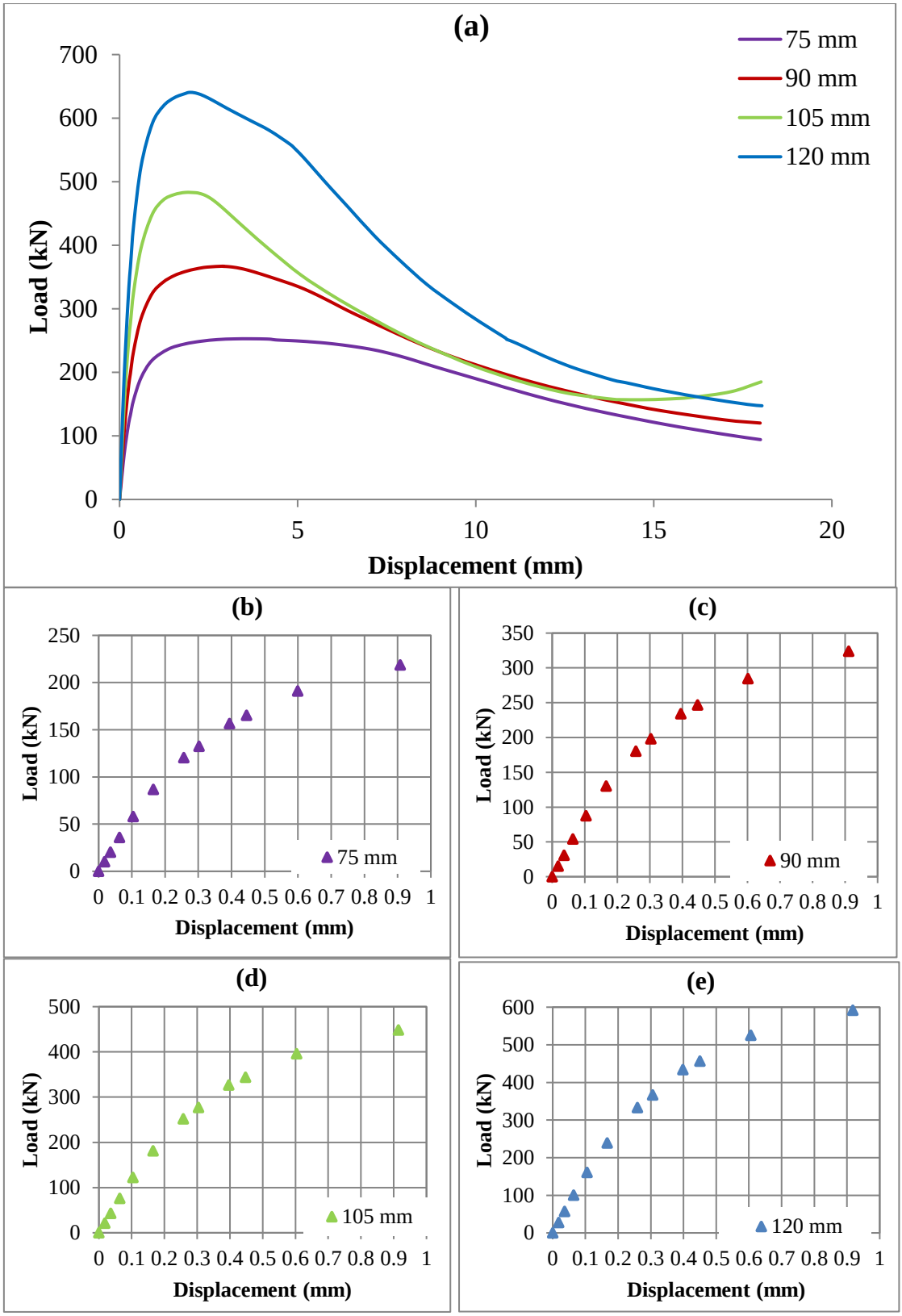

Figure 7.33: Parametric study of FF two-way slabs.

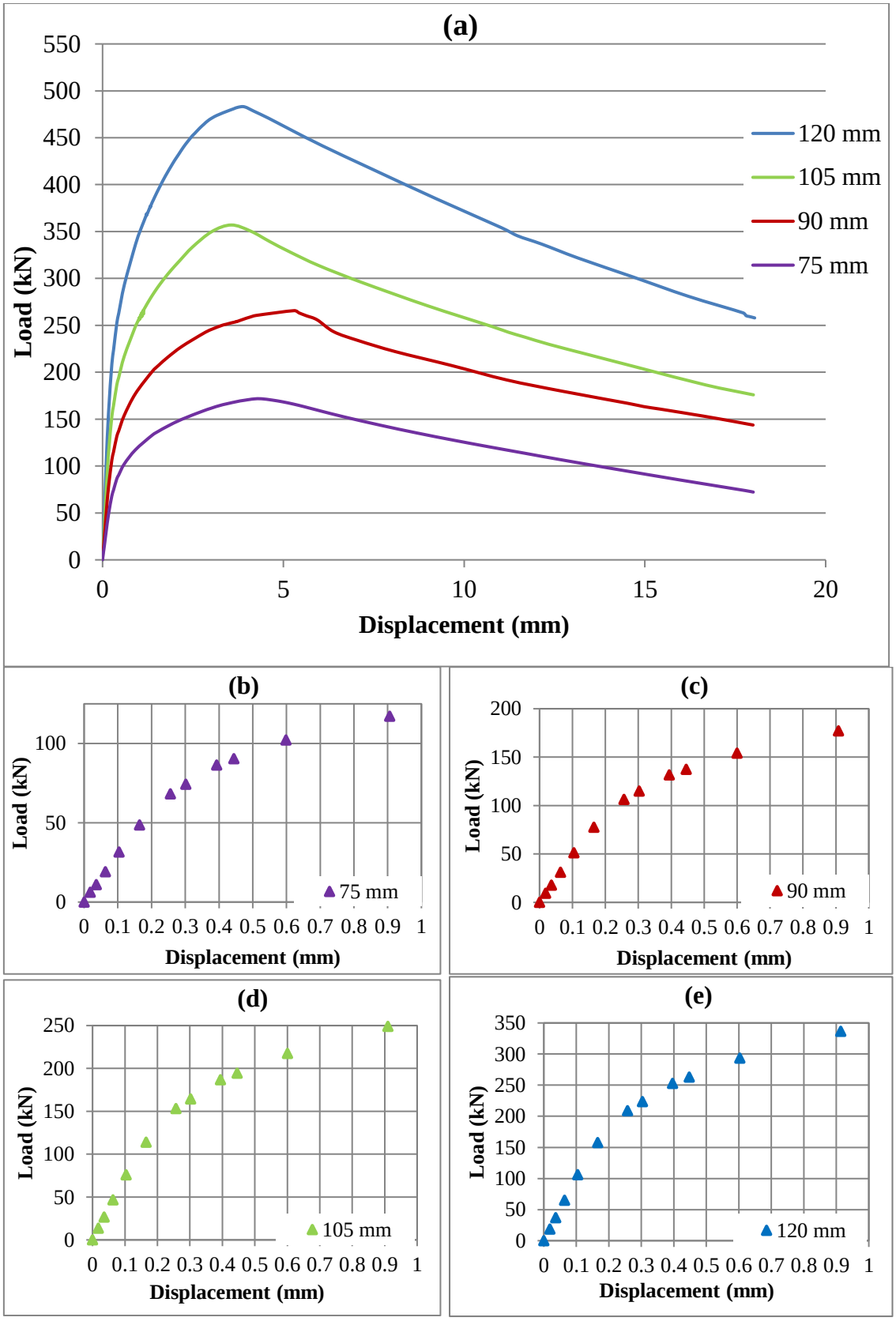

Figure 7.34: Parametric study of SS one-way slabs.

Table 7.4: Parametric results for both FF and SS one-way slabs.

Thickness (mm)	Fully fixed			Simply supported		
	Linear elastic load (kN)	End of strain-hardening		Linear elastic load (kN)	End of strain-hardening	
		Ultimate load (F_{ns}) (kN)	Displacement w_{ns} (mm)		Ultimate load (F_{ns}) (kN)	Displacement w_{ns} (mm)
75	132.4	252.1	3.2	74.2	171.6	4.2
90	197.9	367.1	3.0	114.8	270.4	4.7
105	276.8	482.5	2.2	164.2	350.7	4.1
120	366.2	640.4	2.0	223.6	482.5	3.9

7.4 Comparison of Results of Two-way Slabs

The results of the numerical model developed in Chapter 6 for two-way slabs are presented in this section. These results are compared to corresponding experimental data provided in Chapter 5, to validate the FE analysis in terms of failure mode, load-displacement relationships and crack patterns. The capacity of the model to capture the structural behaviour of two-way slabs with different geometry and boundary conditions is evaluated. The developed FE model was then used to conduct parametric studies for slabs with larger thicknesses.

7.4.1 Failure Modes

During the experiments, the loads were applied using displacement control subjected to a static loading in both the FF and SS series. To ensure that the static condition was also met in the numerical analyses, the reaction forces, stresses, deflection and plastic strain were set as output items. After the model was completed, as expected the numerical analysis was unable to simulate the failure modes (tensile cracks) of the two-way slabs described in Chapter 5. This is a limitation of the homogenous models adopted in this study, and can only be simulated by those models considering the random heterogeneity (Su et. al., 2011) or those where the crack position is known in advance (Meda and Plizzari, 2004). As explained in Section 7.2.1, due to the limitation of the CDP model, the physical cracks cannot be obtained. However, it is capable of showing the stress distribution for both FF and SS boundary conditions as shown in Figure 7.35 and Figure

7.36, respectively. The figures show that the stress distribution is similar for all the FF slabs and that two plastic hinges form in each side of the support. The plastic hinges form at the support and centre of the slab and the stress concentration is highest in these areas. The model appears to capture the failure mode of the slabs reasonably with both boundary conditions. As expected, the high stress concentration occurred at the slab centre for both FF and SS slabs and this behaviour was confirmed in the model. However, as mentioned in Chapter 5, despite taking all these measures for ensuring the fixity of the support edges with the FF boundary conditions, the results of some of the thick slabs (45 and 60 mm) indicate that the stiffness of the support edges may have varied. This resulted in the formation of more than four macrocracks in some of the thick specimens with FF boundary conditions. To investigate this further, a different boundary stiffness was applied to the edges that were resting on the steel frame only, as shown in Figure 7.37.

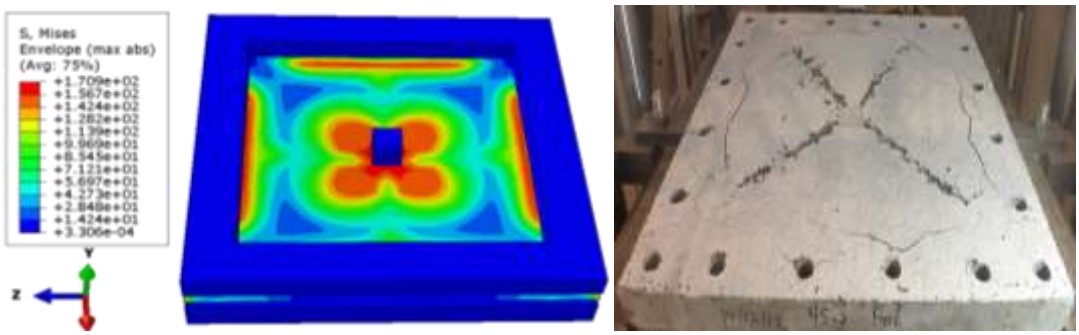

Figure 7.35: Stress contours against experimental failure mode for the 45 mm two-way slabs with FF boundary conditions.

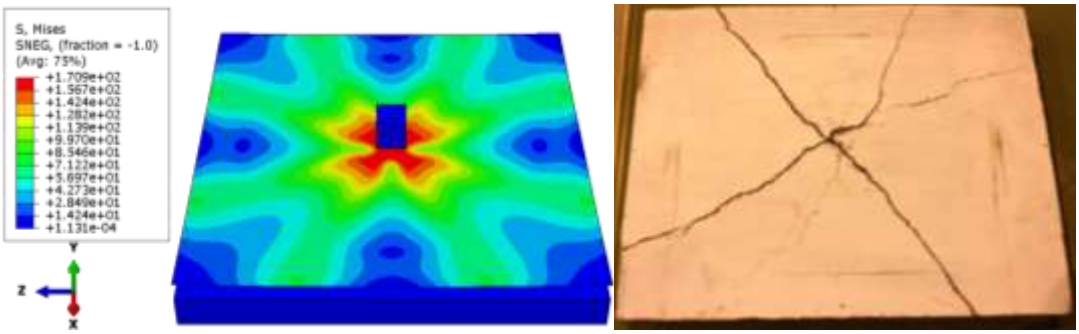

Figure 7.36: Stress contours against experimental failure mode for the 45 mm two-way slabs with SS boundary conditions.

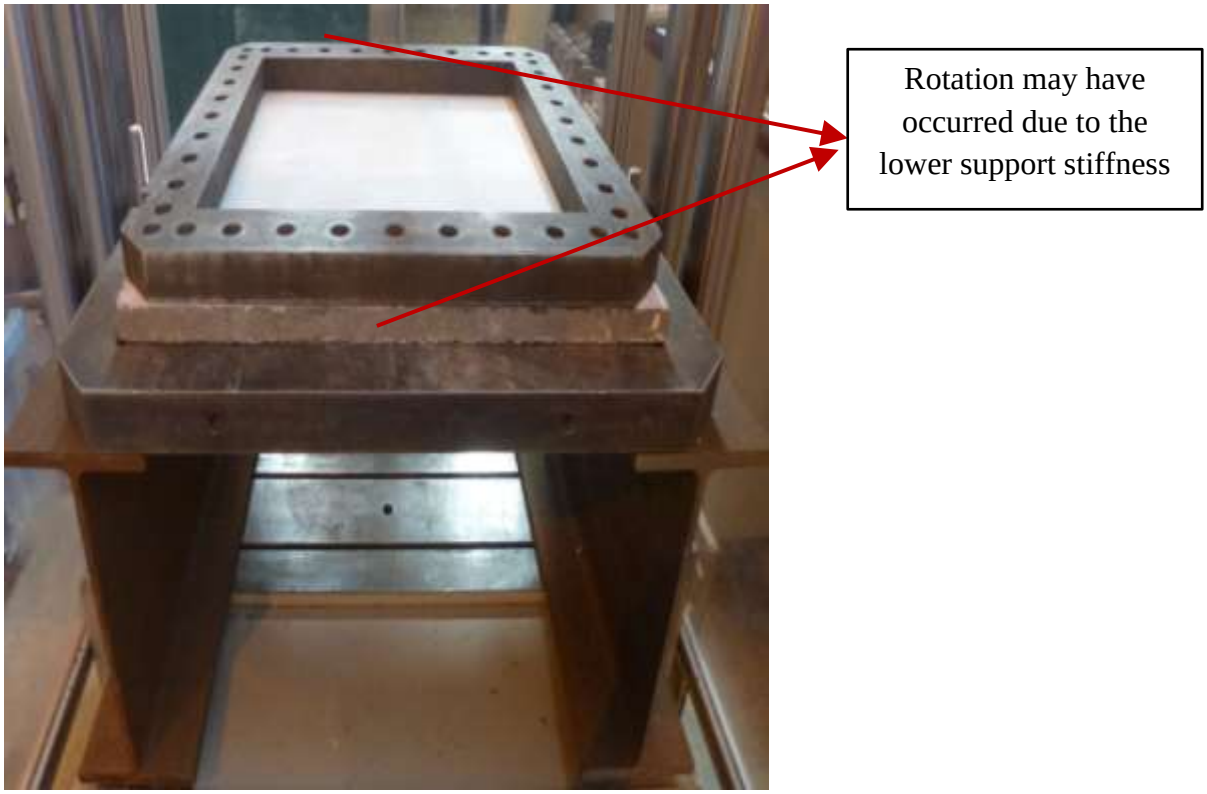

Figure 7.37: Variation of support stiffness for FF boundary condition slabs.

As mentioned, despite the limitation of CDP to reproduce the physical cracks, the location of crack formation can be obtained using PE contour lines. Similar to the one-way slabs, it can be seen that the model reasonably shows the approximate crack locations in both FF and SS boundary conditions as shown Figure 7.38 and Figure 7.39, respectively. Furthermore, during the experiment, compressive cracks in slabs with FF boundary conditions appeared at the centre of the slab edges and extended towards the corner, where this behaviour was confirmed in the FE analyses, as shown in Figure 7.38a. However, as the cracks in two-way slabs became highly complex and the number of cracks changes from one thickness to another, the model became limited in capturing the experimental behaviour. Therefore, a further investigation of two-way slabs using discrete modelling which is beyond the scope of this study, is recommended in the future studies when all the required parameters for such a model become available.

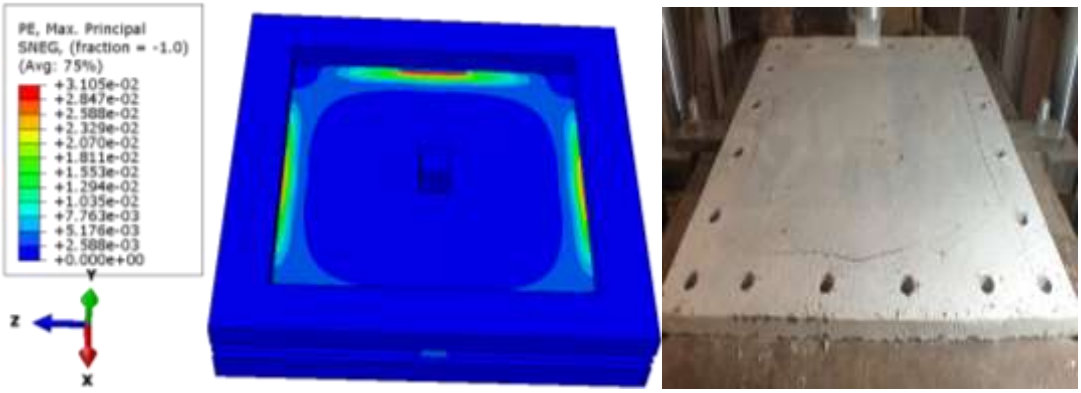

(a) FE and experimental top face

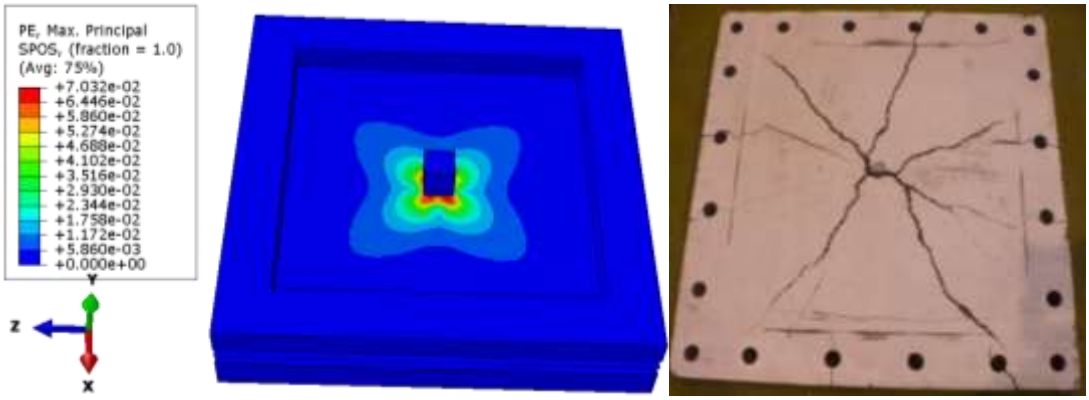

(b) FE and experimental bottom face.

Figure 7.38: Damage result for 45 mm two-way slab with FF boundary condition.

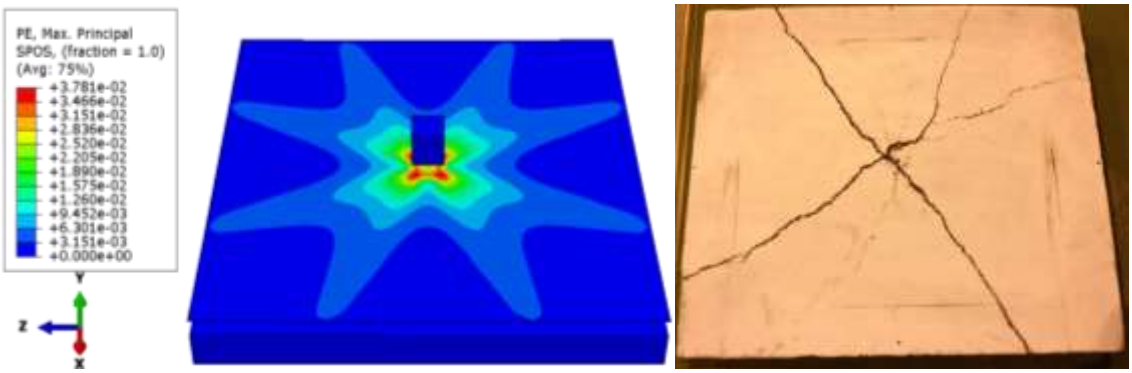

Figure 7.39: Damage result for 45 mm one-way slab with SS boundary condition.

Similar to the one-way slabs, during the experiments, the corner of the slabs with the SS boundary condition rotated in the opposite direction to the load and this rotation was significant compared to the slab's overall central deformation. No rotation was recorded for slabs with FF boundary conditions. The FE analysis using the CDP model confirmed this, thus the complete slab for FF45 and SS45 was modelled to demonstrate this (as shown in Figure 7.40.

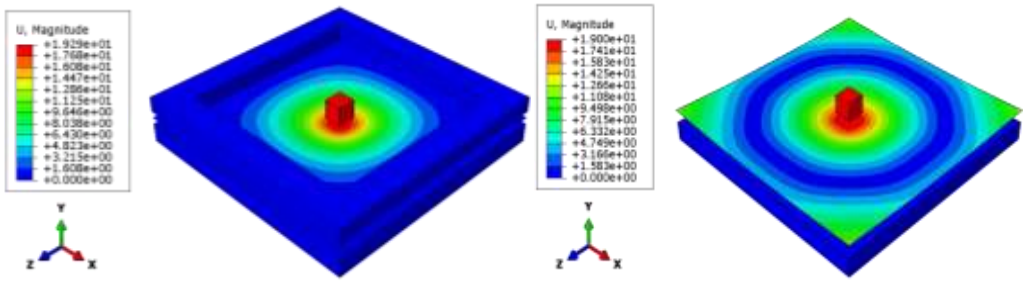

(a) FF boundary condition (b) SS boundary condition

Figure 7.40: Deformation of two-way slabs.

7.4.2 Support Sensitivity Analysis

As mentioned previously, using dial gauges during the experiments confirmed that negligible rotation had occurred at the supports. However, the minimum reading that the dial gauges could record was 1 mm. Therefore, there is a possibility that the two edges which were resting on the steel frame only, as shown Figure 7.37, might have rotated by less than 1 mm during the slab testing. This is particularly possible for two-way thick slabs (45 and 60 mm) with FF boundary conditions. This resulted in a variation in boundary condition stiffnesses with lower stiffness in two edges compared to the other two. To replicate this behaviour, different stiffnesses were applied to the two edges which were believed to have rotated during the slab testing. In total, four different stiffnesses were investigated. In the first and second attempts, the edges were allowed to rotate by 0.25 and 0.5 mm, respectively. While, in the third and fourth attempts, the edges were allowed to rotate by 0.75 and 1 mm, respectively. The weaker edges were applied to the edges that were rotating around the z-axis, while the other two edges which were rotating in the x-axis were fixed.

Since, the 60 mm thick slabs carried the highest load compared to other slabs, this size was used in the CDP model investigation. The results of all four cases of different stiffnesses are shown in Figure 7.41. Due to the allowance of rotations at two of the edges, instabilities developed in the course of the step when the 1 mm case was investigated. Instabilities in nonlinear static problems can be due to the geometrical nature of the problem or material nature, such as material softening (ABAQUS, 2013) as was the case in this study. The instability causes the local transfer of strain energy from one part of the model to neighbouring parts (for example, from the slab to the support plates), and global solution methods are no longer applicable. This issue has to be solved either dynamically or with the aid of (artificial) damping. ABAQUS/Standard provides a solution using an automatic mechanism to stabilise the problem through the automatic addition of volume-proportional damping to the model. The applied damping factors can change with time to account for changes over the duration of the step or they can be constant throughout the step. Three solutions are provided to solve the instability in ABAQUS/ Standard and these are: (a) calculating the damping factor based on the dissipated energy fraction, (b) directly specifying the damping factor, and (c) using the damping factor from the previous general step. Using the trial and error investigation, it was found using a default value of damping factor of 0.0002 stabilised the model. Therefore, the default value was used in all four cases. In addition, to ensure that the slab in the model behaved in a similar way to how it may have occurred during the experiment, the top plate and the slab top face were constrained using the surface-to-surface tie option tool, to ensure that the top plates were rotating as the two edges of the slab rotate around the z-axis during the analysis.

Looking at Figure 7.41, it can be seen that the rotation has a slight effect on the stress distribution within the slab. Stress at the slab centre covered a wider area compared to the result for the fully fixed slab in Figure 7.35. It also appears that the stress at the top face of the slab adjacent to the weaker edges becomes more dominant as the edge rotation was increased. For instance, looking at Figure 7.41a, it can be seen that the stress contours for the 1 mm case was less apparent when compared to the stress contours for the 0.25 mm case in Figure 7.41d. In general, the reduction in support stiffness has a small effect on the crack propagation and cracking in the slab which began at the slab centre where the load was acting, progressed towards the corner of the slab. The diagonal cracks were consistent in all the cases, showing four major cracks at the location where cracks formed during the experiments. In spite of using different boundary stiffnesses, the model was

not able to reproduce the six cracks which occurred in some of the two-way slabs with FF boundary condition. As mentioned previously, this is the limitation of the model in capturing the failure mode of two slabs especially with FF boundary conditions. Therefore, it is recommended that further research is needed to develop a model such as the heterogeneous model which can capture the failure mode of two-way slabs better. However, to obtain all the requirement parameters for such a model, further experimental works, such as single fibre pull-out testing and X-ray computed tomography scans are essential. These testing would allow the user to obtain 3D images to build FE models so that the realistic microstructures of the UHPFRC are modelled, hence failure modes might be better captured. In addition, further testing of two-way slabs with FF boundary conditions similar to the thick slabs tested in this study and slabs with greater thickness are recommended to better understand the failure mode of two-way slabs.

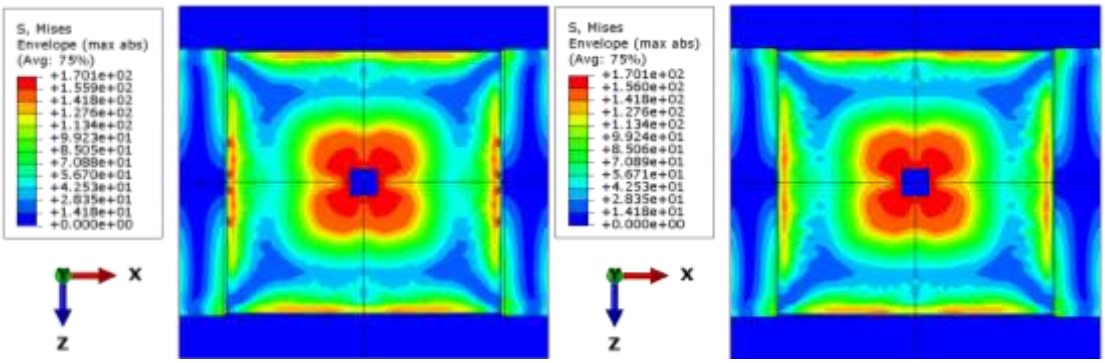

(a) allowing for 1 mm displacement (b) allowing 0.75 mm displacement

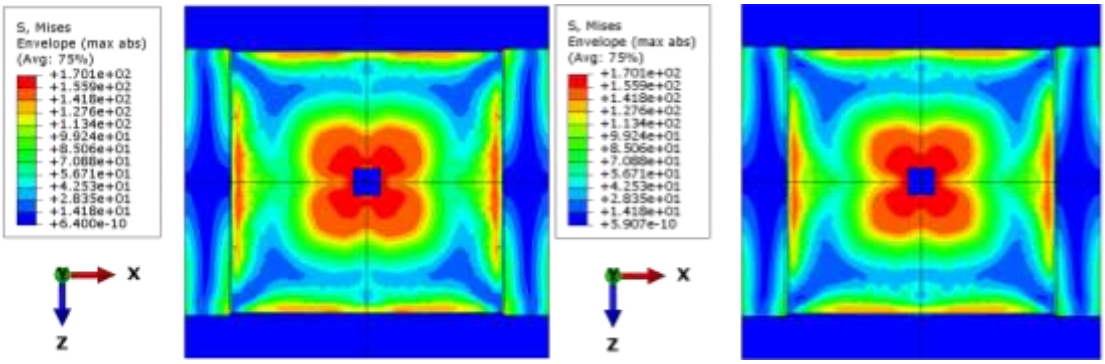

(c) allowing 0.5 mm displacement (d) allowing 0.25 mm displacement

Figure 7.41: Crack propagation of 60 mm two-way slabs with different stiffness.

7.4.3 Load-displacement curves

In order to present the numerically determined load-displacement relationships, the reaction force and displacement at the slab centre were determined. The load was taken as the vertical reaction, which was generated based on the applied load on the UHPFRC slabs. The displacement was taken at the node where it was measured in the experiment. After all the models were run, the three and four load–displacement curves for all the specimens from the bending tests and the average curve are compared with the CDP-based numerical results in Figure 7.42 to 7.45 for FF boundary conditions and Figure 7.46 to 7.49 for SS boundary conditions, respectively, for each slab thickness.

The load-displacement relationships in the linear elastic region in both the FF and SS series were accurately captured by the numerical simulation. A considerable sudden change at the end of the elastic region can be seen in the experiment curves for thick slabs in FF boundary conditions compared to SS boundary conditions. This has caused a small discrepancy between the numerical and experimental results in pseudo-strain hardening region in slabs with 45 and 60 mm thick with FF boundary conditions. This sudden change could be due to the differences in the number of cracks in thin slabs (25 and 35) mm compared to thick slabs (45 and 60) mm.

As explained for one-way slabs, the no cracking condition at the SLS, which does not allow for any cracking to occur, proposed by (AFGC, 2002) may be conservative. Looking at the two-way slabs test results, similar to the one-way slabs, the cracking load occurs at a very small displacement as shown in Table 7.5 for FF and Table 7.6 for SS boundary conditions. For slabs with FF boundary conditions, the load to cause microcracking for the 25 mm slabs, ranged from 10 to 11 kN which are considerably lower than the ultimate loads that ranged from 31 to 35 kN as shown in Table 7.5. Similarly for the 35 mm slabs, microcracks started to appear when the load reached approximately 19 to 21 kN. These loads are also considerably smaller when compared to the ultimate load that ranged from 71 to 73 kN as shown in Table 7.5. A similar behaviour is also noticed for both 45 and 60 mm slabs and the cracking load ranged from 46 to 48 kN and 76 to 79 kN while the ultimate loads were 115 to 119 kN and 185 to 211 kN, respectively.

The difference between the first cracking load and the ultimate load is also observed for two-way slabs with SS boundary conditions. The load to cause the appearance of

microcracks for the 25 and 35 mm slabs ranged approximately from 5 to 7 kN and 13 to 14 kN, respectively. The ultimate loads were 20 to 22 kN for 25 mm slabs and 43 to 45 kN for 35 mm slabs as shown in Table 7.6. For thick slabs (45 and 60 mm), the recorded cracking loads were 30 to 31 kN and 65 to 68 kN, respectively. Similarly, the ultimate loads were significantly greater and ranged from 73 to 82 kN for 45 mm slabs and 141 to 143 kN for 60 mm slabs as shown in Table 7.6. This again demonstrates that the SLS criterion proposed by AFGC, may be conservative for designing a UHPFRC slab. The difference between the first cracking load and the ultimate load in two-way slabs was also significant and ranged from 52% to 70% for the two-way slab thicknesses. Therefore, further tests are needed to better understand the crack behaviour of UHPFRC as the no cracking criterion proposed by AFGC is conservative

Moreover, a considerable variation in the strain-hardening region can be seen in slabs with the same thickness in the experimental results. As explained in Chapter 5, this is due to the change of fibre-bridging in the cracked areas in slabs with larger thicknesses, allowing fibres in the matrix being more randomly distributed. In other words, controlling fibre distribution and orientation in the fibre concrete is impossible and the behaviour of load-displacement curves is significantly dependent on the amount of fibres in the cracked area. However, this variation in the nonlinear stage of UHPFRC is not something new. Concrete has also been known to have a considerable variation in nonlinear behaviour. Moreover, the variation in the strain-hardening stage can become a further concern when it comes to fibre concrete and this is due to the randomness of the fibres within the matrix. Therefore, it is recommend to adopt a mixing procedure which can control and ensure the uniform fibre distribution within the matrix as well as the allowance of variation of at least 10%. It is also important to mention that this recommendation is based on the mix design and procedure used in this study. Nevertheless, further experiments with larger slabs such as full-sized structures have to be tested in order to adopt the recommendation in design.

The F_s and F_{ns} for each slab specimen with experimental averages for both FF and SS boundary conditions are given in Table 7.5 and Table 7.6, respectively. The CDP model compared well with the experiment and, except for the TWO-WAY-FF60 slab which gave 7% error, the errors between the average of the experimental F_s and the numerical F_{ns} results are less than 3%. In the analysis, the strain-hardening and softening behaviour

is controlled by the properties introduced in the model, thus it would not be surprising if some scatter was observed in the nonlinear regions, especially in the thicker slabs.

Furthermore, except for TWO-WAY-FF60 slab, the SD of the F_s is less than 4 kN and this gives a SE of less than 2.5 kN. The CV indicates that there is little fluctuation in the ranges from 1.3% to 9.6% in the ratio of the experimental values to the average value and confirms the accuracy of the experiments. Similarly for the one-way slabs, it is suggested that the variation of 10% in the F_s needs to be considered in designing both thin UHPFRC slabs ($t < 3l_f$) such as 25 and 35 mm and thick UHPFRC slabs ($t > 3l_f$) such as 45 and 60 mm when the ultimate load is considered.

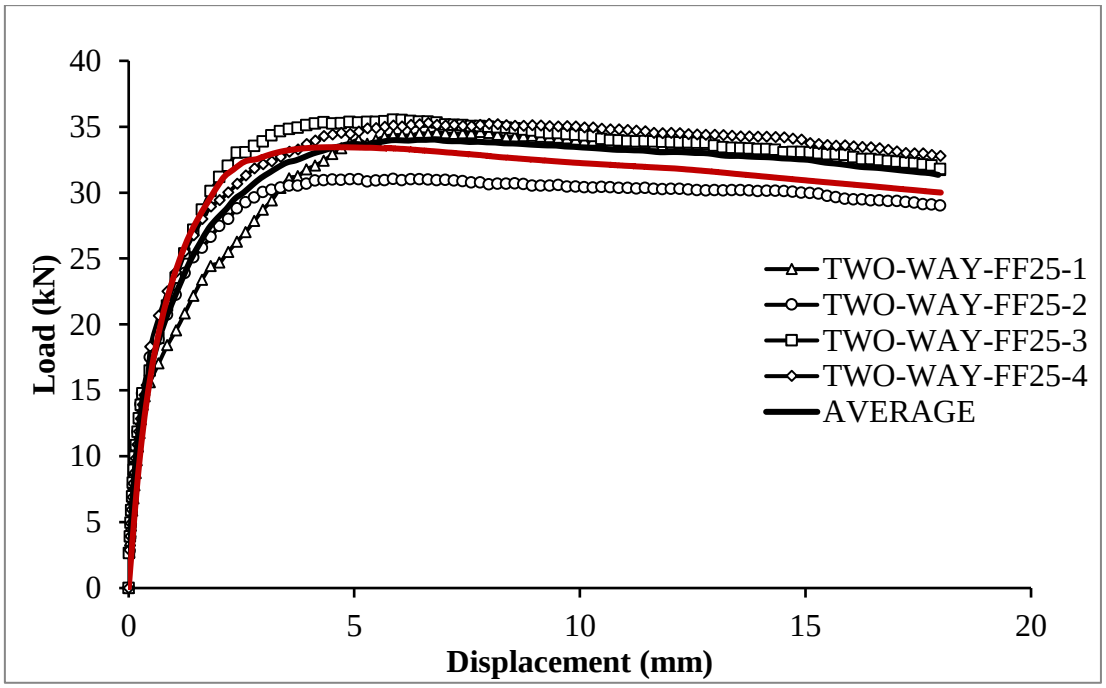

Figure 7.42: Load-displacement curves for FF25 slabs.

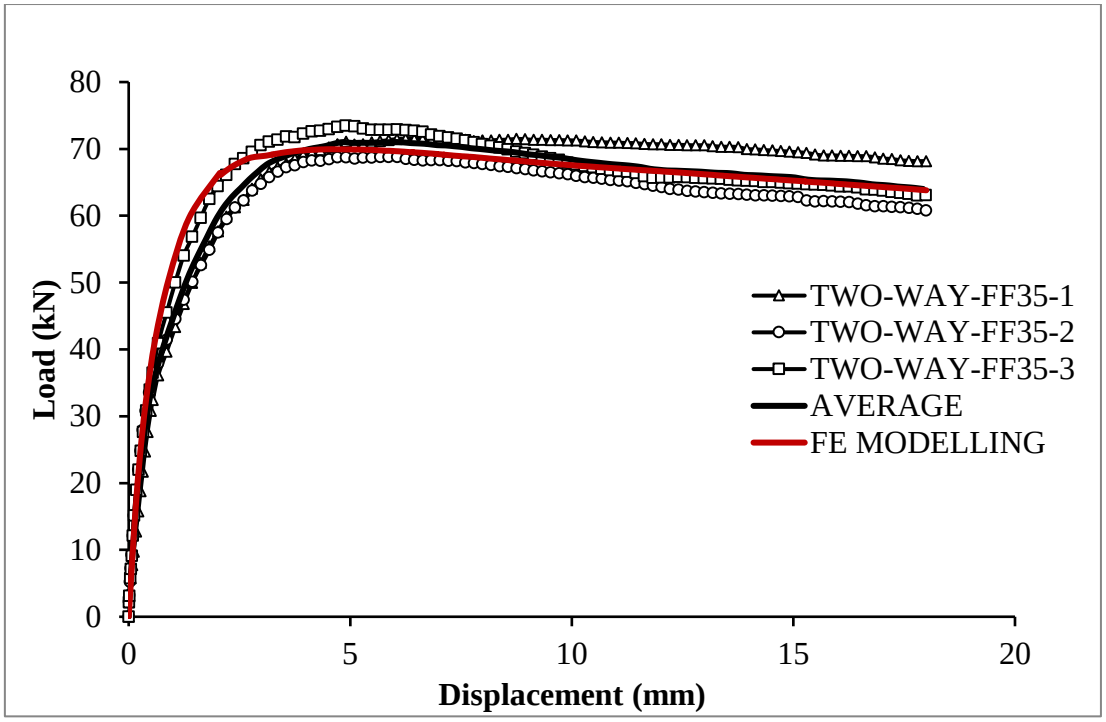

Figure 7.43: Load-displacement curves for FF35 slabs.

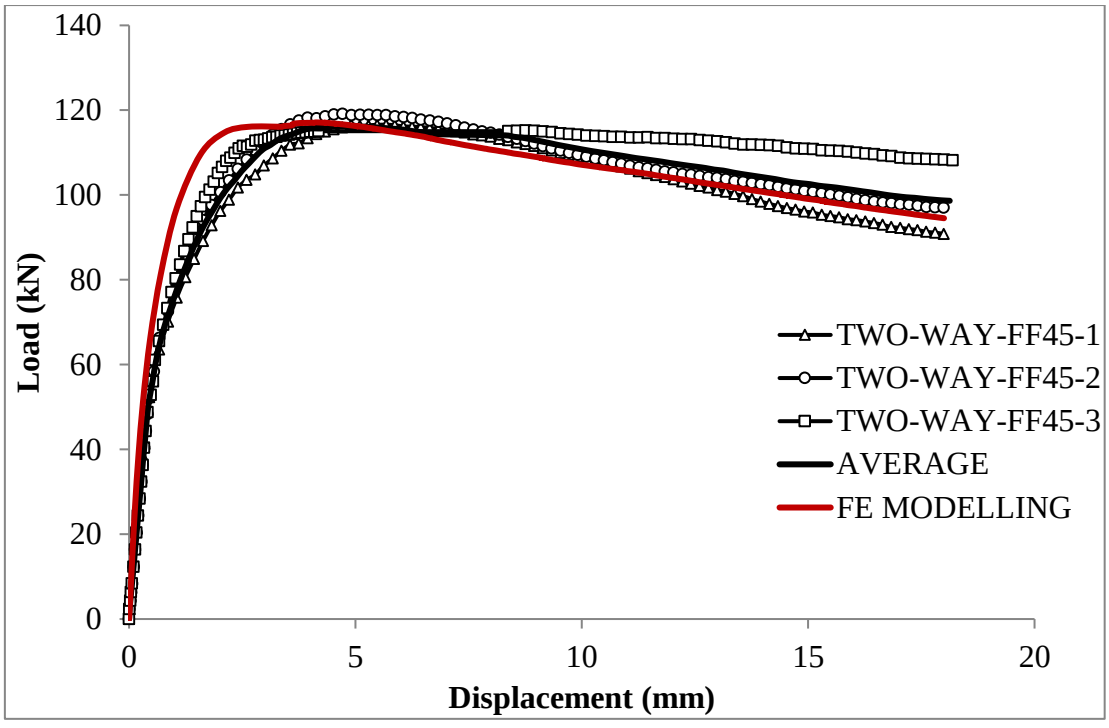

Figure 7.44: Load-displacement curves for FF45 slabs.

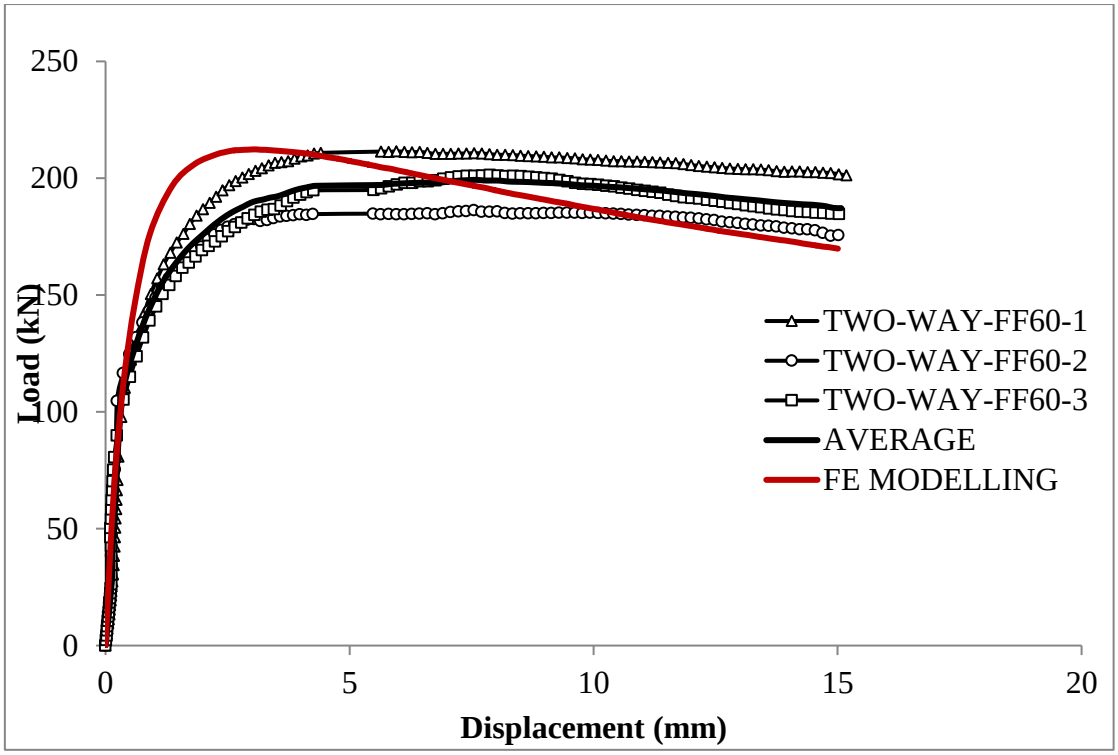

Figure 7.45: Load-displacement curves for FF60 slabs.

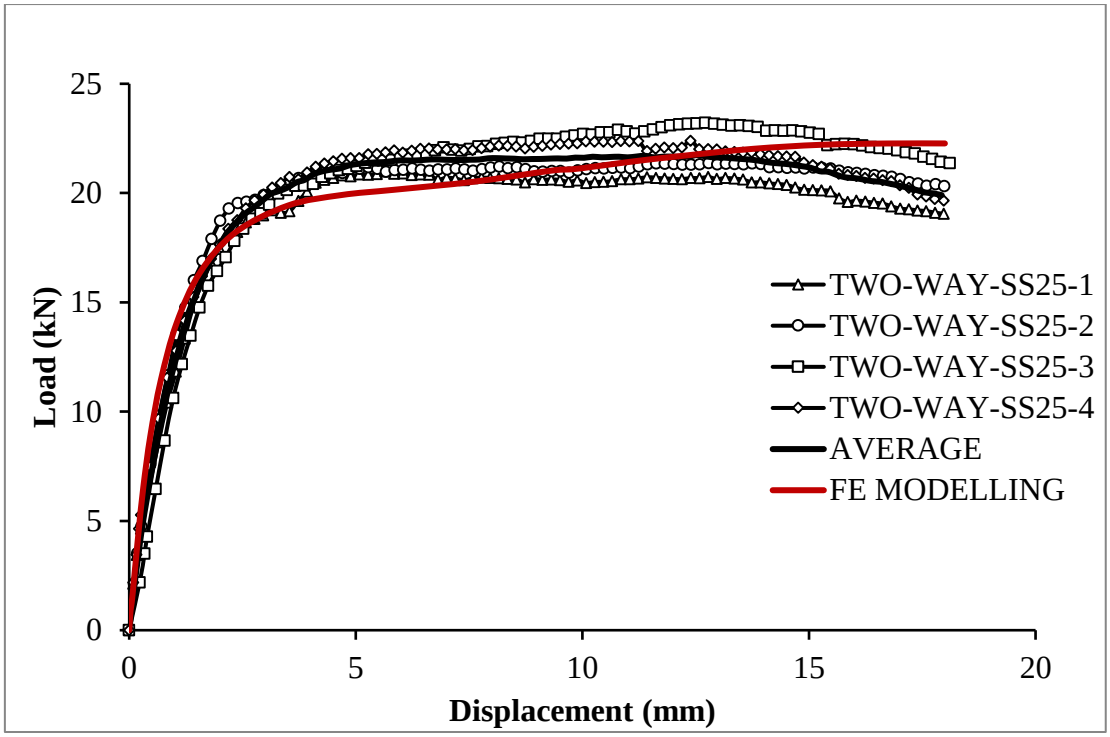

Figure 7.46: Load-displacement curves for SS27 slabs.

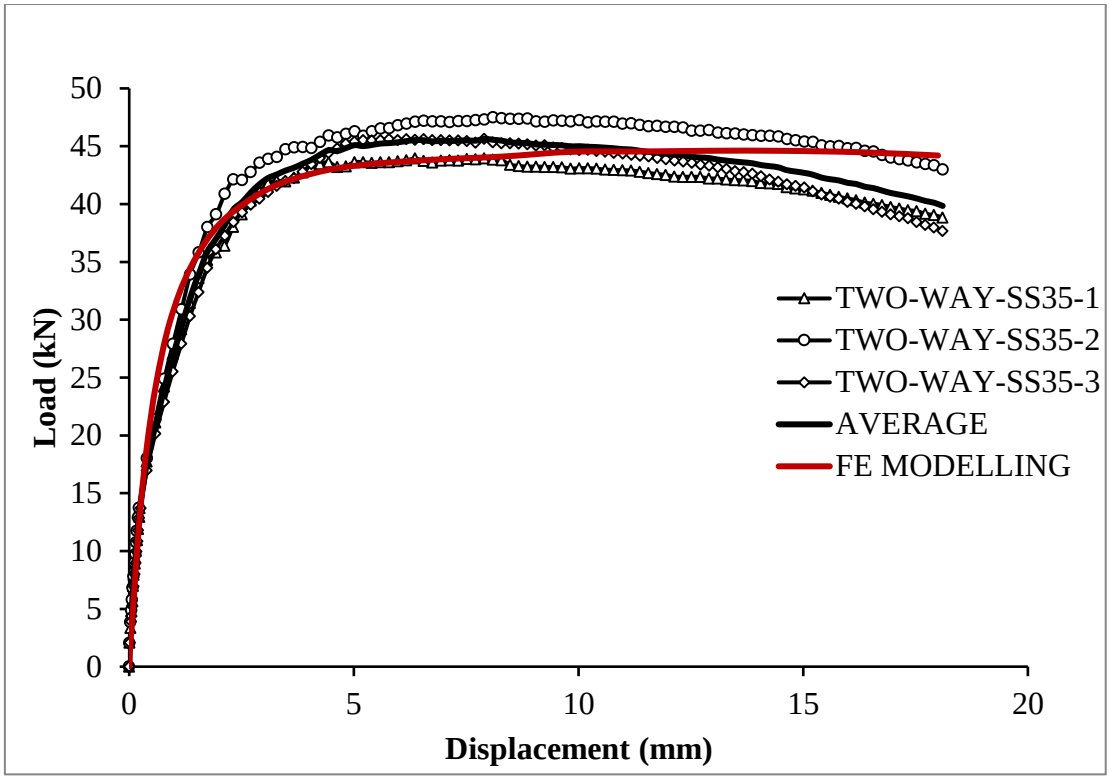

Figure 7.47: Load-displacement curves for SS35 slabs.

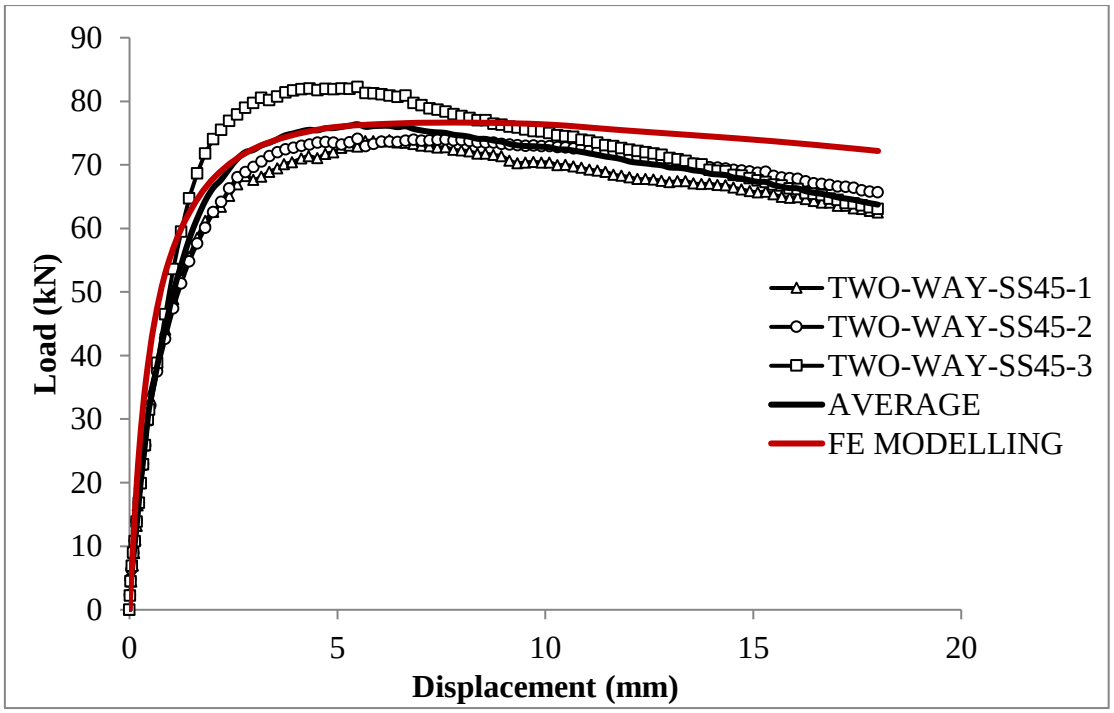

Figure 7.48: Load-displacement curves for SS45 slabs.

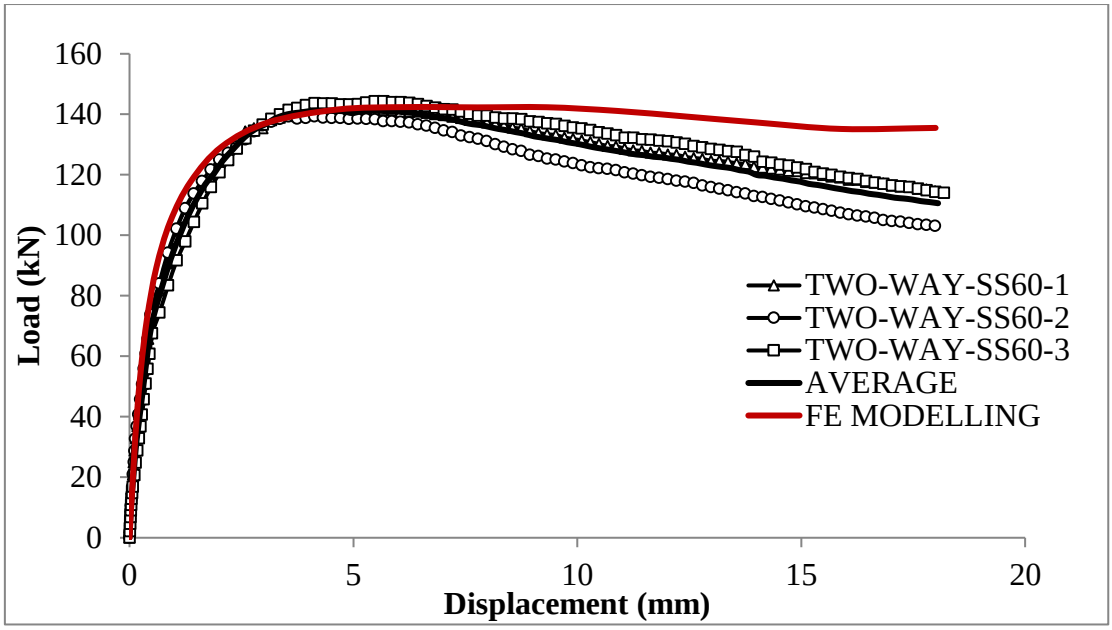

Figure 7.49: Load-displacement curves for SS60 slabs.

It is important to acknowledge that the CDP model shows a relatively stiffer numerical response in the softening region, for SS slabs with thicknesses of 45 mm and 60 mm, and this may be due to the non-uniform fibre distribution and orientation within the matrix. Specimens with higher thicknesses allow fibres to disperse more randomly, resulting in less fibre contribution perpendicular to the tensile cracks. This may mean there are fewer fibre-bridges between the two cracked faces and thus a decrease in stress was observed especially in the softening region. Thinner slabs impose restrictions on the possible fibre orientation, where fibres tend to align along the length of the specimens (Kameswara Rao, 1979, Soroushian and Lee, 1990, Association Francaise de Genie Civil–Service d'etudes Techniques des Routes et Autoroutes (AFGC/SETRA). 2002).

Furthermore, in the FE analysis, fibre distribution and orientation were not taken into account due to the model limitation. Figure 7.42 to 7.45 show that the slip between the slab edges and support considerably influenced the stiffness and therefore resulted in a much steeper deflection in the softening region in slabs in the SS series compared to those with FF supports. This is more pronounced in the thicker slabs such as 45 and 60 mm.

Moreover, for each slab thickness, a different batch was used to cast the specimens during the manufacturing process. Thick slabs may have been affected by fibre balling due to the large quantity of fibres used during the mixing procedure. The fibres may not be

distributed uniformly through the matrix, which resulted in a steeper slope in the softening region. In general, in all the simulations, the slab underwent three main regions, which were observed in slab tests as shown in Figure 7.42 to 7.45. Despite the changes in the slab geometry as well as boundary conditions and in total sixteen different parameters were considered, the CDP model has captured the structural behaviour of the slab accurately, especially in the first and second regions. The UHPFRC mechanical and durability properties are very different from those in OC. In addition, due to the fibre-bridging in UHPFRC, softening behaviour can be obtained where in OC this is not the case. Therefore, the existing OC design method such as the section analysis and the yield line method, especially in fixed boundary conditions cannot provide accurate results.

Nowadays, FE analyses are largely used for both linear and nonlinear analyses due to the limitation of physical tests of the structure (Bathe, 2007). It has contributed to the design standard especially in concrete structures as FE analysis assists in the design of structures especially slabs with complex geometry and loading conditions where other methods require conservative approximations and assumptions to be made (Deaton, 2005). Attempts to extend existing design standards to UHPFRC, is a complicated and challenging task, and it is limited as shown by Spasojevic (2008). It is also inappropriate for a design standard developed for OC to be applied directly to UHPFRC as it requires numerous assumptions due to the absence of reinforcing bars and randomly mixed fibres in the matrix. Producing an analytical design approach based on numerous assumptions is inaccurate and unsafe as shown in Chapters 4 and Chapter 5, thus the use of OC design standards to UHPFRC is not recommended.

Although, to date, the AFGC recommendations is the most reliable source for the design of UHPFRC members, it states that further studies are essential to advance knowledge in design standards of UHPFRC and its use in structures. To design any concrete structure for normal design loads, only linear and nonlinear regions up to the ultimate load are the main interest in design. The FE analyses in this study can reasonably predict both regions for UHPFRC. Therefore, the model could contribute to the advancement of knowledge in this area and be of interest for validating the existing design methods of UHPFRC structures. However, the model needs to be validated experimentally with larger slabs such as the real life-sized structures, in order to be used in practice.

Table 7.5: Slabs experimental and numerical results with FF boundary conditions.

Specimens		Experiment				Numerical ultimate load F_{ns} (kN)	Error $(F_s-F_{ns})/F_s$	Standard Deviation SD/ Error SE (kN)	Coefficient of Variation (CV)
Name	No	Cracking load F_c (kN)	average F_c (kN)	Ultimate load F_s (kN)	average F_s (kN)				
TWO-WAY-FF25	1	10.1	10.8	34.0	33.7	33.4	0.8%	3.2/ 1.6	9.6
	2	11.6		31.0					
	3	10.9		35.3					
	4	10.6		34.5					
TWO-WAY-FF35	1	19.1	20.0	71.0	70.8	69.9	1.2%	1.7/ 0.9	2.4
	2	20.3		68.7					
	3	20.8		72.9					
TWO-WAY-FF45	1	46.4	47.3	116.6	117.0	117.07	0.0%	1.6/ 0.9	1.4
	2	46.9		119.1					
	3	48.7		115.2					
TWO-WAY-FF60	1	76.4	77.7	211.5	197.3	212.0	7.4%	10.9/ 6.3	5.5
	2	77.8		185.0					
	3	78.9		195.1					

Table 7.6: Slabs experimental and numerical results with SS boundary conditions.

Specimens		Experiment				Numerical ultimate load F_{ns} (kN)	Error $(F_s\text{-}F_{ns}) / F_s$	Standard Deviation SD/ Error SE (kN)	Coefficient of Variation (CV)
Name	No	Cracking load F_c (kN)	average F_c (kN)	Ultimate load F_s (kN)	average F_s (kN)				
TWO-WAY-SS25	1	5.0	5.4	20.8	21.2	21.7	2.3%	0.4/ 0.2	2.1
	2	5.1		21.1					
	3	5.2		21.2					
	4	6.3		21.6					
TWO-WAY-SS35	1	13.2	13.8	43.6	45.0	43.4	3.5%	1.1/ 0.6	2.4
	2	13.7		46.2					
	3	14.6		45.3					
TWO -WAY-SS45	1	30.5	31.2	73.0	76.1	76.6	0.4%	4.1/ 2.4	5.5
	2	31.4		73.3					
	3	31.8		82.0					
TWO-WAY-SS60	1	65.4	66.7	141.2	141.0	142.4	1.0%	1.8/ 1.1	1.3
	2	66.8		138.7					
	3	67.9		143.2					

7.4.4 Two-way Slabs Parametric Study

The comparison between numerical and experimental results provided in this chapter demonstrated the reliability and accuracy of the model in capturing the structural behaviour of UHPFRC slabs. In order to extend the range of applications of UHPFRC members and to contribute to the advancement of knowledge in the development of UHPFRC design standards, a parametric study was carried out using the developed FE model that focused exclusively on the linear elastic and the ultimate load carrying capacity. To do this, slabs with both FF and SS boundary conditions with four greater thicknesses were considered: 75, 90, 105 and 120 mm. To present the results of the parametric study, the load-displacement relationships were determined. The results of the parametric assessment are shown in Figure 7.50 and Figure 7.51 for both FF and SS slabs, respectively.

Although, the results show that the elastic regions began to transform to the pseudo-strain hardening region after the displacement of 0.20 mm, this transformation is more pronounced at a displacement of approximately 0.30 to 0.40 mm for all thicknesses in both FF and SS boundary conditions, as shown in Figure 7.50b-e and Figure 7.51b-e, respectively. These results were similar to the result of the thicknesses that were tested in this study. Because the load is sustained by the matrix only, slab thickness had no effect on the linear elastic region. This confirms the accuracy of the FE model for capturing the structural behaviour of UHPFRC in the linear elastic region, thus the model is reliable for designing UHPFRC in the serviceability limit state. The loads at the end of this region were approximately 165.5, 255.5, 355.1 and 449.3 kN for slabs with FF boundary conditions and 106.4, 162.5, 230.7 and 312.6 kN for slabs with SS boundary conditions, as shown in Table 7.7. However, because the transformation from linear to nonlinear is very smooth, it is difficult to know the exact value where the change occurs. Therefore, the above values may vary by between 1-5% of the exact load. The results also show that an increase in slab thickness by 15 mm with FF boundary conditions increases the linear load by approximately 100 kN, whereas, this is not the case in slabs with SS boundary conditions. The percentage increase in linear load increased with the increase of slab thickness and it was varied from 30% to 60% with both SS and FF boundary conditions.

As shown in Table 7.7, slabs with FF boundary conditions reached the end of the pseudo-strain hardening region where fibres began to pull-out at a load of approximately 345.6

kN for 75 mm thick slabs. As the slab thickness increased to 90 mm, the ultimate load increased to 502.1 kN with the percentage increase of approximately 45%. After the 105 mm thick slabs was analysed, the ultimate load increased to 680.1 kN and a percentage increase of 35% was recorded. Finally, a load of 909.2 kN was recorded when 120 mm thick slabs were studied, which gives a percentage increase of 33%. This clearly illustrated that the percentage increase in the ultimate load reduced with an increase of the slab thickness. Slabs with SS boundary conditions were also shown to have a similar trend. The result of parametric studies exhibited that the percentage increase for slabs with thicknesses of 75 mm was 71% when compared to slabs with thickness 60 mm, as shown in Table 7.7. The percentage increase continued to reduce and an increase in the ultimate load of 32% was recorded when 120 mm slabs were analysed. This is clear evidence that the relationship between increases at the ultimate load carrying capacity and the specimen thickness is nonlinear and this nonlinearity develops further as the thickness increases. The results of the parametric studies also agree with the experimental data that the linear elastic stage ends at a small displacement. Therefore, the no cracking SLS criterion proposed by the AFGC which did not allow for cracks to occur in the elastic region may be excessively conservative.

In the softening region, the limitation of the model becomes more apparent in the two-way slabs and SS boundary conditions, in particular. Looking at Figure 7.51, it can be seen that the curves tend to show a plateau behaviour after the load reaches its ultimate. Therefore, if the softening region is to be considered, experiments with sizes similar to the parametric study sizes are recommended to be undertaken to better describe the model developed in this study. Since in design, it is only the linear and strain-hardening behaviour that are of interest and it appears that the discrepancy between the experimental and the numerical results are less than 5% in these regions. The model can contribute to the advancement of knowledge of the UHPFRC design. Nevertheless, these conclusions need be verified experimentally in order to be used in practice.

In general, the experimental work has given a good understanding of the structural behaviour of two-way slabs. The numerical result has also shown that the model accurately captures the structural behaviour in both linear and nonlinear regions in two-way slabs with both SS and FF boundary conditions.

Table 7.7: Parametric results for both FF and SS two-way slabs.

Thickness (mm)	Fully-fixed			Simply-supported		
	Linear elastic load (kN)	End of strain-hardening		Linear elastic load (kN))	End of strain-hardening	
		Ultimate load F_{ns} (kN)	Displacement w_{ns} (mm)		Ultimate load F_{ns} (kN)	Displacement w_{ns} (mm)
75	165.5	345.6	3.2	106.4	239.6	4.6
90	255.5	502.1	3.5	162.5	349.1	4.6
105	355.1	680.1	3.2	230.7	477.1	4.7
120	449.3	909.2	3.5	312.6	641.4	4.7

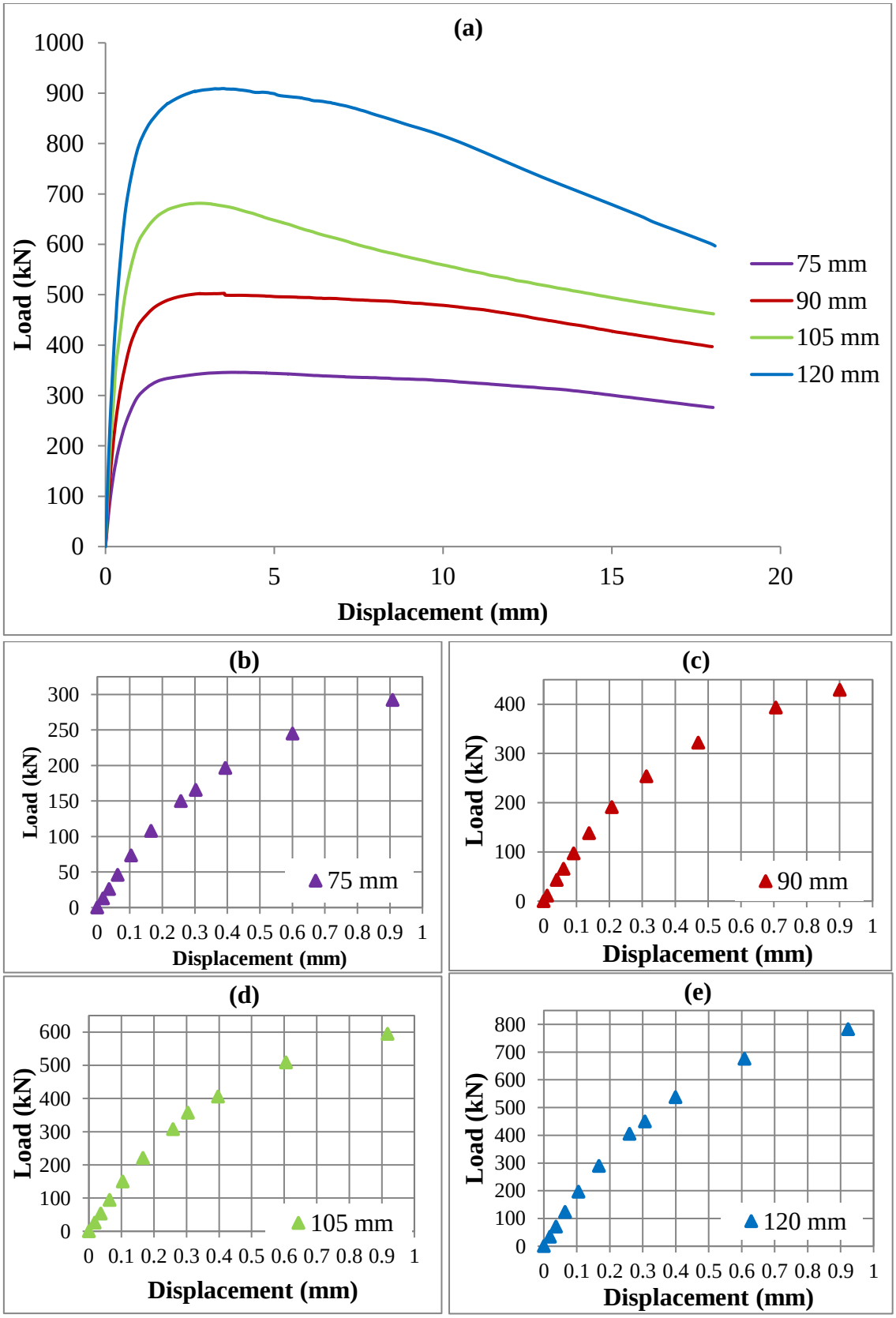

Figure 7.50: Parametric study of fully fixed two-way slabs.

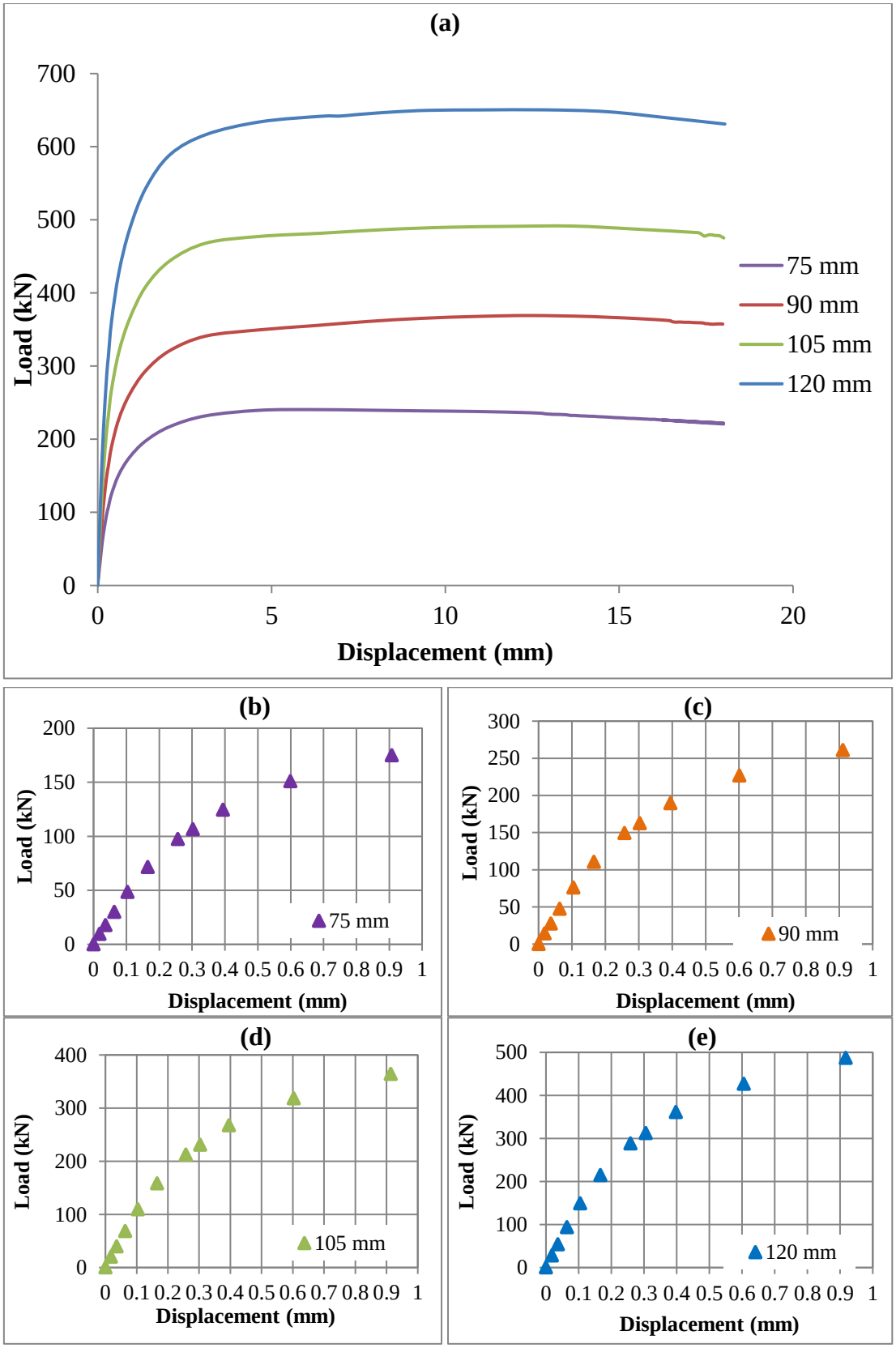

Figure 7.51: Parametric study of simply supported two-way slabs.

7.5 Concluding Remarks

The numerical models were compared with the experimental data from notched-three-point beams, one-way and two-way slabs and show good agreement. Compared to previous analytical and numerical studies, the model developed in this study can predict the full structural behaviour of UHPFRC beams and slabs in all loading stages. Existing models can only predict the linear or linear and strain-hardening behaviour and only for a limited geometry, whereas the model developed in this study can predict a range of parameters with various boundary conditions. With regard to the beams, the CDP model confirmed that the size effect on the nominal flexural strength of those beams up to 150 mm depth is very small and can be ignored. The model parametric studies have also confirmed that the size effect is negligible for the beams up to 300 mm in depth.

Comparison of behaviour predicted by the CDP model and experimental material properties shows that the model developed to investigate UHPFRC slabs and beams can accurately reproduce the uniaxial tension and compression response of UHPFRC at all loading stages. However, the model using a single element investigation shows sensitivity on convergence to reproduce the material properties. Whereas, lower softening behaviour under uniaxial tension and lower peak stress for uniaxial compression were observed. Nevertheless, the trend of the CDP outcome is close to the experimental data demonstrating the ability of the developed models to capture the overall physical behaviour of UHPFRC.

With regards to the slabs, the CDP model showed that, expect for the two-way thick slabs with FF boundary conditions (45 and 60 mm), the full load-displacement curves for both one-way and two-way slabs with both FF and SS boundary conditions can be predicted. Although, different stiffnesses were applied to the support conditions in two-way slabs, the model was found to be limited in capturing the physical crack propagation of thick slabs (45 and 60 mm).

The FE model was also used to study slabs with larger thicknesses that were too expensive or impractical to be tested, through a parametric study. The studies showed that with an increase of slab thickness, the percentage increase of the peak load decreased. The discrepancy between the numerical and the experimental approach in the softening region became more apparent when the parametric sizes were investigated. Therefore, it was

recommended that slabs with sizes similar to the parametric sizes should be tested to further validate the model. However, the transformation from linear elastic to strain-hardening was found to be the same throughout the thicknesses, which is similar to the experimental tests.

The occurrence of fibre pull-out behaviour in one-way slabs in the FF series appears to be more influenced by the boundary conditions than thickness when compared to two-way slabs. Due to the uncertainty in fibre distribution and orientation in the matrix, it was recommended that variations of 10% and 25% in pseudo-strain hardening and strain softening regions, respectively, be considered in designing UHPFRC members. This is particularly recommended for slab thickness that are greater than 45 mm thick as fibres are more randomly distributed and less restricted by the specimen's wall effect.

The no cracking SLS criterion proposed by the AFGC which did not allow for cracks to occur in the elastic region was found to be excessively conservative as the cracking load occurs with a very small displacement (less than 0.5 mm) for both one-way and two-way slabs.

In general, using accurate tensile and compressive material properties as input, the CDP numerical model that was developed and validated by experimental data in this study can usefully predict the structural behaviour of UHPFRC beams and slabs up to the ultimate load. This evidence suggests the FE model developed could also be used to model other UHPFRC structures when the tensile traction-displacement curve obtained from experiments is used to model tension softening.

CHAPTER 8

CONCLUSIONS AND RECOMMENDATIONS

Throughout this research, it was found that there were very few studies available in the open literature regarding the structural behaviour of UHPFRC members, especially slabs. This study is one of a few to investigate the structural behaviour of UHPFRC slabs. A detailed literature review was conducted on the material properties, mechanical behaviour, existing design methods and the current state of knowledge. The aim of this study was to characterise the collapse and failure modes of UHPFRC beams and slabs, with different boundary conditions under static loading. An extensive experimental programme was conducted to provide the data on the structural behaviour in order to achieve the aim of the study.

Firstly, three point bending tests were carried out on rectangular prisms with different notch depths to study the fracture parameters including load-CMOD relationship, failure modes and size effect. Secondly, an extensive experimental investigation on one-way and two-way spanning slabs with varying thicknesses and different boundary conditions was conducted to determine the structural behaviour through the application of a specially developed custom experimental setup. In addition, an experimental investigation based on fibre counting at crack locations to determine the relationship between the fibre distribution and slab thickness was undertaken. The relationship between the thickest slab (60 mm) and full-sized structures in terms of fibre distribution and orientation is also discussed.

Thirdly, only a limited number of boundary and load conditions can be obtained from experiments due to the practicalities and limitation of time and funding. In addition, because the cost of experimental studies is still relatively high, especially for large-sized structures, FE analyses were also developed to model the response of the structures accurately and efficiently. The FE model was validated by material properties testing (uniaxial tension and compression) and experimental results. The FE model were further validated using single element model investigations. The analyses considered both linear and nonlinear behaviour up to the ultimate load carrying capacity of the slabs. It offers a reliable and cost-effective alternative to laboratory testing. The FE models were also used to study how the structural behaviour of UHPFRC members was influenced by thickness through a parametric study.

In general, the response of UHPFRC slabs and beams were examined through both experimental and numerical studies. From the evaluation of the results of this current study, it was concluded that slab thickness and boundary conditions have a significant effect on failure mode, crack pattern and the load-displacement relationship. Physical examination of fibre distribution at the crack location showed that fibres tended to be perpendicular to the cross-section in thin members due to the specimen wall effect, causing more fibres to bridge between the two cracked faces. Whereas, in thick members, fibres were less affected by the specimen wall effect and more randomly orientated in the matrix, resulting in less fibre bridging between the two cracked faces. In terms of beam specimens, it was concluded that the fibre distribution of full-sized beams may be similar to those tested in this study. It was also concluded that the fibre orientation and distribution in full-sized structures is unlikely to differ much from the largest slab tested here by less than 10%. However, these conclusions will have to be verified experimentally with full-sized structures if they are to be used more extensively.

The size effect behaviour of UHPFRC can be ignored or existing size effect theory may need to be modified in the light of this study. In addition, the structural behaviour of UHPFRC can be captured by the FE analysis if representative material properties are known. However, further consideration needs to be given if the model is to be used to investigate the UHPFRC at element level.

8.1 Notched Beams

The beam specimens with different geometries were manufactured and tested. The experimental data has been produced through three-point bending tests under static loading. FE analyses were developed to simulate the experimental results. The modified three-point bending test setup described in Chapter 3 was used to record the load-CMOD relationship. A total of fifteen beams, with five depths (d = 30, 60, 90, 120 and 150 mm) and the same width (b= 150 mm) and span (l=500 mm) were tested to failure. From this the following conclusions can be drawn:

- The effect of the new type Eurocast200 superplasticiser on the UHPFRC constituents was investigated using flow tables, density and cube compressive tests. The new superplasticiser was found to be more effective than the one used in previous studies in terms of workability but similar in strength.

- The results showed that all the beam specimens failed in flexure with a single macrocrack that propagated from the tip of the notch upward due to the loading condition imposed by the notches in the testing configuration. Therefore, no shear failure was detected in the specimen sizes tested in this study. However, it is important to mention that consideration must be given to a possibility of shear failure for specimens with depths greater than those tested in this study or specimens similar to those tested in this study but without a notch.

- The load-CMOD relationship showed that the beam specimens underwent three different stages: pure elastic, pseudo-strain hardening and strain softening. All the failures occurred due to fibre pull-out not yielding of the fibres due to the high yielding point of the steel fibres (2000 MPa).

- The nominal flexural tensile strength for all the other beams was around 20 MPa and the strength did not depend on the size of the element. This clearly indicates that the size effect in concrete can be eliminated through the use of a material with a relatively high ductility such as UHPFRC.

- An examination of fibre distribution using physical fibre counting where cracks occurred was carried out. The examination showed that the number of fibres contributing to the fibre bridging action in the cracked area is not proportional to an increase in the specimen depth. It showed that the ratio of fibres bridged between the two cracked faces per depth of beam reduced as the beam depth increased.

- It was concluded that the fibre distribution of full-sized beams may be similar to those tested (the thicker beam) in this study. However, this conclusion will have to be verified experimentally with full-sized structures if they are to be used more extensively

- The results also showed that the bending behaviour of UHPFRC members are different from conventional concrete and the existing size effect law of conventional concrete needs to be modified or a new theory of size effect required when designing UHPFRC members.

- FE analysis (ABAQUS) was used to model the response of the beams. The failure process was accurately modelled by the CDP model developed in this study. The model can also predict the structural behaviour of UHPFRC beams in terms of load-CMOD curves in all loading stages. It is important to mention that this conclusion is purely based on 2D modelling.

- Reliable material properties were required as input to adequately describe the localised response of the material in a FE analysis which involved accounting for linear, nonlinear and damage behaviour.

- The FE model was validated by material properties testing (uniaxial tension and compression). The model accurately reproduced the response of UHPFRC at all loading stages. The models were further validated using single element modelling, where it showed some sensitivity to reproduce the material properties. Lower softening behaviour under uniaxial tension and lower peak stress for uniaxial compression were observed. Nevertheless, the similar trend of the CDP results to

the experimental data demonstrated the ability of the developed models to capture the overall physical behaviour of UHPFRC structures.

- Because the cost of experimental studies is still relatively high whether in academia or industry, especially for large-sized structures, an extra CDP-based FE simulations for beams with d =180, 210, 240 and 300 mm were carried out for size effect analysis. The results from parametric studies have also confirmed that the size effect is negligible for beams up to 300 mm in depth.

8.2 One-way Slabs

To understand the response of one-way slab structures, a detailed experimental examination was conducted. Due to the uncertainty of true boundary conditions of slabs in engineering structures, especially in bridges, the experimental study was conducted with two defined boundary conditions, fully fixed (FF) and simply supported (SS). Two series of 660 by 660 mm slabs were tested under the bending test. The first series was conducted on 13 slabs with FF boundary conditions and four different thicknesses of 25, 35, 45 and 60 mm, while the second series was conducted on 13 slabs with SS boundary conditions and four different thicknesses of 2**7**, 35, 45, and 60 mm. The effect of slab thickness on fibre distribution and uniformity of fibre distribution within the matrix was examined using a physical fibre counting investigation at the crack locations for each slab thickness. The experimental data was used to validate the FE analysis. Parametric studies for sizes up to 120 mm slab depth were also carried out and the following conclusions were drawn:

- Slabs with both SS and FF boundary conditions were tested using the custom experimental setup and these were seen to fail in flexure with a single macrocrack initiating from the centre towards the middle of the free edges of the slab.

- Similar to the beams, the one-way slabs exhibited three main phases: linear, pseudo-strain hardening and strain softening.

- Examination of the physical distribution of fibres at the crack location showed that fibres tended to be perpendicular to the cross-section in thin members due to the specimen wall effect, causing more fibres to bridge between the two cracked faces.

- The physical inspection also showed that there were a few spots of poor fibre distribution that could be seen in thick slabs but these spots were not predominant enough to characterise the general picture of the fibre distribution within the crack location of the slabs. This result agrees with previous studies which are available in the literature.

- No fibre balling was observed in any of the one-way slab specimens and this confirmed the reliability and consistency of the mix design used in this current study.

- Microcracks in both the FF and SS slab series were initiated at a displacement of around 0.3-0.4 mm. The maximum load was reached in both series at displacements of approximately 5 mm for slabs with 25, 27 and 35 mm thickness and 3 to 4.5 mm for slabs with 45 and 60 mm thicknesses.

- The transformation from elastic to strain-hardening for slabs with thicknesses of 25 and 35 mm in both series were similar and it covered a wide range of displacements approximately between 0.35 to 5 mm, whereas this transformation zone was approximately between 0.35 to 4.5 mm for slabs with thicknesses of 45 and 60 mm.

- As the thickness increased, the ductility of the slabs reduced due to the crack width which is considerably smaller in thin slabs compared to the thick slabs. This is due to the fact that, for the same bending angle in thin slabs, fibres bridge between the two cracked faces whereas in thick slabs the fibres pull-out.

- The results showed that changes in thickness had no influence on the effective flexural tensile strength (f_{st}) of the slabs. It was found that the f_{st} was to be around

4.0 to 4.8 MPa and 6.7 to 7.1 MPa for FF and SS boundary conditions, respectively. Again this confirmed that the size effect is negligible in one-way UHPFRC structures.

- The results from the experimental study showed that the boundary conditions have less effect on the pseudo-strain hardening behaviour in one-way slabs when compared with two-way slabs.

- As reported in the literature, a small variation has always been seen in conventional concrete and fibre concrete in nonlinear regions. Due to the uncertainty in fibre distribution and orientation in the matrix, the UHPFRC used in this study has also shown a small variation in the nonlinear region. Therefore, it is recommended that a variation of between 10% and 25% in pseudo-strain hardening and strain softening regions, respectively, should be considered when designing one-way UHPFRC members. Nevertheless, further experimental testing would be required in order for this recommendation to be used in design.

- The no cracking SLS criterion proposed by the AFGC which does not allow for cracks to occur in the elastic region was found to be excessively conservative as the cracking load occurs with a very small displacement (less than 0.5 mm) in this study. This has also been reported in the literature. Further research using full-sized structures would be required in order for this recommendation to be confirmed.

- The CDP model showed that the structural behaviour in terms of load-displacement curves and failure mode can be predicted for one-way slabs with both FF and SS boundary conditions with thicknesses in the range from 25 mm to 60 mm. However, for the ONE-WAY-SS27, the model showed small increase in stiffness in the softening region when compared to the UHPFRC response.

- The parametric study for slab thicknesses up to 120 mm showed that with the increase in thickness, the percentage increase of the peak load reduced. The parametric study also showed that the FE model can be used to capture the overall

structural behaviour of one-way slabs with different geometries. However, it is recommended to undertake experiments with sizes similar to the parametric study in order to confirm the conclusions regarding the effect of slab thickness on the cracking and ultimate load carrying capacity.

8.3 Two-way Slabs

An extensive experimental investigation was also conducted on a limited number of two-way UHPFRC slabs with various thicknesses. This was done by testing the slab specimens in the laboratory to induce failure that may occur due to the application of a point load. The FE analysis using ABAQUS was developed to predict the experimental data. The experimental work consisted of two series. The first series was carried out on 13 slab specimens with FF boundary conditions while the second series was conducted on 13 slabs with SS boundary conditions. The slab chosen for the investigation in this study was 660 x 600 mm with four different thicknesses: 25, 35, 45 and 60 mm for both boundary conditions. To further examine the effect of slab thickness on fibre distribution and orientation, and to verify that the mixing and casting procedures used to make UHPFRC slabs resulted in the steel fibres being uniformly distributed. Physical investigations of the number of fibres were counted at the locations where cracks had occurred. Based on the experimental and numerical results, and the parametric study for sizes up to 120 mm, the following conclusions can be drawn:

- All the slabs with both FF and SS boundary conditions were tested using a custom experimental setup. These were found to fail in flexure with similar failure crack patterns. Cracks initiated from the centre of the slab propagated towards the corners and edges of the slab.

- Slabs in the FF series failed with four macrocracks for the thinner UHPFRC slabs 25 and 35 mm, while six macrocracks occurred in some of the thicker specimens, 45 and 60 mm. This larger number of cracks was believed to be due to the effect of boundary conditions where the support stiffness in one of the two adjacent edges was greater compared to the other two edges.

- Slabs in the SS series were more consistent throughout the range of varying slab thickness and all the slabs failed with four diagonal macrocracks.

- The load-displacement curves showed that the UHPFRC slabs underwent three main regions similar to the beams and one-way slabs: linear, pseudo-strain hardening and strain softening.

- Slab thickness can influence the fibre distribution and orientation within the matrix. As the thickness increased, the ratio (N/t) was reduced because fibres were less likely to be perpendicular to the direction of the force. So fibres were distributed in the matrix more freely, thus the fibre-bridging action reduced in the thicker slabs.

- Due to the uncertainty in fibre distribution and orientation in the matrix, similar to the one-way slabs, the results showed a small variation in the nonlinear region. Therefore, it is recommended that a variation of between 10% and 25% in pseudo-strain hardening and strain softening regions, respectively, should be considered in designing UHPFRC members in two-way slabs.

- Changes in thickness have very little influence on the effective flexural tensile strength (f_{st}) of slabs with the SS boundary conditions and it was found to be around 6 to 7 MPa. Once again, this confirms that size effect can be ignored in the design of UHPFRC two-way spanning slabs with SS boundary conditions.

- The slab boundary conditions can have a considerable effect on the load-displacement behaviour. Slabs in the SS slab series showed significant deformation in the strain hardening region compared to the FF slab series.

- The no cracking SLS criterion for two-way slabs was found to be excessively conservative as the cracking load occurs with a very small displacement (less than 0.5 mm) in this study.

- The FE analysis based on the CDP model was developed using ABAQUS. The numerical model clarifies the result obtained from the experiment in terms of load-displacement relationship and ultimate load carrying capacity. However, the model was not able to capture the failure mode of two-way slabs and this is a limitation of the model developed in this study.

- Except for the thick slabs (45 and 60 mm) with FF boundary conditions, the full load-displacement curves for two-way slab conditions can be predicted. In thick slabs, the model tends to show an increase in stiffness in the tension softening region.

- In terms of the structural behaviour of UHPFRC, existing models can only predict the linear or nonlinear strain hardening behaviour and only for a limited geometry, whereas the model developed in this study can predict a range of parameters with various boundary conditions.

- The parametric study for slab thicknesses up to 120 mm showed that with the increase of thickness, the percentage increase of the peak load reduced and the trend of the load-displacement curve agreed with the experimental tested data.

- The results suggest that the FE model developed in this study could be used to model other UHPFRC structures where the tensile traction-displacement and stress-strain curves obtained from experiments is used to model both tension softening and compression hardening, respectively.

8.4 Recommendations for Future Work

The research presented has investigated the structural behaviour of UHPFRC beams and slabs experimentally and numerically. The FE analysis has shown that the performance of experimental response with various parameters presented here can be captured accurately. However, due to the time and funding, not all of the possibilities have been explored. It is therefore; recommended that the following work is undertaken in future studies:

- In this study, the beam depth was used to investigate size effect phenomena. Therefore, it is recommended that further experimental work with UHPFRC beams spanning a larger range of sizes (especially change in length) need to be tested before a definitive conclusion on size effect can be drawn. Although, all the beams in this study failed in flexure, consideration must be given to the possibility of shear failure if larger beams are to be tested.

- The specimens were notched with a ratio of depth/notch = 6 but it is recommended that experimental studies of different depth/notch ratio should be carried out to further investigate the effect of notch on the failure mode and flexural nominal strength. Experimental works on beams without notches should be carried out to investigate the effect of the notch on the beam failure modes and flexural tensile strength so that a direct comparison between notched and unnotched beams can be made.

- Up-to-date, heterogeneous models accounting for the fibre-bridging is based on perfect bonding between the fibre and the concrete. These models have only investigated basic geometries. Therefore, it is recommended that heterogeneous models accounting for true fibre-matrix bonding and fibre distribution for different geometries and boundary conditions should be attempted to simulate non-symmetric crack paths, for two-way slabs in particular.

- Additional LVDT's are recommended to be placed under the slab to monitor the displacement at particular points, which are based on the likely location of crack propagation so that the critical failure point on the slab can be monitored.

- More experimental investigations on both one-way and two-way slabs are required to consider different loading positions (centre edges and corner load) to demonstrate the possible failures that could occur due to the application of a point load on the floor such as heavy machinery in the warehouse, laboratory machines in the building and office cabinets.

- Further experimental work considering uniform distributed load are required. The results of these could be compared with the point load tests carried out in Chapters 4 and 5 so that the effect of load conditions on failure mode, crack patterns and ultimate load carrying capacity can be determined.

- The current state of art of fibre examination is limited to a small range of specimen sizes. Therefore, the assessment of distribution of fibres in larger UHPFRC specimens should be studied using computerised imaging techniques. This allows an extended FE analysis to be used to accurately capture the slab tensile crack patterns in two-way slabs and other loading positions where complex cracking may occur.

- Thickness and support conditions were judged to be the most important parameters in this present study. Therefore, parametric studies were carried out on varying slab thicknesses only and the results showed good correlation based on the tested thicknesses. It is recommended that slabs with larger spans and different boundary conditions be tested. The results can then be used to further validate the FE model developed in this study.

- Further testing of two-way slabs with FF boundary conditions similar to the thick slabs tested in this study and slabs with greater thicknesses is recommended to better understand the failure modes of two-way slabs.

REFERENCES

ABAQUS. 2013. *ABAQUS: User's Manual*. Concrete Damaged Plasticity, SIMULIA , 1-1306.

ABDALLA, H. M. & KARIHALOO, B. L. 2003. *Determination of size-independent specific fracture energy of concrete from three-point bend and wedge splitting tests*. Magazine of Concrete Research, 55**,** 2, 133-142.

ACI COMMITTEE 544.1R. 2002. *State-of-the-Art Report on Fiber Reinforced Concrete*. Manual of Concrete Practice, ACI**,** 1-66.

ACI COMMITTEE 544. 1999. *Design Considerations for Steel Fiber Reinforced Concrete*. Manual of Concrete Practice, ACI**,** 1-18.

ACI COMMITTEE. 1987. *Silica Fume in Concrete*. ACI Materials Journal, ACI**,** 1-9.

ACKER, P. & BEHLOUL, M. 2004. *Ductal Technology: A Large Spectrum of Properties, A Wide Range of Applications*. Proceedings of the International Symposium on Ultra High Performance Concrete, fib, Kassel, German, 11-23.

AÏTCIN, P.-C. 1998. *High Performance Concrete*, Taylor & Francis**,** 1-527.

AL-AZZAWI, A. A., ALI, A. S. & RISAN, H. K. 2006. *Behavior of Ultra High Performance Concrete Structures*. ARPN Journal of Engineering and Applied Sciences, 6**,** 5, 95-109.

ALANI, A. M., ABOUTALEBI, M. & KING, M. J. 2013. *Influence of fibre content on crack propagation rate in fibre-reinforced concrete beams*. International Journal of Civil , Environmental, Structural, Construction and Achitectural Engineering, 7**,** 9, 652-658.

ASSAKKAF, I. 2002. *Chapter 6a Shear and Diagonla Tension in Beams.* Reinforced Concrete. 1-33.

ASSAKKAF, I. 2004. *Chapter 4a Shear in Beams.* Reinforced Concrete Design. 1-22.

ASSOCIATION FRANCAISE DE GENIE CIVIL–SERVICE D'ETUDES TECHNIQUES DES ROUTES ET AUTOROUTES (AFGC/SETRA). 2002. *Ultra High Performance Fibre-Reinforced Concretes Recommendation by SETRA-AFGC*. SETRA-AFGC**,** 1-98.

ASTM STANDARD A820. 2011. *Standard Specification for Steel Fibres for Fiber-Reinforced Concrete*. ASTM**,** 1-4.

BACHE, H. H. 1981. *Densified Cement/Ultra-Fine Particle-Based Materials*. Second International Conference on Superplasticizers in Concrete, Aalborg Portland, Ottawa, Ontario, Canada, 1-35.

BALAGURU, P. & KENDZULAK, J. 1987. *Mechanical Properties of Slurry Infiltrated Fiber Concrete (SIFCON)*. ACI Special Publication, 105, 247-268.

BALAGURU, P. N. & SHAH, S. P. 1992. *Fiber-Reinforced Cement Composites*, McGraw-Hill, New York**,** 1-531.

BALOUCH, S., FORTH, J. & GRANJU, J. L. 2010. *Surface corrosion of steel fibre reinforced concrete*. Cement and Concrete Research, 40**,** 3, 410-414.

BARNETT, S. J., LATASTE, J.-F., PARRY, T., MILLARD, S. G. & SOUTSOS, M. N. 2010. *Assessment of fibre orientation in ultra high performance fibre reinforced concrete and its effect on flexural strength*. Materials and Structures, 43**,** 7, 1009-1023.

BARNETT, S. J., SOUTSOS, M. N., MILLARD, S. G. & BUNGEY, J. H. 2006. *Strength Development of Mortars Containing Ground Granulated Blast-Furnace Slag: Effect of Curing Temperature and Determination of Apparent Activation Energies*. Cement and Concrete Research, 36**,** 3, 434-440.

BARR, B. & TOKATLY, Z. 1991. *Size Effects in Two Compact Test Specimen Geometries*. Applications of Fracture Mechanics to Reinforced Concrete, 63-93.

BARROS, J. A. O. & FIGUEIRAS, J. A. 1998. *Experimental Behaviour of Fibre Concrete Slabs on Soil*. Mechanics of Cohesive-frictional Materials, 3**,** 3, 277-290.

BASTIEN-MASSE, M. & BRÜHWILER, E. 2014. *Ultra high performance fiber reinforced concrete for strengthening and protecting bridge deck slabs*. Bridge Maintenance, Safety, Management And Life Extension, Crc Press-Taylor & Francis Group, 2176-2182.

BATHE, K.-J. 2007. *On Reliable Finite Element Methods for Extreme Loading Conditions*. Extreme Man-made and Natural Hazards in Dynamics of Structures. Springer**,** 71-102.

BAZANT, Z. P. 1984. *Size Effect in Blunt Fracture: Concrete, Rock, Metal*. Journal of Engineering Mechanics, 110**,** 4, 518-535.

BAZANT, Z. P. 1991. *Fracture Processes in Concrete, Rock and Ceramics*. Proceedings of the International RILEM/ESIS Conference, Noordwijk, Netherlands, 1, 417-429.

BAŽANT, Z. P. 1989. *Identification of Strain-Softening Constitutive Relation from Uniaxial Tests by Series Coupling Model for Localization*. Cement and Concrete Research, 19**,** 6, 973-977.

BAZANT, Z. P. & CAO, Z. 1987. *Size Effect in Punching Shear Failure of Slabs*. ACI Structural Journal, 84**,** 1, 245-253.

BAZANT, Z. P. & CHEN, E.-P. 1997. *Scaling of Structural Failure*. Applied Mechanics Reviews, 50**,** 10, 593-627.

BAZANT, Z. P. & KAZEMI, M. T. 1991. *Size Effect on Diagonal Shear Failure of Beams Without Stirrups*. ACI Structural Journal, 88**,** 3, 268-276.

BAŽANT, Z. P. & KIM, J. K. 1984. *Size Effect in Shear Failure of Longitudinally Reinforced Beams*. ACI Journal, 81, 456-468.

BAZANT, Z. P. & SENER, S. 1988. *Size Effect in Pullout Tests*. ACI Materials Journal, 85**,** 5, 347-351.

BAŽANT, Z. P. & SUN, H. H. 1987. *Size Effect in Diagonal Shear Failure: Influence of Aggregate Size and Stirrups*. ACI Materials Journal, 84**,** 4, 259-272.

BAZANT, Z. P. & XI, Y. 1991. *Statistical Size Effect in Quasi-Brittle Structures: II. Nonlocal Theory*. Journal of Engineering Mechanics, 117**,** 11, 2623-2640.

BAZANT, Z. P., XI, Y. & REID, S. G. 1991. *Statistical Size Effect in Quasi-Brittle Structure: I. Is Weibull Theory Applicable?* Journal of Engineering Mechanics, 117**,** 11, 2609-2622.

BAZANT, Z. P. & XU, K. 1991. *Size effect in fatigue fracture of concrete*. ACI Materials Journal, 88**,** 4, 390-399.

BENNETT, D. 2002. *MDF and DSF the New Ultra High Strength Concrete*. British Cement Association**,** 1-3.

BENSON, S. & KARIHALOO, B. 2005a. *CARDIFRC-Development and Mechanical Properties. Part I: Development and Workability*. Magazine of Concrete Research, 57, 6**,** 347-352.

BENSON, S. & KARIHALOO, B. 2005b. *CARDIFRC–Development and Mechanical Properties. Part III: Uniaxial Tensile Response and Other Mechanical Properties*. Magazine of Concrete Research, 57, 8**,** 433-443.

BENSON, S., NICOLAIDES, D. & KARIHALOO, B. 2005. *CARDIFRC-Development and Mechanical Properties. Part II: Fibre distribution*. Magazine of Concrete Research, 57, 7**,** 421-432.

BIGGS, R. M., BARTON, F. W., GOMEZ, J. P., MASSARELLI, P. J. & MCKEEL JR, W. T. 2000. *Finite Element Modeling and Analysis of Reinforced-Concrete Bridge Decks*. Charlottesville, Virginia, Virginia Transportation Research Council**,** 1-26.

BONNEAU, O., LACHEMI, M., DALLAIRE, E., AÏTCIN, P. C. & DUGAT, J. 1997. *Mechanical Properties and Durability of two Industrial Reactive Powder Concretes*. ACI Material Journal, 286-290.

BRAESTRUP, M. W. 2010. *Yield Line Theory and Concrete Plasticity*. Magazine of Concrete Research, 60**,** 8, 549.

BRITISH GEOLOGICAL SURVEY 2004. *Mineral Planning Factsheet on Silica Sand-Report to Support the Research Project*. UK, Natural Environment Research Council**,** 1-10.

BRITISH STANDARDS INSTITUTION BS 1881-116. 1983. *Part 116: Method for Determination of Compressive Strength of Concrete Cubes*. Concrete Testing, BS**,** 1-10.

BRITISH STANDARDS INSTITUTION BS 1881-127. 1990. *Part 127: Method of Verifying the Performance of a Concrete Cube Compression Machine Using the Comparative Cube Test*. Concrete Testing, BS**,** 1-16.

BRITISH STANDARDS INSTITUTION BS 4551-1. 1998. *Methods of Testing Mortars, Screeds and Plasters*. Part 1. Physical testing, BS**,** 1-32.

BRITISH STANDARDS INSTITUTION BS EN14651:2005+A1. 2007. *Test Method for Metallic Fibre Concrete. Measuring the Flexural Tensile Strength (Limit of Proportionality (LOP), residual)*. BS**,** 1-20.

BRITISH STANDARDS INSTITUTION BS EN 1997-1. 2000. *Cement-Part 1: Composition, Specifications and Conformity Criteria for Common Cements*. British Standards Institution, London,

CEMENT & CONCRETE ASSOCIATION C&CA. 1965. *Recent Developments in Yield-line Theory*, Cement and Concrete Association**,** 1-74.

CHANH, N. V. 2004. *Steel fiber reinforced concrete*. Proceedings of the JSCE/VIFCEA Joint Seminar on Concrete, . Faculty of Civil Engineering Ho chi minh City university of Technology, Vietnam, 108-116.

CHEN, G. M., CHEN, J. F. & TENG, J. G. 2012. *On the Finite Element Modelling of RC Beams Shear-Strengthened with FRP*. Construction and Building Materials, 32, 13-26.

CHEN, J. F., CHEN, G. M. & TENG, J. G. 2009. *Role of Bond Modelling in Predicting the Behaviour of RC Beams Shear-Strengthened with FRP U-Jackets*. Proceedings of the

9th International Symposium on Fibre Reinforced Polymer for Concrete Structures (FRPRCS9), Sydney, Australia, 1-14.

CHEN, J. F. & TAO, Y. 2011. *Finite Element Modelling of FRP-to-Concrete Bond Behaviour Using the Concrete Damage Plasticity Theory Combined with a Plastic Degradation Model*. CICE 2010 - The 5th International Conference on FRP Composites in Civil Engineering, Springer Berlin Heidelberg, Beijing, China, 1-6.

CHEN, L. & GRAYBEAL, B. A. 2011a. *Modeling Structural Performance of Second-Generation Ultrahigh-Performance Concrete Pi-Girders*. Journal of Bridge Engineering, 17**,** 4, 1-52.

CHEN, L. & GRAYBEAL, B. A. 2011b. *Modeling Structural Performance of Ultrahigh Performance Concrete I-Girders*. Journal of Bridge Engineering, 17**,** 5, 754-764.

COLLEPARDI, S., COPPOLA, L., TROLI, R. & COLLEPARDI, M. 1997. *Mechanical Properties of Modified Reactive Powder Concrete*. ACI Special Publications, 173, 1-22.

CORINALDESI, V. & MORICONI, G. 2003. *Mechanical Properties and Thermal Conductivity of Reactive Powder Concrete Materials*. International Conference on Advances in Concrete and Structures, RILEM Publications SARL, 766-773.

COSKUN, H. 2002. *Construction of Simcon Retrofitted Reinforced Concrete Columns*. Doctor of Philosophy (PhD), North Carolina State University**,** North Carolina, United States, 1-280.

CUCCHIARA, C., LA MENDOLA, L. & PAPIA, M. 2004. *Effectiveness of stirrups and steel fibres as shear reinforcement*. Cement and Concrete Composites, 26**,** 7, 777-786.

DAGAR, K. 2012. *Slurry infiltrated fibrous concrete (SIFCON)*. International Journal of Applied Engineering and Technology, 2, 99-100.

DAVID, O. F. 2011. *Sustainable Durable Architectural Ecocem Green Cement, Presentation*. ECOCEM, 1-30.

DAWOOD, H. M. M. M. 2010. *Seismic Behavior Design of Segmental Precast Post-tensioned*. Master of Science in Civil Engineering (Master's), Washington State University**,** Washington, United States, 1-138.

DE LARRARD, F. & SEDRAN, T. 1994. *Optimization of Ultra-High-Performance Concrete by the Use of a Packing Model*. Cement and Concrete Research, 24**,** 6, 997-1009.

DEATON, J. B. 2005. *A Finite Element Approach to Reinforced Concrete Slab Design*. Degree Master of Science (Master's), Georgia Institute of Technology**,** Georgia, United States, 1-170.

DEUTSCHER AUSSCHUSS FUR STAHLBETON/ GERMAN ASSOCIATION FOR REINFORCED CONCRETE (DAFSTB). 2003. *A state of Art Report on Ultra High Performance Concrete UHPC*. Germany, DAfStb**,** 1-60.

DONATELLO, S., TYRER, M. & CHEESEMAN, C. R. 2009. *Recent Developments in Macro-Defect-Free (MDF) Cements*. Construction and Building Materials, 23**,** 5, 1761-1767.

DØSSLAND, Å. L. 2008. *Fibre Reinforcement in Load Carrying Concrete Structures*. Doctor of Philosophy (PhD), The Norwegian Inst. of Technology**,** Trondheim, Norway, 1-288.

DRABIK, M., MOJUMDAR, S. C. & SLADE, R. 2002. *Prospects of Novel Macro-Defect-Free Cements for the New Millennium*. Ceramics-Silikaty, 46**,** 2, 68-73.

DUGAT, J., ROUX, N. & BERNIER, G. 1996. *Mechanical Properties of Reactive Powder Concretes*. Materials and Structures, 29**,** 4, 233-240.

DUPONT, D. 2003. *Modelling and Experimental Validation of the Constitutive Law (s-e) and Cracking Behaviour of Steel Fibre Reinforced Concrete*. Doctor of Philosophy (PhD), University of Leuvan**,** Leuvan, Belgium, 1-256.

ELLOBODY, E. & BAILEY, C. G. 2008. *Behaviour of Unbonded Post-Tensioned One-way Concrete Slabs*. Advances in Structural Engineering, 11**,** 1, 107-120.

ELLOBODY, E., YOUNG, B. & LAM, D. 2006. *Behaviour of Normal and High Strength Concrete-Filled Compact Steel Tube Circular Stub Columns*. Journal of Constructional Steel Research, 62**,** 7, 706-715.

FAIRBAIRN, E. M. R., TOLEDO FILHO, R. D., BATTISTA, R. C., ROSA, J. I., FORMAGINI, S. & BRANDÃO, J. H. 2006a. *Experimental and Numerical Analysis of UHPFRC Plates and Shells.* In: KONSTA-GDOUTOS, M. (ed.) Measuring, Monitoring and Modeling Concrete Properties. Springer Netherlands**,** 49-58.

FAIRBAIRN, E. M. R., TOLEDO FILHO, R. D., FORMAGINI, S., ROSA, J. I., BATTISTA, R. C., FISCHER, G. & LI, V. C. 2006b. *Experimental Analysis and Modeling of Ultra High Performance Fiber Reinforced Concrete Plates*. International RILEM Workshop on High Performance Fiber Reinforced Cementitious Composites in Structural Applications, RILEM Publications SARL, 295-302.

FARNAM, Y., MOOSAVI, M., SHEKARCHI, M., BABANAJAD, S. K. & BAGHERZADEH, A. 2010. *Behaviour of Slurry Infiltrated Fibre Concrete (SIFCON) Under Triaxial Compression*. Cement and Concrete Research, 40**,** 11, 1571-1581.

FERRARA, L. & MEDA, A. 2006. *Relationships between fibre distribution, workability and the mechanical properties of SFRC applied to precast roof elements*. Materials and Structures, 39**,** 4, 411-420.

FORTH, J. P., MU, R., SCOTT, R. H., JONES, A. E. & BEEBY, A. W. 2014. *Verification of cracked section shrinkage curvature models*. Proceedings of the Institution of Civil Engineers-Structures and Buildings, 167**,** 5, 274-284.

FUJIKAKE, K. 2014. *Impact performance of ultra-high performance fiber reinforced concrete beam and its analytical evaluation*. International Journal of Protective Structures, 5**,** 2, 167-186.

FURLAN, S. & DE HANAI, J. B. 1997. *Shear behaviour of fiber reinforced concrete beams*. Cement and Concrete Composites, 19**,** 4, 359-366.

GHALIB, M. A. 1980. *Moment Capacity of Steel Fiber Reinforced Small Concrete Slabs*. ACI Journal Proceedings, 77**,** 4, 247-257.

GOPALARATNAM, V. & SHAH, S. 1986. *Properties of Steel Fiber Reinforced Concrete Subjected to Impact Loading*. ACI Journal Proceedings, 83**,** 1, 117-126.

GOWRIPALAN, N. & GILBERT, R. I. 2000. *Design Guidelines for Ductal-Prestressed Concrete Beams*. The University of New South Wales, Sydney, Australia**,** 1-54.

GRAYBEAL, B. A. 2006. *Material Property Characterization of Ultra-High Performance Concrete*. Georgetown Pike,, 1-188.

GRAYBEAL, B. A. & HARTMANN, J. L. 2003. *Strength and Durability of Ultra-High Performance Concrete*. Concrete Bridge Conference, Portland Cement Association, Skokie, Illinois, USA, 1-20.

GRÜNEWALD, S. 2004. *Performance-based design of self-compacting fibre reinforced concrete*. PhD Thesis, TU Delft, Delft University of Technology**,** 1-233.

HABEL, K. 2004. *Structural Behaviour of Elements Combining Ultra-High Performance Fibre Reinforced Concretes (UHPFRC) and Reinforced Concrete*. Doctor of Philosophy (PhD), École Polytechnique Fédérale de Lausanne**,** Lausanne, Switzerland, 1-222.

HABEL, K., VIVIANI, M., DENARIÉ, E. & BRÜHWILER, E. 2006. *Development of the Mechanical Properties of an Ultra-High Performance Fiber Reinforced Concrete (UHPFRC)*. Cement and Concrete Research, 36**,** 7, 1362-1370.

HACKMAN, L. E., FARRELL, M. B. & DUNHAM, O. O. 1992. *Slurry Infiltrated Mat Concrete (SIMCON)*. Concrete International, 14, 12**,** 53-56.

HANNANT, P. J. 1978. *Fibre Cements and Fibre Concretes*, New York, John Wiley & Sons Ltd**,** 1-219.

HARRIS, D. K. 2004. *Characterization of Punching Shear Capacity of Thin UHPC Plates*. Master of Science (Master's), Virginia Polytechnic Institute and State University**,** Virginia, United States, 1-146.

HASSAN, A. M. 2013. *Ultra High Performance Fibre Reinforced Concrete for Highway Bridge Applications*. Doctor of Philosophy (PhD), University of Liverpool**,** Liverpool, United Kingdom, 1-288.

HASSAN, A. M. T. & JONES, S. W. 2012. *Non-Destructive Testing of Ultra High Performance Fibre Reinforced Concrete (UHPFRC): A Feasibility Study for Using Ultrasonic and Resonant Frequency Testing Techniques*. Construction and Building Materials, 35**,** 0, 361-367.

HASSAN, A. M. T., JONES, S. W. & MAHMUD, G. H. 2012. *Experimental Test Methods to Determine the Uniaxial Tensile and Compressive Behaviour of Ultra High Performance Fibre Reinforced Concrete (UHPFRC)*. Construction and Building Materials, 37, 874-882.

HERBERT, E. N. & LI, V. C. 2013. *Self-Healing of Microcracks in Engineered Cementitious Composites (ECC) Under a Natural Environment*. Materials, 6**,** 7, 2831-2845.

HERTZ, K. 1984. *Heat-induced Explosion of Dense Concretes*. Danmarks Tekniske Højskole**,** 1-20.

HENTZ, S., DAUDEVILLE, L & DONZE, F. V. 2009. *Discrete element modeling of a reinforced concrete structure***.** J. Mech. Behav. Mater., 19, 4, 249–258

HIGGINS, D. 2005. *Soil Stabilisation with Ground Granulated Blast Furnace Slag*. UK, Cementitious Slag Makers Association (CSMA)**,** 1-15.

HILLERBORG, A., MODÉER, M. & PETERSSON, P. E. 1976. *Analysis of Crack Formation and Crack Growth in Concrete by Means of Fracture Mechanics and Finite Elements*. Cement and Concrete Research, 6**,** 6, 773-781.

HOGNESTAD, E. 1953. *Yield-Line Theory for the Ultimate Flexural Strength of Reinforced Concrete Slabs*. ACI Journal Proceedings, 49**,** 3, 637-656.

HONG, K. N., KANG, S. T., KIM, S. W., PARK, J. J. & HAN, S. H. 2010. *Material Properties of Air-Cured Ultra-High-Performance Steel-Fiber-Reinforced Concrete at Early Ages*. International Journal of the Physical Sciences, 5**,** 17, 2622-2634.

HORII, H., HASEGAWA, A. & NISHINO, F. 1989. *Fracture Process and Bridging Zone Model and Influencing Factors in Fracture of Concrete.* In: SHAH, S. & SWARTZ, S. (eds.) Fracture of Concrete and Rock. Springer New York**,** 205-219.

INGERSLEV, A. 1921. *Om en Elementar Beregningsmetode af Krydsarmerede Plader (on a Simple Analysis of Two-Way Slab).* Ingeniøren, 507-515.

INGERSLEV, Å. 1923. *The Strength of Rectangular Slabs*. Journal of the Institution of Civil Engineers, 1**,** 1, 3-14.

ISLAM, M. M., CHOWDHURY, M. A., AMIN, S., MITU, S. M., BALA, M., ISLAM, Z., RAHMAN, M. S., SALEKIN, M. S., HOSSAIN, M. S., ISLAM, M. R. & SIDDIGUE, A. 2014. *Finite Element modeling and analysis of RC beams made of steel fiber reinforced concrete (SFRC): Critical investigation of the flexural and shear capacity enhancements*. Proceedings of the 2nd International Conference on Civil Engineering for Sustainable Development, 916-922.

JANG, S.-J., KANG, D.-H., AHN, K.-L., PARK, W.-S., KIM, S.-W. & YUN, H.-D. 2015. *Feasibility of Using High-Performance Steel Fibre Reinforced Concrete for Simplifying Reinforcement Details of Critical Members*. International Journal of Polymer Science, 1-13.

JAPAN SOCIATY OF CIVIL ENGINEERS(JSCE). 2008. *Recommendation for Design and Construction of High Performance Fiber Reinforced Cement Composites with Multiple Fine Cracks (HPFRCC).* JSCE**,** 1-113.

JI, W. Y., AN, M. Z., YAN, G. P. & WANG, J. M. 2004. *Study on Reactive Powder Concrete Used in the Sidewalk System of the Qinghai-Tibet Railway Bridge*. International Workshop on Sustainable Development and Concrete Technology, Beijing, China, 333-338.

JOHANSEN, K. W. 1932. *Beregning af Krydsarmerede Jernbetonpladers Brudmoment*. Bygningsstatiske Meddelelser, 3**,** 1, 1-18.

JOHANSEN, K. W. 1943. *Brudlinieteorier,* I kommission hos J. Gjellerup**,** 1-189.

JOHANSEN, K. W. 1962. *Yield-Line Theory*, Cement and Concrete Association**,** 1-181.

JOHANSEN, K. W. 1972. *Yield-Line Formulae for Slabs*, Cement and Concrete Association London**,** 1-106.

JOHARI, M. A. M., ALTWAIR, N. M. & HASHIM, S. F. S. 2013. *Fracture and Tensile Characteristics of Engineered Cementitious Composites Containing POFA.* Advances in Cement Research, 25**,** 4, 189-199.

JONES, L. L. & WOOD, R. H. 1967. *Yield-Line Analysis of Slabs*, London, Thames & Hudson Ltd/Chatoo &Windus**,** 1-405.

KAMEN, A., DENARIE, E. & BRUHWILER, E. 2007. *Thermal Effects on Physico-Mechanical Properties of Ultra-High-Performance Fiber-Reinforced Concrete*. ACI Materials Journal, 104**,** 4, 415-423.

KAMESWARA RAO, C. V. S. 1979. *Effectiveness of Random Fibres in Composites*. Cement and Concrete Research, 9**,** 6, 685-693.

KANG, S.-T. & KIM, J.-K. 2011. *The Relation Between Fiber Orientation and Tensile Behavior in an Ultra High Performance Fiber Reinforced Cementitious Composites (UHPFRCC)*. Cement and Concrete Research, 41**,** 10, 1001-1014.

KANG, S.-T., LEE, Y., PARK, Y.-D. & KIM, J.-K. 2010. *Tensile Fracture Properties of an Ultra High Performance Fiber Reinforced Concrete (UHPFRC) with Steel Fiber*. Composite Structures, 92**,** 1, 61-71.

KANG, S. T., LEE, B. Y., KIM, J. K. & KIM, Y. Y. 2011. *The effect of fibre distribution characteristics on the flexural strength of steel fibre-reinforced ultra high strength concrete*. Construction and Building Materials, 25**,** 5, 2450-2457.

KARIHALOO, B. 1999. *Size Effect in Shallow and Deep Notched Quasi-Brittle Structures.* Fracture Scaling. Springer**,** 379-390.

KARIHALOO, B., ALAEE, F. & BENSON, S. 2002. *A New Technique for Retrofitting Damaged Concrete Structures*. Proceedings of the ICE-Structures and Buildings, 152, 309-318.

KARIHALOO, B. L. & WANG, J. 2000. *Mechanics of Fibre-Reinforced Cementitious Composites*. Computers & Structures, 76**,** 1–3, 19-34.

KARIHALOO, B. L., WANG, J. & GRZYBOWSKI, M. 1996. *Doubly Periodic Arrays of Bridged Cracks and Short Fibre-Reinforced Cementitious Composites*. Journal of the Mechanics and Physics of Solids, 44**,** 10, 1565-1586.

KEENAN, W. 1969. *Strength and behavior of restrained reinforced concrete slabs under static and dynamic loadings*. DTIC Document**,** 1-152.

KENDALL, K., HOWARD, A., BIRCHALL, J., PRATT, P., PROCTOR, B. & JEFFERIS, S. 1983. *The Relation Between Porosity, Microstructure and Strength, and the Approach to Advanced Cement-Based Materials [and Discussion]*. Philosophical Transactions of the Royal Society of London. Series A, Mathematical and Physical Sciences, 310**,** 1511, 139-153.

KHALOO, A. R. & AFSHARI, M. 2005. *Flexural Behaviour of Small Steel Fibre Reinforced Concrete Slabs*. Cement and Concrete Composites, 27**,** 1, 141-149.

KIM, J.-K. & YI, S.-T. 2002. *Application of Size Effect to Compressive Strength of Concrete Members*. Sadhana, 27**,** 4, 467-484.

KIM, S. W., KANG, S. T., PARK, J. J. & RYU, G. S. 2008. *Effect of filling method on fibre orientation and dispersion and mechanical properties of UHPC*. Proceedings of Second International Symposium on Ultra High Performance Concrete, Kassel, Germany (Kassel University Press), 185-192.

KNAPTON, J. 2003. *Ground Bearing Concrete Slabs,* Thomas Telford**,** 1-293.

KOOIMAN, A. G. 2000. *Modelling steel fibre reinforced concrete for structural design*. Ph.D. Thesis, Delft University of Technology, Rotterdam**,** 1-184.

KOSMATKA, S. H., PANARESE, W. C. & PORTLAND CEMENT, A. 2002. *Design and Control of Concrete Mixtures.* Portland Cement Association Skokie**,** 149-177.

KOTSOVOS, M. 1986. *Shear failure of reinforced concrete beams*. Engineering Structures, 9**,** 1, 32-38.

KRSTULOVIC-OPARA, N., DOGAN, E., UANG, C.-M. & HAGHAYEGHI, A. R. 1997. *Flexural Behavior of Composite RC-Slurry Infiltrated Mat Concrete (SIMCON) Members*. ACI Structural Journal, 94**,** 5, 502-511.

KRSTULOVIC-OPARA, N. & MALAK, S. 1997a. *Micromechanical Tensile Behavior of Slurry Infiltrated Continuous-Fiber-Mat Reinforced Concrete (SIMCON).* ACI Materials Journal, 94**,** 5, 373-384.

KRSTULOVIC-OPARA, N. & MALAK, S. 1997b. *Tensile Behavior of Slurry Infiltrated Mat Concrete (SIMCON).* ACI Materials Journal, 94**,** 1, 39-46.

LABIB, W. & EDEN, N. 2006. *An Investigation Into the Use of Fibres in Concrete Industrial Ground-Floor Slabs*. Liverpool John Moores University, Liverpool, 1-13.

LANKARD, D. R. 1984. *Properties, Applications: Slurry Infiltrated Fiber Concrete (SIFCON)*. Concrete International, 6, 44-47.

LANKARD, D. R. & NEWELL, J. K. 1984. *Preparation of Highly Reinforced Steel Fiber Reinforced Concrete Composites*. ACI Special Publication, 81, 287-306.

LAPPA, E., BRAAM, C. & WALRAVEN, J. 2006. *Bending Performance of High Strength Steel Fibre Reinforced Concrete.* Measuring, Monitoring and Modeling Concrete Properties. Springer**,** 133-138.

LATASTE, J.-F., BARNETT, S. J., PARRY, T. & SOUTSOS, M. N. 2009. *Determination of fibres orientation in UHPFRC and evaluation of their effect on mechanical properties*. Non Destructive Testing in Civil Engineering, Nantes, France, 1-8.

LE, T. T. 2008. *Ultra High Performance Fibre Reinforced Concrete Paving Flags*. Doctor of Philosophy (PhD), The University of Liverpool**,** Liverpool, United Kingdom, 1-366.

LEI, Y., NEMATOLLAHI, B., MOHAMED SAID, A. B., GOPAL, B. A. & YEE, T. S. 2012. *Application of Ultra High Performance Fiber Reinforced Concrete–The Malaysia Perspective*. International Journal of Sustainable Construction Engineering and Technology, 3**,** 1, 26-44.

LEPECH, M. & LI, V. C. 2003. *Preliminary Findings on Size Effect in ECC Structural Members in Flexure*. Proceedings of the Seventh International Symposium on Brittle Matrix Composites, Warsaw, Poland, 57-66.

LEPECH, M. & LI, V. C. 2004. *Size Effect in ECC Structural Members in Flexure*. Proceedings of FRAMCOS-5, Vail, Colorado, USA, 1059-1066.

LEPECH, M. D. & LI, V. C. 2008. *Large-Scale Processing of Engineered Cementitious Composites*. ACI Materials Journal, 105**,** 4, 358-366.

LEWIS, J. 1993. *Microstructure-Property Relationships in Macro-Defect-Free Cement*. MRS Bulletin, 18**,** 3, 72-77.

LI, J. & YAO, Y. 2001. *A Study on Creep and Drying Shrinkage of High Performance Concrete*. Cement and Concrete Research, 31**,** 8, 1203-1206.

LI, S., CHEN, J., BISBY, L., HU, Y. & TENG, J. 2012. *Strain Efficiency of FRP Jackets in FRP-Confined Concrete-Filled Circular Steel Tubes*. International Journal of Structural Stability and Dynamics, 12**,** 01, 75-94.

LI, V. C. 1993. *From Micromechanics to Structural Engineering -the Design of Cementitious Composites for Civil Engineering Applications*. JSCE Journal of Structural Mechanics and Earthquake Engineering, 10**,** 2, 37-48.

LI, V. C. 2003. *On Engineered Cementitious Composites (ECC)*. Journal of Advanced Concrete Technology, 1**,** 3, 215-230.

LI, V. C. & KANDA, T. 1998. *INNOVATIONS FORUM: Engineered Cementitious Composites for Structural Applications*. Journal of Materials in Civil Engineering, 10**,** 2, 66-69.

LI, V. C., LEPECH, M., FISCHER, G. & LI, V. 2006. *General Design Assumptions for Engineered Cementitious Composites (ECC)*. International RILEM Workshop on High Performance Fiber Reinforced Cementitious Composites in Structural Applications, RILEM Publications SARL, 269-277.

LI, V. C., LIN, Z. & MATSUMOTO, T. 1998. *Influence of Fiber Bridging on Structural Size-Effect*. International Journal of Solids and Structures, 35**,** 31-32, 4223-4238.

LI, V. C., WANG, Y. & BACKER, S. 1991. *A Micromechanical Model of Tension-Softening and Bridging Toughening of Short Random Fiber Reinforced Brittle Matrix Composites*. Journal of the Mechanics and Physics of Solids, 39**,** 5, 607-625.

LI, V. C., WARD, R. & HMAZA, A. M. 1992. *Steel and synthetic fibers as shear reinforcement*. ACI Materials Journal, 89**,** 5, 499-508.

LILLIU, G. & VAN MIER J.G.M. (2003). *3d lattice type fracture model for concrete*. Engineering Fracture Mechanics, 70, 927-941.

LIU, J., DRIVER, R. G. & LUBELL, A. S. 2008. *Rehabilitation and Repair of Reinforced Concrete Short Columns with External Steel Collars*. University of Alberta. Department of Civil and Environmental Engineering**,** 1-303.

LUBLINER, J., OLIVER, J., OLLER, S. & OÑATE, E. 1989. *A Plastic-Damage Model for Concrete*. International Journal of Solids and Structures, 25**,** 3, 299-326.

LUTHER, M. D. 1990. *High-Performance Silica Fume (Microsilica)-Modified Cementitious Repair Materials*. Transportation Research Record**,** 1284

MAGUREANU, C., SOSA, I., NEGRUTIU, C. & HEGHES, B. 2010. *Bending and shear behavior of ultra-high performance fiber reinforced concrete*. High Performance Structures and Materials, 112, 79-89.

MAGUREANU, C., SOSA, I., NEGRUTIU, C. & HEGHES, B. 2012. *Mechanical Properties and Durability of Ultra High Performance Concrete*. ACI Materials Journal, 109**,** 2, 177.

MALHOTRA, V. M. 1989. *Optimization of Superplasticizer Type and Dosage in Fly Ash and Silica Fume Concrete*. Proceedings Third International Conference on Superplasticizers and Other Chemical Admixtures in Concrete: , American Concrete Institute, Ottawa, Canada, 425-443.

MALHOTRA, V. M. & CARETTE, G. G. 1982. *Silica Fume*. Concrete Construction, 27**,** 5, 443-446.

MALLAT, A. & ALLICHE, A. 2011. *A Modified Tensile Test to Study the Behaviour of Cementitious Materials*. Strain-An International Journal for Experimental Mechanics, 47**,** 6, 499-504.

MARKOVIĆ, I. 2006. *High-Performance Hybrid-Fibre Concrete: Development and Utilisation*. Doctor of Philosophy (PhD), Delft University Press**,** The Netherlands, 228.

MARTI, P., PFYL, T., SIGRIST, V. & ULAGA, T. 1999. *Harmonized Test Procedures for Steel Fiber-Reinforced Concrete*. ACI Materials Journal, 96**,** 6, 676-686.

MEDA, A. & PLIZZARI, G. A. 2004. *New Design Approach for Steel Fiber-Reinforced Concrete Slabs-on-Ground Based on Fracture Mechanics*. ACI Structural Journal, 101**,** 3, 298-303.

MEGSON, T. H. G. 2005. *Chapter 19-Yield Line Analysis of Slabs.* Structural and Stress Analysis (2). Oxford: Butterworth-Heinemann**,** 625-639.

MEHTA, P. K. & AITCIN, P. C. 1990. *Microstructural Basis of Selection of Materials and Mix Proportions for High Strength Concrete*. Proceedings of the 2th International Symposium on High Strength Concrete, 265-286.

MIELENZ, R. 1984. *History of Chemical Admixtures for Concrete*. Concrete International, 6**,** 4, 40-53.

MOBASHER, B., STANG, H. & SHAH, S. P. 1990. *Microcracking in Fiber Reinforced Concrete*. Cement and Concrete Research, 20**,** 5, 665-676.

MOSLEY, W. H., BUNGEY, J. H. & HULSE, R. 2012. *Reinforced Concrete Design to Eurocode 2*, Palgrave MacMillan**,** 1-448.

MURAKAMI, H. & ZENG, J. Y. 1998. *Experimental and Analytical Study of SIMCON Tension Members*. Mechanics of Materials, 28**,** 1–4, 181-195.

NAAMAN, A. 1992. *SIFCON: Tailored Properties for Structural Performance*. High Performance Fiber Reinforced Cement Composites, E & FN Spon, 18-38.

NAAMAN, A. 1999. *Fibers with Slip-Hardening Bond*. Proceeding of the Third International RILEM Workshop on High Performance Fiber Reinforced Cement Composites (HPFRCC 3), RILEM Publications, Mainz, 3, 371-386.

NAAMAN, A. E., MOAVENZADEH, F. & MCGARRY, F. J. 1974. *Probabilistic Analysis of Fiber-Reinforced Concrete*. Journal of the Engineering Mechanics Division, 100**,** 2, 397-413.

NAMMUR JR, G. & NAAMAN, A. E. 1989. *Bond Stress Model for Fiber Reinforced Concrete Based on Bond Stress-Slip Relationship*. ACI Materials Journal, 86**,** 1

NEVILLE, A. M. 2011. *Properties of Concrete. 5th ed*, Harlow, UK : Prentice Hall/Pearson Education**,** 1-872.

NEWMAN, J. B. & CHOO, B. S. 2003. *Advanced Concrete Technology (Concrete Properties)*, Butterworth-Heinemann**,** 1-350.

NEZHENTSEVA, A., SØRENSEN, E. V., ANDERSEN, L. V. & SCHULER, F. 2013. *Distribution and Orientation of Steel Fibres in UHPFRC*. Department of Civil Engineering, Aalborg University**,** 1-44.

NICOLAIDES, D. 2005. *Fracture and Fatigue of CARDIFRC*. Doctor of Philosophy (PhD), Cardiff University**,** Cardiff, United Kingdom, 3-16.

NIELSEN, M. P. 1964. *Limit Analysis of Reinforced Concrete Slabs*. University of Copenhagen**,** Copenhagen, Denmark., 1-166.

NWANKWO, E., SOLEIMAN FALLAH, A. & LOUCA, L. A. 2013. *An Investigation of Interfacial Stresses in Adhesively-Bonded Single Lap Joints Subject to Transverse Pulse Loading*. Journal of Sound and Vibration, 332**,** 7, 1843-1858.

ODLER, I. 2005. *Special Inorganic Cements*, Taylor & Francis**,** 1-314.

ONER, A. & AKYUZ, S. 2007. *An Experimental Study on Optimum Usage of GGBS for the Compressive Strength of Concrete*. Cement and Concrete Composites, 29**,** 6, 505-514.

OOI, E. & YANG, Z. 2010. *Efficient Prediction of Deterministic Size Effects Using the Scaled Boundary Finite Element Method*. Engineering Fracture Mechanics, 77**,** 6, 985-1000.

ORTIZ, M. 1988. *Microcrack Coalescence and Macroscopic Crack Growth Initiation in Brittle Solids*. International Journal of Solids and Structures, 24**,** 3, 231-250.

OSBORNE, G. J. 1999. *Durability of Portland blast-Furnace Slag Cement Concrete*. Cement and Concrete Composites, 21**,** 1, 11-21.

PANSUK, W., SATO, H., SATO, Y. & SHIONAGA, R. 2008. *Tensile behaviors and fiber orientation of UHPC*. Proceedings of second international symposium on ultra high performance concrete, Kassel, Germany, 161-168.

PARK, R. & GAMBLE, W. L. 2000. *Reinforced Concrete Slabs*, John Wiley & Sons Ltd**,** 339-346.

PERRY, V. H. 2003. *A Revolutionary New Material for New Solutions, Technical Forum Presentation, Lafarge North America.* Overview of UHPC Technology, Materials, Properties, Markets and Manufacturing, Lafarge North America. , 1-38.

PETERSSON, Ö. 1998. *Preliminary Mix Design-Final Report of Task 1, Brite Euram project (BE 96-3801)-Rational production and improved working environment through using SCC, Document RT1_v2. doc*. 1-41.

PLUMB, R. C. 1989. *Antique windowpanes and the flow of supercooled liquids*. J. Chem. Educ. 66, 12, 994-996.

POON, C. 1998. *The Influence of Admixtures on the Microstructure and Water Stability of Macro-Defect Free Cement*. Journal of Materials Science Letters, 17**,** 18, 1593-1595.

POPOOLA, O. O., KRIVEN, W. M. & YOUNG, J. F. 1991. *Microstructural and Microchemical Characterization of a Calcium Aluminate-Polymer Composite (MDF Cement)*. Journal of the American Ceramic Society, 74**,** 8, 1928-1933.

PRAGER, W. & HODGE, P. G. 1951. *Theory of Perfectly Plastic Solids*, John Wiley & Sons Ltd**,** 1-264.

PUERTAS, F., SANTOS, H., PALACIOS, M. & MARTÍNEZ-RAMÍREZ, S. 2005. *Polycarboxylate Superplasticiser Admixtures: Effect on Hydration, Microstructure and Rheological Behaviour in Cement Pastes*. Advances in Cement Research, 77-89.

RACKY, P. 2004. *Cost-effectiveness and sustainability of UHPC*. Proceeding from International Symposium on Ultra High Performance Concrete (UHPC), Kassel, 797-806.

RAO, H. S., GHORPADE, V. G., RAMANA, N. V. & GNANESWAR, K. 2010. *Response of SIFCON Two-Way Slabs Under Impact Loading*. International Journal of Impact Engineering, 37**,** 4, 452-458.

RESPLENDINO, J. & PETITJEAN, J. 2003. *Ultra-High-Performance Concrete: First Recommendations and Examples of Application*. 2003 International Symposium on High performance Concrete, Kassel, Germany, 1-18.

RICHARD, P. & CHEYREZY, M. 1995. *Composition of Reactive Powder Concretes*. Cement and Concrete Research, 25**,** 7, 1501-1511.

RICHARD, P. & CHEYREZY, M. H. 1994. *Reactive Powder Concretes with High Ductility and 200-800 MPa Compressive Strength*. ACI Special Publications, 144, 507-518.

ROBERTS, T. M. & HO, N. L. 1982. *Shear failure of deep fibre reinforced concrete beams*. International Journal of Cement Composites and Lightweight Concrete, 4**,** 3, 145-152.

ROESLER, J. R., LANGE, D. A., ALTOUBAT, S. A., RIEDER, K.-A. & ULREICH, G. R. 2004. *Fracture of Plain and Fiber-Reinforced Concrete Slabs Under Monotonic Loading*. Journal of Materials in Civil Engineering, 16**,** 5, 452-460.

ROSSI, P., ACKER, P. & MALIER, Y. 1987. *Effect of Steel fibres at Two Different Stages: the Material and the Structure*. Materials and Structures, 20**,** 6, 436-439.

ROSSI, P., ARCA, A., PARANT, E. & FAKHRI, P. 2005. *Bending and Compressive Behaviours of a New Cement Composite*. Cement and Concrete Research, 35**,** 1, 27-33.

ROUMALDI, J. P. & BATSON, G. B. 1963. *Mechanics of Crack Arrest in Concrete*. Engineering Mechanics Division,, 89**,** 3, 147-168.

SAKAI, E., AKINORI, N., DAIMON, M., AIZAWA, K. & KATO, H. 2008. *Influence of Superplasticizer on the Fluidity of Cements with Different Amount of Aluminate Phase*. Second International Symposium on Ultra High Performance Concrete, 85-92.

SANDHU, G. S. 1970. *The Yield Line Analysis of Concrete Slabs*, Manhattan, Kansas, Kansas State University**,** 1-114.

SANTOS, R. S., RODRIGUES, F. A., SEGRE, N. & JOEKES, I. 1999. *Macro-Defect Free Cements Influence of Poly(vinyl alcohol), Cement Type, and Silica Fume*. Cement and Concrete Research, 29**,** 5, 747-751.

SAS, G., BLANKSVÄRD, T., ENOCHSSON, O., LIC, T., TÄLJSTEN, B., PUURULA, A. & ELFGREN, L. 2011. *Flexural-Shear Failure of a Full Scale Tested RC bridge Strengthened with NSM CFRP. Shear capacity analysis*. Journal of Structural Engineering, 189-206.

SCHACHINGER, I., HILBIG, H. & STENGEL, T. 2008. *Effect of Curing Temperature at an Early Age on the Long-Term Strength Development of UHPC*. Proceedings of the Second International Symposium on UHPC, 205-212.

SCHLEYER, G., BARNETT, S., MILLARD, S., WIGHT, G. & REBENTROST, M. 2011. *UHPFRC Panel Testing*. Structural Engineer, 89**,** 23-24, 34-40.

SEBAIBI, N., BENZERZOUR, M. & ABRIAK, N. E. 2014. *Influence of the Distribution and Orientation of Fibres in a Reinforced Concrete with Waste Fibres and Powders*. Construction and Building Materials, 65**,** 0, 254-263.

SHAH, S. & YOUNG, J. 1990. *Current Research at the NSF Science and Technology Center for Advanced Cement-Based Materials*. American Ceramic Society Bulletin, 69**,** 8, 1319-1331.

SHANNAG, M. J. & HANSEN, W. 2000. *Tensile Properties of Fibre-Reinforced Very High Strength DSP Mortar*. Magazine of Concrete Research, 52, 2**,** 101-108.

SIDDIQUE, R. & KHAN, M. I. 2011. *Silica Fume.* Supplementary Cementing Materials. Springer**,** 67-119.

SKALNY, J., MARCHAND, J. & ODLER, I. 2002. *Sulfate Attack on Concrete*, London and New York, Taylor and Francis**,** 1-217.

SOROUSHIAN, P. & LEE, C.-D. 1990. *Distribution and Orientation of Fibers in Steel Fiber Reinforced Concrete*. ACI Materials Journal, 87**,** 5, 433-439.

SOUTSOS, M. N., MILLARD, S. G., KARAISKOS, K., FISCHER, G. & LI, V. 2006. *Mix Design, Mechanical Properties, and Impact Resistance of Reactive Powder Concrete (RPC)*. International RILEM Workshop on High Performance Fiber Reinforced Cementitious Composites in Structural Applications, RILEM Publications SARL, 549-560.

SPASOJEVIC, A. 2008. *Structural Implications of Ultra-High Performance Fibre-Reinforced Concrete in Bridge Design*. Doctor of Philosophy (PhD), École Polytechnique Fédérale de Lausanne**,** Lausanne, Switzerland, 1-203.

SPASOJEVIC, A., REDAELLI, D., RUIZ, M. F. & MUTTONI, A. 2008. *Influence of Tensile Properties of UHPFRC on Size Effect in Bending*. Ultra High Performance Concrete (UHPC), Second International Symposium on Ultra High Performance Concrete, Kassel, Germany, 303-310.

SPIRATOS, N., MAILVAGANAM, N. P., MALHOTRA, V. M. & JOLICOEUR, C. 2003. *Superplasticizers for Concrete: Fundamentals, Technology, and Practice*, Supplementary Cementing Materials for Sustainable Development, Incorporated**,** 1-322.

SRAVANA, P., SRINIVASA, R. P. & SESHADRI, S. T. 2010. *Flexural behaviour of glass fibre reinforced self compacting concrete slabs*. 35th Conference on Our World in Concrete & Structures, CI-Premier PTE LTD, Singapore, 1-9.

STÄHLI, P., CUSTER, R. & VAN MIER, J. G. 2008. *On flow properties, fibre distribution, fibre orientation and flexural behaviour of FRC*. Materials and Structures, 41**,** 1, 189-196.

SU, X. T., YANG, X., Z. J & LIU, G. H. 2011. *A Discrete Cohesive Crack Model for Fibre Reinforced Concrete with Randomly Oriented Fibres*. The 3rd International Symposium on Computational Mechanics (ISCM III) and the 2nd Symposium on Computational Structural Engineering (CSE II), Taipei, 1-2.

SWADDIWUDHIPONG, S. & SEOW, P. E. C. 2006. *Modelling of Steel Fiber-Reinforced Concrete Under Multi-Axial Loads*. Cement and Concrete Research, 36**,** 7, 1354-1361.

TER MATEN, R. 2011. *Ultra High Performance Concrete in Large Span Shell Structures*. Master Thesis, Delft University of Technology**,** Delft, Netherlands, 1-310.

TONG, P. & BATCHELOR, B. D. V. 1971. *Compressive membrane enhancement in two-way bridge slabs*. ACI Special Publication, 30**,** 12, 271-286.

TOUTLEMONDE, F. & RESPLENDINO, J. 2011. *Designing and Building with UHPFRC: State of the Art and Development*, London, ISTE Ltd**,** 1-814.

U.S DEPARMENT TRANSPORTATION/THE FEDERAL HIGHWAY ADMINISTRATION (FHWA). 2006. *Material Property Characterization of Ultra-High Performance Concrete*. Georgetown Pike, FHWA**,** 1-188.

VAN MIER, J. G. M. 1992. *Scaling in Tensile and Compressive Fracture of Concrete*. Elsevier Applied Science, London/New York**,** 91-135.

VONK, R. A. 1992. *Softening of Concrete Loaded in Compression*. Doctor of Philosophy (PhD), Technische Universiteit Eindhoven**,** Eindhoven, Netherlands, 1-234.

WALRAVEN, J. C. 2009. *High Performance Fiber Reinforced Concrete: Progress in Knowledge and Design Codes*. Materials and Structures, 42**,** 9, 1247-1260.

WANG J. 1994. *Development and application of a micro-mechanics based numerical approach for the study of crack propagation in concrete*. PhD thesis, Swiss Federal Institute of Technology,

WANG, S. & LI, V. C. 2005. *Polyvinyl Alcohol Fiber Reinforced Engineered Cementitious Composites: Material Design and Performances*. International Workshop on HPFRCC Structural Applications, University of Hawaii and University of Michigan, USA, 1-8.

WEIBULL, W. 1939. *Statistical Theory of Strength of Material*. Royal Swedish Academy of Engineering, 1-45.

WEIBULL, W. 1951. *A Statistical Distribution Function of Wide Applicability*. Journal of applied mechanics, 18**,** 3, 293-297.

WILLE, K. & NAAMAN, A. E. 2012. *Pullout Behavior of High-Strength Steel Fibers Embedded in Ultra-High-Performance Concrete*. ACI Materials Journal, 109**,** 4, 1-10.

WILLE, K., NAAMAN, A. E. & EL-TAWIL, S. 2011a. *Optimizing Ultra-High-Performance Fiber-Reinforced Concrete*. Concrete International, 33**,** 9, 35-41.

WILLE, K., NAAMAN, A. E. & PARRA-MONTESINOS, G. J. 2011b. *Ultra-High Performance Concrete with Compressive Strength Exceeding 150 MPa (22 ksi): A Simpler Way*. ACI Materials Journal, 108**,** 1, 46-54.

WILLE, K. & PARRA-MONTESINOS, G. J. 2012. *Effect of Beam Size, Casting Method, and Support Conditions on Flexural Behavior of Ultra-High-Performance Fiber-Reinforced Concrete*. ACI Materials Journal, 109**,** 3, 379-388.

WILLE, K., TUE, N. V. & PARRA-MONTESINOS, G. J. 2014. *Fiber distribution and orientation in UHP-FRC beams and their effect on backward analysis*. Materials and Structures, 47**,** 11, 1825-1838.

YAN, A., WU, K. & ZHANG, X. 2002. *A Quantitative Study on the Surface Crack Pattern of Concrete with High Content of Steel Fiber*. Cement and Concrete Research, 32**,** 9, 1371-1375.

YANG, I. H., JOH, C. & KIM, B. S. 2011a. *Flexural Response Predictions for Ultra-High-Performance Fibre Reinforced Concrete Beams*. Magazine of Concrete Research, 63**,** 1, 1-15.

YANG, I. H., JOH, C. & KIM, B. S. 2011b. *Flexural strength of ultra high strength concrete beams reinforced with steel fibers*. Procedia Engineering, The Twelfth East Asia-Pacific Conference on Structural Engineering and Construction, 14, 793-796.

YANG, S. L., DIAO, B. & YE, Y. H. 2011c. *Influence of Fiber Geometry on the Mechanical Properties of Ultra-High Performance Fiber Reinforced Concrete (UHPFRC)*. Advanced Materials Research, 243, 510-513.

YANG, X. S., LEES, J. M. & MORLEY, C. T. 2005. *Nonlinear Finite Element Analysis of Structures Strengthened with Carbon Fibre Reinforced Polymer: A Comparison Study*. ICCS 2005: 5th International Conference, USA, 2005. Proceedings, Part I, 751-56

YU, Q. 2007. *Size Effect and Design Safety in Concrete Structure Under Shear*. Doctor of Philosophy (PhD), Northwestern University**,** Evanston, Illinois, United States, 1-479.

ZANNI, H., CHEYREZY, M., MARET, V., PHILIPPOT, S. & NIETO, P. 1996. *Investigation of Hydration and Pozzolanic Reaction in Reactive Powder Concrete (RPC) Using Si NMR*. Cement and Concrete Research, 26**,** 1, 93-100.

ZARAIS, P. D. 2003. *Shear Compression Failure in Reinforced Concrete Deep Beams*. Journal of Structural Engineering ASCE, 129**,** 4, 544-553.

ZENG, J., KLINGENBERG, P. & BAYASI, Z. 2000. *Slurry Infiltrated Mat Concrete (SIMCON) for Rehabilitation of Bridges and Pavements*. ACI Special Publication, 185, 55-68.

ZHANG, J. & LI, V. C. 2004. *Simulation of Crack Propagation in Fiber-Reinforced Concrete by Fracture Mechanics*. Cement and Concrete Research, 34**,** 2, 333-339.